Johan Meyers
Bernard Geurts
Pierre Sagaut
Editors

ERCOFTAC Series

Quality and Reliability of Large-Eddy Simulations

Springer

Quality and Reliability of Large-Eddy Simulations

ERCOFTAC SERIES

VOLUME 12

Series Editors

R.V.A. Oliemans, *Chairman ERCOFTAC,*
Delft University of Technology, Delft, The Netherlands

W. Rodi, *Deputy Chairman ERCOFTAC,*
Universität Karlsruhe, Karlsruhe, Germany

Aims and Scope of the Series

ERCOFTAC (European Research Community on Flow, Turbulence and Combustion) was founded as an international association with scientific objectives in 1988. ERCOFTAC strongly promotes joint efforts of European research institutes and industries that are active in the field of flow, turbulence and combustion, in order to enhance the exchange of technical and scientific information on fundamental and applied research and design. Each year, ERCOFTAC organizes several meetings in the form of workshops, conferences and summerschools, where ERCOFTAC members and other researchers meet and exchange information.

The ERCOFTAC Series will publish the proceedings of ERCOFTAC meetings, which cover all aspects of fluid mechanics. The series will comprise proceedings of conferences and workshops, and of textbooks presenting the material taught at summerschools.

The series covers the entire domain of fluid mechanics, which includes physical modelling, computational fluid dynamics including grid generation and turbulence modelling, measuring-techniques, flow visualization as applied to industrial flows, aerodynamics, combustion, geophysical and environmental flows, hydraulics, multi-phase flows, non-Newtonian flows, astrophysical flows, laminar, turbulent and transitional flows.

For other titles published in this series, go to
www.springer.com/series/5934

Quality and Reliability of Large-Eddy Simulations

Edited by

Johan Meyers
Katholieke Universiteit Leuven, Leuven, Belgium

Bernard J. Geurts
University of Twente, Enschede, The Netherlands

and

Pierre Sagaut
Université Pierre et Marie Curie — Paris 6, Paris, France

Springer

Editors
Johan Meyers
Katholieke Universiteit Leuven
Department of Mechanical Engineering
Celestijnenlaan 300A
3001 Leuven
Belgium

Bernard J. Geurts
University of Twente
Mathematical Sciences
7500 AE Enschede
Netherlands

Pierre Sagaut
Universite Paris VI
D'Alembert Institute
4 place Jussieu
75252 Paris Cedex 5
France

ISBN: 978-1-4020-8577-2 e-ISBN: 978-1-4020-8578-9

Library of Congress Control Number: 2008927470

Printed on acid-free paper

9 8 7 6 5 4 3 2 1

springer.com

Preface

Computational resources have developed to the level that, for the first time, it is becoming possible to apply large-eddy simulation (LES) to turbulent flow problems of realistic complexity. Many examples can be found in technology and in a variety of natural flows. This puts issues related to assessing, assuring, and predicting the quality of LES into the spotlight. Several LES studies have been published in the past, demonstrating a high level of accuracy with which turbulent flow predictions can be attained, without having to resort to the excessive requirements on computational resources imposed by direct numerical simulations (see, e.g., [1]). This is also corroborated in the current volume, which contains the proceedings of the first QLES meeting on Quality and Reliability of Large-Eddy Simulation, held October 22–24, 2007 in Leuven (QLES07).

The setup and use of turbulent flow simulations requires a profound knowledge of fluid mechanics, numerical techniques, and the application under consideration. The susceptibility of large-eddy simulations to errors in modelling, in numerics, and in the treatment of boundary conditions, can be quite large due to nonlinear accumulation of different contributions over time, leading to an intricate and unpredictable situation. A full understanding of the interacting error dynamics in large-eddy simulations is still lacking. To ensure the reliability of large-eddy simulations for a wide range of industrial users, the development of clear standards for the evaluation, prediction, and control of simulation errors in LES is summoned. The workshop on Quality and Reliability of Large-Eddy Simulations (QLES2007) provided one of the first platforms specifically addressing these aspects of LES. Its main objective was to address fundamental aspects of the LES-quality issue by bringing together mathematicians, physicists, and engineers, thereby confronting entirely different approaches to the subject, doing justice to the complexity of this field. The problem of treating one flow problem correctly is easily an order of magnitude more challenging than the feasibility problem of doing one simulation at all. The latter illustrates the state-of-the-art in LES of a decade ago, while the former represents a more timely challenge.

One of the main difficulties arising in the evaluation of errors in large-eddy simulation, is the nonlinear accumulation of different error sources. Most notorious is the possible interaction between subgrid-scale modelling errors and numerical errors [9, 33]. A problem which is not so well recognized, is the fact that there is no consensus on the definition of errors among researchers. Moreover, differing views exist on the role of the subgrid-scale model relative to that of the numerics in LES. Obviously, such differences handicap the exchange of ideas on accuracy and reliability of LES. These elements will be addressed in some more detail next, to provide an introduction to the current volume.

In early large-eddy simulations, subgrid-scale models were nothing more than a numerical stabilization mechanism [29], regularizing the coarse-mesh solution of the Navier–Stokes equations. Later (see, e.g. [18, 17]) a physical interpretation was linked to the subgrid-scale model, based on the formal application of a low-pass filter to the Navier–Stokes equations. In particular, attention was given to an analysis of the exchange of energy between so-called resolved and unresolved scales, corresponding roughly to scales larger or smaller than the width of the presumed spatial filter, respectively. In modern-day LES, both approaches still exist, i.e., numerical stabilization of the Navier–Stokes equations versus a physics-based subgrid-scale model.

Many examples exist of physics-based models, such as the Lilly–Smagorinsky model [18], backscatter models [22], VMS-Smagorinsky models [12], and several of their variants [28, 32, 25, 31, 13, 26]. Mathematically, these models are used to close the low-pass filtered Navier–Stokes equations. Hence, a natural point of reference for the definition of errors are the low-pass filtered results from either direct numerical simulations or experiments [34]. In such a framework, it was realized early on that, apart from subgrid modelling issues, also numerical discretization was central for the quality of LES [20]. In Mansour's approach [20], a spectral cut-off filter is considered, and spectral discretization is used as a point of reference for the quality of a numerical discretization scheme. In this context, Ghosal [9] pointed out that discretization and modelling errors are of the same order of magnitude, and further work along these lines was presented in [4, 3]. In a different approach to numerical errors Mason [21] proposed to increase the ratio of the filter scale to the grid size Δ/h. At high values of Δ/h, any consistent numerical discretization will converge to a grid-independent solution. Using this framework to define discretization and modelling error, Vreman, Geurts & Kuerten [33] showed a strong interaction between both error sources when $\Delta = h$. In this context, it was also shown that $\Delta/h > 1$ does not necessarily guarantee a reduction in total errors [33, 7, 23]. From a computational-cost point of view, both $\Delta/h > 1$ and higher order numerics are expensive, and avoided in most large-scale computations of realistic applications. In addition, recent research seems to suggest that low-order schemes and $\Delta/h = 1$ may be beneficial to the global simulation error at coarse resolutions [24].

In an alternative approach to LES one may introduce a direct regularization of the Navier–Stokes equations. In this case a change is made to the dynamical properties of the equations, such that they can be accurately solved at a much coarser mesh than DNS. Such an alteration can be performed on the level of the continuous equations, e.g., addressing the convective nonlinearity, as is done in Leray regularization [8, 16], in the NS-α model [5], or in the ADM approach [30, 15]. Alternatively, it has been suggested that this 'regularization' may be absorbed into the discretization scheme; examples are the spectral vanishing viscosity method [14], MILES [6], and several others [11, 10]. In contrast to the classical subgrid-scale model approach described above, in a numerical stabilization approach, no explicit distinction is made between numerical errors and modelling errors. This is a cause of deep methodological disagreements among different LES practitioners – an element that re-appears in several of the contributions.

We believe that the main challenge for LES today is not lying anymore in the development of new modelling or regularization approaches. Aside from the important, unresolved problem of LES and high-Re boundary layers, most of these techniques produce very satisfactory results when used appropriately. Rather, a main challenge is in the development of a transparent standard which helps practitioners in the correct use of LES. A fully consistent theory on errors in LES still requires a huge amount of work. While empirical qualitative comparisons with reference data have been used for decades to conclude on possible improvements in the numerics and physical closures, a mathematically grounded quantitative error measure, like the one proposed by Hoffman, is certainly needed. The definition of such an error measure is a tricky issue, since it appears that in some flows the error can evolve in an counter-intuitive way [33, 27]. A related issue is LES sensitivity: how sensitive is a given LES result to computational setup parameters? A reliable simulation must be stable, in the sense that a small variation of the setup parameters should not yield a dramatic change in the quality of the results. Here again, only very few results are available, and advanced mathematical tools are required (e.g. [19]).

For Reynolds-averaged Navier–Stokes simulations, which are nowadays commonly used in industry, advice on best practise is well known, e.g., ERCOFTAC's Best practice guidelines [2]. Certainly, such an exercise would also be extremely useful for LES. This motivated a concerted effort to arrive at 'Best practice for LES' as identified as a central target of the COST Action 'LESAID', that started in 2006. However, for LES more should be possible: not only guidelines for good quality, but also a 'first-principles' framework may be feasible, in which the quality of LES is guaranteed. It was this context which motivated the organization of a dedicated workshop on quality and reliability of LES. Different contributions were grouped into four sessions. This is also reflected in the current book, which is divided into four parts, i.e., (1) Numerical and mathematical analysis of subgrid-scale-model and discretization errors,

(2) Computational error-assessment, (3) Modelling and error-assessment of near-wall flows, (4) Error assessment in complex applications.

For the organization we relied considerably on the members of the scientific committee: N. A. Adams (Technische Universität München, Germany), M. Baelmans (Katholieke Universiteit Leuven, Belgium), A. Boguslawski (Politechnika Czestochowska, Poland), D. Carati (Université Libre de Bruxelles, Belgium), E. Dick (Universiteit Gent, Belgium), D. Drikakis (Cranfield University, United Kingdom), A. G. Hutton (QinetiQ, United Kingdom), J. Jiménez (Universidad Politecnica Madrid, Spain), M. V. Salvetti (Università di Pisa, Italy), and G. S. Winckelmans (Université Catholique de Louvain, Belgium). We gratefully acknowledge their help.

The workshop on quality and reliability of large-eddy simulations was supported financially by a number of institutions. On a European scale, support was provided by COST Action P20 'LESAID' (LES – Advanced Industrial Design) and ERCOFTAC (European Research Community on Flow, Turbulence and Combustion). At the Belgian level, financial support was provided by the Research Foundation – Flanders (FWO – Vlaanderen), and by the research council of the K.U.Leuven. This support was crucial to the organization of this workshop and is gratefully acknowledged.

Leuven,
January 2008

Johan Meyers
Bernard J. Geurts
Pierre Sagaut

References

1. Andren A, Brown AR, Graf J, Mason PJ, Moeng C-H, Nieuwstadt FTM, Schumann U (1994) Large-eddy simulation of a neutrally stratified boundary layer: a comparison of four computer codes. Quarterly Journal of the Royal Meteorological Society 120:1457–1484
2. Casey M, Wintergerste T (2000) Best Practice Guidelines. ERCOFTAC Special Interest Group on "Quality and Trust in Industrial CFD"
3. Chow FK, Moin P (2003) A further study of numerical errors in large-eddy simulations. Journal of Computational Physics 184:366–380
4. Fedioun I, Lardjane N, Gökalp I (2001) Revisiting numverical errors in direct and large eddy simulations of turbulence: physical and spectral analysis. Journal of Computational Physics 174:816–851
5. Foias C, Holm DD, Titi ES (2001) The Navier–Stokes-alpha model of fluid turbulence. Physica D–Nonlinear Phenomena 152:505–519
6. Fureby C, Grinstein FF (1999) Monotonically integrated large eddy simulation of free shear flows. AIAA Journal 37:544–556
7. Geurts BJ, Fröhlich J (2002) A framework for predicting accuracy limitations in large eddy simulations. Physics of Fluids 14(6):L41–L44

8. Geurts BJ, Holm DD (2003) Regularization modeling for large-eddy simulation. Physics of Fluids 15(1):L13–L16
9. Ghosal S (1996) An analysis of numerical errors in large-eddy simulations of turbulence. Journal of Computational Physics 125:187–206
10. Grinstein FF, Margolin LG, Rider WJ (2007) Implicit large eddy simulation: computing turbulent fluid dynamics. Cambridge University Press
11. Hickel S, Adams NA, Domaradzki JA (2006) An adaptive local deconvolution method for implicit LES. Journal of Computational Physics 213:413–436
12. Hughes TJR, Mazzei L, Oberai AA (2001) The multiscale formulation of large eddy simulation: decay of homogeneous isotropic turbulence. Physics of Fluids 13(2):505–512
13. Jeanmart H, Winckelmans G (2007) Investigation of eddy-viscosity models modified using discrete filters: A simplified "regularized variational multiscale model" and an "enhanced field model". Physics of Fluids 19, Art no 055110
14. Karamanos G-S, Karniadakis GE (2000) A spectral vanishing viscosity method for large-eddy simulations. Journal of Computational Physics 163:22–50
15. Layton W, Neda M (2007) A similarity theory of approximate deconvolution models of turbulence. Journal of Mathematical Analysis and Applications 333:416–429
16. Leray J (1934) Sur les movements d'un fluide visqueux remplaissant l'espace. Acta Mathematica 63:193–248
17. Leslie DC, Quarini GL (1979) The application of turbulence theory to the formulation of subgrid modelling procedures. Journal of Fluid Mechanics 91(1):65–91
18. Lilly DK (1967) The representation of small-scale turbulence in numerical simulation experiments. In: Proceedings of IBM Scientific Computing Symposium on Environmental Siences. IBM Data Processing Division, White Plains, New York
19. Lucor D, Meyers J, Sagaut P (2007) Sensitivity analysis of LES to subgrid-scale-model parametric uncertainty using polynomial chaos. Journal of Fluid Mechanics 585:255–279
20. Mansour NN, Moin P, Reynolds WC, Ferziger JH (1979) Improved methods for large eddy simulations of turbulence. In: Durst F, Launder BE, Schmidt FW, Whitelaw JH (eds) Turbulent shear flows I:286–401. Springer, Berlin Heidelberg New York
21. Mason PJ, Callen NS (1986) On the magnitude of the subgrid-scale eddy coefficient in large-eddy simulations of turbulent channel flow. Journal of Fluid Mechanics 162:439–462
22. Mason PJ, Thomson TJ (1992) Stochastic backscatter in large-eddy simulations of boundary layers. Journal of Fluid Mechanics 242:51–78
23. Meyers J, Geurts BJ, Baelmans M (2003) Database-analysis of errors in large-eddy simulation. Physics of Fluids 15(9):2740–2755
24. Meyers J, Geurts BJ, Sagaut P (2007) A computational error assessment of central finite-volume discretizations in large-eddy simulation using a Smagorinsky model. Journal of Computational Physics 227:156–173
25. Meyers J, Sagaut P (2006) On the model coefficients for the standard and the variational multi-scale Smagorinsky model. Journal of Fluid Mechanics 569:287–319
26. Meyers J, Sagaut P (2007) Evaluation of Smagorinsky variants in large-eddy simulations of wall-resolved plane channel flows. Physics of Fluids 19, Art no 095105

27. Meyers J, Sagaut P (2007) Is plane channel flow a ffriendly test-case for the testing of LES subgrid models? Physics of Fluids 19, Art no 048105
28. Nicoud F, Ducros F (1999) Subgrid-scale stress modelling based on the square of the velocity gradient tensor. Flow, Turbulence and Combustion 62(3):183–200
29. Smagorinsky J (1963) General circulation experiments with the primitive equations: I. The basic experiment. Monthly Weather Review 91(3):99–165
30. Stolz S, Adams NA, Kleiser L (2001) The approximate deconvolution model for large-eddy simulations of compressible flows and its application to shock-turbulent-boundary-layer interaction. Physics of Fluids 13:2985–3001
31. Stolz S, Schlatter P, Kleiser L (2005) High-pass filtered eddy-viscosity models for large-eddy simulations of transitional and turbulent flow. Physics of Fluids 17, Art no 065103
32. Vreman AW (2004) An eddy-viscosity subgrid-scale model for turbulent shear flow: algebraic theory and applications. Physics of Fluids 16(10):3670–3681
33. Vreman B, Geurts B, Kuerten H (1996) Comparison of numerical schemes in large-eddy simulations of the temporal mixing layer. International Journal for Numerical Methods in Fluids 22:297–311
34. Winckelmans GS, Jeanmart H, Carati D (2002) On the comparison of turbulence intensities from large-eddy simulation with those from experiment or direct numerical simulation. Physics of Fluids 14(5):1809–1811

Contents

Part IV Error Assessment in Complex Applications

Contributors

Nikolaus A. Adams
Institute of Aerodynamics, Technische Universität München, 85747 Garching, 85747 Garching, Germany.

Yacine Addad
School of Mechanical, Aerospace and Civil Engineering, University of Manchester, Manchester M60 1QD, UK

Mirosław Łuniewski
Institute of Fluid-Flow Machinery, Polish Academy of Sciences, Fiszera 14, 80952 Gdańsk, Poland

Andrea Aprovitola
Department of Aerospace and Mechanical Engineering, Second University of Naples, Aversa (CE), Italy

Christophe Bailly
LMFA, ECL, 36 avenue Guy de Collongue, UMR CNRS 5509, Ecole Centrale de Lyon, 69134 Ecully, France; Institut Universitaire de France

R.J.M. Bastiaans
Combustion Technology, Department of Mechanical Engineering Eindhoven University of Technology, PO Box 513, 5600 MB Eindhoven, The Netherlands

Rickard E. Bensow
Department of Shipping and Marine Technology, Chalmers University of Technology, SE 412 96 Göteborg, Sweden

Julien Berland
SINUMEF, ENSAM, 151 boulevard de l'Hôpital, 75013 Paris, France

Christophe Bogey
LMFA, UMR CNRS 5509, Ecole Centrale de Lyon, 69134 Ecully, France

Andrzej Boguslawski
Institute of Thermal Machinery, Czestochowa University of Technology, Al. Armii Krajowej 21, 42-200 Czestochowa, Poland

Aaron M. Botnick
School of Meteorology, University of Oklahoma, Norman, OK 73019, USA

Guillaume Boudier
CERFACS, 42 Avenue G. Coriolis, 31057 Toulouse cedex, France

L. Bricteux
Université Catholique de Louvain (UCL), Mechanical Engineering Department, Division TERM, and Center for Systems Engineering and Applied Mechanics, 1348 Louvain-la-Neuve, Belgium.

Stewart Cant
Cambridge University, Engineering Department, Trumpington Street, Cambridge CB2 1PZ, UK

Ian P. Castro
School of Engineering Sciences, University of Southampton, SO17 1BJ, UK

R. Cocle
Université Catholique de Louvain (UCL), Mechanical Engineering Department, Division TERM, and Center for Systems Engineering and Applied Mechanics, 1348 Louvain-la-Neuve, Belgium

Ralf Deiterding
Oak Ridge National Laboratory, P.O. Box 2008 MS6367, Oak Ridge, TN 37831, USA

Marta de la Llave Plata
Cambridge University, Engineering Department, Trumpington Street, Cambridge CB2 1PZ, UK

Filippo Maria Denaro
Department of Aerospace and Mechanical Engineering, Second University of Naples, Aversa (CE), Italy

P. Domingo
LMFN, CORIA – CNRS, Institut National des Sciences Appliquées de Rouen, France

Stanislaw Drobniak
Institute of Thermal Machinery, Czestochowa University of Technology Al. Armii Krajowej 21, 42-200 Czestochowa, Poland

Evgeni Fedorovich
School of Meteorology, University of Oklahoma, Norman, OK 73019, USA

Christer Fureby
Department of Shipping and Marine Technology, Chalmers University of Technology, SE 412 96 Göteborg, Sweden; Defense Security Systems Technology, The Swedish Defense Research Agency – FOI, SE 147 25 Tumba, Stockholm, Sweden

Ulka Gaitonde
School of Mechanical, Aerospace and Civil Engineering, University of Manchester, Manchester M60 1QD, UK

Margot Gerritsen
Department of Energy Resources Engineering, Stanford University, Green Earth Sciences Building, Stanford, CA, USA 94305-2220

Bernard J. Geurts
Mathematical Sciences, University of Twente, PO Box 217, 7500 AE Enschede, The Netherlands; Applied Physics, Eindhoven University of Technology, PO Box 513, 5600 MB Eindhoven, The Netherlands

Ghader Ghorbaniasl
Vrije Universiteit Brussel, Department Of Mechanical Engineering, Pleinlaan 2, 1050 Brussels, Belgium

Laurent Y. M. Gicquel
CERFACS, 42 Avenue G. Coriolis, 31057 Toulouse cedex, France

Andreas Hauser
Corporate Technology, Power & Sensor Systems, Siemens AG, Günther-Scharowsky-Str. 1, 91050 Erlangen, Germany

Stefan Hickel
Institute of Aerodynamics, Technische Universität München, 85747 Garching, Germany

Johan Hoffman
School of Computer Science and Communication, KTH, SE-100 44 Stockholm, Sweden

Marek Jaszczur
AGH – University of Science and Technology, 30-059 Krakow, Al. Mickiewicza 30, Poland

Markus Klein
Institute for Energy and Powerplant Technology, Technical University of Darmstadt, Petersenstrasse 30, 64297 Darmstadt, Germany

Leonhard Kleiser
Institute of Fluid Dynamics, ETH Zurich, 8092 Zurich, Switzerland

Michael Kornhaas
Technische Universität Darmstadt, Department of Numerical Methods in Mechanical Engineering, Petersenstraße 30, 64287 Darmstadt, Germany

J. G. M. Kuerten
Department of Mechanical Engineering, Technische Universiteit Eindhoven, P.O. Box 513, 5600 MB Eindhoven, The Netherlands

A. Labovschii
Department of Mathematics, University of Pittsburgh, Pittsburgh, PA, USA

Chris Lacor
Vrije Universiteit Brussel, Department of Mechanical Engineering, Pleinlaan 2, 1050 Brussels, Belgium

Dominique Laurence
School of Mechanical, Aerospace and Civil Engineering, University of Manchester, Manchester M60 1QD, UK

W. Layton
Department of Mathematics, University of Pittsburgh, Pittsburgh, PA, USA

G. Lodato
LMFN, CORIA – CNRS, Institut National des Sciences Appliquées de Rouen, France

Máté Márton Lohász
Department of Fluid Mechanics, Budapest University of Technology and Economics, Bertalan L. Str. 4–6, Budapest 1111, Hungary

Manuel Lombardini
Graduate Aeronautical Laboratories, California Institute of Technology, Pasadena, CA 91125, USA

C. Manica
Departamento de Matemática Pura e Aplicada, Universidade Federal do Rio Grande do Sul, Porto Alegre-RS- Brazil

Cristian Marchioli
Centro Interdipartimentale di Fluidodinamicae Idraulica and Dipartimento di Energetica e Macchine, Università di Udine, 33100 Udine, Italy

Johan Meyers
FWO – Vlaanderen (Science Foundation – Flanders); Department of Mechanical Engineering, Katholieke Universiteit Leuven Celestijnenlaan 300A, B3001 Leuven, Belgium

Sebastian B. Müller
Institute of Fluid Dynamics, ETH Zurich, 8092 Zurich, Switzerland

M. Neda
Department of Mathematics and Science, University of Nevada, Las Vegas, NV, USA

Angela O. Nieckele
Department of Mechanical Engineering, Pontifícia Universidade Católica do Rio de Janeiro – PUC/Rio, R. Marquês de S. Vicente 225, Gávea, 22453-900 Rio de Janeiro, RJ, Brazil

Thierry J. Poinsot
Institut de Mécanique des Fluides de Toulouse, Avenue C. Soula, 31400 Toulouse, France

Luis M. Portela
Delft University of Technology, Prins Bernhardlaan 6, 2628 BW, Delft, The Netherlands

Mathieu J. B. M. Pourquie
Laboratory for Aero- and hydrodynamics, dept of Mech Engng, Mekelweg 2, 2628 CD Delft, Netherlands

Jacek Pozorski
Institute of Fluid-Flow Machinery, Polish Academy of Sciences, Fiszera 14, 80952 Gdańsk, Poland

D.I. Pullin
Graduate Aeronautical Laboratories, California Institute of Technology, Pasadena, CA 91125, USA

L. Rebholz
Department of Mathematics, University of Pittsburgh, Pittsburgh, PA, USA

Stefano Rolfo
School of Mechanical, Aerospace and Civil Engineering, University of Manchester, Manchester M60 1QD, UK

Pierre Sagaut
Universite Paris VI, D'Alembert Institute, 4 place Jussieu, 75252 Paris CX 5, France

Maria-Vittoria Salvetti
Dipartimento di Ingegneria Aerospaziale, Università di Pisa, 56122 Pisa, Italy

Luiz E.B. Sampaio
Department of Mechanical Engineering, Pontifícia Universidade Católica do Rio de Janeiro – PUC/Rio, R. Marquês de S. Vicente 225, Gávea, 22453-900 Rio de Janeiro, RJ, Brazil

Michael Schäfer
Technische Universität Darmstadt, Department of Numerical Methods in Mechanical Engineering, Petersenstraße 30, 64287 Darmstadt, Germany

Alfredo Soldati
Centro Interdipartimentale di Fluidodinamica e Idraulica and Dipartimento di Energetica e Macchine, Universität di Udine, 33100 Udine, Italy

Philippe R. Spalart
Boeing Commercial Airplanes, Seattle, WA 98124, USA

Gabriel Staffelbach
CERFACS, 42 Avenue G. Coriolis, 31057 Toulouse cedex, France

I. Stanculescu
Department of Mathematics, University of Pittsburgh, Pittsburgh, PA, USA

Dörte C. Sternel
Technische Universität Darmstadt, Department of Numerical Methods in Mechanical Engineering, Petersenstrase 30, 64287 Darmstadt, Germany

Mikhail Kh. Strelets
New Technologies and Services, St.-Petersburg 197198, Russia

Péter Tóth
Department of Fluid Mechanics, Budapest University of Technology and Economics, Bertalan L. Str. 4-6, Budapest 1111, Hungary

Andrey Travin
New Technologies and Services, St.-Petersburg 197198, Russia

C. Trenchea
Department of Mathematics, University of Pittsburgh, Pittsburgh, PA, USA

Artur Tyliszczak
Institute of Thermal Machinery, Czestochowa University of Technology, Al. Armii Krajowej 21, 42-200 Czestochowa, Poland

A.W. Vreman
Combustion Technology, Department of Mechanical Engineering Eindhoven University of Technology, PO Box 513, 5600 MB Eindhoven, The Netherlands;

Vreman Research, Godfried Bomansstraat 46, 7552 NT Hengelo, The Netherlands

L. Vervisch
LMFN, CORIA – CNRS, Institut National des Sciences Appliquées de Rouen, France

G. Winckelmans
Université Catholique de Louvain (UCL), Mechanical Engineering Department, Division TERM, and Center for Systems Engineering and Applied Mechanics, 1348 Louvain-la-Neuve, Belgium.

Gabriel Wittum
Simulation in Technology, University of Heidelberg, Im Neuenheimer Feld 368, 69120 Heidelberg, Germany

Zheng-Tong Xie
School of Engineering Sciences, University of Southampton, SO17 1BJ, UK

Part I

Numerical and Mathematical Analysis of Subgrid-Scale-Model and Discretization Errors

Architecture of Approximate Deconvolution Models of Turbulence*

A. Labovschii[1], W. Layton[1], C. Manica[2], M. Neda[3], L. Rebholz[1], I. Stanculescu[1], and C. Trenchea[1]

[1] Department of Mathematics, University of Pittsburgh, Pittsburgh, PA, USA ayl2@pitt.edu, wjl+@pitt.edu, ler6@math.pitt.edu, ius1+@pitt.edu, trenchea@pitt.edu

[2] Departamento de Matemática Pura e Aplicada, Universidade Federal do Rio Grande do Sul, Porto Alegre-RS- Brazil, carolina.manica@ufrgs.br

[3] Department of Mathematical Sciences, University of Nevada, Las Vegas, NV, USA, monika.neda@unlv.edu

Abstract. This report presents the mathematical foundation of approximate deconvolution LES models together with the model phenomenology downstream of the theory. This mathematical foundation now begins to be complete for the incompressible Navier–Stokes equations. It is built upon averaging, deconvolving and addressing closure so as to obtain the physically correct energy and helicity balances in the LES model. We show how this is determined and how correct energy balance implies correct prediction of turbulent statistics. Interestingly, the approach is simple and thus gives a road map to develop models for more complex turbulent flows. We illustrate this herein for the case of MHD turbulence.

Keywords: Deconvolution, Energy cascade, Helicity, MHD

1 Introduction

Approximate deconvolution models (ADMs) for large eddy simulation (LES) are systematic (rather than ad hoc). See, for example, [1, 2, 50, 52, 51, 53] for the work of Stolz, Adams, Kleiser and coworkers and [18, 19, 20, 21] for Geurts' work. They can achieve high theoretical accuracy and shine in practical tests; they contain few or no fitting/tuning parameters. The ADM approach has thus proven itself to be very promising with fundamental reasons for its effectiveness, which we discuss herein. The basic (and *ill-posed*) problem of approximate de-convolution is: (Section 2)

$$\text{given } \overline{u} \ (+ \textit{noise}) \text{ find } \textit{useful} \text{ approximations } D(\overline{u}) \text{ of } u \text{ that lead to } \textit{accurate} \text{ and } \textit{stable} \text{ LES models.} \tag{1}$$

* This work was partially supported by NSF Grant DMS 0508260

Indeed, given an approximate deconvolution operator D with accuracy $O(\delta^\alpha)$:

$$\phi = D\overline{\phi} + O(\delta^\alpha) \text{ for smooth functions } \phi \tag{2}$$

the closure problem can be solved approximately to accuracy $O(\delta^\alpha)$ by

$$\overline{uu} \Leftarrow \overline{D(\overline{u})D(\overline{u})} \quad (\ + O(\delta^\alpha) \ ).$$

With the above closure approximation inserted in the SFNSE and adding a time relaxation term $\chi(w - D(\overline{w}))$ we obtain an ADM given by

$$w_t + \nabla \cdot (\overline{D(w)D(w)}) - \nu\triangle w + \nabla q + \chi(w - D(\overline{w})) = \overline{f}(x) \, , \text{ and } \nabla \cdot w = 0.$$

The key to an ADMs physical fidelity and robust mathematical theory is having the correct global energy balance. In Section 3 we show that provided D and $I - D$ are SPD, with the weighted norms $(v, w)_D := (D_N v, w)_{L^2(\Omega)}$ and $\|w\|_D^2 := (w, w)_D$, we have

$$\frac{1}{2}[\|w(T)\|_D^2 + \delta^2\|\nabla w(T)\|_D^2] + \int_0^T \nu\|\nabla w\|_D^2 + \nu\delta^2\|\triangle w\|_D^2 + \chi(w - D(\overline{w}), w)_D dt$$
$$= \frac{1}{2}[\|\overline{u}_0\|_D^2 + \delta^2\|\nabla\overline{u}_0\|_D^2] + \int_0^T (f, w)_D \, dt.$$

This energy equality is the key to both the rigorous theory (Section 3) and turbulent phenomenology (Section 4). In fact, *its derivation gives a roadmap to development of both for LES models for coupled NS systems.* For example, ADM's have been extended successfully to fully coupled MHD turbulence (including the possibility of using different averaging radii for the different physical effects) in [27, 25, 26]. For MHD turbulence, the full ADM LES models derived conserve all appropriate integral invariants and predict Alfvén waves with the correct wave speeds – critical effects of MHD turbulence.

A correct prediction of turbulent flow means getting the energy balance and rotational structures correct. In the large, this means the ADMs energy and helicity statistics, $\widehat{E}(k)$ and $\widehat{H}(k)$ (Section 4), are correct over the resolved scales:

$$\widehat{E}(k) \simeq \alpha_{model}\varepsilon_{model}^{2/3}k^{-5/3}, \ \widehat{H}(k) \simeq C_{model}\gamma_{model}\epsilon_{model}^{-1/3}k^{-5/3}, \text{ for } k \leq \frac{\pi}{\delta}. \tag{3}$$

In the presence of boundaries the difficult problems of commutativity, near wall modeling and filtering through a boundary still arise. These problems have motivated reconsideration of the oldest ideas in fluid dynamics: using simple regularizations of the NSE instead of complex models. We have shown that deconvolution can produce dramatic improvement in NSE regularizations as well. Three are presented in Section 5: the Leray deconvolution regularization, the NS-alpha and the NS-omega regularizations.

Overall, strong stability + high accuracy leads to good things in LES models. We also believe that deconvolution ideas have strong independent value and can be used to improve most (or all) LES models and NSE regularizations.

2 Approximate Deconvolution

1. **The van Cittert deconvolution operator**. See [7], D_N is a family of inverses to G using N steps of fixed point iterations.

   Algorithm 1 [*van Cittert Algorithm*]: *choose* $\mathbf{u}_0 = \overline{\mathbf{u}}$. *For* $n = 0, 1, 2, ...,$ $..., N-1$ *perform* $\mathbf{u}_{n+1} = \mathbf{u}_n + \{\overline{\mathbf{u}} - G\mathbf{u}_n\}$. *Set* $D_N\mathbf{u} := \mathbf{u}_N$.

   A mathematical theory of the van Cittert deconvolution operator and LES models is developing [1, 6, 15] and [30]. For example, it is known that if G is SPD then $D_N : L^2(Q) \to L^2(Q)$ is a bounded operator.
2. **The Accelerated van Cittert deconvolution operator.** Relaxation parameters can be included in Algorithm 1 at little additional computational cost.

   Algorithm 2 [*Accelerated van Cittert Algorithm*]: *Given relaxation parameters* ω_n, *choose* $\mathbf{u}_0 = \overline{\mathbf{u}}$. *For* $n = 0, 1, 2, ..., N-1$ *perform* $\mathbf{u}_{n+1} = \mathbf{u}_n + \omega_n\{\overline{\mathbf{u}} - G\mathbf{u}_n\}$. *Set* $D_N^\omega\mathbf{u} := \mathbf{u}_N$.

   Proposition 1. *Let the averaging operator be the differential filter* $G\boldsymbol{\varphi} := (-\delta^2\triangle + I)^{-1}\boldsymbol{\varphi}$. *If* $\omega_i > 0$, *for all* i, *then* $D_N^\omega : \mathrm{L}^2(Q) \to \mathrm{L}^2(Q)$ *is SPD.*

   Proof. The proof follows from [[38], Lemma 3.2].

   Optimal values of the relaxation parameters ω_i, for $i = 0, 1, 2, 3, 4$ were calculated in [38], Table 1. With these values,
   D_N and D_N^ω lead to a very accurate solution of the
3. **Tikhonov regularization deconvolution operator.** Given $\overline{\mathbf{u}}$ and $1 > \mu > 0$, since G is SPD, an approximate solution to (1) can be calculated as the unique minimizer in $L^2(Q)$ of the Tikhonov functional

$$F_\mu(\mathbf{v}) = \frac{1}{2}(G\mathbf{v}, \mathbf{v}) - (\overline{\mathbf{u}}, \mathbf{v}) + \frac{\mu}{2}(\mathbf{v} - G\mathbf{v}, \mathbf{v}).$$

   The resulting deconvolution operator is

$$D_\mu = ((1-\mu)G + \mu I)^{-1}. \tag{4}$$

   The family of operators D_μ has the following properties, [49]

   - for any $\mu > 0$, D_μ is a bounded SPD operator,
   - $\lim_{\mu\to 0} D_\mu\overline{\boldsymbol{\varphi}} = \boldsymbol{\varphi}$ for all $\boldsymbol{\varphi} \in L^2(Q)$.

   The transfer function of the Tikhonov deconvolution operator is $\widehat{D}_\mu = \frac{1+k^2}{1+\mu k^2}$ and as $\mu \to 0$, D_μ is very accurate.

3 Theory of Approximate Deconvolution Models

In the absence of boundaries, the SFNSE is $\nabla \cdot \overline{u} = 0$ and

$$\overline{u}_t + \nabla \cdot (\overline{D(\overline{u})D(\overline{u})}) - \nu \triangle \overline{u} + \nabla \overline{p} + \nabla \cdot (\overline{uu - D(\overline{u})D(\overline{u})}) = \overline{f}(x). \tag{5}$$

An LES model results from dropping the residual stress $uu - D(\overline{u})D(\overline{u})$. The residual stress, $uu - D(\overline{u})D(\overline{u})$, is directly related to the deconvolution error $u - D(\overline{u})$ since

$$uu - D(\overline{u})D(\overline{u}) = [u - D(\overline{u})]u + D(\overline{u})[u - D(\overline{u})].$$

Thus, the more accurately the deconvolution problem can be solved, the more accurately (on the large scales) the closure problem is solved.

3.1 The Zeroth Order Model

The zeroth order van Cittert operator is $D = I$ or $\phi = \overline{\phi} + O(\delta^2)$:

$$\overline{u}\,\overline{u} \Leftarrow \overline{\overline{u}\,\overline{u}} + O(\delta^2)$$

and yields the zeroth order ADM:

$$w_t + \nabla \cdot (\overline{w}\,\overline{w}) - \nu \triangle w + \nabla q = \overline{f}(x), \text{ and } \nabla \cdot w = 0. \tag{6}$$

All the key mathematical results for approximate deconvolution models were first proven for the (inaccurate) zeroth order model and the proofs in the general case were based on the ideas developed for it. We start with the most important example.

Theorem 3. *(from [28]) Consider (6) with L-periodic boundary conditions and the initial condition $w(x,0) = \overline{u}_0(x)$. Let the averaging operator be the differential filter: $G = A^{-1}, A = -\delta^2 \Delta + 1$. Then, strong solutions to the zeroth order model exist uniquely and satisfy the energy equality:*

$$\begin{aligned} \frac{1}{2}\left[\|w(t)\|^2 + \delta^2 \|\nabla w(t)\|^2\right] + \int_0^t \left[\nu \|\nabla w(t')\|^2 + \nu \delta^2 \|\triangle w(t')\|^2\right] dt' \\ = \frac{1}{2}\|u_0\|^2 + \int_0^t (f(t'), w(t'))dt'. \end{aligned} \tag{7}$$

Proof. (Sketch) The key to the model, like the NSE, is to make the nonlinear term vanish by an appropriate choice of test function. In the zeroth order model's case we observe

$$(\nabla \cdot (\overline{w}\,\overline{w}), Aw) = (A^{-1} \nabla \cdot (w\ w), Aw) = (\nabla \cdot (w\ w), w) = 0.$$

Thus, the key to the model is taking the inner product of (6) with Aw. Since

$$(\nabla q, Aw) = (q, \nabla \cdot Aw) = (q, A\nabla \cdot w) = 0,$$

we have

$$(w_t, Aw) + (\nabla \cdot (\overline{w\ w}), Aw) - \nu(\triangle w, Aw) + (\nabla q, Aw) = (\overline{f}, Aw). \quad (8)$$

Integrating by parts each term gives

$$\frac{1}{2}\frac{d}{dt}[(w,w) + \delta^2(\nabla w, \nabla w)] + [\nu(\nabla w, \nabla w) + \delta^2(\triangle w, \triangle w)] = (f(t), w).$$

Theorem 3 has many important consequences.

- Existence, uniqueness and regularity of strong solutions, [29].
- Correct prediction of turbulent flow statistics through the resolved scales, [37].
- Convergence (modulo a subsequence) as the $\delta_j \to 0$ to a weak solution of the Navier–Stokes equations, [29].
- Optimal estimates of the model error ($\|\overline{u}_{NSE} - w_{LES}\|$) by the model's consistency error (or residual stress), [29].
- Exact conservation of a model energy and global existence for the Euler ADM, see [29, 28].
- Results on model vortex structures, see [29, 41].

Boundaries include the issues of filtering through a boundary and finding effective boundary conditions for (non-local) flow averages or near-wall laws. In [42] both important problems were circumvented by a clean and computationally attractive formulation of discrete differential filters.

3.2 Energy Balance of General ADMs

The extension to the van Cittert family was accomplished by Dunca [14] and Dunca and Epshteyn [15]. Beyond van Cittert deconvolution, current research, [49], investigates general deconvolution models. Let D denote a general approximate deconvolution operator

$$\|D\|_{L(L^2(\Omega)\to L^2(\Omega))} < \infty \text{ and } D\ \overline{\phi} \simeq \phi \text{ in some useful sense.}$$

The associated *base* approximate deconvolution is

$$w_t + \nabla \cdot (\overline{Dw\ Dw}) - \nu\triangle w + \nabla q = \overline{f}(x)\ , \text{ and } \nabla \cdot w = 0. \quad (9)$$

Like the $N = 0$ case, the consistency error/residual stress tensor of the base ADM is

$$\tau(u,u) = uu - D(\overline{u})D(\overline{u}).$$

Finding the energy balance of the general model depends upon: given w, construct an associated function $\Phi(w)$ with

$$(\nabla \cdot (\overline{DwDw}), \Phi(w)) = \cdots = (v \cdot \nabla v, v) = 0.$$

Taking $\Phi(w) = ADw$ we find (with $v = D(w)$) from (9)

$$\begin{aligned}(\nabla \cdot (\overline{DwDw}), ADw) &= (A^{-1}\nabla \cdot (DwDw), ADw) = (\nabla \cdot (D(w)D(w)), D(w)) \\ &= (v \cdot \nabla v, v) = 0.\end{aligned}$$

This gives the analog of the energy estimate (7) in Theorem 3 since

$$(w_t, ADw) - \nu(\triangle w, ADw) = (\overline{f}(x,t), ADw). \tag{10}$$

This is a deconvolution weighted version of the same energy estimate as the $N = 0$ case. If the operators involved commute and the operator D is SPD then this just represents a weighting of the usual L^2 norm and inner product.

We thus have the essential condition and reweightings

$$D \text{ is SPD and } (u,v)_D := (u, Dv), \|u\|_D^2 = (u,u)_D.$$

Proposition 2. *Let G be the differential filter $G = A^{-1}$ where $A = -\delta^2\Delta + 1$. Then, the van Cittert approximate deconvolution operator is symmetric positive definite (and Δ, A, and D commute).*

Proof. Both A^{-1} and $(I - A^{-1})$ are SPD. For example, $(I - A^{-1})$ is a SPD since

$$(\phi, (I - A^{-1})\phi) = \text{ (letting } \psi = A^{-1}\phi) = \delta^4\|\triangle\psi\|^2 + \delta^2\|\nabla\psi\|^2 > 0$$

for $\phi \neq 0$. Eliminating the intermediate steps in Algorithm 1, D_N is clearly SPD since it is a sum of SPD operators:

$$D_N = \sum_{n=0}^{N} (I - A^{-1})^n.$$

Integrating by parts each term in the energy equation (10) gives

$$\frac{1}{2}\frac{d}{dt}[\|v\|_D^2 + \delta^2\|\nabla v\|_D^2] + [\nu\|\nabla v\|_D^2 + \nu\delta^2\|\triangle v\|_D^2] = (f(t), w)_D.$$

The above clearly identifies the ADM energy and energy dissipation rate. The ADM kinetic energy, conserved exactly if $\nu = f = 0$, and energy disipation rate are given by

$$E_{ADM}(w) = \frac{1}{2|\Omega|}[\|w\|_D^2 + \delta^2\|\nabla w\|_D^2],\ \varepsilon_{ADM}(w) = \frac{\nu}{|\Omega|}\|\nabla w\|_D^2 + \frac{\nu\delta^2}{|\Omega|}\|\triangle w\|_D^2.$$

These are the essential ingredients (together with complementing mathematical technicalities) of the following result of Stanculescu [49].

Theorem 4 (ADM Energy Equality). *Suppose that $\triangle, A, D$ commute, D is SPD. Then, a unique strong solution of the general ADM exists. Further, the following energy equality holds*

$$E_{ADM}(w)(t) + \int_0^t \varepsilon_{ADM}(w)dt' = E_{ADM}(w)(0) + \int_0^t \frac{1}{|\Omega|}(f, w)dt'.$$

From the energy equality, mathematical and physical theories of the general ADM follow.

- **The Leray theory of the model:** Existence, uniqueness and regularity of strong solutions, [28, 29, 14, 15, 49, 6] and

$$w_{ADM} \to u_{NSE}, \text{ as } \delta_j \to 0.$$

- **High Accuracy:** for the large scales. For $D = D_N$

$$\max_{[0,T]} \|\overline{u} - w\|^2 + \int_0^T \nu \|\nabla(\overline{u} - w)\|^2 dt' \leq C(u, \mathrm{Re})\delta^{4N+4}.$$

- **Physical fidelity:** correct prediction of turbulent flow statistics, i.e. (3) holds, [35, 36, 32], see also Section 4.

4 ADM Phenomenology

In 1961 helicity's inviscid invariance was discovered [44, 43]. Helicity is a *rotationally* meaningful quantity that can be checked for accuracy in a simulation. There is considerable evidence that both energy and helicity exhibit cascades and the details of their respective cascades are intertwined, [3]. Recent theoretical studies, which have been experimentally confirmed [8], have suggested a joint energy and helicity cascade through the inertial range of wave numbers

$$\widehat{E}(k) \simeq C_E \epsilon^{2/3} k^{-5/3}, \qquad \widehat{H}(k) \simeq C_H \gamma \epsilon^{-1/3} k^{-5/3},$$

where k is wave number, ϵ the time averaged energy dissipation rate, γ the time averaged helicity dissipation rate and C_E, C_H constants, [9, 13].

4.1 Energy Cascade of Approximate Deconvolution Models

The correctness of LES energy cascades of was studied by Muschinksy [45], and later by Holm, Olson and Titi [16] for NS-α and [35, 36] for ADMs. If we set $\chi = 0$ and apply A to the ADM it becomes:

$$\frac{\partial}{\partial t}\left[\mathbf{w} - \delta^2 \triangle \mathbf{w}\right] + D_N(\mathbf{w}) \cdot \nabla D_N(\mathbf{w}) - \nu\left[\triangle \mathbf{w} - \delta^2 \triangle^2 \mathbf{w}\right] + \nabla P = \mathbf{f}.$$

Since D_N is spectrally equivalent to the identity (uniformly in k, δ, nonuniformly in N) the nonlinear interaction $D_N(\mathbf{w}) \cdot \nabla D_N(\mathbf{w})$ (like those in the NSE) will pump energy from large scales to small scales. The viscous terms in the above equation will damp energy at the small scales (more strongly than in the NSE in fact). Lastly, when $\nu = 0$, $f \equiv 0$ the model's kinetic energy is exactly conserved (Theorem 4).

Thus, the family of ADMs satisfies all the requirements for the existence of a Richardson - like energy cascade for E_{model}. Select the (time averaged) variables with units (denoted $[\cdot]$):

- $\widehat{E}_{model}$ - ADM energy spectrum, $[E_{model}] = length^3 time^{-2}$,
- ε_{model} - energy dissipation rate, $[\varepsilon_{model}(k)] = length^2 time^{-3}$,
- k - wave-number with $[k] = length^{-1}$ and
- δ - averaging radius with $[\delta] = length$.

Choosing primary dimensions *mass*, *length* and *time*, form 2 dimensionless ratios, Π_1 and Π_2. Choosing ε and k for the repeating variables we obtain $\Pi_1 = \varepsilon_{model}^a k^b \widehat{E}_{model}$ and $\Pi_2 = \varepsilon_{model}^c k^d \delta$ for some a, b, c, d. Applying the Π-theorem gives

$$\widehat{E}_{model} = \varepsilon_{model}^{2/3} k^{-5/3} f(k\delta).$$

Economy suggests that $f(\Pi_2) = \alpha_{model}$, [36] and thus

$$\widehat{E}_{model}(k) = \alpha_{model} \varepsilon_{model}^{2/3} k^{-5/3}.$$

However, interesting conclusions result from the difference between $E(\mathbf{w})(t)$ and $E_{model}(\mathbf{w})(t)$. Parseval's equality gives $\widehat{E}_{model}(k) = (I + \delta^2 k^2)^{-1} \widehat{E}(k)$ so

$$\widehat{E}(k) = \frac{\alpha_{model} \varepsilon_{model}^{2/3} k^{-5/3}}{1 + \delta^2 k^2}. \tag{11}$$

Equation (11) gives two wave-number regions depending on which term in the denominator is dominant: 1 or $\delta^2 k^2$. The transition point is the cutoff wave-number $k = \frac{\pi}{\delta}$. We thus have (Fig. 1)

$$\widehat{E}(k) \simeq C \varepsilon_{model}^{\frac{2}{3}} k^{-\frac{5}{3}}, \text{ for } k \leq \frac{\pi}{\delta}, \quad \widehat{E}(k) \simeq C \varepsilon_{model}^{\frac{2}{3}} \delta^{-2} k^{-\frac{11}{3}}, \text{ for } k \geq \frac{\pi}{\delta}.$$

Related studies have also established the following:

- *Kraichnan's dynamic argument.* In [32] the dynamical argument of [24] strongly supported $f(\Pi_2) \equiv$ constant.
- *The microscale of ADMs.* When $\chi = 0, \eta_{model}$ is, [36],

$$\eta_{model} \simeq Re^{-\frac{3}{10}} L^{\frac{2}{5}} \delta^{\frac{3}{5}} (N+1)^{-\frac{3}{10}}.$$

- *The joint helicity-energy cascade.* In [32], the model's energy and helicity cascade (3) was established.

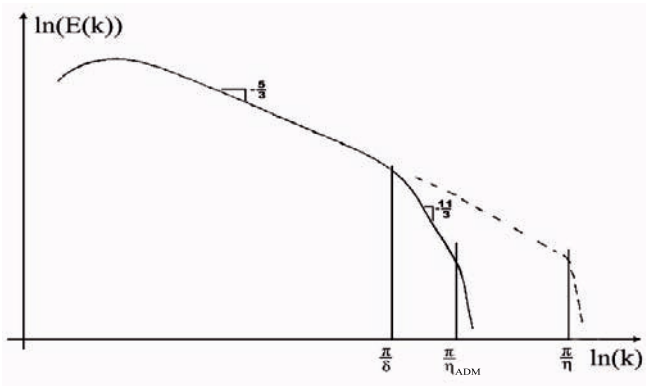

Fig. 1 Spectrum of kinetic energy of ADMs

- *Time relaxation* induces the desired micro-scale, $\eta_{model} \approx \delta$, [36].
- *Other filters.* With $G = (-\delta^2 \Delta + 1)^{-1}$, scales begin to be truncated at $l = O(\delta)$ by an enhanced decay of the energy and helicity of $k^{-11/3}$. The exponent $-11/3$ occurs because the filter decays as k^{-2}. With a Gaussian filter, $\eta_{model} \simeq \delta$.

5 Deconvolution Regularizations of the NSE

Three high order families of regularizations of the (unfiltered) Navier–Stokes equations have recently been proposed and studied. They are the Leray-deconvolution model [31, 34, 48],

$$v_t + D_N \overline{v} \cdot \nabla v + \nabla q - \nu \Delta v = f, \quad \nabla \cdot v = 0, \tag{12}$$

the NS-α-deconvolution model [46, 47],

$$v_t - D_N \overline{v} \times (\nabla \times v) + \nabla q - \nu \Delta v = f, \quad \nabla \cdot D_N \overline{v} = 0 \tag{13}$$

and the NS$-\overline{\omega}$ deconvolution model, [39, 33],

$$v_t - v \times \nabla \times D_N(\overline{v}) + \nabla q - \nu \Delta v = f \quad \text{and } \nabla \cdot v = 0.$$

All are high-order accurate $O(\delta^{2N+2})$. Also, (12) and (13) include for $N = 0$ the Leray-α [12, 40] and NS-α models [10, 11, 16, 17, 22] which both have accuracy $O(\delta^2)$.

5.1 The Leray-Deconvolution Regularization of the NSE

The consistency error of (12) is $O(\delta^{2N+2})$. Thus with the Leray deconvolution model accuracy can be increased by cutting δ (and thus the mesh), or by holding δ constant and increasing the order of approximate deconvolution N.

Theorem 5. *(from [31]) The problem (12) admits a unique solution* $v \in L^\infty(0,T;H^1) \cap L^2(0,T;H^2), q \in L^2(0,T,L^2), v_t \in L^2(0,T;H^{-1})$ *satisfying*

$$\|v(t)\|^2 + 2\nu \int_0^t \|\nabla v\|^2 \, dt' = \|v_0\|^2 + \int_0^t (f,v) \, dt'. \tag{14}$$

For smooth solutions of the NSE the error satisfies

$$\|u - v\|^2 + \nu \int_0^T \|\nabla(u-v)\|^2 dt \leq C(u, Re)\delta^{2N+2}.$$

The filter-and-deconvolve process can be efficiently treated (as in Baker [4]). By time-extrapolating the first term of the nonlinearity, $O(\Delta t^2)$ accuracy is maintained and only known terms are filtered and deconvolved, [34]. The CNLE (Crank-Nicolson with Linear Extrapolation) method for computing solutions to the Leray-deconvolution method was studied in [34]. Discrete filtering ($A_h^{-1}\phi := \overline{\phi}^h$) and discrete deconvolution (D_N^h) in a finite element space X_h, are defined by

$$\delta^2(\nabla\overline{\phi}^h, \nabla\chi) + (\overline{\phi}^h, \chi) = (\phi, \chi) \;\; \forall \chi \in X^h, \quad D_N^h \phi := \sum_{n=0}^{N} (I - A_h^{-1})^n \phi. \tag{15}$$

It is proven in [34] that the consistency of discretely applying approximate deconvolution to a discretely filtered variable is of high order.

Lemma 1. *(from [34]) If* X_h *contains degree* k *piecewise polynomials,*

$$\|\phi - D_N^h \overline{\phi}^h\| \leq C(N,\phi)(\delta h^k + h^{k+1} + \delta^{2N+2}). \tag{16}$$

This lemma is the key in [34] to showing solutions of trapezoidal finite element schemes for (12) converge at the rate of $O(\Delta t^2 + h^k + h^{2N+2})$. Choosing N to balance the exponents allows for optimal convergence. For $N = 0$ (i.e. Leray-α), optimal convergence cannot be obtained if $k \geq 3$.

In [34], two and three dimensional numerical examples of trapezoidal FEM for (12) are given. The 3d computations were done in Matlab using Taylor-Hood tetrahedral elements on an $h = 1/32$ mesh. The 3d tests compared errors and helicity for the scheme for the NSE and Leray-deconvolution for $N = 0, 1, 2$.

Figure 2 shows error versus time for CNLE finite elements schemes for the NSE, and Leray-deconvolution $N = 0, 1, 2$ on the periodic unit box. The Reynolds number was Re=5000, and f and u_0 were computed from the known solution $u = \langle \cos(2\pi(z+t)), \sin(2\pi(z+t)), \sin(2\pi(x+y+t)) \rangle$. From the figure, errors in the Leray-deconvolution models increases at a much slower rate than for the NSE. For the L^2 error, a dramatic decrease in error can be seen in the $N = 1, 2$ models vs. $N = 0$ and NSE.

Figure 3 shows, for the CNLE finite element computations for the NSE and Leray-deconvolution $N = 0, 1, 2$, energy and helicity versus time for a flow

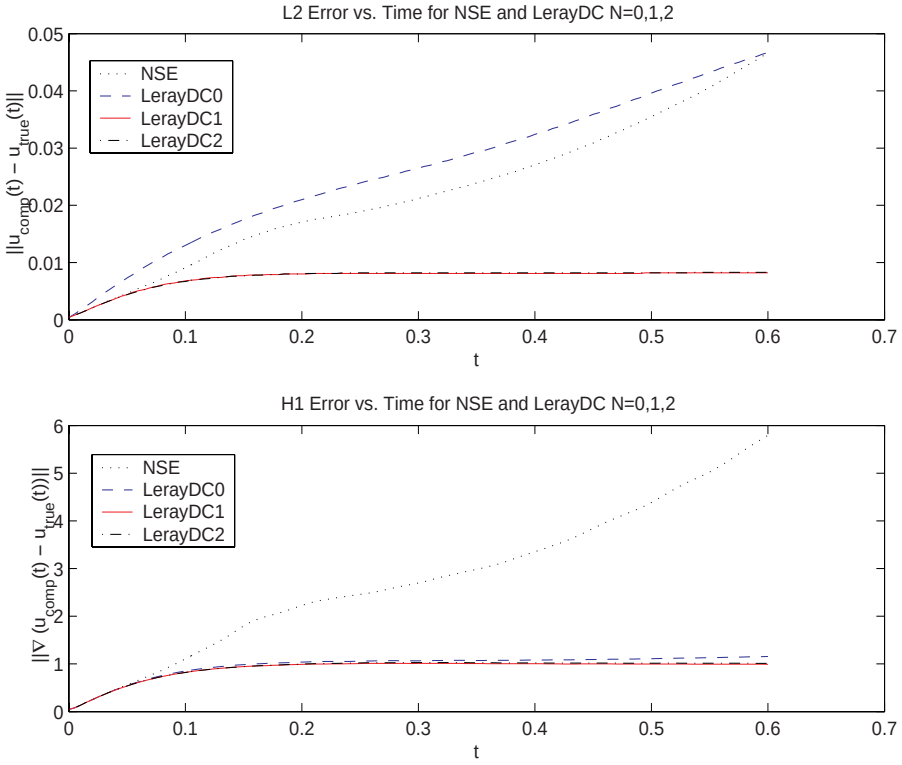

Fig. 2 L^2 and H^1 error vs time for CNLE FEM, $h = 1/32$, Re=5000, and $u = \langle \cos(2\pi(z+t)), \sin(2\pi(z+t)), \sin(2\pi(x+y+t)) \rangle$

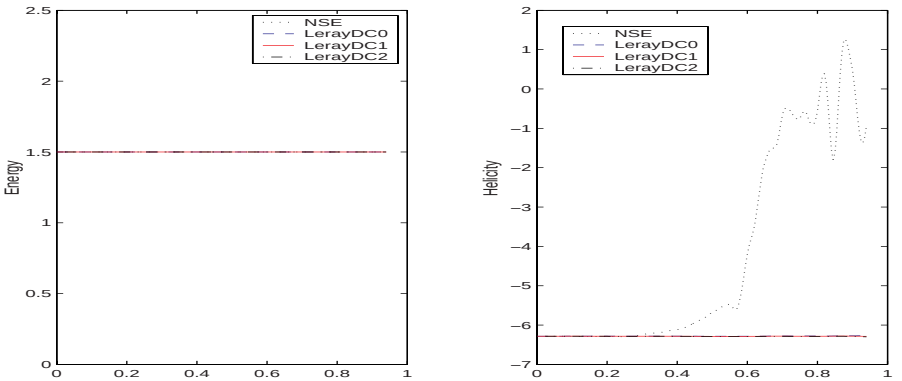

Fig. 3 Energy and helicity vs. time of an extrapolated Crank-Nicholson scheme simulation of a flow with initial condition $u_0 = \langle \cos(2\pi z), \sin(2\pi z), \sin(2\pi x + y) \rangle$, $\nu = f = 0$, and $h = 1/32$ for the NSE and LerayDC $N = 0, 1, 2$. Energy is conserved by all the schemes, but LerayDC schemes approximately conserves helicity while the NSE scheme does not

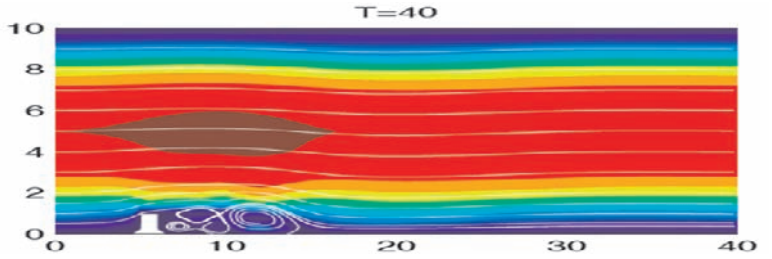

Fig. 4 DNS of Navier–Stokes with 45,138 degrees of freedom

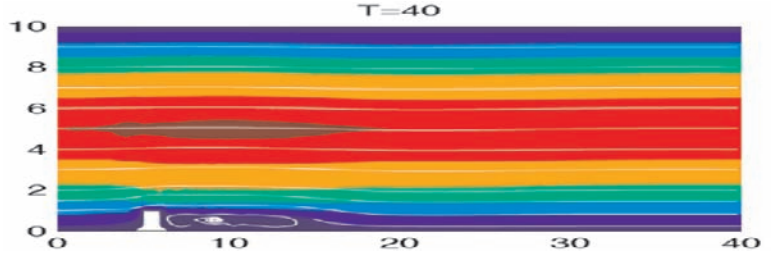

Fig. 5 Leray-α ($N = 0$ Leray-deconvolution) on 5,845 d.o.f.

with initial condition $u_0 = \langle \cos(2\pi z), \sin(2\pi z), \sin(2\pi(x+y)) \rangle$, no viscosity or external force ($\nu = f = 0$), and an $h = 1/32$ uniform discretization of the periodic unit cube. In the continuous case, all of these models conserve both energy and helicity under these conditions. For all four models simulations, energy is exactly conserved. In the helicity graph, the Leray-deconvolution models approximately conserve helicity while the NSE simulation does not.

Two dimensional numerical examples are also given in [34] for two dimensional transitional flow ($\nu = 1/600$) over a forward and backward facing step. Figure 4 shows the true solution of this problem, run for the Navier–Stokes equations on a very fine mesh ($45,138$ degrees of freedom), and show the solution at time $T = 40$ seconds. Here it is seen that eddies form behind the step, shed, and new eddies form. Since the purpose of turbulence modeling is to use them with many less d.o.f. than for a DNS, we run the same problem on a much coarser mesh (only $5,845$ d.o.f.) for the Leray-α model and for the Leray-deconvolution $N = 2$ models. Figure 5 shows the results for the Leray-α model: an eddy forms behind the step and stretches out. The Leray$-\alpha$ model is too dissipative. However, for the Leray-deconvolution $N = 2$ model shown in Fig. 6 on that same mesh, eddies are seen to break off and new ones form behind the step.

The analysis and computations of [31, 34] make a strong case that Leray-deconvolution preserves solution properties, adds accuracy, decreases error and increases physical fidelity.

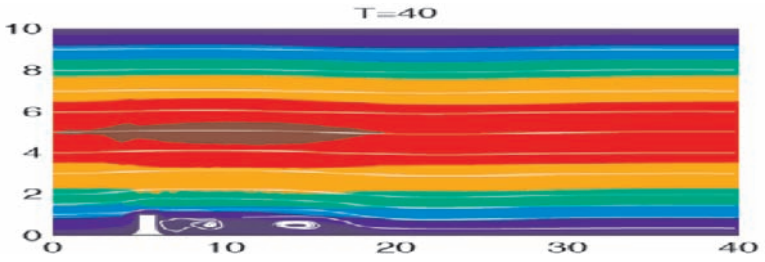

Fig. 6 Leray-deconvolution $N = 2$ simulation on 5,845 degree of freedom mesh

5.2 The NS-α-Deconvolution Regularization of the NSE

The NS-α-deconvolution model [46] is a helicity-corrected Leray-deconvolution model. One drawback of Leray-deconvolution is an inaccurate treatment of three dimensional rotation. Helicity is as important as energy for understanding three dimensional turbulent flow [43, 13, 9]. However, the nonlinear effects of the Leray-deconvolution model non-physically create and dissipate helicity [48]. By adding a helicity-correcting term to Leray-deconvolution (see [46]), a model which treats helicity in a physically accurate manner is recovered: the NS-α-deconvolution model.

Since NS-α-deconvolution has only very recently been proposed, the mathematical theory behind this model has not yet been developed as far as that of the Leray-deconvolution model (but this work is currently underway!). What has been proven is that the NS-α-deconvolution model conserves both a model energy and helicity, and is nonlinearly stable [46]. Define the natural energy and energy dissipation norms of NS-α-deconvolution:

$$\|v\|^2_{E(NS\alpha D)} := \frac{1}{|\Omega|}(v, D_N\overline{v}) = \frac{1}{2|\Omega|}\left[\|\overline{v}\|^2_D + \delta^2\|\nabla\overline{v}\|^2_D\right]$$
$$\|v\|^2_{\epsilon(NS\alpha D)} := \frac{\nu}{|\Omega|}(\nabla v, \nabla D_N\overline{v}) = \frac{\nu}{|\Omega|}\left[\|\nabla\overline{v}\|^2_D + \delta^2\|\Delta\overline{v}\|^2_D\right].$$

Theorem 6. *(From [46]) Solutions of NS-α-deconvolution on a periodic domain in three dimensions, for $\nu = f = 0$, conserve both energy and helicity: For $T > 0$,*

$$\|v(T)\|_{E(NS\alpha D)} = \|v(0)\|_{E(NS\alpha D)}, \quad (v(T), \nabla \times v(T)) = (v(0), \nabla \times v(0)).$$

While if $\nu > 0$ and $f \neq 0$

$$\|v(T)\|^2_{E(NS\alpha D)} + \nu\int_0^T \|\nabla v\|^2_{\epsilon(NS\alpha D)}dt \leq \|v_0\|^2_{E(NS\alpha D)} + C(N)\nu^{-1}\|f\|^2_{L^2(H^{-1})}.$$

In [47], a trapezoidal FEM for NS-α that preserves both energy and helicity is analyzed. It extends to a similar scheme for NS-α-deconvolution. The convergence analysis for the generalized scheme shows its velocity converges

to a NSE solution at the rate of $O(\Delta t^2+h^k+h^{2N+2})$, where (P_k, P_{k-1}), $k \geq 2$ elements are used. For the higher order elements, using $N = 0$ will give sub-optimal convergence rates. However, if $N \geq \frac{1}{2}k-1$ optimal convergence rates can be obtained. Numerical results to test this theory are currently underway, as are experiments to compare the NS-α scheme ($N = 0$) to the NS-α-deconvolution ($N \geq 1$) scheme.

6 Complex Fluids: the Case of MHD Turbulence

Magnetically conducting fluids arise in important applications including plasma physics, geophysics and astronomy. The difficulties of accurately modeling and simulating turbulent flows are magnified many times over in the MHD case. They are evinced by the more complex dynamics of the flow due to the coupling of Navier–Stokes and Maxwell equations via the Lorentz force and Ohm's law. The MHD equations are central to plasma confinement, controlled thermonuclear fusion, liquid-metal cooling of nuclear reactors, electromagnetic casting of metals, MHD sea water propulsion.

Let $u(t,x), p(t,x), B(t,x)$ be the velocity, pressure, and the magnetic field of the flow, driven by the velocity body force f and magnetic field force curl g:

$$\begin{aligned} &u_t + \nabla\cdot(uu) - \frac{1}{\mathrm{Re}}\Delta u + \frac{S}{2}\nabla(B^2) - S\nabla\cdot(BB) + \nabla p = f,\\ &B_t + \frac{1}{\mathrm{Re_m}}\nabla\times(\nabla\times B) + \nabla\times(B\times u) = \nabla\times g,\\ &\nabla\cdot u = 0, \nabla\cdot B = 0. \end{aligned} \tag{17}$$

Here Re, $\mathrm{Re_m}$, and S are the Reynolds, the magnetic Reynolds and the coupling number, respectively, see , e.g. [23].

If $^{-\delta_1}$, $^{-\delta_2}$ denote two local, spacing averaging operators with different lengthscales for different physical processes that commute with the differentiation, then averaging (17) gives the following non-closed equations for $\overline{u}^{\delta_1}$, $\overline{B}^{\delta_2}$, $\overline{p}^{\delta_1}$ in $(0,T)\times\Omega$:

$$\begin{aligned} &\overline{u}^{\delta_1}_t + \nabla\cdot(\overline{uu}^{\delta_1}) - \frac{1}{\mathrm{Re}}\Delta\overline{u}^{\delta_1} - S\nabla\cdot(\overline{BB}^{\delta_1}) + \nabla\Big(\frac{S}{2}\overline{B^2}^{\delta_1} + \overline{p}^{\delta_1}\Big) = \overline{f}^{\delta_1},\\ &\overline{B}^{\delta_2}_t + \frac{1}{\mathrm{Re_m}}\nabla\times(\nabla\times\overline{B}^{\delta_2}) + \nabla\cdot(\overline{Bu}^{\delta_2}) - \nabla\cdot(\overline{uB}^{\delta_2}) = \nabla\times\overline{g}^{\delta_2},\\ &\nabla\cdot\overline{u}^{\delta_2} = 0, \quad \nabla\cdot\overline{B}^{\delta_2} = 0. \end{aligned} \tag{18}$$

The usual closure problem which we study here arises because $\overline{uu^T}^{\delta_1} \neq \overline{u}^{\delta_1}\,\overline{u}^{\delta_1}$, $\overline{BB^T}^{\delta_1} \neq \overline{B}^{\delta_1}\,\overline{B}^{\delta_1}$, $\overline{uB^T}^{\delta_2} \neq \overline{u}^{\delta_1}\,\overline{B^T}^{\delta_2}$. We study (17) hence (18) subject to periodic boundary conditions. The closure problem is to replace the tensors $\overline{uu^T}^{\delta_1}$, $\overline{BB^T}^{\delta_1}$, $\overline{uB^T}^{\delta_2}$ with tensors $\mathscr{T}(\overline{u}^{\delta_1},\overline{u}^{\delta_1})$, $\mathscr{T}(\overline{B}^{\delta_2},\overline{B}^{\delta_2})$, $\mathscr{T}(\overline{u}^{\delta_1},\overline{B}^{\delta_2})$, respectively, depending only on $\overline{u}^{\delta_1}, \overline{B}^{\delta_2}$ and not u, B.

Call w, q, W the approximations to $\overline{u}^{\delta_1}, \overline{p}^{\delta_1}, \overline{B}^{\delta_2}$, the zeroth order MHD ADM is given by:

$$\begin{aligned} &w_t + \nabla \cdot (\overline{ww}^{\delta_1}) - \frac{1}{\mathrm{Re}} \Delta\, w - S\nabla \cdot (\overline{W\,W}^{\delta_1}) + \nabla q = \overline{f}^{\delta_1}, \\ &W_T + \frac{1}{\mathrm{Re_m}} \nabla \times (\nabla \times W) + \nabla \cdot (\overline{Ww}^{\delta_2}) - \nabla \cdot (\overline{wW}^{\delta_2}) = \nabla \times \overline{g}^{\delta_2}, \\ &\nabla \cdot w = 0, \quad \nabla \cdot W = 0. \end{aligned} \tag{19}$$

The model considered can be developed for quite general averaging operators, see e.g. [1]. The choice of averaging operator in (19) is the differential filter $(-\delta^2 \Delta + I)^{-1}$. (We use different lengthscales for the Navier–Stokes and Maxwell equations).

The main theoretical result in [27] states that a unique strong solution of the MHD LES model (19) exists globally in time, for large data and general $\mathrm{Re}, \mathrm{Re}_m > 0$ and that it satisfies an energy equality.

Theorem 7. *Let $\delta_1, \delta_2 > 0$ be fixed. For any $(\overline{u_0}^{\delta_1}, \overline{B_0}^{\delta_2}) \in V$ and $(\overline{\boldsymbol{f}}^{\delta_1}, curl\, \overline{\boldsymbol{g}}^{\delta_2}) \in L^2(0,T;H)$, there exists a unique strong solution (w, W) to (19) in $L^\infty(0,T;H^1(\Omega)) \cap L^2(0,T;H^2(\Omega))$ and $w_t, W_t \in L^2((0,T)\times\Omega)$. Moreover,*

$$E(t) + \int_0^t \epsilon(\tau) d\tau = E(0) + \int_0^t \mathscr{P}(\tau) d\tau,$$

where

$$\begin{aligned} E(t) &= \frac{{\delta_1}^2}{2} \|\nabla w(t,\cdot)\|_0^2 + \frac{1}{2}\|w(t,\cdot)\|_0^2 + \frac{{\delta_2}^2 S}{2}\|\nabla W(t,\cdot)\|_0^2 + \frac{S}{2}\|W(t,\cdot)\|_0^2, \\ \epsilon(t) &= \frac{{\delta_1}^2}{\mathrm{Re}}\|\Delta w(t,\cdot)\|_0^2 + \frac{1}{\mathrm{Re}}\|\nabla w(t,\cdot)\|_0^2 + \frac{{\delta_2}^2 S}{\mathrm{Re_m}}\|\Delta W(t,\cdot)\|_0^2 + \frac{S}{\mathrm{Re_m}}\|\nabla W(t,\cdot)\|_0^2, \\ \mathscr{P}(t) &= (\boldsymbol{f}(t), w(t)) + S(\nabla \times \boldsymbol{g}(t), W(t)). \end{aligned}$$

In the proof we use the semigroup approach of [5], based on the machinery of nonlinear differential equations of accretive type in Banach spaces. The other results derived for the model (19) in [27] concern: (i) *regularity of the solution*, (ii) *error estimates for the model*, (iii) *conservation laws* and (iv) the model predicts Alfvén waves correctly.

References

1. Adams NA, Stolz S (2001) Deconvolution methods for subgrid-scale approximation in large-eddy simulation. In: Geurts BJ (Eds) Modern simulation Strategies for turbulent flow:21–44. R.T. Edwards, Flourtown.
2. Adams NA, Stolz S (2002) A subgrid-scale deconvolution approach for shock capturing. J Comp Phys 178: 391–426

3. André JC, Lesieur M (1977) Influence of helicity on the evolution of isotropic turbulence at high Reynolds number. J Fluid Mech 81:187–207
4. Baker G (1976) Galerkin approximations for the Navier–Stokes equations. Harvard University.
5. Barbu V, Sritharan SS (2001) Flow invariance preserving feedback controllers for the Navier–Stokes equation. J Math Anal Appl 255(1):281–307
6. Berselli LC, Iliescu T, Layton W (2006) Mathematics of large eddy simulation of turbulent flows. Springer, Berlin
7. Bertero M, Boccacci B (1998) Introduction to inverse problems in imaging. IOP Publishing Ltd
8. Bourne J, Orszag S (1977) Spectra in helical three-dimensional homogeneous isotropic turbulence. Phys Rev Lett E 55:7005–7009
9. Chen Q, Chen S, Eyink G (2003) The joint cascade of energy and helicity in three dimensional turbulence. Phys Fluids 15(2):361–374
10. Chen S, Foias C, Holm D, Olson E, Titi E, Wynne S (1998) The Camassa-Holm equations as a closure model for turbulent channel and pipe flow. Phys Rev Lett 81:5338–5341
11. Chen S, Holm D, Margolin L, Zhang R (1999) Direct numerical simulations of the Navier–Stokes alpha model. Physica D 133:66–83
12. Cheskidov A, Holm DD, Olson E, Titi ES (2005) On a Leray-α model of turbulence. Proc R Soc Lond Ser A: Math Phys Eng Sci 461(2055):629–649
13. Ditlevsen P, Giuliani P (2001) Cascades in helical turbulenc. Phys Rev E 63, Art no 036304:1–4.
14. Dunca A (2004) Space averaged Navier–Stokes equations in the presence of walls. Ph.D. thesis, University of Pittsburgh
15. Dunca A, Epshteyn Y (2006) On the Stolz-Adams deconvolution model for the large eddy simulation of turbulent flows. SIAM J Math Anal 37(6):1890–1902
16. Foias C, Holm DD, Titi ES (2001) The Navier–Stokes-alpha model of fluid turbulence. Physica D 152-153:505–519
17. Foias C, Holm DD, Titi ES (2002) The three dimensional viscous Camassa-Holm equations, and their relation to the Navier–Stokes equations and turbulence theory. J Dyn Differ Equ 14(1):1–35
18. Geurts BJ (1997) Inverse modeling for large eddy simulation. Phys Fluids 9:3585–3587
19. Geurts BJ (2003) Elements of direct and large eddy simulation. Edwards, Flourtown
20. Geurts BJ, Holm DD (2003) Regularization modeling for large-eddy simulation. Phys Fluids 15(1):L13–L16
21. Geurts BJ, Holm DD (2006) Leray and LANS-alpha modeling of turbulent mixing. J Turbul 7, Art no 10:1–42
22. Guermond JL, Oden JT, Prudhomme S (2003) An interpretation of the Navier–Stokes-alpha model as a frame-indifferent Leray regularization. Phys D 177(1–4):23–30.
23. Gunzburger MD, Meir AJ, Peterson J (1991) On the existence, uniqueness, and finite element approximation of solutions of the equations of stationary, incompressible magnetohydrodynamics. Math Comp 56(194):523–563
24. Kraichnan R (1971) Inertial-range transfer in two- and three- dimensional turbulence. J Fluid Mech 47:525–535
25. Labovschii A, Trenchea C (in preparation) Identification of averaging radii for the LES in MHD flows.

26. Labovschii A, Trenchea C (2007) Large eddy simulation for MHD flows. Tech report, University of Pittsburgh
27. Labovschii A, Trenchea C (in preparation) Approximate deconvolution models for large eddy simulation for MHD flows. Tech report, University of Pittsburgh
28. Layton W, Lewandowski R (2003) A simple and stable scale-similarity model for large eddy simulation: energy balance and existence of weak solutions. Appl Math Lett 16(8):1205–1209
29. Layton W, Lewandowski R (2006) On a well-posed turbulence model. Discrete and Continuous Dynamical Systems—Series B 6:111–128
30. Layton W, Lewandowski R (2006) Residual stress of approximate deconvolution large eddy simulation models of turbulence. J Turbul 46, Art no 2:1–21
31. Layton W, Lewandowski R (2008) A high accuracy Leray-deconvolution model of turbulence and its limiting behavior. Anal Appl 6(1):1–27
32. Layton W, Manica C, Neda M, Rebholz L (2007) The joint Helicity-Energy cascade for homogeneous, isotropic turbulence generated by approximate deconvolution models. Adv Appl Fluid Mech, to appear
33. Layton W, Manica C, Neda M, Rebholz L (2007) Numerical analysis and computational comparisons of the NS-alpha and NS-omega regularizations. Tech report, University of Pittsburgh
34. Layton W, Manica C, Neda M, Rebholz L (2008) Numerical analysis and computational testing of a high accuracy Leray-deconvolution model of turbulence. Numer Meth PDEs 24(2):555–582
35. Layton W, Neda M (2006) The energy cascade for homogeneous, isotropic turbulence generated by approximate deconvolution models. Tech. report, University of Pittsburgh
36. Layton W, Neda M (2007) A similarity theory of approximate deconvolution models of turbulence. J Math Anal Appl 333(1):416–429
37. Layton W, Neda M (2007) Truncation of scales by time relaxation. J Math Anal Appl 325(2):788–807
38. Layton W, Stanculescu I (2007) K-41 optimized approximate deconvolution models. Int J Comp Sci and Math 1(2–4):396–411
39. Layton W, Trenchea C, Stanculescu I (2008) Theory of the NS-omega model. Tech report, University of Pittsburgh
40. Leray J (1934) Essay sur les mouvements plans d'une liquide visqueux que limitent des parois. J Math Pur Appl, Paris Ser IX 13:331–418
41. Lewandowski R (2006) Vorticities in a LES model for 3D periodic turbulent flows. J Math Fluid Mech 8:398–422
42. Manica CC, Kaya-Merdan S (2006) Convergence analysis of the finite element method for a fundamental model in turbulence. Tech report, University of Pittsburgh (`http://www.math.pitt.edu/techreports.html`)
43. Moffatt HK, Tsinober A (1992) Helicity in laminar and turbulent flow. Annu Rev Fluid Mech 24:281–312
44. Moreau JJ (1961) Constantes d'unilot tourbilloinnaire en fluide parfait barotrope. C R Acad Sci Paris 252:2810–2812
45. Muschinski A (1996) A similarity theory of locally homogeneous and isotropic turbulence generated by a Smagorinsky-type LES. J Fluid Mech 325:239–260
46. Rebholz L (submitted) A family of new high order NS-alpha models arising from helicity correction in Leray turbulence models. TR MATH 06-19, University of Pittsburgh

47. Rebholz L, Miles W (submitted) Computing NS-alpha with greater physical accuracy and higher convergence rates.
48. Rebholz LG (2007) Conservation laws of turbulence models. J Math Anal Appl 326(1):33–45
49. Stanculescu I (2007) Existency theory of abstract approximate deconvolution models of turbulence. Tech report, University of Pittsburgh
50. Stolz S, Adams NA (1999) An approximate deconvolution procedure for large-eddy simulation. Phys Fluids 11:1699–1701
51. Stolz S, Adams NA, Kleiser L (2001) An approximate deconvolution model for large-eddy simulation with application to incompressible wall-bounded flows. Phys Fluids 13:997–1015
52. Stolz S, Adams NA, Kleiser L (2001) The approximate deconvolution model for LES of compressible flows and its application to shock-turbulent-boundary-layer interaction. Phys Fluids 13:2985–3001
53. Stolz S, Adams NA, Kleiser L (2002) The approximate deconvolution model for compressible flows: isotropic turbulence and shock-boundary-layer interaction. In: Friedrich R, Rodi W (eds) Advances in LES of complex flows. Kluwer, Dordrect

Adaptive Turbulence Computation Based on Weak Solutions and Weak Uniqueness

Johan Hoffman

School of Computer Science and Communication, KTH, SE-100 44 Stockholm, Sweden, jhoffman@csc.kth.se

Abstract. We review our work on adaptivity and error control for turbulent flow, and we present recent developments on turbulent boundary layer flow. The computational method G2 is not based on filtering of the Navier-Stokes (NS) equations, and thus no Reynolds (subgrid) stresses are introduced. Instead the mathematical basis is ϵ-weak solutions to the NS equations and weak uniqueness of such ϵ-weak solutions. Based on this mathematical framework we construct adaptive finite element methods for the computation of (mean value) output in turbulent flow, where the mesh is refined with respect to a posteriori estimates of the error in the output of interest. The a posteriori error estimates are based on stability information from the numerical solution of an associated dual (adjoint) problem with data given by the output of interest. To model turbulent boundary layer separation we use a skin friction boundary layer model, and we also consider the case of zero skin friction corresponding to solving the inviscid Euler equations with slip boundary conditions, which we refer to as an EG2 method. The results of EG2 computations suggest a new resolution to the d'Alembert paradox, and a new scenario for turbulent boundary layer separation.

Keywords: Turbulent flow, Adaptive mesh refinement, A posteriori error estimation, Duality, Finite element method, Turbulent boundary layer separation

1 Introduction

In this paper we review our work on adaptive turbulence computation, and report on recent work on turbulent boundary layer separation.

For efficiency in high Reynolds number flow computations, a locally varying degree of resolution is necessary, with relatively low resolution of laminar, smooth flow and high resolution of turbulent wakes, shocks and boundary layers. Phenomena demanding high resolution is usually very localized and thus local mesh refinement can drastically reduce the number of degrees of freedom in a computation, compared to using a uniform mesh. The precise location of such phenomena is not known a priori, since separation, transition and shocks are part of the solution, and thus adaptive mesh refinement

J. Meyers et al. (eds.), Quality and Reliability of Large-Eddy Simulations,

based on a posteriori error estimation is needed. To asses the quality of a computed solution we also need a posteriori error estimates, since a priori error estimation necessarily is crude without feedback from the computation.

A framework for adaptivity and a posteriori error estimation for Galerkin finite element methods (FEM) was developed in the 1990s, primarily by the groups of Johnson at Chalmers [16], Rannacher at Heidelberg University [3], and Süli at Oxford University [20]. A posteriori error estimates for an output of interest was derived in terms of a computable residual and the solution of a linearized dual (or adjoint) problem. In CFD, applications of adaptive finite element methods based on this framework have been increasingly advanced, with e.g. computations of laminar incompressible flow in [2, 19, 23, 4], and laminar compressible flow in [39, 22, 1, 8, 6, 7, 50]. To extend this framework also to turbulent flow a number of major challenges had to be addressed, including the mathematical problem of existence and uniqueness of solutions to the underlying Navier-Stokes (NS) equations, and the computational problem of high computational cost and insufficient resolution.

The extension of the framework for a posteriori error estimation to turbulent flow was initially [24, 25] approached in the setting of large eddy simulation (LES), where the error was estimated with respect to the filtered solution, resulting in an error estimate consisting of a FEM discretization error and a subgrid modeling error, where the subgrid modeling error had to be estimated with respect to an a priori model of the true Reynolds stresses (using e.g. a scale similarity model, see [49]). Although providing a framework for a posteriori error estimation for LES, the main drawback of the approach in [25] is the presence of the true Reynolds stresses in the modeling error estimate. For other work on error estimation in LES, see e.g. [49, 18, 15, 13, 14, 52].

To characterize turbulent flow mathematically we may identify two main approaches: (i) methods based on averaging (filtering) of the NS equations in the spirit of Reynolds [47] and Kolmogorov [41, 42, 40], such as RANS and LES [49], introducing Reynolds (subgrid) stresses that need to be modelled in turbulence (subgrid) models, and (ii) methods from functional analysis based on weak solutions of NS equations proven to exist by Leray [43] in 1934, without any explicit averaging of the equations apart from the weak form of the equations, and without introducing any Reynolds stresses. The weak form of the equations, with the equations multiplied by a set of smooth test functions and integrated, is also the basis for FEM. Even though Leray himself referred to his weak solutions as turbulent solutions, the study of weak solutions to characterize turbulent flow is very limited. One may get the impression that the result of existence of a weak solution is mainly seen as just a step towards proving existence of also a classical solution, formulated as one of the Clay $1 million Prize problems [9], although progress in this direction has been very slow since the proof of Leray.

For high Reynolds numbers direct numerical simulation (DNS) of NS equations is not possible due to the computational cost, and instead computing underresolved approximate solutions is the only option. In the averaging

approach (i) such numerical approximations, using a suitable discretization method, are interpreted as mean values of underlying DNS solutions, whereas in (ii) one may interpret FEM approximations as approximate weak solutions to NS equations [30, 32].

A key issue for underresolved turbulent flow is (turbulent) viscous dissipation; in most discretization methods of NS equations numerical viscosity is introduced, and in (i) viscosity is also introduced by the turbulence model. In assessing the quality of a numerical approximation using the averaging framework (i) one is then typically faced with the following challenges; to separately estimate the numerical error and the modeling error, which involve estimating the true Reynolds stresses, and to distinguish between numerical and modeling viscosity.

A main difference between (i) and (ii) is also that in (i) the underlying NS equations are modified (by averaging), but in (ii) the equations are the same but the degree of satisfaction of the equations is relaxed from pointwise satisfaction to only satisfaction in mean value. In particular, in (ii) no extra terms appear (no Reynolds stresses) and thus one should potentially be able to circumvent the closure problem (turbulence modeling); by using FEM to directly compute approximate weak solutions.

To justify the use of weak solutions to model turbulent flow, one needs to specify what output of a turbulent flow is modelled; a weak solution is not a pointwise approximation of a turbulent velocity field (as in a DNS), and not an obvious mean value of an underlying turbulent velocity field either (as in RANS or LES). In addition, there is no uniqueness result for weak solutions, and the existence result by Leray does not extend to inviscid flow so that weak solutions to the Euler equations cannot be proven to exist.

In [30, 32] a new mathematical framework for characterizing turbulent flow is presented based on ϵ-weak solutions, a relaxation of Lerays concept of a weak solution (thus opposite the Clay Prize problem, which asks for a more regular solution than Leray), and weak (output) uniqueness. It is shown that a certain least squares stabilized finite element method, referred to as a General Galerkin (G2) method, produces ϵ-weak solutions, and that such a solution is unique with respect to certain mean value output. That is, a G2 solution is a well defined mathematical object that can be shown to produce a unique output, such as the drag and lift of an airplane, for example. We note that this theory also trivially extends to the inviscid Euler equations, where the G2 solution is shown to satisfy a local energy estimate with dissipation of kinetic energy in turbulence and shocks [30, 32]. Based on this mathematical framework, adaptive G2 methods are constructed and shown to be very efficient in the computation of e.g. drag for bluff bodies in [31, 26, 27, 29]. For related work on dissipative (exact) weak solutions to the Euler equations see [12], where we note that the existence of (exact) weak solutions is only an assumption.

We note that often a numerical approximation can be interpreted within any of the two frameworks (i) and (ii); a G2 solution may be interpreted as

LES with implicit filtering by the finite element mesh and the least squares stabilization acting as a subgrid model, and a finite volume LES approximation may be proven to be an ϵ-weak solution. See e.g. [21, 5] for discussions on the dual interpretation of numerical stabilization and subgrid models.

The results in [31, 26, 27, 29] indicate that for simple geometries it is possible, to a relatively low cost, to adaptively resolve laminar boundary layers for accurate prediction of separation. On the other hand, turbulent boundary layers are too computationally demanding for any computer of today or tomorrow, and alternative approaches are needed. To model flow with turbulent boundary layers one typically divides the flow into an interior domain and a boundary layer, where the boundary layer provides boundary conditions for the interior domain. To provide realistic boundary conditions various approaches have been presented to model the boundary layer [48, 51], for example based on boundary layer theory (BLT) or turbulence modeling. Inspired by the work in [36, 38, 37, 35] where a slip with friction boundary condition is used to study reattachement of a low Reynolds number LES (with the friction based on BLT), in [28] a simple model for a turbulent boundary layer is suggested which is just a friction boundary condition where the friction parameter is given by the skin friction of the turbulent boundary layer. By reducing the skin friction parameter, corresponding to increasing the Reynolds number (see e.g. [51]), in [28] it is shown that this simple model is capable of predicting the delayed separation of a turbulent boundary layer in drag crisis of a circular cylinder.

The limiting case of zero skin friction corresponds to solving the Euler equations with slip boundary conditions using G2, which we refer to as an EG2 method [28]. In EG2 computations of the flow past an airfoil we obtain good agreement with experiments, capturing the correct separation under increasing angle of attack [33]. We note that with EG2 we have no boundary layer, and without any boundary layer, separation in accordance with the standard model (see e.g. [46, 51]); with kinetic energy dissipation in the boundary layer together with an adverse pressure gradient, is not possible and thus there must be another mechanism for separation. In [33] we present a new scenario for separation based on the pressure gradient in the normal direction; that is a force balance in the direction normal to the boundary rather than in the tangent direction as in the standard model. In particular, EG2 computations suggest a new resolution of the d'Alembert paradox [34], different from the generally accepted one by Prandtl [46] based on BLT.

This paper is structured as follows: in Section 2 we briefly review the framework for ϵ-weak solutions, weak uniqueness, and a posteriori error estimation for incompressible flow, and in Section 3 we present recent work on turbulent boundary layer flow and separation.

2 A Framework for Adaptive Turbulence Computation

In this section we present a framework for adaptive turbulence computation based on weak solutions of the fundamental equations. The mathematical basis is ϵ-weak solutions and weak uniqueness, and in computations we use a weighted least squares stabilized finite element method, which we refer to as a General Galerkin (G2) method. We present a posteriori error estimates, and recall some results for benchmark problems illustrating the adaptive algorithm.

2.1 The Navier-Stokes Equations

The incompressible Navier–Stokes (NS) equations for a constant temperature Newtonian fluid with constant kinematic viscosity $\nu > 0$ enclosed in an open domain Ω in $\mathbb{R}^3$, together with suitable boundary conditions, take the form:

$$R(\hat{u}) = 0, \quad \text{in } \Omega \times I, \tag{1}$$

for $\hat{u} = (u, p)$, with $u(x,t)$ the *velocity vector* and $p(x,t)$ the *pressure* at (x,t), $I = (0,T)$ is a time interval, and $R(\hat{u}) \equiv \bar{R}(\hat{u}) - (f,0) = (\bar{R}_1(\hat{u}), \bar{R}_2(u)) - (f,0)$, with

$$\begin{aligned} \bar{R}_1(\hat{u}) &= \dot{u} + u \cdot \nabla u + \nabla p - \nu \Delta u, \\ \bar{R}_2(u) &= \nabla \cdot u. \end{aligned} \tag{2}$$

A given flow may be characterized by the *Reynolds number* $Re = UL/\nu$, where U and L are representative velocity and length scales, respectively. The Reynolds number characterizes the relative importance of viscous and intertial effects in the flow, with the limiting case of $Re = \infty$ corresponding to the inviscid Euler equations with $\nu = 0$ in (1).

A *strong (or classical) solution* to NS equations is a function $\hat{u}$ that satisfies the equations exactly, making the *residual* pointwise zero: $R(\hat{u}) = 0$. The existence of a strong solution to NS equations is an open problem, listed as one of the Clay Institute $1 million Prize problems [9].

The only existence result available for NS is instead the one by Jean Leray, who in 1934 proved the existence of a so called *weak solution* [43], satisfying the NS equations in a mean value sense: $\hat{u}$ is a weak solution if

$$((R(\hat{u}), \hat{v})) = 0, \tag{3}$$

for all *test functions* $\hat{v}$ in a *test space* $\hat{V}$ with norm $\|\cdot\|_{\hat{V}}$, consisting of suitable differentiable functions, and $R(\hat{u})$ is assumed to belong to a space dual to $\hat{V}$, and $((\cdot,\cdot))$ denotes a duality pairing. The proof of Leray critically depends on the viscous term in the NS equations, and thus does not extend to the inviscid Euler equations, for which no existence result is available.

2.2 Definition of ϵ-Weak Solutions

In [30, 32] the concept of an *ϵ-weak solution* is introduced, as a relaxation of the weak solution of Leray, which is an approximate weak solution with a residual less than ϵ measured in a weak norm. We define for $\hat{v} = (v, q) \in \hat{V}$,

$$\begin{aligned}((R(\hat{u}), \hat{v})) \equiv ((\dot{u}, v)) + ((u \cdot \nabla u, v)) - ((\nabla \cdot v, p)) \\ + ((\nabla \cdot u, q)) + ((\nu \nabla u, \nabla v)) - ((f, v)),\end{aligned} \tag{4}$$

where

$$\hat{V} = \{\hat{v} = (v, q) \in [H^1(Q)]^4 : v \in L_2(H_0^1(\Omega))^3\},$$

and $((\cdot, \cdot))$ is the $[L_2(Q)]^m$ inner product with $m = 1, 3$, or a suitable duality pairing, over the space-time domain $Q = \Omega \times I$. In order for all the terms in (4) to be defined, we ask $u \in L_2(I; H_0^1(\Omega)^3)$, $(u \cdot \nabla)u \in L_2(I; H^{-1}(\Omega)^3)$, $\dot{u} \in L_2(I; H^{-1}(\Omega)^3)$, $p \in L_2(I; L_2(\Omega))$, and $f \in L_2(I; H^{-1}(\Omega)^3)$, where $H_0^1(\Omega)$ is the usual Sobolev space of vector functions being zero on the boundary Γ and square integrable together with their first derivatives over Ω, with dual $H^{-1}(\Omega)$. As usual, $L_2(I; X)$ with X a Hilbert space denotes the set of functions $v : I \to X$ which are square integrable.

Definition 1. *We define $\hat{u} \in \hat{V}$ to be an ϵ-weak solution if*

$$|((R(\hat{u}), \hat{v}))| \leq \epsilon \|\hat{v}\|_{\hat{V}} \quad \forall \hat{v} \in \hat{V}, \tag{5}$$

where $\|\cdot\|_{\hat{V}}$ denotes the $H^1(Q)^4$-norm, and we define $\hat{W}_\epsilon$ to be the set of ϵ-weak solutions for a given $\epsilon > 0$.

Note that for simplicity we here ask also the solution $\hat{u}$ to belong to the test space $\hat{V}$, which require more regularity than necessary; for the formulation (5) to make sense, it is sufficient that $R(\hat{u})$ belongs to $\hat{V}'$, the dual space of $\hat{V}$. Equivalently, we may say that $\hat{u} \in \hat{V}$ is an ϵ-weak solution if

$$\|R(\hat{u})\|_{\hat{V}'} \leq \epsilon,$$

where the norm $\|\cdot\|_{\hat{V}'}$ is a weak norm measuring mean values of $R(\hat{u})$ with decreasing weight as the size of the mean value decreases. Pointvalues are thus measured very lightly.

We note that a strong solution $\hat{u}$ to the NS equations is an ϵ-weak solution for all $\epsilon \geq 0$, while an ϵ-weak solution for $\epsilon > 0$ may be viewed as an approximate weak solution. In Theorem 3 the existence of ϵ-weak solutions is established for any $\epsilon > 0$, a result which also includes the case of the inviscid Euler equations with $\nu = 0$.

2.3 Weak Uniqueness and the Dual Problem

No uniqueness result is available for weak solutions, but for ϵ-weak solutions we can introduce the notion of weak (output) uniqueness [30, 32]. We then

define a *quantity of interest*, or *output*, related to a given ϵ-weak solution $\hat{u}$, in the form of a scalar quantity

$$M(\hat{u}) = ((\hat{u}, \hat{\psi})), \tag{6}$$

which represents a mean-value in space-time, where $\hat{\psi} \in L_2(Q)$ is a given weight function. In typical applications the output could be drag or lift of a body in the flow.

We now seek to estimate the difference in output of two ϵ-weak solutions $\hat{u} = (u, p)$ and $\hat{w} = (w, r)$. We thus seek to estimate a certain form of *output sensitivity* of the space $\hat{W}_\epsilon$ of ϵ-weak solutions. To this end, we introduce the following linearized dual problem of finding $\hat{\varphi} = (\varphi, \theta) \in \hat{V}$, such that

$$a(\hat{u}, \hat{w}; \hat{v}, \hat{\varphi}) = ((\hat{v}, \hat{\psi})), \quad \forall \hat{v} \in \hat{V}_0, \tag{7}$$

where $\hat{V}_0 = \{\hat{v} \in \hat{V} : v(\cdot, 0) = 0\}$, and

$$\begin{aligned} a(\hat{u}, \hat{w}; \hat{v}, \hat{\varphi}) \equiv ((\dot{v}, \varphi)) + ((u \cdot \nabla v, \varphi)) + ((v \cdot \nabla w, \varphi)) \\ + ((\nabla \cdot \varphi, q)) - ((\nabla \cdot v, \theta)) + ((\nu \nabla v, \nabla \varphi)), \end{aligned}$$

with u and w acting as coefficients, and $\hat{\psi}$ is given data.

This is a linear convection-diffusion-reaction problem in variational form, u acting as the convection coefficient and ∇w as the reaction coefficient, and the time variable runs "backwards" in time with initial value $(\varphi(\cdot, T) = 0)$ given at final time T imposed by the variational formulation. The reaction coefficient ∇w may be large and highly fluctuating, and the convection velocity u may also be fluctuating.

Choosing now $\hat{v} = \hat{u} - \hat{w}$ in (7), we obtain

$$((\hat{u}, \hat{\psi})) - ((\hat{w}, \hat{\psi})) = a(\hat{u}, \hat{w}; \hat{u} - \hat{w}, \hat{\varphi}) = ((R(\hat{u}), \hat{\varphi})) - ((R(\hat{w}), \hat{\varphi})), \tag{8}$$

and thus we may estimate the difference in output as follows:

$$|M(\hat{u}) - M(\hat{w})| \leq 2\epsilon \|\hat{\varphi}\|_{\hat{V}}. \tag{9}$$

By defining the *stability factor* $S(\hat{u}, \hat{w}; \hat{\psi}) = \|\hat{\varphi}\|_{\hat{V}}$, we can write

$$|M(\hat{u}) - M(\hat{w})| \leq 2\epsilon S(\hat{u}, \hat{w}; \hat{\psi}), \tag{10}$$

and by defining

$$S_\epsilon(\hat{\psi}) = \sup_{\hat{u}, \hat{w} \in \hat{W}_\epsilon} S(\hat{u}, \hat{w}; \hat{\psi}), \tag{11}$$

we get the following theorem which expresses output uniqueness of $\hat{W}_\epsilon$:

Theorem 1. *For two ϵ-weak solutions $\hat{u}, \hat{w} \in \hat{W}_\epsilon$, we have that*

$$|M(\hat{u}) - M(\hat{w})| \leq 2\epsilon S_\epsilon(\hat{\psi}), \tag{12}$$

for $M(\cdot)$ defined by (6), and $S_\epsilon(\hat{\psi})$ defined by (11).

The size of the stability factor $S_\epsilon(\hat{\psi})$ reflects the output sensitivity, where we expect $S_\epsilon(\hat{\psi})$ to increase as the mean value becomes more local. In practice, there is a lower limit for ϵ, typically given by the maximal computational resoures, and thus $S_\epsilon(\hat{\psi})$ effectively determines the computability of different outputs.

Analytical estimates of $S_\epsilon(\hat{\psi})$ typically lead to exponential growth in ∇w, but computing approximations of the dual solution corresponding to drag and lift coefficients in turbulent flow, we find values of $S_\epsilon(\hat{\psi})$ which are in the range of $10^2 - 10^3$ [30], for which it is possible to choose ϵ so that $2\epsilon S_\epsilon(\hat{\psi}) < 1$, with the corresponding outputs thus being well defined (up to a certain tolerance). We attribute the fact that $\hat{\varphi}$ and derivatives thereof are not exponentially large, to cancellation effects from the oscillating reaction coefficient ∇w, with the sum of the real parts of the eigenvalues of ∇w being very small, with the sign being about as often positive as negative, see [30]. These cancellation effects seem to be impossible to account for in purely theoretical estimates, because knowledge of the underlying flow velocity is necessary.

2.4 Computation with G2 Methods

In computations we use stabilized finite element methods of the form: Find $\hat{U} \equiv \hat{U}_h \in \hat{V}_h$, where $\hat{V}_h \subset \hat{V}$ is a finite dimensional subspace defined on a computational mesh in space-time of mesh size h, such that

$$((R(\hat{U}), \hat{v})) + ((hR(\hat{U}), \bar{R}(\hat{v}))) = 0, \quad \forall \hat{v} \in \hat{V}_h, \tag{13}$$

where $R(\hat{U}) \equiv \bar{R}(\hat{U}) - (f, 0) = (\bar{R}_1(\hat{U}), \bar{R}_2(U)) - (f, 0)$, and for $\hat{w} = (w, r)$,

$$\begin{aligned} \bar{R}_1(\hat{w}) &= \dot{w} + U \cdot \nabla w + \nabla r - \nu \Delta w, \\ \bar{R}_2(w) &= \nabla \cdot w, \end{aligned} \tag{14}$$

with elementwise definition of second order terms. We refer to these methods as General Galerkin (G2) methods, and we thus refer to $\hat{U}$ as a *G2 solution*. Under suitable assumptions, choosing $\hat{v} = \hat{U}$ in (13) gives the following energy estimate [30]:

Theorem 2. *For $f = 0$, the solution $\hat{U}$ in (13) satisfies the following energy estimate:*

$$\frac{1}{2}\|U\|^2 + ((\nu \nabla U, \nabla U)) + ((hR(\hat{U}), R(\hat{U}))) \leq \frac{1}{2}\|u^0\|^2. \tag{15}$$

The term $((R(\hat{U}), v))$ corresponds to Galerkin's method and the term $((hR(\hat{u}), \bar{R}(\hat{v})))$ corresponds to a weighted residual least squares method with stabilizing effect expressed in (15). In particular, in [26] it is shown that the G2 dissipation in computations satisfies a law of finite dissipation (see [17]), with the dissipative term $((hR(\hat{U}), R(\hat{U})))$ being independent of h after some mesh refinement.

The following theorem guarantees the existence of an ϵ-weak solution to the NS equations for any $\epsilon > 0$, including also the inviscid case of the Euler equations with $\nu = 0$:

Theorem 3. *Assume that M_U, the maximum of the computed velocity $U(x,t)$, is bounded for all $h > 0$, then $\hat{U}$ is an ϵ-weak solution with $\epsilon = C_U\|hR(\hat{U})\|$, where $C_U = (C_i + M_U)$ and C_i is an interpolation constant. Theorem 2 also gives that $\epsilon \leq C\sqrt{h}$, with C depending on C_i, M_U and $\|u^0\|$.*

Theorem 3 shows that a G2 solution $\hat{U}$ is an ϵ-weak solution, and computing $\hat{U}$ we can directly determine the corresponding ϵ.

2.5 A Posteriori Error Estimation and an Adaptive Algorithm

We now let $\hat{u}$ be an ϵ-weak solution of the NS equations with ϵ small and we let $\hat{U}$ be a G2 solution, which can be viewed to be an ϵ_{G2}-weak solution with

$$\epsilon_{G2} = C_U\|hR(\hat{U})\| >> \epsilon. \tag{16}$$

By Theorem 1 we get the following a posteriori error estimate for a mean value output $M(\cdot)$ given by a function $\hat{\psi}$:

Theorem 4. *For a mean value output $M(\cdot)$ defined by (6), with $\hat{U}$ a G2 solution and $\hat{u} \in W_\epsilon$, and ϵ_{G2} defined by (16), we have that*

$$|M(\hat{u}) - M(\hat{U})| \leq (C_U\|hR(\hat{U})\| + \epsilon)S_{\epsilon_{G2}}(\hat{\psi}), \tag{17}$$

where $S_{\epsilon_{G2}}(\hat{\psi})$ is the stability factor defined by (11).

We note that for weak uniqueness the residual only needs to be small in a weak norm, and correspondingly for computability the G2 residual only needs to be small when weighted by h. This means that for accurate approximation of a mean value output $M(\cdot)$, the NS equations do not need to be satisfied pointwise, corresponding to a pointwise small residual, but only in an average sense, corresponding to the residual being small only in a weak norm. In computations we find that in fact the G2 residual typically is large pointwise for solutions corresponding to accurate approximation of mean value output, such as the drag of a bluff body.

Based on a sharper version of Theorem 4 with elementwise dual weights of the local residuals, see e.g. [27], we construct adaptive algorithms of the form:

Algorithm 5 (Adaptive G2) *Given an initial coarse computational space mesh $\mathcal{T}^0$, start at $k = 0$, then do*

(1) Compute approximation of the primal problem using $\mathcal{T}^k$.
(2) Compute approximation of the dual problem using $\mathcal{T}^k$.
(3) If the error is less than the tolerance, then STOP, else:

(4) Refine a fraction of the elements in $\mathcal{T}^k$ with largest local contribution to the global error.
(5) Set $k = k + 1$, then goto (1).

Examples in [31, 26, 27, 29] of computing drag for bluff body problems, show a very efficient method with accurate approximation of drag, lift, pressure coefficients and Strouhal numbers etc. using very few degrees of freedom compared to *ad hoc* refined computational meshes.

3 Turbulent Boundary Layers

In this section we review our recent and ongoing research on turbulent boundary layer flow. The computational cost of resolving laminar boundary layers by the mesh may be reasonable in many applications, but for turbulent boundary layers this is not an option. Instead the typical approach is to divide the computational domain into an interior part and a boundary layer, where the solution in the boundary layer provides boundary conditions for the interior part. Boundary layer modeling is a very intensive research area, with many different approaches based on e.g. boundary layer theory, turbulence modeling or multiscale resolution, see e.g. [48] for an overview.

3.1 Drag Crisis and Skin Friction Boundary Conditions

A challenging test problem for simulation of turbulent boundary layer separation is drag crisis, which refer to the problem of simulating the flow past a circular cylinder or a sphere at a Reynolds number so high (about 10^5) that the boundary layer undergoes transition to turbulence resulting in a delayed separation with smaller wake and a reduced drag.

To model turbulent boundary layer separation, in [28] a skin friction boundary layer model is introduced which is based on a Navier slip boundary condition with the friction parameter given by the skin friction of the turbulent boundary layer. A similar model was studied in [15, 13, 14, 52] for reattachement in low Reynolds number LES. Experiments indicate that the skin friction is typically decreasing slowly with the Reynolds number ($c_f \sim Re^{-0.2}$ for a flat plate [51]), and thus decreasing skin friction suggests a model for simulating drag crisis. The results in [28] show that indeed the decreasing skin friction results in delayed separation and a drag corresponding to that of drag crisis in experiments.

We note that drag crisis has earlier been studied computationally, using e.g. DES [10].

3.2 The EG2 Method

A natural question is then what happens when we let the skin friction go to zero, corresponding to the Reynolds number going to infinity? To approach

this question in [28] we again compute the flow past a circular cylinder, now using G2 to solve the inviscid Euler equations with slip boundary conditions, which we refer to as an EG2 method. We know that there exists an exact potential solution to this problem, corresponding to zero drag, and we know that by the Kelvin Theorem no vorticity should be able to develop from an irrotational initial solution as the potential solution.

Although, in the EG2 computations we find that the potential solution is unstable, and instead a turbulent solution develops with strong streamwise vorticity generation at separation. The stability of the potential solution is straight forward to analyze using linear stability analysis, with the stability depending on the real part of the eigenvalues of the gradient of the velocity field [30, 34], which due to the divergence free condition must include unstable eigenvalues unless all eigenvalues have zero real part:

Theorem 6. *Any exact solution $\hat{u}$ to the incompressible Euler equations is (exponentially) unstable unless all eigenvalues of ∇u have zero real part.*

Analyzing also the stability of the vorticity equations one finds that the acceleration of the flow in the streamwise direction at separation generates exponential growth of streamwise vorticity [30, 34], which we find in the computations as the unstable potential solution develops into a turbulent solution with generation of streamwise vorticity at separation (vortex stretching), and since the turbulent (ϵ-weak) solution is not an exact solution the Kelvin Theorem is no longer valid.

3.3 The d'Alembert Paradox

The instability of the potential solution suggests a new resolution to the d'Alembert paradox from 1752 [11], different from the generally accepted one by Prandtl from 1904 [46] being based on boundary layer theory. The d'Alembert paradox points to the obvious lack in agreement between the zero drag potential solution to the Euler equations proven to exist, and experimental observations showing significant drag increasing with the Reynolds number. In particular, the potential solution for the flow past an airfoil has no lift and thus flying would be mathematically impossible, and with the break-through of aviation at the end of the 19th and beginning of the 20th century, with the glider of Otto Lillienthal and the Flyer of the Wright brothers, the phenomenon of flying and the d'Alembert paradox were in great need of an explanation.

To approach this problem two ideas have had major impact on the field: the Kutta-Zhukovsky condition of fixating the separation of the flow past an airfoil to the trailing edge, resulting in a new solution with lift, and the boundary layer theory (BLT) of Prandtl from 1904 [46], postulating the importance of including a viscous boundary layer in the model even for very high Re by substituting the slip boundary condition of the Euler equations for the

no slip boundary condition of the Navier-Stokes equations. Prandtl also suggested a mechanism for separation with loss of kinetic energy of the flow in the boundary layer together with an adverse pressure gradient forcing the velocity in the boundary layer to zero, resulting in separation with recirculation. Even though not explicitly stated in Prandtl's 1904 paper, BLT together with his scenario for separation is generally accepted as the resolution of the d'Alembert paradox, see e.g. [45].

The new resolution of the paradox presented in [34] is fundamenally different from the resolution by Prandtl; being based on the instability of the potential solution and (streamwise) vorticity generation at separation of the turbulent (ϵ-weak) solutions. The two resolutions of the paradox are not compatible, and the vorticity generated at separation in EG2 computations cannot be explained within the paradigm of (the assumption of) an exact (classical) solution to the Euler equations.

3.4 Turbulent Boundary Layer Separation

Computing with EG2 (using a mesh of about 150 000 vertices) the flow past an airfoil NACA 0012 with increasing angle of attack [30], simulating take-off, we find separation of the flow not following the standard model of separation due to (i) loss of kinetic energy in the boundary layer together with (ii) an adverse pressure gradient in the flow direction, resulting in separation with recirculation when the tangential velocity of the flow is reversed.

In EG2 we have no boundary layer, and thus another mechanism must be responsible for separation. In particular, we find that at separation of the flow on the upper surface of the airfoil the flow is not retarded to zero along the boundary as in the standard model, but instead separation occurs as a thin layer is forming in the flow over which the streamwise velocity changes magnitude sharply from the free stream velocity to a much lower velocity that keeps decreasing until the low pressure in the resulting wake is so low that recirculation and turbulence is forming. We also note the streamwise vorticity forming at the trailing edge, as in the case of the circular cylinder, as a consequence of the instability of the potential solution.

The standard model based on Prandtl's 1904 model [46] is formulated as a force balance in the tangential direction along the boundary, whereas in [33] we instead propose an alternative model based on a force balance in the direction normal to the boundary; with separation given by the sign of the normal derivative of the pressure along the boundary.

The EG2 computations also couple to early results on Euler solvers [44], where promising results were obtained for sharp leading edge Delta wings. But without the sharp leading edge, results could not be explained within the framework of exact solutions to the Euler equations. In particular, two main objections were raised; the inability of computing the potential solution, and (ii) the violation of the Kelvin Theorem with vorticity generation without a sharp leading edge. On the other hand, within the framework of EG2 and

ϵ-weak solutions it is straight forward to see that (i) the potential solution cannot be computed since it is unstable, and (ii) the Kelvin Theorem is violated since the resulting EG2 (ϵ-weak) solution does not satisfy the Euler equations pointwise, and thus the assumptions of the Kelvin Theorem are not valid.

Acknowledgements

This paper summarizes recent work including joint work together with Prof. Claes Johnson at KTH. The author also acknowledges financial support from The Swedish Research Council and The Swedish Foundation for Strategic Research.

References

1. Barth TJ (2003) Numerical methods and error estimation for conservation laws on structured and unstructured meshes. Von Karman Institute Lecture Series 04-2003, Brussels, Belgium
2. Becker R, Rannacher R (1996) A feed-back approach to error control in adaptive finite element methods: Basic analysis and examples. East-West J Numer Math **4**:237–264
3. Becker R, Rannacher R (2001) A posteriori error estimation in finite element methods. Acta Numer 10:1–103
4. Braack M, Richter T (2006) Solutions of 3D Navier–Stokes benchmark problems with adaptive finite elements. Comput Fluids 35(4):372–392
5. Brezzi F, Houston P, Marini D, Süli E (2000) Modeling subgrid viscosity for advection-diffusion problems. Computat Meth Appl Mech Eng 190(13–14):1601–1610
6. Burman E (2000) Adaptive finite element methods for compressible flow. Meth Appl Mech Engrg 190:1137–1162.
7. Burman E (2000) Adaptive finite element methods for compressible two-phase flow. Meth Mod Meth App Sci 10(7):963–989
8. Burman E, Ern A, Giovangigli V Adaptive finite element methods for low mach, steady laminar combustion. J Comput Phy 188(2):472–492
9. Clay mathematical institute millenium problems. `http://www.claymath.org/millennium/Navier-Stokes_Equations/`
10. Constantinescu G, Pacheco R, Squires K (2002) Detached-eddy simulation of flow over a sphere. AIAA tech. report 2002-0425
11. d'Alembert J (1752) Essai d'une nouvelle théorie de la résistance des fluides. Paris, `http://gallica.bnf.fr/anthologie/notices/00927.htm`
12. Duchon J, Robert R (2000) Inertial energy dissipation for weak solutions of incompressible Euler and Navier–Stokes solutions. Nonlinearity 13:249–255
13. Dunca A, John V (2004) Finite element error analysis of space averaged flow fields defined by a differential filter. Math Mod Meth Appl Sci 14:603–618

14. Dunca A, John V, Layton WJ (2003) The commutation error of the space averaged Navier–Stokes equations on a bounded domain. In Galdi GP, Heywood JG, Rannacher R (Eds) Contributions to current challenges in mathematical fluid mechanics, Advances in mathematical fluid mechanics 3:53–78. Birkhäuser, Basel
15. Dunca A, John V, Layton WJ (2004) Approximating local averages of fluid velocities: the equilibrium Navier–Stokes equations. Appl Numer Math 49:187–205
16. Eriksson K, Estep D, Hansbo P, Johnson C (1995) Introduction to adaptive methods for differential equations. Acta Numer 4:105–158
17. Frisch U (1995) Turbulence — The Legacy of A. N. Kolmogorov. Cambridge University Press
18. Geurts BJ (2006) Interacting errors in large-eddy simulation: a review of recent developments. J Turbul 7, Art no 55
19. Giles M, Larson M, Levenstam M, Süli E (1997) Adaptive error control for finite element approximations of the lift and drag coefficients in viscous flow. Technical Report NA-76/06, Oxford University Computing Laboratory
20. Giles M, Süli E (2002) Adjoint methods for PDEs: a posteriori error analysis and postprocessing by duality. Acta Numer 11:145–236
21. Guermond JL (1999) Stabilization of Galerkin approximations of transport equations by subgrid modeling. Math Modell Num An 33(6):1293–1316
22. Hartmann R, Houston P (2002) Adaptive discontinuous Galerkin finite element methods for the compressible Euler equations. J Comput Phys 183:508–532
23. Heuveline V, Rannacher R (2003) Duality-based adaptivity in the hp-finite element method. J Numer Math 11(2):95–113
24. Hoffman J (2001) Dynamic subgrid modeling for time dependent convection-diffusion-reaction equations with fractal solutions. Int J Numer Meth Fluids 40:583–592
25. Hoffman J (2004) On duality based a posteriori error estimation in various norms and linear functionals for LES. SIAM J Sci Comput 26(1):178–195
26. Hoffman J (2005) Computation of mean drag for bluff body problems using adaptive DNS/LES. SIAM J Sci Comput 27(1):184–207
27. Hoffman J (2006) Adaptive simulation of the turbulent flow past a sphere. J Fluid Mech 568:77–88
28. Hoffman J (2006) Computation of turbulent flow past bluff bodies using adaptive general Galerkin methods: drag crisis and turbulent Euler solutions. Comput Mech 38:390–402
29. Hoffman J (to appear) Efficient computation of mean drag for the subcritical flow past a circular cylinder using general Galerkin G2. Int J Numer Meth Fluids
30. Hoffman J, Johnson C (2006) Computational turbulent incompressible Flow. Applied Mathematics Body and Soul 4. Springer, Berlin
31. Hoffman J, Johnson C (2006) A new approach to computational turbulence modeling. Comput Methods Appl Mech Engrg 195:2865–2880
32. Hoffman J, Johnson C (2007) Blow up of inviscid Euler solutions. Submitted
33. Hoffman J, Johnson C (2007) Flow separation in fluids with very small viscosity. Submitted
34. Hoffman J, Johnson C (2007) Resolution of d'Alembert's paradox. J Math Fluid Mech, to appear
35. Iliescu T, John V, Layton WJ (2002) Convergence of finite element approximations of large eddy motion. Num Meth Part Diff Equ 18:689–710

36. John V (2002) Slip with friction and penetration with resistance boundary conditions for the Navier–Stokes equations – numerical tests and aspects of the implementation. J Comp Appl Math 147:287–300
37. John V, Layton WJ, Sahin N (2004) Derivation and analysis of near wall models for channel and recirculating flows. Comput Math Appl 48:1135–1151
38. John V, Liakos A (2006) Time dependent flow across a step: the slip with friction boundary condition. Int J Numer Meth Fluids 50:713–731
39. Johnson C (1998) Adaptive finite element methods for conservation laws. In: Advanced numerical approximation of nonlinear hyperbolic equations:269–323. Springer Lecture Notes in Mathematics, Springer, Berlin
40. Kolmogorov AN (1941) Dissipation of energy in locally isotropic turbulence. Dokl Akad Nauk SSSR 32:16–18
41. Kolmogorov AN (1941) The local structure of turbulence in incompressible viscous fluid for very large Reynolds number. Dokl Akad Nauk SSSR 30:299–303
42. Kolmogorov AN (1941) On degeneration (decay) of isotropic turbulence in an incompressible viscous liquid. Dokl Akad Nauk SSSR 31:538–540
43. Leray J (1934) Sur le mouvement d'un liquide visqueux emplissant l'espace. Acta Mathematica 63:193–248
44. Murman EM, Rizzi A (1986) Application of Euler equations to sharp edge delta wings leading edge vortices. AGARD-CP-412, Art no 15
45. Prandtl (2006) Prandtl standard view. `www.fluidmech.net/msc/prandtl.htm`
46. Prandtl L (1904) On motion of fluids with very little viscosity. Third International Congress of Mathematics, Heidelberg. `http://naca.larc.nasa.gov/digidoc/report/tm/52/NACA-TM-452.PDF`
47. Reynolds O (1895) On the dynamical theory of incompressible viscous fluids and the determination of the criterion. Phil Trans R Soc Lond A 186123–164
48. Sagaut P, Deck S, Terracol M (2006) Multiscale and multiresolution approaches in turbulence. Imperial College Press
49. Sagaut P (2001) Large eddy simulation for incompressible flows. Springer, Berlin, Heidelberg, New York
50. Sandboge R (1998) Quantitative error control for finite element methods for one-dimensional compressible flow. Siam J Numer Anal 35(5):2014–2034
51. Schlichting H (1955) Boundary layer theory. McGraw-Hill
52. Vasilyev OV, Lund TS, Moin P (1998) A general class of commutative filters for LES in complex geometries. J Comput Phy 146:82–104

On the Application of Wavelets to LES Sub-grid Modelling

Marta de la Llave Plata and Stewart Cant

Cambridge University, Engineering Department, Trumpington Street, Cambridge CB2 1PZ, UK. md383@cam.ac.uk, rsc10@cam.ac.uk

Abstract. The wavelet-based multi-resolution analysis technique is used to develop a novel approach to the modelling of the sub-grid terms in the large-eddy simulation equations. This new approach is called WaveLES. A numerical framework for the solution of the projected equations is developed for one and three-dimensional problems. The WaveLES method is assessed in *a priori* tests on an atmospheric turbulent time series, and a direct numerical simulation. *A posteriori* tests are carried out for the Burgers equation.

Keywords: Large-eddy simulation, Sub-grid model, Multi-resolution, Wavelets

1 Introduction

The use of wavelets for the numerical solution of flows began with the work of Liandrat and Tchamitchian [11] and Bacry, Mallat and Papanicolaou [2]. New approaches to study and model turbulent flows using the wavelet representation have been investigated by Meneveau [14] and Farge [8]. Based on wavelet thresholding, Farge, Schneider and Kevlahan [9] have proposed the Coherent Vortex Simulation (CVS) technique, which permits the separation of a flow into coherent (organised) and incoherent (random) structures. Wavelet-based methods for the solution of turbulent reacting flows have also been developed by Prosser and Cant [15] and Bockhorn, Frölich and Schneider [5]. In the context of LES, Goldstein and Vasilyev have recently proposed the Stochastic Coherent Adaptive Large-Eddy Simulation (SCALES) technique [10], which combines CVS filtering with the Germano dynamic approach.

The locality property of the wavelet transform (WT), together with its resolution adaptability and, most importantly, its ability to preserve the scale-invariance properties of the analysed signal, makes it a very appealing tool for LES sub-grid (sgs) modelling.

Here, we propose a new approach based on multi-resolution analysis (MRA). Wavelets are used as a basis onto which the N-S equations are projected. The selected basis inherently provides a finite difference (FD) method

J. Meyers et al. (eds.), Quality and Reliability of Large-Eddy Simulations,

for the discretisation of the derivatives, which are expressed in terms of a hierarchy of sparse wavelet spaces. The projected equations are then truncated to the desired level of resolution. The sub-grid scales, required for solving the large-scale field, are computed explicitly through the equations that govern the evolution of the wavelet coefficients.

2 Multi-Resolution Analysis

The principle of MRA, introduced by Mallat in 1989 [12], is to analyse the data at different scale and space resolutions, viewing the signal through windows of different sizes. Large windows will capture the global behaviour, whereas small windows will focus on local features. The MRA can thus be interpreted as a decomposition into approximations at coarser and coarser resolutions. The details, which have been lost when moving from a higher level of approximation to a lower one, are encoded in the *wavelet coefficients*.

An MRA of $\mathbf{L}^2(\mathbb{R})$ is defined by a sequence of nested spaces $\{\mathbf{V}_j\}_{j\in\mathbb{Z}}$,

$$\{0\} \subset ... \subset \mathbf{V}_{j-1} \subset \mathbf{V}_j \subset \mathbf{V}_{j+1} \subset ... \subset \mathbf{L}^2(\mathbb{R}) \tag{1}$$

For each subspace, there exists a function $\phi_{j,k}(x) \in \mathbf{V}_j$, called *scaling function*, which can be obtained by translation and dilation of a *mother scaling function*, $\phi(x) \in \mathbf{L}^2(\mathbb{R})$, as $\phi_{j,k}(x) = \phi(2^j x - k)$. Here $j, k \in \mathbb{Z}$ are the scale and position indeces, respectively.

The projection $P_j(f)$, of a signal $f(x) \in \mathbf{L}^2(\mathbb{R})$ onto a subspace $\mathbf{V}_j$, is expressed in terms of the *scaling function coefficients*, $s_{j,k}$, defined by the inner product between the signal and the scaling functions,

$$P_j(f) = \sum_{k=1}^{2^j} s_{j,k}\phi_{j,k}(x) \ , \ \ s_{j,k} = \langle f(u), \phi_{j,k}(u)\rangle \tag{2}$$

The detail information required to move up one resolution level is contained in the complement space of $\mathbf{V}_j$, namely $\mathbf{W}_j$, such that, $\mathbf{V}_j \oplus \mathbf{W}_j = \mathbf{V}_{j+1}$. The subspaces $\mathbf{W}_j$ are called *wavelet spaces*. If the wavelet basis is orthogonal, then $\mathbf{V}_j$ and $\mathbf{W}_j$ possess the following properties,

$$\mathbf{V}_j \perp \mathbf{W}_j \quad , \quad \mathbf{W}_m \perp \mathbf{W}_n \quad \forall m \neq n \tag{3}$$

The projection $Q_j(f)$, of $f(x)$ onto $\mathbf{W}_j$, is written in terms of the *wavelet coefficients*, $d_{j,k}$, defined by the inner products between the signal and the *wavelet functions*, $\psi_{j,k}(x) \in \mathbf{W}_j$,

$$Q_j(f) = \sum_{k=1}^{2^j} d_{j,k}\psi_{j,k}(x) \ , \ \ d_{j,k} = \langle f(u), \psi_{j,k}(u)\rangle \tag{4}$$

As for the scaling functions, the wavelets are dilates and translates of a *mother wavelet*, $\psi(x) \in \mathbf{L}^2(\mathbb{R}) : \psi_{j,k}(x) = \psi(2^j x - k)$.

2.1 Choice of Wavelets

The orthogonal wavelet family proposed by Daubechies [7] has been selected as basis for the WaveLES technique. Called after their creator, the Daubechies wavelets are fully parametrised and allow a straightforward calculation of the analysis filter. They are characterised by having compact support, and the highest number of vanishing moments compatible with their support width. The number of vanishing moments is related to the regularity of the wavelet, and therefore, to its degree of differentiability.

Since the N-S equations contain derivatives up to order two, we will need wavelets which are at least twice differentiable. The wavelet family with narrower support width to fulfil this condition is the Daubechies six-tap filter (Daub6). This family is defined by six filter coefficients and has three vanishing moments.

2.2 A Word on Notation

The notation used in this paper is similar to that used by Beylkin et al. in [4].

Projection: In the wavelet framework, any variable $f(x)$ can be approximated by its discrete representation in a sufficiently high resolution space $\mathbf{V}_J$, defined by 2^J sample values,

$$f(x) \approx P_J(f) = \sum_{k=1}^{2^J} f_k \phi_{J,k}(x) \tag{5}$$

A coarser representation of f is then given by its projection $P_j(f)$ onto the scaling function space $\mathbf{V}_j$, defined by 2^j scaling function coefficients, and $j < J$.

In the context of LES, we will associate the coarse space $\mathbf{V}_j$ with the LES grid, whose size is $\Delta_{LES} = 2^{-j}$. The full resolution space $\mathbf{V}_J$ is thus equivalent to the DNS field, with grid spacing $\Delta_{DNS} = 2^{-J}$. Hence, the approximations $P_j(f)$ and $P_J(f)$, or in shorthand notation f_j and f_J, will correspond to the LES and DNS flow solutions respectively.

To reconstruct $P_J(f)$ from $P_j(f)$, we must add the unresolved sub-grid scale information included in the wavelet spaces $\{Q_j + Q_{j+1} + \cdots + Q_{J-1}\}(f)$. For compactness, these terms will be grouped under $Q_{j,sgs}(f)$, in shorthand syntax f'_j. Using this notation, the MRA decomposition of a discrete variable f can be expressed as,

$$P_J(f) = P_j(f) + \sum_{i=j}^{J-1} Q_i(f) = P_j(f) + Q_{j,sgs}(f) = f_j + f'_j \tag{6}$$

Reconstruction: The symbol $\mathcal{R}_j^{j_0}[\cdot]$ will designate the operator to reconstruct a vector on subspace $\mathbf{V}_j$ or $\mathbf{W}_j$, in the subspace $\mathbf{V}_{j_0}$, $j_0 \in \mathbb{Z}$. In $\mathbf{V}_{j_0}$,

one can then use the coefficients $\mathcal{R}_j^{j_0}\left[P_j(f)\right]$ and $\mathcal{R}_j^{j_0}\left[Q_j(f)\right]$ to perform the pertinent operations. When the level of origin, j, and destination, j_0, are the same, the superindex is dropped and the operator $\mathcal{R}_{j_0}\left[P_{j_0}(f)\right]$ simply represents the scaling function coefficients of the projection of f on $\mathbf{V}_{j_0}$.

Derivatives: The operators $(P_j\,\partial/\partial x_l\ ,\ P_j\,\partial^2/\partial x_l^2)$ represent the FD approximations on $\mathbf{V}_j$, of the first and second derivatives in the x_l-direction [3]. Similarly, the operators $(Q_j\,\partial/\partial x_l\ ,\ Q_j\,\partial^2/\partial x_l^2)$, denote the FD approximations of the first and second derivatives on $\mathbf{W}_j$. Using abbreviated syntax, $(P_j\,\partial/\partial x_l\ ,\ P_j\,\partial^2/\partial x_l^2)$ will also be written as $(\partial_j^{(l)}\ ,\ \partial_j^{(ll)})$.

3 Wavelet-Based Large Eddy Simulation

The WaveLES method is firstly illustrated for the Burgers equation, which produces a one-dimensional (1D) analogue of the turbulent energy cascade. This simplified system avoids the cumbersome notation of the full three-dimensional (3D) problem. The extrapolation of the methodology to 3D is straightforward and is presented in Sect. 4.2.

3.1 Burgers Equation in Wavelet Bases

The Burgers equation in physical space reads,

$$\frac{\partial u}{\partial t} + \frac{\partial}{\partial x}\left(\frac{u^2}{2}\right) - \nu\frac{\partial^2 u}{\partial x^2} = 0 \tag{7}$$

If we project (7) onto the LES grid and reunite the resolved terms on the left hand side (l.h.s.), we obtain,

$$\begin{aligned}&\frac{\partial}{\partial t}P_j(u) + \frac{1}{2}P_j\frac{\partial}{\partial x}P_j(u)^2 - \nu P_j\frac{\partial^2}{\partial x^2}P_j(u) = \\ &-\frac{1}{2}P_j\frac{\partial}{\partial x}\left(u^2 - P_j(u)^2\right) + \nu P_j\frac{\partial^2}{\partial x^2}\left(u - P_j(u)\right)\end{aligned} \tag{8}$$

The first term on the right hand side (r.h.s.) of (8) is called *convective sgs term*, and will be designated $\partial_j^{(1)}\mathcal{C}_j$. The nature of this term can be brought out by combining expressions (5) and (6),

$$\begin{aligned}\partial_j^{(1)}\mathcal{C}_j &= \partial_j^{(1)}\left(P_J(u) - P_j(u)\right)\left(P_J(u) + P_j(u)\right) \\ &= \partial_j^{(1)}\left(2\,P_j(u)Q_{j,sgs}(u) + Q_{j,sgs}(u)^2\right)\end{aligned} \tag{9}$$

Expansion (9) highlights the existence of two distinct contributions. The first one is due to interactions between the resolved and the sub-grid scales. It will be named res-sgs component. The second one represents the interactions only between the sub-grid scales, called here sgs-sgs component.

Note that, unlike traditional LES, commutation between the projection and difference operators is not assumed. This will generate an additional *viscous sgs component* (second term on the r.h.s. of (8)),

$$\partial_j^{(11)} \mathcal{D}_j = \nu\, \partial_j^{(11)} \left(P_J(u) - P_j(u) \right) = \nu\, \partial_j^{(11)} Q_{j,sgs}(u) \tag{10}$$

3.2 Modelling Approach

The modelling strategy used in WaveLES starts with the observation that, if the flow field has a Kolmogorov-like spectrum, $\kappa^{-\beta}$, and the wavelet basis has sufficient regularity (fast decay of the wavelet function and its derivatives), a good representation of the sgs field is provided by the M first terms in the wavelet series (M-level approach): $Q_{j,sgs}(u) \approx Q_j(u) + \cdots + Q_{j+M-1}(u)$. The evolution of each wavelet component is governed by the projection of (7) onto the subspaces $\mathbf{W}_m$, $m = j, \ldots, j+M-1$,

$$\frac{\partial}{\partial t} Q_m(u) + \frac{1}{2}\, Q_m \frac{\partial}{\partial x} u^2 - \nu\, Q_m \frac{\partial^2}{\partial x^2} u = 0 \tag{11}$$

Invoking the assumptions just made, the full resolution field, u, may be approximated by the sum of the resolved field and the leading terms in the wavelet series, namely, $u \approx P_{j+M}(u) = P_j(u) + Q_{j,sgs}(u)$. Injecting this into (11) yields,

$$\frac{\partial}{\partial t} Q_m(u) + \frac{1}{2}\, Q_m \frac{\partial}{\partial x} P_{j+M}(u)^2 - \nu\, Q_m \frac{\partial^2}{\partial x^2} P_{j+M}(u) = 0 \tag{12}$$

where the index m spans from j to $j+M-1$. Equations (8) and (12) constitute a system of $M+1$ coupled equations for the resolved and the sub-grid fields.

Observe that, in the DNS limiting case, the number of levels considered in the simulation is $M = J - j$, and all the wavelet coefficients, down to the Kolmogorov scale ($\eta \sim 2\Delta_{DNS} = 1/2^{J-1}$), are computed explicitly.

3.3 Practical Implementation

The estimation of the sgs field from (12) requires the definition of a hierarchy of grids with sizes $\Delta_m = 2^{-m}$. Each of these grids will be associated with a wavelet space $\mathbf{W}_m$. This leads to a multi-level approach, in which the number of levels is prescribed by the number of terms considered in the series. We will now proceed to explain how (8) and (12) are solved numerically. For simplicity, we assume that the solution is time advanced using the forward Euler method. The way in which the formulation is presented in this research leaves the way open for the implementation of more sophisticated schemes.

Resolved Non-linear Term: Indeed, multiplication of two coarse-grain variables, $P_j(u)^2$, will generate new coefficients over a range of wavelet spaces.

Clearly, the spread of the product will depend on the nature of the field, but for smooth solutions of the N-S equations a good approximation would be,

$$P_j \frac{\partial}{\partial x} P_j(u)^2 \approx P_j \frac{\partial}{\partial x} \mathcal{R}_j^{j+1} [P_j(u)]^2 \tag{13}$$

which amounts to reconstructing $P_j(u)$ in $\mathbf{V}_{j+1}$, taking the pointwise product of the coefficients $\mathcal{R}_j^{j+1}[P_j(u)]^2$, and applying the differential operator $\partial_j^{(1)}$ to the resulting field. An in-depth discussion on the treatment of non-linearities in wavelet bases can be found in [4].

Unresolved Sub-grid Term: The evaluation of the sgs field requires knowledge of the wavelet coefficients at the designated number of levels, whose evolution is governed by (12). The wavelet coefficients at a generic level m can be computed from,

$$\begin{aligned} Q_m(u)^{n+1} = Q_m(u)^n + \Delta t \Big\{ -\frac{1}{2} Q_m \frac{\partial}{\partial x} \mathcal{R}_{j+M} [P_{j+M}(u)]^2 \\ + \nu Q_m \frac{\partial^2}{\partial x^2} P_{j+M}(u) \Big\}, \end{aligned} \tag{14}$$

where Δt is the time step and the superscript n refers to the solution at time $t_n = n\,\Delta t$. The approximation $P_{j+M}(u)$ is defined on the finest grid considered in the simulation, namely $\mathbf{V}_{j+M}$. It can be evaluated from the values of the detail coefficients available at that time. Observe that the products $P_{j+M}(u)^2$ are calculated in $\mathbf{V}_{j+M}$, as indicated by the use of the operator $\mathcal{R}_{j+M}[\cdot]$.

Once the detail coefficients at time t_{n+1} are known at the required number of levels, the convective and viscous closure terms in (8) can be calculated by assuming $P_J(u) \approx P_{j+M}(u) = P_j(u)^n + Q_{j,sgs}(u)^{n+1}$,

$$\partial_j^{(1)} \mathcal{C}_j^{n+1} \approx \frac{1}{2} \left\{ \partial_j^{(1)} \mathcal{R}_{j+M} [P_{j+M}(u)]^2 - \partial_j^{(1)} \mathcal{R}_j^{j+1} [P_j(u)^n]^2 \right\} \tag{15}$$

$$\partial_j^{(11)} \mathcal{D}_j^{n+1} \approx \nu \left\{ \partial_j^{(11)} P_{j+M}(u) - \partial_j^{(11)} P_j(u)^n \right\} \tag{16}$$

4 A Priori Tests of the WaveLES Technique

Despite the known limitations in the comparison of quantities obtained from LES models against filtered DNS fields, *a priori* testing provides valuable information about the accuracy of the approximation used.

In this work, a so-called DNS quantity is obtained by operating on the full resolution field, defined in $\mathbf{V}_J$, then projecting the outcome on the coarse grid $\mathbf{V}_j$. On the other hand, an LES quantity is derived from the DNS field by truncating its MRA decomposition at the prescribed level. The result of operating on this truncated field is then projected on the coarse mesh $\mathbf{V}_j$.

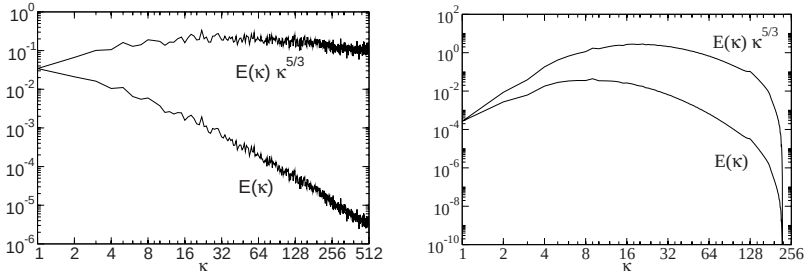

Fig. 1 Fourier spectra of data sets. The spectra have been multiplied by $\kappa^{5/3}$ to highlight the existence of an inertial range. *Left:* Time Series. *Right:* DNS

4.1 A Priori Tests: Turbulent Time Series

The unresolved convective term (15) is evaluated for an atmospheric turbulent time series. The source of these data can be found at `http://www2.isye.gatech.edu/~brani/datapro.html`, where a detailed description of the experimental parameters is provided. Only the horizontal component of the velocity field is considered here, from which the mean has been removed. Making use of Taylor's hypothesis, the data is split into 32 series of 2^{10} samples. The averaged spectrum (left-most plot in Fig. 1) exhibits a clear inertial subrange over a few octaves.

Analysis of Closure Terms

To assess the accuracy of the WaveLES method in capturing the main features of the convective sgs field, (15) has been decomposed into its res-sgs and sgs-sgs components, as defined in Sect. 3.1. This is illustrated in Figs. 2 and 3, for the one and two-level approaches respectively.

The graphs reveal the high fidelity with which the method represents the correlations between resolved and sub-grid scales, as shown by the high values of the correlation coefficient, ρ, above 0.9. The structure and order of magnitude of the sgs-sgs interaction term is relatively well captured, although there is a clear loss of correlation with respect to the res-sgs term. Not surprisingly, the two-level approach leads to a substantial improvement of these correlations. Nevertheless, the fact of adding one more level does not appear to have a significant effect on the res-sgs term. Observe also that the contribution of the res-sgs correlations to the total sgs term $\partial_j^{(1)}\mathcal{C}_j$ prevails over that of the sgs-sgs component.

For brevity, the viscous sgs term is not discussed here. There is no added difficulty in its calculation and the accuracy of its approximation chiefly depends on the regularity of the basis functions. *A posteriori* tests on the Burgers equation show that, for very high-Reynolds-number flows, its contribution can be safely removed from (8).

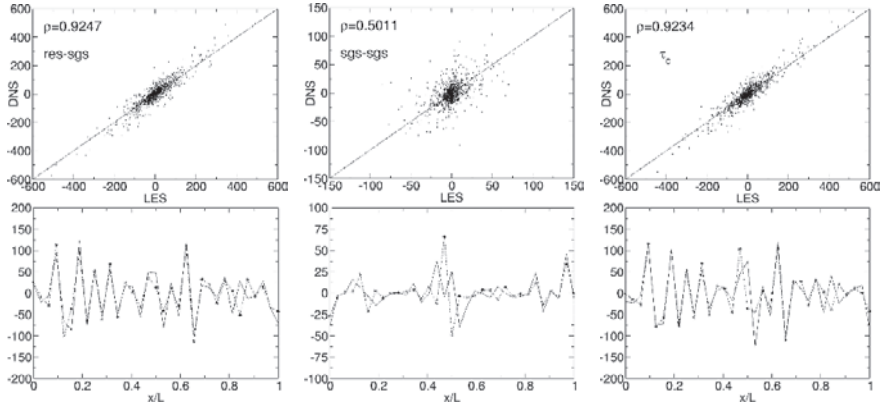

Fig. 2 Convective sgs term ($J = 10$, $j = 5$, $M = 1$). From *left to right*: res-sgs interactions $\partial_j^{(1)}(u_j u_j')$; sgs-sgs interactions $\partial_j^{(1)}(u_j'^2)$; total sgs term $\partial_j^{(1)}\mathcal{C}_j$. The upper panels show the correlations between DNS and LES values. The lower panels compare typical 1D realizations (− DNS; − ∗ − LES)

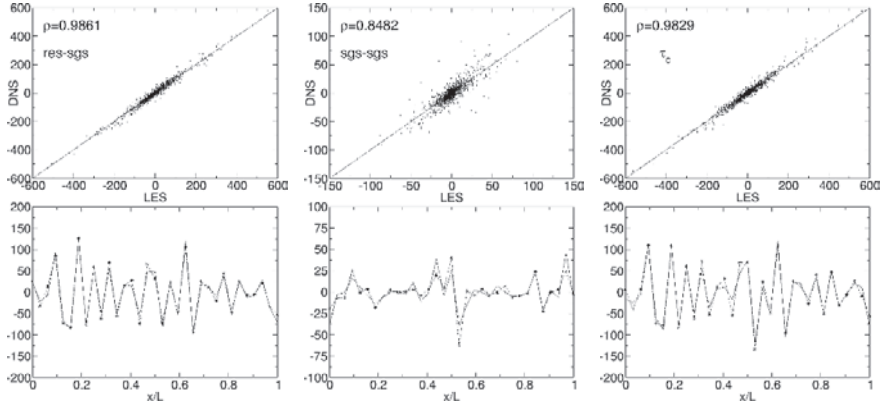

Fig. 3 Convective sgs term ($J = 10$, $j = 5$, $M = 2$). From *left to right*: res-sgs interactions $\partial_j^{(1)}(u_j u_j')$; sgs-sgs interactions $\partial_j^{(1)}(u_j'^2)$; total sgs term $\partial_j^{(1)}\mathcal{C}_j$. The upper panels show the correlations between DNS and LES values. The lower panels compare typical 1D realizations (− DNS; − ∗ − LES)

4.2 A Priori Tests: DNS Turbulence

The validity of the WaveLES technique for 3D problems is assessed in *a priori* tests on a DNS of decaying isotropic turbulence. The flow field was computed using a pseudo-spectral code with anti-aliasing, *FERGUS*, developed by Cant [6]. The number of Fourier modes used in the simulation was 256 in each direction. The Reynolds number, based on the Taylor microscale, was $Re_\lambda \approx$

60. The simulation was run for about 1.5 eddy-turnover times in order to obtain a well developed spectrum (see right graph in Fig. 1).

3D Formulation and Notation

A separable 3D MRA [13] consists in the tensor product of 1D spaces in each of the axis directions, $\mathbf{V}_j^3 = \mathbf{V}_j^x \otimes \mathbf{V}_j^y \otimes \mathbf{V}_j^z$. As in 1D, the approximation of a variable $f(\mathbf{x})$ at scale 2^j is defined by its projection on $\mathbf{V}_j^3 \in \mathbf{L}^2(\mathbb{R}^3)$.

Following the notation used throughout this paper, we will denote by $P_j^3(f)$ the projection of f onto the LES grid, $\mathbf{V}_j^3$ ($\Delta_{LES} = 2^{-3j}$). The full resolution DNS is now given by $P_J^3(f)$ ($\Delta_{DNS} = 2^{-3J}$), which defines a projection on $\mathbf{V}_J^3$. Hence, the incompressible N-S equations in wavelet bases read,

$$P_j^3 \frac{\partial}{\partial x_k} P_j^3(u_k) = -P_j^3 \frac{\partial}{\partial x_k} \left(P_J^3(u_k) - P_j^3(u_k) \right) \tag{17}$$

$$\frac{\partial}{\partial t} P_j^3(u_k) + P_j^3 \frac{\partial}{\partial x_l} \left(P_j^3(u_k) P_j^3(u_l) \right) + \frac{1}{\rho} P_j^3 \frac{\partial}{\partial x_k} P_j^3(p) - \nu P_j^3 \frac{\partial^2}{\partial x_l^2} P_j^3(u_k) =$$

$$-P_j^3 \frac{\partial}{\partial x_l} \left(P_J^3(u_k) P_J^3(u_l) - P_j^3(u_k) P_j^3(u_l) \right) \tag{18}$$

$$+\nu P_j^3 \frac{\partial^2}{\partial x_l^2} \left(P_J^3(u_k) - P_j^3(u_k) \right) - \frac{1}{\rho} P_j^3 \frac{\partial}{\partial x_k} \left(P_J^3(p) - P_j^3(p) \right) \tag{19}$$

where the differences $\{P_J^3(f) - P_j^3(f)\}$ represent the unknown sgs field. By analogy with the 1D case, it will be referred to as $Q_{j,sgs}^3(f)$.

Observe that the approximation of the N-S equations in $\mathbf{V}_j^3$ generates two additional unresolved components. The first one is called *mass conservation sgs term* (r.h.s. of (17)). This term can be unambiguously evaluated once the hierarchy of wavelet coefficients is known. The second one is the *pressure sgs term*, second element in (19), which is not known explictly. For incompressible flows, it is standard practice to conceive the pressure as variable which is used to enforce mass conservation. A pressure-correction method can therefore be used to calculate this contribution. Due to shortness of space, a more detailed discussion of these terms is not included in this paper.

Analysis of Closure Terms

Let us now focus on the non-linear sgs term (18). We believe that the comments made in Sect. 4.1 in relation to the viscous sgs term (first element in (19)) hold equally in the 3D case.

Figures 4 and 5 show the correlations between DNS and LES, for the res-sgs and sgs-sgs terms, respectively. This is done for the three components of the convective sgs term in the x-momentum equation. The analysis on the six other components yielded similar results, as expected for an isotropic flow. The correlation coefficients are very close to one for the res-sgs component, and around 10% lower for the sgs-sgs interaction term. These results are in

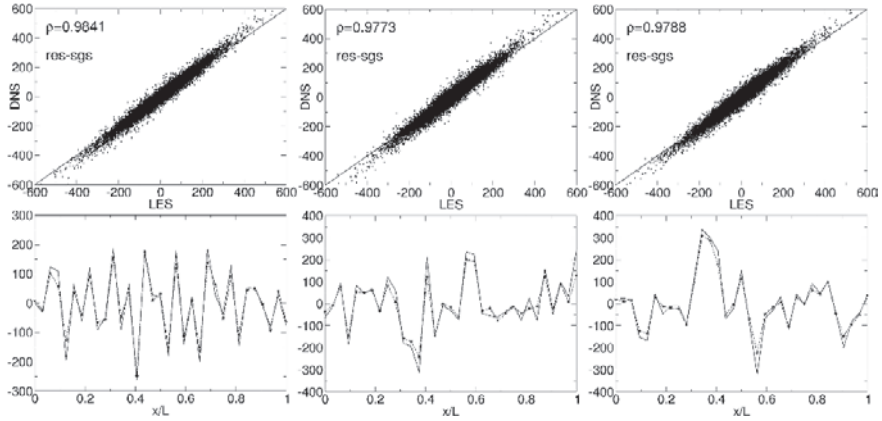

Fig. 4 Convective res-sgs term in the x-momentum equation ($J = 8$, $j = 5$, $M = 1$). From *left to right*: $\partial_j^{(1)}(u_j u_j')$, $\partial_j^{(2)}(u_j v_j')$, and $\partial_j^{(3)}(u_j w_j')$. The upper panels show the correlations between DNS and LES values. The lower panels compare typical 1D realizations ($-$ DNS; $-*-$ LES)

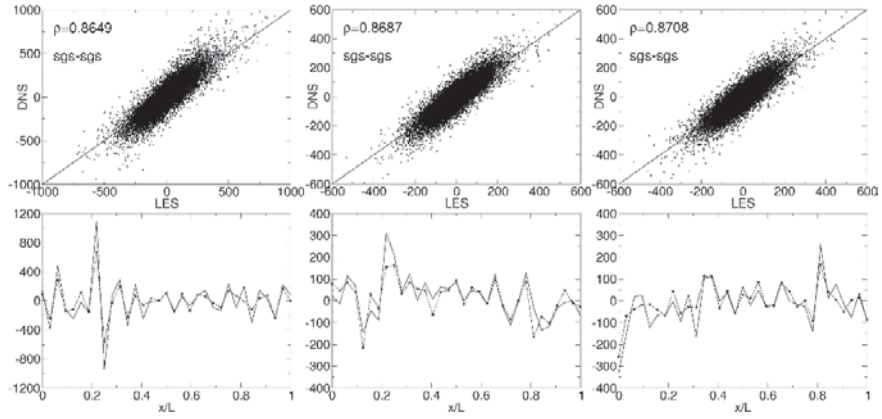

Fig. 5 Convective sgs-sgs term in the x-momentum equation ($J = 8$, $j = 5$, $M = 1$). From *left to right*: $\partial_j^{(1)}(u_j'^2)$, $\partial_j^{(2)}(u_j' v_j')$, and $\partial_j^{(3)}(u_j' w_j')$. The upper panels show the correlations between DNS and LES values. The lower panels compare typical 1D realizations ($-$ DNS; $-*-$ LES)

agreement with those obtained for the atmospheric data. The better approximation obtained here is partly due to a slightly steeper decay of the spectrum at the cut-off wave number in the DNS turbulence (lower Reynolds number). The correlation coefficients for the total convective sgs field in the momentum equations, not shown here, turned out to be in the order of 0.95. As anticipated, slightly lower than that of the res-sgs term alone.

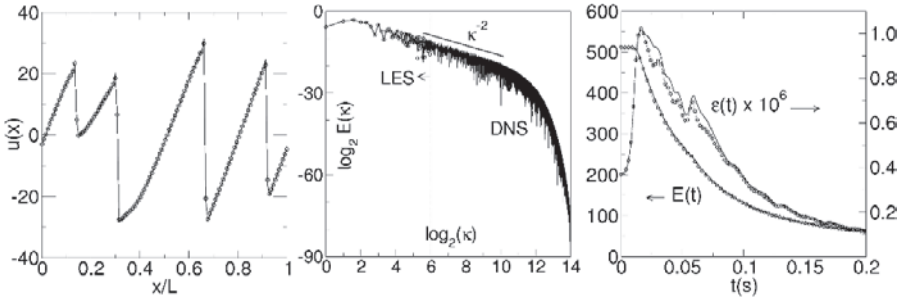

Fig. 6 Solution of the Burgers equation. From *left to right*: velocity profiles at t=0.06s, Fourier spectra at t=0.06s and temporal evolution of the mean kinetic energy and dissipation, $\varepsilon = \langle(\partial_j^{(1)} u_j)^2\rangle$. In all graphs (- DNS; • LES)

5 A Posteriori Tests: Burgers Turbulence

This section reports the main results of applying the WaveLES technique to the solution of (8). The associated full resolution DNS field is also computed for comparison. An initial Gaussian random field is specified by means of a Batchelor-Townsend spectrum. No external forcing is applied and the solution consists of a freely decaying ensemble of shock fronts. The parameters of the simulation are the following: $\nu = 1/15000$, $J = 15$, $j = 7$ and $M = 2$. The contribution of the viscous sgs term (10) is neglected in (8).

Figure 6 compares the outcome of the simulations at time t=0.06s. The agreement between the projected DNS and the LES velocity profiles is very good overall, the highest errors occurring in the vicinity of the discontinuities. Despite these local errors, the resolved part of the energy spectrum is neatly captured, and an excellent match is found in the decay of kinetic energy. On the other hand, the level of dissipation appears to be slightly lower in the LES. However, the trend and the order of magnitude of the dissipation field are very well predicted.

6 Conclusions

A systematic approach to the solution of the LES equations has been proposed based on the wavelet transform. There is no model or parametrisation involved in the methodology. This new technique provides a consistent mathematical formulation for the decomposition of the flow into large and small scales, and gives deep insight into the physics of the turbulent cascade.

A numerical framework has also been developed for the solution of the resolved and sub-grid scale equations. Fast algorithms for the wavelet transform, as well as for the derivation and multiplication of functions in wavelet basis exist in the literature [3, 4]. Furthermore, the wavelet representation

naturally lends itself to the implementation of more sophisticated space-time adaptive schemes [1].

The WaveLES method has been successfully assessed in *a priori* tests on turbulence data from DNS and experiment. *A posteriori* tests have been performed on the Burgers equation. The results of these analyses appear very encouraging and demonstrate the potential of our approach as a powerful alternative to traditional LES.

The implementation and actual simulation of the 3D problem is the subject of future work. The extension of the method to complex geometries will also be investigated by considering the use of more flexible wavelet filters, such as the *Second Generation Wavelets* developed by Sweldens [16].

Acknowledgements

This research has been funded by the UK Engineering and Physical Sciences Research Council, with additional support from Zonta International through the Amelia Earhart Fellowship Program. The authors thank R. Prosser and A.J. Lowe for useful discussions.

References

1. Alam JM, Kevlahan NK-R, Vasilyev OV (2006) J Comput Phys 214:829–857
2. Bacry E, Mallat S, Papanicolaou G (1992) Math Model Numer Anal 26:793–834
3. Beylkin G, Coifman R, Rokhlin V (1991) Commun Pure Appl Math 44:141–183
4. Beylkin G, Keiser JM (1997) J Comput Phys 132:233–259
5. Bockhorn H, Fröhlich J, Schneider K (1999) Combust Theor Model 3:177–198
6. Cant RS (1999) FERGUS: A User Guide. Cambridge University.
7. Daubechies I (1992) Ten Lectures on Wavelets. SIAM.
8. Farge M (1992) Annu Rev Fluid Mech 24:395–457
9. Farge M, Schneider K, Kevlahan N (1999) Phys Fluids 11:2187–2201
10. Goldstein DE, Vasilyev OV (2004) Phys Fluids 16:2497–2513
11. Liandrat J, Tchamitchian P (1990) Resolution of the 1D regularised Burgers equation using a spatial wavelet approximation. NASA, ICASE Report
12. Mallat S (1989) IEEE Trans Pattern Anal Mach Intell 11:674–693
13. Mallat S (1998) A Wavelet Tour of Signal Processing. Academic Press
14. Meneveau C (1991) J Fluid Mech 232:469–520
15. Prosser R, Cant RS (1998) J Comput Phys 147:337–361
16. Sweldens W (1996) J Appl Comput Harmon Anal 2:186–200

Analysis of Truncation Errors and Design of Physically Optimized Discretizations

Stefan Hickel and Nikolaus A. Adams

Institute of Aerodynamics, Technische Universität München, 85747 Garching, Germany. sh@tum.de

Abstract. Further development of Large Eddy Simulation (LES) faces as major obstacle the strong coupling between subgrid-scale (SGS) model and the truncation error of the numerical discretization. Recent analyzes indicate that for certain discretizations and certain flow configurations the truncation error itself can act as implicit SGS model. In this paper, we explore how implicit SGS models can be derived systematically and propose a procedure for design, analysis, and optimization of nonlinear discretizations. Implicit LES can be made rigorous by requiring that the numerical dissipation approximates the SGS dissipation obtained from the analysis of nonlinear interactions in turbulence.

Keywords: Truncation error, Optimization, Subgrid-scale modeling, Implicit LES

1 Introduction

In classical numerical analysis, discretization coefficients are usually chosen in such a way that the formal order of accuracy of a discretization is maximum. This approach holds for direct numerical simulation but not for large-eddy simulation (LES), where the chosen grid resolution essentially defines the range of represented scales. At a finite grid size, truncation errors interfere with the turbulence models. Thus, free discretization coefficients should be selected in such a way that the superposition of all contributions (truncation errors, modeling terms, and modeling errors) is optimal. Further development of LES faces a major obstacle in the strong coupling between subgrid-scale (SGS) modeling and the truncation error of the numerical discretization. SGS models generally operate on scales that are marginally resolved by the underlying numerical method. This mutual interference can have large and generally unpredictable effects on the accuracy of the solution. On the other hand, one can exploit this link by developing discretization methods from subgrid-scale models, or vice versa. Approaches where SGS models and numerical discretizations are fully merged are called implicit LES, a comprehensive review on such methods is given in the book of Grinstein et al. [10].

J. Meyers et al. (eds.), Quality and Reliability of Large-Eddy Simulations,

Previous approaches to implicit SGS modeling rely on the application of preexisting discretization schemes, which have been developed for other purposes, to fluid-flow turbulence. Consequently methods with suitable implicit SGS model are usually found by trial and error. Recent analyses have shown that stabilizing an under-resolved simulations by upwind or non-oscillatory schemes is insufficient for accurately representing SGS turbulence, although some general trends can be reproduced [8, 6, 5]. Employing implicit LES for prediction, however, requires numerical methods that are specially designed, optimized, and validated for the physical problem to be considered. A full coupling of SGS model and discretization scheme cannot be achieved without incorporating physical reasoning into the design of the implicit SGS model.

The objective of this work is to improve on the aforementioned modeling uncertainties by exploring how implicit subgrid-scale modeling can be approached systematically. For this purpose, methods of design, analysis, and optimization of nonlinear discretizations for implicit LES are devised. Previous approaches frequently have led to the belief that an implicit subgrid-scale model is generally inferred by the choice of discretization. This is not necessarily the case. In fact, implicit subgrid-scale models can be designed deliberately. The following systematic procedure for implicit SGS modeling is proposed:

Discretization design: First, a general nonlinear discretization scheme is developed on the basis of standard approaches. These, however, are modified in such a way that the resulting truncation error can be controlled. The resulting scheme should be as simple as possible to facilitate computation at reasonable cost, and as complex as necessary to allow for implicit modeling.

Modified-differential-equation analysis: The general discretization method is analyzed with respect to its implicit SGS modeling capabilities. A suitable tool is an analysis of the modified-differential equation (MDEA). Based on Taylor-series expansions of the solution, such an analysis allows to determine the relation of the implicit model to any given explicit SGS model [18, 7]. However, MDEA of more complex nonlinear discretization schemes for nonlinear three-dimensional differential equations is practically impossible. An alternative approach for complex discretizations is an a-posteriori analysis of the spectral numerical dissipation.

SGS-model calibration: In the final step, appropriate values of the parameters inherent to the discretization scheme are determined. With implicit LES we do not aim at formally highest order of accuracy. Instead, discretization coefficients are optimized in such a way that the truncation error acts as a physically motivated SGS model in regions where the flow is turbulent, while maintaining a second-order accurate central discretization in regions where the flow is laminar.

In the following we report on the application of this procedure in the development of a nonlinear discretization for implicit LES.

2 A Subgrid-Scale Modeling Environment for ILES

For brevity of notation, the following summary is given for the one-dimensional case and a generic nonlinear transport equation

$$\partial_t u + \partial_x F(u) = 0 \ . \tag{1}$$

Following Leonard [16] the discretized equation is obtained by convolution with a homogeneous filter kernel G and the subsequent discretization of the filtered equations

$$\partial_t \overline{u}_N + G * \partial_x F_N(u_N) = -G * \partial_x \tau_{SGS}, \tag{2}$$

where the overbar denotes the filtering $\overline{u} = G*u$, and the subscript N indicates grid functions obtained by projecting continuous functions onto the numerical grid $x_N = \{x_j\}$. This projection corresponds to an additional filtering in Fourier space with a cut-off filter at the Nyquist wave number $\xi_N = \pi/h$, where h is a constant grid spacing.

In the following we consider a top-hat filter. For this filter kernel, the evaluation of Eq. (2) on a computational grid corresponds to Schumann's finite-volume discretization [20]. The subgrid-stress tensor

$$\tau_{SGS} = F(u) - F_N(u_N) \ . \tag{3}$$

originates from the grid projection of non-linear terms and has to be approximated by a subgrid-scale model for closing Eq. (2). *Explicit SGS models* provide approximations or estimations of the unclosed SGS terms which are computed explicitly during time advancement [19, 17]. Most explicit SGS models are based on sound physical theories but were derived without reference to a computational grid and without taking into account a discretization scheme. Solved numerically, however, the discrete approximation of the model interferes with the truncation error

$$\boldsymbol{\mathcal{G}}_N = G * \partial_x F_N(u_N) - \widetilde{G} * \widetilde{\partial}_x \widetilde{F}_N(\widetilde{u}_N) \tag{4}$$

of the underlying discretization scheme, where a tilde indicates the respective numerical approximation. For example, the unfiltered, i.e. continuous, solution u is unknown in an LES. However, an approximation $\widetilde{u}_N$ of the grid function u_N can be obtained from $\overline{u}_N$ by regularized deconvolution [4, 22]. Hence, the solution $\overline{u}_N$ obtained with the discrete operators does not satisfy Eq. (2), but rather a modified differential equation (MDE)

$$\partial_t \overline{u}_N + G * \partial_x F_N(u_N) = \boldsymbol{\mathcal{G}}_N \ . \tag{5}$$

The numerical truncation error can act as an implicit SGS model. Particularly, an explicit SGS model is resembled if the filtered divergence of the model SGS tensor is approximated

$$\mathcal{G}_N \approx -G * \partial_x \tau_{SGS} \ . \tag{6}$$

A suitable framework for implicit LES is available by the finite-volume method, implying reconstruction or deconvolution of the unfiltered solution at cell faces and the approximation of the physical flux function by a numerical flux function. With the *Adaptive Local Deconvolution Method* (ALDM) numerical discretization and SGS modeling are merged entirely [1, 14, 15, 13]. This is possible by exploiting the formal equivalence between cell-averaging and reconstruction in finite-volume discretizations and top-hat filtering and deconvolution in SGS-modeling. A local reconstruction of the unfiltered solution is obtained from a solution-adaptive combination of Harten-type deconvolution polynomials

$$\widetilde{p}^{\mp}_{k,r}(x_{j\pm1/2}) = \sum_{l=0}^{k-1} c^{\mp}_{k,r,l}(x_N)\overline{u}_{j-r+l}, \tag{7}$$

where half-integer indices denote reconstructions at the cell faces. The grid dependent coefficients $c^{\mp}_{k,r,l}$ are chosen such that $\widetilde{p}^{\mp}_{k,r}(x) = u(x) + \mathcal{O}\left(h^k\right)$ [11]. Deconvolution is regularized by limiting the degree k of local approximation polynomials to $k \leq K$ and by permitting all polynomials of degree $1 \leq k \leq K$ to contribute to the approximately deconvolved solution

$$\widetilde{u}^{\mp}(x_{j\pm1/2}) = \sum_{k=1}^{K}\sum_{r=0}^{k-1} \omega^{\mp}_{k,r}(\overline{u}_N)\widetilde{p}^{\mp}_{k,r}(x_{j\pm1/2}). \tag{8}$$

Adaptivity of the deconvolution operator is achieved by dynamically weighing the respective contributions by $\omega_{k,r}(\overline{u}_N)$. A suitable consistent numerical flux function,

$$\widetilde{F}_{j\pm1/2} = F\left(\frac{1}{2}\left(\widetilde{u}^{-}_{j\pm1/2} + \widetilde{u}^{+}_{j\pm1/2}\right)\right) - \sigma_{j\pm1/2}\left(\widetilde{u}^{+}_{j\pm1/2} - \widetilde{u}^{-}_{j\pm1/2}\right), \tag{9}$$

operating on the approximately deconvolved solution provides secondary regularization. $\sigma_{j\pm1/2}$ is a shift-invariant functional of $\overline{u}_N$, for details refer to [1, 14]. The solution-adaptive stencil-selection scheme and the numerical flux function contain free parameters that can be used to adjust the spatial truncation error of the discretization.

3 Modified-Differential-Equation Analysis

The MDEA is based on the assumption that the discrete unfiltered solution in a neighborhood of x_i can be represented by local approximation polynomials of degree K up to $K \leq L$. The polynomial approximation of the filtered solution is

$$\overline{u}_i \doteq \sum_{\mu=0}^{L-1} \breve{u}_i^{(\mu)} \frac{M_\mu(x_i)}{(\mu)!}, \tag{10}$$

where $\breve{u}_i^{(\mu)}$ stand for the order μ derivatives of the approximation polynomial $\breve{u}$ of u at x_i. M_μ is the μ-th moment of the filter kernel

$$M_\mu(x_i) = \int_{-\infty}^{+\infty} (x - x_i)^\mu G(x - x_i) dx \ . \tag{11}$$

The top-hat filter kernel gives

$$M_\mu(x_i) = \begin{cases} 0 & , \mu \ \text{ odd} \\ \dfrac{h_i^\mu}{2^\mu(\mu+1)} & , \mu \ \text{ even.} \end{cases} \tag{12}$$

Taking the order ν derivatives on both sides of Eq. (10), we obtain

$$\overline{u}_i^{(\nu)} \doteq \sum_{\mu=\nu}^{L-1} \breve{u}_i^{(\mu)} \frac{M_{(\mu-\nu)}(x_i)}{(\mu-\nu)!}, \tag{13}$$

for $\nu = 0, \ldots, L-1$. The set of Eq. (13) can be written in matrix form

$$\begin{bmatrix} \overline{u}_i \\ \overline{u}_i' \\ \vdots \\ \overline{u}_i^{(L-1)} \end{bmatrix} = \boldsymbol{C} \cdot \begin{bmatrix} \breve{u}_i \\ \breve{u}_i' \\ \vdots \\ \breve{u}_i^{(L-1)} \end{bmatrix}, \tag{14}$$

where the coefficient matrix $\boldsymbol{C}$ is upper triangular and diagonally dominant [11]. Solving (14) for $\breve{u}_i^{(\nu)}$, $\breve{u}_N$ is obtained in terms of the first $L-1$ derivatives of $\overline{u}_N$. This series expansion for $\breve{u}_N$ can be inserted as approximation for u_N when evaluating the truncation error of a numerical method.

By an analysis of the modified differential equation of a discretization scheme an implicit SGS model can be determined analytically. It can be observed that the Taylor series expansion of the truncation error of nonlinear discretization schemes contains functional expressions which are similar to explicit SGS models. For some discretizations a given explicit SGS model can be matched by adjusting parameters, as demonstrated in the following.

An analysis of ALDM for the 1-D Burgers equation has shown that by adjusting free parameters appropriately the Smagorinsky SGS model can be recovered implicitly: The viscous Burgers equation, where the flux

$$F(u) = \frac{1}{2}u^2 - \nu \partial_x u \tag{15}$$

is to be substituted in Eq. (1), is a popular 1-D model for the 3-D Navier Stokes equations. The Smagorinsky model formulated for the Burgers equation is

$$G * \partial_x \tau_{Smag} = -2C_S h^2 \left|\partial_x \overline{u}\right| \partial_x^2 \overline{u} \ . \tag{16}$$

MDEA of the initial-value problem has been performed for the semi-discretization on equidistant meshes [1]. This is consistent with the spatially-filtered interpretation of the LES equations, i.e., the time step being sufficiently small for the spatial truncation error to be dominant. Model parameters can be identified in such a way that the truncation error $\boldsymbol{\mathcal{G}}_N$ follows as

$$\boldsymbol{\mathcal{G}}_N = 2\,C_S \left|\frac{\partial \overline{u}}{\partial x}\right| \frac{\partial^2 \overline{u}}{\partial x^2}\, h^2 - \frac{1}{6}\, C_S \left|\frac{\partial \overline{u}}{\partial x}\right| \frac{\partial^4 \overline{u}}{\partial x^4}\, h^4 + \mathcal{O}\left(h^6\right) \ . \tag{17}$$

The resulting implicit formulation matches with the explicit model up to order $\mathcal{O}(h^3)$. Note that an interpretation of the higher order terms is difficult for coarse grid resolutions and non-smooth solution.

For the 3-D incompressible Navier-Stokes equations, however, MDEA based on Taylor series expansion turned out to be intractable since the analytical expressions become extremely lengthy. Another reason is the difficulty in solving the pressure-Poisson equation analytically.

Hickel et al. [14] have therefore resorted to an a-posteriori analysis of the spectral numerical viscosity of ALDM in numerical simulations of freely decaying homogeneous isotropic turbulence in the limit of vanishing molecular viscosity. Alternatively to adjusting the model parameters for a given explicit SGS model one can try to find systematically the SGS model that gives the best statistical representation of the SGS effects on the filtered scales. Provided that the grid resolution is sufficient, turbulent subgrid scales are believed to obey general properties such as a Kolmogorov scaling in the inertial wavenumber range. This can be exploited for determining optimal model parameters. Optimization target is a canonical reference flow configuration that represents the essential properties of 3-D Navier–Stokes turbulence.

Using Fourier transforms, the modified differential equation of a generic discretization of the incompressible Navier-Stokes equations can be written in spectral space as

$$\partial_t \widehat{E}(\boldsymbol{\xi}) - \widehat{T}_N(\boldsymbol{\xi}) + 2\nu \boldsymbol{\xi}^2 \widehat{E}(\boldsymbol{\xi}) = \widehat{\boldsymbol{G}}^{-1}(\boldsymbol{\xi}) \widehat{\boldsymbol{u}}_N^*(\boldsymbol{\xi}) \cdot \widehat{\boldsymbol{\mathcal{G}}}_C(\boldsymbol{\xi}) \tag{18}$$

The hat denotes the Fourier transform, i is the imaginary unit, and $\boldsymbol{\xi}$ is the wave-number vector. On the represented wave-number range $|\boldsymbol{\xi}| \leqq \xi_N$ the kinetic energy of the deconvolved velocity is

$$\widehat{E}(\boldsymbol{\xi}) = \frac{1}{2} \widehat{\boldsymbol{u}}_N(\boldsymbol{\xi}) \cdot \widehat{\boldsymbol{u}}_N^*(\boldsymbol{\xi}). \tag{19}$$

The nonlinear energy transfer $\widehat{T}_N(\boldsymbol{\xi})$ is the Fourier transform of the nonlinear term. The right-hand side of this equation is the numerical dissipation

$$\varepsilon_{num}(\boldsymbol{\xi}) = \widehat{\boldsymbol{G}}^{-1}(\boldsymbol{\xi}) \widehat{\boldsymbol{u}}_N^*(\boldsymbol{\xi}) \cdot \widehat{\boldsymbol{\mathcal{G}}}_C(\boldsymbol{\xi}) \tag{20}$$

implied by the discretization. Now we investigate how to model the physical subgrid dissipation ε_{SGS} by ε_{num}. An exact match between ε_{num} and ε_{SGS} cannot be achieved since ε_{SGS} involves interactions with non-represented scales. For modeling it is therefore necessary to invoke theoretical energy-transfer expressions. Employing an eddy-viscosity hypothesis the subgrid-scale dissipation is $\varepsilon_{SGS}(\boldsymbol{\xi}) = 2\nu_{SGS}\xi^2\widehat{E}(\boldsymbol{\xi})$. Similarly, the numerical dissipation can be expressed as

$$\nu_{num}(\boldsymbol{\xi}) = \frac{\varepsilon_{num}(\boldsymbol{\xi})}{2\xi^2\widehat{E}(\boldsymbol{\xi})}. \tag{21}$$

In general ν_{num} is a function of the wavenumber vector $\boldsymbol{\xi}$. For isotropic turbulence, however, statistical properties of (18) follow from the scalar evolution equation for the 3-D energy spectrum

$$\partial_t\widehat{E}(\xi) - \widehat{T}_N(\xi) + 2\nu\xi^2\widehat{E}(\xi) = \varepsilon_{num}(\xi). \tag{22}$$

For a given numerical scheme $\nu_{num}(\xi)$ can be computed from

$$\nu_{num}(\xi) = -\frac{\widehat{G}^{-1}(\xi)}{2\xi^2\widehat{E}(\xi)} \int\limits_{|\boldsymbol{\xi}|=\xi} \widehat{\boldsymbol{u}}_N^*(\boldsymbol{\xi}) \cdot \widehat{\boldsymbol{\mathcal{G}}}_N(\boldsymbol{\xi}) d\boldsymbol{\xi} \tag{23}$$

Convenient for our purposes is a normalization by

$$\nu_{num}^+(\xi^+) = \nu_{num}\left(\xi_N\xi^+\right)\sqrt{\xi_N/\widehat{E}(\xi_N)}, \quad \text{with} \quad \xi^+ = \frac{\xi}{\xi_N}. \tag{24}$$

For an evaluation of the numerical viscosity we consider freely decaying homogeneous isotropic turbulence in the limit of vanishing molecular viscosity which is a critical test case for predicting the proper SGS dissipation. Filtered and truncated highly resolved LES data are used as initial condition. Trial computations are advanced for a small number of time steps and followed by an *a-posteriori* analysis of the data that allows to identify the spectral numerical viscosity of the discretization [14]. Isotropic decaying turbulence does not lose memory of the initial data. To cope with this problem the spectral numerical viscosity from 10 uncorrelated realizations is evaluated and averaged. Each realization is advanced by one time step so that computational cost amounts to 10 time steps per evaluated numerical viscosity.

This methodology can be applied to any discretization scheme, only a dealiased spectral discretization will yield $\nu_{num}^+ \equiv 0$. Figure 1 shows the spectral numerical viscosities of standard finite difference (FD) methods. Central differencing methods are usually energy conserving, however, their dispersive errors re-distribute the kinetic energy between the scales. In average, energy is transferred from medium to large wavenumbers. For most wavenumbers the spectral numerical viscosity of the considered central FD schemes is positive. However, a large negative peak is found at the cutoff wavenumber. Negative dissipation at high wavenumbers results in an energy accumulation. This can lead to numerical instability unless the method is stabilized by adding artificial dissipation. These results are consistent with Ghosal's analysis [9].

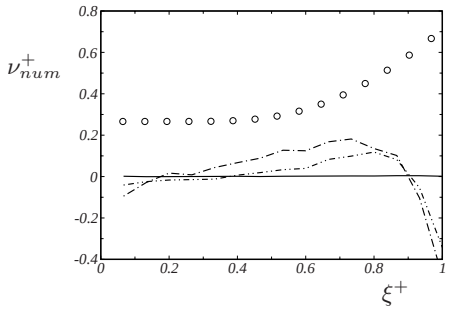

Fig. 1 Spectral numerical viscosity of ——— de-aliased spectral scheme, ·—·—·— 2nd order central FD, —··—··— 4th order central FD ∘ EDQNM theory [3]

4 Optimization of Discretization Coefficients

The assumption of an inertial-range spectrum ranging to infinity and allows for a direct comparison of the numerical dissipation with analytical expressions for the SGS dissipation spectrum. The concept of modeling nonlinear interactions in turbulence by a wavenumber-dependent spectral eddy viscosity was first proposed by Heisenberg [12]. For high Reynolds numbers and under the assumption of a Kolmogorov range Chollet [3] proposes the expression

$$\nu^+_{Chollet}(\xi^+) = 0.441 C_K^{-3/2} \left(1 + 34.47 e^{3.03\xi^+}\right) \tag{25}$$

as best fit to the exact solution. A set of discretization parameters is evaluated by the root-mean-square difference between the spectral numerical viscosity and the spectral eddy viscosity of EDQNM. The employed automatic optimization algorithm follows an evolutionary strategy in which natural biological processes are modeled by simple stochastic search methods. A set of free parameters is considered as genome of a living individual. The algorithm operates on a population of individuals and applies the survival-of-the-fittest principle of the Darwinian theory of evolution. At each generation, a new set of individuals is created by modeled natural processes, such as selection according to the level of fitness, recombination, and random mutation. This process leads to the evolution of a population of individuals that is better adapted to a cost function than the population that it was created from.

Since this algorithm works on populations instead of single individuals, the search is performed in an efficient parallel manner. The numbers of time-steps and realizations for evaluation of the cost function are chosen as a compromise between accuracy and computational feasibility. Surely, they are less than what would be necessary to completely remove the effect of stochastic fluctuations. Thus the resulting cost function is not smooth but exhibits residual fluctuations. Unlike standard gradient-approximation based optimization

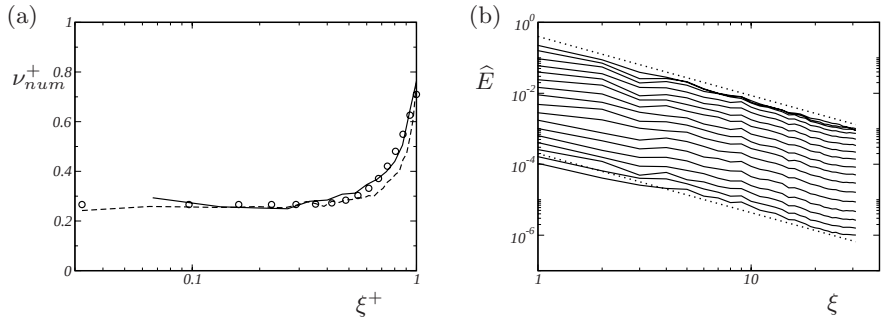

Fig. 2 (**a**) Numerical viscosity of ALDM with optimized parameters compared to the prediction of turbulence theory. ——— LES with $N = 32$, – – – – LES with $N = 64$, ∘ EDQNM theory [3]. (**b**) Instantaneous 3D energy spectra for LES of decaying isotropic turbulence. ——— ALDM; ····· $\widehat{E} \sim \xi^{-5/3}$

methods, evolutionary algorithms can handle such non-smooth cost functions [2]. For further details the reader is referred to [14] and the references therein.

5 Optimized Eddy Viscosity Model

The spectral eddy viscosity of the implicit model with the optimized parameter set yields an excellent match with theoretical predictions as shown in Fig. 2a. It exhibits a low-wavenumber plateau at the correct level and reproduces the typical cusp shape up to the cut-off wavenumber at the correct magnitude. ALDM nonlinearly combines interpolants from several central, upwind, and downwind stencils. The truncation error therefore is not purely dissipative. The probability density function of the numerical viscosity exhibits significant anti-dissipative contributions which represent backscatter, see [14].

The choice of parameters has been validated for LES of decaying homogeneous isotropic turbulence with a Kolmogorov spectrum throughout all represented wavenumbers in the limit $Re \longrightarrow \infty$. The energy spectrum decays self-similarly while preserving the $\xi^{-5/3}$ law up to the largest wavenumbers, see Figure 2b. The observed decay rate of the resolved turbulent kinetic energy $\varepsilon = \partial K/\partial t$ is proportional to the turbulent kinetic energy K to the power of $3/2$ as predicted by the scaling $\varepsilon \sim K^{3/2}L^{-1}$ for self-similar decay of an inertial-range spectrum, i.e. $L = \text{const}$. This agreement is not surprising but confirms the parameter calibration for this particular case at large Reynolds numbers.

For a more demanding test, we present results from a temporal simulation of a transitional wall-bounded flow. The solution is initialized at time $t = t_0$ as a laminar Blasius boundary-layer profile with thickness δ and free-stream velocity U_∞, superimposed with low-amplitude white-noise fluctuations. This

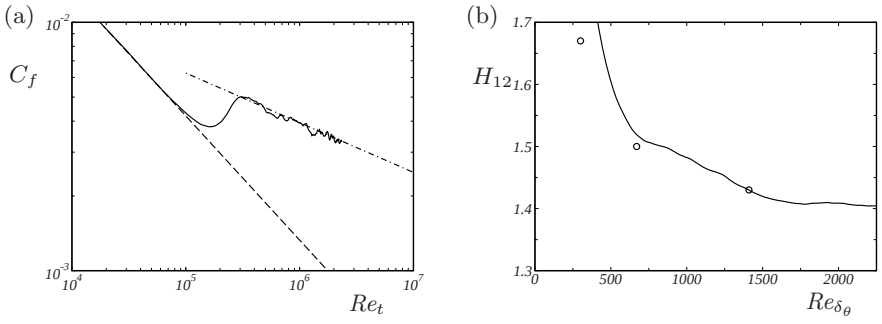

Fig. 3 (**a**) Evolution of friction coefficient C_f. ——— present LES, − − − − laminar theory $C_f \sim (Re_t)^{-1/2}$, ·—·—· turbulent theory $C_f \sim (Re_t)^{-1/5}$. (**b**) Evolution of the shape factor H_{12}. ——— present LES, ∘ DNS

initial disturbance is expected to grow during the simulation and eventually leads to transition of the flow to a turbulent state. Laminar-turbulent transition is one of the most demanding test cases for LES. When white noise is used, most energy is injected into decaying modes and only a low percentage of the disturbance excites the instability modes of the laminar flow. For the onset of transition the SGS model must not affect the growth and amplification of these instable modes. Most eddy-viscosity SGS models do not satisfy this requirement without ad hoc modifications.

The computational box has the extents $48\delta \times 124\delta \times 128\delta$ and is discretized with $48 \times 96 \times 256$ cells in streamwise $\times$ wall-normal $\times$ spanwise directions, respectively. A no-slip condition is imposed at the wall and the free-stream interface is modeled by a decay condition. Periodic boundary conditions are imposed in streamwise and spanwise direction. The large spanwise extent of the computational domain was chosen in order to improve the accuracy of turbulence statistics that are computed from instantaneous snapshots using spatial averaging. Figure 3a shows the friction coefficient $C_f = 2U_\tau^2/U_\infty^2$ for a temporal LES using ALDM. During the growth of the laminar boundary layer the friction coefficient follows the analytical solution $C_f \sim (Re_t)^{-1/2}$, where the Reynolds number is defined as $Re_t = tU_\infty^2/\nu$. One can clearly see that the boundary layer undergoes laminar-turbulent transition. Eventually the friction coefficient follows the turbulent law $C_f \sim (Re_t)^{-1/5}$. The evolution of the shape factor H_{12} is shown in Fig. 3b. The prediction of our temporal LES with ALDM is in good agreement with DNS by Spalart [21] in the later turbulent stages. Results from LES and DNS do not match for the Reynolds number $Re_{\delta^*} = 500$ ($Re_{\delta_\theta} \approx 300$). Spalart's DNS predict turbulent velocity profiles that can hardly be obtained by natural transition at these Reynolds number. In the turbulent regime the performance of the implicit SGS model is evaluated by comparing profiles of mean velocity and Reynolds stresses with DNS data. Figure 4 shows results for the mean velocity profile

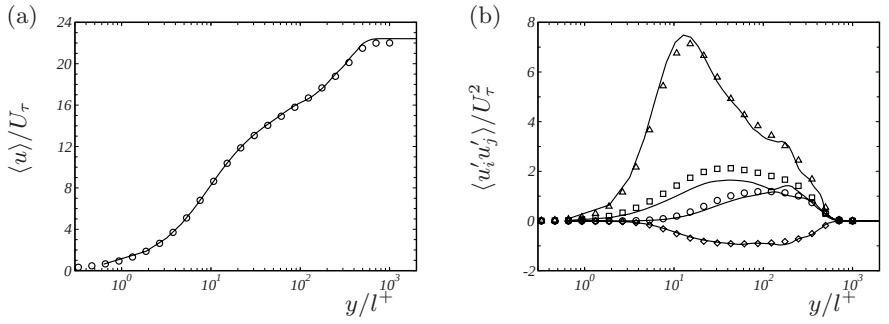

Fig. 4 Profiles of mean velocity and Reynolds stresses for turbulent boundary layer flow at $Re_{\delta_\theta} = 1410$. ——— present LES, symbols denote reference DNS

and Reynolds stresses from LES and DNS at $Re_{\delta_\theta} = 1410$. ALDM apparently predicts the turbulence statistics correctly. It should be noted that the prediction of Reynolds-stress anisotropy by ALDM is better than by common explicit eddy-viscosity models [15].

6 Conclusion

We have presented an approach for the design of physically optimized discretization methods for LES with implicit SGS model. The resulting method is based on the main components of finite-volume discretizations and allows for a full merge of discretization and subgrid-scale model. Although model parameters are determined by isotropic turbulence in the limit of infinite Reynolds number we have shown that the resulting model can be applied also to physically complex flows.

References

1. Adams NA, Hickel S, Franz S (2004) Implicit subgrid-scale modeling by adaptive deconvolution. J Comp Phys 200:412–431
2. Back T, Fogel D, Michalewicz Z (1997) Handbook of Evolutionary Computation. University Oxford Press.
3. Chollet J-P (1984) Two-point closures as a subgrid-scale modeling tool for large-eddy simulations. In: Durst F and Launder B (eds) Turbulent Shear Flows IV, Heidelberg:62–72. Springer, Berlin
4. Domaradzki JA, Adams NA (2002) Direct modeling of subgrid scales of turbulence in large-eddy simulations. J Turb 3, Art no 24
5. Domaradzki JA, Radhakrishnan S (2005). Eddy viscosities in implicit large eddy simulations of decaying high Reynolds number turbulence with and without rotation. Fluid Dyn Res 36:385–406

6. Domaradzki JA., Xiao Z, Smolarkiewicz PK (2003). Effective eddy viscosities in implicit large eddy simulations of turbulent flows. Phys Fluids 15:3890–3893
7. Fureby C, Tabor G, Weller HG, Gosman AD (1997). A comparative study of subgrid scale models in homogeneous isotropic turbulence. Phys Fluids 9:1416–1429
8. Garnier E, Mossi M, Sagaut P, Comte P, Deville M (1999) On the use of shock-capturing schemes for large-eddy simulation. J Comput Phys 153:273–311
9. Ghosal S (1996) An analysis of numerical errors in large-eddy simulations of turbulence. J Comput Phys 125:187–206
10. Grinstein F, Margolin L, Rider W (eds) (2007) Implicit large eddy simulation: computing turbulent flow dynamics. Cambridge University Press
11. Harten A, Engquist B, Osher S, Chakravarthy S (1987) Uniformly high order accurate essentially non-oscillatory schemes, III. J Comput Phys 71:231–303
12. Heisenberg W (1948) Zur statistischen Theorie der Turbulenz. Z Phys A 124:628–657
13. Hickel S, Adams NA (2007) On implicit subgrid-scale modeling in wall-bounded flows. Phys Fluids 19, Art no 105106
14. Hickel S, Adams NA, Domaradzki JA (2006) An adaptive local deconvolution method for implicit LES. J Comput Phys 213:413–436
15. Hickel S, Adams NA, Mansour NN (2007) Implicit subgrid-scale modeling for large-eddy simulation of passive-scalar mixing. Phys Fluids 19, Art no 095102
16. Leonard A (1974) Energy cascade in large eddy simulations of turbulent fluid flows. Adv Geophys 18A:237–248
17. Lesieur M (1997) Turbulence in Fluids, third edn. Kluwer, Dordrecht
18. LeVeque RJ (1992) Numerical methods for conservation laws Birkhäuser, Basel
19. Sagaut P (2005) Large-Eddy Simulation for Incompressible Flows, third edn. Springer, Berlin
20. Schumann U (1975) Subgrid scale model for finite-difference simulations of turbulence in plane channels and annuli. J Comput Phys 18:376–404
21. Spalart PR (1988) Direct simulation of a turbulent boundary layer up to $Re_\theta = 1410$. J Fluid Mech 187:61–98
22. Stolz S, Adams NA (1999) An approximate deconvolution procedure for large-eddy simulation. Phys Fluids 11:1699–1701

Spectral Behavior of Various Subgrid-Scale Models in LES at Very High Reynolds Number

R. Cocle, L. Bricteux, and G. Winckelmans

Université Catholique de Louvain (UCL), Mechanical Engineering Department, Division TERM, and Center for Systems Engineering and Applied Mechanics (CESAME), 1348 Louvain-la-Neuve, Belgium.
roger.cocle@uclouvain.be

Abstract. This study investigates the capabilities of various recent subgrid-scale (SGS) models (the so-called "multiscale" models) for large-eddy simulation (LES), used either in a vortex-in-cell (VIC) method or in a pseudo-spectral (PS) method, and their applicability to the simulation of decaying homogeneous isotropic turbulence (HIT) in the limit of very high Reynolds number (i.e. LES on a large grid and where the molecular viscosity dissipation is negligible compared to the SGS dissipation). The proper coefficient value for each model investigated was obtained by a calibration performed in an earlier study. Various large grid resolutions (128^3, 256^3 and 512^3) are used to compare and to indeed obtain the asymptotic spectral behavior of each model. We are then able to emphasize the behavior of the models, that is not necessarily observable in "small" LES (i.e. in LES at moderate Reynolds number and/or using a smaller mesh). In particular, we show that the multiscale models perform significantly better than the Smagorinsky model: a much wider inertial range is obtained.

Keywords: Large-eddy simulation, Subgrid-scale modelling, Multiscale modelling, High Reynolds number flows, Spectral behavior, Effective viscosity, Hyper-viscosity, Decaying homogeneous isotropic turbulence, Lagrangian methods, Vortex particle method, Vortex-in-cell method, Spectral method

1 Numerical Methods

The governing equations are the Navier-Stokes equations for incompressible flows with constant viscosity and supplemented by a subgrid scale model:

$$\nabla \cdot \mathbf{u} = 0 \tag{1}$$

$$\frac{\partial \mathbf{u}}{\partial t} + (\mathbf{u} \cdot \nabla)\,\mathbf{u} = -\nabla P + \nu \nabla^2 \mathbf{u} + \nabla \cdot \tau^M, \tag{2}$$

where $\mathbf{u}$ is the LES velocity, P is the reduced pressure, ν is the kinematic viscosity, and τ^M is the SGS stress tensor model. We present hereafter the two methods that we use to solve these equations.

J. Meyers et al. (eds.), Quality and Reliability of Large-Eddy Simulations,

1.1 Pseudo-Spectral Solver

The solver used here is based on the Fourier-Galerkin pseudo-spectral (PS) methodology. The time integration of equation (2) is carried out in spectral space using a technique in which the convective and subgrid scale model terms are marched explicitly using the 3rd order Williamson scheme. The nonlinear term is evaluated using a pseudo-spectral algorithm and the dealiasing is done using a phase shift procedure as explained in [2], which ensures energy conservation. The divergence-free character of the velocity field is ensured by reprojection, performed in spectral space.

1.2 Vortex-in-Cell Code

The equations are solved in their vorticity-velocity formulation:

$$\frac{\mathrm{D}\boldsymbol{\omega}}{\mathrm{Dt}} - \nabla \cdot (\mathbf{u}\,\boldsymbol{\omega}) = \nu \nabla^2 \boldsymbol{\omega} + \nabla \cdot \mathbf{T}^M \tag{3}$$

with $\boldsymbol{\omega} = \nabla \times \mathbf{u}$ the LES vorticity field and $\mathbf{T}^M$ the SGS model. The numerical solution of (3) is obtained using the vortex-in-cell (VIC) approach. The vorticity field is represented by regularized vortex particles:

$$\boldsymbol{\omega}_\sigma(\mathbf{x},t) \;=\; \sum_p \boldsymbol{\alpha}_p(t)\; \frac{1}{(\sqrt{\pi}\,\sigma)^3}\; \exp\left(-\frac{|\mathbf{x}-\mathbf{x}_p(t)|^2}{\sigma^2}\right)\;, \tag{4}$$

with $\boldsymbol{\alpha}_p = \int \boldsymbol{\omega}\, d\mathbf{x} = \boldsymbol{\omega}_p\, h^3$ the strength of particle p, $\mathbf{x}_p$ its position, h the discretization size (grid size, also used for particle redistribution), and σ the regularization parameter. Interpolations between particles and grid, as well as particle redistribution, are all done using the M_4' scheme. The vector streamfunction $\boldsymbol{\psi}$ is obtained by solving the Poisson equation $\nabla^2\boldsymbol{\psi} = -\boldsymbol{\omega}$ on the grid using Fishpack [1]. The velocity field (needed for convection and stretching) is then obtained from $\mathbf{u} = \nabla \times \boldsymbol{\psi}$, using 4th order finite differences (FD). The convective part is done using the Lagrangian approach: $d\mathbf{x}_p/dt = \mathbf{u}(\mathbf{x}_p)$; this ensures good convection (i.e., negligible dissipation and dispersion errors). The time variation of the particle strengths (i.e., both the vorticity stretching and the dissipation terms) is evaluated on the grid, using FD. The global time marching procedure is carried out using the Leap Frog scheme for the convection and the Adams-Bashforth scheme for the diffusion. Finally, the divergence-free character of the vorticity field is ensured by reprojection of the discrete vorticity field, which also requires solving a Poisson equation. The details of the method are presented in [5, 14, 4].

2 Subgrid Scale Modeling

We classify the multiscale subgrid scale models in two sets, according to the spectral content of the field on which they are acting:

- *Type I* models ("x-complete" models): models acting on the complete LES field. The SGS stress is then modelled using $\tau_{ij}^M = 2\,\nu_{\rm sgs} S_{ij}$ with $S_{ij} = (\partial u_i/\partial x_j + \partial u_j/\partial x_i)\,/2$ the strain rate tensor. For the vorticity formulation, we use $T_{ij}^M = 2\,\nu_{\rm sgs} Q_{ij}$ with $Q_{ij} = (\partial \omega_i/\partial x_j + \partial \omega_j/\partial x_i)\,/2$.
- *Type II* models ("x-small" models): models acting on a "small-scale" LES field. The SGS stress is then modelled using $\tau_{ij} = 2\,\nu_{\rm sgs}\, S_{ij}^s$ with S_{ij}^s the strain rate tensor of the small scale field. For the vorticity formulation, we use Q_{ij}^S.

The small-scale field is obtained by using the compact (stencil 3) tensor-product discrete filter, and that is iterated n times to produce an order $2n$ filter [8, 3]:

$$\mathbf{u}^{s^{(n)}} = \mathbf{u} - \overline{\mathbf{u}}^{(n)} \tag{5}$$

with

$$\overline{\mathbf{u}}^{(n)} = \left(I - \left(-\delta_x^2/4\right)^n\right)\left(I - \left(-\delta_y^2/4\right)^n\right)\left(I - \left(-\delta_z^2/4\right)^n\right)\mathbf{u} \tag{6}$$

where $\delta_x^2 f_{i,j,k} = f_{i+1,j,k} - 2f_{i,j,k} + f_{i-1,j,k}$. In Fourier space, the filtered field is:

$$\begin{aligned}\widehat{\overline{\mathbf{u}}^{(n)}}(\mathbf{k}) = &\left(1 - \sin^{2n}\left(\frac{k_x\,h_x}{2}\right)\right)\\ &\left(1 - \sin^{2n}\left(\frac{k_y\,h_y}{2}\right)\right)\\ &\left(1 - \sin^{2n}\left(\frac{k_z\,h_z}{2}\right)\right)\widehat{\mathbf{u}}(\mathbf{k})\end{aligned} \tag{7}$$

This classification can be further extended according to the field on which $\nu_{\rm sgs}$ is evaluated (complete or small). The LES length scale is here defined as: $\Delta = (h_x h_y h_z)^{1/3}$. The constants used for the different models were carefully calibrated on HIT at high Reynolds number.

2.1 *Type I* Models

We first present the "x-complete" models. The classical Smagorinsky (SMAG) model is the most common "complete-complete" model:

$$\nu_{\rm sgs} = C_S\,\Delta^2\,(\,2\,S_{ij}S_{ij}\,)^{1/2} \tag{8}$$

with $C_S = 0.027$. A second model is the FSF model [6] (a "small-complete" model). Here, the subgrid viscosity is obtained from the "filtered structure function" $F_2^{s^{(n)}}$:

$$\nu_{\rm sgs} \;=\; C_F^{(n)} \Delta \sqrt{F_2^{s^{(n)}}}\;, \tag{9}$$

where

$$F_2^{s^{(n)}} \;=\; \left\langle \| \,\mathbf{u}^{s^{(n)}}(\mathbf{x}+\mathbf{x}') - \mathbf{u}^{s^{(n)}}(\mathbf{x})\,\|^2 \right\rangle_{|\mathbf{x}'|\,=\,\Delta}\;. \tag{10}$$

The coefficient for $n = 1$ is $C_F^{(1)} = 0.078$. The structure function is evaluated using the nearest neighbors ($3^3 = 27$) values. Note that, in the original FSF model (as investigated here), the small-scale field $\mathbf{u}^{s^{(n)}}$ is obtained by recursive application (n times) of the 2nd order (i.e., stencil 3 and cross-based) FD Laplacian:

$$\mathbf{u}^{s^{(n)}} = \left(-\frac{\Delta^2}{4}\nabla^2\right)^n \mathbf{u} \,. \tag{11}$$

It could also be obtained using the compact tensor-product filter (Eqs.(5, 6, 7)). A third model is the Filtered Smagorinsky model (a "small-complete" model):

$$\nu_{\text{sgs}} = C_{S_2}^{(n)}\, \Delta^2\, (\, 2\, S_{ij}^s S_{ij}^s\,)^{1/2}. \tag{12}$$

The coefficient for $n = 1$ is $C_{S_2}^{(1)} = 0.045$.

2.2 *Type II* Models

We now present the "x-small" models, thus those where the SGS viscosity is applied on the small-scale field ($\mathbf{u}^s$ or $\boldsymbol{\omega}^s$ depending on the formulation for the Navier-Stokes equations). The first "complete-small" model is the "regularized" version, here using the tensor product discrete filter, of the "variational multiscale" model (VM) of [7], used in [8]. The RVM model was also further proposed and tested by [13] and also by [11, 12]. We here use

$$\nu_{\text{sgs}} = C_R^{(n)}\, \Delta^2\, (\, 2\, S_{ij} S_{ij}\,)^{1/2} \,, \tag{13}$$

with $C_R^{(1)} = 0.036$ and $C_R^{(3)} = 0.060$. The second model considered is the regularized version of the "small-small" variational multiscale model. We here use

$$\nu_{\text{sgs}} = C_{R_2}^{(n)}\, \Delta^2\, (\, 2\, S_{ij}^s S_{ij}^s\,)^{1/2} \tag{14}$$

which is here noted RVM_s. This model was proposed and evaluated by [13] and by [11, 12]. The coefficient for $n = 1$ is $C_{R_2}^{(1)} = 0.066$.

2.3 High Order Hyper-Viscosity Model

The hyper-viscosity (HV) SGS model is used solely with the PS code, and as a basis for comparisons to the multiscale models. It reads

$$\tau_{ij}^M = (-1)^p\, \nabla^{2p} (2\, \nu_h\, S_{ij}). \tag{15}$$

On an uniform grid and using a global time scale T_0 in the SGS viscosity (for simplification), this leads to:

$$\nabla \cdot \widehat{\tau}^M(\mathbf{k}) = -C^{(p)} \frac{1}{T_0} (kh)^{2(p+1)} \widehat{\mathbf{u}}(\mathbf{k}). \tag{16}$$

In the present study, we use a very high order HV model ($p = 7$).

3 Results on HIT

We are interested in LES of decaying HIT in the limit of very high Reynolds number (i.e. simulations where the molecular viscosity dissipation is negligible compared to the SGS dissipation). Thus, we deliberately run LES with ν set to zero. The results presented were computed using the VIC and the PS codes. The initial condition was build following the algorithm described by [10]. This initial field then evolved using LES. For the investigations using the VIC code, the following SGS models are used: SMAG, FSF (with $n = 1$), RVM (with $n = 1$ and $n = 3$) and RVM_s. The models investigated using the PS code are the SMAG model, the RVM_s (with $n = 3$) model and the high order HV model.

Figure 1 shows the obtained energy spectra for a 128^3 grid (also time-averaged between $t = 10$ and 40, i.e. when the turbulence is statistically converged). We observe that the *Type II* models with $n = 3$ provide the broader inertial range (i.e., with $k^{-5/3}$ behavior). The width of this captured inertial range decreases with the order of the filter used to obtain the small-scale field (compare RVM with $n = 1$ to RVM with $n = 3$). In opposition, the SMAG and the FSF models do not exhibit any inertial range on such a 128^3 grid. The same conclusion holds for the Filtered Smagorinsky model, even though not shown here. Nevertheless, all spectra are clearly altered by a "bump-like" behavior at the medium to high wavenumbers, though to a lesser extent for the *Type II* models using high order ($n = 3$) filters. This non-physical energy accumulation is present because the shape of the dissipation spectra of the SGS models is never exactly the required one. Indeed, since any SGS model must dissipate, it can never lead to an inertial range obtained over all medium to high wavenumbers of the LES (recall that an inertial range corresponds to an energy cascade without dissipation). Hence, one always obtains the "bottleneck" effect with energy accumulation (bump) followed by dissipation. However, the behavior is much improved when the *Type II* models are used. As they act only at the small scales, their influence on the large scales is reduced and allows to capture a $k^{-5/3}$ inertial range on part of the LES.

This conclusion is also valid for the spectrum obtained using the high order HV model: it provides an inertial range as broad as the *Type II* models with $n = 3$ (even a bit broader), yet the "bump" is more pronounced. Our result compares well with [9] who also shows the presence of the "bottleneck" effect in the energy spectra when a high order HV model is used.

We also investigate the asymptotic behavior of the models when performing LES on larger and larger grids, see Fig. 2. We consider the SMAG model, the RVM_s model and the high order HV model, and we compare the spectra obtained using the PS code and higher resolutions. Such LES has indeed reached its "asymptotic behavior", with self-similar obtained spectra. We also confirm the unequivocal presence of the "bump-like" behavior in all models. As expected, the $k^{-5/3}$ inertial range becomes broader as the grid is taken

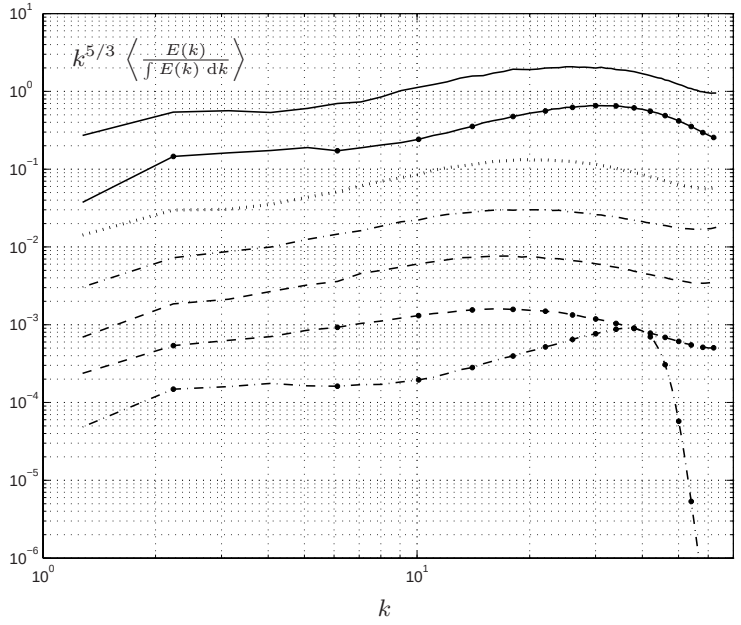

Fig. 1 Compensated and normalized energy spectra for a 128^3 grid (also time-averaged between $t = 10$ and 40; the curves are shifted vertically by 0.5 to better distinguish them): (1) using the VIC code: SMAG (*dash*), FSF (*dash-dot*), RVM with $n = 1$ (*dot*) and RVM with $n = 3$ (*solid*); (2) using the PS code: SMAG (*dash with bullets*), high order HV (*dash-dot with bullets*) and $\mathrm{RVM_s}$ with $n = 3$ (*solid with bullets*)

larger. For instance, the $\mathrm{RVM_s}$ model on a 256^3 grid is able to obtain an inertial range for $4 \leq k \leq 20$ (to be compared to a range $4 \leq k \leq 8$ only for the SMAG model).

4 Conclusions

The results obtained by performing LES of HIT allow to highlight the good spectral behavior of the multiscale subgrid models: those acting on a "small" field. One of the original aspect of this work is that all LES were performed on large grids and at very large Reynolds number, allowing to obtain the asymptotic behavior of each model. The comparisons show that the RVM and $\mathrm{RVM_s}$ models perform significantly better than the Smagorinsky model: a much wider inertial range is obtained. It is also found that, with the same SGS model, the VIC code produces spectra that are very similar to those obtained by the reference PS code (see, e.g., the results with the SMAG model in Fig. 1). Recall that the VIC code also has very good qualities: essentially

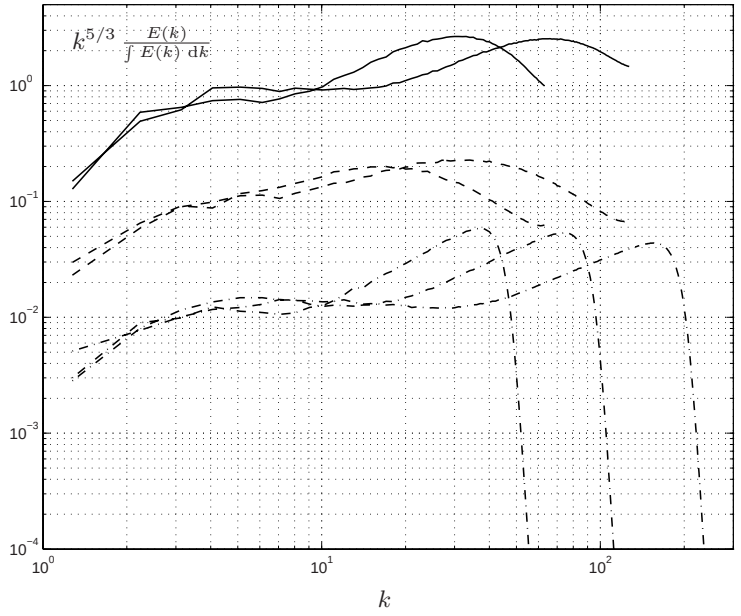

Fig. 2 Compensated and normalized energy spectra when using larger grids (PS code at $t = 20$; the curves are shifted vertically by 0.125 to better distinguish them): $\mathrm{RVM_s}$ with $n = 3$ on 128^3 and 256^3 grids (*solid*), SMAG on 128^3 and 256^3 grids (*dash*), high order HV on 128^3, 256^3 and 512^3 grids (*dash-dot*)

no dispersion and very little numerical dissipation (the PS code has none, of course). The issue of the code numerics interacting with the SGS model is thus of lesser importance in VIC than in other numerical methods.

References

1. Adams J, Swarztrauber P, and Sweet R (1975) Efficient FORTRAN subprograms for the solution of elliptic partial differential equations (FISHPACK ver 4.0). NCAR Technical Note TN/IA-109
2. Canuto C, Hussaini MY, Quarteroni A, Zang TA (1988) Spectral methods in fluid dynamics. Springer, New-York
3. Cocle R, Dufresne L, Winckelmans G (2006) Investigation of multiscale subgrid models for LES of instabilities and turbulence in wake vortex systems. In: Complex Effects in LES: Springer volume, LNCSE series. Springer, Berlin
4. Cocle R, Winckelmans GS, Daeninck G (2007) Combining the vortex-in-cell and parallel fast multipole methods for efficient domain decomposition simulations. J Comp Phys 227(4):2263–2292
5. Cottet G-H, Koumoutsakos PD (2000) Vortex methods, theory and practice. Cambridge University Press, Cambridge

6. Ducros F, Comte P, Lesieur M (1996) Large-eddy simulation of transition to turbulence in a boundary layer spatially developing over a flat plate. J Fluid Mech 326:1–36
7. Hughes TJR, Mazzei L, Oberai AA, Wray AA (2001) The multiscale formulation of large eddy simulation: decay of homogeneous isotropic turbulence. Phys Fluids 13:505–512
8. Jeanmart H, Winckelmans G (2007) Investigation of eddy-viscosity models modified using discrete filters: a simplified "regularized variational multiscale model" and an "enhanced field model". Phys Fluids 19, Art no 055110
9. Lamorgese AG, Caughey DA, Pope SB (2005) Direct numerical simulation of homogeneous tubulence with hyperviscosity. Phys Fluids 17, Art no 015106
10. Rogallo R (1981) Numerical experiments in homogeneous turbulence. NASA Tech Memo 81315, NASA Ames Research Center
11. Stolz S, Schlatter P, Meyer D, Kleiser L (2004) High-pass filtered eddy-viscosity models for LES, In: Friedrich R, Geurts BJ, Métais O (eds) Direct and large-eddy simulation V:81–88. Kluwer, Dordrecht
12. Stolz S, Schlatter P, Kleiser L (2005) High-pass filtered eddy-viscosity models for large-eddy simulations of transitional flow. Phys Fluids 17, Art no 065103
13. Vreman AW (2003) The filtering analog of the variational multiscale method in large-eddy simulation. Phys. Fluids 15:L61–L64
14. Winckelmans G (2004) Vortex methods. In: Stein E, de Borst R, Hughes TJR (eds) Volume 3 (Fluids) of the Encyclopedia of computational mechanics. John Wiley & Sons, New York

Performance Assessment of a New Advective Subgrid Model Through Two Classic Benchmark Test Cases

Luiz E. B. Sampaio[1], Angela O. Nieckele[1], and Margot Gerritsen[2]

[1] Department of Mechanical Engineering, Pontifícia Universidade Católica do Rio de Janeiro – PUC/Rio, R. Marquês de S. Vicente 225, Gávea, 22453-900 Rio de Janeiro, RJ, Brazil. luizebs@mec.puc-rio.br, nieckele@mec.puc-rio.br

[2] Department of Energy Resources Engineering, Stanford University, Green Earth Sciences Building, Stanford, CA, USA 94305-2220. margot.gerritsen@stanford.edu

Abstract. The purpose of this paper is to investigate and validate an alternative subgrid model to be used in Large-Eddy Simulations, based on an advective formulation. Rather than modeling the subgrid tensor that appears in the LES formulation as is commonly done, we directly model the subgrid force vector, imposing two basic requirements. First, it must act only on the smallest scales. Second, it must be of an advective nature, which means it must have a preferred direction aligned with the mass flux. The results for two benchmark test cases show that this approach can successfully represent the effect of the small scales on the resolved ones, while guaranteeing numerical stability and greater robustness in adverse mesh environments, when compared to some traditional eddy-viscosity based models.

Keywords: Turbulence, Large-eddy simulations, Subgrid model

1 Introduction

The vast majority of functional subgrid models currently employed in LES [1] [2] makes use of a diffusive formulation based on the eddy-viscosity assumption. This supposes that the tensor is aligned with the symmetrical part of the velocity gradient, which is generally not true. For this class of subgrid model, an aligned subgrid tensor is obtained by multiplying the strain rate by a scalar, known as eddy-viscosity, which may be derived from a characteristic length and a characteristic velocity. The characteristic length is readily available from the mesh spacing, and usually is taken as the cubic root of the volume of the cell – the control volume in the Finite Volume Method (FVM) case. While this seems appropriated for isotropic regular meshes, it is easy to understand its limitations when dealing with highly anisotropic ones.

J. Meyers et al. (eds.), Quality and Reliability of Large-Eddy Simulations,

Since the subgrid term to be modeled arises from an algebraic manipulation of an advective term, the objective of this paper is to investigate and validate an alternative subgrid model, based on an advective formulation. In such approach, instead of modeling the tensor and take its divergence, as $\nabla \cdot \tau_{\mathbf{SGS}}$, one aims directly at the resulting subgrid force, $\mathbf{f} = \nabla \cdot \tau_{\mathbf{SGS}}$, which has only three components. This force is built in a way to comply with two basic principles: as a LES subgrid model, it must act only in the smallest scales, and, following the motivation exposed in the above paragraph, it must be of advective nature, which means it must have a preferred direction, so that smallest structures aligned with the mass flux are eliminated first, or at least faster.

The idea of representing the subgrid force instead of the subgrid tensor is not new, and has been explored by several authors in the past [3], [4] and [5]. Carati and Wray [5], for instance, derived a transport equation to model the evolution of this subgrid force. In the present work, a direct formulation is proposed instead.

This paper is structured as follows: Section 2 presents the main motivations for new proposal, as well as the description of the advective subgrid model. The results for two benchmark test cases are presented and analyzed in 3. In the first set of tests, the performance of the model is tested employing both isotropic and anisotropic meshes to predict the Homogeneous Isotropic Turbulence (HIT) in a "periodic box". The anisotropic tests are important since, in practical situations with more realistic cases, an isotropic mesh cannot be afforded. The use of anisotropic meshes in these benchmark tests allowed more realistic cases to be covered, without adding further complexity to the test problem geometry and physics. A second set of tests involves turbulent channel flows, where the mesh concentrates in the proximity of the walls. In this later case, we also explore mesh spacing variations in the streamwise direction.

This new approach has been implemented on top of an opensource object-oriented framework [6]. The traditional models used throughout this work are those readily available from OpenFOAM, version 1.4. OpenFOAM source code is publicly available if further implementation detail is sought [7].

2 Subgrid Model

The Navier-Stokes and continuity equations for incompressible flows are:

$$\frac{\partial \mathbf{u}}{\partial t} + \nabla \cdot (\mathbf{u}\,\mathbf{u}) = -\nabla p + \nu \nabla^{\mathbf{2}} \mathbf{u}\,; \quad \nabla \cdot \mathbf{u} = \mathbf{0}\,, \tag{1}$$

with $\mathbf{u}$ the velocity, $p = P/\rho$ the modified pressure, which incorporates the fluid density ρ, and ν the kinematic viscosity.

To reduce the number of degrees of freedom of the original transport equations, the Large-Eddy Simulation (LES) method employs a spatial filtering

operator to select the largest and most energetic structures to be computed, leaving only the small eddies to be modeled [8].

The filtered transport equations can be written as,

$$\frac{\partial \overline{\mathbf{u}}}{\partial t} + \nabla \cdot (\overline{\mathbf{u}}\,\overline{\mathbf{u}}) + \varepsilon_{\mathbf{com}} + \nabla \cdot \tau_{\mathbf{SGS}} = -\nabla \overline{p} + \nu \nabla^{\mathbf{2}} \overline{\mathbf{u}}, \qquad \nabla \cdot \overline{\mathbf{u}} = \mathbf{0}\,, \tag{2}$$

where $\overline{\mathbf{u}}$ is the filtered velocity, and $\overline{p}$ the filtered modified pressure. The commutative error, $\varepsilon_{\mathbf{com}}$, often neglected, is a consequence of commuting the filtering process with a spatial derivative operator. The subgrid tensor, $\tau_{\mathbf{SGS}}$, is the result of commuting the filtering with the outer product ($\mathbf{uu}$). A closed expression can not be found for this subgrid tensor, and hence it must be separately modeled. In order to prevent the artificial accumulation of energy in the smallest modes in numerical simulations, the eddy-viscosity approach models the tensor $\tau_{\mathbf{SGS}}$ as

$$\tau_{\mathbf{SGS}ij} - \frac{1}{3}\ \tau_{\mathbf{SGS}kk}\ \delta_{ij} = -2\ \nu_{SGS}\ \overline{S}_{ij}\,; \quad \overline{S}_{ij} = 0.5\left(\frac{\partial \overline{u}_i}{\partial x_j} + \frac{\partial \overline{u}_j}{\partial x_i}\right), \tag{3}$$

where ν_{SGS} is the subgrid viscosity, and $\overline{S}_{ij}$ is the filtered strain rate.

In the particular case of Finite Volume Method (FVM), the filtering operation may be conveniently confused with the volume integral over the control volume. Therefore, no further filtering is needed, and this process is said to be implicit, or embedded in the FVM.

2.1 Motivation for the Advective Formulation

In eddy-viscosity models a dissipative term is added to the transport equations with the purpose of eliminating or damping the small turbulent structures, which would otherwise be fed and amplified by the energy cascade. As an alternative idea to the widely accepted Boussinesq hypothesis (Eq. 3), we propose a new SGSM approach, in which we enforce the subgrid damping by adding an additional force $\mathbf{f} = \nabla \cdot \tau_{\mathbf{SGS}}$ to the transport equations. Instead of finding an expression for $\tau_{\mathbf{SGS}}$ and adding its divergence to the Navier-Stokes equation, we directly derive the force $\mathbf{f}$ such that the smallest modes supported by the mesh are severely damped, while those with twice or more than twice their wavelength are almost or completely untouched.

A potentially advantageous effect of damping small modes is that the resulting discrete dynamic system is more robust and less prone to numerical instability. Generally, LES practitioners employ non-dissipative central difference schemes to calculate derivatives, avoiding other more stable approaches like upwind methods. Since instability issues are often related to constraints not allowing the use of a regular mesh, the above mentioned effect might prove handy, allowing more flexibility in mesh design. In fact, the methodology presented here was also tested in more stringent mesh environment presenting high stretching ratios [9] with very good results and no stability issues.

2.2 Advective Formulation Methodology

The methodology is illustrated on a representative yet simplified problem, which is the 1-D transport of a passive scalar field by a pure advection obeying the equation:

$$\frac{\partial \phi}{\partial t} + \mathbf{u} \cdot \nabla \phi + f_\phi = 0\,, \tag{4}$$

where f_ϕ is the artificial "force" [3] to be derived, for a general scalar variable ϕ. Later, the methodology will be extended to the more interesting case of a 3-D vector field, where ϕ represents each of the velocity components in a full Navier-Stokes equation.

The first step towards the derivation of a force capable of selectively damping only the smallest modes supported by the mesh is the identification of a fundamental difference between these modes, hereby referred to as undesired or cut-off modes, and the larger modes. A possible way to distinguish them is through the evaluation of the projected gradients of the transported variable ϕ, at the faces of a control volume. If A and B are two adjacent control volume centroids sharing a common face F, the gradient at the cell-center A can be calculated using the Gauss theorem as

$$(\nabla \phi)_A = \frac{1}{\forall_A} \sum_{i=1}^{N_A} \phi_i \, \mathbf{S}_{F_i}\,, \tag{5}$$

where $\forall_A$ is the volume of the cell, N_A is the number of faces of the control volume A, ϕ_i is the transported variable evaluated at face i, and $\mathbf{S}_{F_i}$ is a vector orthogonal to face i, pointing outwards from the cell, with magnitude equal to the face area.

For the projection of the gradient onto the line segment **AB**, at the face F, two possibilities are available: it can be obtained from the interpolations of the gradients at the two neighbor cell centers to the face as

$$\mathbf{AB} \cdot (\nabla \phi)_{\mathbf{avg}} = \mathbf{AB} \cdot \frac{(\nabla \phi)_A + (\nabla \phi)_B}{2}, \tag{6}$$

or, alternatively, from the difference of the transported variable over the distance between cell centers, so that

$$\mathbf{AB} \cdot (\nabla \phi)_{\mathbf{n}} = \phi_B - \phi_A\,. \tag{7}$$

Equations (6) and (7) are presented in a general 3-D form and can be used in any topology, including unstructured meshes, where **AB** denotes the vector from point A to point B. The subscripts A and B refer to the points where gradients are evaluated whereas **avg** and **n** identify how those face gradients

[3] Rigorously, f_ϕ is not a force, unless ϕ has dimension of momentum.

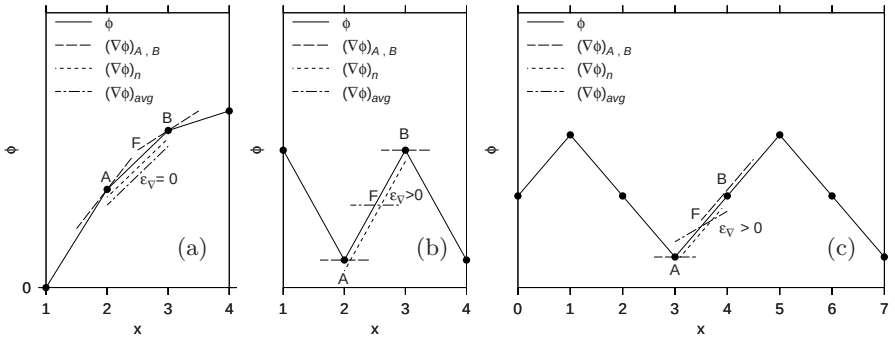

Fig. 1 Different Gradient evaluations for: (**a**) a 2nd degree polynomial mode; (**b**) a cut-off mode; (**c**) a mode with twice the wavelength of the cut-off mode

are calculated. Additionally, an error ε_∇ can be defined as the difference between the two alternative ways of evaluating the gradient projected along **AB**, at the face, given by

$$\varepsilon_\nabla = \mathbf{AB} \cdot \Big[(\nabla\phi)_{\mathbf{n}} - (\nabla\phi)_{\mathbf{avg}} \Big]. \tag{8}$$

In the case of cell centered variables, the gradient at the centroid can not capture the smallest modes, but the face gradient constructed from the two neighbor's difference can. This is why central difference based schemes cannot detect and react to the presence of the smallest modes supported by the mesh, leading to the well known checkered-board pattern. Those modes are then allowed to grow and are the main source of numerical instability, unless some form of artificial damping is provided.

Examining Fig. 1(a), it can be seen that both methods provide the same results for a smooth mode that can be fitted by a second degree polynomial.[4] On the other hand, for the fastest supported mode, as shown in Fig. 1(b), the error ε_∇ is significant and gets bigger as the amplitude of the spatial oscillations is increased. Therefore, ε_∇ is a good candidate for detecting an undesired mode, and estimating how much energy such a mode carries. A subgrid force f_ϕ proportional to ε_∇ will be zero for the smooth mode (Fig. 1(a)) and non-zero for the smallest one (Fig. 1(b)). For modes whose wavelength spans at least four control volumes (Fig. 1(c)), such subgrid force would also be non-zero, but a way around this will be presented shortly, aiming to really restrict its action to the very highest wavenumbers.

The suitability of ε_∇ to build the force f_ϕ can be further appreciated by noticing that, being a gradient, it is almost in the form of an advection term, missing only a velocity factor. The amount of attenuation this force must provide to the variable ϕ can be derived with the help of Fig. 2, where

[4] This is the reason why equal weights instead of linear interpolation were used in Eq. (6). In non-regular meshes, Eq. (7) achieves the lowest truncation error at the midpoint between A and B, in which case $\varepsilon_\nabla = 0$.

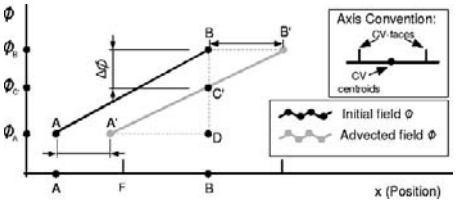

Fig. 2 Advection of scalar field ϕ in a non-uniform velocity field

a piecewise linear representation of the scalar field is advected during the interval Δt. In this figure, the fluid occupying positions A and B would have moved to new positions A' and B', respectively, after the interval Δt.

With the help of Fig. 2, one can derive the decrease in ϕ at cell center B, due to the advection of the piece-wise element connecting points A and B. Supposing that, during the interval Δt, this piece-wise element is always connecting the same fluid particles initially located in the centroids A and B, the change in ϕ depends on the gradient $\nabla\phi_{\mathbf{n}}$ at its upwind face F, and the distance traveled by these particles under advection, $\mathbf{u}_A\Delta t$ and $\mathbf{u}_B\Delta t$. By simple geometry, one can come up with an expression for $\Delta\phi$ in the form

$$f_{\phi_{F_i}} = \frac{\Delta\phi}{\Delta t} = -\frac{(\mathbf{AB}\cdot\mathbf{u}_B)\,\varepsilon_\nabla}{||\mathbf{AB}||^2 + \mathbf{AB}\cdot(\mathbf{u}_B - \mathbf{u}_A)\Delta t}\,. \tag{9}$$

where ε_∇ replaces $\nabla\phi_{\mathbf{n}}$, since the force must only complement the information captured by the smooth interpolated gradient. Here, $f_{\phi_{F_i}}$ is the force associated with the centroid B, due to the influence of the upwind face F_i.

Referring again to Fig. 1, another interesting feature to be explored is that, for the fastest mode shown in Fig. 1(b), the face gradient calculated with Eq. (7) lies outside the range defined by the neighborhood centroid-evaluated ones, at points A and B. This does not happen for the other modes illustrated at Figs. 1(a) and 2(c).

Based on that, the action of the force can be restricted to just the cut-off mode by setting ε_∇ to zero whenever $\mathbf{AB}\cdot(\nabla\phi)_n$ is inside the range limited by the values of $\mathbf{AB}\cdot(\nabla\phi)_A$ and $\mathbf{AB}\cdot(\nabla\phi)_B$. In this paper, a 20% tolerance is allowed for the development of smallest structures, so that the force is non-zero only when $\mathbf{AB}\cdot(\nabla\phi)_n$ surpass the range defined by $[\mathbf{AB}\cdot(\nabla\phi)_A, \mathbf{AB}\cdot(\nabla\phi)_B]$ extended by 20%.

The application of the above methodology to the momentum equation is straightforward. One simply has to replace ϕ by the velocity vector field $\mathbf{u}$.

As in Germano [2], this model is dynamic in the sense that the growth of undesirable modes is immediately detected by the gradient error ε_∇, which in turn controls the forcing f_ϕ in such a way as to damp these modes, without attenuating smoother turbulent structures.

2.3 Numerical Details

All simulations presented in this work have been performed with OpenFOAM, which is a Finite Volume Method based framework for solving partial differential equations in continuum mechanics. All variables are stored at centroids of the control volumes and whenever needed, face values are obtained through a linear interpolation from adjacent cell centers. The spatial discretization of all terms originally found in the Navier-Stokes equation results in a 2nd order scheme. In particular, central differencing is employed for the non-linear term, while the details of the added subgrid forcing was already extensively discussed in 2.2. Time discretization is accomplished with the well known 2nd order backward differencing scheme. The Courant number has been kept below 0.2 in all simulations presented in this paper. The velocity–pressure coupling is achieved with the PISO [10] algorithm.

3 Results

3.1 Homogeneous Isotropic Turbulence

Statistically Steady-State of Forced HIT

The geometry consists of a unit-side cubic box with periodic conditions in all opposite faces, and a very coarse mesh with $32 \times 32 \times 32$ subdivisions in each direction. A pseudo-random body force acting only on the large scales is imposed, following Eswaran and Pope [11], injecting energy and balancing the dissipation rate at small scales. Even with such a coarse mesh, the spectrum of energy is extracted after the flow has reached statistic steady-state, and compared to the theoretical $-5/3$ slope.

Since the primary purpose of these simulations is to evaluate the subgrid models, two extremely high Reynolds number $Re_T = U_{rms}\lambda_T/\nu$, based on the Taylor scale λ_T and on the velocity fluctuation U_{rms}, were tested: $Re_T \approx 3 \times 10^9$ and $Re_T \approx 3 \times 10^4$. Figure 3 presents the resulting spectra from numerical simulations using the Dynamic model [2] and the new proposal (f-LES), for the two different Re_T. The expected $-5/3$ slope is also plotted in the same graph. The large scale random forcing is limited to frequencies below $k/\Delta k = 3$. It is clear that both models present very similar results, which are in accordance to the Kolmogorov universal spectrum. Notwithstanding, it may be argued that "f-LES" performs a little bit better in this particular case, since its resulting slopes are closer to the theoretical value of $-5/3$.

Decaying Homogeneous Isotropic Turbulence

Another important behavior that turbulence simulations must be able to reproduce is the free decaying of kinetic energy and dissipation rate, which

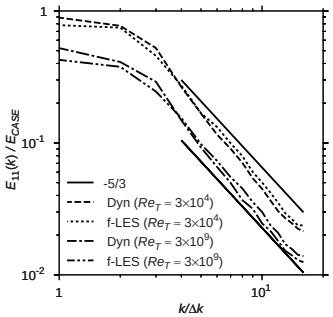

Fig. 3 Spectrum of HIT in a periodic box with 32^3

obeys a logarithmic law during a certain period of time [12], [13]. This is explored in this subsection for the same periodic box of Section 3.1 , in which no "pseudo-random" force is applied. The initial velocity field is chosen so that it has a spectrum containing only large structures. As the flow evolves, the energy stored in the largest scales is transferred to the next smaller scales where there is still no dissipation. The total kinetic energy is thus kept constant in this initial phase, until the energy reaches the Kolmogorov scales, where dissipation takes place. At this point, the viscosity effects start to act, damping the smallest structures. From then on, the total kinetic energy ($\langle K \rangle$) decays logarithmically. In Large Eddy Simulations, this switch from constant to logarithm decay happens when the energy reaches the scales affected by the subgrid model, ideally restricted to the smallest modes supported by the mesh. That being said, the present test case is very useful when assessing how selective subgrid models are in terms of spectrum: those who provide the least dissipation in the initial stage, and the latest transition to logarithm decay in the kinetic energy, are the ones that affect fewer modes in the spectrum.

Figure 4(a) shows the results for the Kinetic Energy as a function of time, obtained from Large Eddy Simulations with two subgrid models and different meshes. The base isotropic mesh ($32 \times 32 \times 32$) had 32 subdivision in each direction, while the anisotropic versions ($64 \times 32 \times 32$ and $128 \times 32 \times 32$) improved the refinement in x-direction by a factor of 2 and 4. The curves for the different cases have been vertically shifted for better visualization, since all simulations started from the same initial velocity field, therefore with the same $\langle K \rangle$. The observed energy evolution in all cases showed a similar pattern, in close agreement to the expected physical behavior described in above paragraphs. The rate of the decaying, however, was overestimated by all models, probably due to the poor mesh resolution. Instead of decaying as $1/t^n$ with n in the range $[1.15, 1.45]$, all subgrid models are predicting a faster decay for the turbulence kinetic energy, with n oscillating in the range $[2.5, 3]$. Regarding this decaying rate, no model proved superior, as they were equally affected by the mesh coarseness.

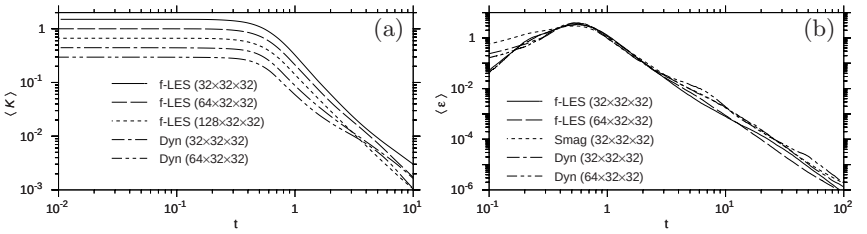

Fig. 4 Comparison of HIT LES behavior in isotropic and anisotropic meshes with different models: (**a**) kinetic energy decaying; (**b**) dissipation rate decaying

From the same Fig. 4(a), one can also infer that both models were little affected by mesh anisotropy, although it may be argued that the dynamic model was a little more sensitive, specially from $t = 1.5$ to 3, when the curves almost crossed.

The dissipation rate also obeys a logarithmic decay from the time the energy reaches the smallest scales on. Before this point, it is clear from Fig. 4(b) that the proposed subgrid model is less dissipative than both the dynamic and Smagorinsky models, with the latter the most dissipative of all. Since the high frequency spectrum is empty in the beginning of the simulations and becomes populated as time goes by, one can conclude that the Smagorinsky model dissipates energy at larger scales when compared to the Dynamic model and the advective forcing model, both of which act more selectively, damping only the smallest modes.

The graphs also show a great consistency between results obtained with meshes with different anisotropy. For the advective subgrid formulation (f-LES), the values of $\langle K \rangle$ are almost independent of the mesh, at least until $t = 10$. On the other hand, the Dynamic model showed a subtle discrepancy, specially in the periods $t = [0.1, 0.3]$, $t = [4, 10]$, and $t = [30, 100]$.

3.2 Turbulent Channel Flows

In this section, we consider the flow between two infinite plates, driven by a pressure gradient, for which extensive Direct Numeric Simulation (DNS) data is available [14]. In the numerical simulations, the infinite width is represented by periodic conditions in the front and back planes, distant 2δ of each other. The domain has a length $L = 4\delta$ in the x-direction and a width $W = 2\delta$ in the z-direction. The inlet and outlet boundary conditions are set to be periodic in velocity and pressure, and a uniform pressure gradient source term is added to the incompressible Navier-Stokes equation to account for the dissipated energy. During the simulations, this pressure gradient value is adjusted so that the Reynolds number based on the mass flux and the channel height (2δ) is 5600 during statistical steady-state. This corresponds to a Reynolds number $Re_\tau = u_\tau \delta / \nu = 180$, where the friction velocity is $u_\tau = \sqrt{\tau / \rho}$.

Two spatial discretizations are tested to evaluate the influence of mesh stretching in the final solution. The first mesh ("MESH A") consists of $40 \times 50 \times 30$ subdivisions, regularly spaced in both streamwise (x) and spanwise (z) directions. A fixed expansion ratio from both walls towards the center, in the y direction, is employed to better represent the different range of scales throughout the domain. The control volume adjacent to the wall measures, in wall units, $(\Delta x^+, \Delta y^+, \Delta z^+) = (18, 1.8, 12)$, while at halfway channel height, the elements span $(\Delta x^+, \Delta y^+, \Delta z^+) = (18, 18, 12)$. This corresponds to an increase of 9.6% in Δy from one control volume to its adjacent, in y-direction.

For the second mesh ("MESH B"), the same number of grid cells was adopted for each direction, but with non-uniform streamwise discretization. Therefore Δy^+ and Δz^+ are exactly the same as in MESH A, while Δx^+ varies from 8.2 (in the inlet and outlet boundaries) to 33 in the middle of the channel. This corresponds to a Δx stretching rate of 7% in the x-direction.

For each of these two meshes, simulations were performed with the Smagorinsky [1] ("Smag"), Dynamic Smagorinsky [2] ("Dyn") and advective forcing ("f-LES") subgrid models. A Van Driest wall function [15] for the subgrid scale length ($\overline{\Delta}$) is required in all simulations involving the Smagorinsky model, in order to damp the eddy-viscosity as the wall is approached. Both the Dynamic model and the model proposed here (f-LES) have, by construction, the ability to automatically adapt the level of subgrid dissipation throughout the computational domain, making the use of wall damping completely unnecessary.

Profiles of first and second order statistics are extracted from the mean field by means of a spatial average over the whole domain, in both x-direction and z-direction. The main results are shown in Fig. 5(a)–(d), where the left column corresponds to the numerical simulations using MESH A, regular in x-direction, while the right column relates to those employing MESH B, irregular in x-direction. The symmetry/antisymmetry of the profiles around $y/\delta = 1$ is a sign that the averaging time was more than adequate to capture the statistic steady-state flow.

In Fig. 5(a) and (b) the streamwise mean velocity profile is normalized by the friction velocity, u_τ, and is plotted against the normalized distance to the wall, $y^+ = u_\tau y/\nu$. The results from "Dyn" and "f-LES" are undistinguishable and match the DNS data from Kim et al. [14] over a wider extension of the viscous sublayer, when compared to the Smagorinsky model. Their inertial subrange is also bigger, as more turbulent structures are captured.

Figure 5(c) and (d) show the profiles of second order statistic of the x and y components of velocity fluctuations, $\overline{u'v'}$, normalized by τ. The results from "Dyn" and "f-LES" are undistinguishable, and in an excellent agreement with DNS data [14] in the case of regular mesh (MESH A, Fig. 5(c)). For the irregular mesh (MESH B), however, there is a small but noticeable deviation from the DNS data near both positive and negative peaks, but "f-LES" and "Dyn" curves are still coincident. On the other hand, the Smagorinsky model greatly underpredicts this cross-fluctuation near the wall ($y/\delta < 0.3$ and $y/\delta >$

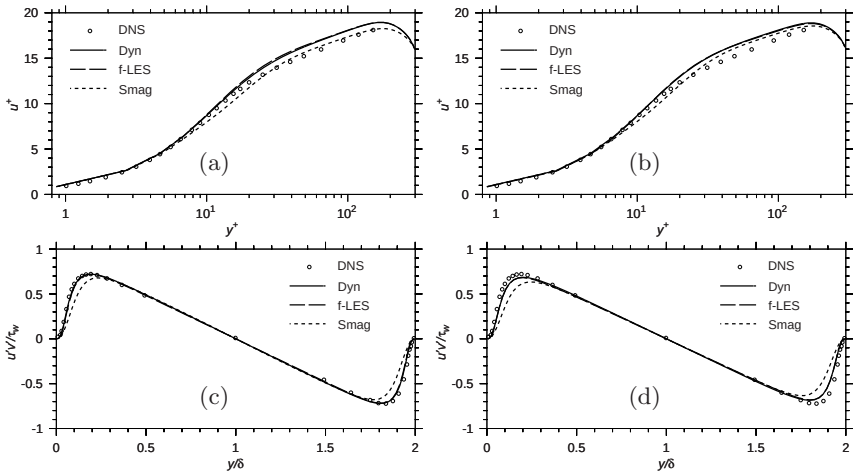

Fig. 5 First and second order statistics for the turbulent flow channel at $Re_\tau = 180$: (**a**) and (**b**) Mean velocity; (**c**) and (**d**) Reynolds tensor, component $\tau_{xy} = \overline{(u'v')}$; Left column corresponds to regular mesh in the streamwise direction, while right column corresponds to irregular mesh in streamwise direction

1.7), in both meshes. As the Dynamic and advective models, the Smagorinsky model also shows a further degradation in the profiles near the peaks when going from MESH A to MESH B, although in this case it may be visually masked by the already big discrepancies relatively to DNS.

4 Final Remarks

The performance of the new subgrid model has been evaluated for the classic test cases involving forcing and decaying of homogeneous isotropic turbulence. The spectrum and decaying rates for kinetic energy obtained with the advective forcing proved to be very similar to those obtained with the dynamic model. A small advantage, however, in terms of diminished range of affected frequencies and more consistency in the decaying rates in anisotropic meshes can be attributed to the new method.

Turbulent channel flow simulations have also been performed in order to compare the model proposed here with traditional Smagorinsky and Dynamic models. For the situations tested in this work, the Dynamic and the advective subgrid model are undistinguishable. Both subgrid models are designed to automatically adapt the dissipation levels in time, according to local requirements, and that is the main reason why they can better represent critical regions when compared to approaches that do not have this capability, like the Smagorinsky model. The proposed model has also shown a promising consistency in predictions when facing different mesh anisotropies, which suggests it can tackle more complex problems.

Acknowledgements

The first two authors gratefully acknowledge the support from CNPq.

References

1. Smagorinsky J (1963) General circulation experiments with the primitive equations. I: the basic experiment. Monthly Weather Review 91(3):99–165
2. Germano M, Piomelli U, Moin P, Cabot WH (1991) A dynamic subgrid-scale eddy viscosity model. Physics of Fluids A 3(7):1760–1765
3. Dantinne G, Jeanmart H, Winckelmans GS, Legat V, Carati D (1998) Hyperviscosity and vorticity-based models for subgrid scale modeling. Journal of Flow, Turbulence and Combustion 59(4):409–420
4. Winckelmans GS, Wray AA, Vasilyev OV, Jeanmart H (2001) Explicit-filtering large eddy simulation using the tensor-diffusivity model supplemented by a dynamic Smagorinsky term. Physics of Fluids 13(5):1385–1403
5. Carati D, Wray AA (2002) Large-eddy simulations with explicit equations for subgrid-scale quantities. In: Proceedings of Summer Program 2002:79–86. Center for Turbulence Research, Stanford University
6. Fureby C, Jasak H, Tabor G, Weller HG (1998) A tensorial approach to computational continuum mechanics using object-oriented techniques. Computers in Physics 12(6):620–631
7. OpenFOAM (2007) `http://www.opencfd.co.uk/openfoam/`
8. Sagaut P (2002) Large eddy simulation for incompressible flows, an introduction. Springer, Berlin Heidelberg New York
9. Sampaio LEB (2006) Large Eddy Simulations of the thin plate separation bubble at shallow incidence, Ph. D. Thesis, Department of Mechanical Engineering, Pontifícia Universidade Católica do Rio de Janeiro, RJ, Brasil (in Portuguese)
10. Issa R (1998) Solution of the implicit discretized fluid flow equations by operator-splitting. Journal of Computational Physics 62:40–65
11. Eswaran V, Pope SB (1988) An examination of forcing in direct numerical simulations of turbulence. Computers and Fluids 16(3):257–278
12. Mansour NN, Wray AA (1993) Decay of isotropic turbulence at low Reynolds number. Physics of Fluids 6(2)808–814
13. Wang H, Sonnenmeier JR, Gamard S, George W (2000) A contribution toward understanding DNS simulations of isotropic decaying turbulence using similarity theory. Turbulence Research Laboratory, State University of New York at Buffalo, Buffalo, NY, USA
14. Kim J, Moin P, Moser R (1987) Turbulence statistics in fully developed channel flow at low Reynolds number. Journal of Fluid Mechanics 177:133–166
15. van Driest ER (1956) On turbulent flow near wall. Journal of Aerospace Sciences 23:1007–1011

Assessment of Dissipation in LES Based on Explicit Filtering from the Computation of Kinetic Energy Budget

Christophe Bogey[1] and Christophe Bailly[1,2]

[1] LMFA, UMR CNRS 5509, Ecole Centrale de Lyon, 69134 Ecully, France.
christophe.bogey@ec-lyon.fr, christophe.bailly@ec-lyon.fr
[2] Institut Universitaire de France

Abstract. Energy dissipation in Large-Eddy Simulations (LES) based on the explicit filtering of the flow variables is investigated. An equation for the turbulent kinetic energy budget including the dissipation resulting from the filtering is first derived from the filtered compressible Navier-Stokes equations. A round jet at Reynolds number 1.1×10^4 is then calculated by LES using explicit filtering. Reference solutions are obtained, and compared to experimental data. The contributions of filtering and viscosity to energy dissipation in the jet are discussed. The filtering activity is found to adjust to the grid and flow properties.

Keywords: Large-eddy simulation, Explicit filtering, Dissipation, Energy budget, Turbulent jet

1 Introduction

In Large-Eddy Simulations (LES), the complexity of turbulent flows is reduced by applying a low-pass filtering to the Navier-Stokes equations [1, 2]. The filter width is usually taken as the mesh size so that one aims in practice at providing solutions for the scales larger than the grid spacing, whereas the smaller scales are removed. However, mathematical and physical modellings are required in order to ensure that solutions to the filtered equations are obtained, and also that they are physically correct.

The low-pass filtering of the non-linear terms of the flow equations first leads to a closure problem by giving subgrid-scale (SGS) terms in the LES equations. SGS models have been proposed, and specially analyzed by *a priori* tests of their correlations with the SGS terms, see in references [3, 4] for instance. One important deficiency of the SGS models is their difficulty in accounting for the physical effects of the subgrid scales. This is in particular the case for the SGS dissipation, which might be under or overestimated according to the models considered [5].

J. Meyers et al. (eds.), Quality and Reliability of Large-Eddy Simulations,

Energy dissipation in LES is a key point that needs to be carefully addressed. Noting that an artificial dissipation is required to regularize the flow, and that eddy viscosity has the same functional form as molecular viscosity, which might be unappropriate [6, 7], LES methods based on high-order/selective filterings have been proposed, and applied successfully to configurations such as isotropic turbulence, channel flows and jets [8, 9, 10, 11, 12]. The basic idea in these methods is to control energy dissipation by minimizing the amount of dissipation on the larger scales [11]. The energy is expected to be diffused when it is transferred to the smaller scales discretized.

One appropriate way for assessing LES quality consists in analysing the energy budgets obtained from the numerical solutions [5, 7, 11, 13, 14]. In the present work, in order to investigate energy dissipation in LES based on explicit filtering, an equation for the budget of the turbulent kinetic energy including the filtering dissipation is thus derived. The terms of the energy budget are calculated explicitly in a self-preserving round jet at Reynolds number 1.1×10^4. The numerical solutions are compared to experiments, and are used to quantify the contributions of filtering and viscosity to energy dissipation in the jet. The filtering activity is finally discussed.

2 Turbulent Kinetic Energy Budget in Compressible LES Based on Explicit Filtering

The equation for the turbulent kinetic energy budget is derived from the filtered compressible Navier-Stokes equations, which can be written, following Vreman et al. [5], in the following form

$$\frac{\partial \overline{\rho}}{\partial t} + \frac{\partial \overline{\rho}\widetilde{u}_j}{\partial x_j} = 0 \tag{1}$$

$$\frac{\partial \overline{\rho}\widetilde{u}_i}{\partial t} + \frac{\partial \overline{\rho}\widetilde{u}_i\widetilde{u}_j}{\partial x_j} = -\frac{\partial \overline{p}}{\partial x_i} + \frac{\partial \widetilde{\tau}_{ij}}{\partial x_j} + \frac{\partial \mathcal{I}_{ij}}{\partial x_j} + \mathcal{R}_i \tag{2}$$

$$\frac{\partial \overline{\rho}\widetilde{e}_t}{\partial t} + \frac{\partial((\overline{\rho}\widetilde{e}_t + \overline{p})\widetilde{u}_j)}{\partial x_j} = -\frac{\partial \widetilde{q}_j}{\partial x_j} + \frac{\partial \widetilde{\tau}_{ij}\widetilde{u}_i}{\partial x_j} + \frac{\partial \mathcal{I}_{ij}\widetilde{u}_i}{\partial x_j} + \mathcal{R}_e, \tag{3}$$

where ρ represents the density, u_i the velocity, p the pressure, τ_{ij} the viscous stress tensor, e_t the total energy density, and q_j the heat flux. The overbar denotes a filtered quantity, and the filtering is assumed to commute with time and spatial derivatives. The tilde denotes a quantity calculated from the filtered variables $\overline{\rho}$, $\overline{\rho u_i}$ and $\overline{p}$. Thus the calculated velocity is $\widetilde{u}_i = \overline{\rho u_i}/\overline{\rho}$ (Favre filtering), and the calculated total energy is $\overline{\rho}\widetilde{e}_t = \overline{p}/(\gamma-1)+\overline{\rho}\widetilde{u}_i\widetilde{u}_i/2$ for a perfect gas (γ is the specific heat ratio). The viscous stress tensor is defined by $\widetilde{\tau}_{ij} = 2\widetilde{\mu}(\widetilde{s}_{ij} - \tilde{s}_{kk}\delta_{ij}/3)$ where $\widetilde{s}_{ij} = (\partial\widetilde{u}_i/\partial x_j + \partial\widetilde{u}_j/\partial x_i)/2$. The viscosity $\widetilde{\mu} = \mu(\widetilde{T})$ is provided by Sutherland's law, and the temperature $\widetilde{T}$ is obtained using the state equation $\overline{p} = \overline{\rho} r \widetilde{T}$. The heat flux is given by $\widetilde{q}_j = -\lambda\partial\widetilde{T}/\partial x_j$

where $\lambda = \widetilde{\mu} c_p/\sigma$ is the thermal conductivity (σ is the Prandtl number and c_p the specific heat at constant pressure). The low-pass filtering of the Navier-Stokes equations makes the so-called subgrid-scale (SGS) terms appear in the right-hand side of Equations (2) and (3). The most important term is the SGS turbulent stress tensor $\mathcal{T}_{ij} = \overline{\rho}\widetilde{u}_i\widetilde{u}_j - \overline{\rho u_i u_j}$, whereas the other terms are included in $\mathcal{R}_i$ and $\mathcal{R}_e$. They are described in references [2, 15].

In the present LES approach, a high-order/selective filtering is used to take into account the dissipative effects of the subgrid scales. This filtering is applied explicitly to the density, momentum and pressure variables, sequentially in the x_i Cartesian directions, in order to remove the wave numbers located near the grid cutoff wave number without significantly affecting the low wave numbers accurately resolved by the numerical methods [11]. Only the fluctuating quantities are involved in the filtering process, which implies, in particular, that it has no effect in a steady laminar flow.

The filtering of the density variable $\overline{\rho}$ in the x_1 direction yields for instance the following filtered quantity, at grid point $(x_1(i_1), x_2(i_2), x_3(i_3))$,

$$\overline{\rho}^{sf}_{i_1,i_2,i_3} = \overline{\rho}_{i_1,i_2,i_3} - \sigma_d \sum_{j=-n}^{n} d_j \left(\overline{\rho}_{i_1+j,i_2,i_3} - \left\langle \overline{\rho}_{i_1+j,i_2,i_3} \right\rangle \right), \tag{4}$$

where σ_d is the filtering strength between 0 and 1, $\langle\cdot\rangle$ represents statistical averaging, and d_j are the coefficients of a centered $(2n+1)$ point filter. One can remark that the explicit filtering process (4) is equivalent to the second-order explicit integration over the simulation time step Δt of the operator

$$D^1\left(\overline{\rho}\right)_{i_1,i_2,i_3} = -\frac{\sigma_d}{\Delta t} \sum_{j=-n}^{n} d_j \left(\overline{\rho}_{i_1+j,i_2,i_3} - \left\langle \overline{\rho}_{i_1+j,i_2,i_3} \right\rangle \right) \tag{5}$$

in the mass conservation equation. A similar remark can be made for the filtering of the momentum variables.

The application of the explicit filtering to the density and the momentum variables can therefore be integrated into the right-hand side of Equations (1) and (2), in the following way

$$\frac{\partial \overline{\rho}}{\partial t} + \frac{\partial \overline{\rho}\widetilde{u}_j}{\partial x_j} = D\left(\overline{\rho}\right) \tag{6}$$

$$\frac{\partial \overline{\rho}\widetilde{u}_i}{\partial t} + \frac{\partial \overline{\rho}\widetilde{u}_i\widetilde{u}_j}{\partial x_j} = -\frac{\partial \overline{p}}{\partial x_i} + \frac{\partial \widetilde{\tau}_{ij}}{\partial x_j} + \frac{\partial \mathcal{T}_{ij}}{\partial x_j} + D\left(\overline{\rho u_i}\right), \tag{7}$$

where the SGS term $\mathcal{R}_i$ is removed, and $D\left(\overline{\rho}\right) = D^1\left(\overline{\rho}\right) + D^2\left(\overline{\rho}\right) + D^3\left(\overline{\rho}\right)$.

In what follows, the equation for the budget of the turbulent kinetic energy in compressible LES based on explicit filtering is determined from Equations (6) and (7). Statistical averaging is denoted by $\langle\cdot\rangle$, and Favre averaging by $[\cdot]$, yielding $[u_i] = \langle\overline{\rho u_i}\rangle / \langle\overline{\rho}\rangle$. The fluctuating velocity is then defined by $u_i' = \widetilde{u}_i - [u_i]$, and the turbulent kinetic energy by $\langle\overline{\rho}\rangle\, k = \left\langle \overline{\rho} u_i'^2/2 \right\rangle$.

Equation 7 is first written in the non conservative form

$$\widetilde{u}_i \underbrace{\left(\frac{\partial \overline{\rho}}{\partial t} + \frac{\partial \overline{\rho}\widetilde{u}_j}{\partial x_j}\right)}_{=D(\overline{\rho})} + \overline{\rho}\frac{\partial \widetilde{u}_i}{\partial t} + \overline{\rho}\widetilde{u}_j\frac{\partial \widetilde{u}_i}{\partial x_j} = -\frac{\partial \overline{p}}{\partial x_i} + \frac{\partial \widetilde{\tau}_{ij}}{\partial x_j} + \frac{\partial \mathcal{T}_{ij}}{\partial x_j} + D\left(\overline{\rho u_i}\right) \quad (8)$$

and multiplied by u_i', leading to the equation

$$\underbrace{\overline{\rho}u_i'\frac{\partial \widetilde{u}_i}{\partial t}}_{A} + \underbrace{\overline{\rho}u_i'\widetilde{u}_j\frac{\partial \widetilde{u}_i}{\partial x_j}}_{B} = \underbrace{-u_i'\frac{\partial \overline{p}}{\partial x_i}}_{C} + \underbrace{u_i'\frac{\partial \widetilde{\tau}_{ij}}{\partial x_j}}_{D} + \underbrace{u_i'\frac{\partial \mathcal{T}_{ij}}{\partial x_j}}_{E} + u_i'D\left(\overline{\rho u_i}\right) - u_i'\widetilde{u}_i D\left(\overline{\rho}\right) \quad (9)$$

Term A in Equation (9) is decomposed as

$$A = \overline{\rho}u_i'\frac{\partial\left[u_i\right]}{\partial t} + \overline{\rho}u_i'\frac{\partial u_i'}{\partial t} = \overline{\rho}u_i'\frac{\partial\left[u_i\right]}{\partial t} + \overline{\rho}\frac{\partial}{\partial t}\left(\frac{u_i'^2}{2}\right) \quad (10)$$

$$= \overline{\rho}u_i'\frac{\partial\left[u_i\right]}{\partial t} + \frac{\partial}{\partial t}\left(\frac{1}{2}\overline{\rho}u_i'^2\right) - \frac{u_i'^2}{2}\frac{\partial \overline{\rho}}{\partial t} \quad (11)$$

and averaged, giving

$$\langle A\rangle = -\left\langle \frac{u_i'^2}{2}\frac{\partial \overline{\rho}}{\partial t}\right\rangle \quad (12)$$

Term B in Equation (9) becomes

$$B = \overline{\rho}u_i'\left[u_j\right]\frac{\partial\left[u_i\right]}{\partial x_j} + \overline{\rho}u_i'u_j'\frac{\partial\left[u_i\right]}{\partial x_j} + \overline{\rho}u_i'\widetilde{u}_j\frac{\partial u_i'}{\partial x_j} \quad (13)$$

with

$$\overline{\rho}u_i'\widetilde{u}_j\frac{\partial u_i'}{\partial x_j} = \overline{\rho}\widetilde{u}_j\frac{\partial}{\partial x_j}\left(\frac{u_i'^2}{2}\right) = \frac{\partial}{\partial x_j}\left(\overline{\rho}\widetilde{u}_j\frac{u_i'^2}{2}\right) - \frac{u_i'^2}{2}\frac{\partial \overline{\rho}\widetilde{u}_j}{\partial x_j} \quad (14)$$

$$= \frac{\partial}{\partial x_j}\left(\overline{\rho}\left[u_j\right]\frac{u_i'^2}{2}\right) + \frac{\partial}{\partial x_j}\left(\overline{\rho}u_j'\frac{u_i'^2}{2}\right) - \frac{u_i'^2}{2}\frac{\partial \overline{\rho}\widetilde{u}_j}{\partial x_j} \quad (15)$$

and one gets after statistical averaging

$$\langle B\rangle = \left\langle \overline{\rho}u_i'u_j'\right\rangle\frac{\partial\left[u_i\right]}{\partial x_j} + \frac{\partial}{\partial x_j}\left(\left\langle \overline{\rho}\frac{u_i'^2}{2}\right\rangle\left[u_j\right]\right) + \frac{\partial}{\partial x_j}\left\langle \overline{\rho}u_j'\frac{u_i'^2}{2}\right\rangle - \left\langle \frac{u_i'^2}{2}\frac{\partial \overline{\rho}\widetilde{u}_j}{\partial x_j}\right\rangle \quad (16)$$

The sum of two expressions (12) and (16) yields

$$\langle A\rangle + \langle B\rangle = \frac{\partial}{\partial x_j}\left(\left\langle \frac{1}{2}\overline{\rho}u_i'^2\right\rangle\left[u_j\right]\right) + \left\langle \overline{\rho}u_i'u_j'\right\rangle\frac{\partial\left[u_i\right]}{\partial x_j} + \frac{1}{2}\frac{\partial}{\partial x_j}\left\langle \overline{\rho}u_i'^2u_j'\right\rangle - \left\langle \frac{u_i'^2}{2}\underbrace{\left(\frac{\partial \overline{\rho}}{\partial t} + \frac{\partial \overline{\rho}\widetilde{u}_j}{\partial x_j}\right)}_{=D(\overline{\rho})}\right\rangle \quad (17)$$

Using averaging, the term C involving pressure in Equation (9) provides

$$\langle C\rangle = -\langle u_i'\rangle \frac{\partial \langle \overline{p}\rangle}{\partial x_i} - \left\langle u_i' \frac{\partial p'}{\partial x_i}\right\rangle = -\langle u_i'\rangle \frac{\partial \langle \overline{p}\rangle}{\partial x_i} - \frac{\partial}{\partial x_i}\langle p' u_i'\rangle + \left\langle p' \frac{\partial u_i'}{\partial x_i}\right\rangle, \quad (18)$$

where the fluctuating pressure is $p' = p - \langle \overline{p}\rangle$. Terms $\langle D\rangle$ and $\langle E\rangle$ are also written as

$$\langle D\rangle = \frac{\partial}{\partial x_j}\langle u_i' \widetilde{\tau}_{ij}\rangle - \left\langle \widetilde{\tau}_{ij}\frac{\partial u_i'}{\partial x_j}\right\rangle \quad (19)$$

$$\langle E\rangle = \frac{\partial}{\partial x_j}\langle u_i' \mathcal{T}_{ij}\rangle - \left\langle \mathcal{T}_{ij}\frac{\partial u_i'}{\partial x_j}\right\rangle. \quad (20)$$

The budgets for the three components of the turbulent kinetic energy are finally obtained by averaging Equation (9)

$$\begin{aligned} 0 = & \underbrace{-\frac{\partial}{\partial x_j}\left(\frac{1}{2}\langle \overline{\rho} u_i'^2\rangle [u_j]\right)}_{\text{mean convection}} \underbrace{-\langle \overline{\rho} u_i' u_j'\rangle \frac{\partial [u_i]}{\partial x_j}}_{\text{production}} \underbrace{-\frac{1}{2}\frac{\partial}{\partial x_j}\langle \overline{\rho} u_i'^2 u_j'\rangle}_{\text{turbulence diffusion}} \\ & \underbrace{-\frac{\partial}{\partial x_i}\langle p' u_i'\rangle}_{\text{pressure diffusion}} \underbrace{+\left\langle p' \frac{\partial u_i'}{\partial x_i}\right\rangle}_{\text{pressure-dilatation}} - \langle u_i'\rangle \frac{\partial \langle \overline{p}\rangle}{\partial x_i} \\ & \underbrace{-\left\langle \widetilde{\tau}_{ij}\frac{\partial u_i'}{\partial x_j}\right\rangle}_{\text{viscous dissipation}} - \left\langle \mathcal{T}_{ij}\frac{\partial u_i'}{\partial x_j}\right\rangle + \frac{\partial}{\partial x_j}\langle u_i' \widetilde{\tau}_{ij}\rangle + \frac{\partial}{\partial x_j}\langle u_i' \mathcal{T}_{ij}\rangle \\ & \underbrace{+\langle u_i' D(\overline{\rho u_i})\rangle}_{\text{filtering dissipation}} - \langle u_i' \widetilde{u}_i D(\overline{\rho})\rangle + \frac{1}{2}\langle u_i'^2 D(\overline{\rho})\rangle \end{aligned} \quad (21)$$

The main terms correspond to mean convection, production, turbulence diffusion, pressure diffusion and pressure-dilatation term, and viscous dissipation. The dissipation induced by the explicit filtering is also included in the energy equation, and can be calculated directly.

3 Application to the Self-preserving Jet

3.1 Parameters

A round jet at Mach number M = 0.9 is computed by LES in order to calculate the budget for the turbulent kinetic energy in the flow self-similarity region, which is usually obtained far from the jet exit and characterized by constant

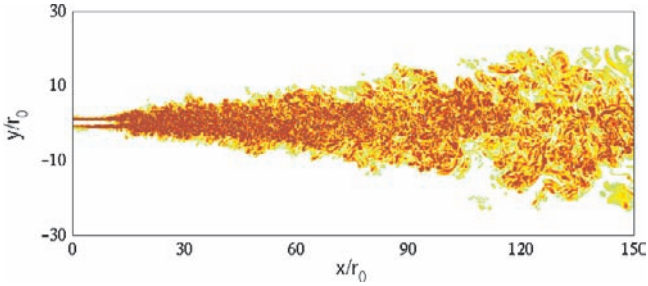

Fig. 1 Snapshot of the vorticity norm in the $x-y$ plane at $z=0$

turbulence intensities along the jet axis [16]. The Reynolds number based on the jet diameter D and velocity u_j is $\mathrm{Re}_D = 1.1 \times 10^4$, corresponding to that of the jet studied experimentally by Panchapakesan & Lumley (P&L) [17].

The LES is performed using low-dissipation and low-dispersion schemes [18], so that the scales discretized at least by four points are neither significantly distorded nor dissipated. Eleven-point centered finite differences are used for space discretization, and an eleven-point selective filtering is applied explicitly to the flow variables as described previously. The effects of the subgrid energy-dissipating scales are then taken into account by the filtering, so that no structural modelling is implemented for the SGS stress tensor ($\mathcal{T}_{ij} = 0$ in (7) and (21)). Time integration is carried out using a low-dissipation six-stage Runge-Kutta method.

The mesh grid is a Cartesian grid symmetrical relative to the jet axis. The x axis is in the jet direction, and the discretizations in the y and z directions are identical. The mesh contains 44 million nodes, and extends axially up to 150 jet radii r_0, as illustrated by the vorticity field in Fig. 1. In the axial direction, the grid spacing is uniform with $\Delta x = r_0/4$. In the transverse directions, the grid spacing is also $\Delta y = r_0/4$ for $6.5r_0 \leq y \leq 23r_0$, but is smaller on the jet axis with $\Delta y = r_0/8$. It is stretched for $y \geq 23r_0$ so that the sideline boundaries are located at $y = 33.5r_0$. Due to the explicit time integration, the time step is $\Delta t = 0.85 \min(\Delta y)/c_{amb}$, where c_{amb} is the ambient speed of sound. For the convergence of statistics, 2×10^6 time steps are performed, leading to a physical time of $Tu_j/D = 9.5 \times 10^4$. The statistical averages of the turbulent quantities are evaluated by computing time averages after a transitory period of 10^5 time steps, when stationary mean flow values are obtained. Note that 22.4 Go of memory is required for the LES, and that 8000 CPU hours have been used on SX5 and SX8 Nec computers.

3.2 Results

As a first validation, the LES results have been compared with corresponding experimental data provided by P&L [17]. Illustrations are given below. The profiles along the jet axis of turbulence intensities u'_{rms}/u_c and v'_{rms}/u_c, where

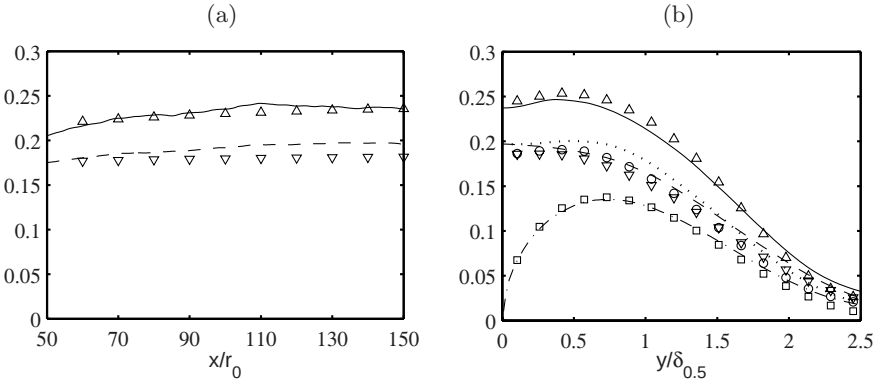

Fig. 2 Profiles of turbulence intensities: u'_{rms}/u_c (——— LES, △ P&L), v'_{rms}/u_c (− − − LES, ▽ P&L), w'_{rms}/u_c (····· LES, o P&L), and $<-u'v'>^{1/2}/u_c$ (− · − · LES, □ P&L); (**a**) along the jet centerline; (**b**) across the jet, averaged over $120r_0 \leq x \leq 145r_0$ (u_c: centerline mean axial velocity, $\delta_{0.5}$: jet half-width)

u_c is the centerline mean axial velocity, are presented in Fig. 2(a). Their values are nearly constant from $x \simeq 120r_0$, which suggests that the jet self-similarity region is reached around this axial location. This behaviour is in good agreement with the measurements of P&L obtained for a jet at the same Reynolds number. In particular the transition towards the region of self-similarity does not appear to be artificially accelerated by the application of the explicit filtering, as it has been observed in jets at lower Reynolds numbers [11] or when an eddy-viscosity subgrid model is used [7].

Considering the centerline profiles of turbulence intensities, the self-preserving jet has been investigated by averaging the flow properties over $120r_0 \leq x \leq 145r_0$. It has been done for the transverse profiles of turbulence intensities and Reynolds stress shown in Fig. 2(b). The LES profiles compare well with the P&L measurements. Other comparisons have been made, regarding the mean-flow development for instance. They can be found in [19].

The budget for the turbulent kinetic energy in the jet has been determined by calculating explicitly all the terms in Equation (21) from the LES fields. The variations along the jet axis of the dominant terms, that correspond to mean convection, production, dissipation, turbulence diffusion, pressure diffusion, and dissipation are presented in Fig. 3(a). The dissipation here is the sum of the viscous dissipation and of the filtering dissipation. The profiles display short oscillations that are of low magnitude, which supports the assertion that the convergence in time of the energy terms is satisfactory. The convergence is however much higher for the production and dissipation terms than for the terms associated with turbulence and pressure diffusions for instance. In addition, in the same way as the turbulence intensities in Fig. 2(a), the energy terms appear to tend to constant values as the axial distance increases, the self-similarity values being visibly reached around $x = 120r_0$.

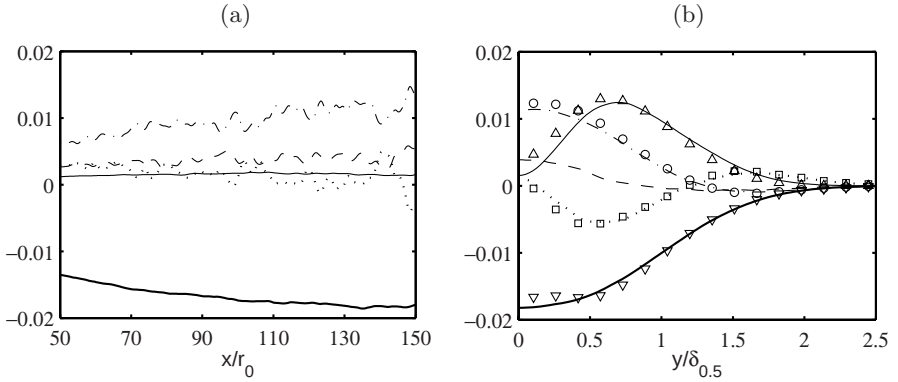

Fig. 3 Turbulent kinetic energy budget: mean convection ($- \cdot - \cdot$ LES, o P&L), production (——— LES, △ P&L), turbulence diffusion ($\cdots\cdots$ LES, □ P&L), pressure diffusion ($- - -$ LES), dissipation (——— LES, ▽ P&L); (**a**) along the jet centerline; (**b**) across the jet, averaged over $120r_0 \leq x \leq 145r_0$ (curves are normalized by $\rho_c u_c^3 \delta_{0.5}$, ρ_c centerline mean density)

The budget for the turbulent kinetic energy calculated across the self-preserving jet is presented in Fig. 3(b). The LES results are in good agreement with the experimental results of P&L, for the production, mean convection, dissipation, and turbulence diffusion terms. This is remarkable, especially since P&L neglected pressure diffusion and obtained dissipation as the balance of the other terms. The present LES thus provides reference solutions, which complements the experimental data.

Our attention is now focused on the dissipation mechanisms involved in the LES, namely the viscous and the filtering dissipations, given respectively by $\langle \epsilon_\mu \rangle = -\langle \widetilde{\tau}_{ij} \partial u_i'/\partial x_j \rangle$ and $\langle \epsilon_{sf} \rangle = \langle u_i' D\left(\overline{\rho u_i}\right) \rangle$ in Equation (21). In earlier works by the authors [7, 11], their contributions have been evaluated in jets, to examine in particular the Reynolds number effects on energy dissipation. In the present study, in order to assess the importance of the filtering, we define, following Geurts and Fröhlich [20], the subgrid-activity parameter

$$s = \frac{\langle \epsilon_{sf} \rangle}{\langle \epsilon_{sf} \rangle + \langle \epsilon_\mu \rangle} \tag{22}$$

which represents also the filtering-activity parameter in the present work.

The profiles of the viscous and filtering dissipations along the jet axis are presented in Fig. 4(a). The sum of the different terms in Equation (21) is plotted as well. It is nearly zero, which suggests that the computation of the energy budget is performed in a suitable manner, and that energy is not significantly damped by time integration. The magnitudes of viscous and filtering dissipations vary with the axial distance. As the jet develops in the downstream direction, the contribution of the filtering decreases, whereas that of viscosity increases, which leads to the lowering of the subgrid-activity

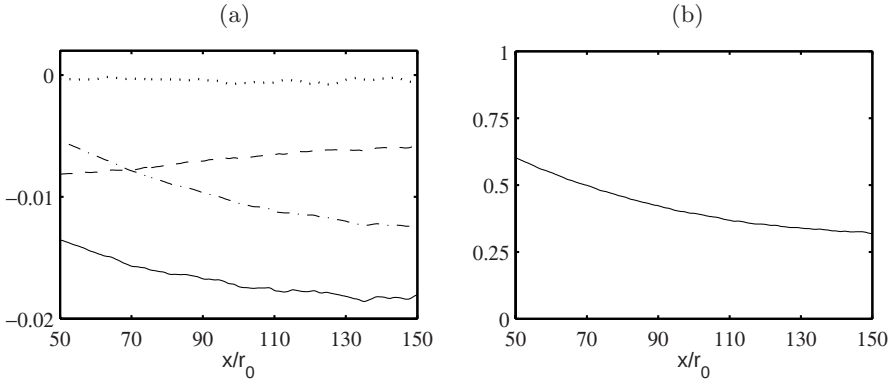

Fig. 4 Profiles along the jet centerline. (**a**) Turbulent energy budget: ——— total dissipation, — · — · viscous dissipation, — — — filtering dissipation, ····· sum of the terms in the energy equation (curves are normalized by $\rho_c u_c^3 \delta_{0.5}$); (**b**) variations of the subgrid-activity parameter s

parameter s in Fig. 4(b). Thus about two-thirds of the energy dissipation is provided by the filtering at $x = 50r_0$, but only one-third at $x = 150r_0$. This behaviour is certainly due to the growth of the turbulent length scales along the jet axis [16]. The mesh spacing being uniform, a more important part of the energy-dissipating scales is then calculated, which reduced the subgrid activity, and hence the role played by the filtering. The contribution of the explicit filtering therefore appears to adjust itself to the flow development.

The dissipation rates obtained across the self-preserving jet for the turbulent kinetic energy and for the three energy components are represented in Fig. 5. In the four cases, as previously in Fig. 4(a), the sum of the different energy terms is also checked to be nearly zero. The viscous dissipation appears to be higher than the filtering dissipation in any case, whatever the radial position may be. The ratio between the two contributions however seems to vary with the position and with the energy component considered. The contribution due to the filtering is for instance seen to decrease close to the centerline. The filtering also visibly dissipates more energy compared with viscosity in the budget for the component w'^2 in Fig. 5(d) than for u'^2 in Fig. 5(b).

In order to quantify the variations of the dissipation rates across the jet, the subgrid-activity parameter s is computed from the profiles of Fig. 5, and presented in Fig. 6. The shapes of the curves obtained for the turbulent kinetic energy and for the energy components are very similar, with a minimum value close to the centerline, a slight increase before a zone displaying nearly constant values for $0.6 \leq y/\delta_{0.5} \leq 2$, and a final growth for $y/\delta_{0.5} \geq 2$. The filtering activity is therefore connected with the radial grid spacing. It is the lower on the jet axis where the radial grid spacing is the smaller with $\Delta y = r_0/8$, does not vary significantly in the central zone where the grid

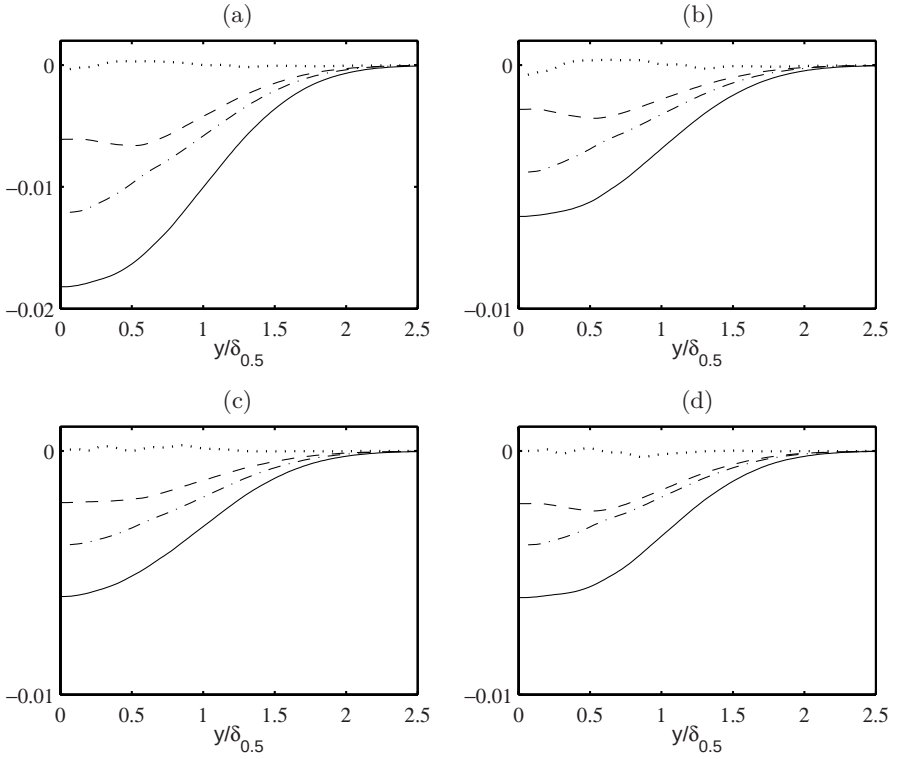

Fig. 5 Profiles obtained across the jet from the budgets for: (**a**) the turbulent kinetic energy k, and for the three energy components, (**b**) u'^2, (**c**) v'^2, (**d**) w'^2, averaged over $120r_0 \leq x \leq 145r_0$; ——— total dissipation, − · − · viscous dissipation, − − − filtering dissipation, ····· sum of the terms in the energy equation (curves are normalized by $\rho_c u_c^3 \delta_{0.5}$)

spacing is uniform with $\Delta y = r_0/4$, and increases in the vicinity of the sideline boundary where the grid is stretched. The influence of the mesh grid is also illustrated in Table 1 reporting the values of the parameter s at $y = 0$ and at $y/\delta_{0.5} = 1.25$. Values of 0.335 and 0.415 are for instance respectively found from the turbulent kinetic energy.

Table 1 allows us also to compare the subgrid activity for the different energy components. On the jet axis, where $\Delta y = \Delta z$, the subgrid activities are the same for the components v'^2 and w'^2 due to the rotation invariance of the flow in a cross-section. The subgrid activity for the component u'^2 however displays another value because of the anisotropy of the flow and of the mesh ($\Delta x = 2\Delta y$) in the $x-y$ section. At the radial position $y/\delta_{0.5} = 1.25$, both the grid and the flow are anisotropic ($\Delta y = \Delta x = \Delta z/2$ for instance). As a result, the filtering activity differs according to the energy components, ranging from 0.385 for the component v'^2 to 0.449 for w'^2. The contribution

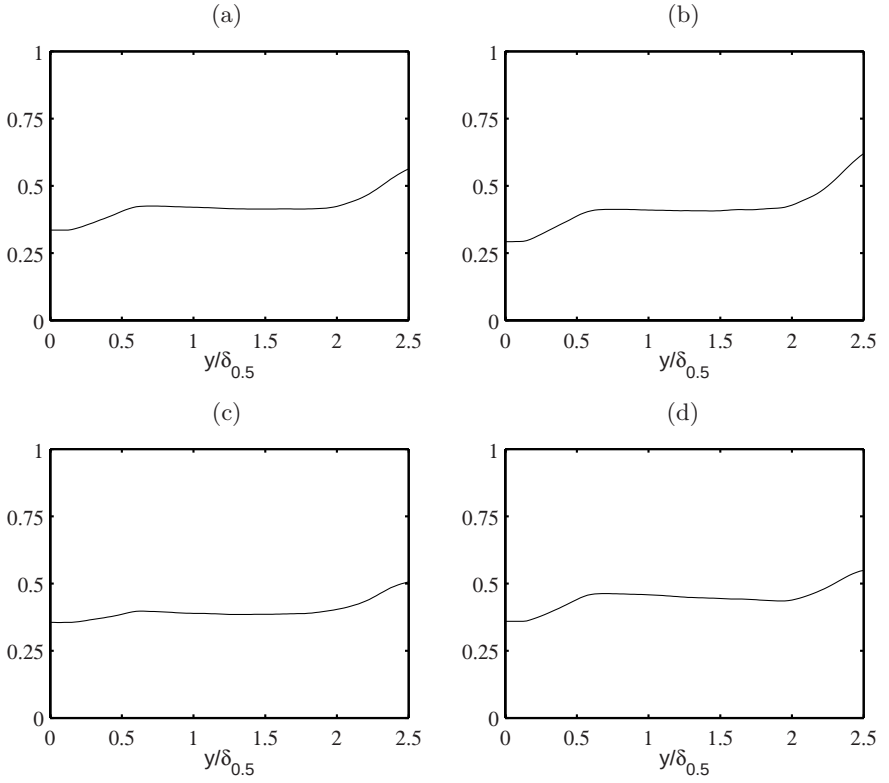

Fig. 6 Profiles of the subgrid-activity parameter s across the jet, averaged over $120r_0 \leq x \leq 145r_0$, calculated from: (**a**) the turbulent kinetic energy k, and from the energy components, (**b**) u'^2, (**c**) v'^2, (**d**) w'^2

Table 1 Subgrid-activity parameter s calculated from the turbulent energy and from the energy components, over $120r_0 \leq x \leq 145r_0$, at $y = 0$ and $y/\delta_{0.5} = 1.25$

	k	u'^2	v'^2	w'^2
$s(y = 0)$	0.335	0.292	0.355	0.359
$s(y/\delta_{0.5} = 1.25)$	0.415	0.407	0.385	0.449

of the explicit filtering to energy dissipation is thus shown to depend both on the grid spacing and on the flow features.

4 Concluding Remarks

An equation for the turbulent kinetic energy budget is proposed for evaluating dissipation in LES based on the explicit filtering, and is calculated in a turbulent self-preserving jet, providing reference solutions for this flow. The filtering

activity is in particular shown to adjust to the grid and flow properties. It is hoped that the present method could be used for other configurations. It also appears as an appropriate tool for investigating the presence of numerical dissipation and Reynolds number effects in LES.

Acknowledgments

The authors gratefully ackmowledge the *Institut du Développement et des Ressources en Informatique Scientifique* (IDRIS) of the CNRS and the *Centre de Calcul Recherche et Technologie* of the CEA (the French Atomic Energy Agency) for providing CPU time on Nec computers and technical assistance.

References

1. Sagaut P (2004) Large-Eddy Simulation for Incompressible Flows, an Introduction. Springer, Berlin
2. Geurts BJ (2004) Elements of Direct and Large-Eddy Simulation. Edwards, Flourtown
3. Meneveau C, Katz J (2000) Annu Rev Fluid Mech 32:1–32
4. Domaradzki JA, Adams NA (2002) J Turb 3, Art no 24
5. Vreman B, Geurts B, Kuerten H (1997) J Fluid Mech 339:357–390
6. Domaradzki JA, Yee PP (2000) Phys Fluids 12:193–196
7. Bogey C, Bailly C (2006) Int J Heat Fluid Flow 27:603–610
8. Stolz S, Adams NA, Kleiser L (2001) Phys Fluids 13(4):997–1015
9. Mathew J, Lechner R, Foysi H, Sesterhenn J, Friedrich R (2003) Phys Fluids 15(8):2279–2289
10. Rizzetta DP, Visbal MR, Blaisdell GA (2003) Int J Numer Meth Fluids 42:665–693
11. Bogey C, Bailly C (2006) Phys Fluids 18, Art no 065101
12. Schlatter P, Stolz S, Kleiser L (2006) Int J Heat Fluid Flow 27:549–558
13. Schlatter P, Stolz S, Kleiser L (2006) In: Lamballais E, Friedrich R, Geurts BJ, Métais O (eds) Direct and Large-Eddy Simulation VI:135–142. Springer, Dordrecht
14. da Silva CB, Métais O (2002) J Fluid Mech 473:103–145
15. Vreman B, Geurts B, Kuerten H (1995) Appl Sci Res 54:191–203
16. Wygnanski I, Fiedler H (1969) J Fluid Mech 38:577–612
17. Panchapakesan NR, Lumley JL (1993) J Fluid Mech 246:197–223
18. Bogey C, Bailly C (2006) J Comput Phys 194:194–214
19. Bogey C, Bailly C (2006) In: Lamballais E, Friedrich R, Geurts BJ, Métais O (eds) Direct and Large-Eddy Simulation VI:285–292. Springer, Dordrecht
20. Geurts BJ, Fröhlich J (2002) Phys Fluids 14(6):41–44

Optimal Unstructured Meshing for Large Eddy Simulations

Yacine Addad, Ulka Gaitonde, Dominique Laurence and Stefano Rolfo

School of Mechanical, Aerospace and Civil Engineering, University of Manchester, Manchester M60 1QD, UK. yacine.addad@manchester.ac.uk, ulka.gaitonde@postgrad.manchester.ac.uk, dominique.laurence@manchester.ac.uk, stefano.rolfo@postgrad.manchester.ac.uk

Abstract. An attempt is made to provide a criterion for optimal unstructured meshing for LES from the knowledge of different turbulence lengthscales. In particular, the performance of a grid based on the Taylor microscales for turbulent channel flow, is investigated, with the final view of facilitating an a priori determination of the mesh resolution required for LES. The grid dictated by the Taylor microscales is more cubical in the centre of the domain than the typical empirical LES grids. Furthermore, it is as fine in the spanwise direction as it is in the wall normal direction. Empirical LES grids, currently widely used, have a very fine (approximately four times finer) wall normal resolution and a coarse (about twice as course) streamwise resolution as compared to a grid based on the Taylor microscales. A remarkable feature is that the mean velocity and streamwise component of fluctuating velocity (classically over-predicted in coarse grid LES) and the wall normal fluctuating velocity are well reproduced on the new grid. The attempt of building an unstructured LES grid based on the Taylor microscale has been found very successful. However, as the Reynolds number is increased this sort of requirement might be excessive and eventualy a criterion such as one tenth of the integral lengthscale could be sufficient.

Keywords: Large-eddy simulation, Grid optimization, Turbulence lengthscales, Taylor microscales

1 Introduction

In general, LES results are in better agreement with experimental evidence compared to RANS if a sufficiently fine grid is employed. However, without a prior knowledge of flow characteristics, it is difficult to ascertain the "sufficient" resolution. As claimed by Celik [1], "a good LES is almost a DNS", i.e. for correct resolution of wall layers and prediction of transition, LES requires an extremely fine grid.

Obviously, as the grid resolution tends to the smallest (i.e. Kolmogorov) scales, LES tends to DNS [2]. The LES philosophy loses its meaning if it

J. Meyers et al. (eds.), Quality and Reliability of Large-Eddy Simulations,

achieves grid independence and the advantage of LES being more economical than DNS on account of resolving only the most energetic eddies, is lost [3]. Physical phenomena, including mixing and combustion, depend strongly on the intensity of turbulent fluctuations and the convection of these fluctuations, exhibited as turbulent dissipation. As a result, prediction of turbulent statistics is as important as that of the mean flow statistics. This makes quality assessment measures imperative for LES in engineering applications.

Most of the prior attempts at reducing computational requirements of LES of wall bounded flows, using structured grids, involved manipulating the grid such that all the near-wall eddies could be resolved without having a large number of grid points in the outer layers. In wall bounded flows, the near wall flow structures are extremely small when compared to the overall flow dimensions. Unfortunately, these small structures play a very important part in the turbulent boundary layer dynamics and therefore need to be well resolved.

In typical mean flow computations, i.e. RANS models, one has to mostly focus on resolving the large mean velocity gradients using grid stretching in the wall-normal direction. In LES, however, a fine near-wall mesh is also required in the direction parallel to the wall. In the previous attempts that were made at reducing the computational requirements, this fine resolution was normally extended into the outer layers. This was not really necessary and consequently, these attempts at lowering computation cost by modifying the grid employed were largely not successful.

A more promising method of reducing the number of outer layer grid points was to use zonal embedded grids [4, 5, 6, 7]. The results thus obtained showed good agreement with previously published numerical as well as experimental results for same flow conditions. The calculations were claimed to require a fraction of the CPU time needed for single zone grid calculation with same near-wall grid density. In addition, the memory requirements were significantly reduced.

In recent years, the grid resolution for LES computations has been made the centre of discussion in many papers that are attempting to provide a sensitive way to measure the quality of the LES predictions [3, 8, 9]. However, apparently this has not been found a straightforward task due to the influence of the numerical dissipation that must be accounted for in the analysis. Thus, some assumptions had to be introduced regarding the global order of the numerical error as well as the scaling of the error like a power with grid refinements. Even with these approximations, the method suggested by Klein [8] for example, request a strict minimum of three LES runs for the same case to be able to obtain any meaningful LES results.

The present work expands toward an alternative method which can be used with any commercial or research CFD code to provide guidance for building a proper grid for LES computations, eventually using a precursor RANS simulation. The next section explains the necessary conditions that one has to

bear in mind for this goal to be fulfilled. This is followed by results of LES computations based on this analysis and some concluding remarks.

2 Turbulence Lengthscales

The first step towards addressing different questions concerning turbulence and turbulent flows is to distinguish between small-scale turbulence and the large scale motions in turbulent flows.

At high Reynolds numbers, the dynamics of the flow is characterized by the existence of a number of different lengthscales. Some of these assume very specific roles in the description and analysis of the flow. A wide range of lengthscales exists, limited at one end by the diffusive action of molecular viscosity (the Kolmogorov scales) and at the other by the dimensions of the flow field.

It is well-known that in SGS models based on the Boussinesq theory by introducing an algebraic eddy-viscosity model, the implicit cut-off filter width, κ_c, has to be positioned in the inertial region of the energy spectrum.

This is easy for HIT decay (homogeneous isotropic turbulence), because the spectrum of the initial field is given or chosen, so one simply ensures that the mesh step h is such that $\kappa_c = 2\pi/2h$ is in the inertial region. Note in passing that the filter width is then $\delta = 2h$ and not $\delta = h$, as (unfortunately) frequently encountered in recent publications. In application other than HIT, three different mesh steps need to be defined for the three directions and these are moreover variable in space, yet there are no guidelines as to how to choose these scales, so generally authors refer to previous successful LES, which only works when the objective is a "post-diction" rather than "pre-diction".

In a non-isotropic context, the following definitions of lengthscales are used.

The integral lengthscale is theoretically defined as the integral of the two point correlation, i.e.

$$L_{ii_k}(y) = \frac{1}{R_{ii}(0,y)} \int_0^\infty R_{ii\_k}(r_k, y)\, dr_k \tag{1}$$

without summation on repeated indices. In general "ii" will be used for the corresponding velocity component and "k" for the co-ordinate direction.

Another large scale is the "energy carrying eddies" scale or "energy lengthscale" obtained by dimensional analysis, and based on RANS model results:

$$L_{RM\_i} = A \frac{< u_i u_i >^3 /2}{\epsilon} \tag{2}$$

For HIT, with the constant A taken close to unity [10], L_{RANS_i} gives some indication of the true integral scale.

These scales are easily computed in the HIT test case. The Taylor microscale is defined as;

$$\lambda_{ii\_k} = \sqrt{\frac{2 < u_i u_i >}{< \frac{\partial u_i}{\partial x_k} \frac{\partial u_i}{\partial x_k} >}} \tag{3}$$

And might be approximated by the HIT derived formula:

$$\lambda_{RM\_i} = \sqrt{15 \frac{< u_i u_i > \nu}{\epsilon}} \tag{4}$$

Extending this outside HIT assumes a relation between componentality and dimensionality (respective velocity components and lengthscale directions), that is not obvious in general but will be seen to be reasonable for near wall flows. The "RM" subscript indicates that estimates of these scales could be provided by a RANS Model; more precisely a low Reynolds Stress transport model if an accurate representation of anisotropy is expected.

Finally, and again for near wall effects, the definition of the Kolmorov scale is extended to include some anisotropy:

$$\eta = (\frac{\nu^3}{\epsilon})^{1/4} \tag{5}$$

$$\eta_i = (\frac{\nu^3}{\epsilon_{ii}})^{1/4} \tag{6}$$

In HIT the longitudinal and the transverse scales are related by

$$\lambda_{11\_1}/\sqrt{2} = \lambda_{22\_1} = \lambda_{33\_1} \tag{7}$$

and

$$L_{11\_1}/2 = L_{11\_2} = L_{22\_1} \tag{8}$$

Figure 1 displays the longitudinal one-dimensional energy spectra obtained from the experiment of Kang et al. [10] at Reynolds number $Re_\lambda = 720$. Added on the figure are the RANS model bases integral scale and the Taylor microscale computed from the Equations (1) and (4) respectively which are valid in HIT so agreement comes as no surprise. Quite obviously also, the integral scales are positioned at the top limit of the inertial range (notice the $-5/3$ slope), the Taylor scales are located more than a decade lower. In fact the Taylor microscale is a combination of the energy scale and the Kolmogorov scale as $\lambda \sim L_{RM}^{1/3} \eta^{2/3}$ so $\lambda / L_{RM} \sim (\eta / L_{RM})^{2/3}$ and an LES based on the Taylor microscale would become over-resolved at higher Reynolds numbers; a bound on the filter scale such as $\Delta = max(\lambda, L_{RM}/10)$ could be recommended.

3 Analysis of Turbulent Channel Flow

We now consider channel flow, with internal flow notations: $1 \sim x$ for streamwise; $2 \sim y$ for wall normal and $3 \sim z$ for spanwise directions.

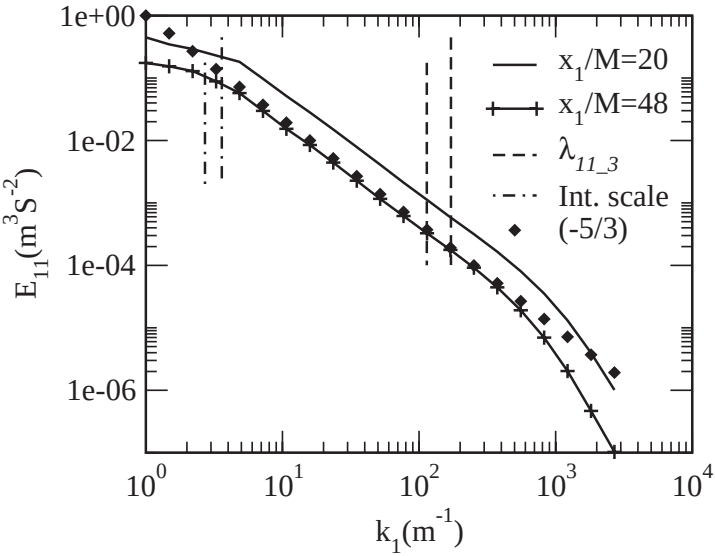

Fig. 1 Comparison between Taylor microscales and the Integral scales in HIT at the two stations 20 and 48 [10]

Results for turbulent channel flow available from direct numerical simulations performed at Reynolds numbers ranging from $Re_\tau = 150$ to 720 [11, 12] were employed to extract velocity and energy spectra, two point correlations and consequently the different turbulent lengthscales.

In Figs. 2 and 3, the Taylor microscales are displayed along with the one-dimensional spectra at two dimensionless distances from the wall. It is no longer possible to identify an inertial range like in the HIT test case. It may be observed from the figures however, that near the wall region is dominated by anisotropic structures up to the Kolmogorov scales, while in the log-layer the flow becomes more isotropic. The Taylor microscales exhibit the same behaviour. It can therefore be reasonably stated that away from the wall, the Taylor microscales should be able to dictate an isotropic grid that is well suited for LES, while near the wall the computation switch to a DNS in which the anisotropy of the structures has to be correctly captured.

Longitudinal lengthscales are divided by 2 or $\sqrt{2}$ for integral and Taylor scales in subsequent graphs.

Figure 4 shows the integral lengthscales as defined from integral of the two point correlation (1), and extracted from the THTLab database [11]. Effectively, the integrations have been stopped when the correlation is lower than 10% to avoid spurious effects of periodicity conditions in the simulations. As could be expected, the streamwise correlations ($k = 1$) show the overwhelming influence of streaks up to $y+ = 100$. For this Re, note that the scales at the wall (y+=0) are roughly the same as those in the core of the flow (80

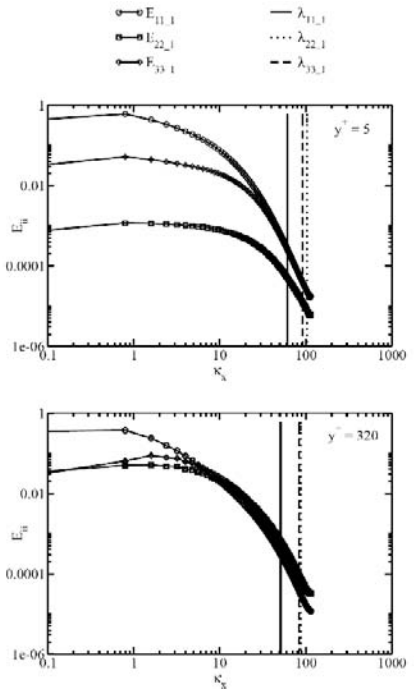

Fig. 2 Streamwise energy spectra from DNS computations at $Re_\tau = 640$

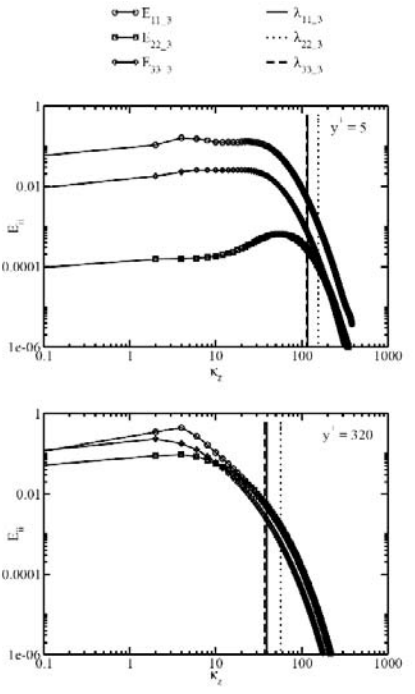

Fig. 3 Spanwise energy spectra from DNS computations at $Re_\tau = 640$

wall units). The spanwise correlations ($k = 2$) on the other hand, show an initially linear growth (roughly scaling with the Von Karman constant 0.41), starting from a wall value of about 20 viscous units. Hence for a well resolved near wall layer one must have $Dx+ \ll 80$ and $Dz+ \ll 20$, which is empirical practice. At the centre, the scatter between components is larger compared to our expectation of isotropic turbulence, but this may be attributed to the fact that large scales require larger statistical samples. However, the streamwise and spanwise scales are coming together. Figure 5 now shows the turbulent energy scales as could be obtained from a RANS model (a perfect model, as DNS data is used as input to the formula). Scaling the mesh steps with these scales is not appropriate as they obviously start from zero, but also decrease at the centre, except the wall normal component which has a monotonic growth and better differentiates between the Log layer and core of the channel (this is in fact one of the assets of Durbin's V2F model).

The scales for the high Reynolds number ($Re_\tau = 720$) are plotted in Fig. 6 as a function of the normalized wall distance. Although omitted here for clarity, similar behaviour was observed for the scales of the other two cases, at lower Re_τ, with their magnitude increasing with decreasing Re_τ.

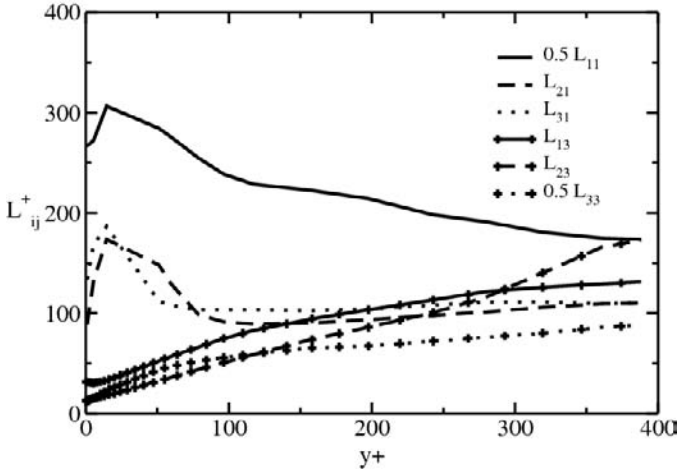

Fig. 4 Integral lengthscales for $Re_\tau = 395$ from DNS [11]. (Correlations integrated only upto 0.1)

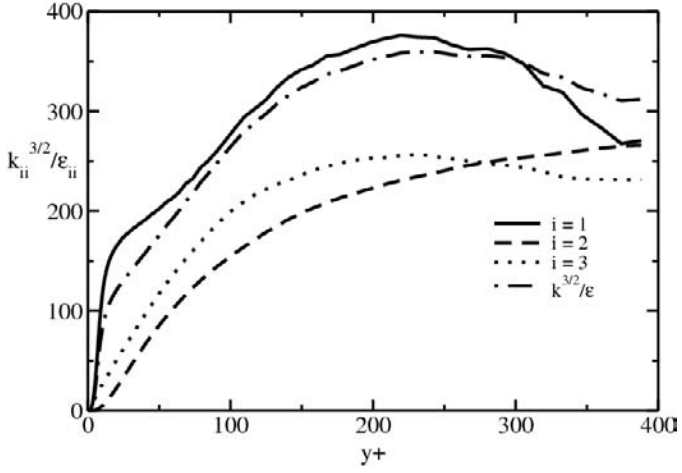

Fig. 5 Energy lengthscales for $Re_\tau = 395$ from DNS [11]. (Correlations integrated only upto 0.1)

The streamwise Taylor microscales ($k = 1$), when divided by $\sqrt{2}$, seem to indicate that a streamwise filter of $\Delta_1^+ = 35$ to 55 viscous units should be sufficient to capture the wall normal velocity fluctuations ($i = 2$) which demand the finest resolution.

It is interesting to notice that the transverse Taylor microscales ($k = 3$) vary similarly to ten times the Kolmogorov scales even upto the centre (for this Re). Both scales show a large variation and anisotropy near to the wall (up to $y+ = 30$), then almost a linear variation, making it difficult to distinguish

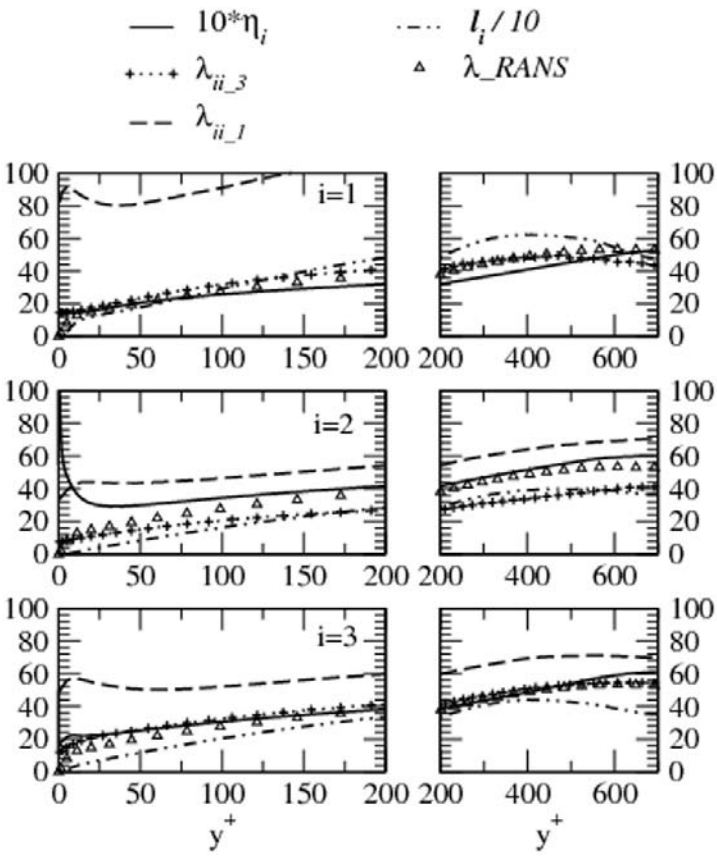

Fig. 6 Comparison between different lengthscales for the channel flow test case at $Re_\tau = 720$

the log-layer region from the core region of the channel. The one-tenth of estimated integral lengthscale as estimated from L_{RM_i}(Equation (2)) was expected to dominate in the central region, but $Re_\tau = 720$ is still too low for this to happen. Near the wall $L_{RM\_i}/10$ decreases very rapidly compared to the Kolmogorov or transverse Taylor scales. The latter suggest $\Delta_3^+ = 15$ at the wall to 45 at the centre which is in line with empirical knowledge. The estimated Taylor scale λ_{RM_i} is quite close to the actual one for $i = 1$ and 3, but shows an overestimation for the wall normal velocity. It also has the disadvantage of going to zero at the wall. Finally the "anisotropic" Kolmogorov scale suggested by Equation (6) is of course isotropic for $y+ > 50$, and is singular at the wall for $i = 2$, and is thus not worth perusing.

From literature it is possible to find that the maximum grid size that is used for DNS is about 5 times the Kolmogorov scales everywhere. Thus, it can be argued that computations using grids based on these scales are

still within the limits of the LES approach. To conclude one may recommend an unstructured mesh such that $\Delta_1 = max(min(\lambda_{ii\_1}, L_{RM}/10))$ and $\Delta_3 = max(min(\lambda_{ii\_3}, L_{RM}/10))$, but with $\lambda_{ii\_k} = max(\lambda_{RM\_k}, \eta/5)$ when the Taylor microscale needs to be guessed from a RANS model. No two point correlation data is available for the wall normal lengthscales, so an estimate $\Delta_2 = max(min(\lambda_{22\_k}), L_{RM}/10)$ is used.

4 Application to Turbulent Channel Flow

Based on the above analysis, a grid has been generated for a plane channel at $Re_\tau = 395$ using the transverse Taylor microscales. The grid density is summarized in Table 1 in comparison of a DNS grid used by Moser et al. [13] and Fig. 7 illustrates the anisotropic cell distribution in the three directions of the domain with a total of 443,272 cells. The commercial code Star-CD has been used for the present simulations. The computations have been carried out using the classical Smagorinsky model with Van Driest damping function.

Table 1 Number of cells in the three directions of the domain

	N_x	N_y	N_z
LES	68 to 200	46	42 to 100
DNS	256	193	192

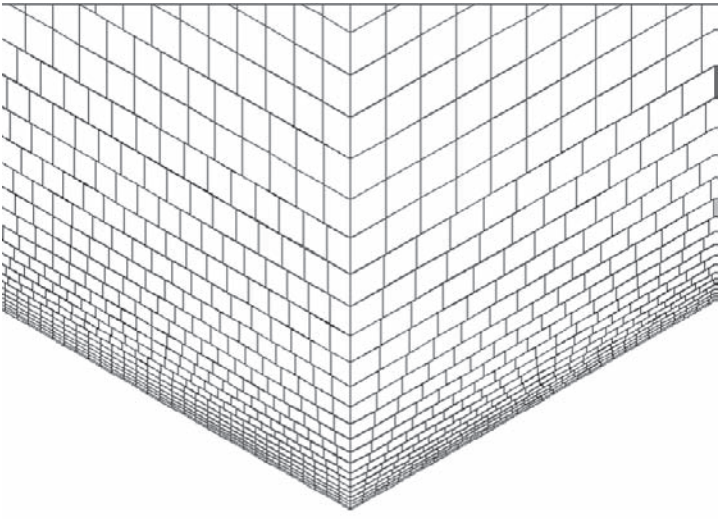

Fig. 7 Grid built for channel flow using Taylor microscales

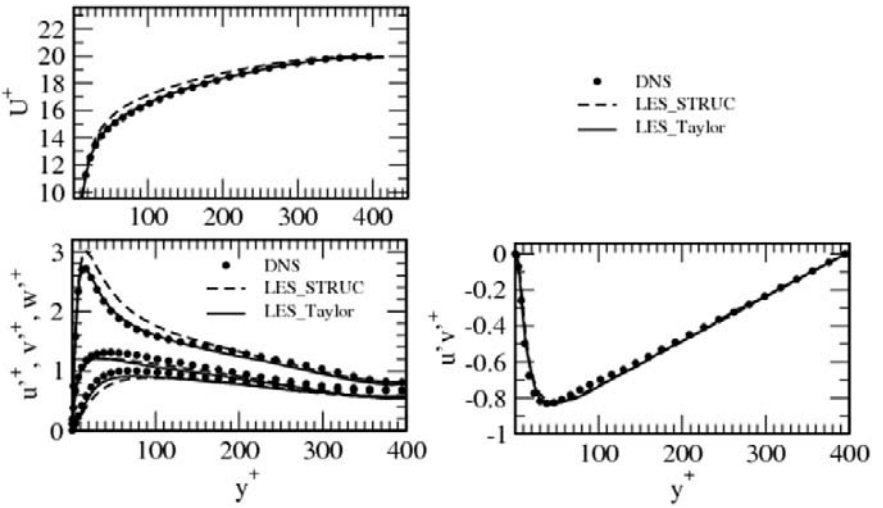

Fig. 8 LES results obtained with the grid generated using Taylor scales (LES Taylor) in comparison with an LES using structured grid (LES STRUC)

Figure 8 illustrates the obtained results in comparison with results from DNS and LES employing structured grids. A remarkable feature is that over-prediction of the mean velocity and streamwise component of fluctuating velocity, usually encountered in LES, are not very pronounced in this simulation. However, some under-prediction of the wall normal and fluctuating velocities occurs, chiefly in the centre of the channel. The velocity profile results very closely follow DNS results and therefore, the attempt of building an LES grid based on the Taylor microscale has been very successful.

5 Conclusions

A grid following the spanwise Taylor microscales in the streamwise, wall normal and spanwise directions gives good agreement of the LES results with those obtained from DNS.

The most important features of this grid, differentiating it from all earlier empirical meshes, are the almost cubical geometry of the cells and the fineness in the spanwise direction. Empirical LES grids, currently very widely used, have a very fine (approximately four times finer) wall normal resolution and a coarse (about twice as coarse) streamwise resolution as compared to a grid based on the Taylor microscales.

The cubical nature of the grid enables the flow vorticity to be effectively captured. Consequently, the turbulent mixing is well taken into account and near wall fluid acceleration is restricted. The results seem to indicate that the

spanwise mesh resolution is very consequential in correctly resolving turbulence in channel flows.

As the present investigation was in progress, a paper by Meyers and Sagaut [14] showed that a very coarse DNS can predict mean profiles surprisingly well, for very specific cell size distributions, but depends strongly on the wall normal resolution and Reynolds number. Nevertheless the present unstructured grid has been build on physically meaningful lengthscales rather than trial and error. The prescribed criteria now need to be tested in different configurations such as jets and separating flows.

References

1. Celik I (2005) RANS/LES/DES/DNS: the future prospects of turbulence modelling. Journal of Fluids Engineering 127:829–830
2. Speziale CG (1998) Turbulence modelling for time-dependent RANS and VLES: a review. AIAA Journal 36:173–184
3. Celik IB, Cehreli ZN, Yavuz I (2005) Index of resolution quality for large eddy simulations. Journal of Fluids Engineering 127:949–958
4. Kallinderis Y (1992) Numerical treatment of grid interfaces to viscous flow. Journal of Computational Physics 98:129–144
5. Rai MM, Moin P (1993) Direct numerical simulation of transition and turbulence in a spatially revolving boundary layer. Journal of Computational Physics 109:169–192
6. Kravchenko AG, Moin P, Moser R (1996) Zonal embedded grids for numerical simulations of wall-bounded turbulent flows. Journal of Computational Physics 127:412–423
7. Addad Y, Laurence D, Talotte C (2002) Large-eddy simulation of a forward-backward facing step for acoustic source identification. 5th Int Symposium on ETME, Maillorca, Spain
8. Klein M (2005) An attempt to assess the quality of large eddy simulations in the context of implicit filtering. Flow, Turbulence and Combustion 75:131–147
9. Jordan SA (2005) A priori assessments of numerical uncertainty in large-eddy simulations. Journal of Fluids Engineering 127(6):1171–1182
10. Kang HS, Chester S, Meneveau C (2003) Decaying turbulence in an active-grid-generated flow and comparisons with large-eddy simulation. Journal of Fluid Mechanics 480:129–160
11. Iwamoto K (2002) Database of fully developed channel flow. THTLAB Internal Reports, Dept of Mech Eng, The Univ of Japan
12. Hu ZW, Sandham ND (2001) DNS databases for turbulent couette and poiseuille flow. Report AFM-01/04, Aerodynamics and Flights Research Group, School of Engineering Sciences, University of Southampton
13. Moser RD, Kim J, Mansour NN (1999) Direct numerical simulation of turbulent channel flow up to $Re_\tau = 590$. Physics of Fluids 11(4):943–945
14. Meyers J, Sagaut P (2007) Is plane-channel flow a friendly case for the testing of large-eddy simulation subgrid-scale models? Physics of Fluids 19, Art no 048105

Analysis of Uniform and Adaptive LES in Natural Convection Flow

Andreas Hauser[1] and Gabriel Wittum[2]

[1] Corporate Technology, Power & Sensor Systems, Siemens AG, Günther-Scharowsky-Str. 1, 91050 Erlangen, Germany. a.hauser@siemens.com
[2] Simulation in Technology, University of Heidelberg, Im Neuenheimer Feld 368, 69120 Heidelberg, Germany. wittum@techsim.org

Abstract. After an introduction to the underlying problem, the governing equations and discretisation schemes, we present in the first part of this contribution the calculation of the model and discretisation error in a turbulent natural convection flow in a tall cavity. It is based on uniform grid refinement and explicit values are given for the error components. In the second part we apply for the same problem local grid adaptation using four different a posteriori error indicators. The computational results are compared with experiments and it is shown, that adaptively refined grids with considerably less elements deliver comparable results gained on finer uniformly refined grids.

Keywords: Model and discretisation error on uniform grids, Local adaptive a posteriori error indicator, Natural convection

1 Introduction

The numerical simulation of turbulent flow is still a challenging task. Turbulence models are applied, because the small turbulent scales in most technologically relevant applications cannot be resolved by today's computer resources. Although Large Eddy Simulation (LES) models the majority of the frequencies in the turbulent spectra, LES still requires rather fine meshes.

An inherent question in LES is the influence of the subgrid-scale model and the computational grid on the overall result, especially when both errors, the model error and discretisation error, are of the same order. This issue will be addressed first in this contribution. In particular, for a natural convection problem both error contributions will be indicated by means of uniform refinement of the grid size on the one hand and varying filter size on the other hand.

As in many flow problems, turbulence is not isotropic throughout the whole computational domain, adaptive methods are predestinated to generate an optimal mesh. This represents the second part of this contribution. Specifically,

J. Meyers et al. (eds.), Quality and Reliability of Large-Eddy Simulations,

the numerical and modeling error is minimised with respect to a given number of elements. Whereas typically only the approximation error is considered, our approach comprises both error components. Four types of error indicators are applied to the natural convection problem: a classical residual based, a hierarchical, a maximum and a gradient indicator for the a posteriori error. Finally, they are compared with numerical results on uniformly refined grids and experimental results.

2 Natural Convection in a Tall Cavity

The numerical investigations are carried out by means of the natural convection problem presented by Betts et al. [1]. A natural convection flow of the fluid air is established by heating one of the vertical walls in a tall cavity as shown in Fig. 1. In such flow problems, the flow characteristic is described by the Rayleigh-number

$$Ra = \frac{g\gamma \Delta T L_0^3}{\nu \kappa},$$

where g stands for gravity, γ for volume expansion, ΔT for characteristic temperature difference, L_0 for characteristic length, ν for kinematic viscosity and κ for thermal diffusivity. Betts and Bokhari showed in this benchmark fully developed turbulence with a Rayleigh number of $Ra = 0.86E{+}6$. Because

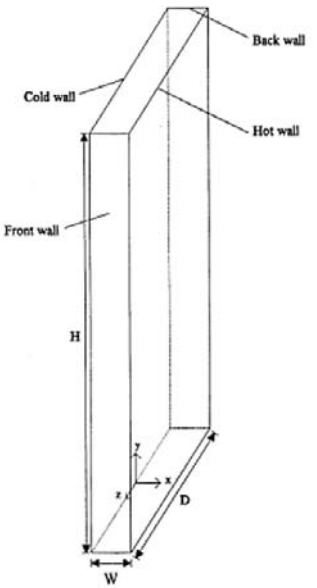

Fig. 1 Natural convection problem in a tall cavity

Table 1 Grid hierarchy of the tall cavity problem

Level i	h_i	#hexa	#nodes	#unknowns
3	0.00950	8192	9945	49725
4	0.00475	65536	72369	361845
5	0.00238	524288	551265	2.75632E+06

of the large length L and the rather small temperature difference of $\Delta T = 17.6K$, turbulent flow can be assumed for constant material properties of air at ambient temperature.

The computational domain is discretised with hexaedra and a uniform grid hierarchy is created by uniform refinement starting from the coarse grid. The grid hierarchy with its mesh sizes, number of elements, nodes and unknowns is shown in Table 1.

3 Mathematical Model and Discretisation

Starting point are the filtered Navier–Stokes equations modeling turbulent fluid flow. Special attention is drawn to the construction of variable filter sizes, which is a prerequisite here for evaluating model and discretisation error.

3.1 Mathematical Model

In order to employ a LES model, the incompressible Navier–Stokes equations are formally filtered and read as follows:

$$\begin{aligned} \frac{\partial \bar{u}_j}{\partial x_j} &= 0 \\ \frac{\partial \bar{u}_i}{\partial t} + \frac{\partial(\bar{u}_j \bar{u}_i)}{\partial x_j} + \frac{\partial \bar{p}}{\partial x_i} - \nu \frac{\partial^2 \bar{u}_i}{\partial x_j \partial x_j} + \frac{\partial \tau_{ij}}{\partial x_j} + \gamma \delta_{i3} g_i (\bar{T} - T_0) &= 0 \\ \frac{\partial \bar{T}}{\partial t} + \frac{\partial(\bar{u}_j \bar{T})}{\partial x_j} - \frac{\partial}{\partial x_j}\left(\kappa \frac{\partial \bar{T}}{\partial x_i}\right) + \frac{\partial q_j}{\partial x_j} &= 0, \end{aligned} \tag{1}$$

where $\bar{u}_i$, $\bar{p}$, $\bar{T}$ represent the filtered velocities, pressure and temperature. The subgrid scale (sgs) tensor τ_{ij} and sgs heat flux q_i close the system. Applying the Smagorinsky model, the sgs terms are defined as follows:

$$\begin{aligned} \tau_{ij} &= \overline{u_i u_j} - \bar{u}_i \bar{u}_j = 2\nu_t |\bar{S}| \bar{S}_{ij} = 2 C_s \Delta^2 |\bar{S}| \bar{S}_{ij} \\ q_j &= \overline{u_i T} - \bar{u}_i \bar{T} = \kappa_t \frac{\partial \bar{T}}{\partial x_i}, \end{aligned}$$

with the sgs strain tensor $\bar{S}_{ij} := (\partial \bar{u}_i / \partial x_j + \partial \bar{u}_j / \partial x_i)/2$, its absolute value $|\bar{S}| = (2\bar{S}_{ij}\bar{S}_{ij})^{1/2}$, the filter size Δ, the Smagorinsky constant with chosen value $C_s := 0.1$, the eddy viscosity ν_t and eddy thermal diffusivity κ_t. The

eddy thermal diffusivity is determined in a very similar manner than the eddy viscosity:

$$\kappa_t = \frac{\nu_t}{Pr_t}.$$

The turbulent Prandtl number Pr_t can be set to one, which is justified in [2].

3.2 Discretisation

The system of partial differential equations is eventually discretised. The spatial discretisation is carried out by a vertex-centered finite volume scheme with colocated variables using continuous, piecewise trilinear ansatz functions. The LBB-stabilisation criterion is met due to a special pressure interpolation, leading to stabilising terms in the continuity equation. The basic idea stems from [3] and the improved scheme was implemented in *UG* [4] by Rentz-Reichert and Nägele [5, 6]. The discretisation is locally flux-conserving and second-order consistent for the second order terms.

In order to avoid time step restrictions induced by the Courant-Friedrichs-Lewy condition, a fully implicit time integration method is used. We apply the A-stable *Fractional-Step-Θ-scheme* [7], which is second order consistent in time requiring the solution of two fractional steps.

3.3 Solving Strategy

Each time step, the system of nonlinear equations has to be solved. The nonlinear solution is found using Newton's method. The nonlinear iteration to solve (1) is considered to have converged, if

$$||d^j_\Theta(\tilde{x}||_2 \leq 10^{-5}||d_\Theta(\tilde{x})||_2,$$

where the nonlinear defect of the iterate $\tilde{x}$ is defined by

$$d^j_\Theta(\tilde{x}_i) := F^{j,j-1}_\Theta(\tilde{x}^{j-1}, \tilde{x}^{j-\Theta}, \tilde{x}^j).$$

Each nonlinear iteration requires the solution of the linear equation derived by linearising 1. The linear system is obtained using a Quasi-Newton linearisation

$$u^n_j \frac{\partial u^n_i}{\partial x_j} \approx u^{n-1}_j \frac{\partial u^n_i}{\partial x_j}, \qquad u^n_j \frac{\partial T^n}{\partial x_j} \approx u^{n-1}_j \frac{\partial T^n}{\partial x_j}$$

obtaining linear convergence [8]. On average, about 4 Newton iterations are required to solve each nonlinear problem. The linear system is solved using the geometric multigrid method with a V(2,2)-cycle applying ILU as a robust smoother. It is accelerated using a Bi-CGStab Krylov-space-method.

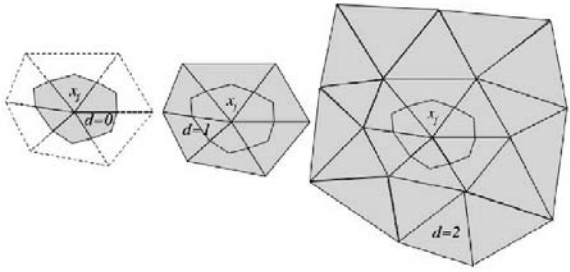

Fig. 2 Different filter sizes for node $\mathbf{x}_j$ on an unstructured grid

3.4 Construction of Variable Filtersizes

In order to evaluate the error components in a LES, the filter widths are of variable size and, hence, are not fixed to the grid size, as it is usually practised. We define an environment $U(\Delta_l^{l-d}(\mathbf{x}_j))$ for the filter size Δ on grid level l, the filter depth $l-d$ at each node $\mathbf{x}_j$ in the computational grid and the relevant elements K from the triangulation τ_l:

$$U(\Delta_l^{l-d}(\mathbf{x}_j)) := \begin{cases} B_j \quad \text{for} \quad d=0 \\ \bigcup\{K' \in \tau_l : K' \cap K'' \neq \emptyset, K'' \in \tau_{l-d} : K'' \cap \mathbf{x}_j \neq \emptyset\} K', \\ \qquad \text{for } d > 0. \end{cases}$$

The smallest filter size is defined by $d=0$ resembling the control volume B_j on level l. The next larger filter size is composed by summing up the elements sharing node $\mathbf{x}_j$. A recursive algorithm adds successively neighbour elements for $d > 1$. Three different filter sizes are exemplified in Fig. 2.

3.5 Numerical Experiments

The resolved kinetic energy, which is defined as

$$E_{res} := \frac{1}{|\Omega|} \int_\Omega \sum_i^d \bar{u}_i' \bar{u}_i' \, dV,$$

is computed on the grid levels l_3, l_4, l_5 with the three different filter sizes $d=0, d=1, d=2$ respectively. As can be seen from Fig. 3, the kinetic energy decreases with increasing filter size. On the other hand, grid convergence for the filter size $d=0$ cannot be stated clearly. But, referring to filter sizes $d=1$ and $d=2$ the solutions converge to the solution on the finest grid level. These data can now be used for evaluating the model and discretisation error.

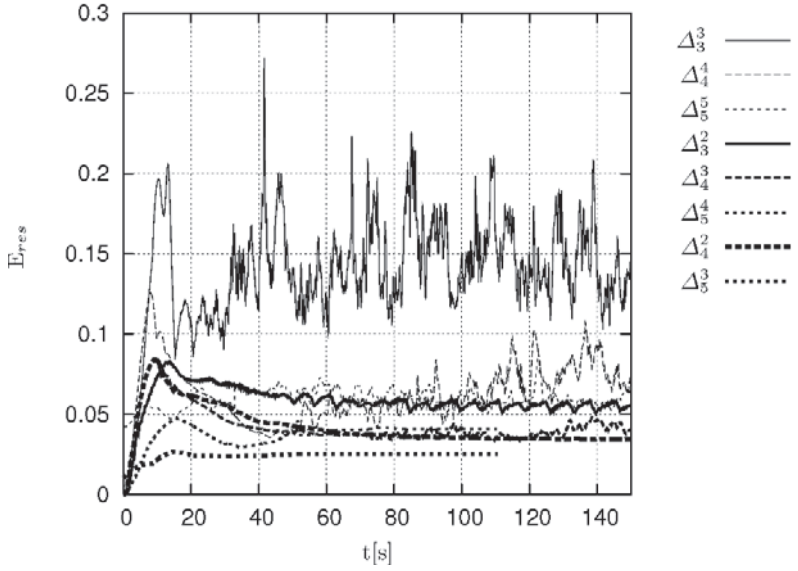

Fig. 3 E_{res} on grid level l_3, l_4, l_5 with three filter sizes $d = 0, d = 1, d = 2$

4 Model and Discretisation Error

The approach for separating both types of errors is described in the following and both errors are given for the computations carried out. Unlike Direct Numerical Simulation, where no turbulence model is used at all, LES incorporates a model error in addition to the discretisation error. The interaction of the two error components especially for second order consistent discretisation schemes, the consistency error of which corresponds to the eddy viscosity, is a priori not clear. Geurts presented in [9] an approach to analyse the influence of the different errors. It should be noted that not the actual error in a mathematical rigorous sense is determined, but rather the tendencies of the two error components. We follow Geurts' ansatz and define the discretisation error *ed* and model error *em* as follows:

$$ed^p_{l_i,l_j} := x_{LES}(\Delta^p_{l_i}) - x_{LES}(\Delta^p_{l_j}), l_j > l_i, \qquad l_i, l_j, p \in \mathbb{N}_0 \tag{2}$$

$$em^p_{l_i,l_j} := x_{LES}(\Delta_{l_j}) - x_{DNS,l_j} \circ G(\Delta^p) \tag{3}$$

The filter size $\Delta^p_{l_i}$ corresponds to the control volume on the coarser grid l_i. This filter size is the same on the finer grid but is resolved by more elements. In (2) the so-called production LES $x_{LES}(\Delta^p_{l_i})$, which assumes an appropriate grid and the control volume as the filter size, is subtracted from a fine LES $x_{LES}(\Delta^p_{l_j})$, in which the grid size is comparatively small. In this way one may extract the discretisation error. On the other hand subtracting an explicitly

Table 2 Model and discretisation errors

$x_{LES}(\Delta^3_{l_3,l_5})$	$x_{LES}(\Delta^3_{l_3,l_4})$	$x_{LES}(\Delta^4_{l_4,l_5})$
$ed^3_{3,5} = 0.1281$	$ed^3_{3,4} = 0.1111$	$ed^4_{4,5} = 0.0283$
$em^3_{3,5} = 0.0110$	$em^3_{3,4} = 0.0068$	$em^4_{4,5} = 0.0044$
$ed/em = 11.6$	$ed/em = 16.3$	$ed/em = 6.4$

filtered DNS in (3) with the filter operator $G(\Delta^p)$ from the fine LES, the discretisation error is small and only the model error remains. With (2) and (3) and with $x := E_{res}$ the error components in the kinetic energy for the computations mentioned above can be estimated. The values are shown in Table 2 and refer to the Rayleygh number given above. From that table it can be stated that the discretisation error is one order of magnitude larger than the model error. In addition, the discretisation error converges faster than the model error.

5 Adaptive LES

In many situations of practical interest, turbulence is not isotropic in the whole domain. Areas, in which high turbulent intensity can be observed, change to low turbulent intensity or even to laminar flow in other regions. With fixed mesh sizes the requirements on the model to deliver accurate results are high. We follow a grid adaptation approach, in which the mesh is adapted locally according to the current solution using the simple Smagorinsky model. Different approaches for adaptive LES exist, like the Stochastic Coherent Adaptive LES [10], where an adaptive wavelet model is used, or the dual weighted residual based a posteriori indicator [11]. Our approach differs from other methods since the mesh is adapted dynamically many times in one computation using classical residual based error indicator as well as indicators suited for LES, like the tracking of the eddy viscosity.

In this section, first the different a posteriori error indicators are described, followed by the quantities on which the indicators are based. The velocity in a seminorm is finally compared with results on uniformly refined grids and experimental results.

5.1 Grid Adaptation Strategy

In order to adapt the grid with respect to a certain criterion, an indicator η_k is evaluated on each element and it is then checked, whether $\eta_K < \epsilon_\eta$, with the error tolerance threshold ϵ_η. If $\eta_K > C_{ref}\epsilon_\eta$, then this element is marked for refinement, in which C_{ref} represents a parameter for refinement. On the other hand, if $\eta_K < C_{coa}\epsilon_\eta$, then this element is marked for coarsening, with the coarsening parameter C_{coa}. In order to keep the mesh within

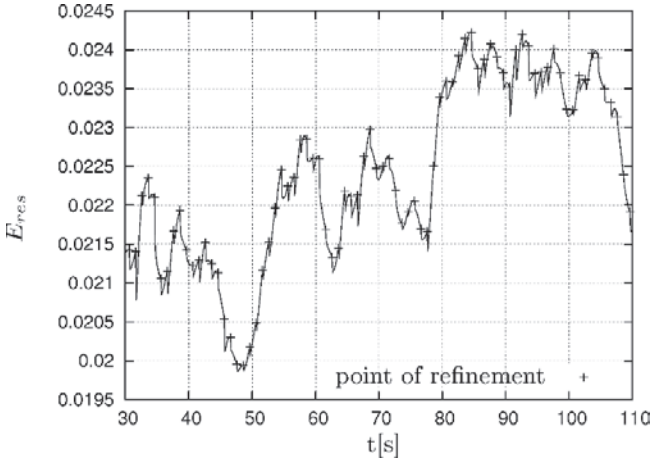

Fig. 4 Points of refinement and kinetic energy over time interval

certain bounds, maximum and minimum grid levels are defined. Hence, the maximum number of elements is determined by the number of elements on the finest grid (maximal grid level), whereas the minimum number of elements is determined by the number of elements on the coarsest grid (minimal grid level). We apply four different a posteriori error indicators: residual based, hierarchical, maximum and gradient error indicator. In the following adaptive computations the minimum grid level is l_3 and the maximum grid level is l_5. This algorithm is performed after each 10th timestep. The points of refinement over a time sequence are shown in Fig. 4. As turbulent flow differs completely from elliptic problems, to which error indicators are applied successfully and with which the error thresholds can be applied as mentioned above, refining grids in turbulent flow problems mean under normal conditions solving a different problem. Against this background the thresholds C_{ref} and C_{coa} must be adapted during the computation. It turned out that this rather technical point of view requires a lot of sensitivity analysis.

5.2 A Posteriori Error Indicators

Four different a posteriori error indicators are applied:

1. residual based
2. hierarchical
3. gradient jump
4. maximum

The residual based error indicator [12] is constructed to detect the discretisation error and is defined as follows:

$$\eta_{res,K} : \omega_r|\eta_r| + \omega_{ju}|\eta_{ju}| + \omega_d|\eta_d|, \tag{4}$$

with the weighting parameters ω for the residual η_r, the gradient jump over the element sides/edges η_{ju} and the divergence η_d.

The hierarchical indicator [13] compares a quantity in two different function spaces:

$$\eta_{hi,K} := ||\phi_1 - \phi_2||,$$

where $\phi_1 \in V_1$ and $\phi_2 \in V_2$ represent a quantity in functional spaces V_1 and V_2 respectively with $V_1 \subset V_2$. Since the geometric multigrid is applied and several grids are available, it is natural to base the function spaces on the grid hierarchy.

The gradient jump indicator [12] computes the gradient jump of a quantity over element sides/edges $bf(K)$. Although strictly speaking, this indicator is a subset of the residual based indicator, it is used as a stand-alone indicator and is defined as follows:

$$\eta_{ju,K} := \left|\left| n_j \frac{\partial u_{h,i}}{\partial x_j} \right|\right|_{bf(K)} \tag{5}$$

Eventually, the maximum indicator simply takes the absolute value of quantity ϕ:

$$\eta_{max} := |\phi_K|$$

The quantities mentioned above can be principally arbitrary. Here, the quantities velocity and eddy viscosity are chosen. An example of an adaptively refined grid is shown in Fig. 5.

The number of elements is kept roughly at $30000(+/-5000)$ elements over the whole time sequence.

5.3 Comparison with Solutions on Uniform Grids and Experiments

In the first instance the adaptive solutions are compared with solutions on uniform grids with respect to kinetic energy. Figure 6 shows this quantity of the four indicators and uniform solutions respectively. It can be noticed that only the residual indicator η_r and maximum indicator $\eta_{max}(\nu_t)$ are capable to approach the characteristics of the uniform solutions Δ_4^4 and Δ_5^5. The other two indicators converge towards the coarse uniform solution Δ_3^3.

Eventually, the different computations are compared with experimental results reported in [1]. More precisely, the vertical velocities along a horizontal line over the short axis at $0.7H$ and $0.5D$ are compared. Figure 7 shows the averaged velocities of the adaptive and uniform computations and the experimental results. Even the uniform computations on the fine grid differ in some intervals of ξ considerably from experimental results. These deviations can be explained in two ways. First, the number of time steps, between 2000 and 5000, is possibly too low for statistical reliable mean values. Secondly, it is observed in the computations that large coherent structures move comparably slow across the domain. The residence time of these structures is

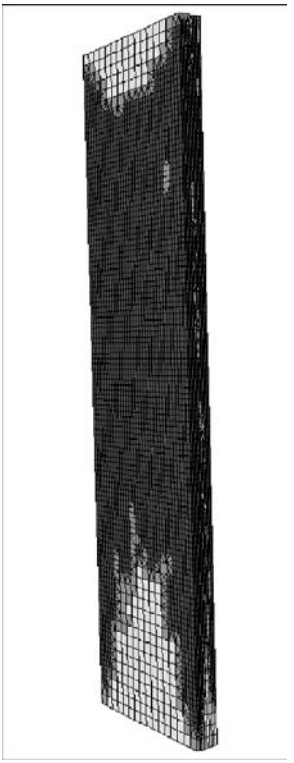

Fig. 5 Adaptively refined grid

comparable to the overall time sequence and, thus, influences the mean values dramatically.

Nevertheless, referring to the computations, it can be seen, that the hierarchical indicator $\eta_{hi}(\nu_t)$ fits least. The maximum indicator $\eta_{max}(\nu_t)$ delivers the best results, whereas the other two indicators $\eta_{ju}(\nu_t)$ and η_r lie somewhere in between.

6 Conclusion

The essence of this contribution is twofold. First, an evaluation of the model and discretisation error within LES of a turbulent natural flow problem is given. It shows that the discretisation error converges faster with decreasing grid size than the model error with decreasing filter size. Secondly, local grid adaptation using four different a posteriori error indicators have been successfully applied to this flow problem. It showed that as well as in the kinetic energy and in the seminorm (vertical velocity along a horizontal line) the maximum error indicator $\eta_{max}(\nu_t)$ seems to be a good choice. A comparable

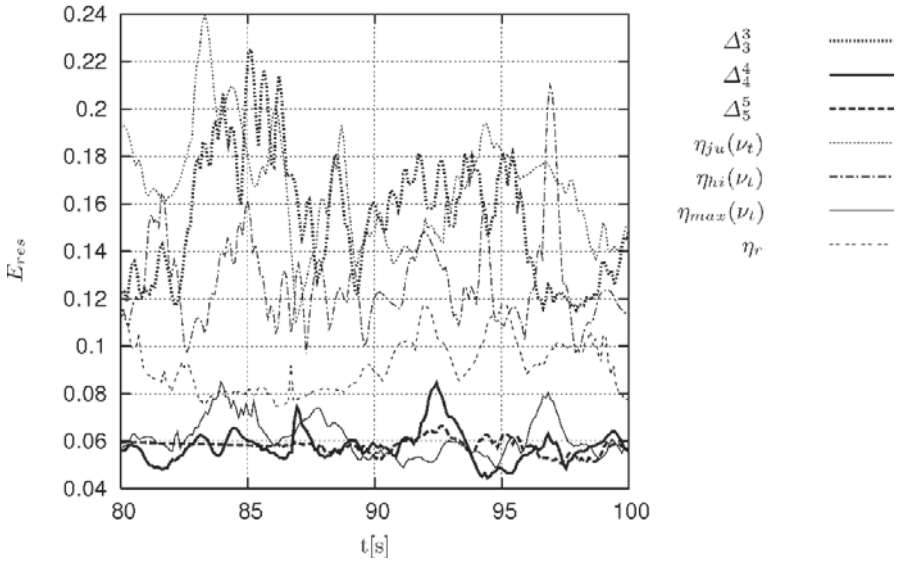

Fig. 6 Adaptive versus uniform solutions

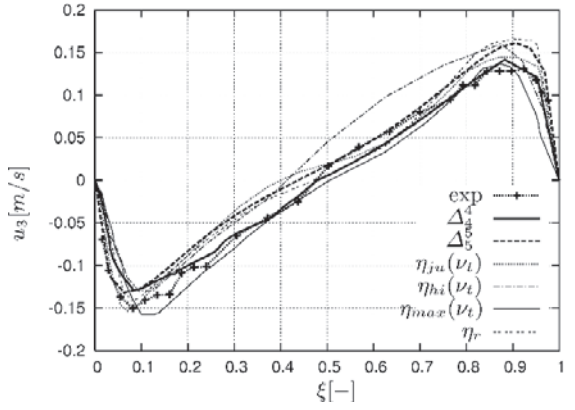

Fig. 7 Vertical velocities along a horizontal line: Comparison between adaptive and uniform computations and experimental results

solution can be obtained by using 50% (grid level 4) or even less than 10% (grid level 5) of the elements on uniform grids.

References

1. Betts PL, Bokhari IH (2000) Int J Heat Fluid Flow 21:675–683
2. Dorfman ASh (1984) J Appl Mech Tech Phys 25(4):572–575
3. Schneider GE, Raw MJ (1987) Numer Heat Trans 11:363–390
4. Bastian P, Birken K, Johannsen K, Lang S, Eckstein K, Neuss N, Rentz-Reichert H, Wieners C (1997) Comput Visual Sci 1:27–40
5. Rentz-Reichert H (1996) Robuste Mehrgitterverfahren zur Lösung der inkompressiblen Navier–Stokes Gleichung: ein Vergleich. PhD Thesis, IWR, Universität Heidelberg
6. Nägele S (2004) Mehrgitterverfahren für die inkompressiblen Navier–Stokes Gleichungen im laminaren und turbulenten Regime unter Berücksichtigung verschiedener Stabilisierungsmethoden. PhD Thesis, IWR, Universität Heidelberg
7. Glowinski R, Periaux J (1987) Supercomputing. State-of-the-Art 381-479
8. Dennis JE, More JJ (1977) SIAM Review 19:46–89
9. Geurts BJ (2004) Elements of direct and large-eddy simulation. Edwards, Fourtown
10. Goldstein DE, Vasilyev OV, Kevlahan NKR (2004) Proceedings of the Summer Program, Center of Turbulence Research
11. Hoffman J (2004) SIAM J Sci Comput 26(1):178–195
12. Verfürth R (1996) A review of a posteriori error estimation and adaptive mesh refinement techniques. Teubner-Wiley, Stuttgart
13. Bey J (1998) Finite-Volumen- und Mehrgitter-Verfahren für elliptische Randwertprobleme. Teubner, Stuttgart

Part II

Computational Error-Assessment

Influence of Time Step Size and Convergence Criteria on Large Eddy Simulations with Implicit Time Discretization

Michael Kornhaas, Dörte C. Sternel, and Michael Schäfer

Technische Universität Darmstadt, Department of Numerical Methods in Mechanical Engineering, Petersenstraße 30, 64287 Darmstadt, Germany
kornhaas@fnb.tu-darmstadt.de

Abstract. Subject of this work is the influence of numerical parameters on quality and efficiency of Large Eddy Simulations. Variations of the time step size and the convergence criterion are considered. The influence of these parameters on mean values and computational time are presented and discussed. The computations were carried out for the well known test case "Periodic flow over a 2D hill".

Keywords: Large eddy simulation, Time step size, Convergence criterion, Efficiency, 2D hill

1 Introduction

Large Eddy Simulation (LES) is a promising way for the simulation of turbulent flow fields of practical relevance. Nevertheless it is still restricted by the capability of today's computers.
To be able to make reliable predictions at a minimum of computational costs, it is necessary to understand the influence of boundary conditions, discretization methods etc. as well as the influence of numerical parameters. This contribution focus on the numerical parameters time step size and the convergence criterion.
The use of implicit time discretization schemes allows time step sizes with corresponding CFL (*Courant-Friedrichs-Lewy*) numbers greater than one. Using a time step size with a maximum CFL number of approximately one, local CFL numbers are smaller than 0.3 for the considered test case (see section 3.1) for the most part of the computational domain (compare Fig. 1). Especially when structured grids are used for the simulation of wall bounded flows, the resolved wall in combination with the maximum acceptable aspect ratio can lead to unnecessarily fine grids in the center of the computational domain where the highest flow velocities occur and, therefore, the highest CFL numbers.

J. Meyers et al. (eds.), Quality and Reliability of Large-Eddy Simulations,

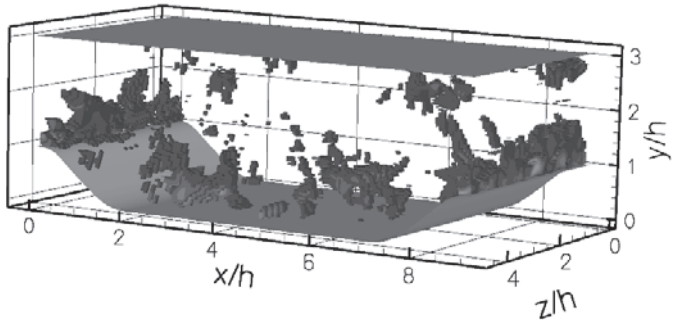

Fig. 1 Spatial distribution of the CFL number for $CFL_{max} \approx 1$. $CFL > 0.3$

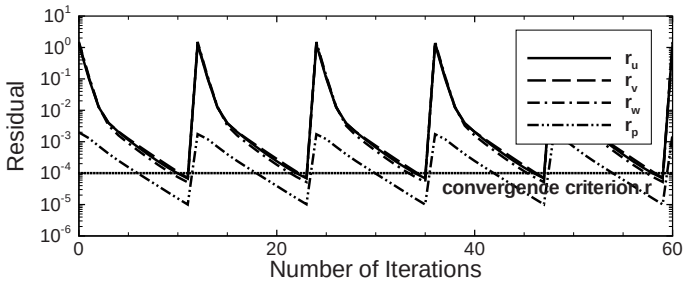

Fig. 2 Convergence behavior for a LES at a fully turbulent state

For statistical analysis it is necessary to calculate relatively big time intervals. The use of larger time steps allows the computation of the required interval with a fewer number of time steps.

Another important numerical parameter is the convergence criterion. It is the basic prerequisite for reliable results. Figure 2 shows a typical convergence behavior of a LES after a fully developed turbulent state is reached. Each "spike" marks one time step. It is obvious that the choice of a stricter convergence criterion leads to longer computational times. Therefore, for efficiency reasons the convergence criterion should not be chosen more restrictive as necessary to get accurate results.

2 Numerical Method and Code Description

To perform the LES the incompressible finite volume solver FASTEST [2] is used. It solves the filtered Navier-Stokes equations on boundary fitted, block structured grids. The convective and diffusive fluxes are approximated with a second-order central difference scheme. Subgrid stresses are computed using

the Smagorinsky model with the dynamic approach of Germano [3]. The implicit Crank-Nicolson scheme is applied for time discretization. The pressure velocity coupling is realized with the SIMPLE algorithm which is embedded in a geometric multi-grid scheme with standard restriction and prolongation [1]. For smoothing the SIP solver is applied.
In each time step it is assumed to have a converged solution if the sum of the residuals r_Φ over all control volumes for each flow quantity Φ is smaller than the convergence criterion r_c

$$r_\Phi = \sum_{j=1}^{N_{CV}} |r_j| < r_c, \tag{1}$$

where N_{CV} is the number of control volumes.

3 Simulations

3.1 The Test Case

The considered test case is the well known "Periodic flow over a 2D hill" (ERCOFTAC test case 9.2) which is a periodic segment of a channel constricted by "2D hills" at the lower wall. The Reynolds number R_h based on the hill height h is approximately 11600. The computational domain is periodic in streamwise as well as in spanwise directions in order to avoid uncertainties due to unknown boundary conditions. Although the simple geometry, the flow shows different features like separation, strong recirculation and reattachment. The geometry of the test case is shown in Fig. 3. The computational domain is of the size $9h \times 3.03h \times 4.5h$.
Since the flow field is statistically 2D, additional averaging in spanwise direction is possible. This reduces the required number of time steps for turbulence statistics significantly.

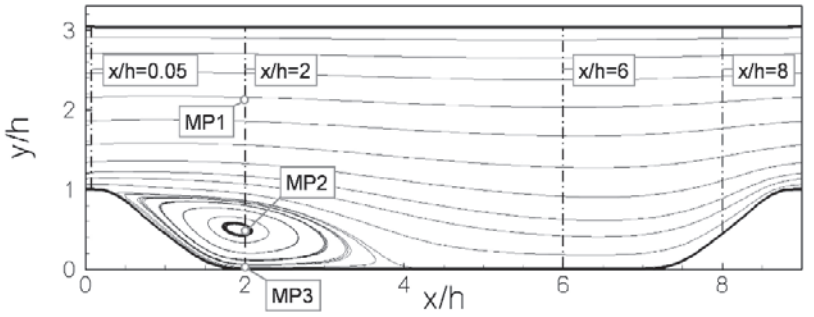

Fig. 3 Geometry of the test case with mean streamlines and locations for the analysis of the mean values as well as monitoring points

3.2 Validation of the Simulation Setup

Influence of the Spatial Resolution

In order to get information about the quality of the perfomed simulations the results of an LES on a 1.47×10^6 control volume (CV) grid – which is used for the parameter studies described in Section 3.3 – are compared with reference data of an LES on a five million CV grid taken from Jang et al. [4] as well as with own reference data of an LES on a 11.8×10^6 CV grid. Figure 4 shows the mean streamwise velocity component $<u>$, normalized with the bulk velocity u_b, for the above mentioned simulations at different locations.

The mean velocities (Fig. 4) obtained with FASTEST on both grids are in very good agreement with the reference data of Jang et al. [4] at all considered locations except at the streamwise position $x/h = 6$. At this position the mean velocity near the lower wall is bigger. The mean streamwise velocities obtained with FASTEST show almost no difference for both grid resolutions. Also the mean fluctuations (Fig. 5) are very similar the data of Jang et al. In the center of the computational domain the fluctuations obtained with FASTEST are smaller than those of data of Jang et al. for the locations $x/h = 0.05$ and $x/h = 8$. At the other considered positions the results are relatively close to the data of Jang et al. but differ from each other for the two grid resolutions. This differences are most likely caused by the relatively short time interval on which averaging was performed and should reduce when averaging is carried on. The error due to the averaging time will be adressed later.
For the following parameter studies the data of the 11.8×10^6 CV LES will be used as reference solution.

Influence of the Averaging Interval

To obtain a statistically converged solution it is necessary to perform time averaging over a sufficiently long time interval. Since many parameter variations

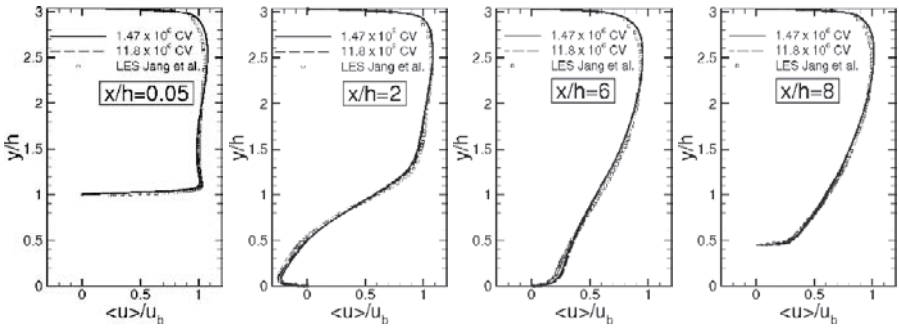

Fig. 4 Validation of the computational setup. Profiles of the normalized mean velocity component $< u > /u_b$ at different locations

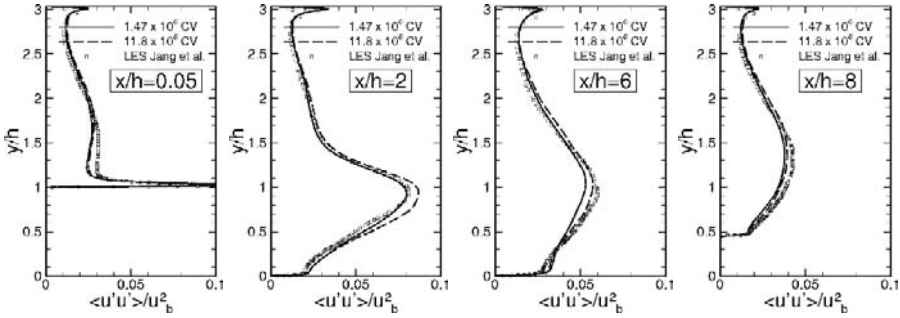

Fig. 5 Validation of the computational setup. Profiles of the normalized mean fluctuations $< u'u' > /u_b^2$ at different locations

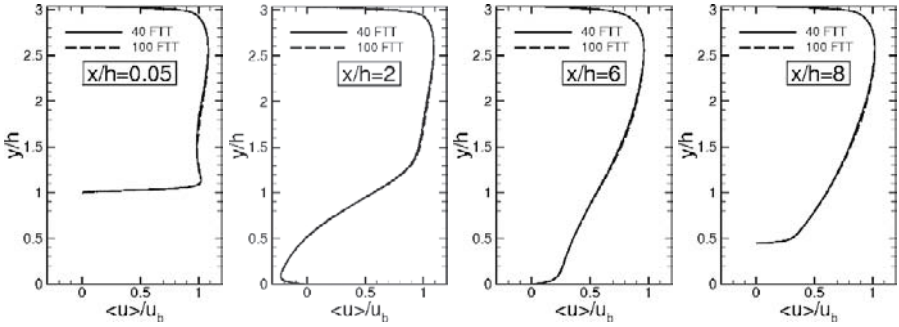

Fig. 6 Validation of the computational setup. Profiles of the normalized mean velocity component $< u > /u_b$ at different locations for different averaging intervals

are considered in this study (see Section 3.3), it is important to find a good compromise between a statistically full converged solution and a relatively short averaging interval in order to keep the simulation time in an acceptable range. To get information about how the chosen averaging interval influences the computational results, different averaging times are considered for one of the most efficient simulations from Section 4.2 with a convergence criterion of $r_c = 10^{-4}$.

The mean streamwise velocity component (Fig. 6) show almost no difference for the considered averaging intervals of 40 and 100 flow through times (FTT). Therefore it can be considered as statistically converged after 40 FTT.

Also the mean streamwise fluctuations (Fig. 7) show a very good agreement for both time intervals at the positions $x/h = 0.05$ and $x/h = 8$. At the other two positions which are strongly influenced by the recirculation zone the differences are bigger. Nevertheless it seems to be a good compromise to use an averaging interval of 40 FTT for the following parameter studies.

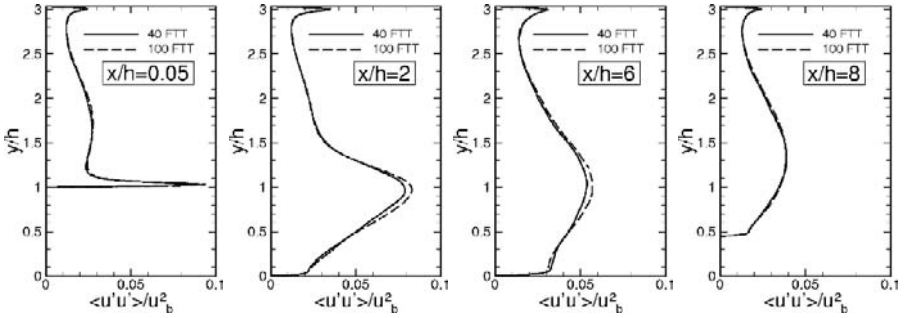

Fig. 7 Validation of the computational setup. Profiles of the normalized mean fluctuations $< u'u' > /u_b^2$ at different locations for different averaging intervals

3.3 Performed Simulations

To gain information how larger time step sizes affect the results of the simulation, computations with different time step sizes and corresponding maximum CFL numbers of approximately 1, 2, and 5 were carried out. Averaging was performed for 40 flow-through times. Additionally a computation with a weak convergence criterion of $r_c = 10^{-1}$ and the biggest considered time step size with $CFL \approx 5$ was carried out.

As mentioned before the convergence criterion r_c is another important numerical parameter which influences the quality of the results as well as the computational time and therefore the efficiency of the calculation. To get information about its effect on results and efficiency, simulations with different convergence criteria ($r_c = 10^{-4}, 10^{-3}, 10^{-2}, 10^{-1}$) were carried out. Another simulation with only one SIMPLE-Iteration per time step without any convergence check was performed as well.

Table 1 gives an overview of the performed simulations. In Section 4 the profiles of the normalized mean streamwise velocity component $<u>/u_b$ as well as the profiles of the normalized mean streamwise fluctuations $<u'u'>/u_b^2$ are compared to each other. Further the convergence behavior and the computational times are evaluated.

Table 1 Overview of performed simulations

Δt (CFL)	5×10^{-5}s (≈ 1)	10^{-4}s (≈ 2)	2.5×10^{-4}s (≈ 5)
Residual $r_c = 10^{-4}$	X	X	X
Residual $r_c = 10^{-3}$	X		
Residual $r_c = 10^{-2}$	X		
Residual $r_c = 10^{-1}$	X		X
1 SIMPLE-Iteration	X		

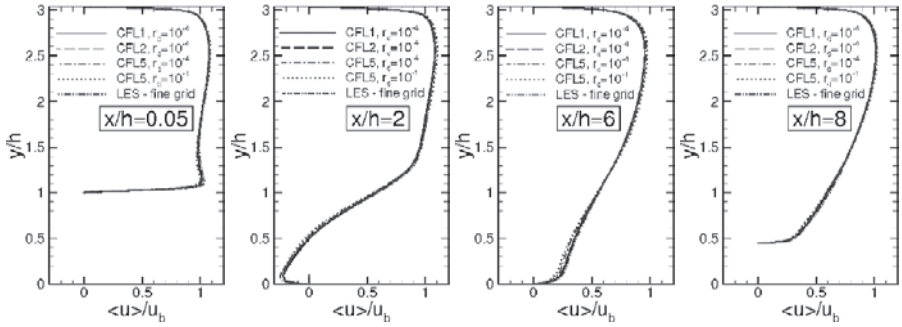

Fig. 8 Influence of the time step size. Profiles of the normalized mean velocity component $< u > /u_b$ at different locations

4 Results

4.1 Influence of the Time Step Size

Figure 8 shows the profiles of the normalized mean streamwise velocity component $< u > /u_b$ for three different time step sizes and corresponding CFL numbers of approximately 1, 2, and 5 for a convergence criterion of $r_c = 10^{-4}$ and for $CFL \approx 5$ also for $r_c = 10^{-4}$. At all considered locations the profiles are in good agreement with the reference solution (LES – fine grid). Also the results for the weakest convergence criterion are not worse than those of the other simulations. There are no significant differences between the results for the averaged velocities for the different time step sizes. In Fig. 9 the profiles of the normalized mean streamwise fluctuations $< u'u' > /u_b^2$ are shown. At the positions $x/h = 0.05$ and $x/h = 8$ profiles are in very good agreement with the reference solution (LES – fine grid) for all simulations with the strict convergence criterion of $r_c = 10^{-4}$. But there are differences at the other two locations. These differences can be explained by the relatively short period of time (40 flow-through times) where averaging was performed.
For the case $CFL \approx 5$ and $r_c = 10^{-1}$ the results differ from the others at the positions $x/h = 0.05$, $x/h = 2$ and $x/h = 6$ even though averaging was performed for the same time interval. It seems that the combination of a big time step size and a weak convergence criterion affects the results of the simulation whereas the sole variation of the time step size (in the considered range) shows no effect to the computational results.

Frequency Spectra

Figure 10 shows streamwise turbulent kinetic energy spectra taken at three different monitoring points (MP) for the smallest time step size with corresponding $CFL \approx 1$ and the largest one with $CFL \approx 5$. The monitoring points are located in the center of the computational domain (MP1), the center of the

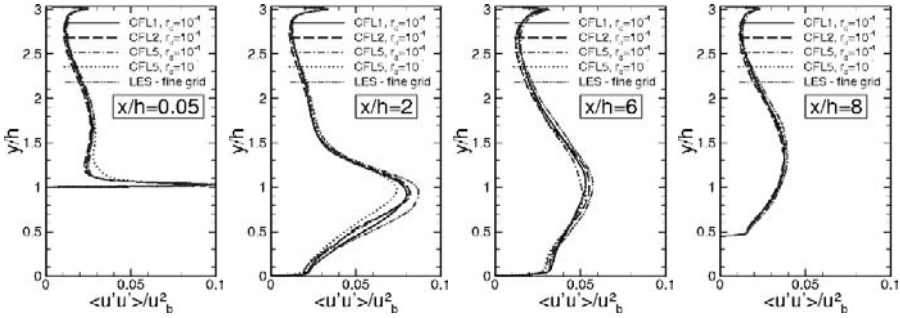

Fig. 9 Influence of the time step size. Profiles of the normalized mean fluctuations $< u'u' > /u_b^2$ at different locations

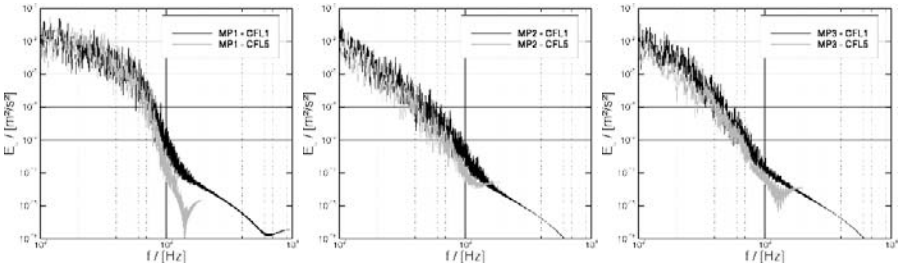

Fig. 10 Influence of the time step size. Streamwise turbulent kinetic energy spectrum taken at three different locations (compare Fig. 3)

recirculation area (MP2) as well as close to the wall (MP3) and the streamwise position $x/h = 2$ (compare Fig. 3). The spectra show the same behavior for both time step sizes at the considered monitoring points up to higher frequencies that contain only little energy. This means that the time step size (at least in the considered range) has only a small effect on the modeled part of the energy spectrum. This indicates clearly that even for $CFL \approx 5$ the time step size is small enough to resolve the relevant scales. Furthermore the highest CFL numbers occur farer away from the wall. This is also reflected in the frequency spectra of MP2 and MP3 that are more similar for the two considered time step sizes.

4.2 Influence of the Convergence Criterion

Figure 11 shows the profiles of the normalized mean streamwise velocity component $<u>/u_b$ for the convergence criteria $r_c = 10^{-1}$ and $r_c = 10^{-4}$ as well as for the case with only one SIMPLE-Iteration per time step. The results for $r_c = 10^{-2}$ and $r_c = 10^{-3}$ are comparable to those of the other simulations and therefore not shown for purposes of clarity. At all considered locations the profiles are in very good agreement with the reference solution (LES – fine grid).

In Fig. 12 the profiles of the normalized mean streamwise fluctuations $<u'u'>/u_b^2$ are shown.
For the different convergence criteria no significant differences between the results for the velocities and fluctuations can be observed. Even the setup without any convergence check and only one SIMPLE-Iteration per time step gives the same results. The differences can again be explained by the relatively small averaging interval.

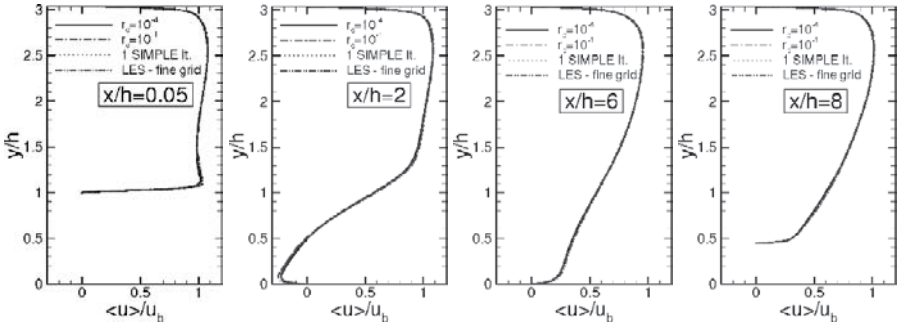

Fig. 11 Influence of the convergence criterion. Profiles of the normalized mean velocity component $< u >/u_b$ at different locations

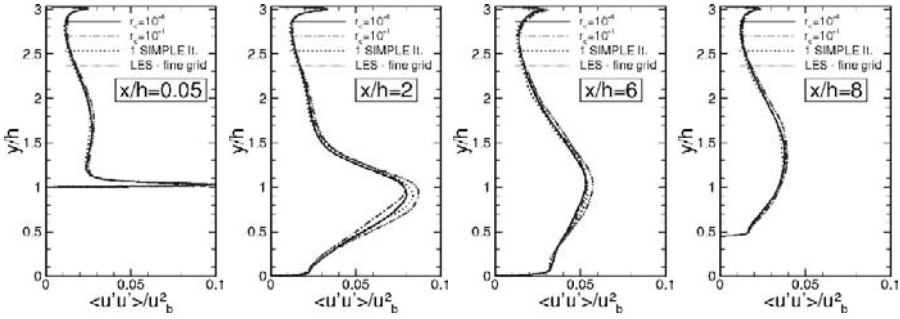

Fig. 12 Influence of the convergence criterion. Profiles of the normalized mean fluctuations $< u'u' >/u_b^2$ at different locations

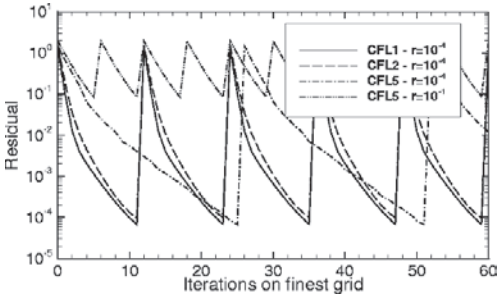

Fig. 13 Convergence behavior for different time step sizes at a fully developed turbulent state

4.3 Comparison of Computational Times

The use of bigger time steps may also affect the convergence behavior because the differences between the time steps are bigger and therefore the initial solution for the new time step may be worse. For this reason the calculation time which is needed for a single time step may also be different. Figure 13 shows the convergence behavior for the three different time step sizes with the corresponding CFL numbers of approximately 1, 2, and 5.
For time step sizes with $CFL \approx 1$ and $CFL \approx 2$ the convergence process is almost identical. The residual reduction is insignificantly smaller for $CFL \approx 2$ than for $CFL \approx 1$ so that the same number of iterations was needed to reach the applied convergence criterion of $r_c = 10^{-4}$. The simulation with $CFL \approx 5$ shows a considerably worse convergence behavior. More than twice as many iterations on the finest grid level were needed to reach the convergence criterion. This case is the only one were a geometric multigrid scheme was applied. For all the other cases the multigrid method did not yield any benefit. The setup with $CFL \approx 5$ and the weak convergence criterion of $r_c = 10^{-1}$ again showed a good convergence behavior.
Figure 14 shows the convergence behavior for different convergence criteria. For the applied convergence criteria the residual reduction per iteration (until the applied convergence criterion was reached) is almost identical. The residual for the case with only one SIMPLE-Iteration is not shown. It stayed almost constant around a value of $r \approx 1.45$. The computational times needed for one time step for the different setups are summarized in Table 2.

5 Conclusions

In this work results of large eddy simulations of the “Periodic flow over a 2D hill” for different convergence criteria and time step sizes were presented and discussed.

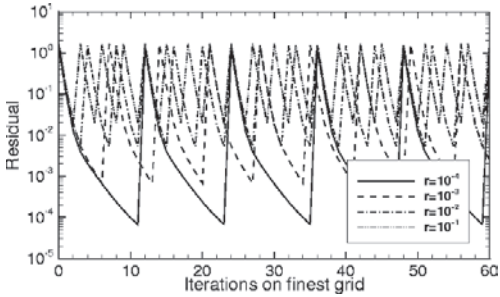

Fig. 14 Convergence behavior for different convergence criteria at a fully developed turbulent state

Table 2 Computational time per time step (2 IBM Power 5 Processors with 1.9 GHz)

Δt (CFL)	5×10^{-5}s (≈ 1)	10^{-4}s (≈ 2)	2.5×10^{-4}s (≈ 5)
Residual $r_c = 10^{-4}$	76.4 s	76.6 s	233.9 s
Residual $r_c = 10^{-3}$	44.2 s	/	/
Residual $r_c = 10^{-2}$	26.6 s	/	/
Residual $r_c = 10^{-1}$	18.5 s	/	38.4 s
1 Simple-Iteration	7.6 s	/	/

For the considered test case the differences of mean velocities and mean fluctuations are negligible for different time step sizes as well as for different convergence criteria in the considered range, except for the case with the biggest time step size and the weakest applied convergence criterion. Even the setup with only one SIMPLE-Iteration per time step gave good results.
So it can be stated that the simulations with the weaker convergence criteria are more efficient.
The case with $CFL \approx 2$ is the most efficient of the three setups with different time step sizes and the strictest convergence criterion. The simulation with the biggest time step size (corresponding $CFL \approx 5$) showed a worse convergence behavior, so that more computational time was needed to simulate a given time interval as with $CFL \approx 2$.
In summary it may be said that for this kind of flow problems (wall bounded flows) where the highest CFL numbers occur in the center of the computational domain and they are rather low close to the wall, the time step size has no influence on averaged results. Also the frequency spectra show the same behavior up to higher frequencies which means that the amount of energy contained in the subgrid scales is approximately the same. For very large time step sizes the convergence behavior gets worse so that more computational time is needed to simulate the desired time interval than with a smaller time step size. For this kind of flow this seems to be the limiting factor for the time step size. So this behavior can be utilized to adjust the time step size during the simulation in order to find the most efficient setup.

Acknowledgements

This work was supported by the DFG within the collaborative research center "Flow and Combustion in future Gas Turbine Combustion Chambers", SFB 568 and the French-German research unit 507, "LES of complex flows".

References

1. Briggs WL, Van Emden H, McCormick SF (2000) A multigrid tutorial. SIAM
2. FASTEST-Manual (2005) Department of Numerical Methods in Mechanical Engineering, Darmstadt, Germany
3. Germano M, Piomelli U, Moin P, Cabot WH (1991) A dynamic subgrid-scale eddy viscosity model. Physics of Fluids A 3(7):1760–1765
4. Jang YJ, Leschziner MA, Abe K, Temmerman L (2002) Investigation of anisotropy-resolving turbulence models by reference to highly-resolved LES data for separated flow. Flow, Turbulence and Combustion 69:161–203

Assessment of LES Quality Measures Using the Error Landscape Approach

Markus Klein[1], Johan Meyers[2], and Bernard J. Geurts[3]

[1] Institute for Energy and Powerplant Technology, Technical University of Darmstadt, Petersenstrasse 30, 64297 Darmstadt, Germany
kleinm@ekt.tu-darmstadt.de
[2] FWO – Vlaanderen (Science Foundation – Flanders); Department of Mechanical Engineering, Katholieke Universiteit Leuven Celestijnenlaan 300A, B3001 Leuven, Belgium. johan.meyers@mech.kuleuven.be
[3] Mathematical Sciences, Faculty EEMCS, University of Twente P.O. Box 217, 7500 AE Enschede, The Netherlands. b.j.geurts@utwente.nl

Abstract. A large-eddy simulation database of homogeneous isotropic decaying turbulence is used to assess four different LES quality measures that have been proposed in the literature. The Smagorinsky subgrid model was adopted and the eddy-viscosity 'parameter' C_S and the grid spacing h were varied systematically. It is shown that two methods qualitatively predict the basic features of an error landscape including an optimal refinement trajectory. These methods are based on variants of Richardson extrapolation and assume that the numerical error and the modelling error scale with a power of the mesh size. Hence they require the combination of simulations on several grids. The results illustrate that an approximate optimal refinement strategy can be constructed based on LES output only, without the need for DNS data. Comparison with the full error landscape shows the suitability of the different methods in the error assessment for homogeneous turbulence. The ratio of the estimated turbulent kinetic energy error and the 'true' turbulent kinetic energy error calculated from DNS is studied for different Smagorinsky parameters and different grid sizes. The behaviour of this quantity for decreasing mesh size gives further insight into the reliability of these methods.

Keywords: Large-eddy simulation, Quality, Assessment measures, Error landscape

1 Introduction

Due to considerable progress of the Large Eddy Simulation (LES) technique combined with a steady increase in computing power, more and more complex flow problems become computationally tractable. Nevertheless, some fundamental problems of the LES formalism remain unsolved. In particular, the application of LES demands for reliable quality assessment procedures.

J. Meyers et al. (eds.), Quality and Reliability of Large-Eddy Simulations,

Numerical and modeling errors have been extensively studied in the past [17, 8, 5, 10, 3, 11] and the investigations led to a better understanding of their interaction and their impact. Several authors attempted to define indices of quality, or error estimators in order to judge the reliability of a given LES. For an overview see, e.g. [2].

Meyers et al. [10, 13] proposed a method to assess LES using a database of pre-computed cases in order to obtain an overview of the error behaviour in the form of so-called error landscapes. In the illustration of this method DNS data of decaying homogeneous isotropic turbulence was adopted yielding a well-defined error surface as a function of grid resolution $N = 1/h$ and model parameter C_S. Though this method yields interesting insights in error-behaviour of LES, it is an *a posteriori* approach, requiring a large number of large-eddy simulations. An alternative was recently proposed by Geurts and Meyers [6] in which an optimal Smagorinsky constant was determined iteratively, at fixed resolution. This method was shown to require about 5 complete large-eddy simulations to reach an accurate estimate of the optimal Smagorinsky parameter. It was illustrated using an error-measure defined relative to DNS data.

This paper explores the possibility of substituting the calculation of the 'true' error, with an estimated simulation error. We investigate estimates in terms of LES data only, and study to what extent an independent 'self-consistent' error-control can be arrived at. The error landscape approach is subsequently used as a tool to assess the quality measures themselves.

2 Error Landscapes

The different error estimators considered in this paper are evaluated using a LES and DNS database consisting of more than 100 simulations of decaying homogeneous isotropic turbulence, recorded at two different Taylor Reynolds numbers $Re_\lambda = 50, 100$ [10]. The following grid resolutions 24^3, 32^3, 40^3, 48^3, 56^3, 64^3, 80^3, 96^3, 128^3 have been used together with 20 different settings for the Smagorinksy parameter in the range from 0.0 to 0.2840.

Meyers et al. [10, 11] consider the time integrated relative turbulent kinetic energy deviation between LES and DNS as an error measure. We propose an analogous measure, in terms of LES data. In the current study, the time-averaging is replaced by averaging over two instants in time $t = 0.5, 1.0$.

Given DNS data for the decay of the turbulent kinetic energy, an error-measure can be defined as:

$$\delta_E(N, C_s) = \left[\frac{\sum_{t=0.5,1.0} \left(E_{LES}(t, N, C_s) - E_{DNS}(t) \right)^2}{\sum_{t=0.5,1.0} E_{DNS}(t)^2} \right]^{1/2} , \qquad (1)$$

For any LES at given N and C_S this yields an impression of the relative error.

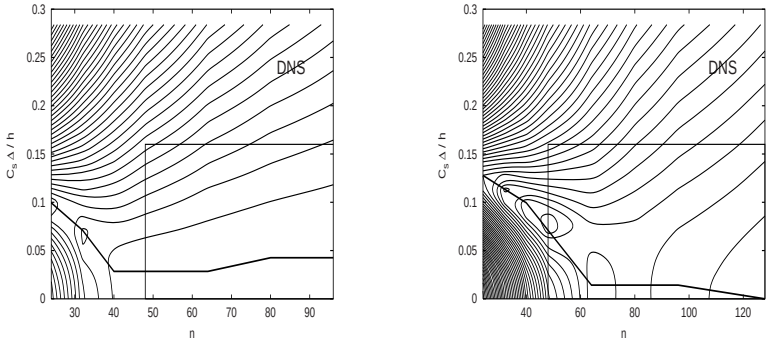

Fig. 1 Error landscapes for $\delta_E(N, C_s)$ obtained from DNS for $Re_\lambda = 50$ (*left*) and $Re_\lambda = 100$ (*right*). The bold line represents the optimal refinement strategy. The box in the figures encloses the parameter range where the error estimators have been evaluated in Section 4

Using the error estimators introduced in Section 3 the presumed deviation based on these estimators can be defined in analogy to (1). We make two alterations: first, the difference between E_{LES} and E_{DNS} is replaced by one of the error estimators introduced below, and second, we normalize the error-measure with a reference value E_{ref} that can be obtained from LES instead of the DNS data as in (1). One could for example think of replacing E_{ref} with $E_{LES}(t, N_{ref}, C_{s,ref})$ or with a value $E_{LES}(t)$ extrapolated from the finest available LES grids. Since this is a normalization, this will only affect to global level of the results, but not the shape of the estimated errors as function of N and C_s. For the purpose of illustration of the method, Equation (2) is in this work normalized with the DNS value.

These two steps can be criticized in many ways and their generality and robustness is not established, but at least the principle provides an operational error assessment that can be directly confronted with the full error-landscape procedure based on (1). In detail, we estimate:

$$D(N, C_s) = \left[\frac{\sum_{t=0.5,1.0} E_{est}(t, N, C_s)^2}{\sum_{t=0.5,1.0} E_{ref}(t, N, C_s)^2} \right]^{1/2} \tag{2}$$

Based on these definitions simulation errors can be shown in the form of so called error landscapes [10, 11] and an optimal refinement strategy can be identified as the Smagorinsky coefficient $\widehat{C}_s(N)$ for which the error $\delta_E(N, C_s)$ or $D(N, C_s)$ is minimal. As an example Fig. 1 shows the error landscapes for $\delta_E(N, C_s)$ for $Re_\lambda = 50$ (left) and $Re_\lambda = 100$ (right) together with the optimal refinement strategy (bold line).

3 LES Quality Measures

Roache [15] gives the following taxonomy for obtaining information for error estimates in the context of RANS simulations. These also apply to LES and are summarized as follows:

1. Additional solutions of the governing equations on other grids
   Grid refinement/coarsening/other unrelated grids
2. Additional solutions of governing equations on the same grid
   Higher/lower order accuracy solutions
3. Auxiliary PDE solutions on the same grid
   Solution of an error equation
4. Auxiliary algebraic evaluations on the same grid; surrogate estimators
   Non conservation of higher order moments (e.g. turbulent kinetic energy), methods developed for grid adaption, convergence of higher order quadratures (e.g. evaluation of a drag coefficient) etc.

This paper focuses on methods which can be applied to the decaying homogeneous isotropic turbulence database established in [10, 13]. We will not consider methods belonging to category 2 or 3. Instead, we focus on four error estimators from category 1 and 4. We restrict ourselves to estimating the turbulent kinetic energy error $E_{DNS} - E_{LES}$ following [2, 1, 4, 7]. It is important to remark that this is a difference between the kinetic energy in the unfiltered reference DNS and the LES. By formally defining a LES filter (denoted here with an overline), $E_{DNS} - E_{LES}$ may be further split into $E_{sgs} = E_{DNS} - E_{\overline{DNS}}$ and $E_{\overline{DNS}} - E_{LES}$ (where $E_{\overline{DNS}}$ is the energy in the filtered DNS). It is the latter difference that is usually defined as the LES simulation error on the kinetic energy [3, 10, 17]. However, for the Smagorinsky model (and many other models), the LES filter is not explicitly defined in the computational method, and implicitly related to the computational mesh at best. Hence, in practice the formal LES filter remains a mathematical abstraction, which makes a precise definition of $E_{DNS} - E_{\overline{DNS}}$ ambiguous.

Therefore, the error estimation methods in [2, 1, 4, 7] follow a more pragmatic approach, i.e. they lump E_{sgs} and $E_{\overline{DNS}} - E_{LES}$ together, trying to estimate the combined term. This may be supported by two empirical observations. First of all, in order to guarantee a good LES prediction, a sufficient amount of energy should be resolved on the computational mesh (e.g., Celik et al. [1] suggest at least 80%). Hence, E_{sgs} should remain small, and may be included in an error estimation. Secondly, for the Smagorinsky model, it was observed that differences in the formal LES filter definition in the calculation of $E_{\overline{DNS}} - E_{LES}$ (including a 'no-filter' case) did not lead to appreciable differences in the overal shape of the error-landscape, and only the absolute levels of the error shifted [10]. Obviously, this observation should be handled with care when other subgrid-scale models are considered.

In the current study, two methods estimate $E_{DNS} - E_{LES}$ based on the turbulent viscosity ν_t obtained during the simulation and hence do not account

for numerical errors unless ν_t is modififed for this purpose. The other two methods use information from additional simulations in order to calculate the error estimate based on variants of Richardson extrapolation.

Similar to the subgrid activity parameter $\langle\epsilon_t\rangle/(\langle\epsilon_t\rangle + \langle\epsilon_\mu\rangle)$ introduced by Geurts and Fröhlich [5], the E_{LESIQ_ν} relates the turbulent viscosity to the laminar viscosity using the following expression (Celik et al. [1]):

$$LESIQ_\nu = \frac{1}{1 + 0.05\left(\frac{\langle\nu+\nu_t\rangle}{\nu}\right)^{0.53}} \tag{3}$$

The LESIQ_ν is a dimensionless number between zero and one. The constants are calibrated in such a way that the index behaves similar to the ratio of resolved to total turbulent kinetic energy, i.e. $\mathrm{E}^{LES}/\mathrm{E}^{DNS}$. An index of quality greater than 0.8 is considered a good LES, 0.95 and higher is considered as DNS [1]. To make it comparable to the other error measures given below, a modified expression (4) is used in this work:

$$E^{est}_{LESIQ_\nu} = \left[1 - \frac{1}{1 + 0.05\left(\frac{\langle\nu+\nu_t\rangle}{\nu}\right)^{0.53}}\right] \cdot E_{DNS} \tag{4}$$

Another frequently used approach for evaluating the subgrid-scale turbulent kinetic energy based on the turbulent viscosity and the filter width Δ is due to Lilly [9],

$$E^{est}_{Lilly} = \nu_t^2 \Big/ (c\Delta)^2, \quad c = 0.094 \tag{5}$$

The LES Index of quality E_{LESIQ} proposed by Celik et al. [1] is based on Richardson extrapolation assuming that the scaling exponents m, n for modelling and numerical error are known and coincide.

$$E^{est}_{LESIQ} = \frac{|E_2 - E_1|}{1 - \beta^n} \tag{6}$$

Two simulations have to be performed on computational grids with grid spacing h resp. βh. The LES turbulent kinetic energy on these two grids is denoted E_1 and E_2.

The evaluation of the error using the sytemactic grid and model variation E_{SGMV} approach [7, 4] is based on three simulations. One standard LES solution, a second LES on a different grid and a third LES using a modified model parameter. It is assumed that the numerical error and the modelling error scale with the mesh size h like $c_n h^n$ resp. $c_m h^m$. The subgrid scale turbulent kinetic engergy is than estimated as:

$$E^{est}_{SGMV} = \left|\frac{(E_3 - E_1)}{(1-\alpha)}\right| + \left|\frac{(E_2 - E_1) - (E_3 - E_1)\frac{(1-\beta^m)}{(1-\alpha)}}{1 - \beta^n}\right| \tag{7}$$

Here E_1 is the standard LES solution, E_2 the coarse grid LES solution and E_3 the LES solution on the standard LES grid, but with a modified model parameter, i.e., $C^2_{S,3} = \alpha\, C^2_{S,1}$. Especially for higher Reynolds number flows $\alpha > 1$ is suggested in order to avoid numerical stability problems. The 1D grid coarsening factor is again denoted by β. Since the method is designed for practical applications grid coarsening is proposed. A value of beta too close to one is not recommended in the context of Richardson extrapolation [15], a value higher than 2 is not of much interest. Throughout, we adopt $\alpha = 4$ and $\beta = 2$. The scaling exponent of the numerical error has been set to $n = 2$. This is based on the fact that a fully second order numerical scheme was used to generate the DNS database. The scaling for the modeling error was set to $m = 2/3$ which is identical to the theoretical prediction [16, 14]. For more details see [2, 4] and the references therein.

4 Assessment of LES Quality Measures

In this section we combine the error landscape approach with the error estimators introduced above, in order to assess their quality and reliability. The SGMV method requires three simulations in order to evaluate the estimated error. In view of the enormous amount of possible combinations to select three LES runs from the database presented in Section 2 the following choice has been made: *(i)* only grid coarsening by a factor of two is considered. *(ii)* for the model variation the model parameter is increased by a factor of four. In case the database did not contain an exact factor four increase, a deviation of up to 25% was allowed. This implies that the estimated error is only available for grid resolution 48^3 or higher. Based on these two criteria all possible combinations of three simulations have been choosen from the database to estimate the simulation error for the SGMV method. The same cases were used for the other error estimators. This serves as the basis for the comparison. It is important to note that the systematic grid and model variation as well as the LESIQ can also be used for values of β less than two. Alternatively also grid refinement, i.e. $\beta < 1$ would be possible. Another option would be to perform the LES simulation with the modified model parameter on the coarse grid instead of the fine grid and certainly the value of α could be changed as well. The presentation of all these variations is however beyond the scope of this work and left for future discussions.

In the remainder of this section we assess the four error estimators using the following guidelines:

- An optimal refinement trajectory can be approximated
- The ratio of estimated and true error $D(N, C_s)/\delta_E(N, C_s)$ should be as close as possible to unity, or in general a constant value, depending on the

reference E_{ref} which is employed. As a minimum requirement this is at least expected for small mesh sizes.
- Overestimation of error, i.e. conservatism, is preferred over underestimation of error.

4.1 Approximative Error Landscapes

Figures 2 and 3 show the error landscapes for $D(N, C_s)$ calculated from the estimators given in (4), (5), (6), (7) for $Re_\lambda = 50$ resp. $Re_\lambda = 100$. We compare these with the error landscape for $\delta_E(N, C_s)$ obtained by using a DNS as point of reference, see Fig. 1. The true error landscapes in Fig. 1 defined relative to DNS data include a window indicating the parameter range in which the error-estimators have been assessed. Note that the horizontal and vertical scales differ. It can be observed that the systematic grid and model variation (SGMV) and the LES index of quality (LESIQ) are able to capture some characteristics of the actual error landscape obtained via DNS. Particularly these two error estimators are capable to predict an optimal refinement strategy as defined in [10]. This is in contrast to E_{LESIQ_ν} and E_{Lilly} which are based on

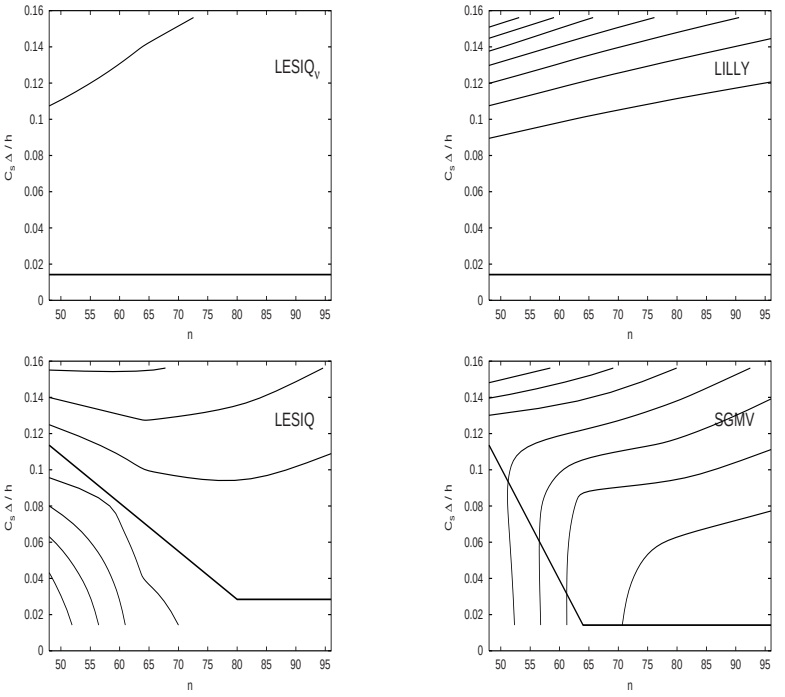

Fig. 2 Error landscapes for $D(N, C_s)$ calculated from 4 different error estimators for $Re_\lambda = 50$. The bold line represents the optimal refinement strategy

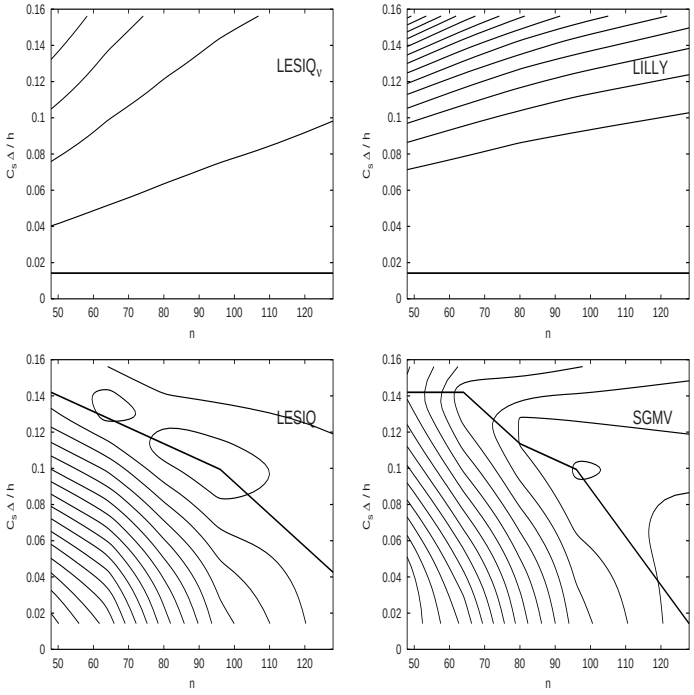

Fig. 3 Error landscapes for $D(N, C_s)$ calculated from 4 different error estimators for $Re_\lambda = 100$. The bold line represents the optimal refinement strategy

a single grid calculation. Here the predicted error basically decreases with the model parameter, hence the optimal model parameter would be zero.

4.2 Convergence of Error Estimators

In addition to the error landscapes it is interesting to investigate the magnitude of $D(N, C_s)$ to $\delta_E(N, C_s)$. Ideally the ratio of both quantities should be as close as possible to one. Due to the fact that the assumption of an assymptotic convergence behavior might not always be fullfilled, larger deviations are expected on coarser grids. However as a minimum requirement $D(N, C_s)/\delta_E(N, C_s)$ should approach unity for decreasing mesh size. Figures 4 and 5 show, for different but fixed model parameters, the ratio of the estimated error and true error $D(N, C_s)/\delta_E(N, C_s)$ for the four different approaches and the two Reynolds numbers. Note the double logarithmic plot.

The following observations can be made:

- $LESIQ_\nu$ diverges from unity for decreasing mesh size, i.e. the error estimate gets worse on finer grids.

- Lilly's approach underpredicts the error considerably. This is consistent with the findings in [7]. For a constant Smagorinsky parameter the estimated error does not converge towards the true error for decreasing mesh size.
- *LESIQ* and *SGMV* converge towards the true error for decreasing mesh size. Bigger discrepancies arise especially from unrealistic low model parameters. Note that the dash-dotted lines correspond to $C_s < 1.0$.
- The *LESIQ* has a tendency to underpredict the error at coarse mesh sizes.
- The SGMV shows a more conservative error estimation behaviour. This is due to the fact that modelling and numerical error are treated separately and that the estimated error is the sum of their absolute values.
- The database consists of many simulations using rahter unphysical model parameters. For $C_s = 0.156$, a value close to the theoretical expecations for isotropic decaying turbulence, especially Lilly's approach and the SGMV show a good performace with $0.5 \leq D(N, C_s)/\delta_E(N, C_s) \leq 2.0$.

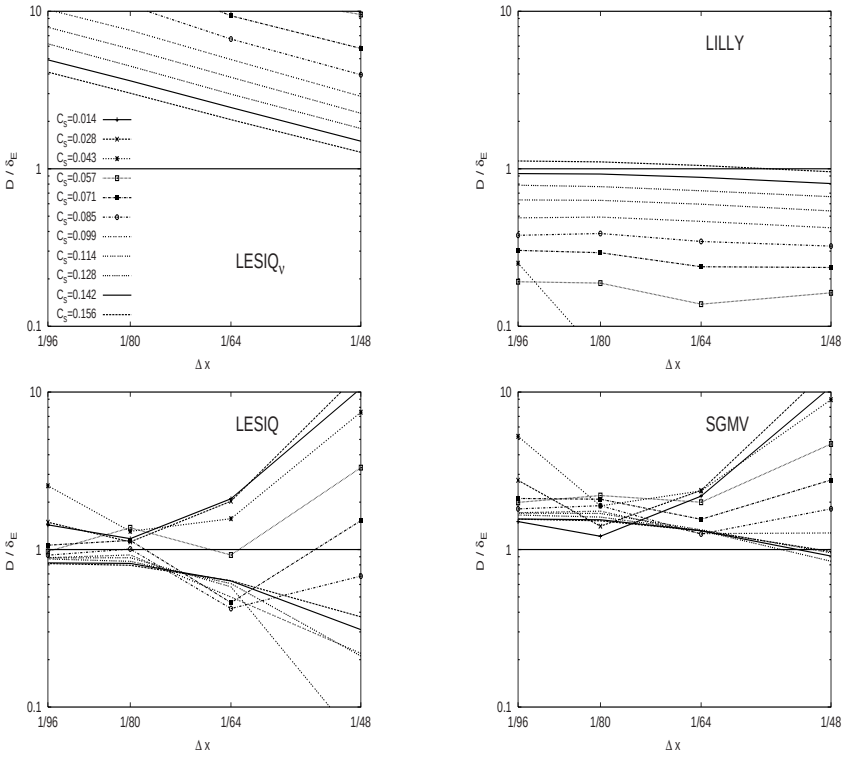

Fig. 4 Estimated error divided by true error plotted against grid resolution for different Smagorinsky parameters at $Re_\lambda = 50$

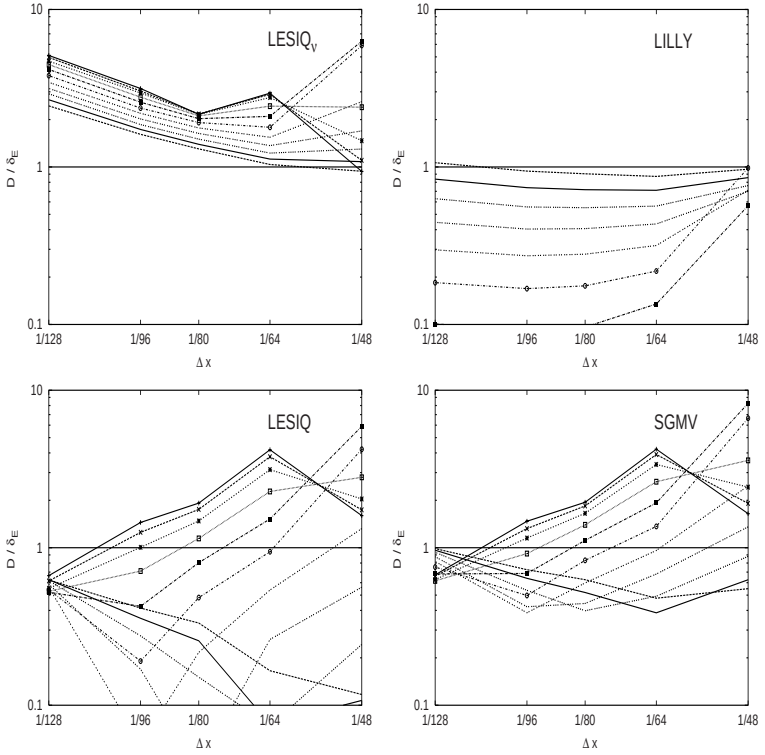

Fig. 5 Estimated error divided by true error plotted against grid resolution for different Smagorinsky parameters at $Re_\lambda = 100$ (see legend in Fig. 4)

5 Conclusion

A large-eddy simulation database of homogeneous isotropic decaying turbulence has been used to assess the following LES quality measures ranging from single grid to three simulation studies: The LESIQ$_\nu$, Lilly's approach to estimate the subgrid scale turbulent kinetic energy, the LES index of quality based on Richardson extrapolation and the systematic grid and model variation (SGMV). The results suggest that only by performing additional simulations on different grids the basic features of an an error landscape, including an optimal refinement trajectory, can be captured. Among these two methods, i.e. LESIQ and SGMV, the systematic grid and model variation provides for the configuration under consideration a more conservative error estimate.

The extension of the present work to different spatial discretization schemes [12] as well as the consideration of other flow propeties as error measures [13]

is part of the work in progress. The application of the systematic grid and model variation and the LESIQ to more complex flow configurations has been discussed in the literature, see [2] for an overview.

Acknowledgments

Financial support by the DFG (German Research Council) SFB568 is gratefully acknowledged.

References

1. Celik IB, Cehreli ZN, Yavuz I (2005) Index of resolution quality for large eddy simulations. ASME Journal of Fluids Engineering 127:949–958
2. Celik I, Klein M, Freitag M, Janicka J (2006) Assessment measures for URANS/DES/LES: an overview with applications. Journal of Turbulence 7, Art no N48
3. Chow FK, Moin P (2003) A further study of numerical errors in large-eddy simulations. Journal of Computational Physics 184:366–380
4. Freitag M, Klein M (2006) An improved method to assess the quality of large eddy simulations in the context of implicit filtering. Journal of Turbulence 7, Art no N40
5. Geurts BJ, Fröhlich J (2002) A framework for predicting accuracy limitations in large eddy simulations. Physics of Fluids 14(6):L41–L44
6. Geurts BJ, Meyers J (2006) Successive inverse polynomial interpolation to optimize Smagorinsky's model for large-eddy simulation of homogeneous turbulence. Physics of Fluids 18, Art no 118102
7. Klein M (2005) An attempt to assess the quality of large eddy simulations in the context of implicit filtering. Flow Turbulence and Combustion 75:131–147
8. Kravchenko AG, Moin P (1997) On the effect of numerical errors in large eddy simulation of turbulent flows. Journal of Computational Physics 131:310–322
9. Lilly DK (1967) The representation of small scale turbulence in mumerical simulation experiments. In: Proceedings of the IBM Scientific Computing Symposium on Environmental Sciences:195–210
10. Meyers J, Geurts BJ, Baelmans M (2003) Database analysis of errors in large-eddy simulation. Physics of Fluids 15(9):2740–2755
11. Meyers J, Geurts BJ, Baelmans M (2005) Optimality of the dynamic procedure for large-eddy simulations. Physics of Fluids 17, Art no 045108
12. Meyers J, Geurts BJ, Sagaut P (2007) A computational error assessment of central finite volume discretizations in large-eddy simulation using a Smagorinsky model. Journal of Computational Physics 227:156–173
13. Meyers J, Sagaut P, Geurts BJ (2006) Optimal model parameters for multi-objective large-eddy simulations. Physics of Fluids 18, Art no 095103
14. Pope SB (2000) Turbulent Flows. Cambridge Universtiy Press
15. Roache PJ (1998) Verification and Validation in Computational Science and Engineering. Hermosa Publishers, Albuquerque

16. Sagaut P (1998) Large Eddy Simulation for Incompressible Flows. Springer, Berlin
17. Vreman B, Geurts B, Kuerten H (1996) Comparison of numerical schemes in large-eddy simulation of the temporal mixing layer. International Journal for Numerical Methods in Fluids 22:297–311

Analysis of Numerical Error Reduction in Explicitly Filtered LES Using Two-Point Turbulence Closure

Julien Berland[1], Christophe Bogey[2], and Christophe Bailly[2]

[1] SINUMEF, ENSAM, 151 boulevard de l'Hôpital, 75013 Paris, France
julien.berland@paris.ensam.fr
[2] LMFA, ECL, 36 avenue Guy de Collongue, 69134 Ecully, France
christophe.bogey@ec-lyon.fr, christophe.bailly@ec-lyon.fr

Abstract. Numerical errors in large-eddy simulation (LES) are investigated using the eddy-damped quasi-normal Markovian (EDQNM) modeling approach, for finite differences of order 2 to 14, and for optimized differentiation schemes. An EDQNM-LES model is derived to evaluate numerical errors, namely the aliasing and the differentiation errors. The results show that the aliasing errors are negligible whereas the interactions between wavenumbers close to the mesh cut-off wavenumber are responsible for a major part of the differentiation errors. In addition, the accuracy of a LES calculation is seen to be improved when explicit filtering of the higher part of the turbulence spectrum is introduced.

Keywords: Large-eddy simulation, EDQNM, Approximate differentiation, Order of accuracy

1 Introduction

Numerical solution of turbulent flow problems can be accomplished using various levels of approximation. In Large-Eddy Simulations (LES), only the larger scales are solved while the smaller ones are taken into account through a SubGrid-Scale (SGS) model [1]. Since the early works of Smagorinsky [2] numerous SGS models have been proposed with the aim of describing the behavior of unresolved scales based on the knowledge of the resolved velocity field. One may for instance refer to the review of Lesieur & Métais [3] for an overview of LES techniques for incompressible flows.

A large variety of SGS modeling procedures have been derived based on physical assumptions applying to the filtered Navier-Stokes equations, and reference to the discretization methods is seldom made. LES performed with explicit models for the residual motions and assuming negligible numerical errors are referred to as *pure physical LES* by Pope [4]. Numerical accuracy in the framework of LES is however a delicate issue.

J. Meyers et al. (eds.), Quality and Reliability of Large-Eddy Simulations,

The investigation of numerical errors in LES requires the design of accuracy estimators which encompass the numerical procedures and the physical model (the filtered Navier-Stokes equations). A first extensive theoretical framework allowing quantitative evaluation of numerical errors in LES has been proposed by Ghosal [5] and has been referred to as *static error analysis* later on by Park & Mahesh [6]. The static error analysis provides a formal model in the spectral space of the numerical implementation of a LES. The numerical errors are then defined by evaluating the deviation of the numerical system from the exact model, and the error is computed assuming a Gaussian state for the velocity field. Two major sources of errors, approximate differentiation and aliasing, have been identified by Ghosal [5]. The static error analysis shows that second-order discretization schemes introduce errors with magnitude larger than the subgrid-scale terms. A filter with a filter-width-to-mesh-size ratio of 8 then needs to be implemented to remove poorly resolved scales. Ghosal's study shows in addition that for eight-order schemes a filter width twice as large as the grid spacing is enough to ensure numerical accuracy. High-order algorithms hence turn out to be more appropriate.

Even if the static error analysis provides insightful details on numerical errors in LES, the method does not fully reproduce the variety of phenomenon involved in simulations. In particular, as pointed out by Park & Mahesh [6], the dynamical interactions cannot be taken into account with a static approach. The *dynamic error analysis* can nevertheless be performed by applying the Eddy-Damped Quasi-Normal Markovian (EDQNM) set of hypothesis to the LES approach in order to design a so-called "EDQNM-LES" model [6]. This theoretical framework permits to compute the time evolution of the kinetic energy spectrum obtained by a LES, which includes the numerical methods, for incompressible homogeneous isotropic turbulence. For instance, Park & Mahesh [6] makes use of the EDQNM-LES approach to study numerical errors in LES.

The present work is an attempt to study the influence of the order of accuracy of discretization algorithms on numerical error magnitudes within LES. Following similar developments to those proposed by Park & Mahesh [6], an EDQNM-LES model is derived to evaluate the time evolution of kinetic energy spectra obtained from LES performed with numerical differentiation methods of various order of accuracy (from 2nd order to 14th order), and with optimized finite difference schemes [7]. The numerical errors in LES are considered for a turbulent field at Reynolds number Re_λ equal to 2500 based on the Taylor scale. The classical EDQNM theory, referred to as "EDQNM-DNS", is first employed to determine reference kinetic energy spectra. The numerical errors are then defined and computed by comparing the EDQNM-LES spectra to the EDQNM-DNS spectra. The EDQNM-DNS and EDQNM-LES models are presented in Section 2 along with the definitions of the numerical errors. The reference solutions and the results of the EDQNM-LES calculations are shown in Section 3. Concluding remarks are finally drawn in Section 4.

2 Two-Point Stochastic Closure for Numerical Error Analysis of LES

2.1 EDQNM-DNS Model

Using the Eddy-Damped Quasi-Normal Markovian (EDQNM) modeling approach, the time evolution of the kinetic energy spectrum $E(k)$ at a wavenumber k, for a freely decaying homogeneous isotropic incompressible turbulent field, can be written as

$$\left(\frac{\partial}{\partial t} + 2\nu k^2\right) E(k) = T(k), \tag{1}$$

where time dependence of the spectrum is implicit and ν stands for the viscosity. The energy energy transfers due to triadic interactions are represented by $T(k)$. The derivation of Equation (1) and the explicit formulation of $T(k)$ are not given here but can be found in Lesieur [8] for instance.

2.2 EDQNM-LES Model

Consider the large-eddy simulation of a freely decaying homogeneous isotropic turbulence with a cut-off wavenumber k_c. The derivation of the EDQNM-DNS model describing the numerical implementation of an LES has been carried analytically by Park & Mahesh [6]. The time evolution of the truncated kinetic energy spectrum $E^\bullet$ ($E^\bullet(k) = 0$ for $k > k_c$) of the LES velocity field is given by

$$\left(\frac{\partial}{\partial t} + 2\nu_t k^2 + 2\nu\chi_k^2 k^2\right) E^\bullet(k) = T_{\mathrm{nl}}(k) + T_{\mathrm{al}}(k), \tag{2}$$

where $T_{\mathrm{nl}}(k)$ corresponds to the energy transfers due to triadic interactions between resolved scales and $T_{\mathrm{al}}(k)$ takes into account aliasing effects occurring when nonlinear terms are discretized [6]. An eddy-viscosity based subgrid-scale model is introduced by imposing a non-zero turbulent viscosity $\nu_t(k)$, which can be defined in the spectral space. The approximate differentiation is characterized by the isotropic ratio χ_k between the norm of the modified wavenumber and the exact wavenumber, with,

$$\chi_k = \frac{1}{4\pi} \int_{\theta\in[0,2\pi]} \int_{\varphi\in[0,\pi]} \frac{\widetilde{k}_\alpha}{k_\alpha} \sin\varphi \, d\varphi d\theta, \tag{3}$$

where k_α is an arbitrary component of $\mathbf{k}$. For instance, for $\alpha = 1$, we have $k_\alpha = k \sin\varphi \cos\theta$.

2.3 Numerical Error Assessment

Numerical Error Definitions

Consider the EDQNM-DNS model. Following a subgrid-scale modeling point of view, a truncation at the wavenumber k_c is introduced into Equation (1):

$$\left(\frac{\partial}{\partial t} + 2\nu k^2\right) E(k) = T^{<}(k|k_c) + T^{>}(k|k_c) \tag{4}$$

where it is assumed that $k < k_c$. The contribution $T^{<}(k|k_c)$ from the resolved scales corresponds to the triadic interactions (k, p, q) such as p and q are lower than k_c. The non-resolved transfers $T^{>}(k|k_c)$ take into account the nonlinear couplings between triads (k, p, q) with p or q greater than the cut-off wavenumber k_c. The subgrid-scale contribution is hence provided by $T^{>}(k|k_c)$ [9].

The numerical errors are defined by comparing the EDQNM-LES model (4) to the EDQNM-DNS formulation (1). Assuming that the LES provides the exact kinetic energy spectrum (i.e. $E^{\bullet}(k) = E(k)$ for $k < k_c$), the difference (1)–(4) between the two governing equations should remain equal to zero, so that

$$\underbrace{T_{\mathrm{nl}}(k) - T^{<}(k|k_c) - 2\nu k^2 \left[E(k) - \chi_k^2 E^{\bullet}(k)\right]}_{\text{differentiation}} + \underbrace{T_{\mathrm{al}}(k)}_{\text{aliasing}} + \underbrace{2\nu_t k^2 E^{\bullet}(k) - T^{>}(k|k_c)}_{\text{s.g.s.}} = 0 \tag{5}$$

Numerical errors can be estimated by the magnitudes of the above terms. The following quantities are then introduced

$$\mathcal{E}_{\mathrm{fd}}(k) = \left|T_{\mathrm{nl}}(k) - T^{<}(k|k_c)\right| + \left|2\nu k^2 \left[E(k) - \chi_k^2 E^{\bullet}(k)\right]\right| \tag{6}$$

$$\mathcal{E}_{\mathrm{al}}(k) = \left|T_{\mathrm{al}}(k)\right| \tag{7}$$

$$\mathcal{M}_{\mathrm{sgs}}(k) = \left|T^{>}(k|k_c)\right|. \tag{8}$$

The differentiation error $\mathcal{E}_{\mathrm{fd}}(k)$ evaluates the inaccuracies due to the approximate differentiation algorithms since it compares in particular the difference between the approximate evaluation of the triadic interactions within the mesh and the exact energy transfers $T^{<}(k|k_c)$ due to the resolved scales. The aliasing errors $\mathcal{E}_{\mathrm{al}}(k)$ provides the magnitude of the aliasing effects. Finally, the amplitude $\mathcal{M}_{\mathrm{sgs}}(k)$ of the subgrid scales contribution deduced from the EDQNM-DNS is employed in this work as an acceptable upper-bound for the numerical errors [5].

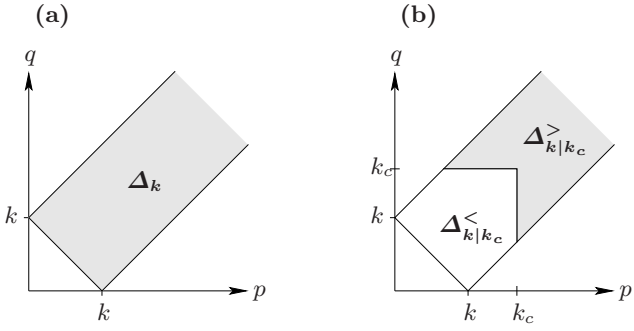

Fig. 1 Sketch in the (p, q)-plane of the integration domains used to compute the nonlinear transfers for the EDQNM calculation. **(a)** Full domain, and **(b)** separation into a resolved and a non-resolved domain given a cut-off wavenumber k_c

Detailed Scale Contribution to the Errors

If we consider the error definitions, it is interesting to assess which scales are mainly responsible for the numerical errors. Let $\mathcal{E}(k)$ be the spectrum of a numerical error. One may show that $\mathcal{E}(k)$ can be written as

$$\mathcal{E}(k) = \iint_{\Delta_k} s(k, p, q)\, dpdq, \tag{9}$$

where $s(k, p, q)$ is the integrand and the integration domain Δ_k, shown in Fig. 1.a, is such as

$$\Delta_k = \Big\{(p, q) \mid k + q \geq p \geq |k - q|\Big\} = \Big\{(p, q) \mid |z| \leq 1\Big\}. \tag{10}$$

While calculating $\mathcal{E}(k)$, one may restrict the domain of integration to scales smaller than a given wavenumber k'. This can be done by replacing the quadrature domain Δ_k in (9) by $\Delta^{<}_{k|k'}$, represented in Fig. 1.b, so that a new quantity $\mathcal{E}^*(k, k')$ is obtained, with

$$\mathcal{E}^*(k, k') = \iint_{\Delta^{<}_{k|k'}} s(k, p, q)\, dpdq \tag{11}$$

Taking the derivative with respect to k' then yields

$$\zeta(k, k') = \frac{\partial}{\partial k'} \left[\mathcal{E}^*(k, k')\right] \tag{12}$$

This quantity $\zeta(k, k')$, referred to as the detailed scale contribution, estimates the net effect on the error $\mathcal{E}(k)$ when scales with wavenumbers between k' and $k' + dk'$ are taken into account in the integral (9).

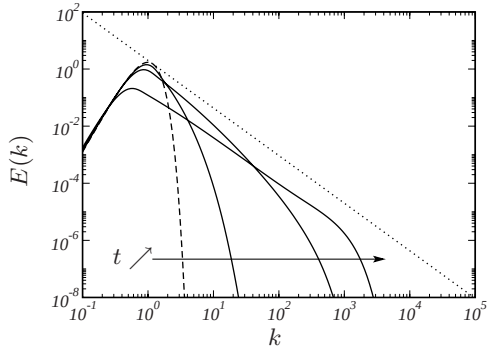

Fig. 2 Time evolution of the kinetic energy spectrum $E(k)$ provided by the EDQNM calculation, as a function of the wavenumber k, for $\mathrm{Re}_\lambda = 2500$. $-\ -\ -$, $E(k, t^* = 0)$; ———, $E(k, t^*)$ for $t^* = 1,\ 2,\ 8$; $\cdot\cdot\cdot\cdot\cdot\cdot\cdot$, $E(k) \propto k^{-5/3}$

3 Results

3.1 Reference Solution (EDQNM-DNS)

The EDQNM calculation has been performed with Reynolds number Re_λ equal to 2500. The dimensionless time $t^* = k_0 v_0 t$ is introduced with $k_0 = 1$ and $v_0 = 1$, which represent typical values of the wavenumber and of the velocity of the energy containing scales. An EDNQM-DNS calculation has been carried out up to $t^* = 20$. The results are evaluated at $t^* = 8$, once the decay of the kinetic energy spectrum has become self-similar. This evolution is illustrated in Fig. 2 where the kinetic energy spectra obtained for $Re_\lambda = 2500$ at t^* equal 0, 1, 2 and 8 are plotted against the wavenumber k. Starting at $t^* = 0$ from an energy distribution mainly clustered on small wavenumbers, the kinetic energy spectral density $E(k)$ then progressively converges towards a turbulent spectrum with a well defined inertial range lying up to the dissipative scales.

3.2 EDQNM-LES

Run Parameters

The EDQNM-LES calculations are performed using the parameters of the EDQNM-DNS. A turbulent field at Reynolds numbers 2500 is considered with a cut-off wavenumber k_c equal to 32. Approximate derivatives are carried out by standard finite differences of order ranging from 2 to 14. To avoid any discussion about numerical errors during the transient evolution of the spectrum, the EDQNM-LES computations are initialized at $t^* = 8$ with the spectra deduced from the EDQNM-DNS, truncated truncated at the cut-off wavenumber k_c.

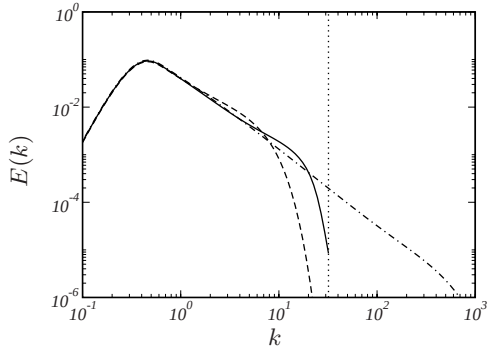

Fig. 3 Evolved kinetic energy spectra at $t^* = 16$ provided by the EDQNM-LES calculations for $\mathrm{Re}_\lambda = 2500$ and $k_c = 32$, for 2nd order and 10th order approximate derivatives, with spectral eddy-viscosity. $- \; - \; -$, 2nd order approximate differentiation; ————, 10th order approximate differentiation; $- \cdot - \cdot -$, EDQNM-DNS reference solution. (The dotted line stands for the LES cut-off wavenumber.)

Evolved Spectra

Approximate differentiation operators unfortunately introduce numerical errors. This trend is illustrated in Fig. 3 where the evolved kinetic energy spectra obtained with the EDQNM-LES model (2) and with the spectral eddy-viscosity of Chollet [10] are plotted at $t^* = 16$ and for $Re_\lambda = 2500$ and $k_c = 32$. The results obtained for the 2nd and 10th order finite differences are presented as well as the reference spectrum of the EDQNM-DNS calculation. Discrepancies between the EDQNM-LES spectra and the reference spectra are clearly visible for both order of accuracy. The wavenumbers close to the mesh cut-off wavenumber are particularly poorly resolved with strong underestimations of the kinetic energy.

3.3 Differentiation Errors

As already pointed out by Park & Mahesh [6], the investigation the present results show that the aliasing effects have a weak influence on the solution quality. The study will therefore focus on the differentiation errors.

Order of Accuracy

Consider first Fig. 4 where the differentiation error $\mathcal{E}_{\mathrm{fd}}(k)$ is plotted against the normalized wavenumber k/k_c for approximate derivatives of order 2, 6, 10 and 14. The results are calculated at the beginning of the calculation ($t^* = 8$) with $Re_\lambda = 2500$ and $k_c = 32$. The modulus of the subgrid-scale contribution $|T^>(k|k_c)|$ is also represented and used as an acceptable upper bound for the

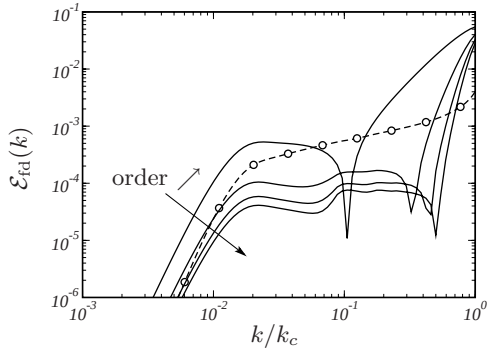

Fig. 4 Differentiation error $\mathcal{E}_{\rm fd}(k)$ as a function of the wavenumber k/k_c for $Re_\lambda = 2500$ and for $k_c = 32$, at $t^* = 8$. Approximate differentiations of order 2, 6, 10 and 14. ———, $\mathcal{E}_{\rm fd}(k)$; $-$ $-\circ$ $-$, magnitude of the subgrid scale contribution $|T^>(k|k_c)|$

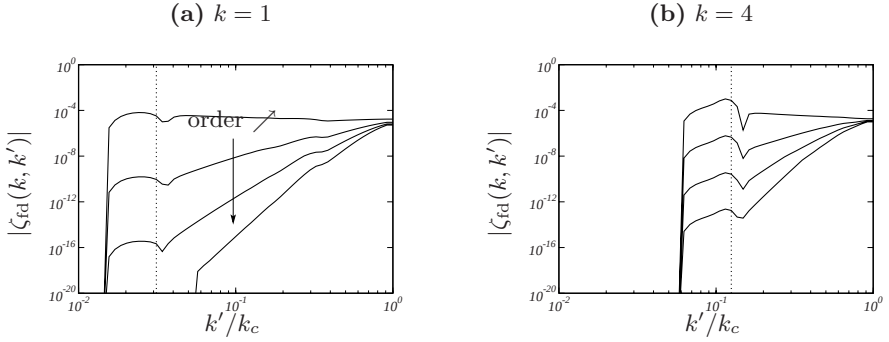

Fig. 5 Detailed scale contribution $|\zeta_{\rm fd}(k,k')|$ to the differentiation errors $\mathcal{E}_{\rm fd}(k)$ as a function of the wavenumber k/k_c for $Re_\lambda = 2500$ and $k_c = 32$, and for various reference wavenumbers k, at $t^* = 8$. Approximate differentiations of order 2, 6, 10 and 14. ———, $|\zeta_{\rm fd}(k,k')|$. Reference wavenumers: **(a)**, $k = 1$; **(b)**, $k = 4$. The dotted line indicates where the reference wavenumber is located on the axis k'/k_c

numerical errors. The error curves exhibit similar shapes with large amplitudes close to the grid cut-off wavenumber, a plateau approximately centered on $k/k_c = 10^{-1}$ and a decrease in k^5 as the wavenumber tends to zero.

One may furthermore observe that increasing the order of accuracy of the discretization tool reduces the numerical errors. The 2nd order scheme indeed yields large differentiation errors, larger than the subgrid-scale energy transfer for most of the wavenumbers supported by the mesh, whereas for higher order schemes the differentiation errors are lower than the reference amplitude $|T^>(k|k_c)|$ is widened. Using a 14th order algorithms for instance,

the numerical errors are negligible for all wavenumbers except those close to the mesh cut-off wavenumber.

It should be noted that increasing the order of accuracy mainly acts on LES accuracy at high wavenumbers. Figure 4 indeed shows that when the formal order is increased the k^5 slope as $k \to 0$ and the plateau level are weakly modified whereas the wavenumber range where differentiation errors are large is severely narrowed. This trend is interesting since one could have expected that the formal order is related to the accuracy at the larger scales.

The relationships between numerical errors and the properties of the approximate differentiation can be interpreted by studying the detailed scale contribution to the numerical errors. The detailed scale contribution $\zeta_{\mathrm{fd}}(k, k')$ to the differentiation error $\mathcal{E}_{\mathrm{fd}}(k)$ is plotted as a function of k'/k_c in Fig. 5(a), (b) for respectively $k = 1$ and $k = 4$. Results are evaluated at $t^* = 8$, for $Re_\lambda = 2500$ and $k_c = 32$, and algorithms of order 2, 6, 10 and 14 are considered. For $k = 1$ and for the 2nd order scheme, the detailed scale contribution shows a maximum in the neighbourhood of $k' = k$, corresponding on the plot to $k'/k_c \simeq 0.03$. The contribution $\zeta_{\mathrm{fd}}(k, k')$ is then seen to slowly decrease when k' tends to the grid cut-off wavenumber k_c. A large range of wavenumbers therefore contributes to the error. When the formal order of the differentiation algorithm is increased, a significant decrease of the contribution from the larger scales is observed. At $k'/k_c \simeq 0.03$, there is for instance about six orders of magnitude between the contribution obtained with the 2nd and with the 6th order schemes. On the other hand, the contributions from the scales close to the mesh cut-off wavenumber appear to be weakly influenced by the order of accuracy. In the neighbourhood of $k' = k_c$, the amplitude of $\zeta_{\mathrm{fd}}(k, k')$ is indeed similar for all the algorithms. This dominant role played by high wavenumbers in the differentiation errors could be explained by the large difference between the exact and the approximate differentiations close to the mesh cut-off wavenumber. Indeed, even though long range interactions between the reference wavenumber $k = 1$ and the wavelengths $k' \sim k_c$ close to the cut-off wavenumber are likely to involve few transfers of energy, the inability of the algorithms to accurately resolve the smaller wavenumber still produces significant numerical errors. It should be noted that according to Fig. 5.(a), small-scale contributions dominate the numerical errors for schemes with order equal or higher than 4.

The same conclusions hold for $k = 4$ in Fig. 5.(b). The contributions from the larger scales ($k'/k_c \sim 0.1$) are seen to decrease with the order of accuracy whereas $\zeta_{\mathrm{fd}}(k, k')$ exhibits non-negligible values in the vicinity of the mesh cut-off wavenumber for all the schemes.

Order of Accuracy vs. Modified Wavenumber Optimization

Increasing the formal order of a discretization scheme is the simplest technique to increase the accuracy of the numerical method. Larger stencil sizes must

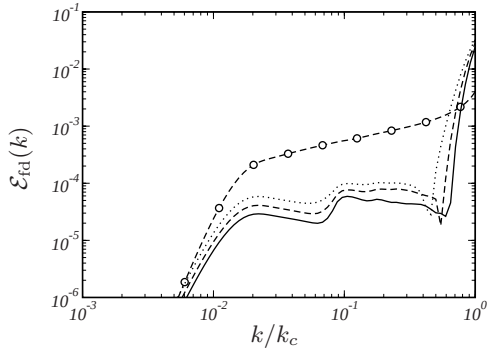

Fig. 6 Differentiation error $\mathcal{E}_{\rm fd}(k)$ as a function of the wavenumber k/k_c for $Re_\lambda = 2500$ and for $k_c = 32$, at $t^* = 8$. $\cdots\cdots\cdots$, 10th standard finite differences; $- - \ -$, 11-point optimized scheme; ———, 13-point optimized scheme; $-\ -\circ\ -$, magnitude of the subgrid scale contribution $|T^>(k|k_c)|$

however be used and the computational cost is increased. Scheme optimization in the Fourier space [11] is an alternative technique allowing to increase the resolution range of approximate derivatives while keeping constant the number of points of the algorithm. Reducing the formal order indeed allows to freely choose some coefficients of the scheme which can be determined by optimizing the modified wavenumber in the spectral space. The accuracy at low wavenumbers is lowered but higher wavenumbers, especially those close to the grid cut-off, are better resolved. Considering the results of the investigation of the detailed scale contribution $\zeta_{\rm fd}(k, k')$ carried out in the former section, the optimized schemes are of special interest since the EDQNM-LES showed that most of the numerical errors are generated by the smallest scales represented on the mesh.

The differentiation error $\mathcal{E}_{\rm fd}(k)$ is plotted in Fig. 6 as a function of k'/k_c for the 4th-order 11-point and 4th-order 13-point optimized finite differences designed by Bogey & Bailly [7]. The results for the standard 10th order scheme is also presented for comparison. The Reynolds number is $Re_\lambda = 2500$ and the mesh cut-off $k_c = 32$. Compared to the 10th standard scheme, the 11-point optimized algorithm provides lower numerical errors. It is worth noting that due to its better accuracy at high wavenumbers, the 11-point optimized scheme results in an error reduction for all the wavenumber range under consideration, including the larger scales with $k/k_c < 10^{-2}$. In a similar manner, the 4th-order 13-point optimized algorithm leads to low differentiation errors over a large interval of wavenumbers. In particular, the poorly resolved wavenumbers close to the mesh cut-off wavenumber lies over a small extent $0.7 < k/k_c < 1$.

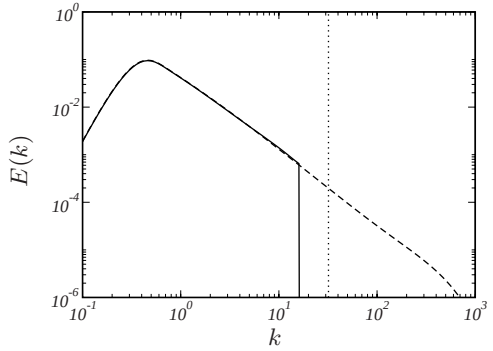

Fig. 7 Evolved kinetic energy spectra at $t^* = 16$ provided by the EDQNM-LES calculation for $\mathrm{Re}_\lambda = 2500$ and $k_c = 32$, for 10th order approximate derivatives, with spectral explicit filtering at $k_f = k_c/2$ and with spectral eddy-viscosity. ————, 10th order finite differences; — — —, EDQNM-DNS reference solution. (The dotted line stands for the LES cut-off wavenumber.)

Explicit Filtering

t has been previously shown that practical discretization tools thus introduce numerical errors over a wavenumber range depending on the order of accuracy. Even though only few wavenumbers are not calculated with accuracy, it may be appropriate to remove these poorly resolved scales. The energy redistribution by the triadic interactions within the resolved scales can indeed lead to a contamination of the full spectrum by numerical errors.

Low-pass filtering with a cut-off wavenumber k_f smaller than the one of the grid (k_c) can reduce numerical errors [5]. The use of explicit filtering is now illustrated using spectral filters with a cut-off wavenumber chosen so that it remains smaller than the accuracy limit k_a of the differentiation algorithm. In the framework of the EDQNM-LES model, spectral filtering is equivalent to setting the kinetic energy spectrum to zero for $k > k_f$, at each time step. Note that in this case the cut-off wavenumber in the spectral eddy-viscosity model of Chollet [10] is equal to the filter cut-off wavenumber.

The improvement in accuracy using filtering is illustrated by performing an EDQNM-LES calculation for the 10th order finite differences at $Re_\lambda = 2500$, with the spectral eddy viscosity model and a filter-width-to-grid-size ratio so that $k_c/k_f = 2$. The waves with fewer than 4 points per wavelength are then removed from the calculation. Figure 7 shows the kinetic energy spectrum obtained at $t^* = 16$ with the EDQNM-LES model and the reference spectrum of the EDQNM-DNS. A good agreement is found over the whole range of resolved wavenumbers. The enhancement of the resolution is especially visible when one compares this spectrum to the one of Fig. 3 which has been obtained without filtering and shows larger discrepancies.

4 Conclusion

The influence on numerical errors of the formal order of the discretization methods in LES has been studied. To quantify the numerical errors, an EDQNM-LES model has been developed in order to evaluate the time evolution of the kinetic energy spectrum obtained by an LES based on approximate differentiation algorithms with given orders. The comparison to the reference spectrum provided by a classical fully-resolved EDQNM approach (EDQNM-DNS) has allowed to define and to calculate the differentiation and the aliasing errors.

The results show that the aliasing errors are negligible. A study of the detailed scale contribution to the differentiation errors furthermore indicates that the interactions between scales in the neighbourhood of the mesh cut-off wavenumber are responsible for the main part of the numerical errors, even at low wavenumbers. This trend is confirmed by considering the 11- and 13-point optimized finite differences. Compared to the standard schemes, the optimized algorithms better resolve short wavelengths and a reduction of the differentiation errors is observed for all wavenumbers. Finally using the EDQNM-LES method, an improvement in accuracy is found to be obtained using explicit filtering.

References

1. Geurts B (2003) Elements of direct and large-eddy simulation. Edwards, Flourtown
2. Smagorinsky J (1963) Mon Wea Rev 91:99–163
3. Lesieur M, Métais O (1996) Annu Rev Fluid Mech 28:45–82
4. Pope S (2204) New J Phys 6:1–24
5. Ghosal S (1996) J Comput Phys 125:187–206
6. Park N, Mahesh K (2007) J Comput Phys 222:194–216
7. Bogey C, Bailly C (2004) J Comput Phys 194:194–214
8. Lesieur M (1987) Turbulence in fluids. Kluwer, Dordrecht
9. Kraichnan R (1976) J Atmos Sci 33:1521–1536
10. Chollet J-P (1984) Two-point closures as a subgrid-scale modeling tool for large-eddy simulations. In: Durst F, Launder BE (eds) Turbulent Shear Flows IV. Springer, Heidelberg
11. Tam C (1995) AIAA J 33:1788–1797

Sensitivity of SGS Models and of Quality of LES to Grid Irregularity

Ghader Ghorbaniasl and Chris Lacor

Vrije Universiteit Brussel, Department Of Mechanical Engineering, Pleinlaan 2, 1050 Brussels, Belgium. ghader.ghorbaniasl@vub.ac.be

Abstract. The present paper investigates the effect of grid irregularity on the results of large eddy simulations in turbulent channel flow at $Re = 180$. Having the error components involved in LES, the grid irregularity effect on the shortcoming of the subgrid scale models and the error of numerical approximation is also assessed. A dynamic version of the WALE model for variable density flows and the variational multi-scale type model based on the dynamic WALE instead of the classical Smagorinsky are implemented. One regular grid and three different disturbed grids are considered. The dynamic WALE model and its VMS version are assessed and compared to the DNS data and to the results obtained from the dynamic Smagorisky model for the three grids. Comparison has shown that the models improve the quality of LES results. It was also noticed that these models, as compared with the dynamic Smagorinsky model, are less affected by grid distortion.

Keywords: Large-eddy simulation, Quality, Dynamic WALE model, Grid irregularity

1 Introduction

With the increase of computing power, the application of LES to industrial type test cases becomes more feasible. However, this type of less academic cases usually require the use of less regular grids, such as unstructured grids. This poses new challenges concerning the quality and the behavior of SGS models on irregular grids as well as possible effects of commutation errors. In the present paper, we will focus on the first aspect.

A complication is that the LES flow field is contaminated by both the inaccuracies resulting from the numerical approximation of the derivatives on the grid (discretization error) and the shortcoming of the model (modeling error). In the present paper, we want to compare LES results for the same test case (channel flow) on a well-behaved Cartesian grid and three different irregular grids, obtained from the Cartesian one by arbitrary displacements of the nodal points. Since both discretization and modeling errors will be

J. Meyers et al. (eds.), Quality and Reliability of Large-Eddy Simulations,

different on the grids, it is essential that both types of errors can be separated if the effect of the grid on the modeling error is to be studied. In the literature, several papers can be found dealing with the separation of errors [1], [2], [3] and [4]. In the present paper, the approach of Vreman et al. [4] is followed, where the separation of discretization and modeling error is done by comparing LES simulations with the same filter but different grid resolutions.

Different SGS models are considered in this study:

1. the dynamic Smagorinsky model (DSM) [5], [6]
2. the wall-adapted local eddy-viscosity (WALE) model, Ducros et al. [7]
3. the variational multi-scale model (VMS), Hughes et al. [8]

In the present paper, a dynamic version of the WALE model, valid for variable density flows, is proposed and tested. The better behaviour of the dynamic WALE model, as compared with the dynamic Smagorinsky, also led us to formulate and test a VMS type model based on the dynamic WALE instead of the standard Smagorinsky. It will be shown that these modifications improve the results for the regular and irregular grids.

The main purpose of this work is to study the grid distortion effect on the quality of LES simulations with the fore-mentioned SGS models. It will be shown that distortion of grids has high influence on the results of the dynamic Smagorinsky model, whereas this effect decreases significantly when the dynamic WALE or VMS of dynamic WALE are used for modeling approach.

This paper is organized as follows: in Section 2 the anisotropic shear stress is briefly discussed and the investigated models are detailed, Section 3 is devoted to a brief summary of approach to separation of errors, test case description and a posteriori tests is presented in Section 4, and finally, in Section 5 conclusions are drawn.

2 The SGS Stress Tensor and Investigated Models

In the case of variable density, the filtered Navier–Stokes equations may be written as

$$\begin{aligned} \frac{\partial \bar{\rho}}{\partial t} + \frac{\partial \bar{\rho}\tilde{u}_i}{\partial x_i} &= 0 \\ \frac{\partial \bar{\rho}\tilde{u}_i}{\partial t} + \frac{\partial \bar{\rho}\tilde{u}_i\tilde{u}_j}{\partial x_j} &= -\frac{\partial \bar{\sigma}_{ij}}{\partial x_j} - \frac{\partial \tau_{ij}^{sgs}}{\partial x_j} \end{aligned} \tag{1}$$

where the Favre filtered field is defined as $\overline{\rho u}/\bar{\rho}$ and the term τ_{ij}^{sgs} is the subgrid-scale shear stress

$$\tau_{ij}^{sgs} = \bar{\rho}(\widetilde{u_i u_j} - \tilde{u}_i\tilde{u}_j) \tag{2}$$

This term cannot be determined using only the resolved flow field $\tilde{u}_i$, and thus it requires modeling. According to equation (2), the subgrid stress is not

strictly deviatoric and one can split it up into a deviatoric and an isotropic tensors as follows,

$$\tau_{ij}^{sgs} = \tau_{ij}^{D} + \tau^{iso}\delta_{ij} \tag{3}$$

where, $\tau^{iso} = \frac{1}{3}\tau_{kk}^{sgs}$, and

$$\tau_{ij}^{D} = \tau_{ij}^{sgs} - \frac{1}{3}\tau_{kk}^{sgs}\delta_{ij} \tag{4}$$

The subgrid-scale stress tensor can be modeled at different levels of complexity. The eddy-viscosity concept is widely used in LES. We shall define in the next section the models based on the eddy-viscosity concept that we have used in the present paper.

2.1 Wall-Adapted Local Eddy-Viscosity (WALE) Model

The basic assumption of all eddy viscosity models is that the unknown subgrid scale stress tensor is proportional to the filtered large scale strain rate tensor. The deviatoric subgrid-stress tensor is approximated by

$$\tau_{ij}^{D} \approx -2\nu_t\bar{\rho}(\tilde{S}_{ij} - \frac{1}{3}\tilde{S}_{kk}\delta_{ij}) = -2\nu_t\bar{\rho}\tilde{S}_{ij}^{D} \tag{5}$$

where ν_t, is the eddy viscosity and $\tilde{S}_{ij}$, is the resolved shear stress tensor. Now the determination of the eddy-viscosity ν_t is required. The WALE model proposed by Ducros et al. [7] is one of the approaches to the eddy-viscosity determination. This approach is specifically designed to return the correct wall-asymptotic y^{+3}-variation of the SGS viscosity (Hinze, 1975) [9]. Although the model has originally been developed for incompressible flows, it can also be used for variable density flows. Following this model, we can have the eddy viscosity as

$$\nu_t = (C_w\Delta)^2|\tilde{S}_w| \tag{6}$$

where

$$|\tilde{S}_w| = \frac{(\tilde{S}_{ij}^{d}\tilde{S}_{ij}^{d})^{3/2}}{(\tilde{S}_{ij}\tilde{S}_{ij})^{5/2} + (\tilde{S}_{ij}^{d}\tilde{S}_{ij}^{d})^{5/4}} \tag{7}$$

and

$$\tilde{S}_{ij}^{d} = \frac{1}{2}(\tilde{g}_{ij}^{2} + \tilde{g}_{ji}^{2}) - \frac{1}{3}\tilde{g}_{kk}^{2}\delta_{ij} \tag{8}$$

with

$$\tilde{g}_{ij}^{2} = \frac{\partial\tilde{u}_i}{\partial x_k}\frac{\partial\tilde{u}_k}{\partial x_j} \tag{9}$$

The term C_w, is the model parameter, which has to be fixed a priori. In order to make this model applicable to real industrial flows, below we will develop the dynamic version of this model for flows with variable density. Being a dynamic model, it will have the great advantage that the coefficient C_w, is not arbitrary chosen (or optimized), but it is computed.

2.2 Dynamic WALE Model

The dynamic procedure was proposed by Germano et al. [10] to allow for the model parameter to vary spatially and temporally by employing an additional filter (test filter) with a filter width $\hat{\Delta}$, larger than the grid spacing, Δ. Applying the test filter to the equations of motion, one can get a subtest stress tensor,

$$T_{ij} = \hat{\bar{\rho}}(\widehat{\breve{u_i}\breve{u_j}} - \breve{\tilde{u}}_i\breve{\tilde{u}}_j) \tag{10}$$

where the symbol $\breve{\cdot}$, is defined as $\breve{\tilde{u}} = \widehat{\bar{\rho}\tilde{u}}/\hat{\bar{\rho}}$. The deviatoric part of the subtest stress can be modeled by

$$\begin{aligned} T_{ij}^D = T_{ij} - \frac{1}{3}T_{kk}\delta_{ij} &\approx -2(C_w\hat{\Delta})^2\hat{\bar{\rho}}|\breve{\bar{S}}_w|(\breve{\bar{S}}_{ij} - \frac{1}{3}\breve{\bar{S}}_{kk}\delta_{ij}) \\ &= -2(C_w\hat{\Delta})^2\hat{\bar{\rho}}|\breve{\bar{S}}_w|\breve{\bar{S}}_{ij}^D \end{aligned} \tag{11}$$

The Favre filtered strain rate at the test scale should be computed as follows,

$$\breve{\bar{S}}_{ij} = \frac{1}{2}(\frac{\partial(\widehat{\bar{\rho}\tilde{u}}_i/\hat{\bar{\rho}})}{\partial x_j} + \frac{\partial(\widehat{\bar{\rho}\tilde{u}}_j/\hat{\bar{\rho}})}{\partial x_i}) \tag{12}$$

One can also determine the Favre filtered tensor $\breve{\bar{g}}_{ij}^2$, at the test scale as

$$\breve{\bar{g}}_{ij}^2 = \frac{\partial(\widehat{\bar{\rho}\tilde{u}}_i/\hat{\bar{\rho}})}{\partial x_k}\frac{\partial(\widehat{\bar{\rho}\tilde{u}}_k/\hat{\bar{\rho}})}{\partial x_j} \tag{13}$$

to obtain the term $|\breve{\bar{S}}_w|$ by

$$|\breve{\bar{S}}_w| = \frac{(\breve{\bar{S}}_{ij}^d\breve{\bar{S}}_{ij}^d)^{3/2}}{(\breve{\bar{S}}_{ij}\breve{\bar{S}}_{ij})^{5/2} + (\breve{\bar{S}}_{ij}^d\breve{\bar{S}}_{ij}^d)^{5/4}} \tag{14}$$

where

$$\breve{\bar{S}}_{ij}^d = \frac{1}{2}(\breve{\bar{g}}_{ij}^2 + \breve{\bar{g}}_{ji}^2) - \frac{1}{3}\breve{\bar{g}}_{kk}^2\delta_{ij} \tag{15}$$

The subgrid stress τ_{ij}^{sgs}, and the subtest stress T_{ij}, can be related to each other through the resolved turbulent stress and Germano identity. Using equations (2) and (10), the resolved turbulent stress, the Leonard stress, which represents the energy scales between the grid filter and the test filter, is defined as

$$L_{ij} = T_{ij} - \hat{\tau}_{ij}^{sgs} = \widehat{\bar{\rho}\tilde{u}_i\tilde{u}_j} - \frac{\widehat{\bar{\rho}\tilde{u}_i}\widehat{\bar{\rho}\tilde{u}_j}}{\hat{\bar{\rho}}} \tag{16}$$

The Leonard stress contains only the resolved scales and it can thus be evaluated from the resolved flow field. Using equations (5), (6) and (11) for the Germano identity, we have

$$L_{ij}^D = T_{ij}^D - \widehat{\tau}_{ij}^D \approx -2(C_w\hat{\Delta})^2\hat{\bar{\rho}}|\breve{\breve{S}}_w|\breve{\breve{S}}_{ij}^D + 2(C_w\Delta)^2\bar{\rho}\widehat{|\tilde{S}_w|\tilde{S}_{ij}^D}$$
$$= 2C_w^2 M_{ij}^D \tag{17}$$

where

$$M_{ij}^D = -(\hat{\Delta}/\Delta)^2\hat{\bar{\rho}}|\breve{\breve{S}}_w|\breve{\breve{S}}_{ij}^D + \bar{\rho}\widehat{|\tilde{S}_w|\tilde{S}_{ij}^D} \tag{18}$$

To obtain the expression for M_{ij}^D, we have neglected the variation of C_w^2, on the test filter width $\hat{\Delta}$. Based on Lilly's work [6], the error square is given by

$$Q = (L_{ij}^D - 2C_w^2 M_{ij}^D)^2 \tag{19}$$

This equation represents a system of equations for the single unknown C_w^2, minimizing the error square, $\partial Q/\partial C_w^2 = 0$, and the fact that, $L_{ij}^D M_{ij}^D = L_{ij}M_{ij}^D$, result in

$$C_w^2 = \frac{1}{2}\frac{< L_{ij}M_{ij}^D >}{< M_{kl}^D M_{kl}^D >} \tag{20}$$

where $< \cdot >$ stands for averaging over the homogenous directions.

2.3 The Variational Multi-Scale Model

The variational multi-scale model (VMS) developed by Hughes et al. [8] corresponds to limiting the Smagorinsky model to the small scales. The main justification behind this model is that most of the shortcomings associated with a Smagorinsky based model are due to their inability to differentiate between small and large scales. In the multi-scale formulation the solution is decomposed into large scale and small scale components,

$$u = u^l + u' \tag{21}$$

In the physical space the following approximation is done for the small scale,

$$u' \approx \tilde{u}^s = \tilde{u} - \hat{\tilde{u}} \tag{22}$$

where $\tilde{u}$ denotes the resolved scales and $\hat{\tilde{u}}$ represents the test filtered field. Another way to obtain the small scale is using the deconvolution technique. Based on this technique and using up to second order accuracy, one can have

$$\tilde{u}^s \approx -\frac{\Delta^2}{24}\nabla^2\tilde{u} \tag{23}$$

The modeling is confined to the small scales. We formulate and test the dynamic WALE based VMS (all-small) model instead of the standard Smagorinsky. We approximate the subgrid stress as

$$\tau_{ij}^{sgs} \approx -2[(C_w\Delta)^2\bar{\rho}|\tilde{S}_w|\tilde{S}_{ij}^D]^s \tag{24}$$

and the subtest stress as

$$T_{ij} \approx -2[(C_w\hat{\Delta})\hat{\bar{\rho}}|\breve{\breve{S}}_w|\breve{\breve{S}}_{ij}^D]^s \tag{25}$$

The superscript s indicates that all the variables inside the square brackets are determined based on the small scales instead of the large scales.

3 Approach to Separation of Errors

The differences between LES and DNS results are the sum of the filtering effect, the modeling error effect caused by the SGS models and the discretization error effect from inaccuracies of the numerical method. Based on Vreman et al. [4] approach, to separate error components, we need to perform the so-called fine-grid LES, in which the filter width is kept constant while the resolution is increased. The discretization error is thus given by

$$e_d =< \tilde{u} >_{LES} - < \tilde{u} >_{finegridLES} \tag{26}$$

The difference between the fine grid LES and the filtered DNS gives the effect of modeling error,

$$e_m =< \tilde{u} >_{finegridLES} - < u >_{filteredDNS} \tag{27}$$

The filtering error can be obtained with

$$e_f =< u >_{filteredDNS} - < u >_{DNS} \tag{28}$$

In equations (26), (27) and (28), $\tilde{u}$ denotes the LES variable and u refers to the DNS data. Obviously, the filtering error does not depend on the SGS models, and it has the same contribution to the total error when different SGS models are used. However, to evaluate SGS models one can avoid using the filtered DNS data by combining the filtering effect with the modeling contribution as follows

$$e_{mf} = e_m + e_f =< \tilde{u} >_{finegridLES} - < u >_{DNS} \tag{29}$$

In the remainder of the article we will refer to this error as a modeling-filtering error, where the modeling error is summed with the filtering error.

4 A Posteriori Tests and Test Case

As already mentioned the turbulent channel flow is chosen as test case. Current results are at a Reynolds number of 180 (based on the friction velocity) but results for higher Reynolds are underway. For the channel considered, $L_x = 4\pi$, $L_y = 2$ and $L_z = 4\pi/3$. Four grids are employed in the calculations: one is a well-behaved Cartesian grid (grid 1) and the three others are irregular grids obtained from grid 1 through distortion in the homogeneous directions. The disturbed grids are obtained by adding a random displacement in the nodes of the regular grid. Based on the size of this displacement, three distorted grids (grid 2, grid 3 and grid 4) are obtained, where grid 4 is the most distorted, grid 2 is the least and grid 3 (cf. Figure 1) is intermediate. All LES use a computational grid of $33 \times 33 \times 33$ points, which corresponds to one-quarter of the DNS resolution in each spatial direction. For spatial

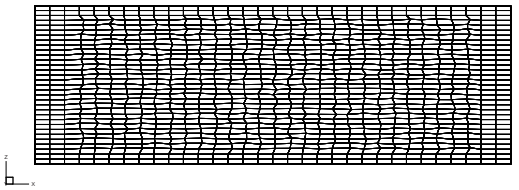

Fig. 1 Schematic of grid 3 is shown

discretization, the second-order central finite volume scheme and for the temporal discretization low storage four-stage second order RK scheme was used. To perform the fine-grid LES three finer grids of $65 \times 65 \times 65$ points associated with the three coarse grids are considered.

It is interesting to note that Meyers et al. [11] have performed grid sensitivity study in their channel-flow DNS at coarse resolutions calculations and suggested the optimal requirement for resolved DNS. The present grid resolution may fall outside these resolution requirements, however, the main purpose of this article was to compare and analyze the performance of different SGS models and since the mesh is the same for all SGS models, the comparative study is valid. First, we investigate the dynamic Smagorinsky, the dynamic WALE and the dynamic WALE based VMS models, when they are applied for the regular grid case. Then, those models will be assessed for the three irregular grids.

In order to have a fair comparison, we should compare LES results with filtered DNS data. Since filtered DNS are in general not available, to evaluate the performance of the models, LES results are compared with unfiltered DNS data. Such a comparison is qualitative at best for the assessment of the results.

4.1 Comparison of the Results for the Regular Grid

In Fig. 2 (Left), we compare results for the mean streamwise velocity. As can be clearly seen, VMS version of the dynamic WALE model (VDW) is the most accurate model. The dynamic Smagorinsky model is the least accurate. The dynamic WALE predicts the results slightly less accurate than its VMS version. As shown in Fig. 2 (Right), the effect of modeling-filtering is smaller than effect of discretization error for all the models. Both the modeling-filtering and numerical errors of the VDW model are the smallest whereas those of the dynamic Smagorinsky are the biggest and of the dynamic WALE are intermediate.

Rms values of streamwise velocity fluctuations is presented in Fig. 3 (Left). Throughout most of the channel, the dynamic WALE and its VMS version model are on top of each other. Both the models overshoot the peak DNS value somewhat more than the dynamic Smagorinsky model but predict the results more accurate than the dynamic Smagorinsky model elsewhere. On

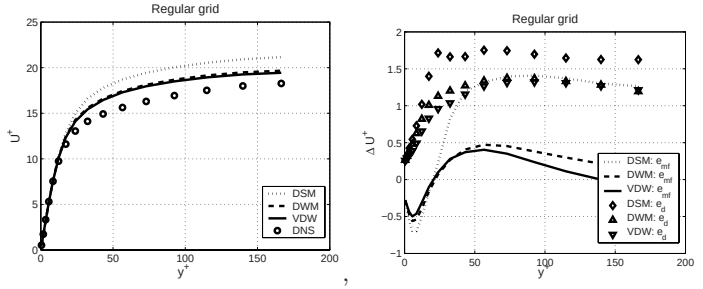

Fig. 2 (*Left*) Mean-velocity profile compared with the DNS data, (*Right*) Related error components

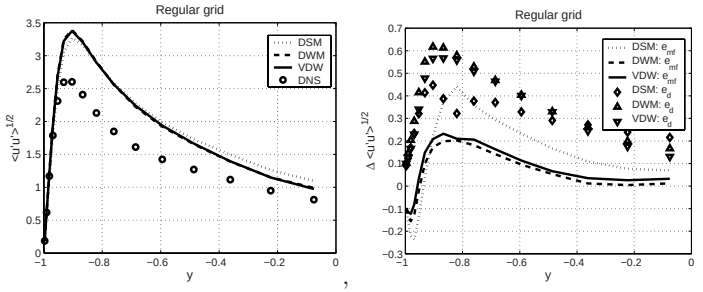

Fig. 3 (*Left*) Rms values of streamwise velocity fluctuations compared with DNS data, (*Right*) The related error components

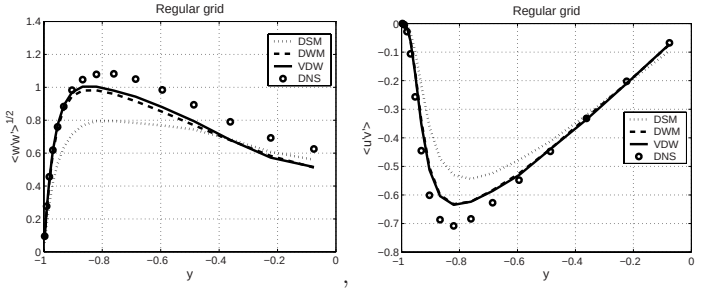

Fig. 4 (*Left*) Rms values of spanwise velocity fluctuations, (*Right*) The x, y-component of Reynolds stress

the right hand side of this figure, the related error components are given. As can been seen, the modeling-filtering error of the VDW is slightly lower than the dynamic WALE one, whereas the discretization error of the VDW is somewhat higher than that of the dynamic WALE. This error for the dynamic Smagorinsky model is the largest. The discretization error of the dynamic Smagorinsky is the smallest at the peak and largest in the middle of the channel.

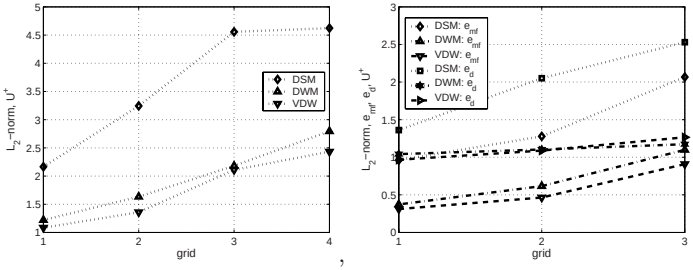

Fig. 5 (*Left*) L2-norms of streamwise mean-velocity, (*Right*) L2-norms of the related error components

Results for rms values of spanwise velocity fluctuations are presented in Fig. 4 (Left). The Smagorisky model produces inaccurate spanwise turbulent intensity profile. The VDW model is again the best. Likewise, the dynamic WALE model predicts the spanwise intensity accurately, slightly less accurate than the VDW. Results of both the dynamic WALE and the VDW models are identical to the DNS data near the wall. The same conclusion was observed for rms values of wall-normal velocity fluctuations.

The x, y-component of Reynolds stress profile is illustrated in Fig. 4 (Right). The dynamic WALE and the VDW models predict the results better than does the dynamic Smagorinsky model. In order to have a fair comparison, the LES modeled contribution was also taken into account in the simulations. Although inclusion of the modeled part improved the dynamic Smagorinsky results considerably, the accuracy of this model was still the least.

Overall, for the regular grid our results indicate that the all-small model is slightly better than the dynamic WALE model and considerably more accurate than the dynamic Smagorinsky model throughout most of the channel for the streamwise mean velocity, the rms wall-normal and spanwise velocity fluctuations and the x,y-component Reynolds stress. The dynamic Smagorinsky model captures the peak of the rms streamwise velocity fluctuations somewhat better than the two others. However, the most accurate models overall is the VDW model. Likewise, the modeling-filtering error effects of the VDW and the dynamic WALE models are significantly lower than one of the dynamic Smagorinsky model.

4.2 Results on the Irregular Grids

In this section, the total error in the LES simulation with the three SGS models applied to the irregular grids is studied.

In order to investigate the SGS models performance, L2-norms of the LES simulations results are considered. First, L2-norms of streamwise mean velocity from the SGS models are plotted in Fig. 5 (Left) for the grids. Herein we notice that the grid irregularity effect on the Smagorinsky model is significantly larger than on the VDW and on the dynamic WALE models. As can

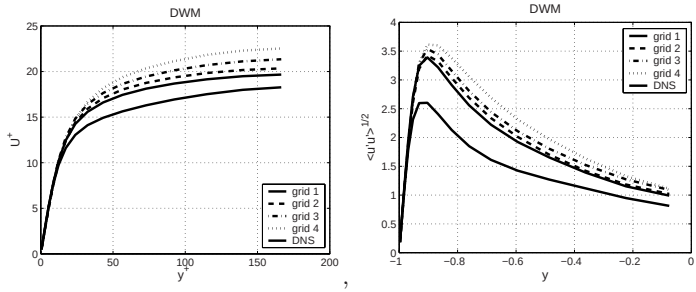

Fig. 6 The results obtained from the DWM compared with the DNS data are shown. (*Left*) Streamwise mean velocity, (*Right*) Rms value of streamwise velocity fluctuations

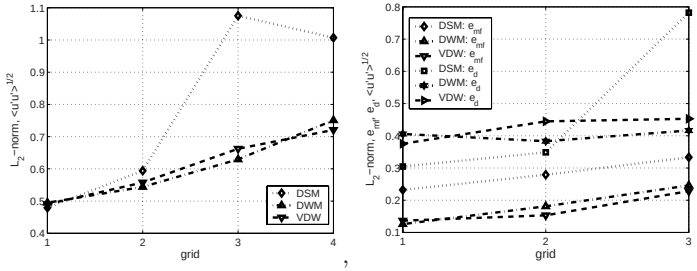

Fig. 7 (*Left*) L2-norms of rms values of streamwise velocity fluctuations, (*Right*) L2-norms of the related error components

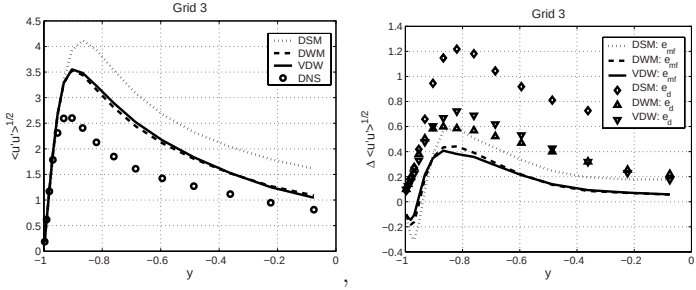

Fig. 8 Rms values of streamwise velocity fluctuations and the associated error components are shown for grid 3

be seen, for all the models the more grid distortion gives the more total error (e.g. see Fig. 6). The VDW is still the most accurate, the dynamic WALE is intermediate and the dynamic Smagorinsky is the least for the different irregular grids. The L2-norms of the error components are given in Fig. 5 (Right). The modeling-filtering error effect of the VDW is the smallest in all the grids. This component for the dynamic Smagorinsky is the largest.

L2-norms of rms values of streamwise velocity fluctuations are plotted in Fig. 7 (Left) for the different grids. On the right hand side of this figure

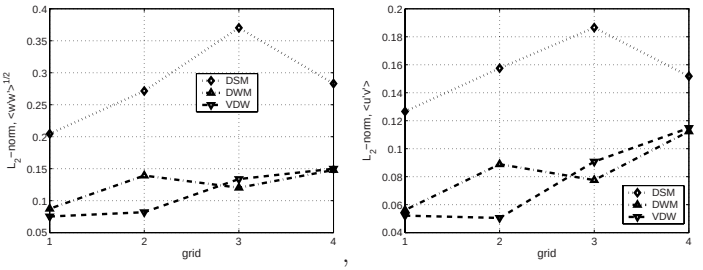

Fig. 9 (*Left*) L2-norms of rms values of spanwise velocity fluctuations, (*Right*) L2-norms of the x, y-component of Reynolds stress

L2-norms of the related error components are illustrated for the three irregular grids. As can be seen, the total error of the dynamic Smagorinsky model increases with the grid irregularity more than those of the dynamic WALE and the VDW models. We can see that for grid 2 and grid 3 the dynamic WALE is the most accurate. For grid 4 the VDW is the most accurate model. For all the irregular grids the total error of the dynamic Smagorinsky is the largest. It should be mentioned that the dynamic Smagorinsky overshoots the peak higher than do the dynamic WALE and the VDW when grid 3 and grid 4 are used (e.g. see Fig. 8). The modeling-filtering error effect for all the SGS models vary uniformly from grid 1 to grid 3, but the discretization error effect of the dynamic Smagorinsky model from grid 2 to grid 3 has rapidly increased.

L2-norms of the spanwise velocity fluctuations and the x, y-component of Reynolds stress are shown in Fig. 9. The all-small is the most accurate model for grid 2. The dynamic WALE is the most accurate model for grid 3. The dynamic Smagrinsky model is still the least accurate for those irregular grids.

5 Conclusion

The dynamic version of the WALE model and the variational multi-scale model based on the dynamic WALE were developed and implemented. The assessment of these models in addition to the dynamic Smagorinsky model were carried out for the turbulent channel flow at Re=180. One regular grid and three different irregular grids were considered for the investigation. Significant improvements in the profiles of mean velocity, rms values of turbulent intensities and the x,y-component of Reynolds stress, as compared to the dynamic Smagorinsky, are obtained for all the grids when using the dynamic WALE model and its VMS version. Overall, we conclude that the dynamic WALE and its VMS version are accurate models, in particular, when the irregular grids are used in the LES simulations. We have also separated the modeling-filtering error effect and the discretization error effect of the models for the grids. We have shown that for each grid and for all the models the discretization error effect is larger than the modeling-filtering error effect.

This behavior can be partially related to the fact that Reynolds number is rather low and the filter width equivalent to grid spacing of the coarse mesh, gives small subgrid contributions and less accurate approximations of derivatives. This is important future research needed to further investigation, in particular, for higher Reynolds number. Finally, it has been shown that the modeling-filtering error effects of the dynamic WALE and the VDW models are lower than that of the dynamic Smagorinsky model for all the grids.

References

1. Ghosal S (1996) An analysis of numerical errors in large-eddy simulations of turbulence, J Comp Phys 125:187–206
2. Gullbrand J, Chow F (2002) Investigation of numerical errors, subfilter-scale models, and subgrid-scale models in turbulent channel flow simulations, Proceedings of the Summer Program, Center for Turbulence Research, NASA Ames/Stanford University
3. Meyers J (2004) Accuracy of large eddy simulation strategies. PhD Dissertation, Katholieke Universiteit Leuven, Belgium
4. Vreman B, Geurts B, Kuerten H (1996) Comparison numerical schemes in LES of the temporal mixing layer. Int J Numer Methods Fluids 22(4):297–311
5. Smagorinsky J (1963) General circulation experiments with the primitive equation. Mon Weather Rev 91(3):99–106
6. Lilly DK (1992) A proposed modification of the Germano subgrid-scale closure method. Phys Fluid A 4(3):633–635
7. Nicoud F, Ducros F (1999) Subgrid-scale stress modeling based on the square of the velocity gradient tensor. Flow Turbulence Combust 62:183–200
8. Hughes TJR, Mazzei L, Oberai AA, Wray AA (2001) The multiscale formulation of large eddy simulation: decay of homogeneous isotropic turbulence. Phys Fluids 13(2)505–512
9. Hinze J (1975) Turbulence. McGraw-Hill, New Yorks
10. Germano M, Piomelli U, Moin P, Cabot W (1991) A dynamic subgrid-scale eddy-viscosity model. Phys Fluid A 3:1760–1765
11. Meyers J, Sagaut P (2007) Is plane-channel flow a friendly case for the testing of large-eddy simulation subgrid-scale models? Phys Fluid 19, Art no 048105

Anisotropic Grid Refinement Study for LES

Péter Tóth and Máté Márton Lohász

Department of Fluid Mechanics, Budapest University of Technology and Economics, Bertalan L. Str. 4-6, Budapest 1111, Hungary
toth@ara.bme.hu, lohasz@ara.bme.hu

Abstract. In this paper an anisotropic grid refinement study is proposed for use in Large-Eddy Simulation. The aim of the method is to compare the effect of different grid refinements. These refinements can be selected systematically in order to fit the grid to the anisotropy of the turbulence. Furthermore it is proposed that the results be compared using multiple objectives, i.e. to separate the effects on the different components of the Reynolds stress tensor. It was attempted to apply the Index of Resolution Quality for quantifying the various refinements. The method was applied to a spatially developing axisymmetric shear layer (round jet). Reynolds stresses, momentum thickness and vortices were plotted for this purpose. The results indicate that grid refinement in different directions has an effect differing both in manner and magnitude. This differing manner is highlighted in the various behaviours of the Reynolds stress components. The index of resolution quality was found to be misleading, since it can underestimate the relative importance of the grid refinement effects.

Keywords: Directional grid refinement, Vortex, Large-eddy simulation

1 Introduction

In the Large-Eddy Simulation (LES) approach a spatial filtering is applied on the turbulent flow and only the scales passed trough the filter are simulated while the smaller ones need to be modelled. Besides the advantage of LES that it resolves the large scales – which are difficult to model – still an important and extensive research field focuses on developing models for the filtered (Sub-Grid) scales. Another important research field in LES is defining guidelines for its proper application, i.e. defining the quality of an existing LES result. This paper contributes to this issue. In practical numerical simulations the filter width can be expressed in terms of the numerical mesh size h. In traditional LES the filter width is the same as the typical mesh size, resulting in large amount of numerical error when resolving the filtered flowfield [5]. The numerical error for LES is defined in [11] as the difference between the

J. Meyers et al. (eds.), Quality and Reliability of Large-Eddy Simulations,

perfect solution of the modelled filtered equation and the one computed using the practical numerical method.

1.1 Need for an Anisotropic Grid

Large scale turbulent structures are highly anisotropic, therefore an anisotropic grid would be optimal for its resolution. Block structured grids can define such a structure, where the anisotropy can be controlled by the cell numbers of the independent edges of the blocks. An arbitrary number of N groups can be selected from these independent edges to control the anisotropy.

1.2 Quality Assessment Criteria for LES

By definition an ideal LES (with a perfect SGS model and without numerical error) should be able to reproduce any smooth (which are not affected by the filtering) quantities perfectly. Most of the turbulent fluctuating quantities are however affected by the filtering and consequently their resolved values (ϕ_{res}) differs from the real one. Thus for fluctuating quantities (e.g. rms), the following approximation was proposed by [2]: $\phi_{tot} = \phi_{res} + \phi_{SGS} + \phi_{num}$, where ϕ_{tot}, ϕ_{SGS} and ϕ_{num} are the total value, the SGS model contribution and the numerical error of ϕ respectively. If ϕ_{tot} is available, the ratio of the resolved value to the total value of ϕ can be expressed. This value is denoted as $LES\_IQ_\phi = \phi_{res}/\phi_{tot}$ in [2]. An LES is defined as good when the smooth quantities are predicted correctly and the amount of the modelled quantities are known. This requires that the large scale motions (typically vortices) – which are believed to produce the anisotropic turbulence – be accurately resolved. [10] argues that if 80% of the turbulent kinetic energy (TKE) is resolved, the LES will be good. This rule can be reformulated for the difference between the total and the resolved value, which needs to be less than 20%. [2] pointed out that even negative values can occur for this difference and therefore a new rule can be formulated: LES_IQ_ϕ needs to be in the 1 ± 0.2 range. This can be extended to every component of the Reynolds stress tensor, using LES_IQ_ϕ to qualify the simulations.

1.3 Estimating the Total Value of ϕ

In this paper two methods are used to estimate ϕ_{tot}. These methods use extrapolation techniques from the results of systematically modified simulations. They were developed for the case when the mesh resolution can be described with a single number ($N = 1$). It is proposed in [8] that the difference between the total value of a quantity and its actual computed (resolved) value can be approximated:

$$\phi_{tot} - \phi_p^{a,b} = \underbrace{c_n\,(bh)^n}_{\phi_{num}} + \underbrace{a c_m\,(bh)^m}_{\phi_{SGS}} \tag{1}$$

Here $\phi_p^{a,b}$ is the resolved value of ϕ for simulation p, with parameters a and b denoting the model variation and the grid refinement parameters respectively. c_n and c_m are constants, which are to be determined. The grid refinement parameter is global, meaning that the grid is refined by b in every spatial direction (all the N edge groups are refined in the same manner). h is the local grid spacing of the base simulation, while n and m are the order of the numerical error, and the subgrid scale model contribution respectively. If $n = m = 2$ is assumed, then only two simulations are needed ($p = 1, 2$) to obtain ϕ_{tot}. Changing only b is proposed by [2], thus the parameters of the required simulations are $[a, b]_{p=1} = [1, 1]$ and $[a, b]_{p=2} = [1, \beta]$, where β is the actual refinement factor. If $n \neq m$, then three simulations are needed ($p = 1, 2, 3$) in order to obtain ϕ_{tot}. There are several possible parameter combinations. If both a and b are varied, then the required simulations are: $[a, b]_{p=1} = [1, 1]$, $[a, b]_{p=2} = [\alpha, \beta]$, $[a, b]_{p=3} = [1, \beta]$, where α is the actual model variation parameter. This combination was proposed by [8], although it was not used to extrapolate the value of ϕ, but to estimate the simulation uncertainty.

1.4 Refinement Assessment for Block Structured Grids

Since the final goal of varying the grid anisotropy is to find an optimal cell size – which fits to the characteristics of the flowfield – a method needs to be defined in order to quantitatively compare the results of the directionally refined simulations. It was attempted to use the index of resolution method described in Sect. 1.3 to quantify the impact of each grid refinement. Since a directional refinement does not converge to the infinite resolution i.e. the total value of ϕ can only be computed by using the original method which applies a global grid refinement (all the N parameters are varied together), it is proposed that a LES_IQ_ϕ be computed by dividing the result on the directionally refined grid by the total value computed using global refinement. This LES_IQ_ϕ – if the methods assumptions are fulfilled – enables us to decide if the effect of the actual refinement is significant.

2 Computational Details

In the present paper the previously described methodology is demonstrated on the near field of a round free jet flow (axisymmetric shear layer).

2.1 Investigated Flow

The flow parameters correspond to the measurements of [3]. The flow was approximated as incompressible and can be characterised by the discharge Reynolds number of $Re = U_0 D/\nu = 106000$, where U_0 is the maximum velocity and D is the inlet diameter.

2.2 Numerical Parameters

The computation was carried out with the commercial code Fluent 6.3 [7], which uses a cell-centred finite-volume method with collocated variable arrangement. For the simulation, the pressure based solver was applied solving the governing equations sequentially and coupling them using the FSM (Fractional Step Method) in a non-iterative manner [7]. The time is advanced using Gear's two step second-order implicit method. Approximately a second order accuracy is reached by using the Bounded Central Differencing scheme [7] for spatial discretisation of the convective terms. The second order scheme was used for the interpolation of the pressure. The spatial derivatives were cell based evaluated.

The simulations used the Smagorinsky model with $C_{s,ref} = 0.1$ (unless otherwise indicated), $\nu_t = (C_{s,ref}\Delta)^2 \sqrt{2S_{ij}S_{ij}}$, where S_{ij} is the resolved rate of strain tensor, $\Delta = \sqrt[3]{V}$ and V is the cell volume.

The $T = 115.2U_0/D$ long statistical sampling was initiated at approximately $T_s = 20U_0/D$ (the approximate end of the temporal laminar-turbulent transition). Constant time-steps were selected for each mesh to have $CFL < 1$.

2.3 Computational Domain and Grid

The computational domain consisting of a cylinder with a streamwise length of $6D$ and diameter of $5.2D$. The block structure of the computational grid can be seen in Fig. 1, with one quarter of the mesh, which is perpendicular to the mean flow is depicted on the right. The cells of the grid are concentrated at $r = 0.5D$, where r is the radial coordinate. This quadrilateral mesh is extruded in the x (streamwise) direction with a non uniform cell distribution. The cells are also concentrated at the inflow boundary. The block structure of the mesh implies that the cell number can be expressed with four variables Ψ, R_1, R_2 and X. The variables Ψ and X directly determine the number of cells in the azimuthal (ψ) and streamwise (x) direction respectively. The number of cells in the radial (r) direction is determined by the R_1, R_2 and Ψ variables, showing that the radial cell number cannot be changed independently from the azimuthal cell number. The block edges are meshed for the refined domains as given in Table 1. The grid notation in the first row of Table 1 (e.g. $b1_{\psi 2}$) shows the refined grid name ($b1$), the refinement direction (ψ) and the refinement factor ($\beta = 2$). The smallest cell of the domain is situated at the inflow boundary in the shear layer and can be characterized by its radial δ_r, circumferential δ_ψ and axial δ_x extent. For the $b1$ base mesh these sizes are $\delta_r = 0.015D$, $\delta_\psi \cong 3\delta_r$ and $\delta_x \cong 1.67\delta_r$. According to the grid refinement parameter β, the smallest cell size for the other grids can be computed from these sizes. The size of the cells increases along the positive x direction up to $x = 4D$, after which it decreases and again concentrates at the outflow boundary. In the outflow plane ($x = 6D$) the cell distribution of the mesh differs

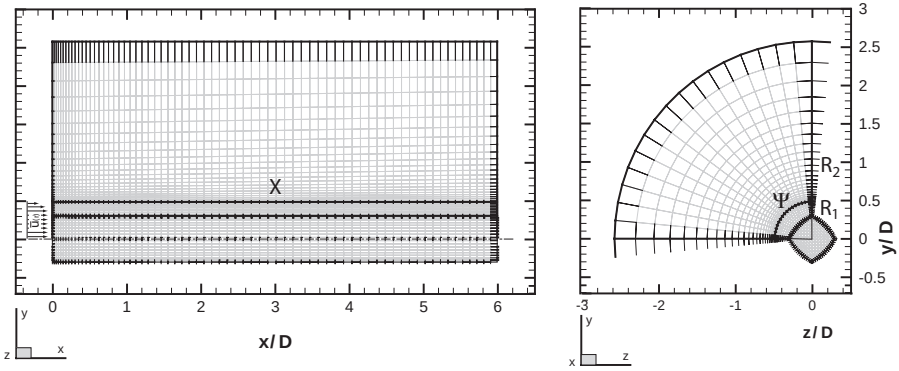

Fig. 1 Block structure of the grid and cross section for the $b1$ mesh. *Left*: $z = 0$ plane. *Right*: $x = 0$ plane. The block resolutions is indicated by Ψ, R_1, R_2 and X

Table 1 Edge cell numbers of the grids, as defined in Fig. 1. The total number of cells is: $X\Psi\,(\Psi + 4\,(R_1 + R_2))$

	$b1$	$b1_{\psi 0.5}$	$b1_{r0.5}$	$b1_{x2}$	$b1_{\psi 2}$	$b1_{r2}$	$b1_{all\sqrt{2}}$	$b2 = b1_{x4}$	$b2_{\psi 2}$	$b2_{r2}$	$b2_{all\sqrt{2}}$
Ψ	17	9	17	17	34	17	24	17	34	17	24
R_1	9	9	5	9	9	18	13	9	9	18	13
R_2	23	23	12	23	23	46	33	23	23	46	33
X	69	69	69	138	69	69	97	276	276	276	390

from the one shown in Fig. 1 right. At this position the cells are uniformly distributed along the edge R_1.

2.4 Boundary Conditions

A velocity inlet boundary condition was prescribed for the region $x = 0, r < 0.5D$. A tangent hyperbolic mean velocity profile ($\bar{u}$) was imposed according to [1]. The initial momentum thickness of the shear layer was defined as $\Theta_0 = 0.005D$. The inflow turbulence was generated by the vortex method [9], with the input parameters of TKE and its dissipation rate. The turbulent kinetic energy profile was calculated from the measurement data of [3] ($TKE = 3/2u_{rms}$). The dissipation rate was $k^{3/2}/l'$ where l' was estimated as $l' = min(0.09\delta_{99}, l)$ and δ_{99} was the 99% boundary layer thickness. The wall shear stress was computed from the mean velocity profile and l was determined by the van Driest formula. The number of the vortices were 190. The far-field condition was prescribed as constant using the pressure outlet condition of [4]. This prescribes a static pressure if the flow leaves the domain and a total pressure if it enters the domain. Reverse flow is set to be perpendicular to the boundary.

3 Results

In the grid refinement study of a free jet starting with the base mesh $b1$ (see Table 1), our goal was to examine the effect of radial, azimuthal and streamwise grid spacing on the results. These three grid parameters were believed to affect the outcome of the LES. The refinement in azimuthal direction was done by changing the cell number parameter Ψ. The refinement in the streamwise direction was accomplished by changing the cell number X. Because the block structure of the grid does not allow a purely radial refinement in the whole domain, radial grid refinement was accomplished by changing the R_1 and R_2 parameters simultaneously. The cell distribution properties remain unchanged along the edges in the refinement procedure. The results are discussed in terms of turbulent kinetic energy (k), Reynolds-stresses $\overline{u'u'}$, $\overline{v'v'}$, $\overline{w'w'}$ $\overline{u'v'}$ (u', v', w' are fluctuation velocity components in the cylindrical coordinate system) and momentum thickness of the shear layer (θ_m). The LES_IQ_ϕ value was computed for TKE and the Reynolds stresses. The simulation data was azimuthally averaged at $r = 0.5D$ in the shear layer of the jet. The discussion is limited to this location.

3.1 Baseline Grid Simulation Study

In the present study the $b1$ mesh was refined with a factor of $\beta = 2$ in all three direction x, ψ, r (simulations: $b1_{x2}$, $b1_{\psi 2}$, $b1_{r2}$). The total value was estimated using $\beta = \sqrt{2}$ in each direction ($b1_{all\sqrt{2}}$), corresponding to a cell number increase by a factor of $2\sqrt{2}$, which was believed to be adequate for the extrapolation. The results can be seen in Fig. 2, and the LES_IQ_ϕ values in Fig. 3.

In terms of the k values, only the globally ($b1_{all\sqrt{2}}$) and the streamwise ($b1_{x2}$) refined grids have changed the results significantly. These results suggest that only refinement in the streamwise direction has significant effect. Considering the normal components of the Reynolds-stresses, it can be seen that the k value is increased because of the $\overline{v'v'}$ and $\overline{w'w'}$ stresses, while the streamwise fluctuation $\overline{u'u'}$ has not changed. The dynamically important shear stress $\overline{u'v'}$ shows that the cell doubling in the streamwise direction has significant impact, but the global refinement only has a small effect and other refinements have not changed the results. The momentum thickness of the shear layer also shows that the streamwise refinement has changed the results. Additionally, the azimuthally refined grids also have some impact on θ_m.

Since the azimuthal and radial grid refinement does not have significant impact on the results, it was investigated to see what would be the impact of a grid coarsening in these directions. The grid resolution of $b1$ was halved in the azimuthal and radial directions and the results of the simulations were plotted in Fig. 2 along with the refined grid data. It became clear that both

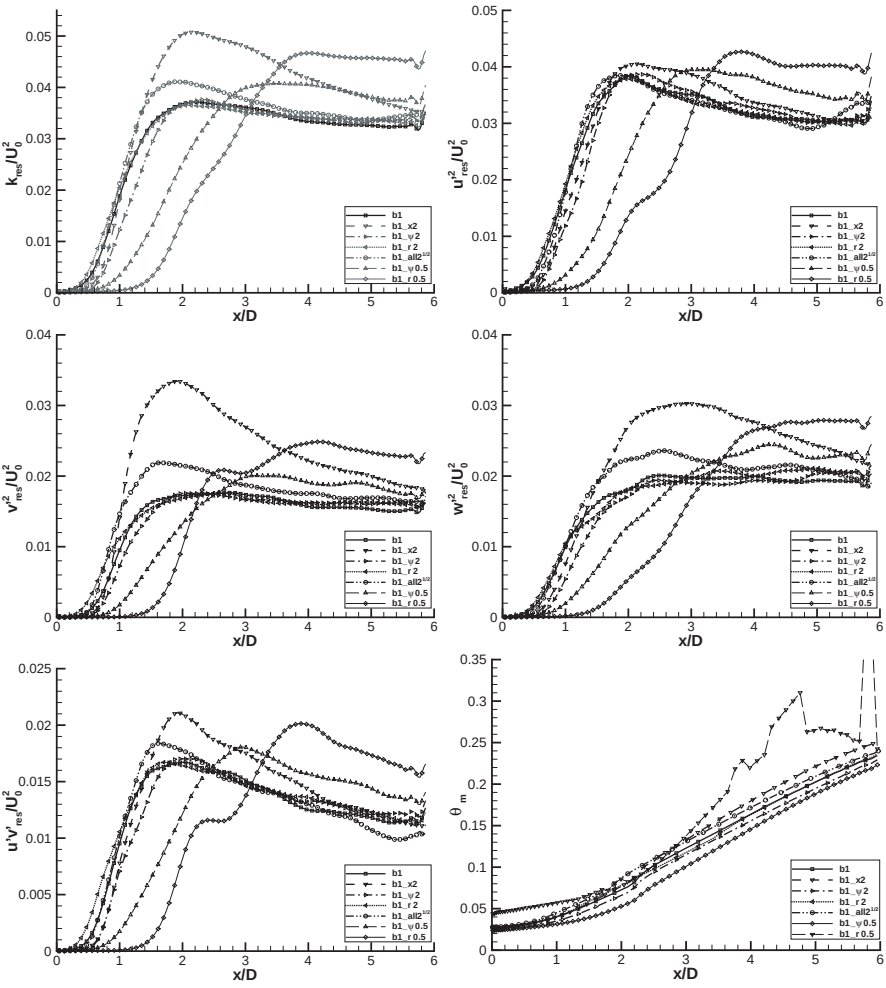

Fig. 2 TKE, Reynolds stress components and momentum thickness for the $b1$ and its refined meshes

the azimuthally and radially coarsened grids had strong impact on the simulation results. The laminar to turbulent transition (k increase) started further downstream than it did on the $b1$ mesh. The momentum thickness of the shear layer increased with radial coarsening and slightly decreased when coarsening azimuthally.

In Fig. 3 the LES_IQ_ϕ values can be seen. The total value of k was extrapolated by the aforementioned methods of [2] and [8]. For the extrapolation using the method of [8] (setting $n = 2$, $m = 2/3$) a simulation with a modified SGS model parameter is required. The contribution of SGS model is halved ($\alpha = 1/2$), thus $C_s = 1/\sqrt{2}C_{s,ref}$ model parameter was used. Differences

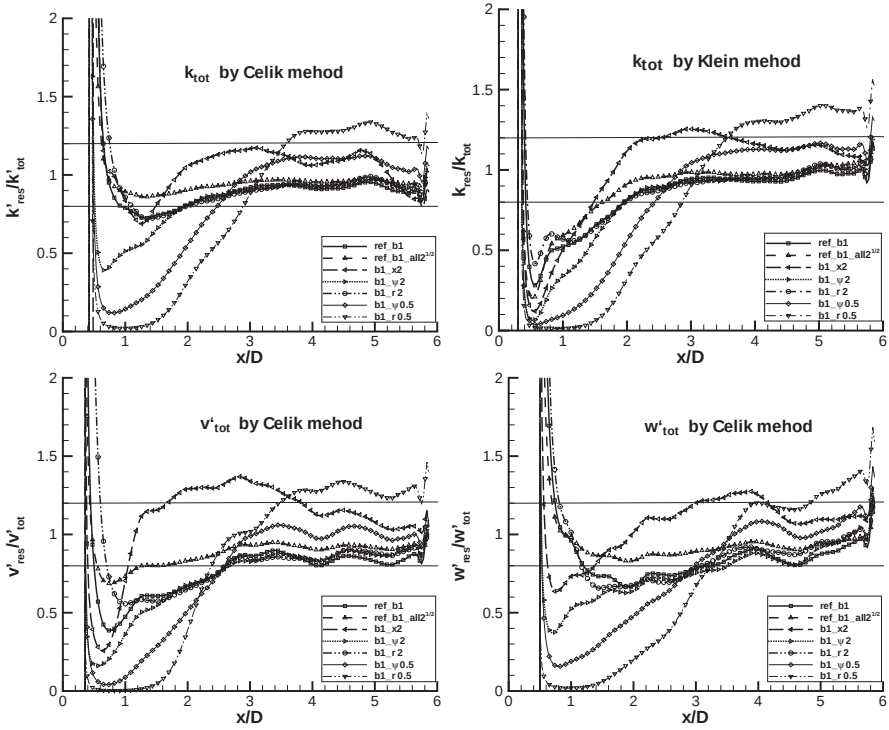

Fig. 3 LES_IQ_ϕ using Celik [2] and Klein [8] method

between the two extrapolation methods can be observed in the $0.4D < x < 2D$ region. Considering the $x > 2D$ part of the curves, all the refined grids run in the range 1 ± 0.2 with [2] and there was only a small overshoot for k using [8]. This shows that the $b1$ mesh and all the refined ones can be accepted as good LES. However the LES_IQ_ϕ of the Reynolds-stresses $\overline{v'v'}$ and $\overline{w'w'}$ indicates that the streamwise refined grid result run out of the aforementioned range.

3.2 Streamwise Grid Refinement Study

Since the streamwise refinement had strong impact on the results, a study on the streamwise refinement was carried out and presented in Fig. 4, using $\beta = \sqrt{2}, 2, 2\sqrt{2}, 4, 8$. Turbulent kinetic energy and Reynolds stresses showed oscillatory convergence behaviour. For clarity, the dependence on the streamwise grid spacing was extracted at $x = 3.5D$ for k and θ_m. From the complete streamwise study emerged that streamwise refinement has strong influences on the normal and spanwise fluctuations, but the effect on streamwise fluctuation and shear stress is not significant.

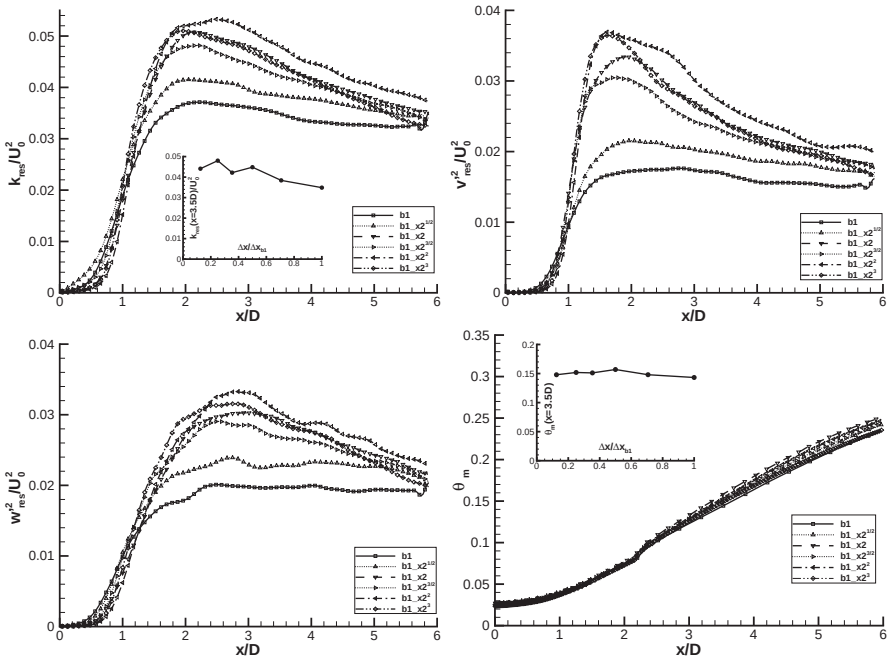

Fig. 4 TKE, Reynolds stress components and momentum thickness for the $b1$ and its streamwise refined meshes

3.3 Refined Grid Simulation Study

A further investigation in directional grid refinement was carried out on the $b1_{x4}$ mesh, which was chosen as the $b2$ base mesh and refined in the same manner as $b1$. The results are depicted in Fig. 5. All of the Reynolds stresses were affected by the refinement in any direction. The strongest impact can be seen on the $\overline{v'v'}$ and $\overline{w'w'}$ stresses. Radial and global grid refinement considerably changed the point of laminar to turbulent transition. The momentum thickness plot also supports this conclusion. Streamwise and azimuthal refinement had effect on the momentum thickness but radial refinement had the strongest impact. According to the LES_IQ_k diagrams none of the meshes satisfy the 1 ± 0.2 criteria except in small regions. However the $b2_{r2}$ mesh was closer to the given range. This refinement study indicates that further directional refinement investigations are needed using the $b2_{r2}$ grid as the base mesh.

3.4 Coherent Structure Behaviour

Since the main question in LES is the accurate resolution of the large (smooth) scales, in this section we have compared the instantaneous flowfields in terms of vortical structures. The vortices are defined as the regions of positive Q,

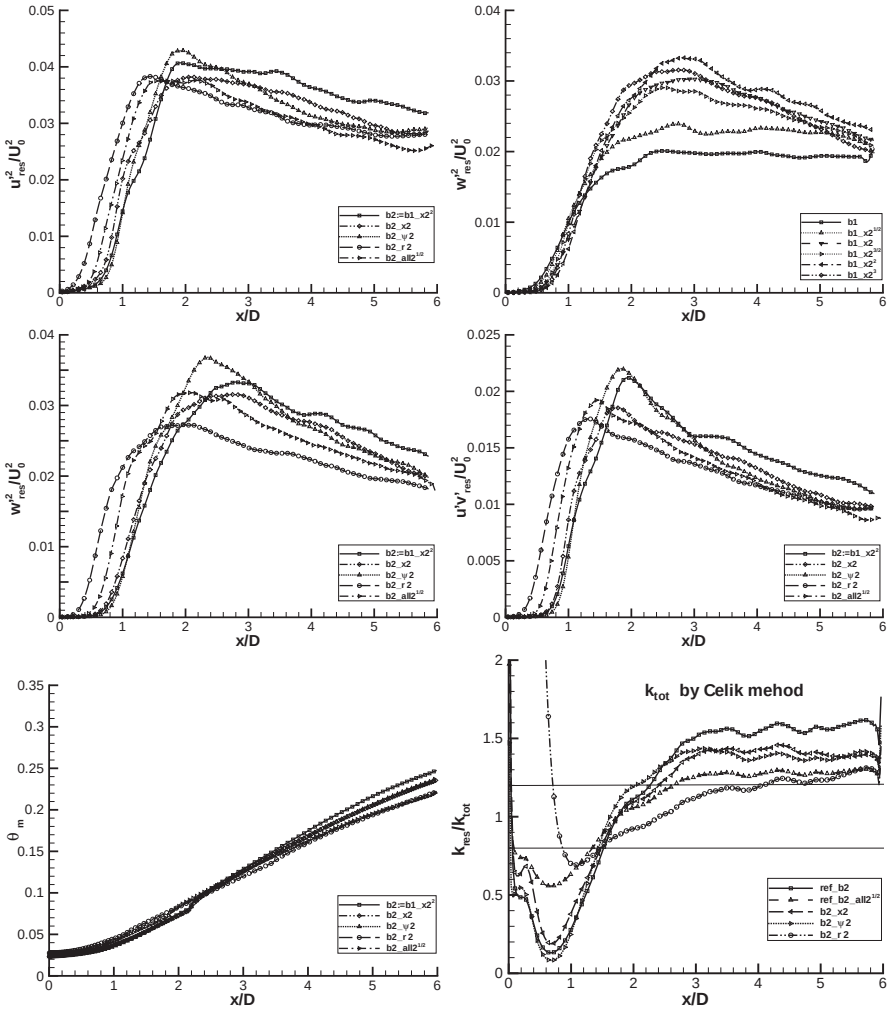

Fig. 5 Reynolds stress components, momentum thickness and LES_IQ_k using [2] for the $b2$ and its refined meshes

which is the second invariant of the velocity gradient tensor [6]. Moreover, positive Q regions show the rotation dominated part of the flow. In Fig. 6 the contours of Q can be seen in the half centre plane together with the rendered isosurface of $Q = 0.2U_0^2/D^2$. These pictures are snapshots of the typical flow structures at arbitrarily chosen simulation time. The formation of Kelvin-Helmholz rollers can be seen at the inlet in the shear layer (where $\partial k/\partial x > 0$) and downstream they are tearing and tilting ($\partial k/\partial x < 0$). It can be seen that on the streamwise refined grid $b1_{x2}$ and $b2$ the intensity of the structures were increased while their size remained approximately the

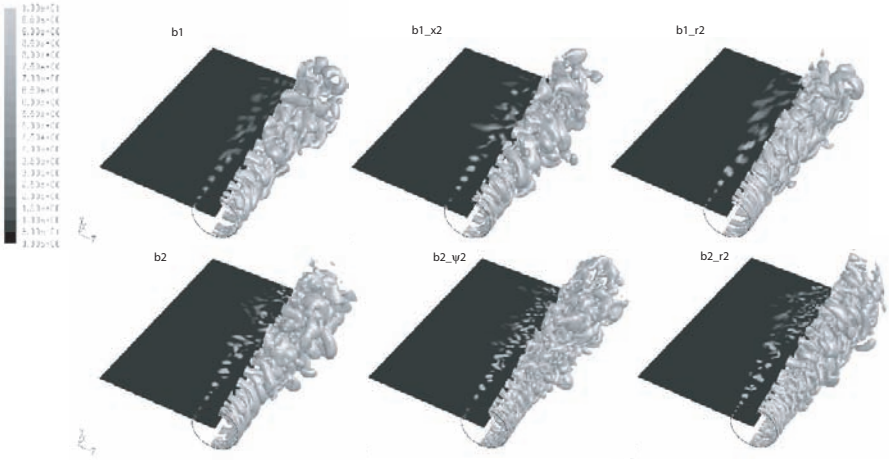

Fig. 6 Q contours in the $y = 0, z < 0$ half-plane and rendered $Q = 0.2U_0^2/D^2$ isosurfaces

same. Smaller, but significant intensity growth could be observed in the case of radially refined grid $b1_{r2}$. In this case the rollers were smoother. These observations support the averaged variable results, where only the streamwise refinement had considerable effect. Considering only the refined grids of $b2$, the $b2_{\psi 2}$ and $b2_{r2}$ show significant changes in the vortex topology. For azimuthal refinement ($b2_{\psi 2}$) the structures were more detailed compared to $b2$ or $b2_{r2}$. On the radially refined grid ($b2_{r2}$) the rollers were created further upstream. Both $b2_{\psi 2}$ and $b2_{r2}$ meshes changed the averaged flow field results as well as the coherent structure topology.

4 Conclusion

In this paper, a proposal for a method has been made to check the anisotropy of computational cells used for LES. The grid refinement study was carried out for a high Reynolds number axisymmetric shear layer simulation. Two conclusions can be drawn from the experiences.

The first one concerns the applicability of the proposed method. It was found that refining the grid in each direction separately highlighted the most under-resolved edges of the grid structure. Therefore, for such grids, the global refinement was inefficient for improving the LES. Taking into consideration individually the components of the Reynolds stress tensor is interesting, since the components are affected differently. An unreliability associated with using the Index of Resolution Quality method of [2] was found through this investigation. One possible reason for this unreliability is that the anticipated monotonic grid convergence was not present (as found in the streamwise refinement study, Sect. 3.2).

The second conclusion is related to the shear layer simulation. The results are believed to help in the understanding of the deficiencies of LES of such flows. The grid resolution in the streamwise, azimuthal and radial directions of the domain were systematically changed. The radial refinements were found to differently influence the results depending on the actual resolution. For a finer streamwise grid, the spatial transition was changed by the radial refinement. The streamwise refinement has notable impact on only the radial and azimuthal fluctuations. Though the grid refinement had a strong influence on the turbulence characteristics, the investigated integral parameter of the flow did not depend strongly on the grid resolution, which supports the general concept that LES is able to reproduce the smooth averaged flow features even at low resolution of TKE.

The vortex extraction method proved to be a useful tool for the explanation of the physical changes caused by the grid refinement, although further work is needed for its complete understanding.

References

1. Bogey C, Bailly C,Juve D (2003) Noise investigation of a high subsonic, moderate Reynolds number jet using a compressible Large Eddy Simulation. Theoretical and Computational Fluid Dynamics 16(4):273–297
2. Celik I, Cehreli ZN, Yavuz I (2005) Index of resolution quality for Large-Eddy Simulations. Journal of Fluids Engineering 127:949–958
3. Crow SC, Champagne FH (1971) Orderly structures in jet turbulence. Journal of Fluid Mechanics 48:547–591
4. Fluent, Inc. (2006) Fluent 6.3 User's Guide
5. Geurts BJ, Frohlich J (2002) A framework for predicting accuracy limitations in large-eddy simulation. Physics of Fluids 14(6):L41–L44
6. Hunt JCR, Wray AA, Moin P (1988) Eddies, streams, and convergence zones in turbulent flows. In: Proceedings of the Summer Program, Center for Turbulence Research, Stanford
7. Kim SE (2004) Large Eddy Simulation using unstructured meshes and dynamic subgrid-scale turbulence models. In: 34th AIAA Fluid Dynamics Conference and Exhibit, Portland, Oregon
8. Klein M (2005) An attempt to assess the quality of Large Eddy Simulations in the context of implicit filtering. Flow Turbulence and Combustion 75:131–147
9. Mathey F, Cokljat D, Bertoglio JP, Sergent E (2006) Assessment of the vortex method for Large-Eddy Simulation inlet conditions. Progress In Computational Fluid Dynamics 6(1–3):58–67
10. Pope SB (2004) Ten questions concerning the large-eddy simulation of turbulent flows. New Journal of Physics 36(6):1–24, 2004
11. Vreman B, Geurts B, Kuerten H (1996) Comparison of numerical schemes in large-eddy simulation of the temporal mixing layer. International Journal for Numerical Methods in Fluids 22(4):297–311

Part III

Modelling and Error-Assessment of Near-Wall Flows

Expectations in the Wall Region of a Large-Eddy Simulation

Philippe R. Spalart[1], Mikhail Kh. Strelets[2], and Andrey Travin[2]

[1] Boeing Commercial Airplanes, Seattle, WA 98124, USA
philippe.r.spalart@boeing.com
[2] New Technologies and Services, St.-Petersburg 197198, Russia
strelets@mail.rcom.ru

Abstract. The expectations fall into two categories. The first relates to the method and how general it should be, how applicable to unstructured grids in complex three-dimensional geometries and very high Reynolds numbers, even if the exercise uses a structured grid in a two-dimensional flow at moderate Reynolds number. The viewpoint is that there should be a known path from the research activity to the creation of a machine or the prediction of weather. If not, the gap in this path takes on a high priority and the work is labeled as preliminary. An example of such a litmus test is whether the grid design requires knowledge of the direction of the skin friction. The second category relates to the fidelity of the description of the turbulence which can be assembled. As an example, the shear stress in a wall-bounded LES is calculated quite well as the sum of a viscous stress, a "modeled" Reynolds stress, and a "resolved" Reynolds stress. However, the same has not been achieved for the other Reynolds stresses, unless the grid is such that Quasi-Direct Numerical Simulation is taking place. Higher-order quantities are even more troublesome. We also discuss a remedy to Log-Layer Mismatch called "Energized Wall-Modeled LES" which is most simple, cost-free, and compatible with grids that are useable in practice. The added term provides visible extra activity, and improves all the Reynolds stresses in addition to the mean velocity.

Keywords: Quality, Reliability, Versatility, Applicability, Large-eddy simulation

1 Introduction

The primary content of this paper is opinion over what are the best priorities in Large-Eddy Simulation, and more generally in turbulence research. In this, the first author's affiliation with industry and brief activity in Atmospheric Boundary Layers has an influence, but is not overwhelming. In simple terms, two distinctions may be made. The first would oppose the "romantic" and the "practical" visions of turbulence research. The second would oppose the "supply" and the "demand" visions. These distinctions are not identical, but

J. Meyers et al. (eds.), Quality and Reliability of Large-Eddy Simulations,

they are correlated in the community. The views advocated here probably differ from those of many attendees at this workshop, but debate is useful. Some of the comments merely extend those made in 1997 when introducing DES [1], but others stem from experience with Wall-Modelled LES (WMLES), particularly in the study by Nikitin et al. [2].

In the romantic vision, research is certainly not done to build weapons or even other machines, let alone to make money (weather and climate forecast receive somewhat more respect). The objective is beauty in resolving questions, which were created by real-life turbulence but have acquired a value of their own. Funding from agencies and companies with practical purposes is accepted, and careers are built. In the practical vision, the needs of the community to predict and manage turbulence in the real world are always kept in mind, although often with a long-term view, sometimes fifty years. An example of romantic problem is that of possible finite-time singularities in the Euler equations; the argument that these are related to the energy cascade (which occurs in real life) is thin. A more extreme example would be to study the Navier-Stokes equations in four dimensions. A less extreme example is to study Decaying Isotropic Turbulence in great depth. There is a tendency in some circles and especially in RANS modelling to approach all turbulent flows as a perturbation of DIT, which has no rational basis and is counter-productive.

Again using simple words, LES studies with a fixed filter width, and grid refinement until the solution is highly accurate, follow the romantic vision. A vision which also has merit considers that the Navier-Stokes equations supplemented with an SGS model, itself tied to a filter of arbitrary size, do not deserve a very accurate solution. This vision considers the SGS model itself as an "error term," which is reduced by narrowing the filter. In simple situations, the eddy viscosity scales with $\epsilon^{1/3}\Delta^{4/3}$ with ϵ the dissipation rate and Δ the grid spacing. Romantic researchers would probably not dispute the idea that making the filter and grid size about the same makes the best use of a given amount of computing, as it allows the resolution of "as much turbulence" as the grid can support. Practical researchers thus view the problem of LES with a fixed filter size as artificial.

Turning to supply and demand, the supply vision considers that the only responsibility of the research community is to provide increasing knowledge and performance, for instance measured by Reynolds number. In numerical work, this kind of progress is guaranteed by the steadily increasing computing power, whereas experimentalists receive only modest help from new technology. In DNS algorithms, no drastic advances have been made in many years, and none are likely in the future. This is for simple geometries, in which spectral methods have been dominant; for complex geometries, much remains to be done to produce a very-low-dissipation shock-capturing unstructured-grid system. The estimate by Moin and Kim [3] that DNS will be possible for airplanes around 2080 with 10^{16} grid points has not been challenged. Disappointingly, recent years have allowed an order-of-magnitude increase in Reynolds number

over the first viable DNS runs, but a much finer determination of the Karman constant, for instance, has been surprisingly resistant. Many studies have shown that LES with near-resolution of the wall layer is roughly 10 times less expensive than DNS. This is helpful, but worth roughly a factor of $10^{1/4}$ in Reynolds number, a small ratio. Another measure is that this approach might be workable in 2074 rather than 2080. This is Quasi-Direct Numerical Simulation, or QDNS, with eddy-viscosity levels of only a few times the molecular viscosity [1]; it is also called "Wall-Resolved LES" by colleagues who have more appreciation for it than present authors do. A valid question to them is: what is the exact purpose of such work? It seems not to contribute to real-life predictions, and also not to constitute pure research, unlike DNS, because it contains an adjustable empirical model and the grid cannot be refined or coarsened much while retaining the same nature of the simulation.

The "demand" view is that much higher Reynolds numbers are needed in the general fields of transportation and weather, so that an LES method is a worthwhile goal only if it allows a quantum leap in Reynolds number. This leads to the position that Wall Modelling remains the principal challenge in LES research. In general, it may be more useful to start from a general method and improve its accuracy, than to restrict work to cases which can be treated accurately and marginally extend the range of such cases.

The advantage of WMLES extend beyond Reynolds number. For instance, it can accommodate rough walls, whether the rough surface is a shirt, a lawn, or a parking lot. Other effects such as non-uniform transpiration can be modelled in a statistical sense.

The arguments in favor of DES [1] do not need to be repeated in detail here. Again the estimate that WMLES of a wing will become possible around 2045 with 10^{11} points has not been challenged to the authors' attention. However, simulations with over 10^9 points are imminent, which may indicate that the rate of increase in computing power has been faster than assumed in 1997. Alternatively, these simulations may not involve generalized coordinates, nor run over the number of time steps deemed necessary for the wing, namely 5×10^6. The wing problem involves a boundary-layer thickness much smaller than the airfoil chord, itself smaller than the span, which in turn is smaller than the length of the trailing vortices which need to be established. The wing simulation suffers from a disparity of both length and time scales, while internal and "academic" turbulence modules may not suffer disparities as severe, making it easier to reach an impressive number of grid points without going through so many eddy turnover times.

While DES is recognized as necessary for large thin boundary layers, the trend to address thicker boundary layers with WMLES instead of RANS, including inside a DES, has been undeniable. It presents a hope of breaking the "accuracy barrier" of RANS in predicting separation. However, it is far from a simple endeavour. The principal obstacles are "Log-Layer Mismatch" or LLM which is discussed at length, and the creation of LES content in an attached boundary layer, which is not discussed here.

2 Grid Design and Wall Modelling

The y axis is normal to the wall, x is in the flow direction, and z lateral. The grid spacings are denoted by Δ, and $\Delta_{\|}$ is representative of Δx and Δz (which are often equal in what follows).

2.1 Wall-Normal Grid Distribution

The established RANS practice requires a first y^+ of about 1, followed by prudent stretching, with a ratio of 1.25 at the most, and then by more nearly uniform spacing in the outer layer. It has worked in WMLES also, when using "integration to the wall" and aiming at cubic cells in the outer layer. Note that the concept of "working" is relative, in the sense that one could possibly blame this practice for LLM, or other problems. The limits on y^+ and stretching ratio derive directly from the logarithmic profile, and the cubic cells provide harmony between the three directions. This could not be the very best manner in which to allocate grid points, especially if one had the freedom of unstructured grids.

At increasing Reynolds numbers, the number of y grid layers increases, but only logarithmically: roughly like $5 \times \log(Re)$, if the stretching ratio is 1.2 [2]. This is very manageable. This integration to the wall creates shallow grid cells, in which RANS reasoning is justified, which constitutes a "theoretical windfall." On the other hand, if the behaviour of the turbulence in cells from $y = 0$ to $y \approx \Delta_{\|}$ is very predictable, a wall-function approach is essentially just as justified physically. It is, however, more difficult to design, program, and keep stable.

2.2 Wall-Parallel Grid Cell Area

Many discussions have centred on the wall-parallel spacings in wall units, Δx^+ and Δz^+, but with upcoming remarks specifically on the aspect ratio $\Delta x^+/\Delta z^+$, it is logical here to address the area $\Delta x^+ \Delta z^+$. The argument against QDNS is not new. An LES method with engineering and weather-forecast potential needs wall modelling, allowing unlimited values for $\Delta x^+ \Delta z^+$, rather than the values around 150 in DNS and maybe 500 in QDNS. WMLES has been exercised at 4×10^6 with impunity. This is not very easy, LLM being the first difficulty, but it is not out of reach any more (§4), and the current level of motivation in the community is gratifying. In fact, the intermediate régime with $\Delta x^+ \Delta z^+$ in the range of a few thousands is more difficult than the fully-fledged wall-modelled régime.

2.3 Wall-Parallel Grid Aspect Ratio

In DNS of two-dimensional flows, it is a fine tradition that the longitudinal grid spacing Δx^+ is about three times larger than the lateral spacing Δz^+,

with values in the vicinity of 21 and 7. This is well justified by examination of the spectra in x and z. Recent DNS work in a three-dimensional but predictable flow, the Ekman layer, aligns the grid in that manner by rotating the freestream vector [4]. These simulations, on structured grids, continue the anisotropic patch shape into the outer region of the flow, out of convenience, even though the anisotropy of the smaller eddies is different, and the Kolmogorov length scale has grown, albeit only like $y^{1/4}$.

The 3-to-1 aspect ratio is also deep-rooted in LES. This is understandable for QDNS, of course, but not as much for WMLES, and one could ask whether it is out of habit. A genuine answer to this would require extensive tests aimed at the computing expense required to reach a certain accuracy. However, such a determination would not have much value to the users of LES, for the following reason.

The flows of interest, for which the accuracy advantage of LES over RANS is worth the expense, all have three-dimensional pressure gradients. These are precisely the flows in which the skin-friction direction is part of the answer, not of the problem statement, so that building it into the grid is not possible. This direction is also very sensitive to parameters such as angle of attack, sideslip, and Mach number. One would have to imagine adaptive gridding with a sensor for the "longitudinal" and "lateral" direction, which would gradually redesign an LES grid while incipient and/or massive separation builds up. Later generations may achieve this, but the conclusion today has to be that a good WMLES method cannot be dependent on the x-z grid aspect ratio. Grid design, including unstructured, needs to produce roughly isotropic cells, and the solver must be tolerant of somewhat different shapes.

3 Resolved and Modeled Reynolds Stresses

When wall modeling is applied, the Reynolds stresses are normally the sum of Modeled and Resolved Reynolds Stresses. It is normal for the Modeled Stresses to rival the Resolved Stresses, even in a simulation of high quality, and a task for the LES research community is to properly represent to the community at large what the correct behaviour is.

3.1 Shear Stress

The stress in question is that in the direction of the mean skin friction. It has very much control, and fortunately its behaviour is well understood. The resolved shear stress is $-\overline{u'v'}$ and, with an eddy-viscosity model, the modeled shear stress is $\overline{\nu_t(u_y + v_x)}$. Figure 1 shows how the two communicate when the grid is refined; the level at which they cross is roughly $1.3\,\Delta_{\|}$. This length scale is equivalent to ν/u_τ for the viscous layer; in DNS, the viscous and Reynolds stress cross at a fixed y^+. At this Reynolds number, the viscous stress is not seen with a linear axis for y. As the grid resolution approaches QDNS, the

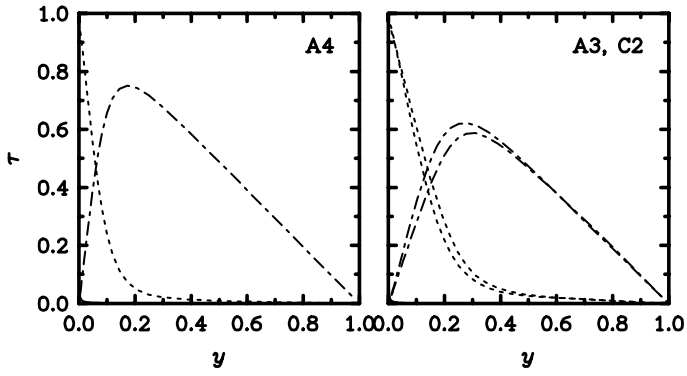

Fig. 1 Components of the shear stress in WMLES. - - -, modeled stress; - — -, resolved stress. *Left*, fine grid; *right*, coarse grid with two codes [2]

modeled stress vanishes. The figure also shows that the scatter when DES is applied in two codes is modest.

The important fact is that, in a successful simulation, the sum of the modeled and resolved shear stresses closely approximates the Reynolds shear stress a DNS would produce. When it does not, the viscous stress $\nu \partial U/\partial y$ must compensate, since the total of the three stresses is imposed, so that U itself is incorrect. This is the essence of LLM and suggests how to remedy it; see §4.

3.2 Other Reynolds Stresses

The stresses besides the dominant shear stress are less well understood, for at least three reasons.

First, the exact or "DNS" behaviour is not known precisely even in a channel, the way it is for the shear stress. It is very plausible that the stresses obey outer scaling of the type $u_\tau^2 f(y/\delta)$ in the outer layer [5]. However, it is now confirmed that they do not obey inner scaling of the type $u_\tau^2 f(y^+)$ in the inner layer, at least at the Reynolds numbers reached. The near-wall peak values show no sign of saturating. Consistently, the stresses do not display the plateau which would be needed to satisfy an overlap argument. It is plausible but not confirmed that u'^2 and w'^2 have a logarithmic layer instead of a plateau [5].

Second, the behaviour of the resolved stresses towards the wall is controlled by the grid spacing in a manner that remains uncertain. As y tends to 0 the DNS spectrum extends to higher and higher wavenumbers k, plausibly with a $1/k$ slope (which gives the logarithmic layer). The LES spectrum is truncated, assuming a structured grid or a similar scaling, which presumably leads to a plateau. However, this is only for u' and w', whereas v' has its own behaviour like the shear stress. The pressure fluctuations, which are most important in

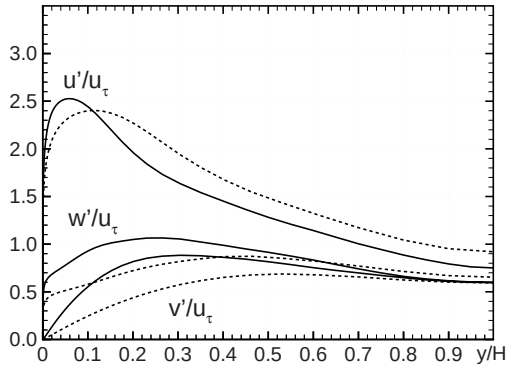

Fig. 2 Resolved diagonal Reynolds stresses in WMLES at $Re_\tau = 20,000$. - - -, coarse grid; —, fine grid

some applications, may have a different pattern yet. This is seen in Fig. 2. Two of the stresses, v' and w', rise on the finer grid as may be expected, but the third one does not rise everywhere, and shows an effect even on the centreline. In addition the asymptotic behaviour is, nearly, for u' and w' to approach the wall as $O(1)$ and v' as $O(y)$, i.e., the inviscid behaviour (they follow y and y^2 in the viscous layer of a DNS, of course). This is due to wall modelling and the high Reynolds number. A look back at the resolved shear stress confirms this: it is close to $O(y)$ behaviour, rather than the viscous y^3. Thus, DNS and WMLES may have drastically different patterns near the wall.

Third, the modeled diagonal stresses produced by a typical RANS model are rather poor. As a result, adding them to the resolved diagonal stresses has little reason to be as successful as it is for the shear stress. One-equation models, of course, produce meaningless diagonal stresses. Two-equation models invariably produce the plateau with $k^+ = 1/\sqrt{C_\mu}$, because their structure leads to the inner and outer laws. They also completely miss the anisotropy which is so pronounced near the wall.

For these three reasons, obtaining accurate diagonal Reynolds stresses from a WMLES is a distant goal. In most applications, it is not an essential one. The wall layer has a dialog with the outer layer based on the shear stress. In other applications, the full rms of a quantity is needed. Pressure comes to mind, for aerodynamic noise purposes, whether community or cabin noise. In such cases, extending the LES spectrum with the correct law, for instance $1/f$, is an option if it is done with care and only after the LES grid is fine enough to indicate the $1/f$ or similar behaviour.

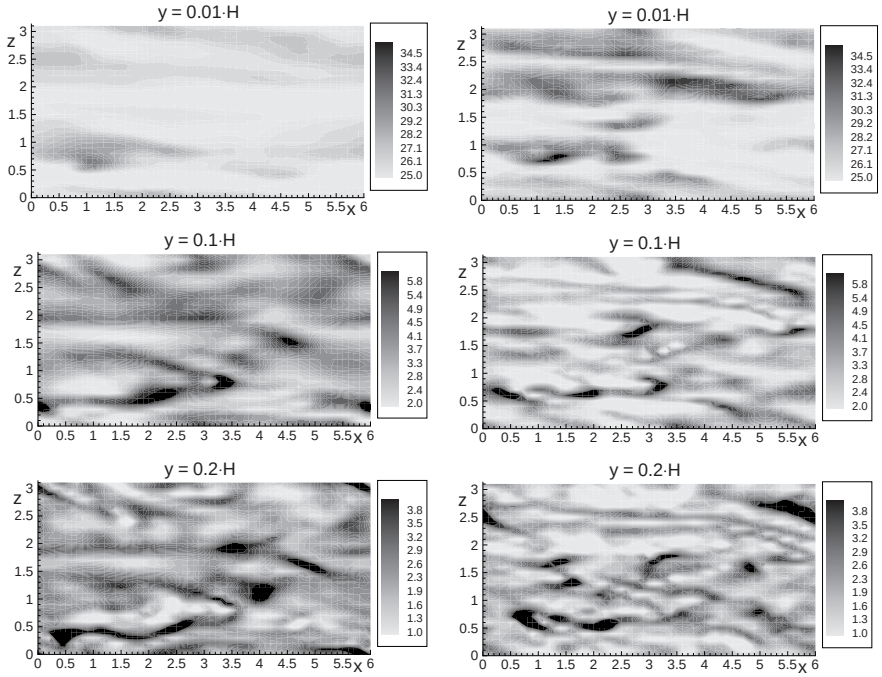

Fig. 3 Response of channel-flow near-wall structures to stimulation. Vorticity magnitude. Grid spacing $\Delta_{\|} = 0.1$. *Left*, simple DES-based WMLES; *right*, EWMLES

4 Partial Solution to Log-Layer Mismatch

This will be called Energized WMLES. This solution is partial in the sense that it has not yet been successfully combined into a non-zonal method with DDES or even the original DES (with $\Delta_{\|}$ large enough to ensure the boundary layer is fully covered by RANS), nor tested with moderate values for Δx^+ and Δz^+, i.e., towards the QDNS régime. On the other hand, it is very simple and applicable to WMLES with any SGS model, for instance Smagorinsky's, pending the calibration of a single constant. It is insensitive to grid aspect ratio and flow direction, and has no need for random numbers, let alone a database. It requires the wall-normal direction, which is physically justified very near a wall, and can be obtained as the gradient of the wall distance. Other approaches to correct sluggish near-wall behaviour in WMLES also are zonal and inappropriate in a RANS boundary layer.

Knowing that LLM is very plausibly linked to a low level of resolved turbulence at heights of the order of $\Delta_{\|}$ [6], the idea is to add a source term to the wall-normal momentum equation,

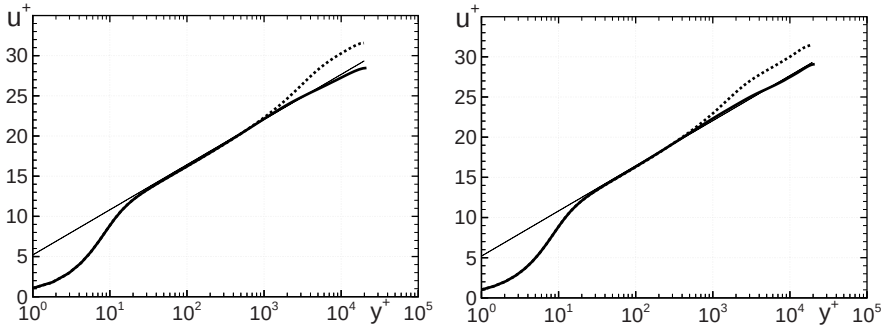

Fig. 4 Response of channel-flow velocity profiles to stimulation. *Left*, coarse grid; *right*, fine grid. - - -, simple DES-based WMLES; — EWMLES

$$\frac{\partial v}{\partial t} = NSE + C_e \; f_e(y) \; \frac{\sqrt{\nu_t S}}{y_0} \; v, \qquad f_e(y) \equiv \sqrt{\pi} \exp\left(-\pi^2 \left(\frac{y}{y_0} - 1 \right)^2 \right), \quad (1)$$

where *NSE* symbolically represents the usual Navier-Stokes terms and S is the modified vorticity of the S-A model (and can be the plain vorticity). The new term boosts the wall-normal fluctuations and therefore the resolved shear stress, and can be adjusted to remove LLM. This was done in channel flow at $Re_\tau = 20,000$ with two grids, one of them fairly coarse ($\Delta_\parallel = H/10$, where H is the channel half-depth) and the other twice as fine in x and z. The effect is clear in Fig. 3; short waves are visibly enhanced. In the outer region, the two simulations are much more similar (not shown).

The involvement of the eddy viscosity ν_t in (1) would probably be helpful when creating LES content in an initially RANS-dominated flow, as high values of the modeled Reynolds stress $\nu_t S$ will naturally stimulate the resolved Reynolds stress. A fair value for the length y_0 is $\Delta_\parallel$, and typical grids will allow an accurate enough resolution of the Gaussian f_e in the y direction. Other functions than the Gaussian which integrate to y_0 would also work, as would somewhat narrower or wider Gaussians. The value of 1.08 for the constant C_e suppresses LLM well in Case C1 of Nikitin et al., which has equal spacing in x and z. This is seen in Fig. 4, which also confirms agreement between the present solutions and those of Nikitin et al. [2]. In addition, the response to grid refinement is good. Without EWMLES, the mismatch merely moves to lower values of y/H when the grid is refined; this is fully consistent with the scaling of errors in the "super buffer layer" with grid spacing. With EWMLES, there remains a much fainter imperfection in the log law, which also "slides" down during grid refinement.

Another view at the hidden limitations of EWMLES in this preliminary version is that it was applied only to channel flow, in which the average wall-normal velocity $\overline{v}$ is zero. In that sense, it would be more accurate to write (1) with $C_e f_e(y) \sqrt{\nu_t S}/y_0 \; (v - \overline{v})$, which brings up the issue of defining $\overline{v}$ in

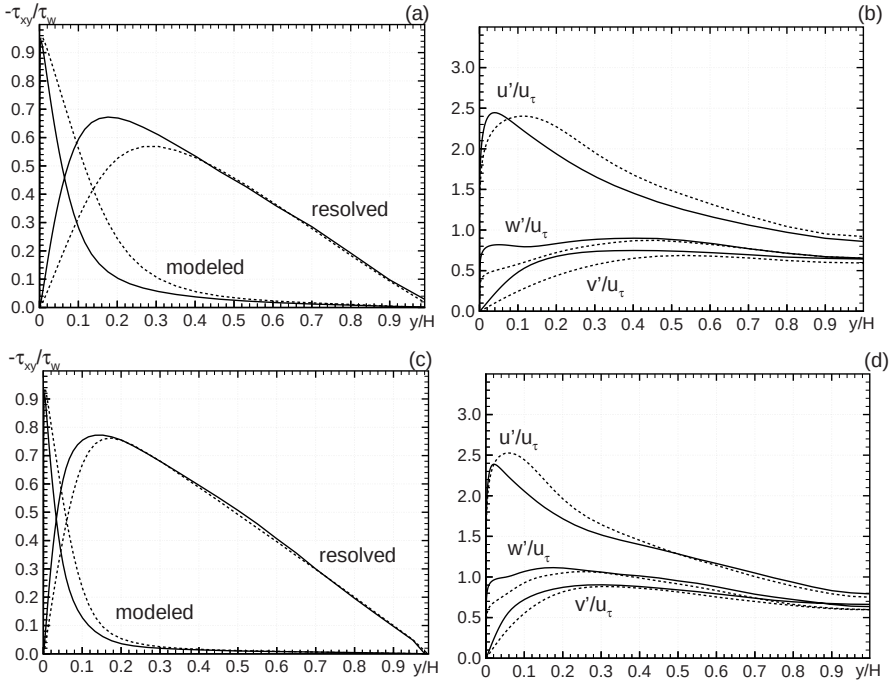

Fig. 5 Response of channel-flow Reynolds-stress profiles to stimulation. - - -, simple DES-based WMLES; —, EWMLES. *Left*, shear stress; *right*, diagonal stresses. *Upper row*, coarse grid; *lower row*, fine grid

general. If $\overline{v}$ is defined by a local filtering operation, the method will resemble the application of a negative eddy viscosity (an idea which the authors have encountered while reviewing recent manuscripts).

Figure 5 presents the Reynolds stresses, with both the effects of EWMLES and of grid refinement. A modeled component is plausible only in the case of the shear stress; for the others, only the resolved stress is shown. The effect of EWMLES on the shear stresses is dramatic: the modeled stress is down by almost half at $y = \Delta_{\|}$. This is consistent with Fig. 4, in that the shear rate dU/dy with LLM is too high by nearly a factor of 2 in that region. The response to grid refinement is correct. With EWMLES the diagonal stresses similarly approach the wall with noticeably higher values, and accentuate the "inviscid" pattern mentioned earlier. Just like grid refinement, EWMLES tends to raise v' and w', but to lower u' over most of the layer.

To summarize, EWMLES may represent a fruitful research direction. It is an illustration of the "demand" view of turbulence research, in that it was strongly constrained to be compatible with grids of simple designs, even unstructured, and not to need any large source of knowledge such as a database (nor even random numbers). This continues the constraints which were set by

Nikitin et al. [2]. The compatibility with overall DES capability is another matter.

5 Outlook

The "vision" comments made do not imply that research is ever completely wasted; in a sense, all problems are worth solving. However, problems in turbulence are so numerous, stubborn and inspiring that identifying the ones with the highest value to society and a hope of progress is not just a trivial matter of survival for the research community. It's part of the mission.

The comments on expectations of fidelity, principally in the realm of WMLES, are not very deep but offer a viewpoint relevant to the validation and comparison of approaches. In addition, the observation from Figs. 1, 2 and 5 that the resolved Reynolds stresses in a high-Reynolds-number WMLES approach the wall with the power laws valid in inviscid flow appears new.

Energized Wall-Modelled LES was presented as work in progress, as much for its simplicity and self-sufficiency as for its accuracy. Still, it conclusively improved both the mean velocity and the Reynolds stresses. It probably deserves testing with other wall models than DES.

References

1. Spalart PR, Jou W-H, Strelets M, Allmaras SR (1997) Comments on the feasibility of LES for wings, and on a hybrid RANS/LES approach. First AFOSR International Conference on DNS/LES, Aug 4–8, 1997, Ruston, Louisiana. In: Liu C, Liu Z (Eds) Advances in DNS/LES. Greyden, Columbus, OH
2. Nikitin NV, Nicoud F, Wasistho B, Squires KD, Spalart PR (2000). An Approach to wall modeling in large-eddy simulations. Phys Fluids 12:1629–1632
3. Moin P, Kim J (1997) Tackling turbulence with supercomputers. Scient Am 276:62–68
4. Johnstone R, Coleman GN, Spalart PR (2008) DNS of the Ekman layer: a step in Reynolds number and cautious support for the log law. Phys Fluids, submitted.
5. Spalart R (1988) Direct simulation of a turbulent boundary layer up to $R_\theta = 1410$. J Fluid Mech 187:61–98
6. Keating A, Piomelli U (2006) A dynamic stochastic forcing method as a wall-layer model for large-eddy simulations. J Turb 7, Art no 12

Large Eddy Simulation of Atmospheric Convective Boundary Layer with Realistic Environmental Forcings

Aaron M. Botnick and Evgeni Fedorovich

School of Meteorology, University of Oklahoma, Norman, OK 73019, USA
botnicam@ou.edu, fedorovich@ou.edu

Abstract. Initializing large eddy simulations (LES) in meteorological applications typically involves prescribing an idealized background atmospheric environment in which simulations are run. This study investigates LES initialization options using realistic atmospheric environmental forcings. Analysis of several simulated convective boundary layer (CBL) cases highlights common sources of initialization-related errors in LES predictions of CBL structure and evolution as compared to observational data. Effects of initialization errors on simulated features of the CBL for different evolution patterns of daytime environmental atmospheric flow are analyzed. Possible approaches toward dynamic adjustment of environmental parameters in LES of atmospheric boundary layer flows are suggested.

Keywords: Large eddy simulation, Initialization, Convective boundary layer, Atmospheric observations, Meteorological radar profiler

1 Introduction

Turbulent flow structure in the clear convective boundary layer (CBL), which is commonly observed in the lower atmosphere during daytime hours, is primarily determined by buoyant heat transfer from the underlying surface. In conjunction with (wind) shear forcing, whose strength can be variable, this driving mechanism generates turbulent motions on a broad range of scales. This leads to a progressive deepening of the boundary layer as long as the surface buoyant forcing remains strong. The CBL typically develops in the stably stratified ambient atmosphere. Stratification strength is usually expressed in terms of the vertical gradient in the background potential temperature profile. This stratification can be weak (sometimes, almost neutral) – in this case, the CBL grows relatively fast. When stratification is strong, it effectively suppresses CBL growth into the free atmosphere aloft impeding entrainment of quiescent free-atmosphere air into the turbulent CBL core. Previous studies have shown that the surface buoyancy flux (combination of temperature

J. Meyers et al. (eds.), Quality and Reliability of Large-Eddy Simulations,

and moisture surface fluxes) in conjunction with the background atmospheric stratification and wind shear are the principal forcing mechanisms in the atmospheric CBL [10, 8, 12, 14, 2, 3]. Parameters of the ambient atmosphere in LES CBL studies conducted so far were typically prescribed in an idealized form, see e.g. [6]. In these applications, LES was used as a tool to evaluate, qualitatively and quantitatively, various physical mechanisms that determine CBL flow structure (in this respect, LES did a great job) rather than predicting particular features of the CBL flow structure under specific environmental conditions. Exceptions, in this sense, were studies by [12], who initialized their LES of sheared CBL with wind and potential temperature profile data from the U.S. Southern Great Plains (SGP) Atmospheric Radiation Measurement Climate Research Facility (ACRF), and by [4], who used observational data from different platforms during one day of the International H_2O Project (IHOP) field campaign in summer of 2002 to initialize LES of CBL in the vicinity of dryline. These two studies provided valuable, although limited (number of cases studied), information about the abilities of LES to handle real CBL flows coupled with the changing ambient atmosphere.

There is growing demand from the atmospheric remote-sensing community for high-resolution data on turbulence structure in atmospheric boundary layer flows to be used in radar and other remote-sensor simulators (see e.g. [13]). The CBL, where the dominant portion of turbulence energy is carried by large eddies with scales on the order of boundary layer depth, appears to be a natural subject for application of an LES-based turbulence data generator. However, in order to provide data for remote-sensor simulators operating under diverse weather conditions in the CBL, the LES should be able to adequately reproduce CBL turbulence dynamics with actual external forcings.

In the present study, LES runs have been conducted with realistic environmental atmospheric settings corresponding to particular summer days of 2004 and 2007 with clear CBLs observed at the SGP site. Besides providing data for evaluation of a radar simulator, the purpose of these numerical experiments was to evaluate accuracy of LES predictions with respect to various CBL features and investigate possible improvements of the LES settings to make the numerical predictions more accurate. After brief description of the employed LES code in Sect. 2, initialization procedures will be considered in Sect. 3, followed by a presentation of the analyzed LES data in conjunction with atmospheric soundings and radar observations in Sect. 4. Potential improvements of the LES setup will be addressed in Sect. 5.

2 Large Eddy Simulation

The LES code in use for this study employs the subgrid closure from [5]. Detailed explanation of the code can be found in [7], with revised boundary conditions described in [6]. Table 1 presents general LES settings employed. The time step for the LES runs was calculated from stability constraints,

Table 1 Settings of LES

Parameter	Setting
Domain size	5.12 x 5.12 x 4.0 km^3
Grid	256 x 256 x 200
Surface fluxes	See Eq. (9)
Geostrophic wind	Derived from RUC data as in Eq. (10)
Time step	Based on stability conditions: $\sim$ 0.6–1.2 s
Lateral BCs	Periodic for all variables
Upper BCs	Neumann with sponge layer in the upper 20% of domain
Lower BCs	No-slip for velocity; Neumann for θ, q, E (subgrid energy); Monin-Obukhov similarity functions as in [7]
Subgrid closure	Deardorff closure scheme as in [5]

varying between 0.4 and 1.2 s. Flow statistics were calculated every 50 time steps using horizontal averaging. Calculated statistics included means, variances, co-variances, and third-order moments. Simulations were initiated with vertical profiles of u (along x axis) and v (along y axis) components of the wind velocity, potential temperature (θ), specific humidity (q), x and y components of the geostrophic wind (u_g, v_g), and time series of fluxes of temperature ($\overline{w'\theta'}$) and moisture ($\overline{w'q'}$) measured at the underlying surface. The geostrophic wind represents the external forcing related to the horizontal gradient of the large-scale pressure field. Initialization procedure details are presented in Sect. 3. The governing equations for the employed LES are the following:

$$\frac{\partial \widetilde{u}_i}{\partial t} = -\frac{\partial \widetilde{u}_i \widetilde{u}_j}{\partial x_j} + g\frac{\widetilde{\theta}_v - \theta_{v_0}}{\theta_{v_0}}\delta_{i3} - \frac{\partial \widetilde{\pi}}{\partial x_i} + f\left(\widetilde{u}_j - u_{g_j}\right)\varepsilon_{ij3} + \frac{\partial}{\partial x_j}\left[\nu\left(\frac{\partial \widetilde{u}_i}{\partial x_j} + \frac{\partial \widetilde{u}_j}{\partial x_i}\right) - \left(\widetilde{u_i u_j} - \widetilde{u}_i\widetilde{u}_j\right)\right], \tag{1}$$

$$\frac{\partial \widetilde{u}_i}{\partial x_i} = 0\,, \tag{2}$$

$$\frac{\partial \widetilde{\theta}_v}{\partial t} = -\frac{\partial \widetilde{u}_i \widetilde{\theta}_v}{\partial x_i} + \frac{\partial}{\partial x_i}\left[\mu\left(\frac{\partial \widetilde{\theta}_v}{\partial x_i}\right) - \left(\widetilde{\theta_v u_i} - \widetilde{\theta}_v\widetilde{u}_i\right)\right], \tag{3}$$

where $i, j = \{1, 2, 3\}$; t is time, $x_i = (x, y, z)$ are the right-hand Cartesian coordinates, $\widetilde{u}_i = (\widetilde{u}, \widetilde{v}, \widetilde{w})$ represent resolved velocity components, $\widetilde{\theta}_v$ is resolved virtual potential temperature, ν is kinematic viscosity, and μ is molecular thermal diffusivity. Components of subgrid stresses and subgrid θ_v flux, respectively, are represented by $\widetilde{u_i u_j} - \widetilde{u}_i\widetilde{u}_j$ and $\widetilde{\theta_v u_i} - \widetilde{\theta}_v\widetilde{u}_i$. Tildes in these equations represent volume averaging. Normalized pressure, $\widetilde{\pi}$, is defined as $\widetilde{\pi} = \left(\widetilde{p} - p_0\right)/\varrho_0$, where $\widetilde{p}$ is resolved pressure, p_0 is hydrostatic atmospheric

pressure, ϱ_0 is constant reference density, and θ_{v_c} is constant reference potential temperature.

Subgrid stress and θ_v flux are parameterized in terms of subgrid eddy viscosity (K_m) and subgrid eddy diffusivity (K_h) following [5]:

$$\widetilde{u_i u_j} - \widetilde{u}_i \widetilde{u}_j = \frac{2}{3} E \delta_{ij} - 2K_m \widetilde{s_{ij}} \,, \tag{4}$$

$$\widetilde{\theta_v u_i} - \widetilde{\theta}_v \widetilde{u}_i = -K_h \frac{\partial \widetilde{\theta}_v}{\partial x_i} \,, \tag{5}$$

where $\widetilde{s_{ij}} = \left(\partial \widetilde{u}_i / \partial x_j + \partial \widetilde{u}_j / \partial x_i\right)/2$ is the deformation tensor for filtered velocity and E is subgrid kinetic energy, which is determined from the following balance equation:

$$\frac{\partial E}{\partial t} + \frac{\partial \widetilde{u}_i E}{\partial x_i} = 2K_m \widetilde{s_{ij}} \frac{\partial \widetilde{u}_i}{\partial x_j} - K_h \frac{\partial \widetilde{\theta}_v}{\partial x_3} + \frac{\partial}{\partial x_i}\left[2K_m \frac{\partial E}{\partial x_i}\right] - \varepsilon \,, \tag{6}$$

where ε represents the subgrid viscous dissipation rate. Eddy viscosity and diffusivity are expressed through mixing length l and E as

$$K_m = 0.12 l E^{1/2} \,, \;\; K_h = \left(1 + 2l/\Delta\right) K_m \,, \tag{7}$$

where $\Delta = \left(\Delta x \Delta y \Delta z\right)^{1/3}$ is effective grid-cell size, and $\varepsilon \propto \left(E^{3/2}/l\right)$. Subgrid mixing length l is evaluated as

$$\begin{aligned} &l = \Delta \qquad \text{if } \partial \widetilde{b}/\partial z \le 0 \,, \\ &l = \min\left\{\Delta \,,\; 0.5 E^{1/2} / \left(\partial \widetilde{b}/\partial z\right)^{1/2}\right\} \qquad \text{if } \partial \widetilde{b}/\partial z > 0 \,. \end{aligned} \tag{8}$$

A Poisson equation for $\widetilde{\pi}$ is constructed by combining the continuity and momentum balance equations as in [11]. This equation is solved numerically by the fast Fourier-transform technique over horizontal planes, and by tridiagonal matrix decomposition in the vertical.

3 Initialization Procedures

An example of typical initialization of LES with idealized atmospheric profiles is illustrated in panel (a) of Fig. 1; note that $u = u_g$ are held constant during the run as is $\overline{w'\theta'_v}$, with θ represented by a steady linear profile. In this study, LES is initialized with realistic environmental profiles schematically shown in panel (b) of Fig. 1. These realistic environmental settings often include multiple inversions (areas of higher stability) and sharp wind changes with height (wind shears). Under realistic conditions, $\overline{w'\theta'_v}$ at the surface is not

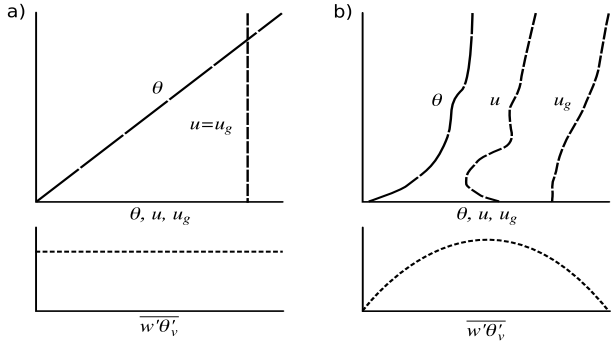

Fig. 1 Schematic representation of idealized (**a**) and realistic (**b**) initial data

taken constant, rather it reflects the evolution of the intensity of solar heating over the course of the day.

Initialization data for this study were collected from the SGP ACRF site in Lamont (north central Oklahoma) equipped with balloon borne instruments and an eddy-correlation system for measurement of surface fluxes. In our LES exercise, only clear CBLs were simulated, narrowing the number of possible cases. Surface fluxes of temperature and moisture were calculated from measured sensible and latent heat fluxes as

$$\overline{w'\theta'} = \frac{H}{\varrho_c\, c_p}\,, \qquad \overline{w'q'} = \frac{LH}{\varrho_c\, L_v}\,, \qquad \overline{w'\theta'_v} = \overline{w'\theta'} + 0.61\theta_{v_0}\overline{w'q'}\,, \quad (9)$$

In the above expressions, $\overline{w'\theta'}$ is surface kinematic temperature flux, $\overline{w'q'}$ is surface kinematic humidity flux, H is sensible heat flux, LH is latent heat flux (heat release from the condensation of water vapor), c_p is specific heat of water, and L_v is latent heat of vaporization. Geostrophic wind components are evaluated from the Rapid Update Cycle (RUC) [1] objective analysis system, these data are available hourly. Geostrophic wind is assumed the same in all vertical nodes of the LES domain. Four RUC grid points surrounding the Lamont (LMN) site are used in calculating horizontal gradients of pressure, deriving the geostrophic wind components as

$$u_g = \frac{-1}{\varrho_c f}\frac{\partial p}{\partial y}\,, \qquad v_g = \frac{1}{\varrho_c f}\frac{\partial p}{\partial x}\,, \qquad f = 2\Omega\sin\phi\,, \quad (10)$$

where f is the Coriolis parameter, Ω is the Earth's angular velocity, and ϕ is the site latitude. Profiles of actual wind, obtained either from RUC and/or from the local sounding at LMN, are interpolated to the vertical nodes of the LES domain. Near-surface portions of these profiles are additionally adjusted in order to match the no-slip condition at the surface, assuming the logarithmic wind profile throughout the lowest LES cell layer.

Two initialization methods were used in this study: local and composite. The local method uses data from the LMN site to obtain initial vertical profiles of θ, q, u, and v, while RUC analyses are used to calculate profiles of u_g and v_g. These profiles are specified only at model initialization time, and are not updated during the run. Surface fluxes, on the other hand, are updated every 30 min. Sounding data for LMN are available every 6 h, with 12 Coordinated Universal Time (UTC) (7 h local time) sounding data used for initialization. The LMN sounding data contain more than ten times that of traditional soundings from U.S. National Weather Service (NWS) sites. This allows more features of vertical atmospheric heterogeneity to be represented in the initial profiles. In contrast, composite initialization uses sounding data from five NWS sites as well as reduced resolution data from LMN aggregated into a single profile via an inverse distance weighted average. This procedure can be used for initialization of LES in locations where local data are not available. Initialized LES is then run for approximately 12 h of simulated time, or until the temperature flux becomes negative (sunset).

4 Case Description and Analysis

In central Oklahoma, only a few summer days normally contain a clear CBL throughout the course of the day. In order to identify clear CBL days, atmospheric radiation data from LMN were used. When no clouds are present, the diurnal distribution of solar radiation flux is represented by a smooth, nearly symmetric curve. As the employed LES uses temporally constant u_g and v_g to account for large-scale pressure forcing, an additional selection criterion was small variability of geostrophic wind throughout the 12 h period of simulation. This condition turned out to be rather restrictive (see discussion below).

The rationale for using atmospheric initialization with realistic environmental settings is to attempt accurate verification of LES statistics via remote-sensing platforms, such as meteorological profiling radars. Meaningful verification is possible if the LES is capable of reproducing a variety of remotely sensed features of the CBL: wind shears (both speed and directional), gradients of temperature and humidity, and capping inversion structure. The elevation, and especially the vertical extent, of the capping inversion are difficult to determine with any precision even in LES. In this study the maximum gradient of θ was used as an indicator of capping inversion height; taken, in turn, as a measure of CBL depth [15].

Pino et al. (2003) [12] attempted similar use of realistic atmospheric settings. However, their initial profiles were low resolution and remained semi-idealized. Their study, nevertheless, suggested that initializing LES with realistic settings was possible. The initial profiles of atmospheric variables in our study matched real atmospheric soundings as closely as possible. We also aimed at closely reproducing the observed sounding after 6 and 12 h of simulation. These times roughly corresponded to midday and sunset.

Prediction accuracy of CBL depth was used as a major criterion for quality of the LES in our application. We labeled a case fair when CBL depth was estimated within a few hundred meters of CBL depth from 0 UTC sounding data (12 h), and winds were in the same direction and close magnitude to those in 0 UTC sounding data. Cases were rated poor if after 12 h, CBL depth was off by a large margin or winds were vastly different from observational data.

4.1 Fair Case – 8 June 2007

Results shown for this case were obtained via the local initialization method, using RUC analyses on a higher-resolution grid (compared to 2004 cases). The considered case represented a unique atmospheric state. During the preceding night, a cold front had passed through LMN, where approximately 1.5 mm of rain fell. At 12 UTC, the upper atmosphere is still in transition between the trough associated with the cold front and the high pressure behind it. The LMN site is under an area of surface high pressure and light winds. Geostrophic wind components are -15 ms^{-1} (u_g) and -5 ms^{-1} (v_g) near the ground, as shown in Fig. 2. Both components considerably (and nearly synchronously) change in the vertical toward the domain top. Twelve h later (0 UTC) the geostrophic wind weakens to near zero as the vast area of high pressure moves further into the central plains.

The vertical wind distribution at 12 UTC displays a low-level jet (LLJ) with the peak wind speed at a height of about 700 m. Near-surface wind shear associated with this jet enhances vertical mixing early in the day. Eventually, as the CBL grows, the LLJ is completely mixed out, and the actual wind distribution becomes close to geostrophic. This can be seen in Fig. 3, where the LES profiles are shown at three times. Atmospheric stratification, according

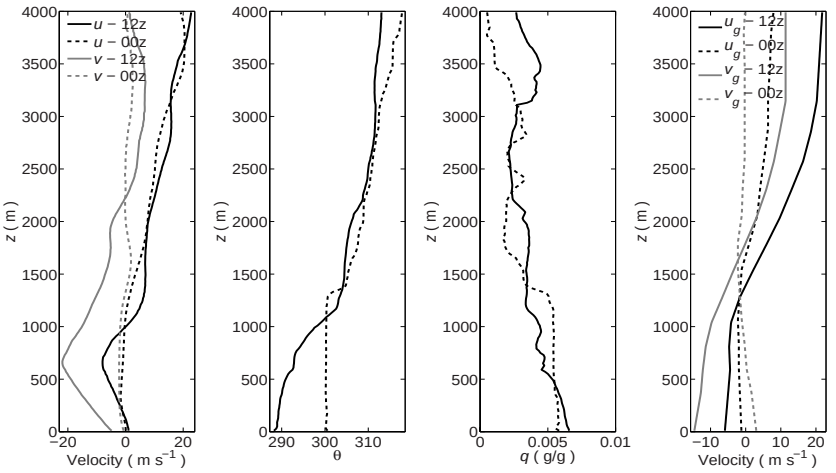

Fig. 2 Initial (12 UTC, *solid lines*) and observed (0 UTC, *dashed lines*) profiles

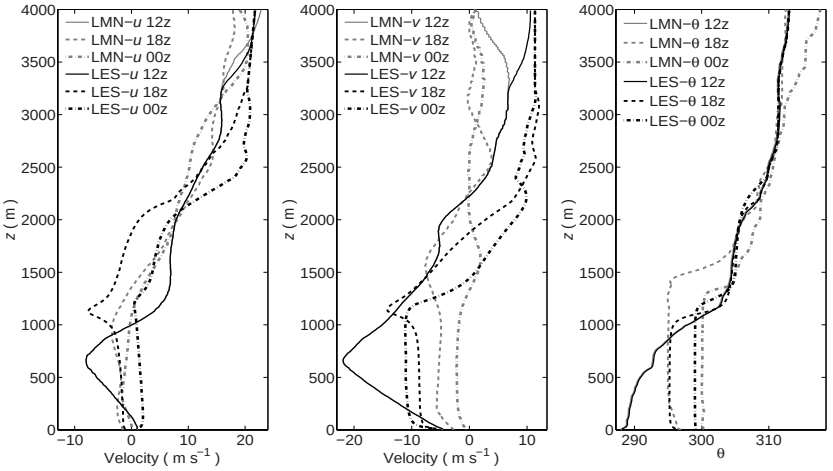

Fig. 3 LES (*black*) and LMN (*gray*) profiles at 12, 18, and 0 UTC for 8 June 2007

to the initial sounding is rather weak throughout the lower 500 m becoming stronger between 800 and 1200 m. This feature causes relatively fast growth of the CBL during the morning hours, with slower growth later in the day. Lamont sounding data at 0 UTC show CBL depth to be about 1300 m, with depth peaking near 1500 m at 18 UTC. A possible explanation for this CBL contraction is the movement of cooler air into the region behind the front that is not captured by the current version of the LES code. However, the CBL evolution predicted by LES for this case decently match the observed temporal changes of CBL depth with time over the main portion of the day. The procedures outlined in Sect. 5, in particular, temporal adjustment of geostrophic wind during the run and accounting for temperature advection, could further improve LES performance under atmospheric conditions similar to those observed in this case.

Meteorological radar profilers are able to detect vertical variability of the CBL structure, as they are sensitive to changes in the refractive index. This index may be directly expressed through air temperature and pressure, and additionally through water vapor mass concentration (specific humidity, q) for humid air. In the refractivity field, the CBL top is clearly seen as the boundary between warm, dry air in the free atmosphere aloft and cooler, moist air inside the CBL. Spatial variability of refractivity is represented by its structure function, C_n^2, defined in [13]. This quantity allows direct calculation from LES data. Radar range-corrected power, η, is related to C_n^2 as $\eta = 0.379 C_n^2 \lambda^{-1/3}$, where λ is the radar wavelength in cm. The LES-derived C_n^2 values for the considered CBL case in this section are compared in Fig. 4 (top panel) with C_n^2 derived from radar profiler measurements at the LMN site for this day. One can see that LES produces C_n^2 fields that closely match the trend in radar

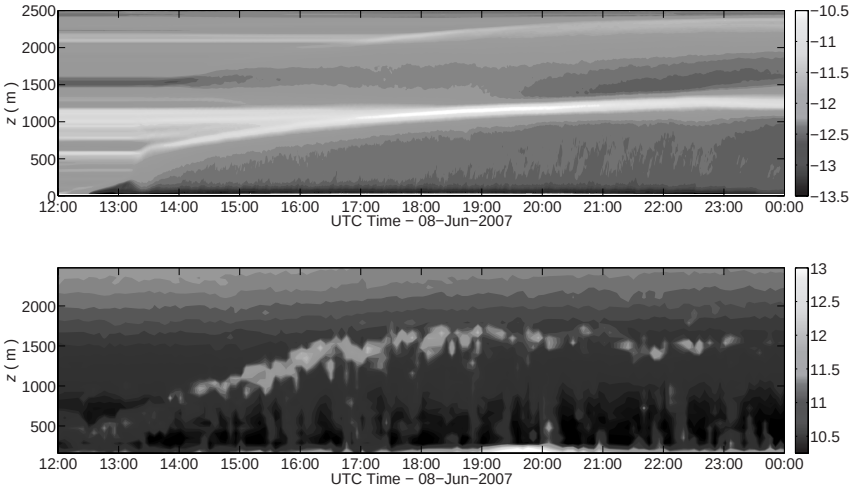

Fig. 4 LES-derived C_n^2 (*top*) and uncalibrated radar-derived C_n^2 (*bottom*)

data. Large values of C_n^2 in both plots show large fluctuations of temperatures and humidity near the CBL top.

4.2 Poor Case – 20 July 2004

Conditions at LMN on 20 July 2004 were characterized by high pressure with an approaching surface low and pre-frontal trough. No rainfall was reported, and winds were light with a 12 ms^{-1} LLJ present. There was minimal warming leading to a slight increase in the background θ profile, and slight changes in the background q profile. Geostrophic wind was almost constant in time in the x direction; however, significant changes took place, over the course of the day, in the y direction, as shown in Fig. 5. It is important to note that the initial θ profile in the considered case is nearly neutral, corresponding to very weak stratification. As a result, by the end of the day, the CBL depth is effectively undefined via sounding data, as mixing of CBL air with weakly stratified environmental air produces a deep CBL with poorly identifiable capping inversion (region with large θ gradient). Overall, the LES well captures this strong mixing and fast growth of the CBL, but it is almost impossible to derive any measurable integral parameters of the CBL (e.g. CBL and entrainment zone depth) for practical applications, see Fig. 6. Although the x component of the actual wind (u) is predicted quite accurately, the y component (v) is off by 8 ms^{-1} and points to the strong over-mixing of the corresponding component of momentum in this case.

Composite profile data were not available for initialization of this case, so it is hard to say whether they would produce better results given the initial background atmospheric state and its evolution over the course of the

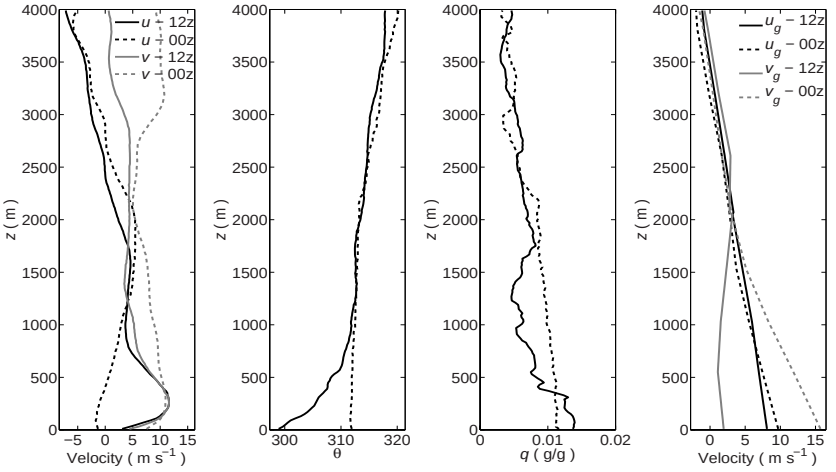

Fig. 5 Initial (12 UTC, *solid lines*) and observed (0 UTC, *dashed lines*) profiles

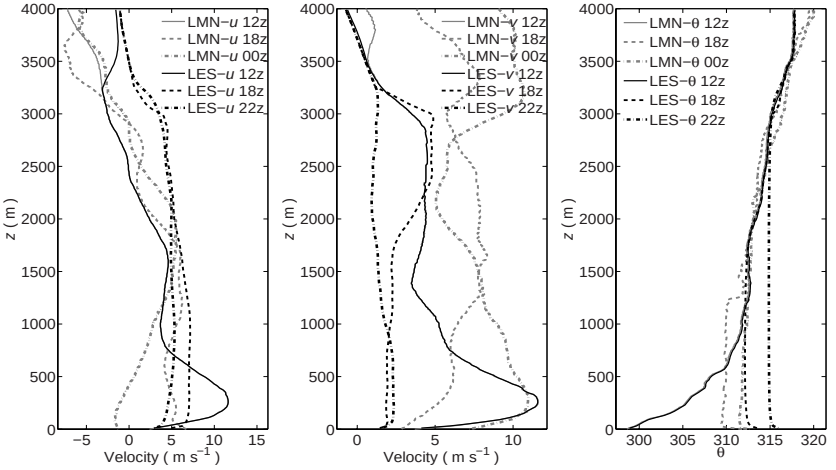

Fig. 6 LES (*black*) and LMN (*gray*) profiles at 12, 18, and 0 UTC for 20 July 2004

day. Apparently, any LES improvements are rather problematic in this case as many of the features that determine the CBL evolution under considered conditions are beyond current capabilities of LES designed for atmospheric boundary layer applications. To adequately account for these features, the LES should either be run in a nested mode with a larger-scale atmospheric model – such option has recently been discussed in [9] – or be fed with data from fine-scale, multi-platform atmospheric observations presently not readily available.

5 Potential Improvements of LES

Eight atmospheric CBL cases were analyzed in the reported LES exercise with the initialization procedures specified in Sect. 3. The performed analyses suggest that certain changes to the LES code may improve the prognostic capability of LES in a realistic atmospheric mode. These changes could include update of geostrophic wind profiles, adjustment of the background θ and q profiles in the process of CBL development, increasing temporal resolution of surface fluxes, and accounting for large-scale temperature advection (thermal wind).

While cases with weak winds and small temporal changes are reproduced well by LES, the majority of simulated cases showed some disparity between output statistics and observational data. With RUC analysis data available hourly, these data can be used to modify u_g and v_g profiles in the LES during the run resulting in a temporally changing geostrophic wind forcing. Availability of surface flux data with 5 min resolution (six time finer than currently employed) would help to more accurately adjust CBL evolution to the primary forcing driving this boundary layer flow.

The employed LES code does not take into account temperature advection associated with baroclinicity (thermal wind). In the context of the present LES exercise, the magnitude of the thermal wind is proportional to the vertical change in geostrophic wind, which can be retrieved from RUC analysis data. Incorporation of temperature advection in the LES equations would allow the θ profile to adjust to this large-scale forcing mechanism. A method for doing this can be found in [14], where LES was applied to simulate baroclinic mixed layers with idealized environmental atmospheric forcings. Generally, advection resulting in the evolution of initial profiles is very likely in the real atmosphere. It would be possible to account for such effects by gradualy adjusting the profiles of θ and q above the CBL, if information about their evolution were available.

Acknowledgements

The authors of this work wish to acknowledge the National Science Foundation (NSF) for their support via grant ATM-0553345. Observational data for this study were obtained from the Atmospheric Radiation Measurement (ARM) Program sponsored by the U.S. Department of Energy, Office of Science, Office of Biological and Environmental Research, Environmental Sciences Division.

References

1. Benjamin SG, Dévényi D, Weygandt SS, Brundage KJ, Brown JM, Grell GA, Kim D, Schwartz BE, Smirnova TG, Smith TL, Manikin GS (2004) An hourly assimilation-forecast cycle: the RUC. Mon Wea Rev 132:495–518

2. Conzemius RJ, Fedorovich E (2006) Dynamics of sheared convective boundary layer entrainment. Part I: methodological background and large-eddy simulations. J Atmos Sci 63:1151–1178
3. Conzemius RJ, Fedorovich E (2006) Dynamics of sheared convective boundary layer entrainment. Part II: evaluation of bulk model predictions of entrainment flux. J Atmos Sci 63:1179–1199
4. Conzemius RJ, Fedorovich E (2007) A case study of convective boundary layer development during IHOP: numerical simulations compared to observations. Mon Wea Rev, to appear
5. Deardorff JW (1980) Stratocumulus-capped mixed layers derived from a three-dimensional model. Bound-Layer Meteor 18:495–527
6. Fedorovich E, Conzemius RJ, Mironov D (2004) Convective entrainment into a shear-free, linearly stratified atmosphere: bulk models reevaluated through large eddy simulations. J Atmos Sci 61:281–295
7. Fedorovich E, Nieuwstadt FTM, Kaiser R (2001) Numerical and laboratory study of a horizontally evolving convective boundary layer. Part I: transition regimes and development of the mixed layer. J Atmos Sci 58:70–86
8. Khanna S, Brasseur JG (1998) Three-dimensional buoyancy and shear-induced local structure of the atmospheric boundary layer. J Atmos Sci 55:710–743
9. Moeng CH, Dudhia J, Klemp J, Sullivan PP (2007) Examining two-way grid nesting for large eddy simulation of the PBL using the WRF model. Mon Wea Rev 135:2295–2311
10. Moeng CH, Sullivan PP (1994) A comparison of shear and buoyancy-driven planetary boundary layer flows. J Atmos Sci 51:999–1022
11. Nieuwstadt FTM (1990) Direct and large-eddy simulation of free convection. In: Proc 9th Internat Heat Transfer Conference 1:37–47. Amer Soc Mech Engrg, New York, Jerusalem, Israel
12. Pino D, Arellano J, Duynkerke PG (2003) The contribution of shear to the evolution of a convective boundary layer. J Atmos Sci 60:1913–1926
13. Scipión D, Chilson PB, Fedorovich E, Palmer RD (2007) A radar simulator based on large eddy simulation for studies of the daytime convective boundary layer. J Atmos Oceanic Technol, submitted
14. Sorbjan Z (2004) Large-eddy simulations of the baroclinic mixed layer. Bound-Layer Meteor 112:57–80
15. Sullivan PP, Moeng CH, Stevens B, Lenschow DH, Mayor SD (1998) Structure of the entrainment zone capping the convective atmospheric boundary layer. J Atmos Sci 55:3042–3064

Accuracy Close to the Wall for Large-Eddy Simulations of Flow Around Obstacles Using Immersed Boundary Methods

Mathieu J. B. M. Pourquie

Laboratory for Aero- and hydrodynamics, dept of Mech Engng, Mekelweg 2, 2628 CD Delft, Netherlands. m.j.b.m.pourquie@tudelft.nl

Abstract. We take a closer look at the behaviour of immersed boundaries close to the immersed boundary. Two kinds of errors usually occur. They are interpolation errors and the error which occurs because we do not exactly satisfy zero penetration velocity near the immersed wall. We try to assess the relative importance of both for the case where the immersed wall coincides with a grid boundary.

Keywords: Immersed boundary method, Error close to immersed wall

1 Introduction

In immersed boundary methods one adds additional momentum sources to the momentum equations to represent the presence of an obstacle. An advantage is that obstacles can be added without making a new grid. For a pressure-correction based model, this leads to another big advantage. In this type of method a Poisson equation for the pressure has to be solved. If obstacles are present one has to use an iterative Poisson solver which typically uses most of the CPU of the problem. If, like with immersed boundary methods, only the momentum equations are changed, the mass conservation procedure does not have to be changed when adding obstacles and very efficient direct Poisson solvers can be used.

When using immersed boundary methods one is often interested in the flow field at some distance from the immersed boundary. However, in case of quantities like heat fluxes the behaviour close to the boundaries is also important because we take derivatives to get the flux and these derivatives depend on quantities in the grid points next to the immersed wall.

In general, for a model which uses pressure correction there are two types of error that occur when using an immersed boundary method. Often a profile is assumed for quantities (velocity components, scalar quantities like temperature) close to the wall, for instance a linear profile. Interpolation/extrapolation then uses more points inside the fluid domain than just one point, which is the

J. Meyers et al. (eds.), Quality and Reliability of Large-Eddy Simulations,

case for a second order code. See Fig. 1. The other type of error arises because the wall-normal velocity component on a wall is not exactly zero. This happens in pressure-correction codes, where after calculation of the momentum equations we do a pressure correction which changes the velocity components by a small, but non-zero amount.

We were interested in the relative importance of the error made by assuming a profile and the error by a non-zero velocity component normal to the wall. This can be assessed by using three methods: a traditional method using an iterative solver, a method which uses a well-known immersed boundary method, namely Verzicco's method [1], and by using a variant of the immersed boundary method which uses the same type of boundary condition as the traditional method and differs only from the traditional method because after the pressure correction the wall-normal velocity component is not exactly 0. In the next sections we will describe the details of the flow simulation model, Verzicco's method and its variant, the geometry calculated and show some results of simulations with the two methods.

2 Numerics

The model is a standard second-order staggered finite-volume model using central differences in space and Adams-Bashforth in time. It uses a pressure-correction scheme and so a Poisson equation has to be solved for the pressure. The Poisson equation solver is either a direct method based on FFT, cyclic reduction and tridiagonal or (in the case of an iterative solver) the Strongly-Implicit method of Stone (SIP, [2]). The iterative solver gave a divergence of the order of 1e-4.

3 Immersed Boundary Method

A simple and robust method for implementing an immersed boundary method which works for all kinds of immersed boundaries (curved, straight, non-moving, moving) was extensively used by Verzicco et al. [1] after an idea of Mohd-Yusof. It adds extra momentum sources to the momentum equations in such a way that the velocity components, when linearly extrapolated from fluid to wall, are 0. See Fig. 1.

Features to note are, that the velocity is forced to follow a linear profile near the boundary and that we use two velocity points inside the fluid near the wall. Adaptions for a higher order polynomial fit are easily made.

The variant we studied (for which some results were shown in [3]) is one in which we assume that the walls of the obstacle coincide with cell walls, so that the obstacles must have flat surfaces. The wall normal components can simply be put equal to 0. For the tangential component we directly look at the stress. This stress is replaced by the one that would exist for a real wall.

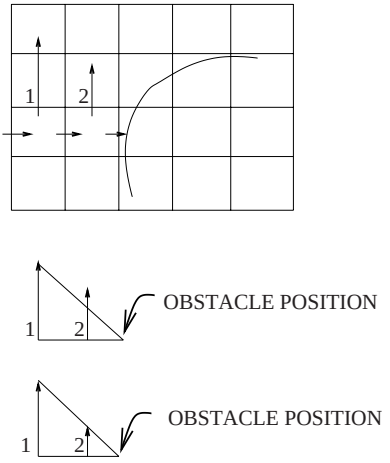

Fig. 1 Cartesian method of Verzicco. After solution of the momentum equations as if no wall is there, velocity components do not extrapolate to 0 on the fictitious wall. The velocity component nearest to the wall is adapted so that it does

See Fig. 2 below. For a scalar we do the same: the flux is replaced by the flux that would exist in case of a real wall, see Fig. 3. A clear disadvantage with respect to Verzicco's method is that the immersed boundary must coincide with cell walls. Also, the way we impose the immersed boundary depends on the discretisation because the old tangential stresses and the old scalar fluxes have to be removed. An advantage is, that no additional extrapolation or interpolation is necessary when compared to traditional methods using a real wall. Also, no extra grid points in the fluid are used when compared to the traditional approach. The only difference is that after pressure correction the wall normal velocity component will be no longer be exactly zero. An additional advantage is that, since we work with the stress, a wall law can be easily used together with this method (the incorrect tangential stress calculated as if no wall is there is replaced by a stress according to a wall law, which is calculated in exactly the same way as for a traditional model). Also, the method can be used inside and outside the obstacle and one does not need to check whether one is inside or outside. Moreover, there are no non-uniqueness questions near corners (velocity points close to a corner of a boundary may be determined by more than one point further into the fluid with Verzicco's method). Although there are advantages for the new variant, it is of course much less generally applicable and mainly useful for studying the flow around rectangular obstacles and for studying the numerics, as we can distinguish between effects caused by pressure correction and by interpolation.

For the passive scalar, no-flux boundary conditions were enforced in the same way for all methods, namely by putting the flux at the wall to 0. A

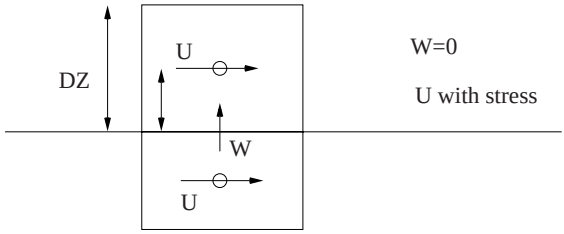

Fig. 2 Variant of immersed boundary method. Velocities are calculated as if no wall is there. After this, the normal velocity on the horizontal cell wall is put to 0, and the contribution from the shear stress which was applied at the horizontal wall (which is then not correct) is subtracted and replaced by the stress that would exist in case of a real wall. The last stress is in discretised form equal to $\mu \frac{U}{1/2dz}$

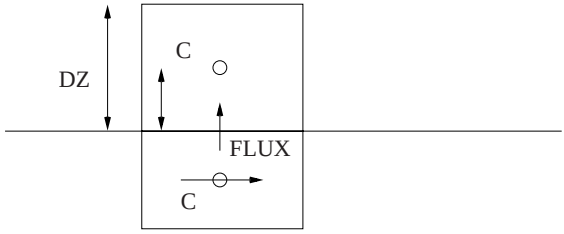

Fig. 3 Variant of immersed boundary method. After solution of the scalar equations as if no wall is there, the scalar flux at the wall is replaced by the flux that would exist for a real wall. For prescribed scalar on the wall, equal to Cw, this flux would be $k \frac{Cw-C}{1/2dz}$

prescribed scalar for Verzicco's method is enforced by imposing a linear profile near the wall for the concentration.

4 Flow Geometry and Simulation Details

The geometry considered is that of flow over a cavity, see Fig. 4. The flow is driven by an imposed pressure gradient, boundary conditions are periodic in main flow direction (at right angles to the cavity), periodic in spanwise direction, free-slip on the top, no-slip on all other boundaries. A scalar is released at the bottom of the cavity, for the scalar we have inflow-outflow boundary conditions in the main flow direction, periodic boundary conditions in the spanwise direction, no-flux at the top and no-flux or prescribed value at the other walls. The tests concern flows without any subgrid model, for a Re number of 1800, and with an LES model and a wall law (Werner-Wengle), with a Re number of 16000, with Re based on cavity height H, a typical velocity scale in the cavity and the viscosity. The subgrid model was simple Smagorinsky with Van driest wall damping. Together with the flow field we

calculated a scalar field for two cases, namely no-flux boundary condition and prescribed scalar on the wall. Grids are quite coarse, 60 cube for the Re 1800 case and 40 cube for the higher Re (LES) case. For the low Re (no SG model) case the wall yplus is around 2 over most of the boundary, with an exception near the right canyon wall where the flow hits the wall. Overthere it is sometimes up to around 6, which is far too big but we let this be so we can see its effect on the results. For the higher Re case we have yplus of around 40, necessitating the use of a wall law.

For the lower Re number case, the simulation was run until the flow had become irregular, after which the simulation was continued for another 100 eddy turnover times, which is defined as the height of the (square) cavity divided by a typical velocity scale in the cavity. Starting from this simulation, simulations were run for another 30 eddy turnover times for the different wall treatments after which statistics were taken over another 100 eddy turnover times. For the higher Re number case, shorter simulation times were used to get data, namely 20 eddy turnover times were allowed to adapt to a new wall treatment, and 20 eddy turnover times were used to get averages.

The penetration velocities (non-zero wall normal velocity components at an immersed wall after the pressure correction) are of order 1e-3 times a typical velocity in the cavity, the maximum occurring near the sharp corners.

The simulations without subgrid model (low Re) used grid refinement near the wall and had a domain height of 7 H (H = canyon height), the simulations with subgrid model (higher Re) used a domain of 4H and used an equidistant model inside the cavity and a grid stretch in vertical direction. Due to the different grid for different Re, the source for the scalar was different and one should not compare concentration values for higher and lower Re.

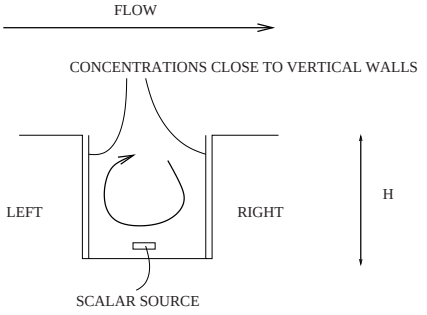

Fig. 4 The canyon geometry. There is flow over the canyon leading to circulation within the canyon. Near the bottom we release a passive scalar

5 Results

We show results for several cases, distinguished according to method (traditional, Verzicco, and the new variant which is called the stress method) and the type of boundary condition for the passive scalar (which is either no-flux of prescribed scalar). We show primarily the results for the passive scalar.

The results plotted are average concentration values and RMS of the concentration for the first grid cell inside the fluid next to the virtual, vertical boundary.

A typical output for the concentrations with no model is given in Fig. 5 left, showing the concentration at the left wall, which is hit by the concentration first, together with the concentration at the right wall which hits the wall after some concentration has escaped to the outside so that values are smaller. These results (and the next four plots) are for no-flux boundary conditions for the scalar.

A comparison between methods for time-averaged concentration is given in Fig. 5 middle, showing concentrations at the left wall and Fig. 5 right, showing concentrations at the right wall. Results are very close.

RMS values of the concentrations are compared in Fig. 6 left and middle for left and right wall. Here differences are seen between the three methods, mostly between Verzicco's method and the other two. The reason for the differences proved to be the fact that the yplus value for the right wall is (far) too big, sometimes around 6, to assume a linear profile. Where yplus is decent (smaller than 2) results are much closer.

Results are also shown for prescribed scalar at the walls, so that the derivatives at the wall have to be accurate. In Figs. 6 right and 7 left we have the concentrations at the left and right wall. Values are smaller than in the no-flux case. Differences are already apparent. In 7 middle and right we see the RMS values compared for left and right wall. Again, differences are biggest for the bigger yplus values. Not unexpectedly, differences are bigger for the prescribed scalar case than for the no-flux case.

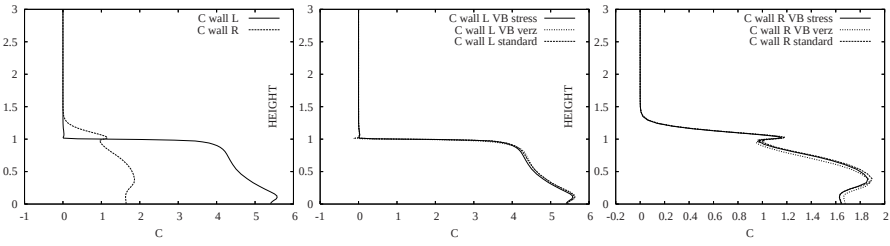

Fig. 5 *Left*: the time-averaged concentration very close to the left and right wall of the canyon. *Middle and right*: Comparison of time-averaged concentration close to the walls between several boundary treatments (indicated with stress for our variant, verz for Verzicco's method and standard for a standard method)

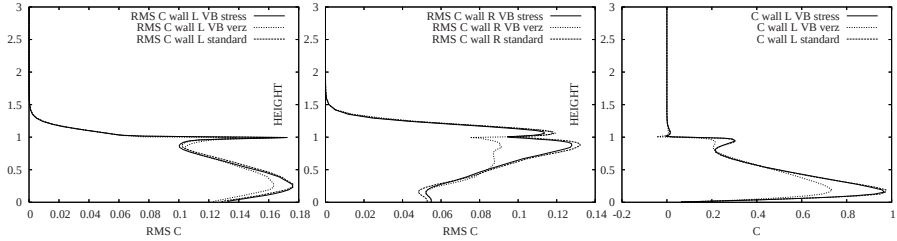

Fig. 6 *Left*: RMS values of concentration at left wall, zero-flux at wall case. *Middle*: RMS values of concentration at right wall, zero-flux at wall case. *Right*: time-averaged values at left wall for prescribed scalar at the walls. Results for calculations using several boundary treatments (indicated with stress for our variant, verz for Verzicco's method and a standard method using an iterative Poisson solver)

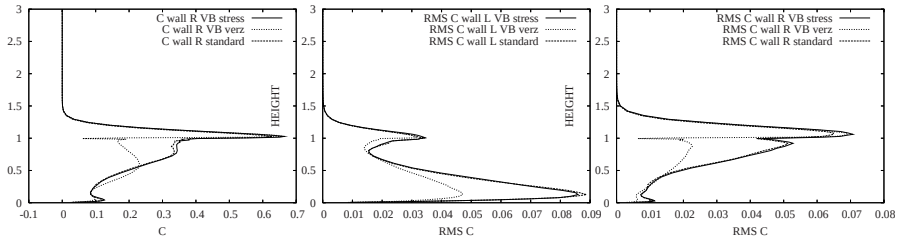

Fig. 7 *Left*: time-averaged values at right wall for prescribed scalar at the walls. *Middle*: RMS values concentration at left wall. *Right*: RMS values concentration at right wall. Results for calculations using several boundary treatments (indicated with stress for our variant, verz for Verzicco's method and a standard method using an iterative Poisson solver)

Finally, for the higher Re number case, a preliminary result for the case of a prescribed scalar (remember, the scalar source is different this time) is shown in Fig. 8. LES has been used, and a wall law has been used to calculate the scalar flux and shear stress at the wall. Only results for the right wall are shown, the time-averaged concentration and RMS of the concentration, only our variant of the immersed boundary and the standard model. Differences are visible but are possibly due to the shorter averaging time.

6 Conclusions

We wanted to see the effect of interpolation and nonzero penetration velocity for immersed boundary methods. As expected, there are differences between all three methods used (standard, Verzicco and stress method). From a comparison between the stress method (which uses standard boundary conditions) and the standard method with iterative Poisson solver differences (resulting

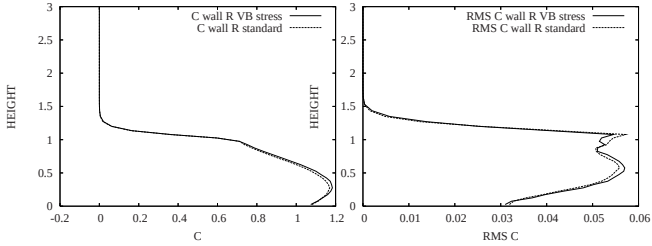

Fig. 8 *Left*: time-averaged values at right wall for prescribed scalar at the right wall. *Right*: RMS values concentration at right wall. Results for calculations using several boundary treatments (indicated with stress for our variant and standard for a standard method using an iterative Poisson solver)

from just the non-zero penetration velocities) are very small for the case calculated. The comparison with Verzicco's method, which assumes a linear profile, indicate that the extra interpolations due to the assumption of a linear profile have a bigger effect than the non-zero penetration velocities. This effect becomes more apparent when the flow profile is more curved. For the zero-flux case, Verzicco's method does well for the scalar for the region where yplus is sufficiently small, but then, zero-flux for the scalar was also imposed exactly for Verzicco's case. For the case of prescribed scalar, differences are bigger, as expected. For yplus sufficiently small, these differences too should disappear.

Summarising, the results indicate that with proper distance from the wall one can use the virtual boundary method for concentration problems for flow around square obstacles, the effect of the non-zero penetration velocity being very small. Extension of our geometry to more complicated problems with multiple obstacles is straightforward ([4]).

References

1. Fadlun EA, Verzicco R, Orlandi P, Mohd-Yusof J (2000) J Comp Phys 161: 35–60
2. Ferziger J, Peric B (2002) Computational Methods for Fluid Dynamics. Springer, Berlin, Heidelberg, New York
3. Pourquie M, Nieuwstadt F (2005) The use of virtual boundary conditions for fast DNS/LES of flow around objects. In Symposium: Atmospheric Flows in Urban Environments, Proceedings McMat
4. Breugem WP, Boersma BJ (2005) Direct numerical simulations of turbulent flow over a permeable wall using a direct and a continuum approach. Phys Fluids 17, Art no 025103

On the Control of the Mass Errors in Finite Volume-Based Approximate Projection Methods for Large Eddy Simulations

Andrea Aprovitola and Filippo Maria Denaro

Department of Aerospace and Mechanical Engineering, Second University of Naples, Aversa (CE), Italy. andrea.aprovitola@unina2.it, denaro@unina.it

Abstract. Filtering in Large Eddy Simulation (LES) is often only a formalism since practically discretization of both the domain and operators is used as implicit grid-filtering to the variables. In the present study, the LES equations are written in the integral form around a Finite Volume (FV) Ω rather than in the differential form as is more usual in Finite Differences (FD) and Spectral Methods (SM). Grid-filtering is therefore associated to the use of an explicit local volume average, by the way of surface flux integrals, and specific LES equations are here described. Moreover, since the filtered pressure characterizes itself only as a Lagrange multiplier used to satisfy the continuity constraint, projection methods are used for obtaining a divergence-free velocity. The choice of the non-staggered collocation is often preferable since is easily extendable on general geometries. However, the price to be paid in the so-called Approximate Projection Methods, is that the discrete continuity equation is satisfied only up to the magnitude of the local truncation error. Thus, the effects of such source errors are analyzed in FD and FV-based LES of turbulent channel flow. It will be shown that the FV formulation is much more efficient than FD in controlling the errors.

Keywords: Large-eddy simulation, Finite volume methods, Explicit and implicit filtering, Projection methods

1 Introduction

Several elements contribute to the effective quality of Large Eddy Simulation (LES) of turbulence, e.g. see [1, 2, 3]. Specifically, they are the mathematical and physical formulation, i.e. filtered equations and turbulence modelling of the Sub-Grid Scales (SGS) terms, as well as the time and space discretization. Of course, the choice of the computational grid is a further component that contributes to succeed in LES.

As regards to numerical methods, there is an extensive literature indicating Spectral Methods (SM) to be largely preferred in case of Cartesian geometries as well as Finite Difference (FD) methods are preferred in more

J. Meyers et al. (eds.), Quality and Reliability of Large-Eddy Simulations,

general geometries. Someway, less attention seems focused on Finite Volume (FV) approaches to LES. When using SM one clearly identifies the LES filter as that one corresponding to the sharp cut-off acting at the Nyquist frequency $k_c = \pi/h$, associated to the truncated Fourier series defined on a grid of step h. On the other hand, it is well known that the LES filter shape in FD-based simulations is often only implicitly defined by the discretization and is not exactly identifiable as, depending on the order of accuracy, the Fourier components turn out to be differently resolved close to k_c. Thus, some authors addressed the use of explicit filtering (pre-filtering) for which one can exactly identify the filter type and control the truncation errors [4, 5, 6]. However, both FD and SM-based formulations are developed by discretizing the differential form of the Navier-Stokes (NS) equations. For FV-based formulations, although the integral form is quite more complicated to be discretized than the differential counterpart (according to [7] three levels of approximation are required, interpolation, differentiation and integration), it appears to be the most opportune since leading to solve discrete equation models, which allow mass, momentum as well as any conservative quantity, to be *a-priori* conserved, no matter of what the actual accuracy order is in effect. On the contrary, it is well known that SM and FD methods do not automatically share such property. This fact is particularly relevant since it is known that the discrete conservation property ensures the correct wave velocity propagation as it is required to reproduce the correct energy dynamic. As a matter of fact, the additional appealing feature of FV-based approaches to LES is in the fact that the local average represents a natural link with the smooth filtering, i.e., the *top-hat* one. Note that FV discretizations of any accuracy order always drive to approximate the top-hat filtered equations, e.g. see [8, 9, 10]. The fluxes surface integrals must be really considered acting as volume filter in order for the proper decomposition of resolved fluxes and congruent SGS modelling to be supplied. Particularly, when a SGS dynamic modelling procedure is used, the presence of the built-in FV filtering induced us to consider the extension of the Germano identity, e.g. see [10]. Note that such peculiarities of FVs are not often fully highlighted, even in recently published paper, e.g., see [6, 11].

Within this framework, solving the NS equations with the hypothesis of fluid incompressibility leads to ensure the mass-conservation constraint $\underline{\nabla} \cdot \mathbf{v} = 0$, everywhere and for all time. That makes the pressure acting only as a Lagrangian multiplier, having no thermodynamic law. In order to alleviate the computational effort of solving Lagrangian constrained system of equations, the velocity and the pressure gradient vector fields are decoupled in the sense provided by the Helmholtz-Hodge decomposition (HHD) theorem [12, 13], leading to the class of the so-called *Projection Methods*, generally used both in Direct Numerical Simulation (DNS) and in LES, no matter of which one among SM, FD or FV methods is practically used.

Considering the complexity of discretizing integrals and derivatives and computing the SGS terms, the use of projection methods on non-staggered computational grids is preferable. However, when using second order

discretizations on such grids, two general approaches arise. On a side, if the discrete continuity equation has to be exactly satisfied then the discrete pressure equation must be defined on a sparse stencil that, owing to the lack of communication between neighbouring nodes (odd-even decoupling), could produce non-physical oscillating solutions. On the other side, if a compact stencil is constrained for obtaining a smooth pressure field, then the discrete continuity constraint can not be satisfied up to machine-accuracy but it converges towards a source term that is proportional to fourth-order derivatives of the pressure field, multiplied by the time-step and the square of the grid step sizes, e.g., see [7]. It is usual [14, 15] to speak in the first case of *Exact Projection Methods* (EPM) whereas one speaks of *Approximate Projection Methods* (APM) in the latter case. Especially in LES, it is important to have control of all the sources of numerical errors that can contaminate the large scales (quasi-inviscid) dynamic and consequently the actions of any SGS model. Since there is no kinetic energy equation resolved for incompressible omothermal flows, it is possible that mass errors introduced by the APM enter indiscriminately into the flow dynamic.

The aim of this paper is to illustrate the preliminary assessments of the study on the mass-errors effect for FV-based LES compared to FD-based ones when the APM is used. The classical test-case of the turbulent channel flow at $\mathrm{Re}_\tau = 590$ is adopted. Furthermore, the results obtained by adopting a recently developed improved discrete divergence-free method are illustrated.

2 Integral and Differential Formulation of the Filtered Equations

In LES approach, the separation between large resolved scales and small unresolved ones is obtained via low-pass filtering. The spatial filtering operation (here, time filtering is not considered) can be expressed as the convolution product between the unfiltered point-wise field, say f, and some suitable filter function G, that is,

$$\overline{f}(\mathbf{x},\, t) = \int G\left(\mathbf{x} - \mathbf{x}';\ \overline{\Delta}\ \right)\ f(\mathbf{x}',\, t) d\mathbf{x}' \equiv G\ * f \tag{1}$$

$\overline{\Delta}$ being the characteristic filter width. The Eq. (1) corresponds to have $\widehat{\overline{f}}\,(\mathbf{k}_w, t) = \hat{G}\,(\mathbf{k}_w)\,\hat{f}\,(\mathbf{k}_w, t)$ in Fourier space, $\mathbf{k}_w$ being the wavenumbers vector. Some classical filters G are, for example, the top-hat in physical space and the sharp spectral cut-off, see [1, 2, 3]. The evolution equations for the large scale field can be formally obtained by applying the filter (1) to each term of the NS equations while supplying some SGS model for the consequent unresolved terms. Then, for given boundary and initial conditions, a certain discretization in time and space allows us updating the LES solution directly in terms of the filtered fields.

However, filtering the NS equation is often implicitly let to domain and operators discretization, e.g. see [1, 4, 5, 6, 11]. The classical filtered equations such as those used in FD or SM approaches, assuming the commutation property holds for filter and differentiation operations, write in differential divergence form as

$$\underline{\nabla} \cdot \overline{\mathbf{v}} = 0 \tag{2}$$

$$\frac{\partial \overline{\mathbf{v}}}{\partial t} + \underline{\nabla} \cdot (\overline{\mathbf{v}\mathbf{v}}) + \underline{\nabla} \overline{P} = \underline{\nabla} \cdot (2\nu \underline{\nabla}^s \overline{\mathbf{v}}) - \underline{\nabla} \cdot \mathbf{T}_D \tag{3}$$

$$\mathbf{T}_D = \overline{\mathbf{v}\mathbf{v}} - \overline{\mathbf{v}}\ \overline{\mathbf{v}} \tag{4}$$

being $P = p/\rho_0$, ν the kinematic viscosity and $\mathbf{T}_D$ the exact unresolved sub-grid tensor, subscript D denoting the differential formulation. It is worthwhile remarking that we consider only the divergence form (3) of the momentum equation, which is suitable for transformation to the integral one, no other energy-preserving forms, such as the skew-symmetric one, being here considered. Without performing an explicit filtering, the real shape of the filtered velocity $\overline{\mathbf{v}}$ will depend on the implicit choice of the filter function G associated to a certain discretization. Using SM, the LES filter is identified as that one corresponding to the sharp cut-off acting at the Nyquist frequency $k_c = \pi/h$. Perhaps, in traditional FD-based LES solution, both the computational grid and the discretization operators "implicitly" act as filtering to the NS equations and the filter shape depends on the type of discretizazion, as it has been reviewed in [5]. Some authors [5, 6] considered, therefore, using an explicit filtering on (3) in order to minimize the discretization error as well as to have a known shape of the actual LES filter.

On the other hand, we will now address how FV-based LES is very attractive since it turns out to be someway in the between of implicit and explicit filtering procedures. In fact, the NS equations written in the integral form around a FV Ω, its measure being indicated by $|\Omega|$, exactly accords with the top-hat homogeneous filtering. That is, one writes

$$\int_{\partial\Omega} \mathbf{n} \cdot \overline{\mathbf{v}}\ dS = 0, \tag{5}$$

$$|\Omega| \frac{\partial \overline{\mathbf{v}}}{\partial t} + \int_{\partial\Omega} \mathbf{n} \cdot (\overline{\mathbf{v}}\ \overline{\mathbf{v}})\ dS + \int_{\partial\Omega} \mathbf{n}\, P\ dS = \int_{\partial\Omega} \mathbf{n} \cdot (2\nu \underline{\nabla}^s \overline{\mathbf{v}})\ dS - \int_{\partial\Omega} \mathbf{n} \cdot \mathbf{T}_I\ dS, \tag{6}$$

$$\mathbf{T}_I = (\mathbf{v}\mathbf{v} - \overline{\mathbf{v}}\ \overline{\mathbf{v}}) - 2\nu\, (\underline{\nabla}^s \mathbf{v} - \underline{\nabla}^s \overline{\mathbf{v}}), \tag{7}$$

being $\overline{\mathbf{v}}$ the divergence-free ($\int_{\partial\Omega} \mathbf{n} \cdot \mathbf{v}\ dS = 0 \Rightarrow \nabla \cdot \overline{\mathbf{v}} = 0$) volume averaged velocity, $\mathbf{n}$ the outward oriented unit normal to the surface $\partial\Omega$ and $\mathbf{T}_I$ the exact unresolved sub-grid tensor, subscript I denoting the integral formulation. It is worthwhile remarking that the adoption of the integral-based LES formulation, leads to a very different definition of the exact unresolved tensor as highlighted by comparing (4) and (7). In the integral form, the SGS

term preserves a local character, the further filtering operation being involved by the volume integration that in our case, by means of the Gauss theorem, applies as surface integral [9, 10]. This appears to be a congruent way to effectively use the conservative integral form rather than adopting an additional volume filtering on the differential one as done in [6]. Furthermore, if the commutation property between filter, derivatives and integrals does not hold, then special filtering must be adopted for the differential form whilst only the continuity equation contains a source term in the integral one, the momentum equation being not changed. As final comment, the local truncation error of a FV scheme always affects the shape of the effective filter but, while increasing the accuracy of a FD method does not help us to exactly identify the actual filter, increasing the accuracy of the fluxes reconstruction of a FV method makes the effective filter tending to the theoretical expected top-hat one. Still now, such distinctive issues between FV and FD-based LES, are not clearly individuated, e.g. see [5, 6, 11].

Here, the closure of both the filtered equations (3) and (6) is obtained by exploiting only the Bousinnesq sub-grid viscosity concept, even if mixed models are however possible. Namely, the deviatoric part of the unresolved tensors is classically modelled like an additional stress term with a point-wise time-dependent eddy viscosity, hereafter denoted by ν_{LES}

$$\mathbf{T}_{LES} \cong -2\nu_{LES}\underline{\nabla}^s\overline{\mathbf{v}}. \tag{8}$$

This way, a modified pressure variable π accounts for the contribution of the isotropic part of the unresolved tensor. The eddy viscosity model (8) is used both for FD and FV approaches, the surface integral in (6) acts as a local filtering in FV while the divergence operator acts point-wisely in FD. The dynamic procedure is then adopted in both formulations. The full details of the dynamic procedure, developed for FV-based LES, are given in [10]. Let us highlight that the goal of this study is not to get the best possible LES solution but is focused to analyse the effects of the APM, for the FD and FV formulation, with a given SGS model. Specifically, a lack in the divergence-free constraint can be responsible of false energy evolution, as for example studied in [16].

3 The Approximate Projection Method for the LES Equations

According to the projection method idea, a velocity-pressure de-coupling based on the HHD theorem of a vector field in a finite domain e.g., see [12, 13], is introduced, allowing us to solve separately first the equation for an intermediate velocity field, say $\mathbf{v}^*$, then projecting it on the sub-space of divergence-free functions. It is known that second order discretization on staggered grids ensures non-spurious modes in the solution, nevertheless the non-staggered

collocation (or cell-centred grid) is often preferable since is much more feasible and easily extendable to general geometries and higher accuracy. However, it is well known that second-order accurate projection methods on cell-centred grids substantially belong to the class of either EPM or APM, e.g. see [14, 15]. In the EPM, the continuity constraint can be satisfied to machine-accuracy but the discrete divergence $\mathbf{D}$ and gradient $\mathbf{G}$ (second order accurate but centred on large stencil, e.g., $2h$) operators produce the discrete elliptic equation $L_H(\phi) \equiv \mathbf{DG}(\phi) = \mathbf{D} \cdot \mathbf{v}^*$ which is affected by lack of communication between neighbouring nodes (odd-even decoupling), producing spurious oscillating solutions. In fact, as can be shown by analyzing the number of zeros of the Fourier symbol, both the operators $\mathbf{D}$ and L_H have an eight-dimension null-space. Conversely, in the APM one does not demand that the discrete system matches the condition for being exactly a projection. The divergence $\mathbf{D}_{APM}$ and gradient $\mathbf{G}_{APM}$ operators (second order accurate but centred on the smallest mesh size h) allow us obtaining a compact Laplace operator $L \equiv \mathbf{D}_{APM}\mathbf{G}_{APM}$ that is only an approximation of the operator L_H, L can be shown to have the null-space of dimension one, corresponding only to the constant mode. The APM-based elliptic equation is $L(\phi) = \mathbf{D} \cdot \mathbf{v}^*$, the RHS being exactly the same of the EPM, but the price to be paid is that the discrete continuity equation is satisfied only up to the magnitude of the local truncation error [7, 14, 15]. The presence of such error at fixed grid measure influences the transfer of kinetic energy for FD or FV methods in different way.

We use the Adams-Bashforth time integration of the convective and horizontal (x and z directions) diffusive terms along with the eddy viscosity model. The vertical diffusive term (y direction) is discretized by the implicit Crank-Nicolson scheme. A small time-step ensures that the second order accuracy in time does not add a supplementary time-filtering. The solution of the intermediate non-solenoidal velocity field is performed by solving the space-time discrete filtered momentum equation (3) or (6) after that the pressure term is disregarded [17]. Depending on the discretization, second order FD and FV methods can or not drive to solve the same algebraic equations, e.g. see [7, 18, 19]. Hence, the discretizations for both FD and FV are now addressed.

3.1 Finite Difference Formulation

Starting from Eq. (3) along with the SGS model (8), the discrete prediction equation for the intermediate non-solenoidal velocity $\tilde{\mathbf{v}}^*$ writes, at a generic grid point i,j,k, as

$$\left[I - \frac{\nu \Delta t}{2}\widetilde{\frac{\partial}{\partial y}}\left(\widetilde{\frac{\partial}{\partial y}}\right)\right]\tilde{\mathbf{v}}^* = \left[I + \frac{\nu \Delta t}{2}\widetilde{\frac{\partial}{\partial y}}\left(\widetilde{\frac{\partial}{\partial y}}\right)\right]\tilde{\mathbf{v}}^n - \Delta t\underline{\widetilde{\nabla}} \cdot \left[\frac{3}{2}\left(\tilde{\mathbf{v}}^n\tilde{\mathbf{v}}^n + \tilde{\mathbf{T}}^n_{LES}\right) - \frac{3\nu}{2}\left(\mathbf{i}\widetilde{\frac{\partial}{\partial x}} + \mathbf{k}\widetilde{\frac{\partial}{\partial z}}\right)\tilde{\mathbf{v}}^n - \frac{\tilde{\mathbf{v}}^{n-1}\tilde{\mathbf{v}}^{n-1}}{2} - \frac{\tilde{\mathbf{T}}^{n-1}_{LES}}{2} + \frac{\nu}{2}\left(\mathbf{i}\widetilde{\frac{\partial}{\partial x}} + \mathbf{k}\widetilde{\frac{\partial}{\partial z}}\right)\tilde{\mathbf{v}}^{n-1}\right] \quad (9)$$

being I the identity operator, $\mathbf{i}$ and $\mathbf{k}$ the unit vectors along x and z directions, respectively. According to notation in [5], the symbol $\tilde{\mathbf{v}}$ has been here

used instead of the $\overline{\mathbf{v}}$ in order to highlight that the implicit grid-filtering has undefined shape in FD, not necessarily corresponding to the top-hat filtering. It is worthwhile remarking that Eq. (9) is based on the divergence form of the differential equation (3), sometime being such form referred as to "finite-volume", e.g. [11]. Often, FD approaches adopts the skew-symmetric form that ensures the discrete conservation and good stability properties. Here, we are interested only in the divergence form which is suitable to be compared to the integral one by means of Gauss theorem. In Eq. (9), the tilde symbol on the derivative indicates the use of classical discrete operators such as

$$\widetilde{\frac{\partial}{\partial x}}\bigg|_{ijk} \widetilde{u}^2 = \frac{\widetilde{u}^2_{i+1,jk} - \widetilde{u}^2_{i-1,jk}}{2\Delta x}; \; \widetilde{\frac{\partial}{\partial x}}\left(\widetilde{\frac{\partial}{\partial x}}\right)\bigg|_{ijk} \widetilde{u} = \frac{\widetilde{u}_{i+1,jk} - 2\widetilde{u}_{ijk} + \widetilde{u}_{i-1,jk}}{\Delta x^2} \quad . \tag{10}$$

It is worthwhile noticing that for the first derivative in (10) one can assess the exact correspondence to the one-dimensional top-hat filtering, that is $\widetilde{\frac{\partial f}{\partial x}} = \frac{1}{2\Delta x}\int_{x-\Delta x}^{x+\Delta x} \frac{\partial f}{\partial x}\, dx$. Conversely, it is easy to show that the discretization of the second derivative in (10) implies a double 1D filtering.

3.2 Finite Volume Formulation

Starting from Eq. (6) along with the SGS model (8), the discrete prediction equation for the intermediate non-solenoidal velocity $\overline{\widetilde{\mathbf{v}}}^*$, at a generic FV centre-node i,j,k, write as

$$\begin{aligned}\left[I - \frac{\nu\Delta t}{2\Delta y}\left(\widetilde{\frac{\partial}{\partial y}}\bigg|_{CS_p^+} - \widetilde{\frac{\partial}{\partial y}}\bigg|_{CS_p^-}\right)\right]\overline{\widetilde{\mathbf{v}}}^* &= \left[I + \frac{\nu\Delta t}{2\Delta y}\left(\widetilde{\frac{\partial}{\partial y}}\bigg|_{CS_p^+} - \widetilde{\frac{\partial}{\partial y}}\bigg|_{CS_p^-}\right)\right]\overline{\widetilde{\mathbf{v}}}^n \\ &- \frac{\Delta t}{2}\left\{3\left[\frac{1}{|\Omega(\mathbf{x})|}\sum_p \Delta S_p \mathbf{n}\cdot\left(\overline{\widetilde{\mathbf{v}}}\,\overline{\widetilde{\mathbf{v}}} + \overline{\widetilde{\mathbf{T}}}_{LES}\right)^n_{CS_p} - \nu\left(\widetilde{D}_1 + \widetilde{D}_3\right)\overline{\widetilde{\mathbf{v}}}^n\right]\right. \\ &\left. - \frac{1}{|\Omega(\mathbf{x})|}\sum_p \Delta S_p \mathbf{n}\cdot\left(\overline{\widetilde{\mathbf{v}}}\,\overline{\widetilde{\mathbf{v}}} + \overline{\widetilde{\mathbf{T}}}_{LES}\right)^{n-1}_{CS_p} + \nu\left(\widetilde{D}_1 + \widetilde{D}_3\right)\overline{\widetilde{\mathbf{v}}}^{n-1}\right\}\end{aligned} \tag{11}$$

having used the mean value-based discrete integrals of convective and SGS fluxes [7] (trapezoidal rule can be also used) and having indicated with ΔS_p the measure of the p-th FV flux-surface being CS_p its node-centre. Furthermore, $CS_p^{\pm}$ denotes the centre of the two horizontal faces across the position y_j and $\widetilde{D}_{1,3}(\ )$ indicates the integro-differential second order discrete operator of the diffusive fluxes along x and z directions, e.g., see [18, 19]. Note that the tilde symbol on the variables is now used in conjunction with the hat symbol in order to indicate that FV-based implicit filtering produces always a numerical approximation of the top-hat filtering. Differently from the FD formulation, since on a non-staggered grid the values on the face-centres CS_p must be reconstructed from the node-centre i,j,k, in order for the FV discretization to be completely defined the interpolation of the convective fluxes

has to be still defined [7]. Reconstruction is here performed at second order of accuracy that is a linear polynomial approximation is adopted. However, following a classical non-staggered formulation with linear interpolation, one would get the same FD discretization type reported in (10), no matter of the fact that the FV approach was used [18, 19], thus, a distinguishably strategy will be adopted as follows.

3.3 Flux Reconstruction Based on the APM Step

Let us first recalling that, according to the APM formulation [14, 15, 18, 19], one relaxes the divergence constraint and constructs an approximate projector, say it simply P. After applying P on the intermediate velocity, one has $P\left(\widetilde{\mathbf{v}}^*\right) = \widetilde{\mathbf{v}}_S^{n+1}$ and $P\left(\overline{\widetilde{\mathbf{v}}}^*\right) = \overline{\widetilde{\mathbf{v}}}_S^{n+1}$ for FD and FV-based LES, respectively. The subscript S denotes that the fact that APM-based velocity introduces a local source mass. Practically, one solves the elliptic equation $L\left(\widetilde{\phi}_C^{n+1}\right) = \mathbf{D}\cdot\widetilde{\mathbf{v}}^*$ and $L\left(\overline{\widetilde{\phi}}_C^{n+1}\right) = \mathbf{D}\cdot\overline{\widetilde{\mathbf{v}}}^*$ for FD and FV, respectively, associated to proper Neumann boundary conditions that provide a unique solution (apart a constant) for the scalar potential field. Note the RHS of the elliptic equation is equivalently obtained by using a linear interpolation with a more compact divergence operator $\mathbf{D}_{APM}$, see [14, 15, 18, 19]. In FV formulation it is well-suited defining an additional set of six normal-to-face velocities on each FV surface S_p, say them $\bar{\tilde{u}}_{f\ i\pm1/2,j,k}^{n+1}, \bar{\tilde{v}}_{f\ i,j\pm1/2,k}^{n+1}, \bar{\tilde{w}}_{f\ i,j,k\pm1/2}^{n+1}$ for x, y and z components, respectively. Such velocities are staggered-like as one can see for example for the x-component

$$\bar{\tilde{u}}_{f\ i\pm1/2,j,k}^{n+1} = \frac{\bar{\tilde{u}}_{i\pm1,j,k}^* + \bar{\tilde{u}}_{i,j,k}^*}{2} \mp \frac{\overline{\widetilde{\phi}}_{i\pm1,j,k}^{n+1} - \overline{\widetilde{\phi}}_{i,j,k}^{n+1}}{\Delta x} \quad . \tag{12}$$

are computable under an exact projection. In fact, if one constructs the discrete divergence constraint $\mathbf{D}_{APM}\cdot\bar{\tilde{\mathbf{v}}}_f^{n+1} = 0$, then one easily sees that the Poisson equation $L\left(\overline{\widetilde{\phi}}_C^{n+1}\right) = \mathbf{D}\cdot\overline{\widetilde{\mathbf{v}}}^*$ is recovered. Therefore, this set of auxiliary staggered normal-to-face velocities is intrinsically divergence-free. Such velocities are then really used for computing $\overline{\widetilde{\mathbf{v}}}^*$ by means of the convective fluxes reconstruction needed in (11), as for example for the component

$$\frac{1}{|\Omega_{ijk}|}\int_{z_k^-}^{z_k^+} d\zeta \int_{y_j^-}^{y_j^+} \left(\overline{u}^2\big|_{x_i^+} - \overline{u}^2\big|_{x_i^-}\right) d\eta \cong \frac{1}{\Delta x}\left[\left(\bar{\tilde{u}}_{f\ i+1/2,j,k}\right)^2 - \left(\bar{\tilde{u}}_{f\ i-1/2,j,k}\right)^2\right] \tag{13}$$

allowing us computing (11). Finally, once a potential field has been obtained from the Poisson problem, one can directly update the node-centre velocity simply computing $\widetilde{\mathbf{v}}_S^{n+1} = \widetilde{\mathbf{v}}^* - \mathbf{G}\widetilde{\phi}_C^{n+1}$ and $\overline{\widetilde{\mathbf{v}}}_S^{n+1} = \overline{\widetilde{\mathbf{v}}}^* - \mathbf{G}\overline{\widetilde{\phi}}_C^{n+1}$ for FD

and FV formulations, respectively. This way, although the same APM-based elliptic equation is used and the final velocities $\widetilde{\mathbf{v}}_S^{n+1}$and $\widetilde{\overline{\mathbf{v}}}_S^{n+1}$ are not exactly divergence-free, the mass error differently spreads in them, depending on the used FD or FV-based method.

Besides, an originally developed procedure, called Double Projection Method (DPM), see [18, 19], exploits the HHD theorem for deriving an additional potential velocity field that, while correcting the FV-based velocity $\widetilde{\overline{\mathbf{v}}}_S^{n+1}$, enforces the discrete continuity. This is accomplished by solving for a second elliptic equation obtained by prescribing that an additional discrete gradient of a scalar function ensures the discrete continuity, that is $\widetilde{\overline{\mathbf{v}}}^{n+1} = \widetilde{\overline{\mathbf{v}}}_S^{n+1} - \Delta t\ \mathbf{G} f_C^{n+1}$. The additional computational effort of the second elliptic solver is justified by the fact that one should use both a refined grid and a small time step to reduce the continuity errors of the APM. The DPM procedure will be also tested for analysing the errors present in LES.

4 Turbulent Channel Flow Simulation

A preliminary analysis of the performances of the APM and DMP formulations [18, 19] in simulating the problem of the plane turbulent channel flow is now reported. The DNS database [20] is considered for comparisons. For the sake of completeness, solutions were obtained both for LES supplied by the dynamical eddy-viscosity modelling procedure [10] as well as without any SGS modelling. According to the FV methodology, the test filtering is chosen to be a horizontal top-hat filter and the SGS coefficients are taken point-wise, no plane-averaged being performed [10]. By using a clipping, the SGS viscosity was set to have only positive values but this is a very invasive criterion and best choices are possible [10]. The computational grid consists of $48 \times 64 \times 64$ grid points, non-uniformly distributed only in vertical direction. The initial condition on the velocity corresponds to a laminar parabolic profile with a superimposed random fluctuation while a constant pressure gradient is supplied as forcing term. The horizontal component of the kinetic energy evolutions at Re_τ =180 are reported in Fig. 1a for the FV and FD-based solutions with and without SGS models. Noteworthy, the FD run without model was never stable, no matter of the time-step used while stable computations (with both APM and DPM) are obtained with the FV-based no-model. The FD-based LES solution supplied by the eddy viscosity modelling was stable.

Effects of the eddy viscosity modelling are clear seen in terms of increasing in the energy level, according to an increase of the flow rate. In Fig. 1b the ensemble averaged stream-wise velocity profiles U^+ are reported in semi-logarithmic scales versus the wall coordinate Y^+. The FV no-model (APM and DPM) simulations well accord to DNS apart for the centre of the channel where turbulence is poorly resolved and it appears a deviation from the logarithmic. On the other hand, the effects of the eddy viscosity modelling appear

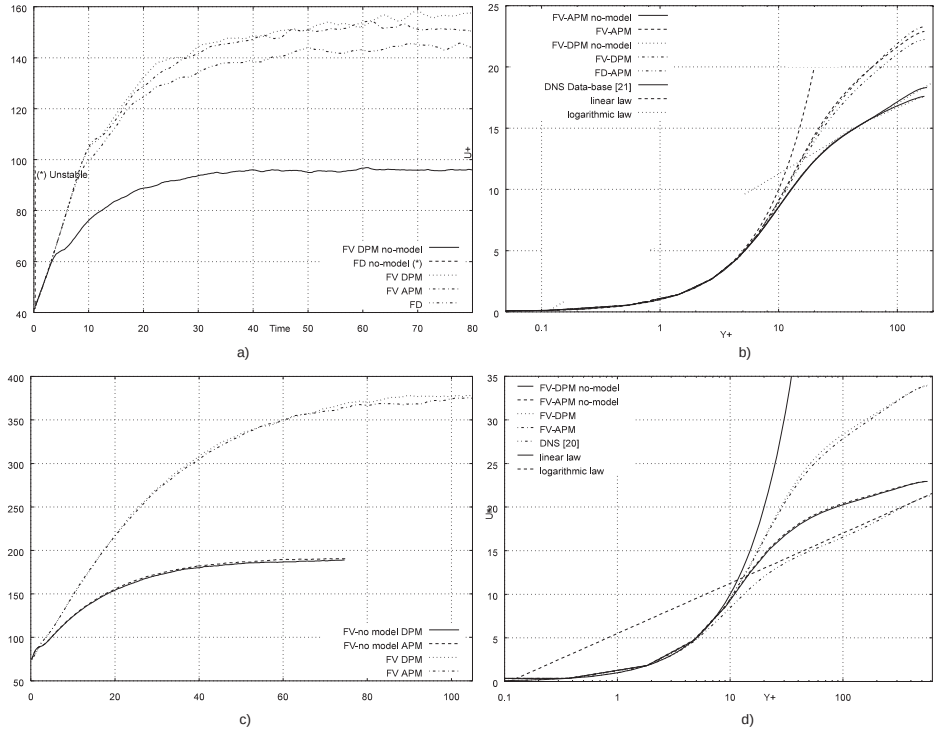

Fig. 1 Re_τ =180: (**a**) horizontal kinetic energy evolution; (**b**) velocity profiles in wall units; Re_τ =590: (**c**) horizontal kinetic energy evolution; (**d**) velocity profiles in wall units

in the higher levels of the velocity profiles, FD being slightly lesser. It is also evident a different slope from the theoretical law. This effect is substantially supposed due to the SGS modelling, since it is present both in FD and FV solutions, but it is worthwhile noticing that in LES context the analytical form of the law of the wall is not necessarily invariant to a filtering operation since the friction velocity of filtered data can be different from the unfiltered ones. Therefore, we assume the LES mean profiles can be only qualitatively compared to DNS, further analysis being required to produce congruent mean profiles. A further set of simulations was performed at higher Reynolds number, that is Re_τ =590, on the same computational grid. In Fig. 1c the horizontal component of the kinetic energy evolutions are reported for the case with and without SGS modelling. Solutions without SGS modelling reached earlier an energy equilibrium. Again, the FD-based solution was unstable. These results confirm the effect of the implicit built-in top-hat filtering associated to the integral formulation. The means velocity profiles illustrated in Fig. 1d highlight the higher values for the no-model simulations that is due only to filtering effects. The LES supplied by the SGS modelling increase the velocity

intensity, and a slope, slightly departing from the logarithmic law, is obtained someway better for the DPM case.

As brief concluding remarks, the better quality of second order FV formulations over FD based on divergence form seems indubitable. In fact, despite of the fact that the FD equations were written in conservative form, stable and quite accurate no-model solutions appeared only for the integral formulation. The action on the kinetic energy evolution appears not controlled by the FD method as unconditional numerical instability occurred. The built-in implicit top-hat filtering in FV formulation appears effective. The action of the eddy-viscosity dynamic model is someway excessive and must be still tuned by choosing a proper clipping criterion. Of course, other SGS modelling such as the deconvolution-based ones can also provide improvement in the solutions.

References

1. Sagaut P (2006) Large Eddy Simulation for incompressible flows. An introduction, 3 ed. Springer, Berlin
2. Berselli L, Iliescu T, Layton W (2005) Mathematics of large eddy simulation of turbulent flows. Springer, Berlin
3. Lesieur M, Métais O, Comte P (2005) Large-eddy simulations of turbulence. Cambridge University Press
4. Lund TS (1997) On the use of discrete filters for large eddy simulation. In: Ann. Research Briefs:83–95. Center for Turbulence Research, Stanford University
5. Gullbrand J, Chow FK (2003) The effect of numerical errors and turbulence models in large-eddy simulations of channel flow, with and without explicit filtering. J Fluid Mech 495:323–341
6. Vreman AW, Guerts BJ (2002) A new treatment of commutation-errors in large-eddy simulation. In: Adv In Turb IX. Proc. European Turbulence Conferences
7. Ferziger JH, Peric M (2001) Computational methods for fluid dynamics. Springer, Berlin Heidelberg New York
8. De Stefano G, Denaro FM, Riccardi G (2001) High order filtering for control volume flow simulations. Int J Num Meth Fluids 37(7):797–835
9. Iannelli P, Denaro FM, De Stefano G (2003) A deconvolution-based fourth order finite volume method for incompressible flows on non-iniform grids. Int J Num Meth Fluids 43(4):431–462
10. Denaro FM, De Stefano G, Iudicone D, Botte V (2007) A finite volume dynamic large-eddy simulation method for buoyancy driven turbulent geophysical flows. Ocean Modell 17(3):199–218
11. Meyers J, Guerts BJ, Sagaut P (2007) A computational error-assessment of central finite-volume discretizations in large-eddy simulation using a Smagorinsky model. J Comput Phys 227:156–173
12. Chorin AJ (1968) Numerical Solution of the Navier–Stokes Equations. Math Comp 22:745–762
13. Denaro FM (2003) On the application of the Helmholtz–Hodge decomposition in projection methods for the numerical solution of the incompressible Navier–Stokes equations with general boundary conditions. Int J Num Meth Fluids 43:43–69

14. Rider WJ (1995) Approximate projection methods for incompressible flow: implementation, variants and robustness. Technical Report LA-UR-200, Los Alamos National Laboratory
15. Almgren AS, Bell JB, Crutchfield W (2000) Approximate projection methods: Part I. Inviscid analsysis. SIAM J Sci Comput 22(4):1139–1159
16. Felten FN, Lund TS (2006) Kinetic energy conservation issues associated with the collocated mesh scheme for incompressible flow. J Comput Phys 215:465–484
17. Denaro FM (2005) Time-accurate intermediate boundary conditions for large eddy simulations based on projection methods. Int J Num Meth Fluids 48:869–908
18. Denaro FM (2006) A 3D second-order accurate projection-based finite volume code on non-staggered, non-uniform structured grids with continuity preserving properties: application to buoyancy-driven flows. Int J Num Meth Fluids 52:393–432
19. Aprovitola A, Denaro FM (2007) A non-diffusive, divergence-free, finite volume-based double projection method on non-staggered grids. Int J Num Meth Fluids 53(7):1127–1172
20. Moser RD, Kim J, Mansour NN (1999) Direct numerical simulation of turbulent channel flow up to Re_τ =590. Phys Fluids 11(4):943–945

Part IV

Error Assessment in Complex Applications

Reliability of Large-Eddy Simulation of Nonpremixed Turbulent Flames: Scalar Dissipation Rate Modeling and 3D-Boundary Conditions

L. Vervisch, G. Lodato, and P. Domingo

LMFN, CORIA – CNRS, Institut National des Sciences Appliquées de Rouen, France. vervisch@coria.fr, lodato@coria.fr, Domingo@coria.fr

Abstract. The intricate coupling between the numerical discretization of scalar field transport and the modeling of unresolved sub-grid scale fluctuations of chemical species is discussed. It is shown how the closures for the sub-grid scale scalar dissipation rate combine modeling of small scale diffusion with two error terms measuring the lack of accuracy in the transport of scalar field fluctuations energy. Then, the need of accounting for the three-dimensional character of turbulent flows at boundaries of computational domains is illustrated.

Keywords: Quality, Reliability, Large-eddy simulation, Boundary conditions, Flames, Chemistry

1 Introduction

Large-Eddy Simulation (LES) of nonpremixed turbulent flames relies on four major ingredients: (i) the Sub-Grid Scale (SGS) modeling of unresolved fluxes of momentum and mass, (ii) the description of chemistry and micro-mixing, (iii) the numerics, and (iv) the boundary conditions. Weakness in one of these ingredients can easily jeopardize turbulent flame LES quality. Two points related to (ii), (iii) and (iv) are considered in this paper. The chemistry and its tabulation are first discussed. The need to transport with accuracy the energy of scalar fields is expressed, along with related implications for subgrid-scale modeling of scalar dissipation rates and micro-mixing. Finally, the importance of boundary conditions is illustrated with LES involving a novel three-dimensional Navier Stokes Characteristic Boundary Conditions approach.

J. Meyers et al. (eds.), Quality and Reliability of Large-Eddy Simulations,

2 Error in Scalar Energy Transport: Impact on Scalar Variance and Dissipation Rate Modeling

Auto-ignition, flame stabilization, recirculating products, which may include intermediate species, and the prediction of some pollutants cannot be addressed without including detailed chemistry in sub-grid scale modeling. The difficulty is twofold: hydrocarbon chemistry involves numerous species and elementary reactions, which cannot all be considered in the LES solution, and, the strongly non-linear character of chemistry is coupled with the sub-grid scale fluctuations of species and temperature, which are not resolved by the grid. This lack of resolution results from the very localized heat release profiles through reaction zones and flames. Typically, under atmospheric pressure, flame thickness is of the order of a tenth of a millimeter with intermediate radical species evolving over even thinner layers inside reaction zones. When compared to combustion chambers of the order of tens of centimeters or even of the order of meters, flames evolve over too short distances to be resolved simultaneously with the eddies controlling large-scale mixing, at least with actual computer capabilities. The tabulation of chemical species behavior prior to LES is one of available options that was investigated to downsize combustion chemistry to make it compatible with flow solvers. This table is then filtered to be used in LES. For instance, presumed-PDF may be used to filter the chemical response, as it is done in the PCM (Presumed Conditional Moment) approach [22, 5, 6]. In nonpremixed systems, the filtering of the chemical table is calibrated from SGS energy of scalars, as the mixture fraction and the progress of reaction.

$Y_v = \widetilde{YY} - \widetilde{Y}\,\widetilde{Y}$ denotes the SGS energy of the reactive scalar Y. The balance equations for $\widetilde{Y}$ and Y_v may be written:

$$\frac{\partial \overline{\rho}\widetilde{Y}}{\partial t} + \nabla \cdot \overline{\rho}\widetilde{\mathbf{u}}\widetilde{Y} = -\overline{\tau}_Y + \nabla \cdot \left(\overline{\rho}\mathcal{D}\ \nabla \widetilde{Y}\right) + \widetilde{\dot{\omega}}_Y \tag{1}$$

$$\begin{aligned}\frac{\partial \overline{\rho}Y_v}{\partial t} + \nabla \cdot \overline{\rho}\widetilde{\mathbf{u}}Y_v = &-\nabla \cdot \left(\overline{\tau}_{Y^2} - 2\widetilde{Y}\overline{\tau}_Y\right) + \nabla \cdot \left(\overline{\rho}\mathcal{D}\ \nabla Y_v\right) \\ &- 2\overline{\tau}_Y \cdot \nabla \widetilde{Y} - 2\overline{s}_{\chi_Y} + 2\left(\widetilde{Y\dot{\omega}}_Y - \widetilde{Y}\widetilde{\dot{\omega}}_Y\right),\end{aligned} \tag{2}$$

where where $\tau_Y = \overline{\rho \mathbf{u} Y} - \overline{\rho}\widetilde{\mathbf{u}}\widetilde{Y}$ and $\tau_{Y^2} = \overline{\rho \mathbf{u} Y^2} - \overline{\rho}\widetilde{\mathbf{u}}\widetilde{Y^2}$ are SGS transport. $\overline{s}_\chi = \overline{\rho\mathcal{D}|\nabla Y|^2} - \overline{\rho}\mathcal{D}|\nabla \widetilde{Y}|^2$ is the SGS scalar dissipation rate. $\dot{\omega}_Y$ denotes the chemical source and usual notations are otherwise adopted.

The modeling of $\overline{s}_\chi$ is a very sensitive point, it impacts on the shape of the presumed probability density function and modifying its expression, or any adjustable parameter entering this expression, strongly modifies flame and flow responses. This is illustrated in Fig. 1 showing $\left\langle \widetilde{Y}_{CO} \right\rangle$, the time average of the filtered CO mass fraction in LES of a lifted jet flame, which is performed with two different expressions of the scalar dissipation rate. The first is the usual linear relaxation hypothesis:

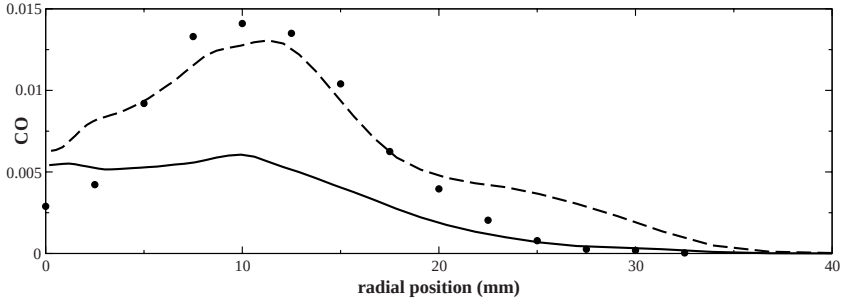

Fig. 1 Radial profiles of CO mass fraction at the lifted turbulent flame base. *Symbol*: measurements [4] *Solid-line*: LES with $\overline{s}_{\chi_Y}$ given by Eq. (3). *Dash-Line*: LES with $\overline{s}_{\chi_Y}$ given by Eq. (4)

$$\overline{s}_{\chi_Y} = \overline{\rho}\frac{Y_v}{\Delta^2/\nu_T} \tag{3}$$

the second is a novel closure proposed by Domingo et al. [6] accounting for the fact that burning favors strong gradients of Y, thereby increasing SGS mixing when the unmixedness $S = Y_v/\widetilde{Y}(1-\widetilde{Y})$ is large [3]:

$$\overline{s}_{\chi_Y} = (1-S)\overline{\rho}\frac{Y_v}{\Delta^2/\nu_T} + S\left(-\overline{\rho}\mathcal{D}|\nabla\widetilde{Y}|^2 + \overline{Y\dot{\omega}}_Y - \overline{Y^{Eq}\dot{\omega}}_Y/2\right), \tag{4}$$

where Δ is the filter size, ν_T the SGS viscosity and Y^{Eq} the value of Y under chemical equilibrium condition, which may depend on position because of non-uniform equivalence ratio. It is discussed in [6] that Eq. (4) is exact when $S \to 1$ and also when $S \to 0$ for a quasi-Gaussian SGS probability density function of Y. Modifying the scalar dissipation rate modeling has a strong impact on the shape of the flame base and on the radial spreading of the burnt gases; then, the prediction of intermediate species as carbon monoxide (CO) is also strongly affected by the modeling of $\overline{s}_{\chi_Y}$ (Fig. 1). Since the turbulent flame simulation is that sensitive to the modeling of the SGS scalar dissipation rate, it is legitimate to wonder whether the choice of the expression for $\overline{s}_{\chi_c}$ can be influenced by direct or indirect interactions with the numerics. Here the simulations where performed using a fourth-order finite volume skew-symmetric-like scheme [8] for the spatial derivatives, a discretization ensuring a correct transport of the energy of the velocity field. The mesh is composed of 2,150,000 nodes with a characteristic mesh size h that varies 0.3 mm $< h <$ 2.5 mm. Its spanwise and streamwise lengths are 28D×28D and 90D, respectively. The filtered structure function model [7] is used to express the unknown SGS transport by velocity fluctuations.

Y_v is the difference between the filtered energy of the scalar and the energy of the resolved scalar field. The transport of Y_v by the large eddies should be

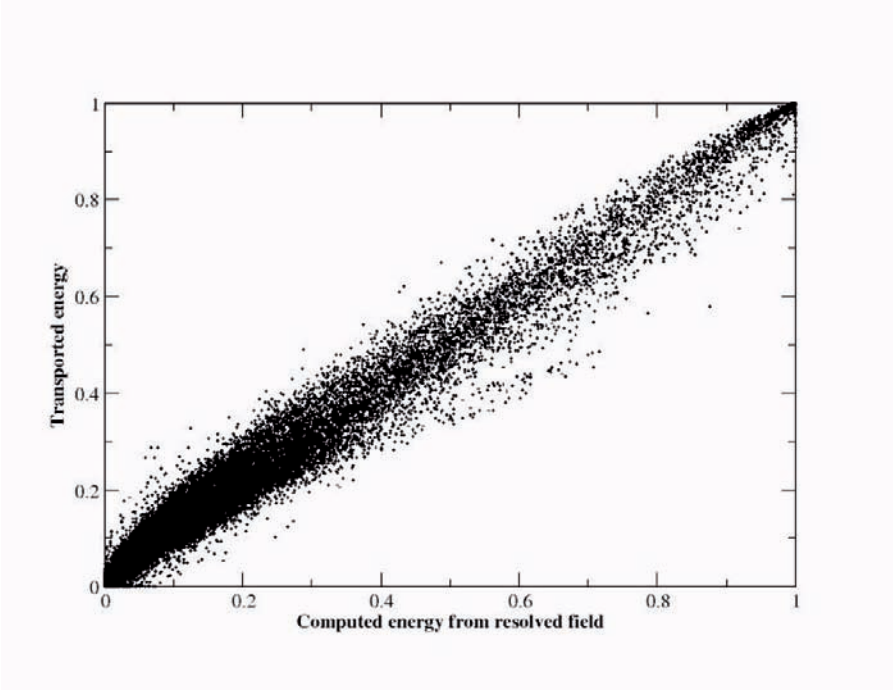

Fig. 2 $\theta = (\widetilde{Y})^2$ solving its balance equation (Eq. 7) versus $(\widetilde{Y})^2$ obtained from the square of the resolved $\widetilde{Y}$ field (Eq. 1), lifted jet-flame [6]

done so that it is coherent with the transport of the resolved energy $(\widetilde{Y})^2$. This can be quantified on LES meshes by two error terms E_Y^u and E_Y^D defined as:

$$E_Y^u = \frac{1}{2}\overline{\rho}\widetilde{\mathbf{u}} \cdot \nabla \widetilde{Y}^2 - \overline{\rho}\widetilde{\mathbf{u}}\widetilde{Y} \cdot \nabla \widetilde{Y} \tag{5}$$

$$E_Y^D = \frac{1}{2}\nabla \cdot \left(\overline{\rho} D^* \nabla \widetilde{Y}^2\right) - \widetilde{Y}\nabla \cdot \left(\overline{\rho} D^* \nabla \widetilde{Y}\right) - \overline{\rho} D^* |\nabla \widetilde{Y}|^2, \tag{6}$$

where ρ is the density, $\mathbf{u}$ the velocity and $D^* = D + D_T$ the sum of the molecular and SGS diffusion coefficient of the scalar Y. Both E_Y^u and E_Y^D vanishes when the numerical discretization conserves scalar energy. These error terms are a direct measure of the departure that may be expected when comparing $\theta = (\widetilde{Y})^2$ obtained from the solving of its balance equation,[1]

$$\frac{\partial \overline{\rho}\theta}{\partial t} + \nabla \cdot \overline{\rho}\widetilde{\mathbf{u}}\theta = -\nabla \cdot (2\widetilde{Y}\ \overline{\tau}_Y) + \nabla \cdot (\overline{\rho}\mathcal{D}\ \nabla\theta) + 2\overline{\tau}_Y \cdot \nabla \widetilde{Y} - 2\overline{\rho} D |\nabla \widetilde{Y}|^2 + 2\widetilde{\dot{\omega}}_Y \widetilde{Y} \tag{7}$$

[1] Hereafter θ always denotes $(\widetilde{Y})^2$ computed from Eq. (7).

with $(\widetilde{Y})^2$ deduced from simply taking the square of $\widetilde{Y}$, obtained from Eq. (1). Such a comparison is shown in Fig. 2 for a passive scalar ($\dot{\omega}_Y = 0$), where $E_Y^u = E_Y^D = 0$ would correspond to a unity slope line. A non-negligible deviation from this line is observed, which illustrates the lack of precision in the transport of scalar energy. In actual simulations, the error terms E_Y^u and E_Y^D are combined with the SGS closure for the scalar dissipation rate, which is in fact a model for the term,

$$\overline{s}_\chi^* = \overline{s}_\chi + (E_Y^u - E_Y^D) \tag{8}$$

leading to different flame results when modifying the numerics, or the mesh, with an obvious impact on LES reliability.

For a given modeling of $\overline{s}_\chi$, the difference $\Delta Y^2 = (\widetilde{Y})^2 - \theta$ informs on the possible variations of Y_v that may be attributed to the combined action of E_Y^u and E_Y^D. The unmixedness factor S, defined above and varying between zero and unity, is constructed for Y_v (Fig. 3(a)) and $Y_v + |\Delta Y^2|$ (Fig. 3(b)). S_Y is one of the control parameters of filtered chemistry [6] and Fig. 3 shows that it is strongly sensitive to error in scalar energy transport.

The development and the use of energy conservative schemes for velocity [12], but also for scalar fields on unstructured mesh thus appears as a major issue of turbulent combustion LES.

3 Three-Dimensional Boundary Conditions for Increasing LES Reliability

Turbulent flames and acoustics are coupled in many combustion systems and, when it is the case, a fully compressible flow solver is needed to accurately simulate mixing and reaction. In such LES, the boundary conditions treatment is usually grounded on relations valid only when the flow is orthogonal to the face boundary. The Navier-Stokes equations are written in terms acoustic wave amplitudes, then one-dimensional characteristic wave equations, coupled with a specific boundary condition (inlet, outlet, wall), are used to determine these waves amplitude, which are finally used in the Navier-Stokes equations to advance the system in time at the boundary [15].

Turbulent flows are not likely to behave as one-dimensional when entering or leaving computational domains. The net result is the generation of flow perturbations at boundaries, which may strongly reduce LES accuracy. These perturbations may be damped by adding artificial dissipation when approaching the boundaries, or the acoustic response of the face boundary may also be tuned via target solutions and relaxation parameters. More or less justified ad-hoc procedures are therefore introduced. Unfortunately, these ad-hoc procedures need to be modified when changing the flow parameters of a given configuration. Then, it becomes quite difficult to really compare different simulations of the same problem, since the boundary treatment has been adjusted for every set of flow parameters, reducing LES reliability.

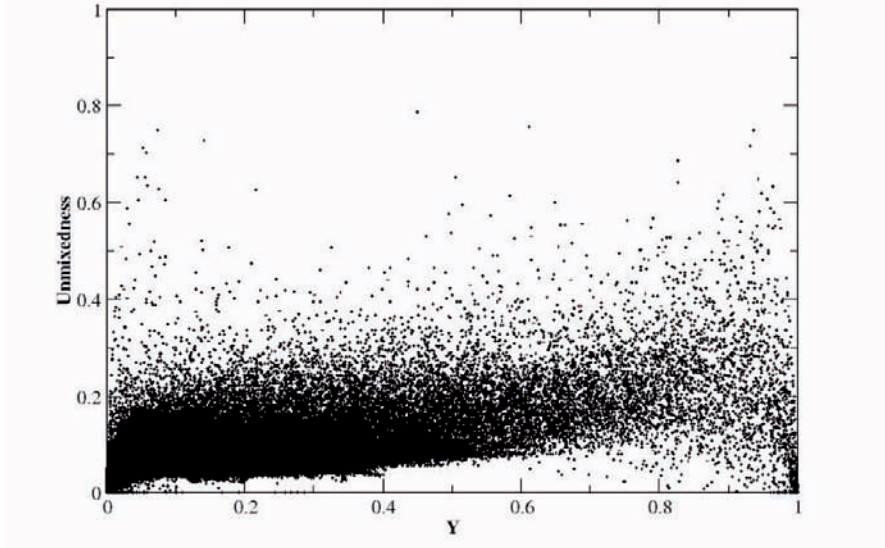

(a)

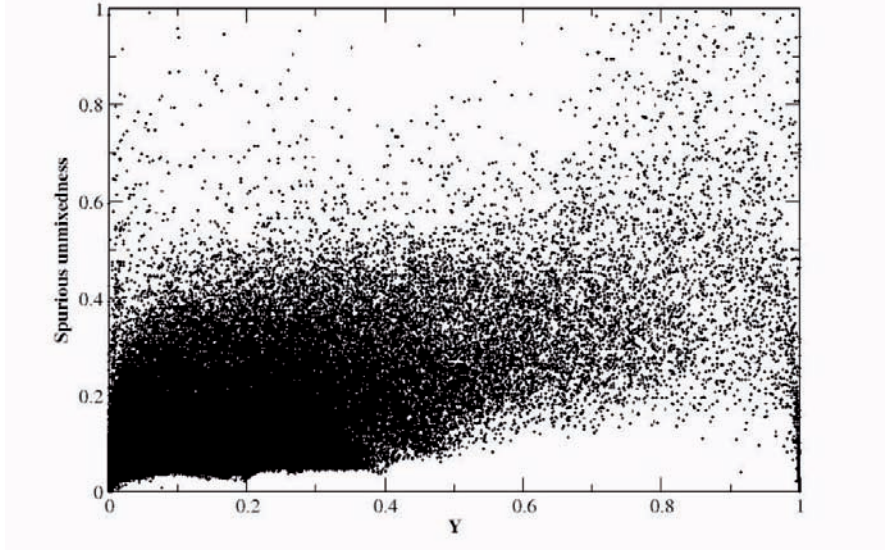

(b)

Fig. 3 (**a**): $S = Y_v/(\widetilde{Y}(1-\widetilde{Y}))$, (**b**): $(Y_v + |\Delta Y^2|)/(\widetilde{Y}(1-\widetilde{Y}))$ versus $\widetilde{Y}$

In this context, numerous developments may be found in the literature concerning boundary conditions and their applications [17, 20, 21, 15, 1, 9, 19, 13, 14, 18, 23, 16, 2]. This section discusses recent developments in boundary conditions treatment by Lodato et al. [11], in which the three-dimensional character of turbulent flows at boundaries is accounted for. This is done by including in the analysis convection and pressure gradients developing in the directions of the boundary plane when computing the amplitudes of the acoustic waves. Because these additional transverse terms are coupled with characteristic waves traveling along directions orthogonal to adjacent boundaries, on edges and corners, three-dimensional characteristic coupled waves must be studied. Moreover, when edges or corners result from intersection of planes having different types of boundary conditions (inlet, outlet, wall), compatibility conditions must be carefully imposed to preserve the well-posedness of the problem.

The full description of three-dimensional Navier-Stokes Characteristic Boundary Conditions (3D-NSCBC) is out of the scope of this paper, details may be found in [11], only the main lines are given along with some results to illustrate the potential of such boundary treatment and its impact on LES reliability.

Characteristic waves are represented by their amplitude time variations $\mathcal{L}_i$, $\mathcal{M}_i$ and $\mathcal{N}_i$ corresponding to the three physical-space directions with the subscript 'i' referring to the i-th characteristic wave (continuity, momentum, energy and scalar). Some waves leave the domain, while others enter from outside, the incoming ones must be specified to close the boundary problem. Usually, only the waves corresponding to the direction normal to the boundary are considered, for instance only the $\mathcal{L}_i$ for a boundary that is orthogonal to the first direction. In 3D-NSCBC, the waves in the three directions are included in the derivation of boundary conditions. At a corner, the system verified by the wave amplitudes reads:

$$\begin{cases} \dfrac{\partial \rho}{\partial t} = \mathcal{W}_\rho(\mathcal{L}_i, \mathcal{M}_i, \mathcal{N}_i) \\ \dfrac{\partial u_k}{\partial t} = \mathcal{W}_{u_k}(\mathcal{L}_i, \mathcal{M}_i, \mathcal{N}_i) \\ \dfrac{\partial p}{\partial t} = \mathcal{W}_p(\mathcal{L}_i, \mathcal{M}_i, \mathcal{N}_i) \\ \dfrac{\partial Z}{\partial t} = \mathcal{W}_Z(\mathcal{L}_i, \mathcal{M}_i, \mathcal{N}_i), \end{cases} \tag{9}$$

where ρ is the density u_k the velocity component in the direction k, Z is a scalar and $\mathcal{W}_m$ denotes functions of wave amplitudes associated to the boundary conditions that is prescribed in terms of $\partial\rho/\partial t$, $\partial u_k/\partial t$, $\partial p/\partial t$ and $\partial Z/\partial t$. Prescribing time evolution of these primitive variables at the boundary, provides a way to estimate $\mathcal{L}_i$, $\mathcal{M}_i$ and $\mathcal{N}_i$ from Eq. (9), so that they can be used to close the full set of Navier-Stokes equation at the boundaries. In Eq. (9), when the boundary is normal to the direction of the waves $\mathcal{L}_i$, the

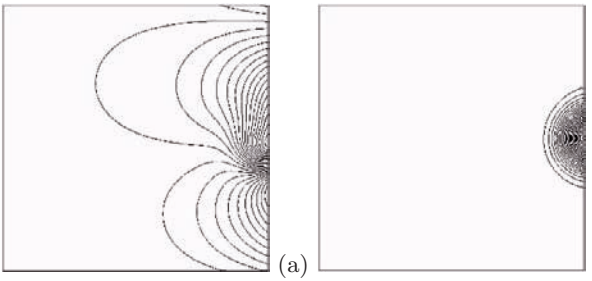

Fig. 4 Vortex test: pressure contours as the vortex crosses the boundary (Ma = 0.00575). Standard NSCBC non-reflecting outflow (**a**); 3D-NSCBC non-reflecting outflow (**b**)

combination of $\mathcal{M}_i$ and $\mathcal{N}_i$ represents the transverse contribution that is usually neglected. For every boundary, a linear system must be combined with compatibility conditions in case of inlet/wall, outlet/wall, inlet/outlet to get the unknown incoming wave amplitudes.

The importance of transverse terms at boundaries is illustrated in Fig. 4 showing the pressure contour when a vortex is traveling through an exit. Unphysical noise is generated by usual non-reflecting outflow, while the novel 3D-NSCBC treatment preserves the correct pressure distribution when the vorticity field leaves the domain.

The propagation of a spherical pressure wave through edges and corners is a stringent test of three-dimensional boundary conditions. Spurious noise is easily generated when waves crosses boundaries, leading to solutions as the one observed in Fig. 5(a). Pressure patterns are generated that are driven by the edges and the corners; the quality of LES can be more than offset by such flow behavior at boundaries. The use of a proper three-dimensional boundary conditions strongly improves the physical behavior of the flow Fig. 5(b): the pressure waves leave the domain preserving their spherical character.

Inlet and outlet of LES (or DNS) computational domains are known to play a key role on the behavior of the interior solution. Moving outflow planes away from the most interesting part of the solution is the most adopted approach to avoid pollution from exit boundaries, this may be accompanied by mesh relaxation or even a so-called 'sponge domain' adding artificial viscosity to damp any extraneous perturbation added to the flow at the boundary. Figure 6 shows LES of a jet having a boundary intentionally located in a zone where turbulence is still fully developed. The computational domain is a box of dimensions $14D \times 5D \times 5D$ with D the diameter, the mesh is composed of $200 \times 80 \times 80$ grid points. The boundary treatment that includes the three-dimensional characteristic waves allows for evacuating the vortex tubes and other turbulent structures without noise or flow deformation Fig. 6(b).

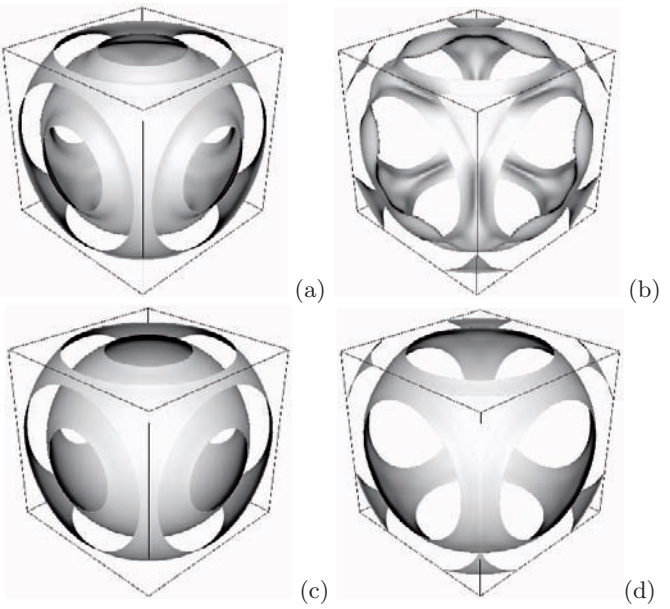

Fig. 5 Spherical pressure wave test: pressure iso-surfaces evolution (iso-value $p/p_{\mathrm{ref}} = 1000$). (**a**–**b**): Standard-NSCBC, (**d**–**f**): 3D-NSCBC non-reflecting outflows

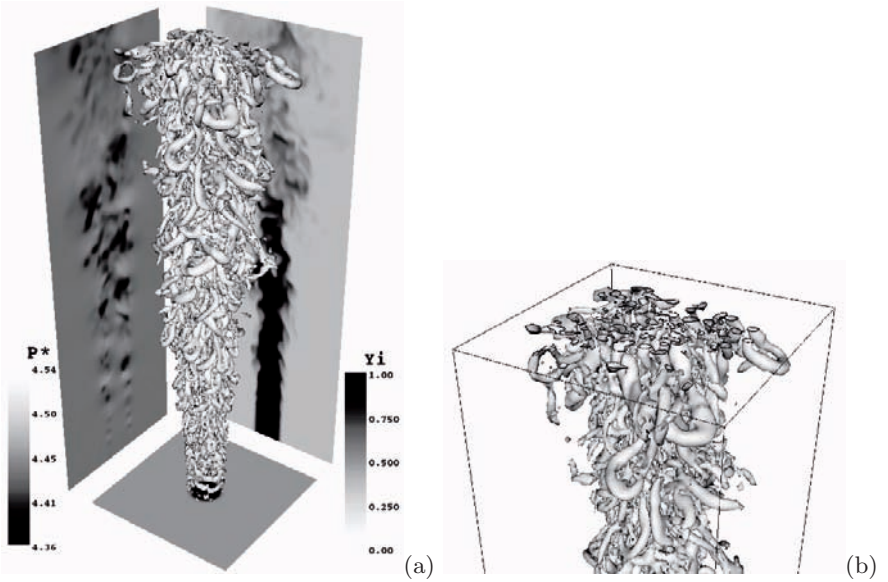

Fig. 6 Free round-jet with 3D-NSCBC. (**a**): Q-criterion = 0.5 contours (*center*), pressure (*left*) and passive scalar (*right*) distributions over orthogonal axial planes ($t = 157.1D/U_{\mathrm{b}}$). (**b**): detail of $Q = 0.5$ contours at the exit boundary

4 Concluding Remarks

Large-Eddy Simulation is highly sensitive to numerical errors and, in many occasions, sub-grid scale modeling is unfortunately entangled with these errors [10]. Sub-grid scale modeling of chemical species fluctuations, based on a measure of the sub-grid scale variance, is directly related with the error introduced when transporting the energy of scalar fields. Accordingly, the modeling of sub-grid scale scalar dissipation rate should not be addressed without discussing also the numerical discretization.

Fully compressible simulations of the Navier-Stokes equations are highly sensitive to boundary conditions. Any specific treatment that calibrate the three-dimensional character of turbulence at boundaries using one-dimensional prototype flows is likely to be deficient when vorticity crosses the boundary. To overcome this inherent difficulty of DNS and LES of compressible flows, the treatment of acoustic waves at boundaries can be expressed in its three-dimensional form, to evacuate turbulence with almost no spurious flow distortion.

References

1. Baum M, Poinsot T, Thévenin D (1995) Accurate boundary conditions for multicomponent reactive flows. Journal of Computational Physics 116(2):247–261
2. Bogey C, Bailly C (2007) An analysis of the correlations between the turbulent flow and the sound pressure fields of subsonic jets. Journal of Fluid Mechanics 583:71–97
3. Bray KNC (1996) The challenge of turbulent combustion. Proceedings of Combustion Institute 26:1–26
4. Cabra R, Chen JY, Dibble RW, Karpetis AN, Barlow RS (2005) Lifted methane-air jet flame in vitiated coflow. Combustion and Flame 143(4):491–506
5. Domingo P, Vervisch L, Payet S, Hauguel R (2005) DNS of a premixed turbulent V-flame and LES of a ducted-flame using a FSD-PDF subgrid scale closure with FPI-tabulated chemistry. Combustion and Flame 143(4):566–586
6. Domingo P, Vervisch L, Veynante D (2008) Large-eddy simulation of a lifted methane-air jet flame in a vitiated coflow. Combustion and Flame 152(3): 415–432
7. Ducros F, Comte P, Lesieur M (1996) Large-eddy simulation of transition to turbulence in a boundary layer developing spatially over a flat plate. Journal of Fluid Mechanics 326:1–36
8. Ducros F, Laporte F, Soulères T, Guinot V, Moinat P, Caruelle B (2000) High-order fluxes for conservative skew-symmetric-like schemes in structured meshes: application to compressible flows. Journal of Computational Physics 161: 114–139
9. Hixon R, Shih SH, Mankabadi RR (1995) Evaluation of boundary conditions for computational aeroacoustics. AIAA Journal 33(11):2006–2012

10. Klein M, Meyers J, Geurts BJ (2008) Assessment of LES quality measures using the error landscape approach. In: Meyers J, Geurts BJ, Sagaut P (eds) Quality and Reliability of Large Eddy Simulation. Springer, Berlin Heidelberg New York
11. Lodato G, Domingo P, Vervisch L (2008) Three-dimensional boundary conditions for direct and large-eddy simulation of compressible viscous flows. Journal of Computational Physics 227(10):5105–5143
12. Morinishi Y, Lund TS, Vasilyev OV, Moin P (1998) Fully conservative higher order finite difference schemes for incompressible flow. Journal of Computational Physics 143(1):90–124
13. Nicoud F (1999) Defining wave amplitude in characteristic boundary conditions. Journal of Computational Physics 149:418–422
14. Okong'o N, Bellan J (2002) Consistent boundary conditions for multicomponent real gas mixtures based on characteristic waves. Journal of Computational Physics 176(2):330–344
15. Poinsot T, Lele SK (1992) Boundary conditions for direct simulations of compressible viscous flows. Journal of Computational Physics 1(101):104–129
16. Polifke W, Wall C, Moin P (2006) Partially reflecting and non-reflecting boundary conditions for simulation of compressible viscous flow. Journal of Computational Physics 213(1):437–449
17. Rudy DH, Strikwerda JC (1980) A nonreflecting outflow boundary condition for subsonic Navier–Stokes calculations. Journal of Computational Physics 36: 55–70
18. Sutherland JC, Kennedy CA (2003) Improved boundary conditions for viscous, reacting, compressible flows. Journal of Computational Physics 191(2):502–524
19. Tam CKW (1998) Advances in numerical boundary conditions for computational aeroacoustics. Journal of Computational Acoustics 6(4):377–402
20. Thompson KW (1987) Time dependent boundary conditions for hyperbolic systems. Journal of Computational Physics 68:1–24
21. Thompson KW (1990) Time dependent boundary conditions for hyperbolic systems, II. Journal of Computational Physics 89:439–461
22. Vervisch L, Hauguel R, Domingo P, Rullaud M (2004) Three facets of turbulent combustion modelling: DNS of premixed V-flame, LES of lifted nonpremixed flame and RANS of jet-flame. Journal of Turbulence 5, Art no 4
23. Yoo CS, Wang Y, Trouvé A, Im HG (2005) Characteristic boundary conditions for direct simulations of turbulent counterflow flames. Combustion Theory and Modeling 9(4):617–646

LES at Work: Quality Management in Practical Large-Eddy Simulations

Christer Fureby[1,2] and Rickard E. Bensow[1]

[1] Department of Shipping and Marine Technology, Chalmers University of Technology, SE 412 96 Göteborg, Sweden
[2] Defense Security Systems Technology, The Swedish Defense Research Agency – FOI, SE 147 25 Tumba, Stockholm, Sweden

Abstract. This paper aims at reviewing some important aspects of Large Eddy Simulation (LES) as applied to engineering applications. In particular we focus on aspects relevant to quality management and validation and verification procedures. After outlining the LES formalism and the numerical methods considered appropriate for engineering applications we discuss particular features of LES that require specific treatment or attention in the validation and verification process. This is illustrated in more detail when different flows are introduced and discussed. Applications are selected from different fields, and are of different complexity, being supported by reference data, to demonstrate a variety of modeling aspects in engineering. Finally, we connect the various aspects of validation and verification with the technical aspects of engineering LES.

1 Introduction

Large Eddy Simulation (LES) is fast becoming a liable alternative for engineering applications, despite its higher cost compared to contemporary methods. The reason is the capability of LES to resolve the large-scale unsteady flow physics, such as coherent structure dynamics, directly on the mesh. This simplifies the modeling of mixing, combustion and multi-phase processes, where inclusion of small scales noticeably improves the quality of the computations, and flow induced noise and vibrations, where small-scale pressure fluctuations are of primary interest. LES should also provide higher accuracy, reliability and versatility compared to the current industry standard in Computational Fluid Dynamics (CFD), being Reynolds Averaged Navier-Stokes (RANS) models, in which only the mean flow is solved for. However, this comes at the price of increased computational cost, sensitivity of problem set-up and solution procedures.

LES of engineering applications, typically outside of the well-validated regime, calls for careful assessment of the quality of the results, and the complications are many and of different character. These include grid refinement

J. Meyers et al. (eds.), Quality and Reliability of Large-Eddy Simulations,

effects, impact of geometric simplifications and imperfections, boundary conditions, physical modeling, etc. The characterization and management of these important issues calls for a closer dialog both between CFD scientists and engineers, and between the CFD community and Experimental Fluid Dynamics (EFD) scientists and engineers.

In this paper, we aim at raising different issues in quality assessment from our portfolio of problems, ranging from canonical flows to challenging engineering problems. Our aim here is not to give a complete picture of the problems that may arise, nor to give a procedure to evaluate the reliability of the results. The disposition of the paper is as follows: We start by giving some background on LES, subgrid modeling and numerical methods. We then discuss the concept of verification and validation in CFD and relate this to complications in applying these ideas to engineering cases in general and LES in particular. Finally, we present a suite of LES results and relate some of the issues in validation to these practical computations.

2 The Large Eddy Simulation Formalism

The starting point of this study is the equations of motions describing incompressible, compressible or reactive flows, which can be comprehensively formulated as,

$$\partial_t(\mathbf{u}) + \nabla \cdot \mathbf{F}(\mathbf{u}, \mathbf{u}) = \mathbf{f}(\mathbf{u}), \tag{1}$$

where $\mathbf{u} = [\rho, \rho\mathbf{v}, \rho E, \rho Y_i]^T$ is the vector of dependent variables, where ρ is the density, $\mathbf{v}$ the velocity, $E = e + \frac{1}{2}\mathbf{v}^2$ the total energy, e the internal energy and Y_i the species mass fractions. In addition, $\mathbf{F} = \mathbf{F}(\mathbf{u}, \mathbf{u}) = [\rho\mathbf{v}, \rho\mathbf{v} \otimes \mathbf{v} + p\mathbf{I} - \mathbf{S}, \rho\mathbf{v}E + p\mathbf{v} - \mathbf{S}\mathbf{v} - \mathbf{h}, \rho\mathbf{v}Y_i - \mathbf{j}_i]^T$ is the flux vector and $\mathbf{f} = \mathbf{f}(\mathbf{u}) = [0, \rho\mathbf{f}, \rho\sigma, \dot{w}_i]^T$ the source term. Following [1, 2, 3, 4] we assume the fluid to be linear viscous ($\mathbf{S} = (\lambda + \frac{2}{3}\mu)(\nabla \cdot \mathbf{v})\mathbf{I} + 2\mu\mathbf{D}_D$) with Fourier heat conduction ($\mathbf{h} = \kappa\nabla T$), Fickian diffusion ($\mathbf{j}_i = D_i\nabla Y_i$) and Arrhenius chemistry ($\dot{w}_i = M_i[P_{ij}\dot{w}_j]$), and satisfying the classical thermal and caloric equations of state ($p = \rho RT$ and $e = h - p/\rho = \int c_v dT$). Moreover, $\mathbf{f}$ is the specific body force and σ the non-mechanical energy source. R is the (composition dependent) gas constant, M_i the species molar mass, μ the viscosity, $\lambda + \frac{2}{3}\mu$ the bulk viscosity, κ the thermal diffusivity, h the enthalpy, c_v the specific heat (at constant volume), D_i the species diffusivity, P_{ij} the Stoichiometric matrix, and $\dot{w}_j$ the j^{th} reaction rate. From a computational view, it may be convenient to express (1) in terms of convective and diffusive fluxes, $\mathbf{F}_C = [\rho\mathbf{v}, \rho\mathbf{v} \otimes \mathbf{v}, \rho\mathbf{v}E, \rho\mathbf{v}Y_i]^T$ and $\mathbf{F}_D = [0, -p\mathbf{I} + \mathbf{S}, -p\mathbf{v} + \mathbf{S}\mathbf{v} + \mathbf{h}, \mathbf{j}_i]^T$, such that $\partial_t(\mathbf{u}) + \nabla \cdot \mathbf{F}_C(\mathbf{u}, \mathbf{u}) = \nabla \cdot \mathbf{F}_D(\mathbf{u}, \mathbf{u}) + \mathbf{f}(\mathbf{u})$.

Most flows are turbulent, and the classical picture of turbulence starts from a sequence of bifurcations in a laminar flow, each of which renders more eddies of smaller and smaller scales. The kinetic energy is found to be of the form $E(k) = C_k\varepsilon^{2/3}k^{-5/3}f(k\ell_K)$, where the length scale $1/k$ corresponds to the

wavenumber k, f is a damping function (for high k) and ℓ_K is the Kolmogorov length scale, at which the smallest turbulent eddies dissipate into heat. Most of the kinetic energy is contained within the (large) integral scales, ℓ_I, from which energy is transported by the cascade process down to the Kolmogorov scales. In most flows, the large-scale flow form coherent structures, containing most of the energy, typically spanning a range of scales from ℓ_I to ℓ_T, where ℓ_T is the (intermediate) Taylor scale. These coherent structures consist of relatively closely bounded vortex filaments that move collectively in the flow, being responsible for most of the large-scale mixing and dynamics. Dimensional analysis suggest that $\ell_K \approx (\nu^3/\varepsilon)^{1/4}$ and $\ell_I/\ell_T \approx Re_I^{1/2}$, where ε is the dissipation, [5], and by assuming equilibrium between production, $P \propto v_I^3/\ell_I$, and dissipation it follows that $\ell_I/\ell_K \approx Re_I^{3/4}$. These relations suggest that a DNS will require $N_{DNS} \approx (\ell_I/\ell_K)^3 \approx Re_I^{9/4}$ cells whereas a LES would only require $N_{LES} \approx (\ell_I/\ell_T)^3 \approx Re_I^{3/2}$ cells. Hence, LES is cheaper than DNS, although still expensive compared to RANS.

The motivation behind the development of LES was to develop a modeling framework that is more accurate than RANS and less expensive than DNS. At present there exists two competing types of LES: *explicit* LES, [1, 2, 3, 6, 7], and *implicit* LES, [8, 9, 10]. Both approaches are based on filtering (1), either explicitly or implicitly, but differ primarily in the way that the unresolved (subgrid) flow physics is modeled. In *explicit* LES, physics based models are used to model these processes, [1, 7, 11], whereas in *implicit* LES the leading order truncation error of specific numerical algorithms are used to emulate these physical processes [10, 12].

In order to separate between resolved and subgrid parts, $\mathbf{u}$ is decomposed as $\mathbf{u} = \bar{\mathbf{u}} + \mathbf{u}'$, where $\bar{\mathbf{u}} = G(\mathbf{x}, \Delta) * \mathbf{u}$ is the resolved part and G the filter kernel with filter width Δ. By applying this filtering operation to the governing Equation (1) we obtain,

$$\partial_t(\bar{\mathbf{u}}) + \nabla \cdot \mathbf{F}(\bar{\mathbf{u}}, \bar{\mathbf{u}}) = -\nabla \cdot \mathbf{B}(\mathbf{u}, \bar{\mathbf{u}}) + \mathbf{f}(\bar{\mathbf{u}}) + \sigma(\mathbf{u}, \bar{\mathbf{u}}), \tag{2}$$

where $\nabla \cdot \mathbf{B}(\mathbf{u}, \bar{\mathbf{u}}) = \overline{\nabla \cdot \mathbf{F}(\mathbf{u}, \mathbf{u})} - \nabla \cdot \mathbf{F}(\bar{\mathbf{u}}, \bar{\mathbf{u}}) = [\nabla \cdot \overline{\mathbf{F}(\mathbf{u}, \mathbf{u})} - \nabla \cdot \mathbf{F}(\bar{\mathbf{u}}, \bar{\mathbf{u}})] + [\overline{\nabla \cdot \mathbf{F}(\mathbf{u}, \mathbf{u})} - \nabla \cdot \overline{\mathbf{F}(\mathbf{u}, \mathbf{u})}]$ is the unresolved transport term and $\sigma(\mathbf{u}, \bar{\mathbf{u}}) = \overline{\mathbf{f}(\mathbf{u})} - \mathbf{f}(\bar{\mathbf{u}})$ is the unresolved source term, both of which require closure modeling to take the subgrid physics into account. The unresolved transport term, $\nabla \cdot \mathbf{B}$, consists of the subgrid term, $\nabla \cdot \overline{\mathbf{F}(\mathbf{u}, \mathbf{u})} - \nabla \cdot \mathbf{F}(\bar{\mathbf{u}}, \bar{\mathbf{u}})$, representing the subgrid physics, and the commutation error term, $\overline{\nabla \cdot \mathbf{F}(\mathbf{u}, \mathbf{u})} - \nabla \cdot \overline{\mathbf{F}(\mathbf{u}, \mathbf{u})}$, representing the fact the differentiation and filtering do not generally commute, [13]. In practice, however, we typically neglect the commutation error term, and take $\nabla \cdot \mathbf{B} \approx \nabla \cdot [\overline{\mathbf{F}(\mathbf{u}, \mathbf{u})} - \mathbf{F}(\bar{\mathbf{u}}, \bar{\mathbf{u}})]$. Furthermore, the flux function $\mathbf{F}$ can be split into its convective and diffusive parts ($\mathbf{F}_D$ and $\mathbf{F}_C$, respectively) such that $\nabla \cdot \mathbf{B} \approx \nabla \cdot [\overline{\mathbf{F}_C(\mathbf{u}, \mathbf{u})} - \mathbf{F}_C(\bar{\mathbf{u}}, \bar{\mathbf{u}})] + \nabla \cdot [\overline{\mathbf{F}_D(\mathbf{u}, \mathbf{u})} - \mathbf{F}_D(\bar{\mathbf{u}}, \bar{\mathbf{u}})]$. The convective part is well-known, e.g. [1, 2, 7], whereas both the diffusive part and the source term, $\sigma(\mathbf{u}, \bar{\mathbf{u}})$, are less familiar since they mainly appear in compressible, reactive and multi-phase LES. For example, our inability to

model σ has contributed to the plethora of turbulent combustion models, [14], available and a better treatment of these terms would be most welcome.

In order to close (2) and to incorporate the effects of the subgrid physics we must provide closure models for $\nabla \cdot \mathbf{B}$, or rather $\mathbf{B}$, and σ. In most LES only the convective contribution to $\nabla \cdot \mathbf{B}$ is considered, i.e. $\nabla \cdot \mathbf{B} \approx \nabla \cdot [\overline{\mathbf{F}_C(\mathbf{u},\mathbf{u})} - \mathbf{F}_C(\bar{\mathbf{u}},\bar{\mathbf{u}})]$, based on which most subgrid models are developed. Although an abundance of subgrid models exist for incompressible LES, e.g. [1], not many of these are further developed to also handle compressible or reactive LES. Examplifying with models for incompressible flow, we have the One Equation Eddy Viscosity (OEEVM) model, [15], the Smagorinsky (SMG) model, [16, 17], the Structure Function Model (SFM), [18], and the Mixed Model (MM), [19, 20]. The former three are of the form $\mathbf{B}_{EV} \approx -2\mu_k \nabla \bar{\mathbf{v}}|_{sym}$, whereas the MM is of the form $\mathbf{B} \approx \overline{\mathbf{F}_C(\bar{\mathbf{v}},\bar{\mathbf{v}})} - \mathbf{F}_C(\overline{\bar{\mathbf{v}}},\overline{\bar{\mathbf{v}}}) + \mathbf{B}_{EV}$, in which μ_k is the subgrid viscosity which is to be modeled differently in the OEEVM, SMG and SFM. The inevitable model coefficients are obtained either by integrating the energy spectra, [1], or through a dynamic procedure, [17]. The subgrid source terms, σ, are often more complicated to handle since they are usually related to other types of physical processes such as reactions, [21]. For reacting flows we may either use flamelet models, [21], or finite rate chemistry models, [14, 21]. In the former, the species (or Y_i) equations are replaced by equations for the mixture fraction, z, and the reaction coordinate, c, in which the reaction is represented by the turbulent flame speed, S_t, as parameterized by the laminar flame speed, S_u^0, and the flame wrinkling, $\Xi = S_t/S_u^0$. In the latter, the filtered source terms in the Y_i-equations are modeled using different models such as the Partially Stirred Reactor (PaSR), [14], model and the Thickened Flame Model (TFM), [22]. This also requires the specification of a reaction mechanism and associated rate parameters. The choice of combustion model is an open issue in current reactive flow LES, and a more systematic treatment is welcome.

Close to walls, the flow becomes dominated by vortices with a characteristic length and spacing much smaller than those of the free flow. Simulating wall bounded flows with LES is thus a challenge since either we need to resolve also the near wall flow structures (*wall-resolved LES*) or we have to model the near wall flow (*wall-modeled LES*), [1]. Wall-modeled LES is at present the only alternative for LES of practical applications, and therefore specific treatment of the near wall flow is needed, [23]. One approach, although not recommended, is to use damping functions to reduce the subgrid viscosity close to the wall, [1], whereas a better approach is to employ dedicated subgrid near wall models. Some of these wall models, e.g. [24, 25], adjust the velocity at the solid wall to enforce the local near wall flow to satisfy the logarithmic law of the wall, whereas other wall models, e.g. [26], simply adjust the subgrid viscosity to achieve the same. As will be described later, the choice of near wall modeling may be very important to the overall flow behavior.

3 Numerical Methods

Here we limit the discussion to unstructured Finite Volume Methods (FVM) since they are most appropriate for engineering LES. Unstructured grids typically allow greater flexibility in generating and adapting grids, but at the expense of increased storage needs. Central to FVM's is that the values of $\mathbf{u}$ are represented by control volume averages, $\mathbf{u}_P$, representing an implicit filtering of (2). Discrete FVM approximations can be derived by means of Reynolds transport theorem so that (2) becomes,

$$\partial_t(\bar{\mathbf{u}}_P) + \tfrac{1}{\delta V_P}\sum_f \left[\mathbf{F}_f^C - \mathbf{F}_f^D + \mathbf{B}_f\right] = \mathbf{f}_P + \sigma_P, \tag{3}$$

where $\mathbf{F}_f^C = \mathbf{F}_C(\bar{\mathbf{u}}_f, \bar{\mathbf{u}}_f)d\mathbf{A}_f$, etc., is the discrete fluxes and $d\mathbf{A}_f$ the area-element of integration. The semi-discretized equations (3) needs to be integrated in time, and rules must be prescribed for how to reconstruct the convective, diffusive and subgrid fluxes, $\mathbf{F}_f^C$, $\mathbf{F}_f^D$ and $\mathbf{B}_f$, to close (3). For high-speed flows, explicit time integration schemes are most appropriate, e.g. based on a Runge-Kutta method, [27], whereas for low-speed flows a semi-implicit multi-step method, [28], is most often used. The flux-reconstruction is crucial, and for the convective fluxes linear or cubic interpolation schemes are recommended, but for engineering applications, monotone or TVD schemes may be necessary. For the remaining fluxes, linear or cubic interpolation schemes are usually applied, and the time-step should be limited by a Courant number of less than about 0.5.

One way to estimate the accuracy of the numerical method is to estimate the leading order truncation error using the Modified Equations Approach (MEA), [29]. Briefly stated, given the differential equations of interest and the numerical method to be used, the MAE provides the differential equations solved numerically. These modified differential equations will thus include the original differential equations together with further terms related to the truncation error of the numerical method. One key aspect of the MEA compared with other approaches is that the truncation error will include whatever non-linearity is related to either the differential equation or the numerical method. Expressions for the leading order truncation of the aforementioned FVM discretization can be found in [12] and [30], and for a 2nd order linear scheme for the momentum equation, the truncation error is $\mathbf{T} = \frac{1}{8}[\rho\bar{\mathbf{v}} \otimes ((\nabla^2\bar{\mathbf{v}})(\mathbf{d} \otimes \mathbf{d}))]_{sym} + \ldots$, where $\mathbf{d}$ is the grid spacing, revealing the nature of the scheme and how it may interact with an explicit subgrid model.

4 Error and Uncertainty Quantification Through Validation and Verification

The procedure used to measure the quality and reliability of a simulation is often labeled *validation and verification (V&V)*. This could be envisaged to give error bars on the simulation results similar to what is standard in EFD, although terminology and principles differ between CFD and EFD. The ideas discussed here are largely inspired by the AIAA guidelines, [31], and we aim at being consistent with that terminology. We also note that in some fields, standards to perform V&V have been developed, at least for stationary RANS, [32]. Many aspects in V&V become however much more complicated for unsteady simulations and LES.

4.1 Verification

Verification deals with assessing that the governing model problem is *solved correctly*, and thus to quantify the numerical error and to show that the code and the method have appropriate convergence properties. This is mainly a mathematics and computer science issue that can be carried out by series expansion of the error followed by estimating the convergence through a systematic grid refinement. This is neither practical nor easily interpreted for LES of engineering cases due to the usually large baseline grids, grid refinement issues and lack of reference data. Another potentially interesting method is the Method of Manufactured Solutions (MMS), [33], but it is not obvious that this approach can be used for 3D unsteady flow problems. We note though that although neither of these methods seems suitable to verify a certain calculation, they can be used to verify the code, implementation of different discretization schemes etc. on a simple set-up. Alternatively, the MEA could be considered one way to estimate the numerical error. However, this process is ambiguous considering the implicit filtering in LES. Another complication is how to verify transient calculations, where two realizations do not need to be identical. We thus seem forced to compare statistical moments of the solution, but then face the problem that correct statistics may be obtained despite an error in the computation.

4.2 Validation

Validation deals with assessing that the *correct model problem* is solved, and thus to estimate errors and uncertainties arising from approximating reality. This is primarily a physics and engineering issue that involves the choice of the model equations, boundary conditions, geometrical approximations etc. The validation process typically involves comparing the computed results with experimental data. In accordance with [31], we try to distinguish between *errors*, whose effect can be estimated and are due to known approximations,

and *uncertainties*, that are potential sources of error due to unknown effects of modeling. The common way to proceed with validation is to attempt to isolate different modeling effects in unit flow cases and for these cases compare with high accuracy results from DNS or experiments. By computing several of these unit flows one can build confidence in the models and approximations used. Validation is thus a continuously ongoing and developing process. The problem when approaching engineering applications is then that all approximations cannot be isolated and tested separately.

4.3 Issues in V&V for LES of Engineering Flows

Setting up an LES computation (or any flow simulation) of an engineering application involves a series of sensitive modeling and approximation steps, subject to the V&V procedure. The most obvious ones are the always present choice of model equations and discretization of these as well as the computational domain. We will here indicate some particularly difficult issues, primarily influencing the validation stage(s).

It needs to be pointed out that in LES, the distinction between verification and validation demands a separation between filtering and discretization that is seldom done in practice. This is even more complicated for Implicit LES (ILES), where the subgrid model error and the discretization error is the same. However, this also suggests that the subgrid model error is, in principle, accessible in LES by varying the filter width independently of the grid resolution (or in ILES by grid convergence). This is in contrast to RANS where the modeling always constitutes an uncertainty. Disregarding the obvious problems with computational resources to perform such studies, comparison and interpretation of results using different filter width may not be straightforward and additional convergence results for different statistical moments of the regularized equations may be needed.

The level of geometrical details that can be included should depend on the number of grid points we can afford and the filter width. In practical LES, the filter width is usually defined implicitly by the control volume size and the filtering of the geometry is not considered other than through the practical aspects in generating the mesh. Most often though, no-slip conditions or wall-modeling are applied which may not be correct for a filtered geometry. This has been discussed in e.g. [1], but no consensus among practitioners has been reached. Hence, effects of surface roughness such as bolts, welds or fillets, and of turbulence triggers in laboratory studies are often neglected, [34].

Effects that stem from the surroundings, whose modeling is denoted supergrid modeling, [35], include the size of the computational domain and the definition of far-field boundary conditions. Defining an appropriate size of the domain is arbitrary for external flows, and for internal flows the same holds for the placement of inlets and outlets. For external flows, the boundaries are often set 'sufficiently far away', but this statement is neither obvious nor sufficient for most cases. In laboratory set-ups, the always-present wind tunnel

or towing-tank walls influence the flow e.g. through blocking, whereas real flows may experience density stratification, conjugate heat transfer effects, fluid structure interaction effects etc. The inflow turbulence characterization and modeling, [36, 37], requires more attention and is currently considered a more important part of the LES model than the subgrid model. For reacting or buoyant flows, the thermal properties of the boundary may also have a strong impact, [38]. Other issues to mention includes non-linear thermal and caloric equations of state, as well as transport properties.

A careful statistical analysis of the computational results should be performed. This concerns the sampling of uncorrelated moments for steady flows, and ensemble averaging from repeated flow realizations for unsteady flows. At present, this is not always straightforward due primarily to limited computational resources, but as they increase, we expect improved statistics that can be better compared to measurement data. For unsteady flow, such as maneuvering simulations, the cost of forming sufficient statistical moments is still daunting.

A necessity for validation is to limit the differences in the experimental and computational set-up. The details of and uncertainty from the experimental geometry and boundary conditions typically reported in a scientific paper are enough to assess and interpret the results, but may lack key details for the computational set-up. It may be alignment issues of the model or the measurement equipment in a wind tunnel, discrepancies in measured reference values, insulation properties of walls, etc. To make progress, increased interaction between the EFD and CFD communities are necessary, and new validation cases should be developed jointly. There is also a need for improved interaction between theorititians and practitioners in LES in order to study and understand the impact of e.g. filtering, commutation errors and wall treatment. Ideally, it also involves modeling of multi-physics processes, where the actual physics is poorly understood or validated, or may be very difficult to tackle experimentally.

5 From Canonical to Engineering Flows

Next, we illustrate these issues using a range of flows – from canonical flows, where the set-up is well-defined and the analysis is straightforward, to flows approaching engineering complexity, where the problems of mimicking the case is considerable and the assessment of resolution and modeling is not easy. Experimental data is provided when available,

5.1 Academic Flows

We first consider the canonical flow associated with fully developed turbulent channel flows at Re-numbers from Re_τ=395 to 1800, [26, 39], all computed on the same 60^3 grid to investigate the capability of handling the near

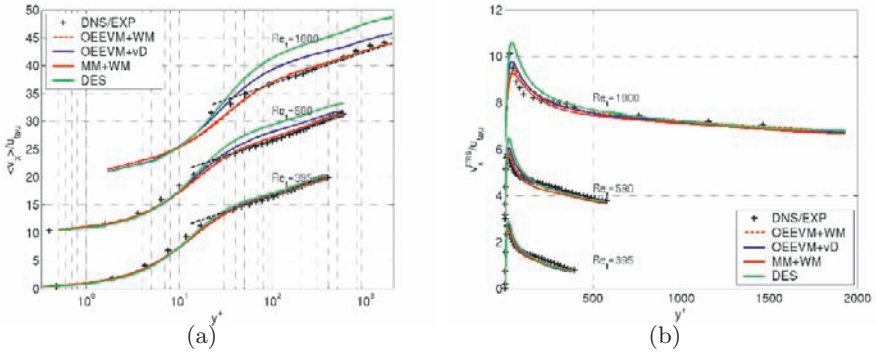

Fig. 1 Fully developed turbulent channel flow at Re_τ=395 to 1800; (**a**) time-average axial velocity in inner scaling and (**b**) axial rms-fluctuations in outer scaling

wall flow, being critical in many practical applications of LES. Comparison is made with DNS data, [40], at Re_τ=395 and 590 and experimental data, [41], at Re_τ=1800. In Fig. 1 we present comparisons of the time-averaged axial velocity, $\langle \bar{v}_x \rangle$, and its rms fluctuations, $v_x^{rms} = \sqrt{\langle \bar{v}_x - \langle \bar{v}_x \rangle \rangle^2}$. From Fig. 1 we find that at the lowest Re_τ number, i.e. at the highest resolution, the differences between the different models are virtually insignificant, but as the relative resolution decreases the impact of the modeling becomes important. At Re_τ=590 both Detached Eddy Simulation (DES) and LES, using the OEEVM together with the van-Driest damping, (OEEVM+vD) overpredict both $\langle \bar{v}_x \rangle$ and v_x^{rms}. At Re_τ=1800 this is even more pronounced with the DES resulting in poor agreement with the measurement data. Improved DES predictions can be obtained if $y^+ < 1$, as for Re_τ=395, due to the built-in constraints of the Spalart-Allmares model. This, however, may be difficult to comply with in complex geometries. We observe that the MM together with the wall-model (MM+WM) yields improved results over the OEEVM together with the wall-model (OEEVM+WM) as a consequence of the assimilation of the scale similarity term in the LES model, [20].

Next, we consider the flow over a surface mounted hill, [42], in a wind tunnel at a Re=130,000, that has been studied by several groups, e.g. [43]. Persson et al. [44], performed a systematic comparison between RANS, DES and LES, studying also the effects of inlet conditions, subgrid models and grid resolution. The key features of the flow are the boundary layer flow over the hill and the free separation on the lee-side of the hill. Several unsteady intertwined vortices are found behind the hill, in particular near the lower wall, as illustrated in Fig. 2. Persson et al. [44], report good agreement between predicted and measured pressure coefficient, C_P, for all LES, and in particular for the LES performed in a domain with an extended approach flow section. A somewhat too long recirculation bubble was found for most LES, whereas the RANS showed a far too long recirculation bubble, cf. [43]. DES with different

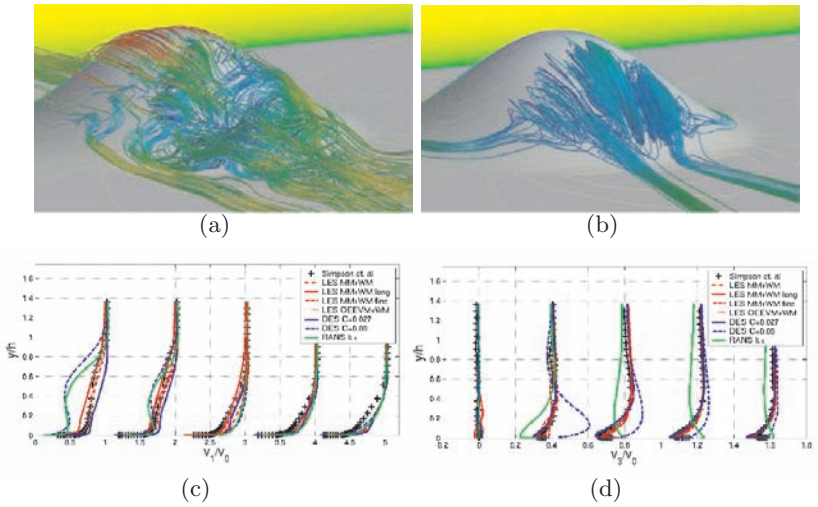

Fig. 2 Flow over a surface mounted hill; (**a**) instantaneous and (**b**) time-averaged flow field, (**c**) streamwise and (**d**) transvers velocities in the wake

inflow turbulence levels, referred to as high and low, was found to result in very different flow representations: The DES with low inflow turbulence behaves as an LES whereas the DES with high inflow turbulence behaves as a RANS. In Fig. 2(c), (d) we present comparisons of the time-averaged axial and spanwise velocity components, $\langle \bar{v}_1 \rangle$ and $\langle \bar{v}_3 \rangle$, respectively. Best agreement is found for the wall-modeled LES (LES MM+WM and LES OEEVM+WM) closely followed by DES low. Both RANS and DES high fall short in predicting the mean flow structures, clearly revealing the weaknesses of these models for flows with strong curvature, and the sensitivity of the supergrid viscosity modeling in DES to the inflow conditions.

5.2 DARPA SubOff AFF1 Bare Hull Body

At the borderline between validation and marine applications, we present also the flow past the DARPA SubOff AFF1 body. The geometry consists of a torpedo-like axisymmetric hull having a cylindrical mid-section making up about half of the hull length, [45, 46]. Simulations have been performed with RANS, DES and LES on grids between 1.5 and 6.0 million cells, at a hull length Re number of 12×10^6, [47], whereas the experimental data are from wind tunnel measurements at David Taylor Model Basin, [46]. This is a challenging flow, especially for LES due to the developing boundary layer over the mid-section and the high Re number, making wall-resolved LES too costly, thus necessitating wall-modeled LES. For the pressure and skin-friction (not shown), good agreement is found for all models at all resolutions. In particular, we notice the good skin-friction predictions obtained with LES, [47], showing

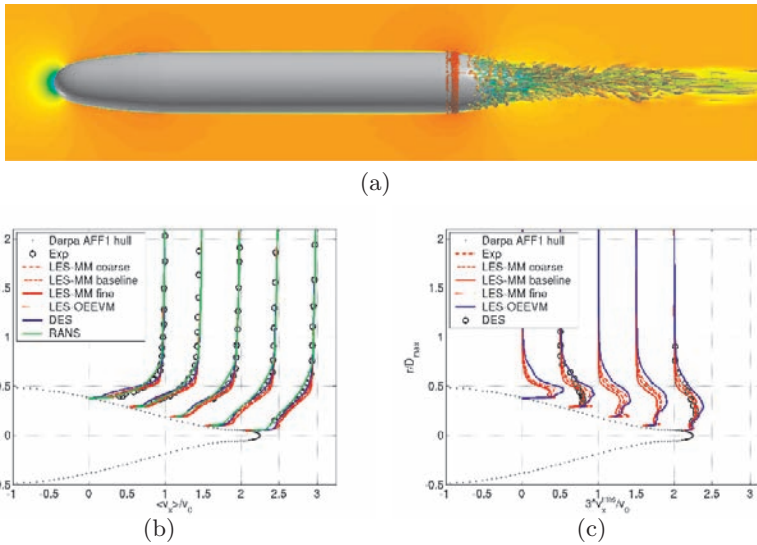

Fig. 3 Results for the Darpa Suboff AFF1; (**a**) flow visualization, (**b**) axial velocity, and (**c**) axial rms-fluctuations. The data is taken along five cuts at the tapered stern

the capability of the wall-model in predicting the wall shear stress, τ_w. The wall-model in itself is simple, but in combination with an accurately predicted outer flow, that includes large-scale dynamics, it allows the appropriate interactions between the inner and outer layers in the near wall region. Concerning the time-averaged velocity profiles, $\langle \bar{v}_x \rangle$, and their rms-fluctuations, v_x^{rms}, Fig. 3(b), (c), there are however noticeable differences between the modeling approaches with RANS performing less accurately than LES and DES. As seen in Fig. 3(c), RANS underpredicts v_x^{rms}, but discrepancies are evident also in $\langle \bar{v}_x \rangle$. We further note that also the coarse grid LES gives good agreement with measurement data, signifying only a weak grid dependency of the first and second order statistical moments of the velocity, although more structures are present in the fine grid LES.

5.3 Supersonic Jet Flows

With more stringent regulations on aircraft noise the aerospace industry is investing in CFD to calculate jet noise. To illustrate supersonic jet flow physics and how this can be predicted by RANS and LES, results based on the Seiner et al. [48], experiments of a Ma 2 jet of diameter D=91.44 mm will be discussed. The computational models originate at the nozzle orifice, at which top-hat profiles are prescribed for ρ, v_x, T, k and ε, thereby excluding the nozzle orifice boundary layer dynamics that may affect the jet boundary layer dynamics. At all other boundaries, wave-transmissive conditions are used to

allow pressure and entropy waves to exit the domain without reflections. For LES, grids of 1.10, 3.72 and 8.80 million cells are used, whereas for RANS only the coarse grid is used. The difference between RANS and LES, and the influence of resolution in LES is illustrated in Fig. 4:(a).

The coarse and fine grid LES show similar flow structures, but with the fine grid LES revealing much more details. Comparing the time-averaged axial velocity, $\langle \tilde{v}_x \rangle$, and the rms-fluctuations, v_x^{rms}, in Fig. 4:(b), show that the fine and medium grid LES agree well with the measurement data whereas the coarse grid LES and the RANS show discrepancies in the potential core and mixing regions. The number of shock-diamonds, as shown by the peaks and valleys in the pressure (see insert in Fig. 4:(a)), velocity and temperature (see Fig. 4:(b)) also differs between the simulations. The medium and fine grid LES predicts the same number of shock-diamonds, suggesting that these grids are sufficiently fine to capture the shock reflection angles in the oscillating jet boundary. RANS and coarse grid LES both fail to predict these key flow features. The influence of the resolution is even more pronounced in the v_x^{rms}-profiles of Fig. 4:(b). Furthermore, we compare jet centerline temperature profiles, $\langle \tilde{T} \rangle$, supporting the conjecture that only the medium and fine grid LES are capable of matching the experimental data. The oblique pressure waves (see insert in Fig. 4:(a)), radiating from a region at the end of the potential core, illustrate the radiating sound waves.

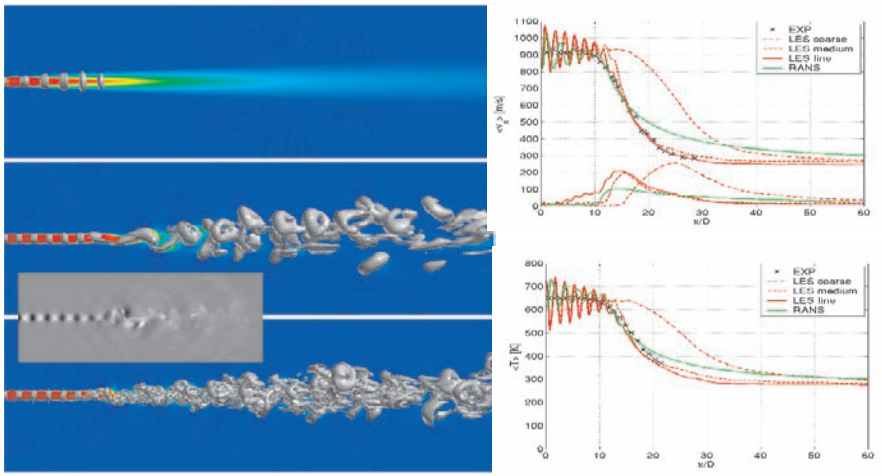

(a) (b)

Fig. 4 Round supersonic jet flows. (**a**) Contours of the axial velocity and isosurfaces of the second invariant of the velocity gradient from RANS (*top*), coarse LES (*middle*) and fine LES (*bottom*). Insert shows the instantaneous pressure distribution. (**b**) Axial profiles of time-averaged axial velocity (*top*) and temperature (*bottom*)

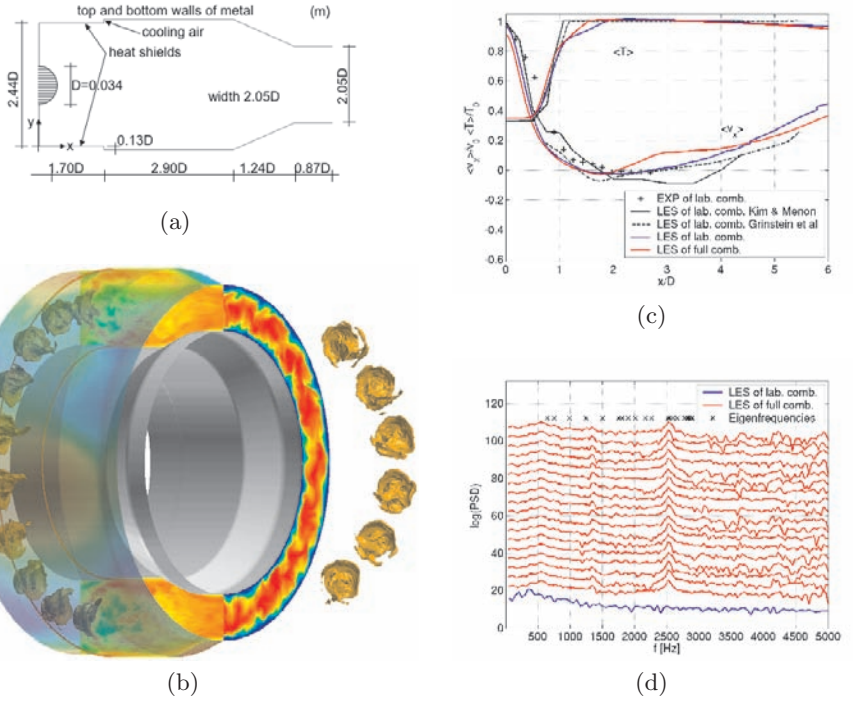

Fig. 5 Annular gas turbine combustor. (**a**) Schematic of the model combustor, (**b**) iso-surfaces of the fuel mass fraction, centerplane axial velocity contours, combustor exit temperature contours and confinement wall pressure contours. (**c**) Time-averaged profiles of the axial velocity and temperature from different cases, and (**d**) frequency contents 1.25D behind each burner in the laboratory and annular combustors

5.4 Annular Multi-Burner Gas Turbine Combustor

Annular gas turbine combustors are used for aeropropulsion, power generation, and marine and land-based propulsion. Although they have an advantage over can combustors in low NO_x levels they often suffer from combustion oscillations that can result in flashback, blowout and mechanical vibrations. Such oscillations are hard to predict at the design stage and correcting actions can be costly. At present, industry is relying on thermoacoustic models, [49], employing RANS for a single burner configuration to predict the mean flame, in order to predict the eigenfrequencies of the combustor. This approach neglects much of the non-linear physics, and improved models are most wanted. Compressible reactive LES with finite rate chemistry have the potential to predict the required features although at a high computational cost.

We here present such results for a model 18 burner annular combustor, developed from the laboratory GE LM6000 combustor, [50, 51], used in other studies, [52, 53]. The geometry is outlined in Fig. 5:(a), and here a CH4/air mixture at an equivalence ratio of 0.56 is burnt at 6.18×10^5 Pa and 644 K at a Re=320,000 and a swirl number of 0.56. Here, the 18 DACRS premixers are modeled by a swirling air/fuel jet, [51], injected through round inlets with diameter D. Hexahedral grids with 10 million cells are used, together with wave-transmissive outlet boundary conditions, and adiabatic, no-slip, wall boundary conditions. A seven species, three-step reaction scheme is employed to model the CH_4 oxidation and the CO and NO_x emission formation, with Arrhenius coefficients optimized to match the laminar flame speed and temperatures of the Gri-Mech 3.0 in lean to rich premixed flames.

In Fig. 5:(b) we show a perspective view of the combustor in terms of an iso-surface of the fuel mass fraction, representing the flame, center-plane contours of the axial velocity, outlet contours of the temperature, outer wall contours of the pressure and six flames shown head on. Each flame takes the shape of a wrenched expanding tube that fold back on itself when approaching the combustor centerline to collapse in a tongue twisted by the helicoidal vortex. The flames are stabilized by the combined effect of swirl and recirculation ahead of the flames and between the flames and the dump plane. Individual flames are different and the outer (semi-transparent) combustor wall is colored by pressure, revealing alternating high and low pressures. In Fig. 5(c), (d) we show time-averaged centerline profiles of the axial velocity $\langle \tilde{v}_x \rangle$ and the temperature $\langle \tilde{T} \rangle$, as well as the pressure Power Spectral Density (PSD) at points 1.20D behind each burner in both the laboratory and annular combustors. The LES results agree well with the data, [50], and with other LES results, [52, 53]. The annular combustor LES suggests different $\langle \tilde{v}_x \rangle$ and $\langle \tilde{T} \rangle$ profiles compared to the single combustor due to the modified dynamics of the helicoidal vortex systems. The differences are more pronounced when viewing the PSD. In particular we find a 2.50 kHz mode in the annular combustor that is absent in the laboratory combustor. Comparing with the confinement pressure distribution and thermoacoustic model results we find that this mode is a spinning mode due to the coupling between the helicoidal vortex systems.

5.5 Submarine During Maneuver

Understanding unsteady separating flows past maneuvering submarines is important to guarantee the operational safety of the ships and their crews, and to reduce the signatures. Separating flows around the hull, sail, and rudders are responsible for the poorly understood forces and moments that can be detrimental to performance. Even if test data exists it is recognized that stability derivatives from model tests, incorporated into the equations of motion, fail to predict some features of transient maneuvers. Thus, the interest in maneuvering simulations is increasing and for reasons of reliability together with

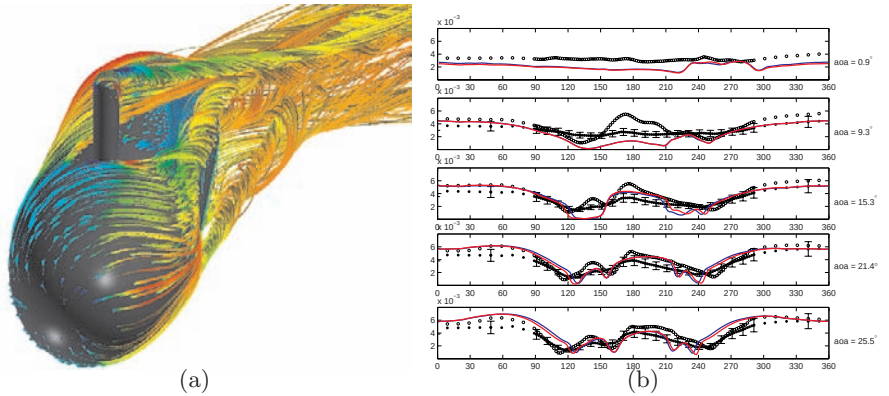

Fig. 6 Results for submarine maneuvering in terms of streamlines and skin friction on the hull. In (**b**) we show a comparison of skin friction profiles at x/L=0.686 at different yaw angles.

the potential of more accurately predicting noise and vibrations, the use of LES is attractive, in spite of its higher cost compared with RANS.

We here show results from a side-slip maneuver for the DARPA Suboff AFF2 configuration, [45, 46], as experimentally studied at Virginia Tech, [54, 55], for quasi-steady and unsteady maneuvers. To simulate this maneuver, we carry out LES with an Arbitrary Lagrangian Eulerian (ALE) formulation, [56], in which the motion is included into the equations of motion through a mesh velocity. Wall-modeled LES is used with grids of 4.3 and 6.3 million cells, graded towards the hull, resulting in wall normal resolution of about $y^+ = 30$. Two different runs are performed, starting from different initial times, to estimate the variability of the flow, [56]. The experimental data, measured at Re=5.5×10^6, was aimed at measuring the separation lines from local minima of the skin-friction, C_f, and hence the error in C_f may be substantial.

The main flow structures are the horseshoe vortex, the development of cross-flow vortices, and the sail-wake. As the horseshoe vortex evolves, it interacts with the hull-boundary layer to create a complex flow with intermittent separation at the stern. During the maneuver, the leeward horseshoe vortex leg turns towards the side of the hull and interacts with the cross-flow vortex that has begun to develop. Continuing the maneuver, this vortex system detaches from the hull, creating a complex vortex system at the stern. The windward horseshoe vortex leg is not affected by the cross-flow in the early stages of the maneuver but later merges with the sail wake. At later stages, several secondary vortices emerge and a very complex system of interacting structures is formed. In the sail wake, high frequency fluctuations are detected and for high angles of attack, separation starts to develop on the leeward side of the sail. Figure 6:(b) compares the time evolution of C_f between the steady and unsteady measurement data and LES results. Differences are detected between

the steady and unsteady data, and the LES appears much closer to the unsteady experimental data, although including some features that resemble the steady experimental data. The two LES runs are similar, but it is evident that both the location and shape of the structures varies from one run to another, illustrating the sensitivity to initial conditions and therefore also to similar effects caused by unsteady boundary condition effects.

6 Discussion

In this section we connect the issues discussed in Sect. 4 to the cases of Sect. 5. The discussion will be brief and is by no means complete but will indicate the kind of questions that will arise when trying to assess the quality of a LES of an engineering application.

Physical process modeling is probably the single most important issue, particularly for engineering applications, and covers a wide range of topics. Examples include the modeling of the stress tensor in a non-newtonian fluid, the equations of state in high speed and reactive flows, the reaction mechanisms and reaction rates in reactive flows, phase change processes (evaporation, condensation and melting) in multi-phase flows, conjugate heat transfer, thermal radiation, acoustics, relative motion and fluid structure interactions. These processes often occur together in engineering applications, which puts exceptional requirements on the code development and on the V&V procedure. Both the gas turbine combustor and the submarine maneuvering are examples of such cases, and must be proceeded by a series of increasingly complex studies, discussed in [14, 26, 39, 53, 57].

Flow modeling concerns mainly the LES closure modeling and is connected to the physical process modeling in terms of the complexity of the flow physics that requires modeling. For incompressible Newtonian fluids this reduces to modeling the subgrid stress tensor, the sensitivity of which is illustrated in Figs. 1, 2 and 3, for different flows. These results, together with other similar studies, imply that the details of the subgrid model are of lesser importance, provided that the grid and the handling of the near wall flow are appropriate. On the other hand, as illustrated in Fig. 1, the importance of the near wall treatment is crucial. The differences between DES and LES are further illustrated in Figs. 2 and 3, providing guidance for more complex flows. In this respect, DES is peculiar since it depends on the (rather arbitrary) choice of inflow data, resulting in LES-like or RANS-like profiles, being in good or marginally good agreement with the reference data, respectively.

The sensitivity to the grid resolution is a classical verification issue that is historically connected to grid refinement or verification in the RANS context. However, for LES it is somewhat different as discussed earlier. For engineering LES, the sensitivity to grid resolution is often difficult to investigate since the baseline grids are usually large or even very large in order to accommodate all details of the geometries involved. Additional complications arise from the

use of unstructured (or hybrid) grids or Adaptive Mesh Refinement (AMR) sometimes required to capture shocks and other discontinuities. The channel flow results suggest that the near wall region is important, and that damping function models and DES does not work unless y^+ is less than about 3, whereas the wall-model, [24, 25, 26], has a wider range of applicability. This is also illustrated by the results for the more challenging Darpa SubOff AFF1 case. On the other hand, the influence of the grid is also evident for the supersonic jet, where grids with typical spacings of Δ and 1.5Δ produce accurate results, whereas a spacing of 2Δ fails. All three grids, however, result in energy spectra with a distinctive $k^{-5/3}$ sub-range. For this case, however, the transitional flow around the end of the potential core may require a higher resolution.

The reason to use *wall-modeled LES* is that the resolution requirements become prohibitively large as the wall is approached. However, most engineering (and some laboratory) surfaces are rough to some extent, either deliberately be means of turbulence triggers (e.g. trip wires, struts or zig-zag tape) aiming at emulating full scale conditions or *per-se* through welds, unfinished surfaces, small technical details, or by fouling. Some studies, e.g. [34], indicate that the detailed design of such triggers creates different boundary layer structures. This is an important issue that has not yet been fully recognized, and we believe that for some flows this overwhelms that of ordinary subgrid modeling since it controls transition, separation and viscous drag. These effects cannot often be resolved, and thus has to be parametrically modeled, preferably as a part of the wall-models, which can be extended to also handle surface roughness. The wall model used here is simple, but still gives good agreement with reference data for channel flows and for flow around different bodies. This is in spite of the lack of trip-wires on the Darpa AFF1 and AFF2 hulls and a steady inflow for the 3D hill. Also the shear stress analysis of the maneuvering submarine gives good results with measured shear stress.

Supergrid modeling, i.e. the influence of the surroundings (wind tunnel, laboratory facility or the open sea) is as already mentioned very important, e.g. [35]. For example, the flows around the 3D hill and the Darpa SubOff AFF1 hull are affected by the turbulence within the wind tunnels, and particularly by the fact that the stern of the Darpa SubOff AFF1 hull exits the tunnel inside of an anechoic chamber. Also for the maneuvering submarine, where slotted walls are used in the wind tunnel, it is difficult to estimate the effect of the walls in the measurements and the boundaries in the computation. For the gas turbine combustor, the swirlers, the guide vanes at the end of the combustion chamber, and the turbine package after the combustor are not included, and instead models have to be employed. Such models lack information about the small-scale turbulence and the acoustic impedance of the real device. To properly analyze such flows systematic variations of velocity profiles, impedances, etc., are therefore required. Also for the supersonic jet there are issues of supergrid modeling, such as the shape of the velocity profiles and the turbulence. By including the nozzle, these effects can be minimized, but to a considerably higher cost. But even then, we are likely to experience the same

problem again, since we can not included the complete engine. Where to stop including features is thus subject to several very complicated approximations.

The final issue in validation is to compare correctly with available data. This involves e.g. handling normalization factors, location of measurement probes and understanding experimental data handling and errors. This is often well documented, but being in contact with the experimentalists simplifies this matter, and is sometimes the only way to obtain critical information, some of which not considered important when the experiment was performed. Another aspect is to consider is the statistical treatment of the LES data. To be consistent with experimental practice, uncorrelated averages should be used instead of running averages that we believe is common in the LES community. When comparing transient results, like the maneuvering submarine, one is also faced with the problem of comparing a single realization of the flow with an ensemble-averaged measurement. In this case, ten maneuvers have been performed without reporting the standard deviation. Estimating the accuracy of the LES in this case is troublesome, to say the least, even if comparisons are made with measured skin friction data.

To summarize, we emphasize the challenges and opportunities involved in quality assessment in LES in particular, and in CFD in general. In order to be useful for engineering, the reliability of LES needs to be proven by a combination of theoretical work on quality and grid resolution indicators and practical experiences. A close collaboration between EFD and CFD is crucial to study and validate effects from approximations and modeling.

Acknowledgements

The authors wish to acknowledge the financial support from the Swedish Armed Forces and the Swedish Defence Material Agency. The authors also wishes to thank N. Alin, J. Tegnér, T. Huuva, U. Svennberg, and M. Liefendahl. All simulations in this article were performed using the OpenFoam (www.openFoam.com) platform.

References

1. Sagaut P (2001) Large Eddy Simulation for Incompressible Flows. Springer, Berlin Heidelberg, New York
2. Pope, SB (2000) Turbulent Flows. Cambridge University Press
3. Lumley JL (Ed.) (1992) Wither Turbulence? Turbulence at the Crossroads, Lecture Notes in Physics 357:344. Springer, Berlin Heidelberg, New York
4. Wilcox, DC (1993) Turbulence Modeling for CFD. DCW Industries
5. Frisch U (1995) Turbulence. Cambridge University Press
6. Ferziger JH, Leslie DC (1979) AIAA 79-1441
7. Lesieur M, Metais O (1996) Annu Rev Fluid Mech 28:45
8. Boris JP, Grinstein FF, Oran ES, Kolbe RL (1992) Fluid Dyn Res 10:199

9. Grinstein FF, Fureby C (2004) Computing in Science and Engineering, March/April issue, p 36
10. Grinstein FF, Margolin L, Rider B (2007) Implicit Large Eddy Simulation: Computing Turbulent Fluid Dynamics. Cambridge University Press
11. Bochev P, Christon M, Collis S, Lehoucq R, Shadid J, Slepoy A, Wagner G (2004) SAND Report SAND2004-2871
12. Drikakis D, Fureby C, Grinstein FF, Liefendahl M (2007) ILES with limiting algorithms. In: Grinstein FF, Margolin L, Rider B (eds) Implicit Large Eddy Simulation: Computing Turbulent Fluid Dynamics, Cambridge University Press
13. Fureby C, Tabor, G (1997) J Theor Fluid Dyn 9:85
14. Fureby C (2007) AIAA Paper No 2007-1413
15. Schumann U (1975) J Comput Phys 18:376
16. Smagorinsky J (1963) Month Wea Rev 91:91
17. Germano M, Piomelli U, Moin P, Cabot WH (1994) Phys Fluids A 3:1760
18. Ducros F, Comte P, Lesieur M (1996) J Fluid Mech 326:1
19. Bardina J, Ferziger JH, Reynolds WC (1980) AIAA Paper 80-1357
20. Bensow RE, Fureby C (2007) J Turbul, to appear
21. Poinsot T, Veynante D (2001) Theoretical and Numerical Combustion, Edwards
22. Colin O, Ducros F, Veynante D, Poinsot T (2000) Phys Fluids 12:1843
23. Piomelli U, Balares E (2002) Annu Rev Fluid Mech 34:349
24. Piomelli U, Moin P, Ferziger JH, Kim J (1989) Phys Fluids A 1:1061
25. Werner A, Wengle H (1991) In: Proceeedings 8th Int Symp on Turb Shear Flows, Munich, Germany, p. 155
26. Fureby C (2007) Ercoftac Bulletin, Marsh Issue
27. Gottlieb S, Shu C-W (1998) Math Comput 67:73
28. Hirsch C (1999) Numerical Computation of Internal and External Flows. John Wiley & Sons
29. Hirt CW (1968) J Comput Phys 2:339
30. Grinstein FF, Fureby C (2007) J Fluids Engng 129:1514
31. AIAA, (1998) AIAA-G-077-1998
32. ITTC (2005) Recommended Procedures and Guidelines, Section 7.5-03
33. Roachee PJ (1998) Verification and Validation in Computational Science and Engineering, Hermosa Publishers
34. Werner S, (2006) Computational Hydrodynamics Applied to an America's Cup Class Kiel. PhD Thesis, Chalmers University of Technology
35. Grinstein FF (2006) AIAA 06-3048
36. Baba Ahmadi MH (2007) Construction of Inlet Conditions for LES. PhD Thesis, University of Exeter
37. Tabor G (2007) Personal communication.
38. Sidwell T, Richards G, Casleton K, Straub D, Maloney D, Strakey P, Ferguson D, Beer S, Woodruff S (2005) AIAA J 44:434
39. Liefendahl M, Persson T, Fureby C (2006) AIAA paper No 2006-0904
40. Moser RD, Kim J, Mansour NN (1999) Phys Fluids 11:943
41. Wei T, Willmarth WW (1989) J Fluid Mech 204:57
42. Byun G, Simpson RL (2005) AIAA 05-0113
43. Davidson L (2005) Test Case 11.2 – 3D Hill. In: Proceedings of the 11th Ercoftac/IAHR Workshop on Refined Turbulence Modeling
44. Persson T, Liefevendahl M, Bensow RE, Fureby C (2005) J Turbul 7, Art no 4
45. Groves, NC, Huang TT, Chang MS (1989) Report DTRC/SHD-1298-01

46. Huang TT, Liu H-L, Groves NC, Forlini TJ, Blanton J, Gowing S (1992) In: Proceedings of 19th Symp on Naval Hydrodynamics, Seoul, Korea
47. Bensow RE, Fureby C, Liefvendahl M, Persson T (2006) In: Proceedings of 26th Sym. on Naval Hydrodynamics, Rome, Italy
48. Seiner JM, Ponton MK, Jansen BJ, Lagen NT (1992) AIAA 92-02-046
49. Walz G, Krebs W, Hoffmann S, Judith H (2002) J Engng for Gas Turb and Power 124:3
50. Hura HS, Joshi ND, Mongia HC, Tonouchi J (1998) ASME-98-GT-444
51. Held TJ, Mongia HC (1998) ASME-98-GT-217
52. Kim W-W, Menon S, Mongia HC (1999) Comb Sci Tech 143:25
53. Grinstein FF, Fureby C (2004) In: Proceedings of the 30th Int Symp on Comb, p 1791
54. Hosder S (2001) Unsteady Turbulent Skin Measurements on a Maneuvering DARPA2 Suboff Model, Virginia Tech
55. Hosder S, Simpson RJ (2001) AIAA Paper 2001-1000
56. Bensow RE, Fureby C (2007) In: Proceedings of 9th Int Symp on Numerical Ship Hydrodynamics, Ann Arbor, MI, USA
57. Alin N, Bensow RE, Fureby C, (2006) Final report, ONR contract No N62558-06-C-2004

Quality of LES Predictions of Isothermal and Hot Round Jet

Artur Tyliszczak, Andrzej Boguslawski, and Stanislaw Drobniak

Institute of Thermal Machinery, Czestochowa University of Technology
Al. Armii Krajowej 21, 42-200 Czestochowa, Poland
atyl@imc.pcz.czest.pl, abogus@imc.pcz.czest.pl

Abstract. The paper presents results of LES computations performed for isothermal and non-isothermal variable density jets using high order numerical code. According to the experimental data and linear stability theory the range of the density ratios between jet and the ambient fluids considered in this work encloses the regimes of absolute and convective type of instability. Much attention is paid to the quality of the solutions depending on the mesh resolution and turbulence intensity imposed at the inlet velocity profile. The differences between the solutions obtained using different (advective/conservative) form of the Navier–Stokes equations are also mentioned.

Keywords: Absolute/Convective instability, Hot jet, Low mach number

1 Introduction

A concept of absolute and convective instabilities was introduced by Landau [9] in the context of hydrodynamic instability of shear layer. He noted that for certain flow conditions a small disturbance could grow in time contaminating the flow upstream and downstream in the case of absolute instability or could be swept away by convective motion in the case of convective instability keeping the disturbance limited in time. Plasma physicists showed experimentally a phenomenon corresponding to absolute instability predicted theoretically by Landau [9]. Briggs [2] and Bers [1] formulated a spatio-temporal linear stability theory which was applied to shear layer instability by Huerre and Monkewitz [6] who analyzed the problem with respect to wakes and in plane mixing layers of variable density. Absolutely unstable round free jets were studied experimentally by Sreenivasan et al. [16] who observed strong oscillations in air-helium jets for the density ratio lower than certain critical value. The exhaustive experimental work on the hot air round jet instability were performed by Monkewitz et al. [14]. The experimental studies of air-helium round jets were continued later by Kyle & Sreenivasan [8]. These two principal experimental works on air-helium round jet by Kyle & Sreenivasan [8]

J. Meyers et al. (eds.), Quality and Reliability of Large-Eddy Simulations,

and on hot-air round jet by Monkewitz et al. [14] delivered the most important data to characterize the instability of variable density jets. Monkewitz et al.[9] by acoustic pressure measurements identified two unstable modes in hot-air jets. The first one, called the Mode I, was observed when the density ratio $S < 0.69$ ($S = \rho_1/\rho_2$, ratio of the jet density to ambient flow density) with characteristic frequency $St_D \approx 0.3$ (D-nozzle outlet diameter). When the density ratio was lowered to $S = 0.65$ another mode called Mode II was identified with characteristic frequency $St_D \approx 0.45$. For density ratio within the range $0.55 < S < 0.65$ both modes Mode I and Mode II coexisted while for density ratio $S < 0.55$ the Mode II dominated and the Mode I was not observed. Kyle & Sreenivasan [8] investigated by LDV velocity fluctuations in round air-helium jet and also observed two unstable modes. The first one called an oscillating mode was observed for the density ratio $S < 0.61$ and was identified as a mode corresponding to Mode II observed by Monkewitz et al. [14] in heated jet. The second mode observed by Kyle & Sreenivasan [8] in air-helium jets, called the broadband mode, which appeared when R/θ (R is the inlet jet radius and θ is the momentum thickness of the shear layer at the nozzle exit) reached large values. It was stated by Kyle & Sreenivasan [8] that this mode did not correspond to Mode I in heated jets as far as both frequency range and density ratios are concerned. Kyle & Sreenivasan [8] observed also a critical shear layer thickness below which oscillating mode vanished what was in contradiction with theoretical finding of Monkewitz & Sohn [15] whose predictions showed that absolutely unstable mode was persistent even for infinitely thin shear layer.

The present paper is devoted to LES predictions of isothermal and heated jets for a variety of the governing parameters like density ratio, inlet shear layer thickness, inlet turbulence level. The main aim of the calculations performed was to study whether using LES the change from the convective to absolute instability in hot jet can be captured as observed in experimental investigations. A special attention in the present studies was attached to the quality of the LES results and sensitivity to mesh resolution for a variety of the flow governing parameters.

2 Numerical method and boundary conditions

In this work we applied the so-called low Mach number expansion [3, 11] which allows for an efficient solution in low Mach number conditions. Motivated by analysis presented in [5] showing considerable influence of the aliasing errors, depending on the form of the Navier–Stokes equations, we consider LES formulation for both the advective and conservative formulation of the non-linear terms of the Navier–Stokes equations.

The subgrid terms which appear after performing LES filtering are modeled using filtered structure function model [4, 13]. Third order low-storage Runge–Kutta method is used to solve equations in time. Within each Runge–

Table 1 The governing parameters and the test case considered

	$R/\theta = 10$	$R/\theta = 20$
$TI = 10^{-4}\%$	A1	A2
$TI = 2\%$	A3	A4

Kutta step the projection method is applied to determine pressure and velocity fields. The spatial discretization is performed with VIth order compact scheme [10] in direction of the jet axis and Fourier approximation in plane perpendicular to the jet. The applied code reveals to be very accurate in various type of jet flows including natural and excited jets [17, 18].

The computational domain is a rectangular box $10D \times 10D \times 16D$. The periodic boundary conditions are assumed on the lateral walls while the inlet boundary conditions are specified in terms of instantaneous velocity (defined by hyperbolic-tangent profile [18] and white noise disturbance with assumed turbulence intensity TI), density and temperature. At the outlet of the computational domain we applied the so-called convective type boundary conditions.

3 Results and Discussion

The systematic studies of the isothermal and hot jet for various flow governing parameters were carried out taking into account influence of the shear layer thickness, density ratios and inlet turbulence level. For each test case also the mesh density influence on the predicted flow structure was analyzed. The flow parameters tested are gathered in Table 1. For the test cases A1-A4 the calculations were performed for three density ratios of the jet density to the ambient fluid $S = 1.0, 0.8, 0.6$. For isothermal jet when the density ratio $S = 1.0$ and for heated jet when $S > 0.8$ the flow is convectively unstable while for the hot jet with density ratio $S < 0.6$ and certain range of the shear layer thickness the absolutely unstable jet is expected as shown by the spatio-temporal linear stability analysis [7] and also confirmed by experimental results. The linear stability analysis shows that the critical density ratio for the shear layer thickness characterized by the parameter $R/\theta = 20$ is equal $S_{crit} \approx 0.7$ while for thicker shear layer characterized by $R/\theta = 10$ the rapid decrease of critical density ratio should be observed and the critical density ratio is equal $S_{crit} \approx 0.5$.Hence it is expected that the flow structure for the hot jet with density ratio $S = 0.6$ should be significantly different for two test cases considered. The choice of the inlet turbulence intensity at the level $TI = 2\%$ and $TI = 10^{-4}\%$ results from the previous studies showing that even quite low turbulence level $TI = 2\%$ can significantly disturb the formation of large scale coherent vortices in isothermal and hot round jet. Figure 1 on the left hand side shows the influence of the mesh density on the mean and fluctuating velocity profiles along the jet axis for isothermal jet test case A4

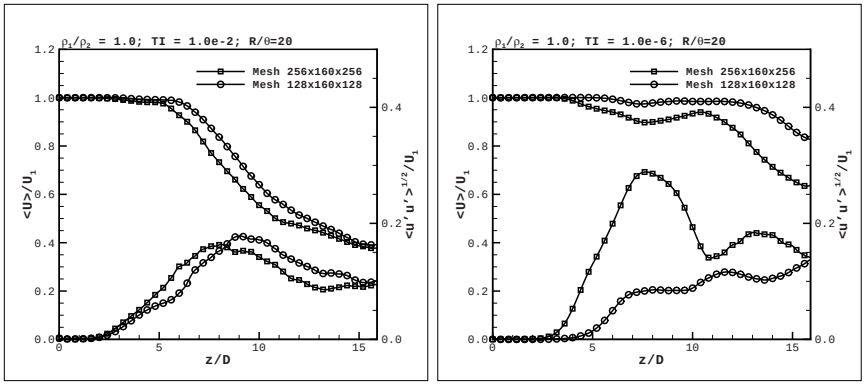

Fig. 1 Mean and fluctuating profile of the axial velocity for $S = 1.0$, $R/\theta = 20$: $TI = 2\%$ (*left figure*) and $TI = 10^{-4}\%$ (*right figure*)

that means for higher inlet turbulence level $TI = 2\%$ and thinner shear layer characterized by parameter $R/\theta = 20$. For finer mesh the potential core of the jet is shorter that is consistent with higher turbulence level growth rate. However, qualitatively the results are similar and the maximum turbulence level at the jet axis is close in both predictions. The influence of the mesh density on the mean and fluctuating velocity turned out to be much stronger in the case of very low inlet turbulence level as shown in Fig. 1 on the right hand side. In this case the prediction obtained with coarser mesh $128 \times 160 \times 128$ shows very long potential core up to distance approximately $x/D = 12$ from the nozzle exit while the results obtained with the finer mesh $256 \times 160 \times 256$ reveals much shorter potential core extending only up to $x/D = 4$ with a local minimum of the mean velocity at the distance $x/D = 7$. This local minimum coincides with the very high turbulence level at the jet axis $< u'u' >^{1/2} /U_1 = 24\%$. Evolution of the axial velocity component spectrum at the shear layer and the jet axis presented in Fig. 2 reveals in the jet near region a dominating peak characterized with non-dimensional frequency based on the jet diameter $St_D = 0.5$. This fluctuation is a result of growing Kelvin-Helmholtz instability. Starting from the distance $x/D = 4$ this fundamental mode is decaying while the subharmonic mode $St_D = 0.25$ is growing rapidly attaining its maximum at the distance $x/D = 8$. Such an evolution of the velocity spectrum is characteristic for the vortex pairing process. The vortex pairing process is clearly shown in Fig. 3 where the Q parameter and axial velocity iso-contours are shown. Formation of large coherent vortices resulting from the vortex pairing process corresponds to the local maximum of the fluctuating velocity at the distance $x/D = 8$ from the nozzle outlet. Further downstream these large scale vortex rings break up due to circumferential instability which is associated with the formation of so called side jets also well characterized by the Q parameter iso-surfaces shown in Fig. 3 on the left hand side. The large scale structures break up is associated with a decay of the fluctuating velocity

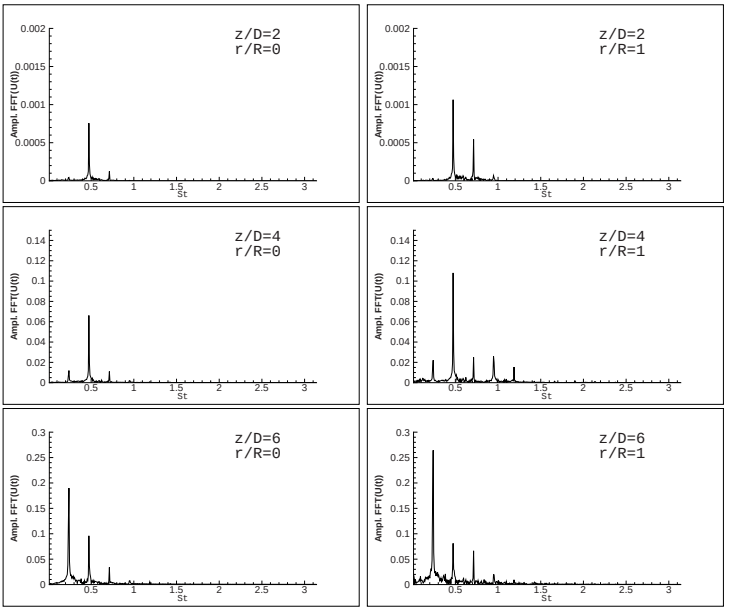

Fig. 2 Evolution of the spectrum of axial velocity component at the shear layer and the jet axis for $S = 1.0$, $R/\theta = 20$, $TI = 10^{-4}\%$, mesh $256 \times 160 \times 256$

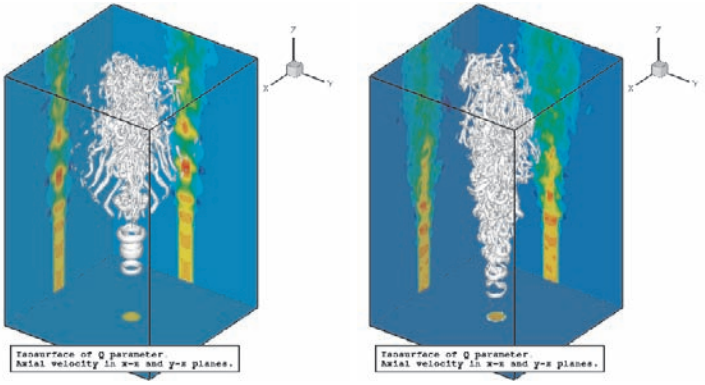

Fig. 3 Isosurface of the instantaneous Q parameter for $S = 1.0$, $R/\theta = 20$, $TI = 10^{-4}\%$ (*left figure*) and $TI = 2\%$ (*right figure*), mesh $256 \times 160 \times 256$

up to the distance $x/D = 10$. Further growth of the fluctuating velocity is a result of the fully turbulent flow as at the distance $x/D = 12$ only a small peak with the frequency $St_D = 0.25$ is present (not shown). The Q parameter at this distance shows also only small scale vortical structures. The results shown above for two test cases characterized by two different inlet turbulence level $TI = 2\%$ and very low value $TI = 10^{-4\%}$ confirm the opinion expressed

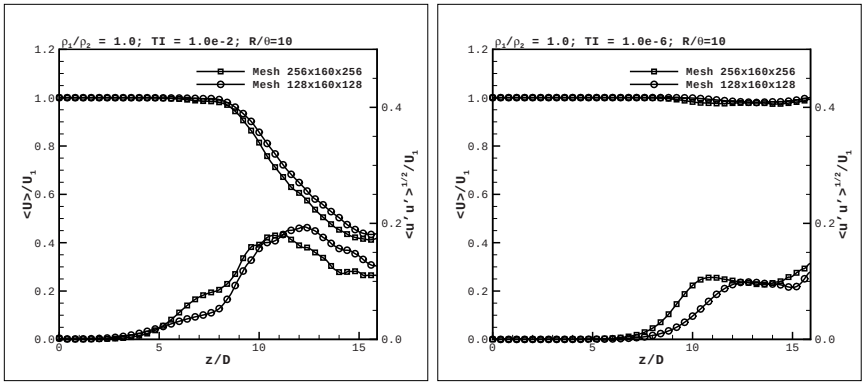

Fig. 4 Mean and fluctuating profile of the axial velocity for $S = 1.0$, $R/\theta = 10$: $TI = 2\%$ (*left figure*) and $TI = 10^{-4}\%$ (*right figure*)

in the paper of Meneveau & Katz [12] that coherent structures may be much larger when the shear layer is laminar. However, the mesh density analysis performed within current studies shows that in this case mesh resolution is crucial for the correct prediction of the coherent vortices with LES method. If the turbulence level is high enough to disturb the process of coherent vortex formation the influence of the mesh resolution is much weaker as shown in Fig. 1. The evidence that the coherent structures are much weaker for the inlet turbulence level $TI = 2\%$ even for high resolution LES predictions is confirmed by analysis of the Q-criterion for this test case shown in Fig. 3 on the right hand side. This conclusion is also confirmed by the axial velocity spectrum (not shown in the paper) where broadband velocity fluctuations around the non-dimensional frequency $St_D = 0.5$ are visible. Next the analysis of the mesh resolution was performed for the test cases A1 and A3 for the thicker shear layer characterized by the parameter $R/\theta = 10$. The mean and fluctuating velocity profiles for inlet turbulence level $TI = 2\%$ and $TI = 10^{-4}\%$ are shown in Fig. 4. As previously for the higher inlet turbulence level the mesh resolution does not change the results qualitatively. It could be interpreted as before that the inlet turbulence level is sufficiently high to disturb the process of vortex formation and the resolution required to predict correctly the large scale coherent vortices is not so important in this case. Although for the finer mesh (Fig. 4 on the right hand side) the higher growth rate of the fluctuating velocity is observed at the distance $x/D = 5 \div 9$ showing that vortex pairing process is captured better than in the case of coarser mesh. However, on the contrary to the previous results obtained for thin shear layer $R/\theta = 20$ shown in Fig. 1, in the case of thicker one $R/\theta = 10$ the mesh refinement does not bring significant change of the results. The Kelvin-Helmholtz instability scales on the shear layer thickness and for thicker shear layer the growth rate of the oscillation is smaller than for thin one. It means that the distance on which the coherent structures are formed is longer and turbulent fluctuations

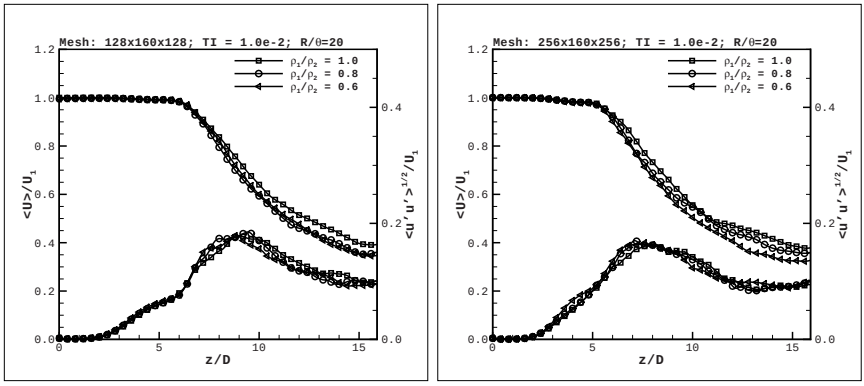

Fig. 5 Mean and fluctuating profile of the axial velocity for $R/\theta = 20$, $TI = 2\%$ and $S = 1.0, 0.8, 0.6$ for the coarse mesh (*left figure*) and the fine mesh (*right figure*)

imposed on the growing vortical structures disturb their formation leading to faster break up. Hence even for extremely low inlet turbulence level in the case of thicker shear layer the conditions for vortex formation are not good enough and high mesh resolution does not improve the results significantly.

The analysis of the quality of LES predictions of the isothermal jet presented so far were continued with the analysis of heated jet for two density ratios $S = 0.8$ and $S = 0.6$. The influence of the density ratio on the mean and fluctuating velocity distribution along the jet axis for the test case A4 ($TI = 2\%$ and $R/\theta = 20$) for coarse and fine mesh is shown in Fig. 5. For both mesh resolutions it is seen that the density ratio does not change the flow structure qualitatively. Even for the lowest density ratio $S = 0.6$ for which the absolute instability is expected, as predicted by linear stability theory, it seems that the change of the instability scenario is not captured well by LES predictions. Again it seems that assumed inlet turbulence level $TI = 2\%$ is sufficiently high to disturb the vortex formation also in the case of heated jet. The situation changes drastically if the laminar shear layer is assumed at the inlet conditions as for the test case A2 for which the velocity profiles are shown in Fig. 6 for the coarser and finer mesh respectively and for various density ratios. For the coarser mesh (Fig. 6 on the left hand side) the results corresponding to the density ratio $S = 0.6$ are not significantly different compared to the isothermal and slightly heated jet ($S = 0.8$). The local maximum of the fluctuating velocity at the distance $x/D = 7$ for the density ratio $S = 0.6$ is higher than in the case of isothermal and slightly heated jet that could be interpreted as a change of the instability mechanism due to density differences. However, surprising results are obtained with the mesh refinement shown in (Fig. 6 on the right hand side). In this case the mean and fluctuating velocity for isothermal flow and slightly heated one are close each other while for the hot jet with density ratio $S = 0.6$ a significant change is observed for both the mean and fluctuating velocity profiles. By contrast to the results obtained

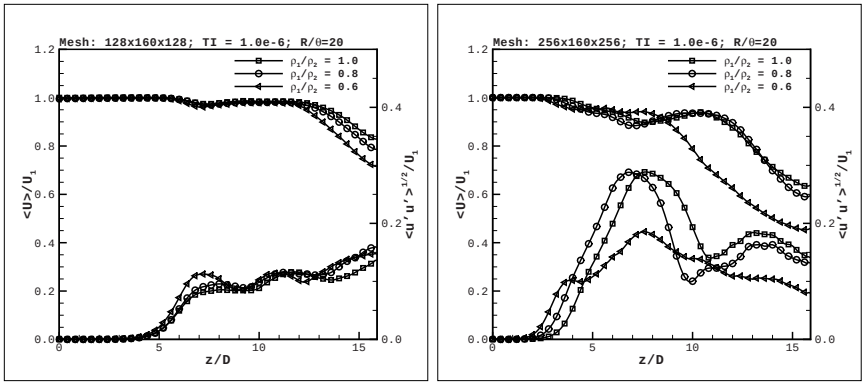

Fig. 6 Mean and fluctuating profile of the axial velocity for $R/\theta = 20$, $TI = 10^{-4}\%$ and $S = 1.0, 0.8, 0.6$ for the coarse mesh (*left figure*) and the fine mesh (*right figure*)

with the coarser mesh the decrease of the density ratio down to $S = 0.6$ leads to lower fluctuating velocity at the distance $x/D = 7$. Moreover comparing the results obtained with the coarser and finer mesh one can observe that the mesh resolution influences much more the results for isothermal and slightly heated jet than the results for the hot jet. It seems that an explanation of such influence of the mesh resolution could be similar to the one discussed above for the case of the jet characterized by thicker shear layer. In the case of the hot jet with the density ratio $S = 0.6$ the instability scenario is changed compared to the isothermal or slightly heated jet. It results with faster break up of large scale coherent structures leading to much lower fluctuating velocity at the jest axis. Hence, because of the flow conditions the large scale structures are not fully formed and the mesh resolution as in the previous case does not influence the LES predictions of the hot jet. The Q parameter isosurfaces for the hot jet with density ratio $S = 0.8, 0.6$ are shown in Fig. 7. It can be seen from this picture that vortical structures are not so large as in the case of isothermal jet shown in Fig. 3.

The problem of the instability mechanism for the hot jet is worth of careful discussion. The question could be posed whether current LES results actually capture correctly the absolute instability phenomenon. Unfortunately, it is a significant difficulty in the physical interpretation of the results presented so far, however some observations proving correctness of the LES prediction of absolute instability can be made. We could already see that there are considerable differences in the mean and fluctuating velocity profiles when the density ratio is lowered to $S = 0.6$ – this could already be interpreted as the change of the instability mechanism. Let us now analyze the spectral characteristics of the flow conditions for isothermal and heated jet. The convective instability present in the isothermal and slightly heated jet scales on the shear layer thickness and for the one considered in current studies, characterized with $R/\theta = 20$, the preferred non-dimensional frequency is $St_D = 0.5$, as shown

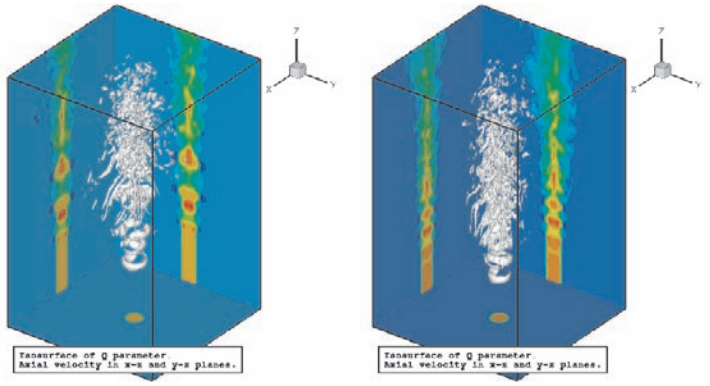

Fig. 7 Isosurface of the instantaneous Q parameter for $R/\theta = 20$, $TI = 10^{-4}\%$ for $S = 0.8$ (*left figure*) and $S = 0.6$ (*right figure*), mesh $256 \times 160 \times 256$

in the velocity spectra in Fig. 2. On the other hand the absolutely unstable mode scales on the jet diameter and as shown by the linear stability theory is characterized by frequency also close to $St_D = 0.5$. This means that both convective and absolute instability could generate oscillations with the same frequency. This is confirmed by the velocity spectra for the hot jet shown in Fig. 8:

- actually there are no additional peaks present comparing to the velocity spectra for the isothermal case (see Fig. 2);
- additionally one may observe that closer to the jet inlet the amplitudes of peaks corresponding to the preferred mode and its subharmonic are much larger for the heated jet with $S = 0.6$ than for the isothermal case.

These observations may suggest superposition of phenomena originating from different sources (one of them is the absolute instability) and therefore the LES prediction of existence of the absolute instability in the heated jet seems to be correct. However, in order to univocally verify this statement it would be necessary to perform LES prediction of the jet characterized with shear layer thinner than $R/\theta = 20$ for which the convective instability should generate fluctuations with higher frequency while the frequency related to the absolute instability should stay unchanged and should correspond to $St_D = 0.5$. In this case one could distinguish both instability mechanisms in the case of the hot jet. Unfortunately thinner shear layer will require considerably higher mesh resolution resulting in much longer CPU time and due to limited computer resources such computations have not been carried out so far.

The last issue considered within the current studies devoted to the quality of LES predictions of the round jet was the problem of the form of the filtered Navier–Stokes equations solved. All the results discussed above were obtained solving advective form of the momentum equations. Nevertheless, motivated by an interesting discussion presented in [5] concerning the level of errors

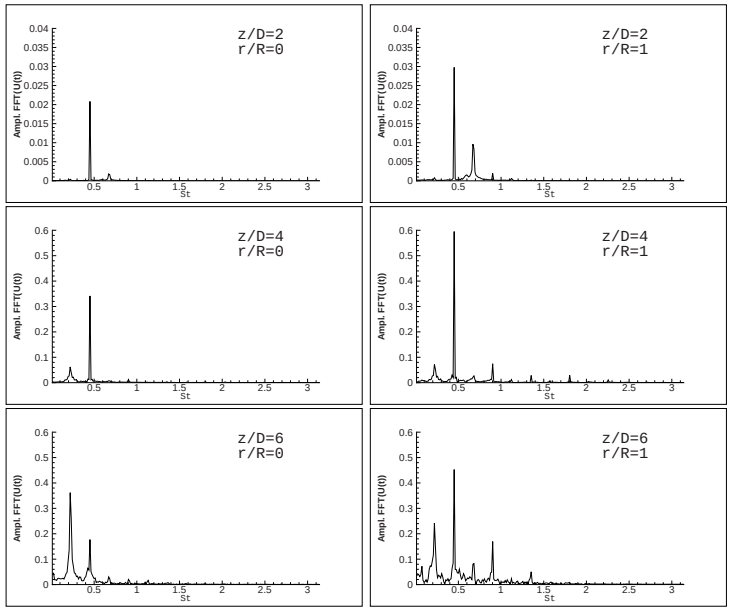

Fig. 8 Evolution of the spectrum of axial velocity component at the shear layer and the jet axis for $S = 0.6$, $R/\theta = 20$, $TI = 10^{-4}\%$, mesh $256 \times 160 \times 256$

arising due to discretisation of the conservative and advective form of the Navier–Stokes equations we decided to perform similar analysis in the present study. Therefore, for most of the test cases presented previously we performed computations using both the advective and conservative form, however due to the limited size of the paper only two cases for the isothermal flow are presented. For the test case A4 (see Fig. 9) it can be seen that if the advective form of the N-S equations is applied, then a little faster growth rate of the fluctuations is predicted in the range $x/D = 5 \div 8$, but the results are in general close each other at least qualitatively. However, surprising results are obtained for lower turbulence intensity (case A2 Fig. 9 on the right hand side). In this case the results obtained with conservative form of the N-S equations are qualitatively different from the corresponding solution of the advective form of the equations. Further studies are necessary to explain this observations but at the current stage it seems that this effect is also related to the existence of the large scale coherent structures present in the solution. For the solution in which the coherent vortices break up faster (or they are not formed) like in the case of higher turbulence intensity, the numerical errors due to the discretization of different form of the equations do not affect the solution significantly. On the other hand the solution seems to be very sensitive to the numerical errors when the fully developed coherent vortices are predicted in the flow field.

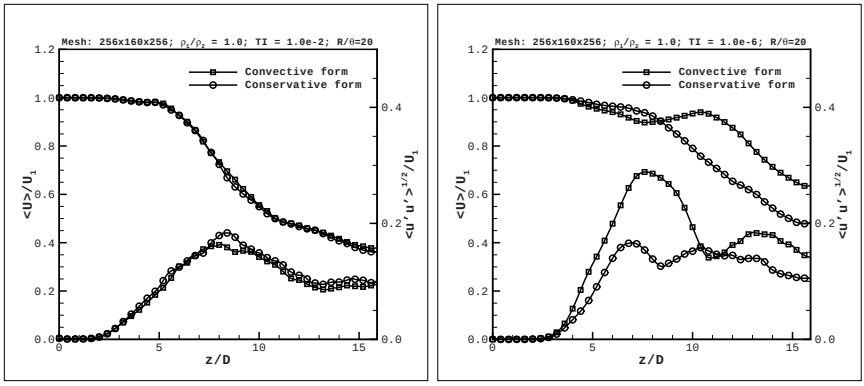

Fig. 9 Mean and fluctuating profile of the axial velocity for $S = 1.0$, $R/\theta = 20$: $TI = 2\%$ (*left figure*) and $TI = 10^{-4}\%$ (*right figure*) for conservative and advective for of the nonlinear term in the N-S equations

4 Conclusions

The paper presents detailed LES studies of isothermal and heated round jet with particular attention devoted to the LES results quality due to mesh resolution and some numerical errors. The influence of the governing parameters like shear layer thickness, inlet turbulence level and density ratio was discussed. It was suggested that the LES results quality is very sensitive to the mesh resolution and numerical errors in all the test cases in which strong large scale vortical structures could develop. In such cases mesh refinement and numerical scheme can change qualitatively the results of the mean and fluctuating velocity profiles. One could also suppose that if the results are affected significantly by the mesh resolution and numerical scheme when strong coherent vortices are present in the solution all these test cases would be very challenging for the subgrid modeling. The LES studies of the flow with large scale coherent structures using a variety of subgrid models is planned for near future.

Acknowledgements

The support for the research was provided within statutory funds BS-1-103-301/2004/P and also the EU FAR-Wake Project No. AST4-CT-2005-012238 and the research grant COST/258/2006 founded by Polish Ministry of Science. The authors are grateful to the Cyfronet Computing Center in Krakow (Poland) for access to the computing resources on Mars PC Cluster.

References

1. Bers A (1975) Linear Waves and Instabilities, Physique des Plasmas. Gordon and Breach, London
2. Briggs RJ (1964) Electron-Stream Interaction with Plasmas. Research Monograph No 29, The MIT Press, Cambridge
3. Cook WC, and Riley JJ (1996) Direct numerical simulation of a turbulent reactive plume on a parallel computer. J Comput Phys 129:263–283
4. Ducros F, Comte P, Lesieur M (1996) Large-eddy simulation of transition to turbulence in a boundary layer developing spatially over a flat plate. J Fluid Mech 326:1–36
5. Fedioun I, Lardjane N, Gokalp I (2001) Revisiting numerical errors in direct and large eddy simulations of turbulence: physical and spectral spaces analysis. J Comput Phys 174:816–851
6. Huerre P, Monkewitz PA (1985) Absolute and convective instabilities in free shear layers. J Fluid Mech 159:151
7. Jendoubi S, Strykowski P (1994) Absolute and convective instability of axisymmetric jets with external flow. Phys Fluids 6:3000
8. Kyle DM, Sreenivasan KR (1993) The instability and breakdown of a round variable density jet. J Fluid Mech 249:619–664
9. Landau LD, Lifshitz EM (1959) Fluid Mechanics. Pergamon Press, Oxford
10. Lele SK (1992) Compact finite difference with spectral-like resolution. J Comput Phys 103:16–42
11. Majda A, Sethian J (1985) The derivation of the numerical solution of the equations for zero Mach number Combustion. Combust Sci Tech 42:185–205
12. Menevau C, Katz J (2000) Scale-invariance and turbulence models for Large-Eddy Simulation. Annu Rev Fluid Mech 32:1–32
13. Metais O, Lesieur M, Comte P (1999) Large-eddy simulations of incompressible and compressible turbulence. In: Transition, turbulence and combustion modelling. Kluwer, Dordrecht
14. Monkewitz PA, Bechert DW, Bariskow B, Lehmann B (1990) Self-excited oscillations and mixing in a heated round jet. J Fluid Mech 213:611–639
15. Monkewitz PA, Sohn KD (1988) Absolute instability in hot jets. AIAA J 26(8):911–916
16. Sreenivasan KR, Raghu S, Kyle D (1989) Absolute instability in variable density round jets. Exp Fluids 7:309
17. Tyliszczak A, Boguslawski A (2006) LES of the jet in low Mach variable density conditions. In: Geurts BJ, Metais O, Lamballais E, Friedrich R (eds) Direct and Large Eddy Simulations VI:575–582. Springer, Berlin
18. Tyliszczak A, Boguslawski A (2007) LES of Variable Density Bifurcating Jets. In: Iacarrino G, Kassinos SC, Langer CA, Moin P (eds) Complex Effects in Large Eddy Simulations. Lecture Notes in Computational Science and Engineering 56:273–288. Springer, Berlin

LES for Street-Scale Environments and Its Prospects*

Zheng-Tong Xie and Ian P. Castro

School of Engineering Sciences, University of Southampton, SO17 1BJ, UK
z.xie@soton.ac.uk, i.castro@soton.ac.uk

Abstract. In this paper we raise several issues, e.g. resolution, Reynolds number dependency, mesh quality and inflow boundary conditions for Large-Eddy Simulation (LES) of street scale flows, scalar dispersion and heat transfer within urban areas. Some of the issues are addressed extensively and some LES results of test cases are presented. The other issues are discussed and commented for further study. Finally we attempt to foresee prospects for the use of LES for urban environments with a computational domain size up to a few kilometers and a resolution down to one meter.

Keywords: Urban canopy layer, Cuboid-shape body, Resolution, Reynolds number dependency, Inflow condition, Efficiency, Point source dispersion, Heat transfer

1 Introduction

There is a growing concern about the urban environment. In our previous work, we have demonstrated that LES is a promising tool for this area [10]. However, in order to establish the credibility of LES as a tool for operational/practical forecast applications, there are many issues which must be addressed, such as:

- Is there a general minimum resolution needed to produce reasonable turbulence statistics? If the answer is 'YES' for the flow, is it also applicable for scalar dispersion?
- Is LES reliable for the high Reynolds numbers typical of urban flows?
- How much does LES accuracy depend on the mesh quality in such cases?
- Efficient inflow boundary conditions (e.g. via appropriate generation of artificial turbulence) need to be coupled to the weather scale flow and the urban boundary layer. What errors are involved in doing this?

* Support of the Natural Environment Research Council under NCAS Grant DST/26/39 is gratefully acknowledged

In this paper, we investigate the quality and reliability of LES for street-scale flows, mainly by undertaking numerical-sensitivity experiments, rather than attempting to quantify the uncertainty and error of LES as in [8].

2 Governing Equations of Large-Eddy Simulation

To ensure a largely self-contained paper, a brief description of the governing equations is given here. More details can be found in [10], hereafter denoted by XC.

The filtered continuity and Navier-Stokes equations are written as follows,

$$\frac{\partial u_i}{\partial x_i} = 0$$
$$\frac{\partial u_i}{\partial t} + \frac{\partial u_i u_j}{\partial x_j} = -\frac{1}{\rho}\left(\frac{\partial p}{\partial x_i} + \delta_{i1}\frac{\partial \langle P\rangle}{\partial x_1}\right) + \frac{\partial}{\partial x_j}\left(\tau_{ij} + \nu\frac{\partial u_i}{\partial x_j}\right). \qquad (1)$$

The dynamical quantities, u_i, p are resolved-scale (filtered) velocity and pressure respectively and τ_{ij} is the subgrid-scale (SGS) Reynolds stress. δ_{i1} is the Kronecker-delta and ν is the kinematic viscosity. $\partial\langle P\rangle/\partial x_1$ is the driving force, a constant streamwise pressure gradient which exists only when periodic inlet-outlet boundary conditions are applied but otherwise vanishes. The Smagorinsky SGS model was used with $C_s = 0.1$. In the near-wall region, the Lilly damping function was also applied. Note that the Smagorinsky model is widely used by researchers to simulate the kind of flow of most concern to us – rough-wall flows – with considerable success [10].

The wall model is generally an important issue for LES, and is no less important than the SGS model if the computational cost is to be minimised. For cases where the fine eddies in the vicinity of the wall are important, it is recommended that $\mathscr{N}_1^+$ is of order of unity ($\mathscr{N}_1^+$ is the distance in wall units between the centroid of the first cell and the wall assuming the $\mathscr{N}$ coordinate is normal to the wall). Note, however, that for a complex geometry, where separation and attachment processes occur, it is impossible to satisfy this criteria everywhere. We argue that, unlike the situation for smooth-wall flows, it is in fact not necessary, at least for obtaining overall surface drag and the turbulent motions at the scale of the roughness elements (buildings), which turn out to be dominant (see XC).

The local wall shear stress is then obtained from the laminar stress-strain relationships:

$$u^+ = \frac{u}{\hat{u}_\tau}, \quad \mathscr{N}^+ = \frac{\rho\hat{u}_\tau\mathscr{N}}{\mu}, \quad \mathscr{N}^+ = u^+, \qquad (2)$$

where $\rho\hat{u}_\tau^2$ is the local wall shear stress. However, if the near-wall mesh is not fine enough to resolve the viscous sublayer, for simplicity it is assumed that the centroid of the cell next to the wall falls within the logarithmic region of the boundary layer:

$$\frac{u}{\hat{u}_\tau} = \frac{1}{\kappa} \ln E \left(\frac{\rho \hat{u}_\tau \mathscr{N}}{\mu} \right), \tag{3}$$

where κ is the von Karman constant and E is an empirical constant. The log-law is employed when $\mathscr{N}^+ > 11.2$. Again, note that for very rough-wall flows there are probably very few regions on the surface of the roughness elements where log-law conditions genuinely occur in practice; however, we have shown earlier that for this type of flow the precise surface condition is unimportant for capturing the element-scale flows and surface drag (see XC).

The entire LES model was implemented in the code described in XC. Crucially, the discretisation for all terms in Eq. (1) was second order accurate in both space and time – lower-order schemes were found not to be adequate but, equally, for the kind of problems addressed here it is not necessary to use schemes that are of even higher order. Inlet boundary conditions were set using a User-Defined-Function, embodying the technique described in the following section.

3 Reynolds Number Dependency and Minimum Resolution

Recently an LES model was used to calculate the turbulent flow over staggered wall-mounted cubes and a staggered array of random height obstacles with area coverage 25%, at Reynolds numbers between 5×10^3 and 5×10^6, based on the free stream velocity and the obstacle height [10]. Three meshes with $8 \times 8 \times 8$, $16 \times 16 \times 16$ and $32 \times 32 \times 32$ grid points respectively per building block were used for flow at the various Reynolds numbers. The significantly coarser mesh than required for a full DNS, i.e. $16 \times 16 \times 16$ grid points per building block, produces sufficiently accurate results. Turbulence generated by urban-like obstacles, e.g. cuboid-shape bodies with sharp edges, is building-block-scale dominated, which suggests that for this type of flow the precise wall condition/subgrid-scale model is unimportant for capturing the element-scale flows and surface drag.

$Re = 5 \times 10^3$ is low enough for the $32 \times 32 \times 32$ resolution to be 'almost' DNS, but flows at $Re = 5 \times 10^4$ and $Re = 5 \times 10^6$, with coarse or fine grids, generated almost identical non-dimensional statistics compared with those at $Re = 5 \times 10^3$, even though the high-frequency end of the spectrum was not well captured in some cases. Also, surface drag obtained using the same resolution was comparable between various Reynolds numbers, as also found in laboratory experiments. The results collectively confirm that Reynolds number dependency, if it does exist, is very weak (except no doubt very close to solid walls), principally because the surface drag is predominantly form drag and the turbulence production process is at scales comparable to the roughness element sizes, as suggested also by wind tunnel experiments.

LES is thus able to simulate turbulent flow over the urban-like obstacles at high Re with grids that would be far too coarse for adequate computation of corresponding smooth-wall flows. A wide inertial sub-range in flows over

urban-like obstacles may also suggest that turbulence reaches a quasi-isotropic state at relatively lower frequency than non-vortex-shedding flows at similar Reynolds numbers, which is another reason why a simple SGS model can give reasonable results. Whilst improvement of the SGS model, *via* more expensive dynamic models for example, may enhance the simulation in the close vicinity of the solid walls at high Reynolds number and, likewise, improvements in the wall model itself may increase accuracy near the element walls, it is much more important to use grids which can resolve the major features of the separated shear layers. The influence of the small-scale motions, captured increasingly inadequately as Re rises, is much lower in these flows than it is in smooth-wall equivalents. This is all greatly beneficial for the numerical simulation of the coupling between weather scale flows and street scale flows. Our major conclusion is thus that LES may be reliably able to simulate turbulent flow over urban areas at realistic Reynolds numbers, with what (in more 'classical' flows) would normally be thought of as inadequate grids. It is suggested that medium sized meshes on the body scale (e.g. 15–20 grid points at least over a typical body dimension) are sufficient for the simulation of a real urban area, at least for obtaining the total drag force or the large-scale flow dynamics.

4 Mesh Type and Wall-Layer Resolution

4.1 Tetrahedral Mesh vs. Hexahedral Mesh

In the computations discussed above, only Cartesian (hexahedral) meshes were used for generic surfaces. In order to simulate the flows over a genuine urban canopy with a more complex geometry, unstructured non-hexahedra meshes inevitably have to be used. Tetrahedral meshes are widely used in CFD because methods which do this are mature, efficient and highly automated [7]. It is worth investigating the reliability and accuracy of the tetrahedral mesh for LES of the urban-type flows.

Fine and coarse tetrahedral meshes (see Fig. 1) were used to simulate the flows in the same computational domain ($4h \times 4h \times 4h$; h cube height) as in [10] for an array of uniform staggered cubes, i.e. four cubes with area coverage 25%. The lengths of the side of the tetrahedral cells were approximately $h/16$ and $h/8$ respectively for fine and coarse meshes(1.3M cells and 0.16M cells respectively in total). The Reynolds number was 5×10^3 based on the free stream velocity and the cube height. The other settings were the same as those in [10].

Figure 2 shows a typical comparison of vertical profiles of the turbulence statistics behind a cube using the hexahedral mesh ($16 \times 16 \times 16$ grid points per cube) and the tetrahedral meshes. Clearly, increasing the resolution of the tetrahedral mesh improves the profiles. However, even the fine tetrahedral mesh (1.3M cells) evidently underestimates the turbulence fluctuations compared to the hexahedral mesh (0.25M cells). Perhaps not surprisingly, the

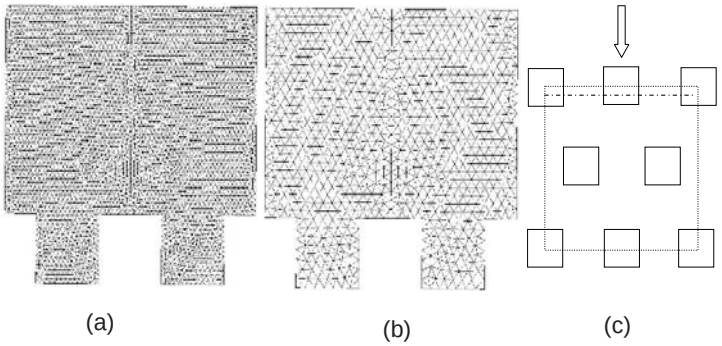

Fig. 1 A vertical cut on the chain-dotted line in (**c**) of tetrahedral meshes for an array of uniform cubes. (**a**), fine mesh(1.3M cells); (**b**), coarse mesh(0.16M cells); (**c**), the square highlighted by the dotted line indicates the plan view of the computational domain

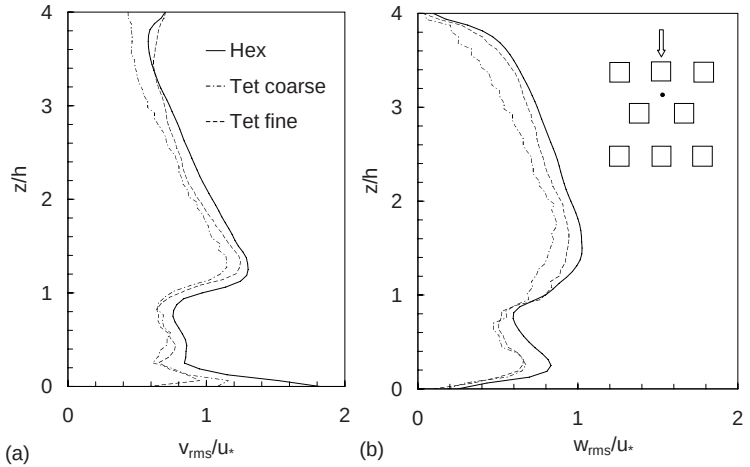

Fig. 2 Comparison of vertical profiles of the turbulence statistics behind cube (indicated by the dot in the inset in (**b**) using hexahedral (0.25M cells) and tetrahedral meshes. (**a**) spanwise and (**b**) vertical fluctuation velocities

accuracy of the tetrahedral meshes, even at the higher resolution, is confirmed as being not so high as that of the uniform hexahedra mesh.

4.2 Polyhedral Mesh vs. Hexahedral Mesh

Polyhedral meshes offer substantially better properties than tetrahedral meshes [7]. However, there is relatively little experience available with such meshes. A polyhedral mesh was validated for flow over (initially) uniform

cubes and then a more random geometry (i.e. 64 staggered blocks with random heights). Only the latter is reported here.

The size of a 'repeating unit' of the obstacle array was 80 mm × 80 mm, within which were placed in regular staggered pattern sixteen 10-mm-square elements having heights chosen from an appropriate normal distribution. Four repeating units were included in the whole computing domain (hence the total number of obstacles is 64), so the domain size was $L_x \times L_y \times L_z = 16h_m \times 16h_m \times 10h_m$, where $h_m = 0.01$ m is the mean height of the obstacles. The Reynolds number was 5000 based on the free stream velocity and the mean height. A three-level hexahedral mesh (2.3 million cells) with $16 \times 16 \times 16$ cells per $h_m \times h_m \times h_m$ in the near wall region (see Fig. 3c), and a three-level polyhedral mesh (1.3 million cells) with $13 \times 13 \times 13$ cells per $h_m \times h_m \times h_m$ in the near wall region (see Fig. 3d) were used.

Essentially identical results were obtained using the polyhedral mesh and hexahedral mesh, despite the much smaller number of cells used in the former. This may suggest that the two meshes are both satisfactory. It is known that

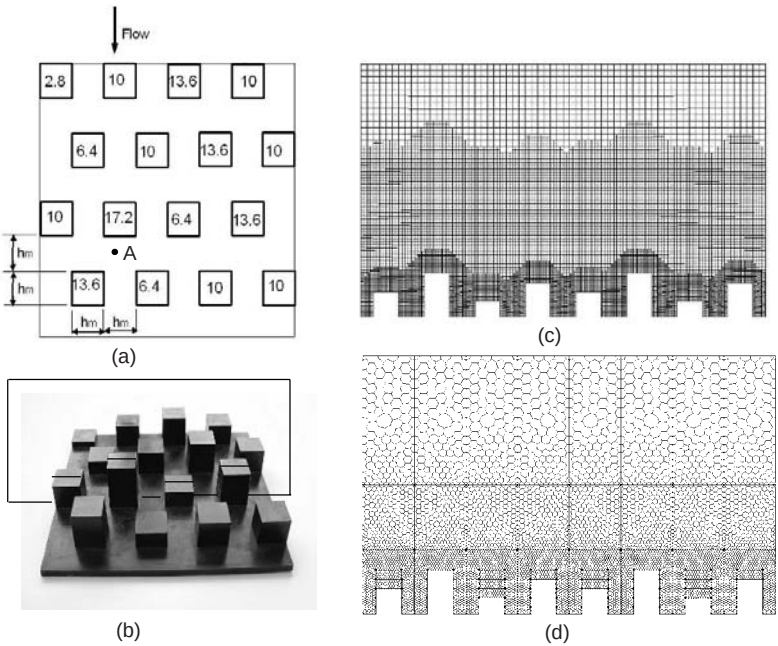

Fig. 3 (**a**), plan view of one repeating unit with numbers indicating the block height in mm; (**b**), a view of one repeating unit used in the laboratory experiment [3]; (**c**), hexahedral mesh ($16 \times 16 \times 16$ grids on the 10 mm cube, 2.3M cells); (**d**), polyhedral mesh ($13 \times 13 \times 13$ grids on the 10 mm cube, 1.3M cells), for an array of obstacles with random heights

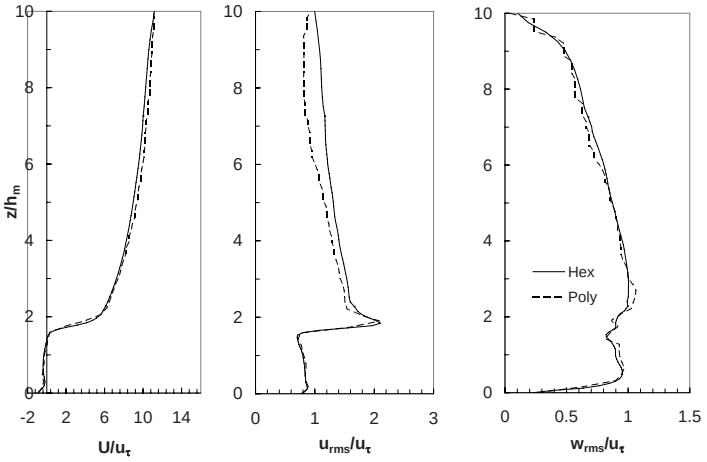

Fig. 4 Vertical profiles of mean velocity and turbulence statistics behind 17.2 mm block (i.e. station A in Fig. 3a) using hexahedral and polyhedral meshes

the former is more flexible for complex geometry than the latter. Furthermore, the results confirm that the polyhedral mesh is more accurate and less memory consuming than the widely used tetrahedral mesh. Figure 4 presents streamwise mean velocity and velocity r.m.s profiles behind the 17.2 mm block, i.e. station A in Fig. 4a.

4.3 Importance of Wall-Layer Resolution

How important are the wall-layers on the building surfaces? The computation domain typically may contain tens or hundreds of buildings. For instance, the DAPPLE geometry (http://www.dapple.org.uk/), which is one we are currently simulating, has nearly one hundred buildings. To resolve all of the wall layers would be extremely expensive at present.

LES was applied to calculate the turbulent flow over staggered wall-mounted uniform cubes with area coverage 25% at Reynolds number of 5000 based on the free stream velocity and the cube height. The computational domain and the other settings were the same as those in §4.1. A pure polyhedral mesh of more than 0.1 million cells with $13 \times 13 \times 13$ grid points per cube was used (Fig. 5a, C20SA). A second polyhedral mesh with a similar number of cells but with five wall-layers on the solid surfaces was also used (Fig. 5b, C20SB). The distances in wall units of the centroid of the first cell from the wall, z_1^+, for C20SA and C20SB were approximately 7.8 and 1 respectively, based on the global friction velocity u_*. Note that the distances in wall units of the centroid of the first cell from the wall based on the local friction velocity, z_{l1}^+, were much lower, because obstacle form drag provides the dominant part of the total drag. Figure 6 shows a comparison of vertical

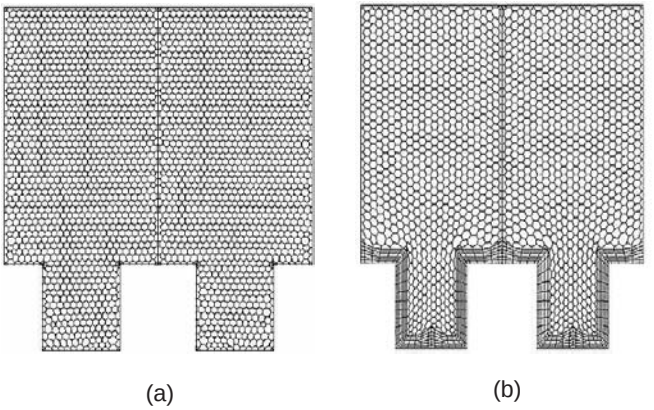

Fig. 5 Polyhedral meshes without (**a**) and with (**b**) wall-layers for an array of uniform cubes. Computational domain as in Fig. 1c

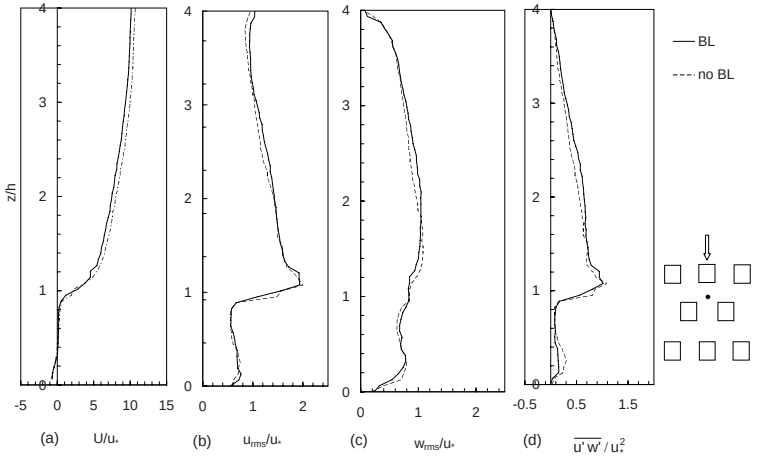

Fig. 6 Comparison of vertical profiles of mean velocity and turbulence statistics between meshes with (BL, C20SB) and without (no BL, C20SA) wall-layers

profiles of normalised mean streamwise velocity U, velocity fluctuations u_{rms} & w_{rms} and Reynolds shear stress $-\overline{u'w'}$. The differences between 'BL' and 'no BL' are hardly discernible, which suggests that it is not crucial to resolve the wall-layers on the building surfaces if the details within the wall-layers are not of particular interest.

By using numerical experiments like these, we have concluded that full resolution of the wall-layers is not important for the global turbulence statistics, nor for the mean drag of the complete surface. Note, however, that if heat transfer processes are important the same conclusion may well not hold.

5 Inflow Conditions and Large-Scale Unsteady Flows

Coupling weather-scale computations (for example from the UK Met Office's weather code, the Unified Model) to smaller-scale computations of flow and dispersion within urban environments requires a particularly efficient means of providing dynamically changing turbulence data at the inlet of the computational domain. This is especially true if the street-scale flows are to be modelled using LES.

Autocorrelation functions of typical turbulent shear flows have forms not too dissimilar to decaying exponentials. A digital-filter-based generation of turbulent inflow conditions exploiting this fact was developed [11] as a suitable technique for LES computation of spatially developing flows. The artificially generated turbulent inflows satisfy prescribed profiles of integral length scales and the Reynolds-stress-tensor. The method is more suitable for developed turbulent shear flows, e.g. the flow over an urban area, than the one proposed by [4]. It is also much more efficient than, amongst others, Klein's methods because at every time step only one set of two-dimensional (rather than three-dimensional) random data is filtered to generate a set of two-dimensional data with the appropriate spatial correlations. These data are correlated with the data from the previous time step by using an exponential function based on two weight factors.

In [12], LES of plane channel flows and flows over a group of staggered cubes has provided satisfactory validation of the technique, with results showing good agreement with simulations using periodic inlet-outlet boundary conditions and reasonable agreement with data from other sources – both DNS and laboratory experiments. These satisfactory validations, the fact that the results are not too sensitive to the precise form of the prescribed inlet turbulence, and the high efficiency of the technique, together suggest that the method will be very useful for practical simulations of urban-type flows.

Understanding the mechanism by which the urban boundary layer and the regional weather model are coupled aerodynamically and thermodynamically is known to be vital but is still in its infancy. Unsteadiness of the large scale driving wind probably has significant impact on the turbulent flows within the urban boundary layer [9]. For implementing dynamic spatial boundary conditions derived from the unsteady output of much larger-scale computations, like those available from the UK Met Office's Unified Model (UM), coupled with the new small-scale turbulence inflow method described as in §5, tools need to be developed to simulate flows over genuine urban geometry.

The question arises as to how such tools can be validated. Both pure oscillatory flow and a combined oscillatory flow with an added mean current have attracted researchers' attention for decades, with most studies being experimental [1, 2, 9]. As a validation, for investigating unsteady large-scale driving flows, we numerically simulated a combined oscillatory throughflow and mean current (here labelled as C20SOI) over a group of cube arrays (eight rows of cubes, see Fig. 9c) using the inflow-generating method. An assumption

was made here that at the inlet the turbulent fluctuations (u_{rms}, v_{rms} and w_{rms}) are in phase with the mean streamwise velocity defined by

$$U = U_0[1.0 + 0.5\sin(2\pi t/T)], \tag{4}$$

where U is the phase averaged streamwise velocity, U_0 is the mean streamwise velocity of the current, $T = 322.6h/u_*$ is the (relatively long) oscillation period, h is the height of the cube and u_* is the mean friction velocity. This assumption might not be too unreasonable for street-scale urban flows which are driven by the geostrophic wind.

For the same computational domain, a second LES run was conducted with a combination of a steady and an oscillatory pressure gradient and with streamwise periodic boundary conditions. This is labelled C20SOP and the unsteady pressure gradient is defined by

$$\frac{dP}{dx} = -\frac{\rho}{D}\{u_*[1.0 + 0.5\sin(2\pi t/T)]\}^2, \tag{5}$$

where $D = 4h$ is the depth of the domain and ρ is the density. The resulting mean streamwise velocity can be written as $U = U_0[1 + \alpha\sin(2\pi t/T - \phi)]$, where α and ϕ (the phase lag) are parameters to be obtained by using a fitting method. The velocity $r.m.s$ values ($u_{rms}, v_{rms}, w_{rms}$) are assumed to be of similar form to this equation.

Results obtained from the two driving methods are illustrated in Fig. 7, which shows the algebraically averaged profiles of the phase-averaged statistics obtained by the two methods and compared with the previous steady flow case (§4.1). The 'Oscillatory, body force' case is in marginally better agreement with the 'Steady, body force' than the 'Oscillatory, inflow' case, in particular within the canopy. The discrepancies might have two sources: (1) in Eq. (5) there is a higher frequency component, $\rho\{u_*0.125[1 - \cos(4\pi t/T)]\}$; (2) the phase of U, $u_{rms}, v_{rms}, w_{rms}$ lags that of dP/dx (see Eq. (5)).

Hence, an investigation of the mechanisms in the combined oscillatory throughflow superposed on a mean current was also attempted. We found that the phase lags of U, $\overline{u'w'}$, u_{rms} and w_{rms} are approximately 45 degree at all heights for C20SOP. This is reflected in the surface drag; Fig. 8 shows time series of the driving force, i.e. the body force in Eq. (5), and the total instantaneous drag on the sixteen cubes; a clear 45 degree phase lag is seen.

Figure 9 shows a comparison of phase averaged streamwise velocity between C20SOI and C20SOP. Note that here for C20SOP the phase is $2\pi t/T - \phi$ and that the phase-averaged statistics for C20SOI were obtained behind row seven (the 'dot' in Fig. 7, r.h.s.). Figure 9b shows that at all heights for C20SOI the streamwise velocity keeps the same phase, whereas Fig. 9a for C20SOP shows a very slight variation of phase lag with height. Nevertheless, the data in Fig. 9a and b have an almost identical pattern. The phase averaged turbulence statistics (u_{rms}, w_{rms} and $\overline{u'w'}$) also show almost identical patterns in the two cases. We conclude that our inflow turbulence generation method is adequate for cases where there are long-time-scale variations at the upstream boundary.

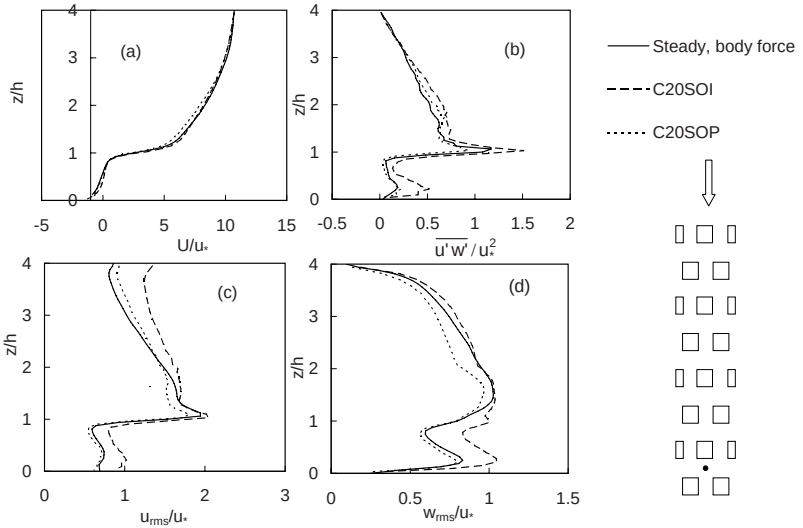

Fig. 7 Algebraically averaged profiles of the phase-averaged statistics

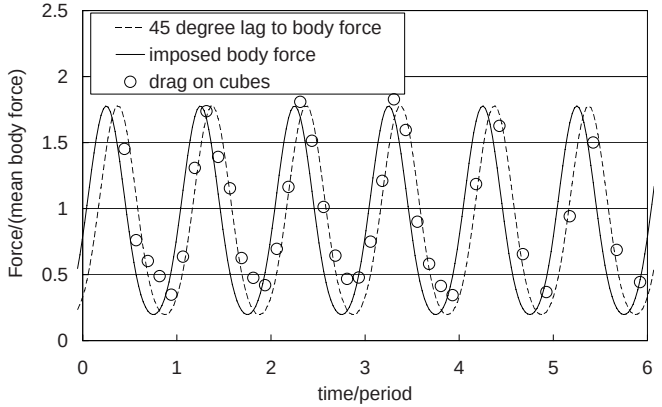

Fig. 8 Driving force and total instantaneous drag on cubes

6 Conclusions

Currently such LES simulations (using steady large-scale boundary conditions obtained from the UM), like those for the Marylebone Road area of London recently studied at both field and laboratory scale under the DAPPLE project (http://www.dapple.org.uk/), are showing great promise. The inflow and polyhedral mesh techniques have been applied for the turbulent flow and point source dispersion over the DAPPLE field site, which is located at the intersection of Marylebone Road and Gloucester Place in Central London. The computational domain size was 1200 m (streamwise) × 800 m (lateral) × 200 m (in full scale), with a resolution down to approximately one meter.

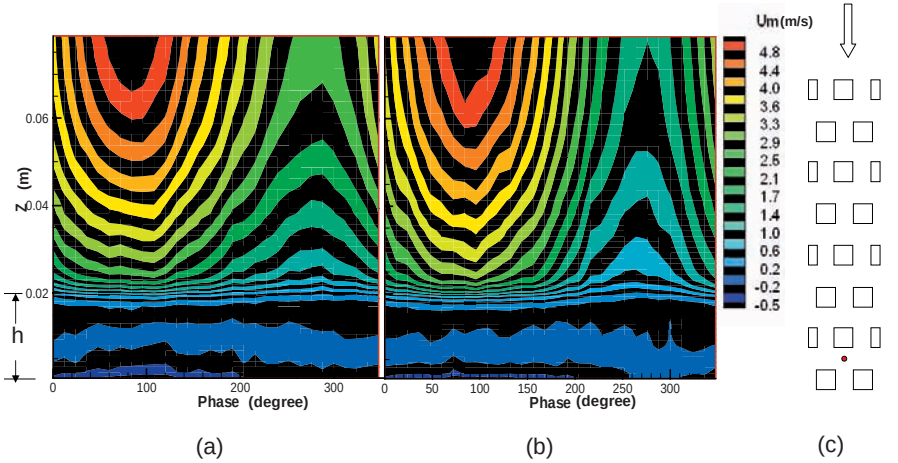

Fig. 9 Vertical profiles of phase averaged streamwise velocity. (**a**), C20SOP: body force driving; (**b**), C20SOI: inflow; (**c**): plan view of the 8 rows of cubes

Numerical simulations have focused on the case of southwesterly winds and a tracer release at York St. between Monatgue St. and Gloucester Place. The mean velocity and the Reynolds stress profiles at fourteen sites and mean concentration at ten sites are in good agreement with the wind tunnel experiments conducted under the DAPPLE programme (at EnFlo, University of Surrey) and, incidentally, have been found to be significantly better than results obtained using RANS techniques.

On the basis of our current success, we are optimistic about the reliability and affordability of LES for simulating flow and scalar dispersion within and above usefully-sized sub-domains of a city region, at a resolution down to one meter. Problems involving significant heat transfer effects are, however, likely to pose even greater challenges.

References

1. Al-Asmi K (1992) PhD Thesis, Department of Mechanical Engineering, University of Surrey
2. Chang YS, Scotti A (2004) J Geohys Res 109:1–16
3. Cheng H, Castro IP (2002) Bound-Lay Meteorol 104:229–259
4. Klein M, Sadiki A, Janicka J (2003) J Comp Phys 86:652–665
5. Lim HC, Castro IP, Hoxey RP (2007) J Fluid Mech 571:97–118
6. Lodahl CR, Sumer BM, Fredsøe J (1998) J Fluid Mech 373:313–348
7. Peric M (2004) ERCOFTAC Bull 62:25–29
8. Roache PJ (1997) Annu Rev Fluid Mech 29:123–160
9. Sleath JFA (1987) J Fluid Mech 182:369–409
10. Xie Z-T, Castro IP (2006) Flow Turbul Combust 76(3):291–312
11. Xie Z-T, Castro IP (2006) J Hydrodyn, Ser B 18(3, sup 1):259–264
12. Xie Z-T, Castro IP (2008) Flow Turbul Combust, to appear, DOI 10.1007/s10494-008-9151-5

Large Eddy Simulations of the Richtmyer–Meshkov Instability in a Converging Geometry

Manuel Lombardini[1], Ralf Deiterding[2], and D. I. Pullin[1]

[1] Graduate Aeronautical Laboratories, California Institute of Technology, Pasadena, CA 91125, USA. manuel@caltech.edu
[2] Oak Ridge National Laboratory, P.O. Box 2008 MS6367, Oak Ridge, TN 37831, USA

Abstract. This work presents on-going research on large-eddy simulations of shock-generated mixing in Richtmyer-Meshkov flow in converging geometries. A hybrid numerical method is used on each subgrid of the mesh hierarchy within the AMROC (adaptive mesh refinement object oriented C++) framework: it is a shock capturing method but reverts to a centered scheme with low numerical viscosity in regions of smoother flow. The stretched-vortex subgrid-scale model allows for the capturing of the small-scale mixing process between the two fluids. Results presented focus on the evolution of the mixing layer and its internal statistics including various spectra and p.d.f.s of mixed molar and mass fractions. A detailed quantitative analysis has also been conducted including space-time histories of instantaneous cylindrical shell-averages of diverse quantities, taken concentrically to the main shocks. Comparisons are made with the planar Richtmyer-Meshkov instability with reshock studied by Vetter and Sturtevant (1995) [1] and Hill et al. (2006) [2].

Keywords: Large-eddy simulations (LES) with strong shocks, Richtmyer-Meshkov instability (RMI), Compressible turbulent mixing, Adaptive mesh refinement (AMR)

1 Introduction

1.1 Flow Description

The RMI occurs when an interface between two fluids of different density is impulsively accelerated by a shock wave depositing baroclinic vorticity on the interface. Such instability can be seen as the impulsive limit of the Rayleigh-Taylor instability [3, 4]. Examples of the occurrence of the RMI in converging geometries are present in experiments aiming to achieve inertial confinement fusion or in natural phenomena such as supernova collapse. While the linear regime of the purely azimuthal RMI has been recently analyzed [5], two-dimensional simulations of the instability in polar imploding and exploding

J. Meyers et al. (eds.), Quality and Reliability of Large-Eddy Simulations,

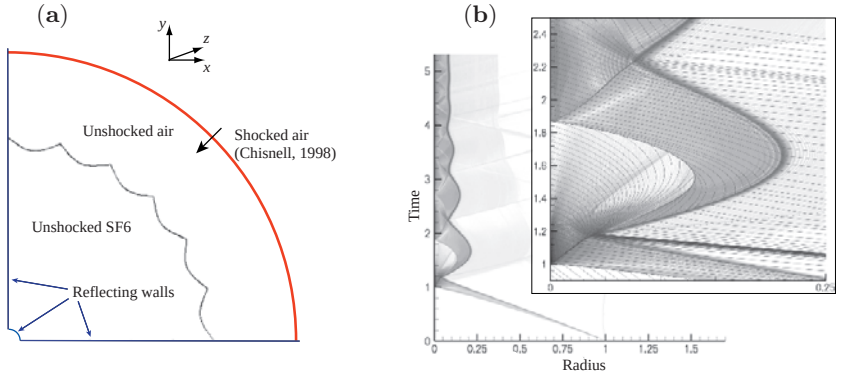

Fig. 1 (***a***) Initial flow description. (***b***) One-dimensional wave diagram (r, t) obtained by studying the radially symmetric converging-shock/unperturbed-interface interaction; characteristics $u_r - a$ (sound speed a) are superposed on the close-up; time is dimensionalized by the implosion time, radius by initial position of the interface

geometries using a front-tracking method have also been performed [6]. The latter work has related the first reshock event but has not pursued any study of the three-dimensional turbulent mixing following.

Figure 1(a) depicts a converging cylindrical shock impacting a perturbed, cylindrically-shaped density interface that separates (light) air from (heavy) SF_6 (Atwood number $A = 2/3$), both at rest. The transmitted shock converges inwards, reflects off the apex, and reshocks the highly distorted interface, initiating a strong turbulent mixing. Multiple reshock events follow, as inferred from Fig. 1(b). While the planar interaction between a shock and a 'heavy SF_6 to light air' contact produces a reflected rarefaction wave, each (heavy to light) reshock interaction generates a reflected wave that focuses on a shock, and reflects at the apex as a new shock that drives the next reshock interaction. The successive reshock events occur with lower intensity but in a self-similar way, eventually concentrating the heavy fluid inside. Stronger initial incident shocks trap the heavy fluid closer to the apex.

1.2 Initial and Boundary Conditions

It is assumed that shock-wave/boundary-layer interaction does not play a dominant role in the growth of the turbulent mixing zone (TMZ) and slip boundary conditions can be applied at the reflected walls. Periodic boundary conditions are used in the z-direction of the cylinder axis. The measured location and extent of the TMZ suggest that the turbulent region does not reach the inner cylindrical wall, which is used to regularize the apex (cf. Fig. 1(a)). It can also be employed to prescribe zero-gradient boundary conditions over an outer cylindrical boundary.

The flow behind the cylindrical converging shock is initialized with the approximate solution of Chisnell [7], whose self-similar structure has been preliminary confirmed by simulations of a single converging shock. In addition, the Guderley exponent, characterizing the shock position history, has been confidently computed before and after apex reflection. This choice of initial conditions completely avoids spurious waves and leaves only the shock thickness as intrinsic length scale. Simulations have been performed for the incident shock strength $M_I = 1.3$ and 2.0, where M_I is the Mach number of the shock immediately before impact onto the interface.

The interface is initially located around the mean radial position $r = R_0$ and has a fully resolved intrinsic thickness. In order to ensure an effective mixing, the shape of the interface is specified as a linear combination of a regular perturbation in both azimuthal and axial directions $|\sin(n\theta)\sin(kz)|$ with wavelengths comparable at the reshock time and amplitude about 5% of R_0, and a symmetry-breaking perturbation with amplitude that has a random phase and a prescribed power spectrum with peak wavelength close to R_0.

2 Equations of Motion and Subgrid Modeling

2.1 Favre-Filtered Navier-Stokes Equations

The reshock process produces a large dynamical range of turbulent scales, necessitating the use of LES. If the overbar denotes the filtering operation, any Favre-filtered quantities is defined by $\widetilde{f} = \overline{\rho f}/\overline{\rho}$, and the LES equations of motion in conservative form are obtained by Favre-filtering the Navier-Stokes equations, separating the large scales to be simulated from the small scales to be modeled:

$$\frac{\partial \overline{\rho}}{\partial t} + \frac{\partial \overline{\rho}\widetilde{u}_j}{\partial x_j} = 0, \tag{1}$$

$$\frac{\partial \overline{\rho}\widetilde{u}_i}{\partial t} + \frac{\partial (\overline{\rho}\widetilde{u}_i\widetilde{u}_j + \overline{p}\delta_{ij})}{\partial x_j} = \frac{\partial d_{ij}}{\partial x_j} - \frac{\partial \tau_{ij}}{\partial x_j}, \tag{2}$$

$$\frac{\partial \overline{E}}{\partial t} + \frac{\partial (\overline{E} + \overline{p})\widetilde{u}_j}{\partial x_j} = \frac{\partial}{\partial x_j}\left(\overline{\kappa}\frac{\partial \widetilde{T}}{\partial x_j}\right) + \frac{\partial d_{ji}\widetilde{u}_i}{\partial x_j} - \frac{\partial q_j^T}{\partial x_j}, \tag{3}$$

$$\frac{\partial \overline{\rho}\widetilde{\psi}}{\partial t} + \frac{\partial \overline{\rho}\widetilde{\psi}\widetilde{u}_j}{\partial x_j} = \frac{\partial}{\partial x_j}\left(\overline{\rho}\widetilde{D}\frac{\partial \widetilde{\psi}}{\partial x_j}\right) - \frac{\partial q_j^{\psi}}{\partial x_j}, \tag{4}$$

where the filtered total energy $\overline{E}$, pressure $\overline{p}$, and deviatoric Newtonian stress tensor d_{ij} of the mixture are given by

$$\overline{E} = \frac{\overline{p}}{\widetilde{\gamma} - 1} + \frac{1}{2}\overline{\rho}\widetilde{u}_k\widetilde{u}_k + \frac{1}{2}\tau_{kk}, \;\; \overline{p} = \frac{\overline{\rho}R\widetilde{T}}{\widetilde{m}}, \tag{5}$$

$$d_{ij} = \overline{\mu}\left(\left(\frac{\partial \widetilde{u}_i}{\partial x_j} + \frac{\partial \widetilde{u}_j}{\partial x_i}\right) - \frac{2}{3}\frac{\partial \widetilde{u}_k}{\partial x_k}\delta_{ij}\right). \tag{6}$$

The scalar ψ defines the local mixture composition between air ($\psi = 0$) and SF_6 ($\psi = 1$). The mean molecular weight is defined as a function of the respective molecular weight by $1/\widetilde{m} = ((1-\widetilde{\psi})/m_{\text{air}} + \widetilde{\psi}/m_{\text{SF}_6})$. The average specific heat ratio is given by $\widetilde{\gamma} = \widetilde{c}_p/(\widetilde{c}_p - R/\widetilde{m})$, where $\widetilde{c}_p = ((1-\widetilde{\psi})c_{p,\text{air}} + \widetilde{\psi}c_{p,\text{SF}_6})$. Temperature-dependent transport properties of the mixture, i.e. viscosity $\overline{\mu}$, heat conduction $\overline{\kappa}$, and diffusivity $\widetilde{D}$, obey usual binary mixing rules and pure component mixing properties. Hereinafter, filtered and Favre-filtered quantities are identified with resolved-scale quantities computed in the LES, and overbars and tildes are voluntarily ignored.

2.2 Application of the Stretched-Vortex Subgrid Model

While conventional LES models generally consider only resolved-scale transport, and do not attempt to capture the small-scale mixing process between the two fluids, the stretched-vortex subgrid-scale (SGS) model [8] extended to compressible flows [9] and subgrid scalar transport [10] is based on an explicit structural modeling of small-scale dynamics. It utilizes stretching vortices as the essential subgrid element in the closure of Favre-filtered Navier-Stokes equations by providing the subgrid stress tensor τ_{ij}, the turbulent temperature flux q_i^T, and the mixture fraction flux q_i^ψ (see [2] for detailed expressions of the subgrid tensors). In this model, the flow within a computational grid cell results from an ensemble of straight, nearly axisymmetric vortices aligned with a direction obtained from a weighting of local resolved-scale vorticity and strain rate orientations. The subgrid spiral vortices are local approximate solutions of the Navier-Stokes equations [11] and the scalar transport equations [12]. Note that the structural nature of this model has also facilitated the mathematical development of a multiscale treatment of the activity beyond the resolution cut-off and predictions of subgrid mixing properties [2].

3 Computational Approach

3.1 AMROC Framework

The resolution requirements imposed by the physics of the flow vary greatly both spatially and temporally for this simulation. The parallel block-structured adaptive mesh refinement framework AMROC developed by Deiterding [13] proves to be decisive for the converging RMI, where the interface is expected to travel down to the inner apex and coarse resolution is sufficient for the outer region. Discrete conservation of mass, momentum, and energy is accomplished by using a flux-based conservative finite-difference approach. Figure 2 shows the mixing zone and the refinement levels used at different stages of the simulation. The base grid ((x, y, z)-resolution of $83 \times 83 \times 51$) is refined twice, with factors $(2, 2)$, such that the finest equivalent resolution would be $332 \times 332 \times 204$.

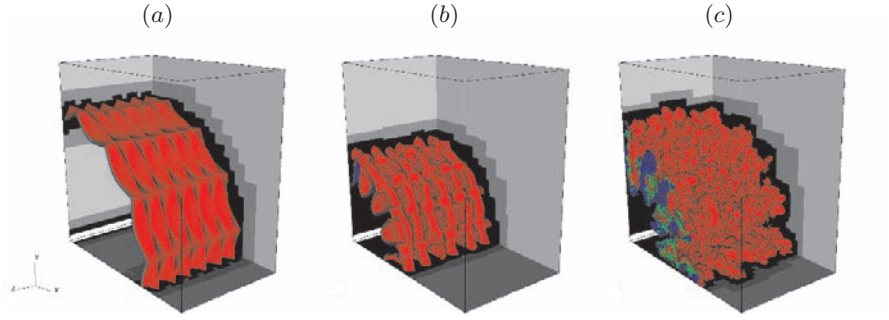

Fig. 2 Differently colored iso-surfaces for $\psi = 75\%$, 50%, and 25% visualize the evolution of the TMZ: (***a***) initially, (***b***) after the first shock interaction, (***c***) after the first reshock. The gray levels on the background planes represent the domains of different mesh refinement. Case $M_0 = 1.3$

3.2 Hybrid Numerical Method

The numerical method is formulated for uniform Cartesian grids and is effectively applied to each subgrid of the mesh hierarchy. A ghost fluid approach [14] is utilized to numerically incorporate the non-Cartesian reflective wall boundary conditions arising at the small cylinder regularizing the apex (cf. Section 1.2). The overall method is an extension of the hybrid scheme by Hill & Pullin [15] to SAMR meshes with non-Cartesian embedded boundaries. A weighted, essentially non-oscillatory (WENO) scheme is used to capture discontinuities such as shock waves or fine/coarse mesh interfaces, but switches to a low-numerical dissipation, explicit, tuned center-difference scheme (TCD) in the smooth or turbulent regions, optimal for the functioning of explicit LES such as the SGS stretched-vortex method. To ensure discrete numerical stability of the inviscid terms (momentum, scalar and energy convection terms), the centered discretization is written in a stable, energy preserving formulation adapted to compressible flows [16]: the TCD flux at cell walls has a skew-symmetric form described in detail in [17].

WENO-TCD Switching Technique

Around discontinuities, the WENO scheme computes fluxes at cell walls based on a weighted convex combination of candidate stencils that minimizes interpolation across shocks. For the subgrid activity to be correctly computed, thereby assuring the quality of the LES, the use of WENO is restrained to regions containing shock waves only. Instead of using purely geometrical criteria based, for instance, on curvature of pressure and/or density (as in [15, 17] and other hybrid methods cited within), a new WENO/TCD switching method has been created to better extract the physical nature of the compressible flow, therefore optimizing the use of WENO.

To illustrate the technique, consider the local one-dimensional Riemann problem at every cell wall of the computation domain. An approximate solution, denoted by a subscript $\star$, can be computed using Roe-averaged quantities from the given left state (cell center i) and right state (cell center $i+1$). Lax' entropy conditions allow for characterizing the type of the waves $u-a$ and $u+a$ (shock or rarefaction wave) connecting the right or left state from the central state $\star$. A shock is produced for the wave $u\pm a$ if $u_r \pm a_r < u_\star \pm a_\star < u_l \pm a_l$. The strength of these inequalities is evaluated within a threshold value $\alpha_{\mathrm{Lax}}/a_\star$ in order to eliminate weak acoustic waves that could be easily handled by the TCD scheme. For better efficiency and flexibility, this criterion is combined with a geometrical test based on the mapping $\phi(\theta) = 2\theta/(1+\theta)^2$ of the normalized pressure gradient $\theta = |p_{i+1} - p_i|/|p_{i+1} + p_i|$ inspired from slope-limiting techniques. A threshold for the latter geometrical criterion is defined by α_{Map}.

Two and three-dimensional versions of this new switching algorithm have been developed to treat complex configurations such as oblique waves, curved shocks, and more general shock waves not aligned with the computational grid. Comparisons with sensors relying on pressure fluctuations alone were performed as verification tests on complex 1D examples (planar shock-contact interaction with reshock, radially symmetric cylindrical and spherical converging shock-contact interaction with reshock, shock-entropy wave interaction, colliding blast waves, vacuum test), and multi-dimensional examples as well (planar RMI, cylindrical converging RMI, supersonic shear layer, inclined supersonic jet). The values of α_{Lax} and α_{Map} giving superior results to former criteria are both around 1%.

4 Shell-Averaged Statistics

4.1 General Definitions

The natural symmetry of the problem results in defining as 'shell' a cylindrical segment of radius r extending in both θ and z directions. Shell-averaged flow quantities are presented on both the resolved and the subgrid scales. Using brackets to denote a shell-average at position r and time t, we define for any quantity $Q(\boldsymbol{x}, t)$:

$$Q(\boldsymbol{x}, t) \equiv \langle Q \rangle(r, t) + Q'(r, \theta, z, t) \equiv \widetilde{Q}(r, t) + Q''(r, \theta, z, t), \tag{7}$$

$$\widetilde{Q}(r, t) \equiv \frac{\langle \rho Q \rangle}{\langle \rho \rangle}, \;\; \mathrm{Var}_\rho(Q) \equiv \widetilde{Q''^2} = \widetilde{Q^2} - \tilde{Q}^2 = \frac{\langle \rho Q^2 \rangle}{\langle \rho \rangle} - \frac{\langle \rho Q \rangle^2}{\langle \rho \rangle^2}, \tag{8}$$

where the tilde now represents the Favre-like shell-average. Note that its computation involves first the interpolation of Cartesian fields over a shell that can possibly cross diverse AMR patches being handled by different processors, then averaging the sampled fields. Favre-like shell-averaged statistics of

the turbulent activity such as resolved-scale turbulent kinetic energy (TKE) $\langle K \rangle$, subgrid TKE $\langle k \rangle$ (per unit mass), resolved-scale dissipation $\langle \epsilon_{res} \rangle$, and subgrid energy transfer $\langle \epsilon_{sgs} \rangle$ read as follows:

$$\langle K \rangle = \frac{1}{2}\mathrm{Var}_\rho(u_i u_i),\ \langle k \rangle = \frac{\langle \tau_{ii} \rangle}{2\langle \rho \rangle},\ \langle \epsilon_{res} \rangle = \frac{\langle d'_{ij} S'_{ij} \rangle}{\langle \rho \rangle},\ \langle \epsilon_{sgs} \rangle = -\frac{\langle \tau'_{ij} S'_{ij} \rangle}{\langle \rho \rangle}. \quad (9)$$

Turbulent intensity u' computed from the total TKE, turbulent Reynolds number Re_T based on u' and on the total turbulent dissipation, and turbulent Mach number M_T can be defined as

$$u' = \sqrt{\frac{2(\langle K \rangle + \langle k \rangle)}{3}},\ Re_T = \frac{u'(u'^3/(\langle \epsilon_{res} \rangle + \langle \epsilon_{sgs} \rangle))}{\langle \mu/\rho \rangle},\ M_T = \frac{u'}{\langle a \rangle}. \quad (10)$$

Above shell-averaged quantities are dimensionless. The characteristic length scale of our problem is R_0. Characteristic density and speed are ρ_0 and $a_0 = \sqrt{\gamma_{\mathrm{air}} p_0/\rho_0}$ corresponding to the unshocked region of air. The characteristic turbulent kinetic energy per unit mass is chosen as a_0^2, time as R_0/a_0, and turbulent dissipation as $\mu_{\mathrm{air}} a_0^2/(\rho_0 R_0^2)$.

4.2 Shell-Averaged Statistics vs. Time

We define the mixing zone thickness δ and its center r_c according to the integral definitions as

$$\delta(t) = 4\int_{r_{min}}^{r_{max}} (1 - \langle \psi \rangle)\langle \psi \rangle \mathrm{d}r, \quad r_c(t) = 4\int_{r_{min}}^{r_{max}} \frac{r}{\delta}(1 - \langle \psi \rangle)\langle \psi \rangle \mathrm{d}r. \quad (11)$$

To study the statistical properties of the spike and bubble structures, we define from $\langle \psi \rangle$ the 75% air (resp. SF_6) shell mean position r_s (resp. r_b) as the portion of heavy (resp. light) fluid penetrating into the light (resp. heavy) fluid, also called spike (resp. bubble). Figure 3 shows the history of the mixing layer growth. Sharp compressions of the mixing zone characterize the initial shock-interface interaction and the first reshock. Each of these phases are followed by a growth of the mixing zone. A second reshock is apparent at a dimensionless time of approximately 2. The volume-averaged total TKE vs. time (not shown) confirms these two reshock events, where a noticeable amounts of vorticity and kinetic energy have been deposited across the mixing layer. The weaker reshocks that follow (cf. Section 1.1 contribute to extend the already thickened mixing zone further. As the mixing zone expands outwards, the growth decelerates to finally reach a stable position, while the volume-averaged total TKE continues to decay as well as Re_T evaluated at r_c (not shown). At later times, Re_T is about 10 times higher than its equivalent in the planar case. Compared to the planar RMI (Figs. 5 and 11 of [2]), the cylindrical converging RMI shows a stronger and longer mixing zone growth as well as a longer decay of TKE.

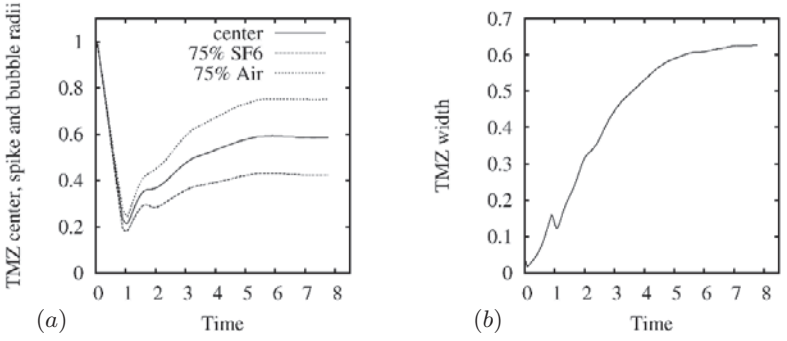

Fig. 3 (***a***) Average TMZ center r_c, bubble r_b and spike positions r_s, and (***b***) TMZ growth rate δ, vs. time ($M_0 = 2.0$)

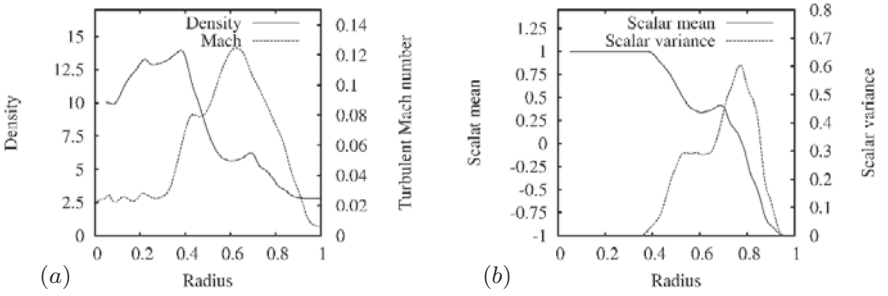

Fig. 4 (***a***) Shell-averaged density $\langle\rho\rangle$ and turbulent Mach number M_T, and (***b***) scalar mean $\langle Y\rangle$ and dissipation $\mathrm{Var}_\rho(Y)$, vs. radius ($t = 3.8$, $M_0 = 1.3$)

4.3 Shell-Averaged Statistics vs. Radius at Later Times

The scalar function displayed Fig. 4(b) is defined by $Y = 2\psi - 1$ such that $Y \epsilon [-1, 1]$. The shell-averaged scalar variance characterizes the extent of the TMZ, with two peaks denoting the dominant bubble and spike portions. It is observed that compressibility effects during the evolution of the mixing zone peak at its center and, excluding shock interaction events, late time turbulence is weakly compressible with M_T in the range 0.06–0.012 within the TMZ (Fig. 4(a)).

Thanks to the stretched-vortex subgrid model, shell-averaged subgrid quantities can be directly estimated. Figure 5(a) shows that later during the TKE decay, the resolved TKE is about 50 times the subgrid TKE ($\sim$ 10 times in the planar case). The subgrid dissipation is of the order of 200 times its resolved counterpart ($\sim$ 100 times in the planar case) as shown in Fig. 5(b), while prior to reshock it was only about 20 times larger (not shown). This indicates that the turbulence scales fully develop only after reshock.

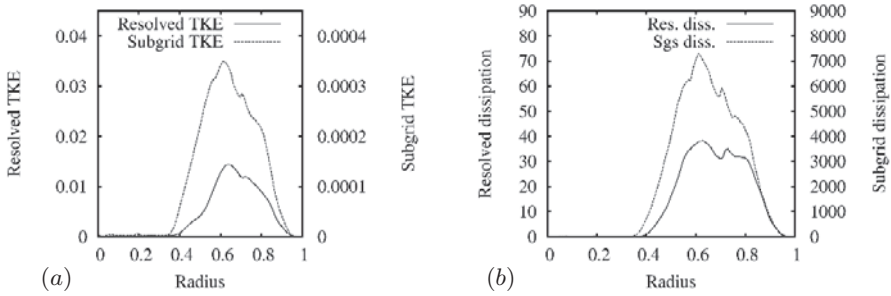

Fig. 5 (***a***) Resolved and subgrid TKE $\langle K \rangle$ and $\langle k \rangle$, and (***b***) resolved and subgrid dissipation $\langle \epsilon_{res} \rangle$ and $\langle \epsilon_{sgs} \rangle$, vs. radius ($t = 3.8$, $M_0 = 1.3$)

5 Studying the Turbulent Mixing

Other tools, such as power spectra and probability density functions (p.d.f.s), are utilized here to study the properties and the quality of the resolved turbulent flow. Velocity components, density, passive scalar, as well as subgrid stretched vortex axis orientation angles, have been interpolated over cylindrical shells going through the TMZ at radii r_c (TMZ center), r_b (bubbles) and r_s (spikes), at very late times.

5.1 Instantaneous One-Dimensional Spectra

Applying Fourier transforms in the periodic z-direction and averaging the power spectrum coefficients over the θ-direction, various power spectra are plotted as a function of the axial wavenumber k_z in Fig. 6(a, b). The data exhibits decay at highest wavenumbers approaching Kolmogorov-like $k^{-5/3}$ scaling. Except for u_z, minimal aliasing errors are observed at the highest wavenumbers. A change in the numerical representation of the subgrid stress tensors is currently being considered to solve this issue. We recall that no explicit filtering of any kind was performed, and WENO is not used across the TMZ. Density and scalar spectra correlate well as shown in Fig. 6(b).

5.2 Instantaneous Two-Dimensional Spectra

Using symmetries, a full cylindrical flow field can be reconstructed and any shell of given radius r exhibits periodicity in the azimuthal direction as well as the axial one. Considering the unfolded shell as an (s, z)-plane, with s the arc $s = r\theta$, a (k_θ, k_z)-power spectrum can be derived. Figure 7(a) shows that the u_r two-dimensional power spectrum is rather isotropic, as also observed for the other velocity components as well as density and scalar spectra (not shown). We can therefore legitimately assume that the turbulent flow over a cylindrical shell has two isotropic directions, while in the planar case directions transverse

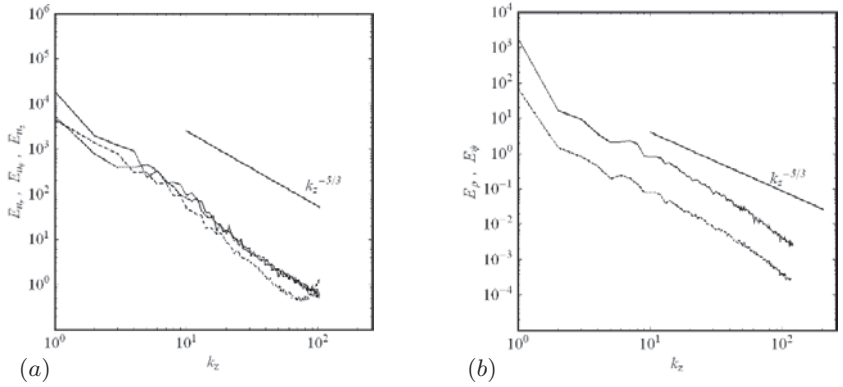

Fig. 6 (***a***) k_z-power spectra of the velocity components u_r (*solid line*), u_θ (*dotted line*), u_z (*dashed line*); (***b***) density (*solid line*) and scalar (*dashed line*) (shell $r = r_c$, $t = 8.2$, $M_0 = 2.0$)

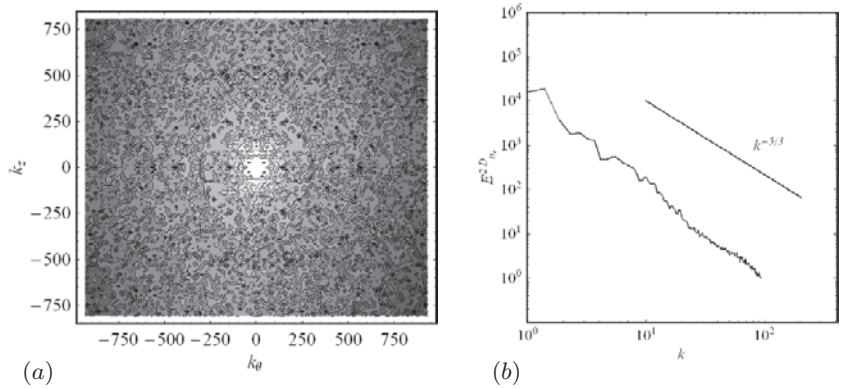

Fig. 7 u_r velocity component (***a***) (k_θ, k_z)-power spectrum (physical wavenumbers represented in arbitrary units), and (***b***) radial k-spectrum (shell $r = r_c$, $t = 8.2$, $M_0 = 2.0$)

to the flow are obviously equivalent. A radial k-spectrum, with $k = \sqrt{k_z^2 + k_\theta^2}$, is displayed in Fig. 7(*b*) and compared to the Kolmogorov scaling $k^{-5/3}$.

5.3 Instantaneous p.d.f.s of the Mixing

In order to study the inhomogeneity of the turbulent mixing due to the different structures (spikes and bubbles), that act differently on either side of the TMZ, we sample scalar (or mixture fraction) and density fields interpolated over a given cylindrical shell to create the Reynolds joint density-mixture fraction p.d.f. that follows:

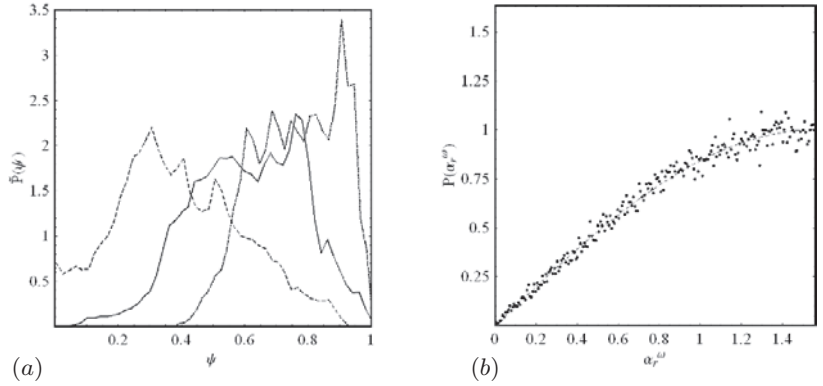

Fig. 8 (***a***) P.d.f.s of the mixture fraction at r_c (*solid line*), r_b (*dotted line*), and r_s (*dashed line*); (***b***) p.d.f. of the vorticity local orientation angle with $\mathbf{e}_r$ (shell $r = r_c$, $t = 8.2$, $M_0 = 2.0$)

$$\tilde{\mathrm{P}}(\psi; \boldsymbol{x}, t) \equiv \frac{1}{\langle\rho\rangle} \int \rho \mathrm{P}(\rho, \psi; \boldsymbol{x}, t) \mathrm{d}\rho, \tag{12}$$

Before reshock, the two fluids are mostly unmixed, and the p.d.f. shows two peaks for values of the mixture fraction of 0 and 1. After the first reshock, the p.d.f. at the shell cutting through the TMZ center r_c exhibits a strong central mode, while for the shells r_b and r_s, the two peaks have moved towards the TMZ center, away from the pure fluid values 0 and 1, indicating mixing progress. It is observed that the strength of these two regions of the TMZ with high density gradients is sustained by the successive reshocks carrying pressure gradients in the radial direction. The bimodal nature of the mixing at the center of the TMZ is apparent at later times (Fig. 8(*a*)), but seems to tend to a wide single mode as time evolves and reshocks become weaker.

5.4 Instantaneous p.d.f.s of the Subgrid Vortex Orientation

In order to understand the influence of the model on the turbulent properties of the flow mixing, we study the isotropy of both vorticity and principal rate of strain fields (cf. Section 2.2) by displaying the p.d.f. of these various angles with respect to the local cylindrical basis $(\mathbf{e}_r, \mathbf{e}_\theta, \mathbf{e}_z)$ over the r_c-shell. Results demonstrate that the principal strain rate at the TMZ center is somewhat anisotropic in the radial direction $\mathbf{e}_r$ (not shown), while the vorticity orientates isotropically as shown for example for the vorticity radial orientation α_r^ω in Fig. 8(*b*) (similar results not shown here apply to the two other angles). Recall that for an isotropic distribution of angles α with respect to a fixed axis, the corresponding p.d.f. is $\sin(\alpha)$ (dashed line in Fig. 8(*b*)).

6 Conclusion

The Richtmyer-Meshkov instability with reshock has been studied in a canonical cylindrical converging geometry. Compressible large-eddy simulation using the stretched-vortex subgrid model has been used to study the turbulent mixing occurring between an outside light and an inside heavy fluid. A low-dissipation tuned-centered stencil used away from shocks has allowed for accurately computing different turbulent statistics.

The successive reshocks prove to be responsible for the intense growth of the mixing zone. After the second reshock event, a long decay of the turbulent energy is observed. At later times, the growth stabilizes and the turbulent mixing zone remains weakly compressible. Various late time energy spectra taken at the center of the mixing zone show an inertial subrange approaching the universal $k^{-5/3}$ scaling. The late time mixing in the converging geometry exhibits a similar but somewhat less pronounced bimodal aspect than in the planar case. The local isotropic nature of the flow has been scrutinized through diverse statistics over cylindrical shells penetrating through the mixing layer. Current work consists of formulating the effect of curvature on the turbulent activity and exploring the 'heavy to light' converging RMI flow.

Acknowledgments

The authors would like to acknowledge the helpful conversations with D.J. Hill. This work is supported by the ASC program of the Department of Energy under subcontract no. B341492 of DoE contract W-7405-ENG-48.

References

1. Vetter M, Sturtevant B (1995) Shock Waves 4:247–252
2. Hill DJ, Pantano C, Pullin DI (2006) J Fluid Mech 557:29–61
3. Richtmyer RD (1960) Commun Pure Appl Math 13:297–319
4. Meshkov EE (1969) Sov Fluid Dyn 4:101–108
5. Mikaelian KO (2005) Phys Fluids 17(9), Art no 094105
6. Zhang Q, Graham MJ (1998) Phys Fluids 10(4):974–992
7. Chisnell RF (1998) J Fluid Mech 354:357–375
8. Misra A, Pullin DI (1997) Phys Fluids 9:2443–2454
9. Kosovic B, Pullin DI, Samtaney R (2002) Phys Fluids 14:1511–1522
10. Pullin DI (2000) Phys Fluids 12:2311–2319
11. Lundgren TS (1982) Phys Fluids 25:2193–2203
12. Pullin DI, Lundgren TS (2001) Phys Fluids 13:2553–2563
13. Deiterding R (2005) In: Plewa T et al (eds) Adaptive mesh refinement – theory and applications. Springer, New York
14. Fedkiw RP, Aslam T, Merriman B, Osher S (1999) J Comput Phys 152(2):457–492
15. Hill DJ, Pullin DI (2004) J Comput Phys 194:435–450
16. Honein AE, Moin P (2004) J Comput Phys 201:531–545
17. Pantano C, Deiterding R, Hill DJ, Pullin DI (2007) J Comput Phys 221(1):63–87

Quality Assessment in LES of a Compressible Swirling Mixing Layer

Sebastian B. Müller and Leonhard Kleiser

Institute of Fluid Dynamics, ETH Zurich, 8092 Zurich, Switzerland
sebastian@ifd.mavt.ethz.ch, kleiser@ifd.mavt.ethz.ch

Abstract. We apply large-eddy simulation (LES) to simulate the nonlinear evolution of a subsonic circular swirling mixing layer, a round jet surrounded by slow co-flow with an additional swirl component present only in the narrow shear layer. The growth of viscous spatial instabilities and transition to turbulence of the swirling mixing layer are investigated. LES results are assessed at different resolutions and compared with reference results from direct numerical simulation (DNS).

Keywords: Large-eddy simulation, Approximate deconvolution model, Compressible flow, Transition to turbulence, Swirling mixing layer

1 Introduction

Swirling mixing layers occur in many technical applications. Typical examples are leading-edge vortices on delta wings or flame holders in combustion devices. Good mixing is crucial in designing combustion systems for different applications. Detailed understanding of the physics of swirling jet flows and mixing layers is essential for the development of new turbulence and mixing models. To improve the understanding of the underlying flow physics, substantial research efforts have been undertaken in the past decades. These efforts primarily aimed at modeling basic elements of swirling motion and to determine the associated stability characteristics. The addition of swirl can enhance the mixing of circular mixing layers and jet flows. In the present investigation, the predictive capability of large-eddy simulation (LES) is studied for transition to turbulence in a subsonic swirling circular mixing layer.

Transitional and turbulent flows support a wide range of temporal and spatial scales of motion. As a consequence, accurate simulation methodologies are required to reliably predict the flow. In direct numerical simulations (DNS), all scales of turbulence are numerically resolved, while in Reynolds-averaged Navier-Stokes computations (RANS) all scales of turbulence are modeled. In LES, the large-scale motion of a transitional or turbulent flow field is resolved

J. Meyers et al. (eds.), Quality and Reliability of Large-Eddy Simulations,

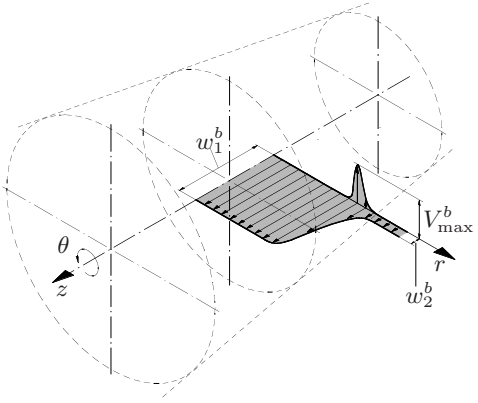

Fig. 1 Swirling mixing layer configuration

and the effects of the small, unresolved scales on the large ones are modeled. The subgrid-scale modeling strategy is based on the idea that the large scales are primarily dependent on the geometry as well as a few important integral characteristics, while the small scales tend to be more universal and are therefore expected to be modeled more easily. LES aims to bridge the gap between expensive DNS, which are limited to moderate Reynolds numbers, and RANS, which need (sometimes heavily complex) turbulence models that sometimes fail to predict turbulent flows accurately and are often inappropriate for the analysis of transitional and turbulent flows. The investigation of such flows using LES comprises an important research activity for the engineering sciences. In this contribution, we present LES results using the approximate deconvolution model (ADM) [13] as subgrid-scale closure. LES results are assessed at different resolutions and compared with reference results from direct numerical simulation (DNS).

2 Simulation Methodology

Figure 1 illustrates the flow configuration under consideration. It consists of a subsonic circular swirling mixing layer, i.e. a round jet surrounded by slow coflow with an additional swirl component which is present only in the narrow shear layer. Our results have been obtained with a highly accurate code for DNS (and LES) solving the (filtered) Navier-Stokes equations for compressible flow in cylindrical coordinates. We consider the nonlinear disturbance development and transition to turbulence of the laminar layer perturbed at the inflow by viscous spatial instabilities obtained from linear theory. Swirling mixing layers at Mach number $Ma = 0.8$ are investigated. The Reynolds number of the flow under consideration is chosen as $Re = 5000$ (using the jet radius

and centerline values as reference quantities). The maximum swirl velocity is set to $V^b_{\max} = 0.4$.

Our DNS/LES code relies on the conservative formulation of the compressible Navier-Stokes equations expressed in cylindrical coordinates and a mapping from Cartesian to cylindrical coordinates is employed. This eliminates problems related to the specific numerical treatment of additional centrifugal and Coriolis force terms that arise in other (e.g. weakly conservative) formulations.

At the inflow plane, Dirichlet boundary conditions are applied on all five conservative variables to precisely define the time-dependent inflow. In addition, a damping sponge zone is imposed to absorb any upstream-traveling acoustic disturbances. At the radial and outflow boundaries non-reflecting conditions (accounting for the curvilinear radial boundary) are employed and supplemented by sponge layers to enforce ambient values for pressure and density. The inflow forcing is based on the superposition of viscous spatial linear instabilities consisting of individual wavelike solutions of the form

$$\hat{q}(r) \exp\left\{\mathrm{i} \cdot (\alpha z + n\theta - \omega t)\right\},$$

where $\hat{q}$ is the complex eigenfunction, $\alpha = \alpha_r + i\alpha_i$ the complex streamwise wavenumber, n the azimuthal wavenumber and ω the circular frequency. For the base flow type under consideration, inviscid [7] and viscous [10] linear stability investigations have been performed. The present simulations employ an axisymmetric ($n = 0$) and two helical $n = 1$ instabilities with positive and negative circular frequency. Additional simulations were performed to analyze the swirl-enhanced mixing behavior using different combinations of instability waves [9].

The DNS results have been validated by employing two different high-order discretization schemes at otherwise identical resolution and boundary conditions. One simulation employs up to tenth-order (at interior points) compact central schemes [6] for spatial dicretization of the convective as well as diffusive terms, yielding an overall fourth-order scheme. These central compact schemes are combined with a secondary filter $\hat{Q}_5\hat{G}$ after every other time step to ensure numerical stability. The other simulation relies on upwind-biased schemes [1] for the convective terms instead of compact central schemes. The secondary filtering is not used in this simulation. For the LES, convective as well as diffusive terms are discretized with up to tenth-order (at interior points) compact central schemes [6], yielding an overall fourth-order scheme. In the azimuthal direction a Fourier spectral method is employed. Secondary filtering or upwind-biased schemes are not used in the LES. For time advancement the LDDRK scheme by Berland et al. [3] is used to provide an efficient and accurate low-storage integration scheme. A necessary condition for a stable time integration is that the eigenvalues of the spatially discretized linearized Navier-Stokes equations lie within the stability domain of the Runge-Kutta scheme. This stability criterion is maintained by an appropriately chosen time-step size derived from the scalar model advection-diffusion equation [9]. Near

the polar axis the azimuthal grid spacing becomes excessively fine. To avoid unnecessarily small time steps, the number of retained Fourier modes is linearly reduced towards the pole. For further details concerning the numerical simulation methodology we refer to [9] and [11].

The size of the computational domain is $L_z \times L_r = 24 \times 10$. The resolution of our DNS is $N_r \times N_\theta \times N_z = 255 \times 150 \times 445$ grid points while the LES employ $N_r \times N_\theta \times N_z = 87 \times 40 \times 187$ (LES-Low) and $N_r \times N_\theta \times N_z = 109 \times 60 \times 235$ (LES-High) grid points, respectively. These spatial LES resolutions correspond to approximately 3.8% and 9% of the spatial DNS resolution. The computational mesh is refined in the radial and the axial direction by coordinate transformations following the work of Bayliss et al. [2] and Bodony [4]. The grid density distribution in the axial direction consists of three major sections: a gradual refinement covering the initial transitional region, followed by a uniform grid region towards the subsequent turbulent region, and a moderate grid coarsening in the outflow-boundary zone. In the radial direction a specific requirement on a transformation arises from the singularity treatment according to [8] which is adopted in the present work and demands that the mapping is smooth and symmetric with respect to $r = 0$. It is apparent that the region around the shear layer imposes the most stringent resolution requirement on the radial grid distribution.

As subgrid-scale closure we employ the ADM subgrid-scale model, see [13]. The relaxation parameters χ_ρ,$\chi_{\rho u}$, and χ_E have been chosen to be constant in space and time. Case LES-Low was performed using ad-hoc values $\chi_\rho = \chi_{\rho u} = \chi_E = 111 (= 1/\Delta t)$. Case LES-High was performed with the values: $\chi_\rho = 50 (= 0.5/\Delta t)$, $\chi_\rho = 75 = (0.75/\Delta t)$ and $\chi_\rho = 100 (= 1/\Delta t)$, and $\chi_\rho \equiv \chi_{\rho u} \equiv \chi_E$, respectively. The results corresponding to LES-High are based on a value of 100 for the relaxation parameters unless stated otherwise.

3 Results

The computational time for each LES is documented in Table 1 together with corresponding values for the DNS, demonstrating that LES computations require only a fraction ($\approx$1–2%) of the computational cost of a DNS.

An overview of the instantaneous flow behavior is provided by λ_2-isosurface visualizations in Fig. 2. As can be seen the large-scale behavior in the

Table 1 CPU time of direct and large-eddy simulations (NEC SX-5, CSCS)

Case	Time (h)
DNS using upwind-biased scheme [1]	1459
LES using ADM, high resolution (LES-High)	27.6
LES using ADM, low resolution (LES-Low)	12.6

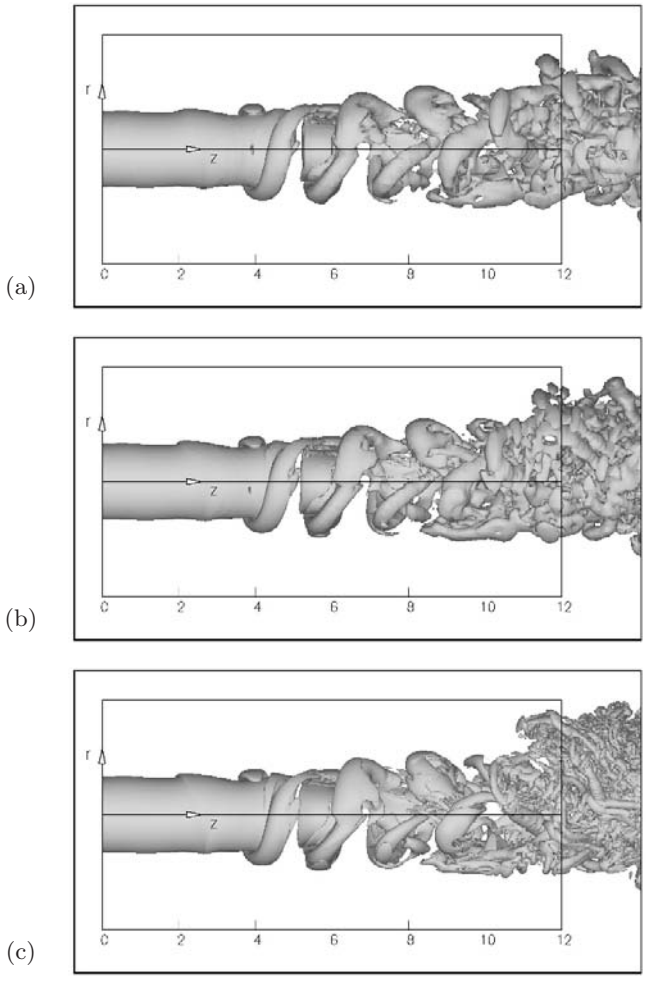

Fig. 2 Visualization of the instantaneous flow field using the second invariant ($\lambda_2 = -0.05$) for LES and DNS. (**a**) Case LES-Low; (**b**) case LES-High; (**c**) DNS

transitional region is very close to the DNS for both LES cases. Note that the slightly chiseled appearance of the isosurface for the LES is due to the visualization on the coarse grids.

Statistical averaging was performed in time over the same sampling period as in the DNS. A total of 1400 DNS flow fields were interpolated onto the respective LES grid and filtered with the primary filter $\hat{G}$. All statistics are based on these particular filtered fields. Errors due to a spline interpolation in the radial and axial directions of the DNS flow fields are attenuated by application of the primary filter.

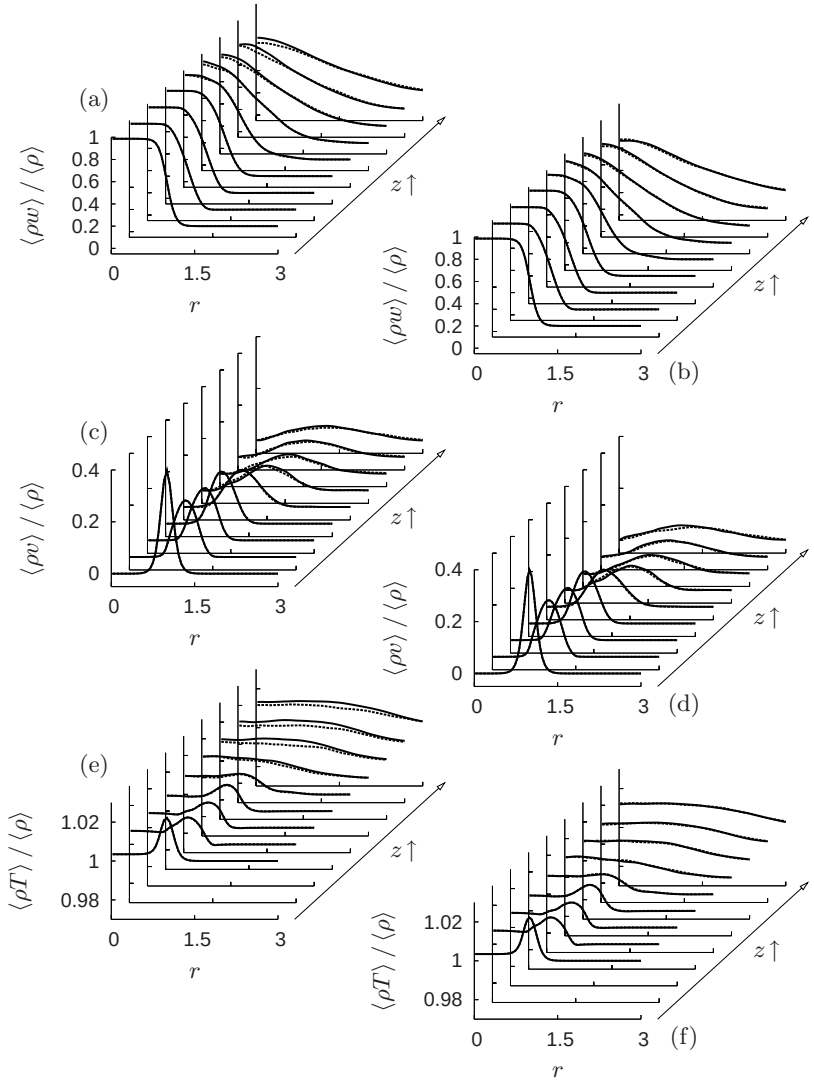

Fig. 3 Axial development of mean flow. *Dashed lines*: LES-Low/LES-High, *solid line*: DNS using upwind-biased schemes [1] interpolated onto LES grid and filtered using primary filter. (**a**), (**c**), (**e**): Favre-averaged axial and azimuthal velocity and temperature, case LES-Low. (**b**), (**d**), (**f**): Favre-averaged axial and azimuthal velocity and temperature, case LES-High

Figure 3 shows the Favre-averaged axial and azimuthal velocity and the temperature. A total of nine downstream positions have been chosen as documented in Table 2. The overall agreement is already quite acceptable in case

Table 2 Downstream positions z_i of statistical data evaluations

i	1	2	3	4	5	6	7	8	9
z_i	0.00	5.50	6.50	7.50	10.5	13.0	15.5	17.0	20.0

LES-Low, but further improved in case LES-High. The RMS of the axial and azimuthal velocities as well as temperature are shown in Fig. 4. Clear improvements are observed for case LES-High and for the most part of these statistics the LES-High results were identical with DNS within line thickness. Slight discrepancies between LES and filtered DNS continue to be visible in the turbulent kinetic energy, Reynolds shear stresses and velocity-temperature correlations [9].

We specifically considered the downstream development of the axial velocity along the centerline as this location was prone to the largest differences in the two DNS computations (see also [9]). Figure 5 displays the mean axial velocity and the corresponding RMS fluctuation along the centerline for LES-Low. Basically the mean axial velocity of the LES starts to drop down slightly upstream of the DNS prediction and the fluctuations become larger starting in the breakdown region $z \approx 10$. For case LES-High and variations in the value of $\chi_\rho, \chi_{\rho u}$ and χ_E, the largest differences were observed along the centerline (Fig. 6). In the turbulent region ($z \approx 15 \div 20$) the deviations from the reference DNS data are most pronounced for the mean axial velocity and the corresponding RMS fluctuation. For smaller values of $\chi_\rho, \chi_{\rho u}$ and χ_E, the RMS values become increasingly higher within this region. The differences can be attributed to variations in the parameter as this was the only modification done for the LES simulations.

An additional comparison between LES-High and filtered DNS data was performed for the two-point correlation defined by

$$\mathcal{R}_q(z_0, \eta) = \frac{\left\langle q'(z_0) q'(z_0 + \eta) \right\rangle}{\left\langle q'^2(z_0) \right\rangle^{1/2} \left\langle q'^2(z_0 + \eta) \right\rangle^{1/2}},$$

where q is an arbitrary quantity, $'$ denotes its temporal and azimuthal fluctuation, and η is the separation distance. Figure 7 displays two-point correlations for the radial, azimuthal and axial velocity as well as for the pressure fluctuations. Values are averaged in time and azimuthal direction. The comparison shows excellent agreement.

The downstream development of the temporal Fourier amplitudes of the three instabilities excited at the inflow has been analyzed and compared to filtered DNS data. In Fig. 8 we show this modal growth for the three disturbances as well as their higher harmonics. The comparison of LES-High to the filtered DNS data shows quite satisfying agreement. Even the growth of the disturbance generated by the nonlinear product of the instabilities and with a

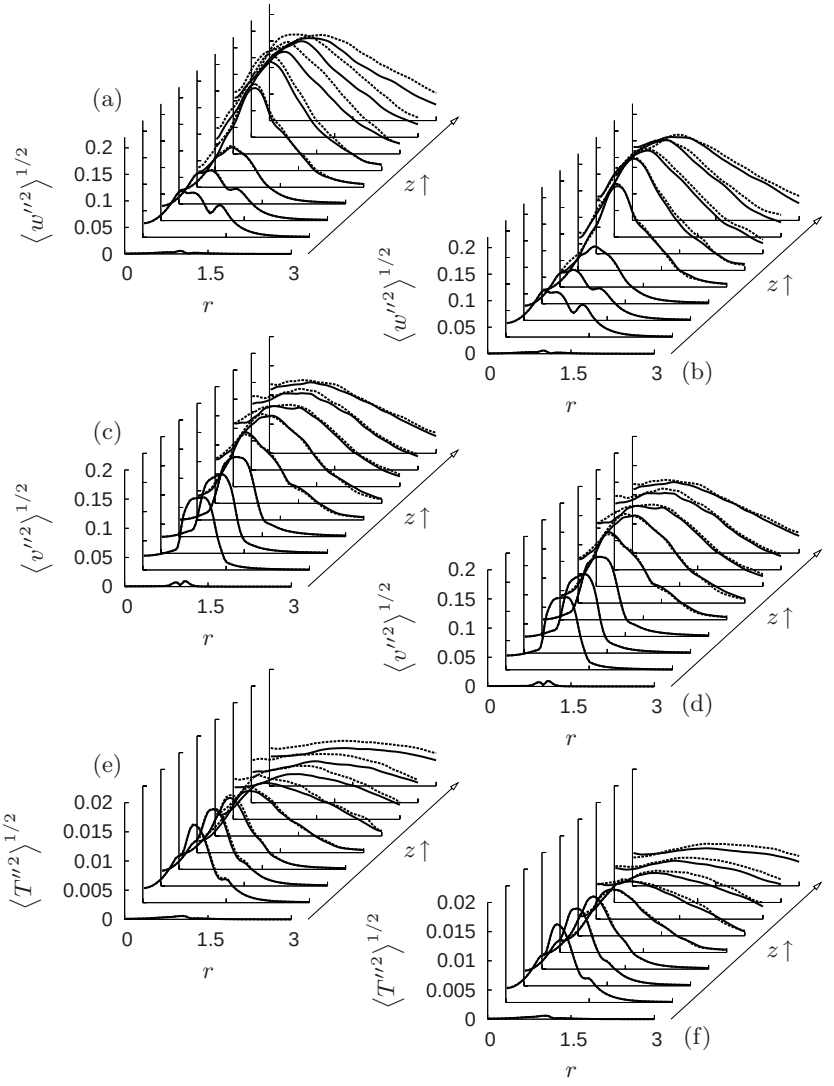

Fig. 4 Axial development of RMS fluctuations. *Dashed lines*: LES-Low/LES-High, *solid line*: DNS using upwind-biased schemes [1] interpolated onto LES grid and filtered using primary filter. (**a**), (**c**), (**e**): RMS of axial and azimuthal velocity and of temperature, case LES-Low. (**b**), (**d**), (**f**): RMS of axial and azimuthal velocity and of temperature, case LES-High

frequency corresponding to the sum or difference of the primary instabilities is in good agreement with the filtered DNS data. Only the higher harmon-

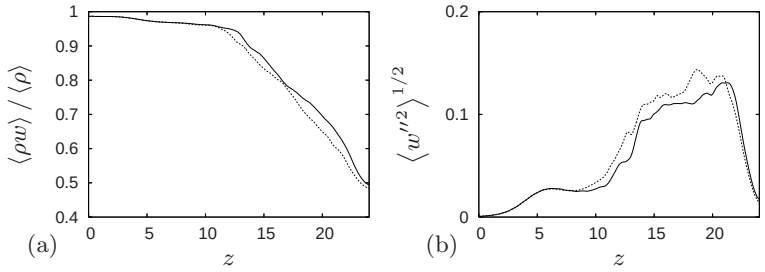

Fig. 5 Axial development of mean and RMS velocity. *Solid line*: DNS using secondary filtering [9] interpolated onto LES grid and filtered using primary filter. *Dotted line*: LES-Low (**a**) Mean axial centerline velocity, (**b**) RMS of mean axial velocity along centerline

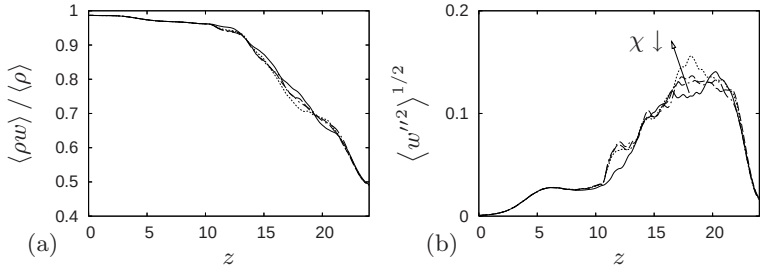

Fig. 6 Axial development of mean and RMS velocity. *Solid line*: DNS using upwind-biased schemes [1] interpolated onto the LES grid and filtered using primary filter. *Dotted line*: LES-High using $\chi_\rho = \chi_{\rho w} = \chi_E = 50$, *dashed line*: LES-High using $\chi_\rho = \chi_{\rho w} = \chi_E = 75$, *dashed-dotted line*: LES-High using $\chi_\rho = \chi_{\rho w} = \chi_E = 100$. (**a**) Mean axial centerline velocity, (**b**) RMS of mean axial velocity along centerline

ics show some appreciable differences although the basic growth behavior is captured very well.

Overall we find quite good agreement between the case LES-High and filtered DNS data for all discussed quantities. Concerning the mean flow fluctuations, the case LES-Low already achieves acceptable results.

4 Conclusions

High resolution DNS data has been used to assess the predictive capability of LES using the ADM subgrid-scale model [13] with constant (in space and time) relaxation parameters, for which ad-hoc values were chosen. Varying these parameters did not yield substantial differences concerning the present LES. The computations showed acceptable or very good agreement of detailed mean-flow and spectral statistics with filtered DNS data.

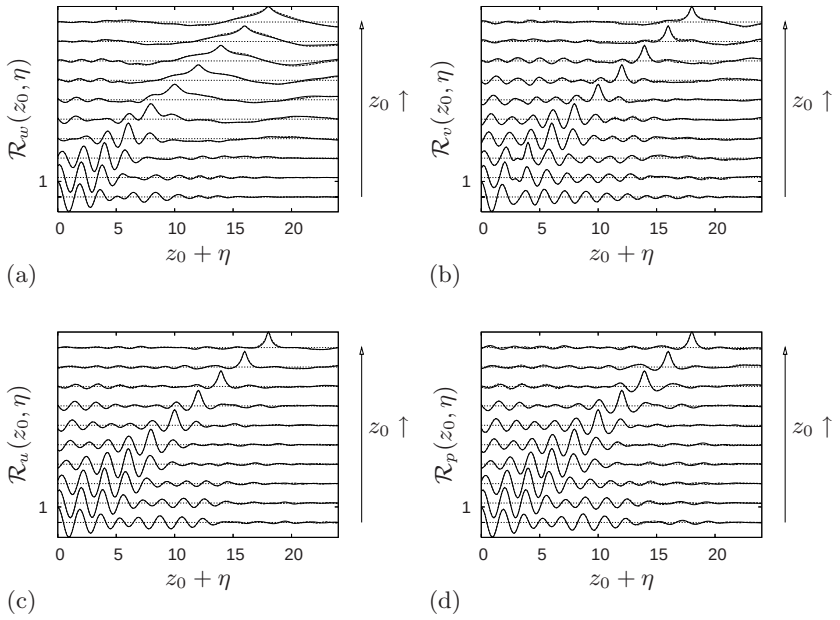

Fig. 7 Two-point statistics at $r = 1$ and axial positions $z_0 = 2 \cdot m$, $m = 0 \ldots 9$ at $r = 1$. *Dashed line*: LES-High, *solid line*: DNS using upwind-biased schemes [1] interpolated onto LES grid and filtered using primary filter. (**a**) Axial velocity fluctuations, (**b**) azimuthal velocity fluctuations, (**c**) radial velocity fluctuations, (**d**) pressure fluctuations

In addition to providing for subgrid energy transfer [5], the relaxation term is beneficial in three respects related to numerical discretization. First, stability of the compact finite-difference operators used herein for LES is ensured (i.e. unstable eigenvalues of the spectrum corresponding to this spatial derivative operator, including the effect of mapping from computational to physical space, are moved to the left in the complex plane). Secondly, the consecutive usage of first-derivative finite-difference operators in computing diffusive terms yields a lack of dissipation in the smallest scales [6]. The relaxation term allows for dissipation in exactly this high-wavenumber band, i.e. in the small scales. Finally, the magnitude of aliasing errors which arise due to nonlinear products on a finite grid can be expected to be lower as the energy at high wavenumbers is reduced [5]. The minimum value of each relaxation coefficient should ensure that the stability of the finite-difference operators is ensured. Increasing the value of the relaxation coefficients limits the time step size for a stable integration. For problems in which a fine time step is necessary for accuracy or stability to obtain e.g. highly-resolved temporal signals as required in aeroacoustics (see, e.g., [12]) the choice of large values for the relaxation parameters can be regarded as unproblematic.

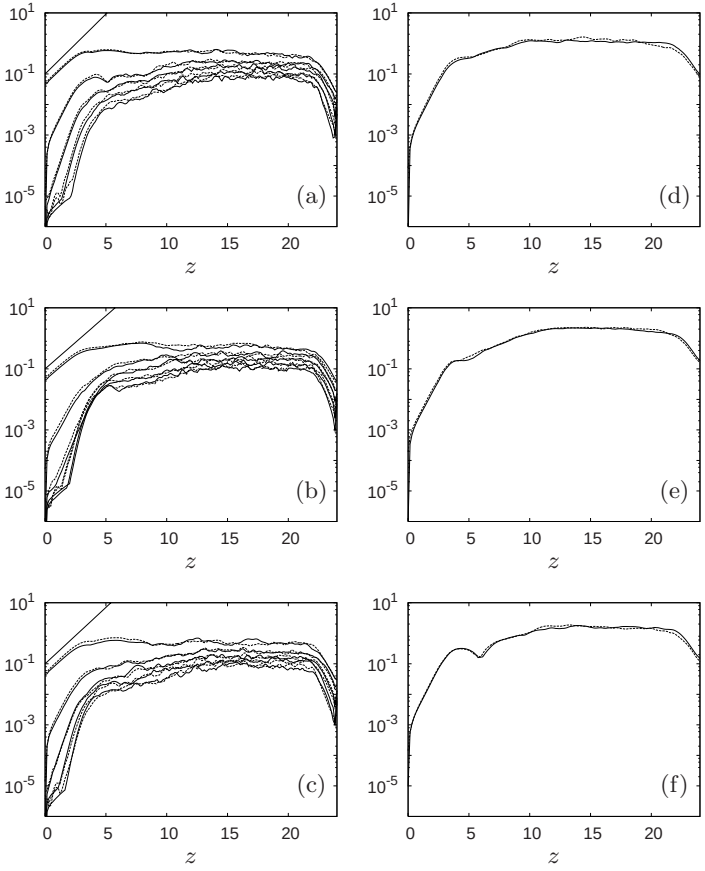

Fig. 8 Downstream development of Fourier amplitudes of axial mass flux. Shown are the growth of the inflow disturbances with highest growth rate and the corresponding first and non-linearly generated higher harmonic disturbance amplitudes. These amplitudes appear in a monotonic manner. *Solid lines*: DNS data using upwind-biased schemes [1] interpolated onto LES grid and filtered using primary filter. ; *dashed lines*: LES-High. The *thin solid lines* represent the growth according to spatial linear stability theory. (**a**) $\omega_0 = 2.046$, $l \cdot \omega_0$; (**b**) $\omega_1 = -1.652$, $l \cdot \omega_0$; (**c**) $\omega_2 = 1.931$, $l \cdot \omega_0$; $l = 1, \ldots, 5$; (**d**) $\omega = \omega_0 + \omega_1$; (**e**) $\omega = \omega_1 + \omega_2$; (**f**) $\omega = \omega_0 - \omega_2$

Acknowledgments

The computations were performed at the Swiss National Supercomputing Center (CSCS) Manno. We would like to thank our colleagues at the Institute of Fluid Dynamics for stimulating discussions.

References

1. Adams NA, Shariff K (1996) A high-resolution hybrid compact-ENO scheme for shock-turbulence interaction problems. J Comput Phys 127(1):27–51
2. Bayliss A, Class A, Matkowsky BJ (1995) Adaptive approximation of solutions to problems with multiple layers by Chebyshev pseudo-spectral methods. J Comput Phys 116(1):160–172
3. Berland J, Bogey C, Bailly C Low-dissipation and low-dispersion fourth-order Runge-Kutta algorithm. Comput Fluids 35(10):1459–1463
4. Bodony DJ (2004) Aeroacoustic prediction of turbulent free shear flows. PhD thesis, Stanford University
5. Domaradzki JA, Adams NA (2002) Direct modelling of subgrid scales of turbulence in large eddy simulations. J Turbul 3, Art no 24
6. Lele SK (1992) Compact finite difference schemes with spectral-like resolution. J Comput Phys 103(1):16–42
7. Lu G, Lele SK (1999) Inviscid instability of compressible swirling mixing layers. Phys Fluids 11(2):450–461
8. Mohseni K, Colonius T (2000) Numerical treatment of polar coordinate singularities. J Comput Phys 157(2):787–795
9. Müller SB (2007) Numerical investigations of compressible turbulent swirling jet flows. Diss. ETH No. 17375, ETH Zurich, Zurich, Switzerland. Available online from `http://e-collection.ethbib.ethz.ch`
10. Müller SB, Kleiser L (2006) Viscous and inviscid spatial stability analysis of compressible swirling mixing layers. Submitted
11. Müller SB, Kleiser L (2007) Large-eddy simulation of vortex breakdown in compressible swirling jet flow. Comp Fluids, to apppear. `doi:10.1016/j.compfluid.2007.04.010`
12. Singh KK, Mongeau L, Frankel SH, Gore JP (2007) Effect of co- and counter-swirl on noise from swirling flows and flames. AIAA J 45(2):651–661
13. Stolz S, Adams NA, Kleiser L (2001) The approximate deconvolution model for LES of compressible flows and its application to shock-turbulent-boundary-layer interaction. Phys Fluids 13(10):2985–3001

Accuracy of Large-Eddy Simulation of Premixed Turbulent Combustion

A. W. Vreman[1,2], R. J. M. Bastiaans[1], and B. J. Geurts[3,4]

[1] Combustion Technology, Department of Mechanical Engineering Eindhoven University of Technology, PO Box 513, 5600 MB Eindhoven, The Netherlands. R.J.M.Bastiaans@tue.nl
[2] Vreman Research, Godfried Bomansstraat 46, 7552 NT Hengelo, The Netherlands
[3] Mathematical Sciences, University of Twente, PO Box 217, 7500 AE Enschede, The Netherlands
[4] Applied Physics, Eindhoven University of Technology, PO Box 513, 5600 MB Eindhoven, The Netherlands

Abstract. The accuracy of large-eddy simulation (LES) of a turbulent premixed Bunsen flame is investigated in this paper. To distinguish between discretization and modeling errors, multiple large-eddy simulations, using different grid size h but the same filterwidth Δ, are compared with the direct numerical simulation (DNS). In addition, large-eddy simulations using multiple Δ but the same ratio Δ/h are compared. The chemistry in the LES and DNS is parametrized with the standard steady premixed flamelet for stochiometric methane-air combustion. The subgrid terms are closed with an eddy-viscosity or eddy-diffusivity approach, with an exception of the dominant subgrid term, which is the subgrid part of the chemical source term. The latter subgrid contribution is modeled by a similarity model based upon 2Δ, which is found to be superior to such a model based upon Δ. Using the 2Δ similarity model for the subgrid chemistry the LES produces good results, certainly in view of the fact that the LES is completely wrong if the subgrid chemistry model is omitted. The grid refinements of the LES show that the results for $\Delta = h$ do depend on the numerical scheme, much more than for $h = \Delta/2$ and $h = \Delta/4$. Nevertheless, modeling errors and discretization error may partially cancel each other; occasionally the $\Delta = h$ results were more accurate than the $h \leq \Delta$ results.

Keywords: Large-eddy simulation, Accuracy tests, Turbulent combustion, Premixed flamelets

1 Introduction

Large-Eddy Simulation (LES) of combustion as research topic has gained an increasing amount of attention in recent years. The subject is complicated,

J. Meyers et al. (eds.), Quality and Reliability of Large-Eddy Simulations,

because questions regarding LES methodology and modeling issues related to chemistry need to be considered simultaneously. In order to be able to perform three-dimensional time-dependent simulations of turbulent flows with combustion, it is usually not realistic to solve transport equations for all species occurring in the chemical reaction process. Therefore, it is common to apply a reduction technique to limit the number of transport equations that need to be carried in three dimensions. One group of reduction techniques is formed by the flamelet approaches [1, 2, 3, 4, 5, 6]. In flamelet approaches, results from one-dimensional computations with detailed chemistry (flamelets) are mapped to one or a few representative variables. Subsequently, the mapping functions, which are represented by a one- or multidimensional table, are used in the three-dimensional computation of a specific application.

LES of turbulent combustion is complicated, because in most cases neither turbulent structures nor the thickness of the flame can be properly resolved on the computational mesh. Thus, in addition to subgrid modeling of the turbulence, subgrid modeling of the chemical reaction process, which appears in the equations as one or more nonlinear source-terms, needs to be considered. The purpose of the present paper is to develop LES for turbulent combustion further and to study its accuracy. For the latter purpose we follow the strategy proposed in Ref. [7] (and revisited for example in Ref. [8]) and perform LES for multiple mesh sizes $h \leq \Delta$, where the filterwidth Δ is held fixed. Modeling and discretization errors are thus separated, since discretization errors reduce if h is reduced and Δ, the length-scale of the smallest resolved structures in the simulation, is kept constant.

To test LES of turbulent combustion we have chosen a premixed Bunsen flame, similar to experiments by Filatyev et al. [9] and simulations by Bell et al. [10]. The size of the flame is somewhat smaller in our case, to enable well-resolved Direct Numerical Simulation (DNS) with moderate computational effort. In the present paper both DNS and LES assume flamelet chemistry, but unlike LES, the DNS resolves both flame thickness and turbulence down to the Kolmogorov length-scale. Therefore the DNS does not require subgrid modeling, and it can be used to test and develop LES models.

The outline of the paper is as follows. In Section 2 we specify the governing equations, the approach of subgrid modeling, and the numerical discretization. In Section 3 results are shown for the premixed Bunsen flame and LES is compared to DNS. Conclusions are summarized in Section 4.

2 Computational Method

2.1 The Unfiltered Equations

The Navier-Stokes equations with parametrized premixed chemistry read:

$$\frac{\partial \rho}{\partial t} + \frac{\partial \rho u_j}{\partial x_j} = 0, \tag{1}$$

$$\frac{\partial \rho u_i}{\partial t} + \frac{\partial \rho u_i u_j}{\partial x_j} = -\frac{\partial p}{\partial x_i} + 2\frac{\partial \mu S_{ij}}{\partial x_j}, \tag{2}$$

$$\frac{\partial \rho c}{\partial t} + \frac{\partial \rho u_j c}{\partial x_j} = \frac{\partial}{\partial x_j}\Big(\rho D \frac{\partial c}{\partial x_j}\Big) + \omega_c, \tag{3}$$

$$\rho = f_1(c), \tag{4}$$

$$T = f_2(c), \tag{5}$$

$$\omega_c = f_3(c), \tag{6}$$

where the summation convention over repeated indices is used, while ρ, $\mathbf{u}$, p, T, and c represent density, velocity vector, pressure, temperature, and progress variable. The progress variable is based upon the scaled mass fraction of O_2 and is scaled such that it equals zero in the unburnt and one in the burnt regions. This mass fraction is selected as progress variable because, unlike many other species (CO_2 for example), the mass fraction of O_2 satisfies the requirement of strict monotonicity on the entire flamelet. The functions f_j (plotted in Fig. 1) denote the quantities that are retrieved from the flamelet database. The flamelet database is composed of a single flamelet, obtained by solving the premixed flamelet equations with detailed chemistry using the GRI 3.0 reaction scheme for a stoichiometric methane-air mixture [3].

It is remarked that T is almost reversely proportional to ρ; T is prescribed by the combustion approximation, an approximate equation of state [3]. In addition the rate of strain is defined by

$$S_{ij} = \tfrac{1}{2}\Big(\frac{\partial u_i}{\partial x_j} + \frac{\partial u_j}{\partial x_i} - \frac{2}{3}\frac{\partial u_k}{\partial x_k}\delta_{ij}\Big), \tag{7}$$

while the viscosity μ is a function of temperature according to Sutherland's three-coefficient law. The thermal diffusivity is equal to

$$\lambda/c_p = 2.58 \cdot 10^{-5}(T/298\ \mathrm{K})^{0.69}, \tag{8}$$

where λ is the thermal conductivity and c_p the specific heat [11]. The diffusivity ρD_c is equal to λ/c_p divided by the Lewis number of O_2 (1.11).

2.2 Subgrid Modeling

Whereas DNS with flamelet chemistry solves the unfiltered equations, LES solves the filtered equations. The basic filter definition in LES is given by $\overline{\rho} = G\rho$, where G is the filter operator, a convolution integral operator with top-hat filter kernel with width Δ. In variable density flows it is convenient to use the density-weighted or Favre filter as well, defined by $\tilde{u}_i = \overline{\rho u}_i/\overline{\rho}$.

The filtered equations are obtained by application of the basic filter operations to the equations in the previous subsection. The nonlinearities in

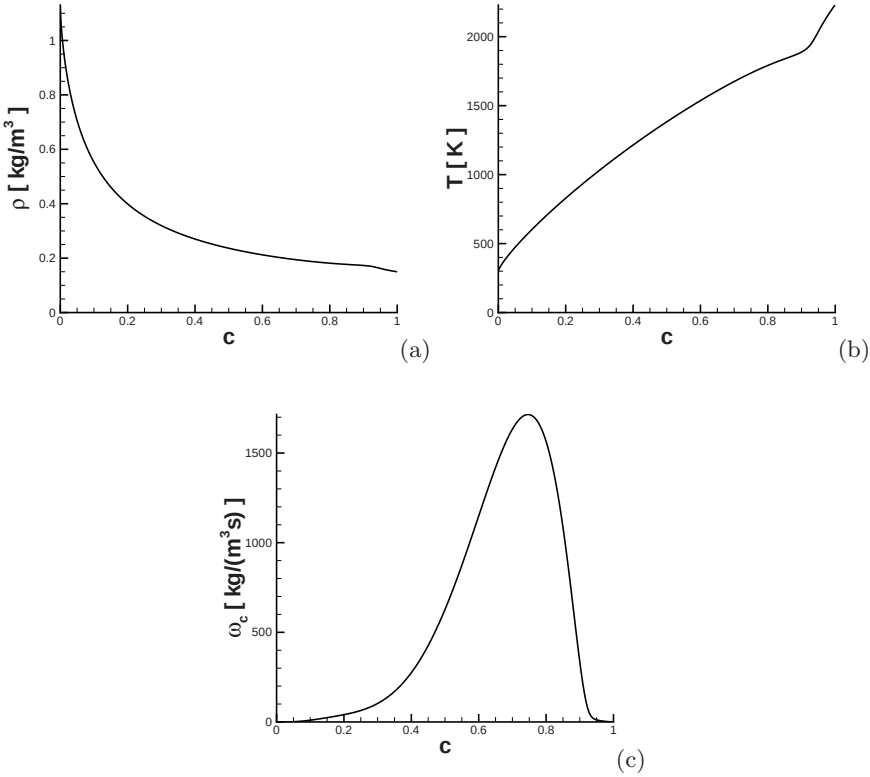

Fig. 1 Visualization of the flamelet database (functions $f_i(c)$): density (**a**), temperature (**b**) and chemical source term (**c**)

the equations lead to unknown terms, which are either modeled, or neglected. Subgrid terms arising from the nonlinearity of the viscous terms are neglected, while the subgrid terms arising from the convective terms are closed by adding an eddy-viscosity μ_t to the molecular viscosity in the momentum equations and an eddy-diffusivity μ_t/Sc_t with $Sc_t = 0.4$ [4] to the molecular diffusivity in the scalar equation. For the eddy-viscosity the following model is used [12]:

$$\mu_t = \overline{\rho} C \Big(\frac{\beta_{11}\beta_{22} - \beta_{12}^2 + \beta_{11}\beta_{33} - \beta_{13}^2 + \beta_{22}\beta_{33} - \beta_{23}^2}{\alpha_{kl}\alpha_{kl}} \Big)^{1/2}. \tag{9}$$

Here the tensor β equals the gradient model:

$$\beta_{ij} = \Delta_k \alpha_{ki} \alpha_{kj}, \qquad \alpha_{ki} = \frac{\partial \tilde{u}_i}{\partial x_k}, \tag{10}$$

where Δ_k is the filterwidth in direction x_k; $\Delta_1 = \Delta_2 = \Delta_3 = \Delta$ is used throughout this paper. The model constant is related to the Smagorinsky

constant $C = 2.5C_S^2$; in this work we take $C = 0.07$. Model (9) has shown to be as accurate as the dynamic subgrid model in non-reacting wall-bounded and free shear flow [12].

Due to the nonlinearity of the chemical parametrization (nonlinearities in f_1 to f_3), non-standard subgrid terms arise, $\overline{f_i(c)} - f_i(\tilde{c})$. Geurts [13] proposed to model these non-standard terms with approximate deconvolution. Here we use a similar strategy, but in order to compensate for the fact that a deconvolution retrieves resolved scales only, we slightly alter the common methodology and apply the deconvolution at a larger scale; the filterwidth of the 'inverted' filter H now equals 2Δ. Thus the unknown quantities $\overline{f_i(c)}$ are modeled by

$$Hf_i(2\tilde{c} - H\tilde{c}), \tag{11}$$

where H is the top-hat filter with filterwidth 2Δ. In fact the quantity between brackets can be expressed as $c = \tilde{c} + c''$ in case the subgrid fluctuation c'' is modeled by $\tilde{c} - H\tilde{c}$. This is a scale-similarity hypothesis [14], and thus Eq. (11) is essentially a similarity model. However, $\tilde{c} - H\tilde{c}$ is also the first term in the series expansion of the deconvolution operator [15]. To extend the deconvolution, more terms may be added to approximate c, but we do not pursue this here.

2.3 Numerics

We used a straightforward and efficient numerical implementation to solve the equations with parametrized chemistry. The variable density approach involved a Poisson equation for the pressure, similar to other low-Mach methods [4, 5].

For the continuity and momentum equations the standard finite volume method was employed, with second-order central differencing on a staggered Cartesian mesh. The discrete convective terms would conserve kinetic energy if the density were constant. Because of its stability properties a hybrid time-stepping scheme was used to integrate the moment equations, Adams-Bashforth for the convective and forward Euler for the viscous terms.

The scalar equation was recast into the equivalent advective formulation. Then the Van Leer third-order accurate MUSCL scheme, which is TVD, was applied to the advective terms. Thus the spatial discretization of the scalar equation introduced numerical diffusion, which was not the case in the momentum equations. However, for the scalar equation numerical diffusion is hard to avoid if we want to keep the scalars in between their physical bounds on coarse grids. The scalar was updated with pure forward Euler since for an upwind method the hybrid time-stepping scheme has less advantages than for central differencing (used in the momentum equation).

Within each time-step the scalar equation was updated first. The explicit filter H that occurs in the model for the reaction terms was discretized with the Simpson rule. Then the momentum equations were updated to obtain the

uncorrected velocities. Imposing the continuity equation provided then a Poisson equation for the pressure, which was solved using multigrid. Each timestep ended with the correction of the velocities using the pressure gradient. More details about the pressure correction algorithm can be found in Ref. [16].

3 Results

3.1 Flow Conditions

In this section we present DNS and LES results for a planar Bunsen flame. The configuration of the premixed stoichiometric methane-air Bunsen flame simulated was a spatial planar jet of the unburnt mixture (mean centerline velocity $U_0 = 3\text{m/s}$ and $T = 298\text{K}$), surrounded by a co-flow with hot products (velocity 7m/s and $T = 2240\text{K}$). The slot width of the burner equalled 8mm, different from otherwise similar experiments [9] and simulations [10, 16].

The DNS was performed on a uniform grid with 320 points in the inhomogeneous streamwise direction (z), 256 points in the inhomogeneous normal direction (y), and 160 points in the spanwise homogeneous (periodic) direction (x). Each grid cell was cubic and the grid size was 0.1 mm. The time step of the DNS, $\delta t = 0.2 \cdot 10^{-5}\text{s}$, was verified to be sufficiently small. The outflow boundary conditions in the normal and streamwise direction assumed Neumann conditions for the three velocity components. The pressure satisfied Neumann conditions at the streamwise in- and outflow, while it was held constant in the normal outflow planes. The mean inflow profiles were based on tangent hyperbolic profiles with a thickness of 0.384 mm (based on maximum derivative).

In the experiments by Filatyev et al. [9] the inflow turbulence was generated by a suitable grid that set the length-scale of the turbulence. For the present simulation results, the velocity at the core of the inflow was perturbed with random uniform noise, which was filtered to control the turbulence length-scale. No inflow perturbations were added to the mean of the progress variable. The inflow velocity perturbations were constructed such that they were the same for each simulation in the present section, both DNS and LES. For each velocity component, and each $\delta t_0 = 10^{-6}\text{s}$, random numbers between -1 and 1 were generated on the DNS inflow plane (160×256). Then these random numbers were filtered, applying a box-filter of $l_0 = 5.2\text{mm}$ in the spatial directions, and a temporal exponential filter. For a signal q, the temporal filter was discretized by

$$\hat{q}_{n+1} = (1 - \frac{\delta t_0 \sqrt{12}}{l_0/U_0})\hat{q}_n + \frac{\delta t_0 \sqrt{12}}{l_0/U_0} q_n. \tag{12}$$

The perturbation was initialized with $\hat{q}_0 = 0$. The width of this temporal filter based on its second-order moment equals l_0/U_0. Subsequently, periodic boundary conditions were imposed in both spatial directions, and then the

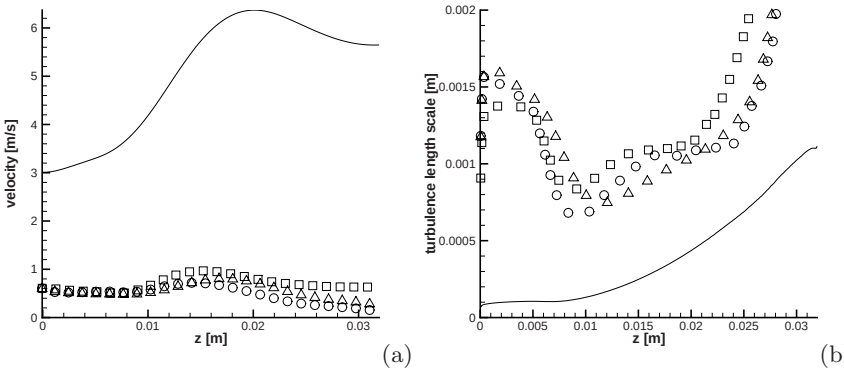

Fig. 2 (**a**) Centerline mean streamwise velocity (*solid*) and streamwise (*square*), normal (*circle*) and spanwise (*triangle*) turbulence intensities.
(**b**) Centerline Kolmogorov length-scale (*solid*) and Taylor micro-scales based on streamwise (*square*), normal (*circle*) and spanwise (*triangle*) velocity component

Table 1 Overview of simulations

Simulation	Δ [mm]	h [mm]	Inclusion source-term subgrid model	Scalar clipping	δt [10^{-5}s]	Line in Figs. 4, 5
DNS	–	0.1	–	no	0.2	thick solid
LES0	0.8	0.8	no	no	2.0	long dash
LES1a	0.8	0.8	yes	no	2.0	thin solid
LES1b	0.8	0.4	yes	no	1.0	dashed
LES1c	0.8	0.2	yes	no	0.5	dash-dotted
LES1d	0.8	0.8	yes	yes	2.0	thin solid
LES2	0.4	0.4	yes	no	1.0	dotted

spatial filter with length l_0 was performed. After the filtering, the inflow was multiplied with 1650 (to obtain the inflow intensities mentioned later on) and confined to the center jet (using a tangent hyperbolic function of the same shape as the mean inflow profiles). Finally, for the large-eddy simulations, the discrete inflow plane was injected to the simulation grid of each specific case.

The turbulence generated by these inflow conditions quickly developed, and at $z = 1$mm it was characterized by a turbulent intensity of 0.6m/s, a Taylor length-scale λ of 0.14mm, such that $Re_\lambda = 50$. The Kolmogorov length-scale at this location equalled 0.09mm, which was properly resolved by the DNS grid. Centerline mean velocity, turbulence intensities, and turbulence length-scales are shown in Fig. 2.

Six large-eddy simulations were performed, with uniform cubical grid cells. An overview of these simulations is provided in Table 1. The coarsest LES was at least three orders of magnitude less expensive than the DNS, because in

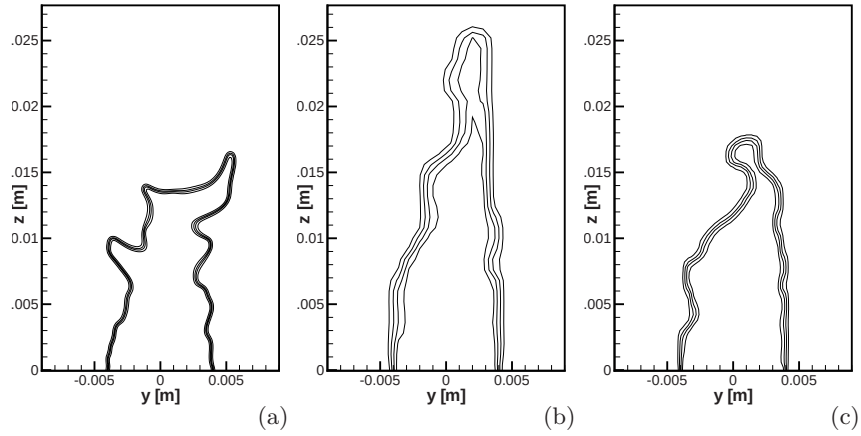

Fig. 3 Snapshots of progress variable in the plane $x = 0$ at $t = 0.2\,\mathrm{s}$. Isocontours 0.2, 0.4, 0.6 and 0.8. DNS (**a**); LES1a $h = \Delta = 0.8\,\mathrm{mm}$ (**b**); LES2 $h = \Delta = 0.4\,\mathrm{mm}$ (**c**)

each spatial direction the mesh was 8 times coarser than in the DNS and the time-step was 10 times larger.

3.2 Comparison between LES and DNS

The LES results are discussed in the following five paragraphs. First, we discuss the LES results along the first line of grid refinement (h decreases with $\Delta = h$). Second, we discuss the LES-results along the second line of grid refinement (h decreases and Δ remains constant). Third, we demonstrate the effect of the reaction subgrid model, by comparison with a simulation in which reaction subgrid modeling was ignored. Fourth, we discuss and illustrate the issue of clipping the scalar. Fifth, we explain how the results prompted us to formulate the similarity/deconvolution model at 2Δ instead of Δ.

First, LES results along the $\Delta = h$ refinement strategy are shown in Figs. 3 and 4a along DNS results. The snapshots (Fig. 3) show that, compared to DNS, both the gradient of the scalar and the amount of wrinkling are reduced in the LES. Both reduce with increasing Δ. The mean statistics of the two large-eddy with different resolutions are remarkably similar according to Fig. 4a, which shows time-averaged scalar contours for $c = 0.75$, the contour of maximum source term (see Fig. 1c).

Second, we not only varied the mesh-size h with Δ/h held fixed (equal to one), but we also investigated the accuracy of the LES by refining the grid with Δ kept constant (LES1a-c), see Fig. 4b. The results of LES1b and LES1c are almost the same, which indicates that the discretization errors are small for these cases with $h \leq \Delta/2$. Thus the difference between LES1bc and DNS

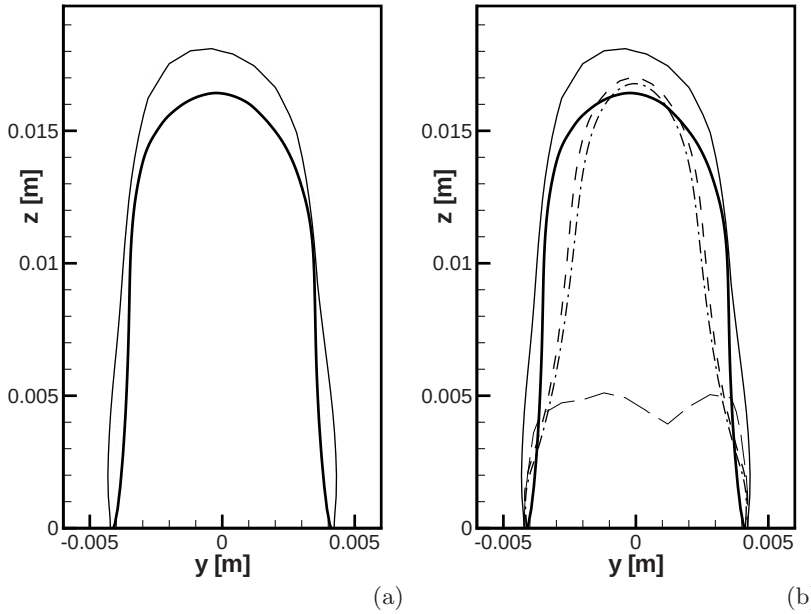

Fig. 4 Isocontour 0.75 of the mean progress variable: (**a**) refinement strategy $\Delta = h$; (**b**) refinement strategy with Δ held fixed, the effect of no subgrid source term is also included here.
DNS (*thick solid*); LES1a (*thin solid*, $h = \Delta = 0.8\,\text{mm}$); LES2 (*dotted*, $h = \Delta = 0.4\,\text{mm}$); LES1b (*dashed*, $h = \Delta/2 = 0.4\,\text{mm}$); LES1c (*dash-dotted*, $h = \Delta/4 = 0.2\,\text{mm}$); LES0 (*long dash*, no subgrid source term)

is an estimate for the modeling errors. However, discretization errors are not small in LES1a, as there is significant deviation between LES1a and the more resolved simulations LES1bc. Surprisingly, LES1a predicts the mean source term better than LES1bc do (Fig. 5b). This illustrates that for this quantity the significant discretization error on the coarse grid cancels the modeling error to some extent [7, 8].

Third, Figs. 4b and 5 show a very large effect of the subgrid modeling of the source term. LES performed very poor when no subgrid model was employed for the source term (LES0, where $\omega(\tilde{c})$ was used to model $\overline{\omega(c)}$); The long-dash line in Fig. 4b shows that LES0 predicted a flame which was much too short and hardly came off the burner, represented by the inflow condition. The subgrid eddy-viscosity and subgrid eddy-diffusivity was still switched on in this case.

The fourth issue in this results section addresses a nuisance of the similarity/deconvolution model, namely that it does not garantuee that the

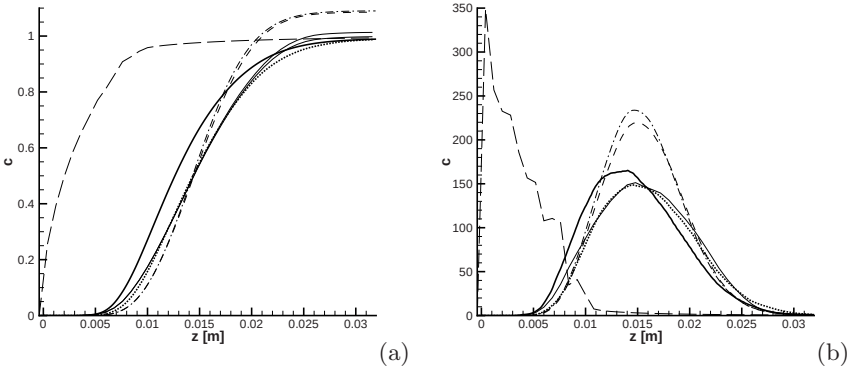

Fig. 5 Centerline statistics; mean progress variable (**a**) and mean source term (**b**) (subgrid modeling included where applicable). DNS (*thick solid*); LES0 (*long dash*, no subgrid source term), LES1ad (*thin solid*, $h = \Delta = 0.8\,\mathrm{mm}$, without and with clipping values larger than one), LES1b (*dashed*, $h = \Delta/2 = 0.4\,\mathrm{mm}$), LES1c (*dash-dotted*, $h = \Delta/4 = 0.2\,\mathrm{mm}$), LES2 (*dotted*, $h = \Delta = 0.4\,\mathrm{mm}$)

maximum of the scalar remains smaller than the physical bound. Overshoots (up to approximately 1.2) were observed, which can be inferred from the results of LES1a-c for $z \geq 0.02$m in Fig. 5a. Fortunately, these overshoots appear to have a very small effect upon the statistics. This is shown by the results of simulation LES1d, in which the scalar was clipped after each time step and thus forced to remain between 0 and 1. A small difference between LES1d and LES1a can be observed in Fig. 5, while there were too small visible differences to include this run into Figs. 4 and 5b.

Finally, it is remarked that, in order to obtain acceptable LES results on the coarse grid, it was necessary to apply the source-term similarity model at the scale 2Δ (and not at Δ). We shortly desribe what happened when we applied the similarity model at the scale Δ (for the case with $\Delta = h = 0.8$mm). Since then the filterwidth of H equalled the grid size, it was convenient to approximate H with a truncated Taylor expansion, $H \approx I + (\Delta^2/24)\nabla^2$. However, the flame resulting from that simulation turned out to be even smaller than the result of LES0, in which no model for the subgrid source term was used. As H with filterwidth Δ appeared to be inappropriate for the present case, we started to use H with filterwidth 2Δ. This choice turned out to be quite beneficial. The formal justification to use 2Δ instead of Δ is that a deconvolution can never retrieve all scales in actual LES, simply because the finest physical scales cannot be recognized by the grid. Here we deliberately used a deconvolution step with a 'wrong' filterwidth to 'overrelax' the scales larger than Δ, compensating for the missing unretrievable scales. Apparently, this was a successful strategy for the Bunsen flame application.

4 Conclusions

Large-eddy simulations with premixed flamelet chemistry were compared with DNS. The test-case was a premixed Bunsen flame with turbulent inflow characterized by $Re_\lambda = 50$. The turbulent flame was verified to be in the thin reaction zone regime, with the inflow u'/s_{L0} about 1.6 and the Karlovitz number around 16 (ratio of the gradient thickness of the progress variable and the Kolmogorov length, u' is the turbulent intensity, $s_{L0} = 0.36$m/s is the laminar burning velocity). The turbulent burning velocity was about $2.5s_{L0}$. This DNS, resolved down to the Kolmogorov scale, was used to test LES at much coarser grids. A similarity (or first-step deconvolution model) was used to include subgrid reaction effects. It was found to be important to apply the similarity model at 2Δ, in order to compensate for the unretrievable subgrid scales. When the model was applied at the basic filterwidth, flash-back occurred (the flame did not come off the burner, represented by the inflow condition). A similar thing occurred when subgrid reaction effects were ignored altogether. However, when they were included with the similarity model at scale 2Δ, reasonable results were obtained. A drawback of the model is that physical upperbound of the scalar is violated (overshoots of about 20%). However, sofar this drawback has no serious implications; an additional simulation in which the scalar was clipped at each time-step to satisfy the physical constraint provided almost the same results.

The accuracy of LES was investigated in detail. Two types of grid refinements were considered: grid refinement where both h and Δ were decreased; and grid refinement where h was decreased and Δ stayed constant. The first type of grid refinement altered the mean scalar statistics only slightly. The second type of grid refinement, which had larger effect, serves to distinguish between discretization and modeling errors. It appeared that discretization errors had considerable influence for $h = \Delta$, but not necessarily a bad influence, since for the chemical source term for example, the results for $h = \Delta$ were closer to the DNS than for $h = \Delta/2$. Results for $h = \Delta/2$ and $h = \Delta/4$ were quite similar, which indicates that for $h \leq \Delta/2$ the effects of discretization errors were small.

Acknowledgements

This research was funded by Stichting Technische Wetenschappen, grant number EWO.5874.

References

1. Peters N (2000) Turbulent Combustion, Cambridge University Press, Cambridge

2. Van Oijen JA, De Goey LPH (2000) Modelling of premixed laminar flames using flamelet-generated manifolds. Combust Sci Tech 161:113–137
3. Van Oijen JA (2002) Flamelet-generated manifolds: development and application to premixed laminar flames. PhD Thesis, University of Technology Eindhoven
4. Pitsch H, Steiner H (2000) Large-eddy simulation of a turbulent piloted methane/air diffusion flame (Sandia flame D). Phys Fluids 12:2541–2554
5. Pierce CD, Moin P (2004) Progress-variable approach for large-eddy simulation of non-premixed turbulent combustion. J Fluid Mech 504:73–97
6. Domingo P, Vervisch L, Payet S, Hauguel R (2005) DNS of a premixed turbulent V flame and LES of a ducted flame using a FSD-PDF subgrid scale closure with FPI-tabulated chemistry. Comb Flame 143:566–586
7. Vreman B, Geurts B, Kuerten H (1996) Comparison of numerical schemes in large-eddy simulation of the temporal mixing layer. Int J Num Meth Fluids 22:297–311
8. Meyers J, Geurts BJ, Baelmans M (2003) Database analysis of errors in large-eddy simulation, Phys Fluids 15:2740–2755
9. Filatyev SA, Driscoll JF, Carter CD, Donbar JM (2005) Measured properties of turbulent premixed flames for model assessment, including burning velocities, stretch rates, and surface densities. Comb Flame 141:1–21
10. Bell JB, Day MS, Grcar JF, Lijewski MJ, Driscoll JF, Filatyev SA (2007) Numerical simulation of a laboratory-scale turbulent slot flame. Proc Comb Inst 31:1299–1307
11. Smooke MD, Giovangigli V (1991) Formulation of the premixed and non-premixed test problems. In: Smooke MD (ed) Reduced kinetic mechanisms and asymptotic approximations for methane-air flames. Springer Verlag, Berlin, 1–28
12. Vreman AW (2004) An eddy-viscosity model for turbulent shear-flow: algebraic theory and applications. Phys Fluids 16:3670–3681
13. Geurts BJ (2006) Regularization modeling for large-eddy simulation of diffusion flames. Proceedings ECCOMAS CFD 2006, Delft University of Technology
14. Bardina J, Ferziger JH, Reynolds WC (1984) Improved turbulence models based on LES of homogeneous incompressible turbulent flows. Department of Mechanical Engineering, Report No TF-19, Stanford
15. Stolz S, Adams NA, Kleiser L (2001) An approximate deconvolution model for large-eddy simulation with application to incompressible wall-bounded flows. Phys Fluids 13:997–1015
16. Vreman AW, van Oijen JA, de Goey LPH, Bastiaans RJM (2007) Large-eddy simulation of turbulent combustion using premixed flamelet chemistry. Proceedings 2nd ECCOMAS Thematic Conference on Computational Combustion, Delft University of Technology

Mesh Dependency of Turbulent Reacting Large-Eddy Simulations of a Gas Turbine Combustion Chamber

Guillaume Boudier[1], Gabriel Staffelbach[1], Laurent Y. M. Gicquel[1], and Thierry J. Poinsot[2]

[1] CERFACS, 42 Avenue G. Coriolis, 31057 Toulouse cedex, France
lgicquel@cerfacs.fr
[2] Institut de Mécanique des Fluides de Toulouse, Avenue C. Soula, 31400 Toulouse, France. poinsot@imft.fr

Abstract. Convergence of reacting LES predictions for an aeronautical gas turbine combustion chamber is analysed in terms of mesh resolution. To do so three fully unstructured meshes containing respectively 1.2, 10.6 and 43.9 million tetrahedra are used to compute this fully turbulent reacting flow. Resolution criteria obtained from the mean velocity and reacting fields depict different convergence behaviors. Reacting fields and more specifically combustion regimes are seen to be slightly grid dependent while maintaining mean global combustion quantities.

Keywords: Large-eddy simulation, Turbulent reacting flows, Complex application, Grid resolution

1 Introduction

Recent developments in large scale computer architectures allow to consider (cf. www.top500.org) LES to predict turbulent reacting flows in gas turbine engines. For example, a compressible LES computation for a sector of an existing helicopter combustion chamber [1] provided insights on the reliability of such applications. To quantify the quality of these predictions, comparisons against RANS and experimental measurements were provided. The statistical convergence for the mean temperature field was also addressed based on an industrial criterion quantifying the radial temperature heterogeneities at the exit of the burner. Even though such computations (see also [2]) show the feasibility of complex geometry LES, studies of the sensitivity of the various statistical fields to grid resolution, LES modeling, numerical scheme, are still required to establish the true reliability of LES for such complex applications.

The impact of grid resolution on the simulation is considered here. To do so, the fully compressible, multi-species reacting LES performed in [1] is

J. Meyers et al. (eds.), Quality and Reliability of Large-Eddy Simulations,

reproduced on two other meshes yielding three fully unsteady turbulent reacting predictions of the same configuration.The numerical scheme is second-order accurate in time and space (Lax-Wendroff integration scheme) and the LES models are: the Smagorinsky closure for the sub-grid stress, gradient diffusion models for the species and heatflux sub-grid scale vectors with constant turbulent Schmidt and Prandtl numbers. The turbulent combustion model is the Dynamic Thickened Flame Model (DTF) [3, 4, 5, 6, 7]. In that case, thickening is local and automatically obtained in the computation for a cell to laminar flame thickness ratio fixed at 3. The three tetrahedra meshes contain respectively 1.2, 10.6 and 43.9 millions cells. Refinement from one mesh to the other is primarily enforced in the primary zone where combustion occurs.The three predictions are gauged against each other for various mean flow quantities.

The paper is organized as follows. An overview of the parallel LES solver, models and computational parameters is given. The studied configuration is then described along with the set of Boundary Conditions (BC) and a presentation of the three meshes used to study reacting LES. LES predictions are analysed in Section 4 from a statistical point of view. Specific care is devoted to the combustion quantities and the convergnce of the statistics is assessed.

2 Numerics

The fluid considered follows the ideal gas law, $p = \rho\, r\, T$ and $e_s = \int_0^T C_p\, dT - p/\rho$, where e_s is the mixture sensible energy, T the temperature, $C_p = \sum_{\alpha=1}^{N} C_{p,\alpha}\, Y_\alpha$ the fluid heat capacity at constant pressure and r is the mixture gas constant, which varies with composition and is obtained by $r = \frac{R}{W} = R \sum_{\alpha=1}^{N} \frac{Y_\alpha}{W_\alpha}$, where $R = 8.314\ \mathtt{kgm^2/(s^2K)}$ and W_α is the molecular weight of the species α. The viscous stress tensor, the heat diffusion vector and the species molecular transport use classical gradient approaches. The fluid viscosity follows Sutherland's law, the heat diffusion coefficient follows Fourier's law, and the species diffusion coefficients are obtained using a constant species Schmidt number and diffusion velocity corrections for mass conservation [4]. Note that throughout the work, the variations of the molecular coefficients resulting from the unresolved fluctuations are neglected so that the various expressions for the molecular coefficients become only functions of the filtered field [4].

The application of the LES filtering operation to the instantaneous set of compressible Navier-Stokes transport equations with chemical reactions yields the LES equations which need modelling for the system to be closed [8, 9]. The unresolved SGS (Sub-Grid Scale) stress tensor $\overline{\tau_{ij}}^t = \overline{\rho}\ (\widetilde{u_i u_j} - \widetilde{u}_i \widetilde{u}_j)$, is usually addressed through the concept of SGS turbulent viscosity model and the Boussinesq assumption [10] which reads (Smagorinsky [11]):

$$\overline{\tau_{ij}}^t - \frac{1}{3}\, \overline{\tau_{kk}}^t\, \delta_{ij} = -2\, \overline{\rho}\, \nu_t\, \widetilde{S}_{ij}, \tag{1}$$

with,

$$\widetilde{S}_{ij} = \frac{1}{2}\left(\frac{\partial \widetilde{u}_i}{\partial x_j} + \frac{\partial \widetilde{u}_j}{\partial x_i}\right) - \frac{1}{3}\,\frac{\partial \widetilde{u}_k}{\partial x_k}\,\delta_{ij}. \tag{2}$$

In Eqs. (1) and (2) $\widetilde{S}_{ij}$ is the resolved strain tensor and ν_t is the SGS turbulent viscosity. The Smagorinsky model [11] is used here and expresses ν_t as:

$$\nu_t = (C_S \triangle)^2 \, \|S\|. \tag{3}$$

In Eq. (3), $\triangle$ denotes the filter characteristic length and is approximated by the cubic-root of the cell volume, C_S is the model constant ($C_S = 0.18$) and $\|S\| = (2\,\widetilde{S_{ij}}\widetilde{S_{ij}})^{1/2}$.

The SGS species flux $\overline{J_i^\alpha}^t = \overline{\rho}\,(\widetilde{u_i Y_\alpha} - \widetilde{u_i}\widetilde{Y_\alpha})$ is modelled by use of the species SGS turbulent diffusivity $D_t^\alpha = \nu_t / Sc_t^\alpha$, where Sc_t^α is the turbulent Schmidt number ($Sc_t^\alpha = 0.9$ for all α). The SGS energy flux $\overline{q_i}^t = \overline{\rho}\,(\widetilde{u_i E} - \widetilde{u_i}\widetilde{E})$ is also modelled by use of a thermal diffusivity along with a turbulent Prandtl number $Pr_t = 0.9$, so that $\lambda_t = \overline{\rho}\,\nu_t\,C_p/Pr_t$:

$$\overline{J_i^\alpha}^t = -\overline{\rho}\left(D_t^\alpha\,\frac{W_\alpha}{W}\,\frac{\partial \widetilde{X}_\alpha}{\partial x_i} - \widetilde{Y_\alpha}\,V_i^c\right) \quad \text{and} \quad \overline{q_i}^t = -\lambda_t\,\frac{\partial \widetilde{T}}{\partial x_i} + \sum_{\alpha=1}^{N} \overline{J_i^\alpha}^t\,\widetilde{h}_s^\alpha. \tag{4}$$

In Eq. (4) the mixture molecular weight W and the species molecular weight W_α can be combined with the species mass fraction to yield the expression for the molar fraction of species α: $X_\alpha = Y_\alpha W/W_\alpha$. V_i^c is the diffusion correction velocity resulting from the Hirschfelder Curtis approximation [4] and $\widetilde{T}$ is the modified filtered temperature which satisfies the modified filtered state equation [12, 13, 14], $\overline{p} = \overline{\rho}\,r\,\widetilde{T}$. Finally, $\widetilde{h}_s^\alpha$ stands for the enthalpy of species α. Although the performance of the models could be improved through the use of a dynamic formulation [12, 15, 16, 17, 18], they are considered sufficient to address the present investigation.

The flame/turbulence interaction is modelled using the Dynamic Thickened Flame (DTF) model. The model leads to a flame thickness which is multiplied by F and more easily resolved on a coarser mesh. While in reacting zones, diffusion and source terms issued from the thickened reaction are well resolved and turbulence is solely represented by the efficiency function E [19], molecular and thermal diffusion cannot be over-estimated by a factor F in mixing zones where no combustion occurs (it would yield over-estimated mixing and wrong flame positions). Dynamic thickening is introduced to account for these points [4, 5, 6, 7, 20]. The baseline idea of the Dynamic Thickened Flame model (DTF) is to detect reaction zones using a sensor S and to thicken only these reaction zones, leaving the rest of the flow unmodified. Thickening, which is proportional to the grid resolution, locally adapts the combustion process to reach a numerically resolved flame front which affects the flame wrinkling and interactions at the SGS level are supplied by the efficiency function [4, 5, 6, 7, 20].

Dealing with reacting fluids, modelling of the chemical kinetics needs also to be supplied. For simplicity, a one-step chemistry model (Eq. (5)) is derived for $C_{10}H_{16}$ based on a detailed model of $C_{10}H_{16}$/Air combustion with 43 species and 174 steps (Turbomeca private communication).

$$C_{10}H_{16} + 14O_2 \longrightarrow 10CO_2 + 8H_2O. \tag{5}$$

The reduced one-step scheme guaranties proper flame speed predictions only in the lean regime (i.e. with equivalence ratios, $\Phi < 1$). For the target configuration, such a chemical scheme is not sufficient to predict proper flame position since the local equivalence ratio reaches a wide range of values. To circumvent such a shortcoming the pre-exponential constant of the one-step scheme is adjusted versus local equivalence ratio to reproduce the proper flame speed dependency on the rich side [21]. The final expression for the rate of reaction is,

$$\dot{\mathcal{Q}} = A(\Phi) \left(\frac{\rho\, Y_{C_{10}H_{16}}}{W_{C_{10}H_{16}}}\right)^{n_1} \left(\frac{\rho\, Y_{O_2}}{W_{O_2}}\right)^{n_2} exp(\frac{-T_a}{T}) \qquad (\mathtt{mol.\,m^{-3}\,s^{-1}}), \tag{6}$$

where $n_1 = 1.5, n_2 = 0.55, T_a = 3608.4\,\mathtt{K}$ and the $A(\Phi)$ function is $A(\Phi) = \frac{3.84\,10^{14}}{2}(1+\mathtt{tanh}(\frac{1.39-\Phi}{0.26})) + \frac{0.33}{4}(1+\mathtt{tanh}(\frac{\Phi-1.6}{0.8}))(1+\mathtt{tanh}(\frac{1.85-\Phi}{0.8}))$. The adjusted one-step scheme matches the detailed scheme reasonably well in terms of flame speed and adiabatic temperature for premixed laminar flames at 8 *bar*, which is the target pressure for the full combustor.

3 Target Configuration

The configuration (Fig. 1) corresponds to a helicopter combustion chamber where fuel is injected using an inverted cane injection system, also called pre-vaporizer [1]. The computational domain focuses on a 36 degree section of a full annular reverse-flow combustion chamber designed by Turbomeca (Safran group). A premixed gaseous mixture of $C_{10}H_{16}$ enters the chamber through the pre-vaporizer, Fig. 1. Fresh gases are consumed in the primary zone, delimited by the chamber dilution holes and the liner dome of the combustion chamber, Fig. 1. To ensure full combustion, this region of the chamber is fed with air by primary jets located on the inner liner, Fig. 1. Burnt gases are then cooled by dilution jets or cooling films located on the inner and outer liners as well as on the return bend of the combustion chamber. Multi-perforated plates also ensure local wall cooling in areas of the chamber shown on Fig. 1. The operating point corresponds to cruising conditions and is the same for the three grids.

Grid characteristics are summarized in Table 1 in terms of number of cells, points and minimum/maximum cell volumes. The meshes are refined in the primary zone, particularly in the lower part where combustion occurs, and in the regions of cooling films. The Navier-Stokes Characteristic Boundary

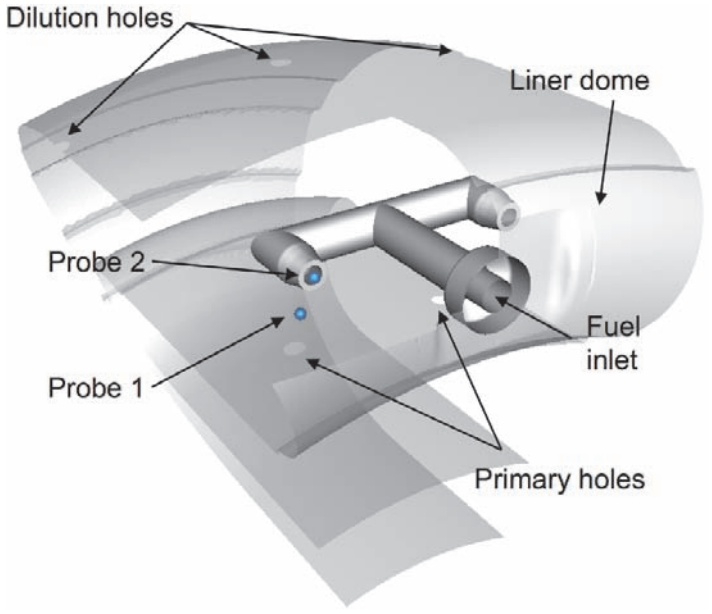

Fig. 1 Computational domain of the helicopter chamber considered in this work

Table 1 Mesh characteristics used for the coarse, the intermediate and fine LES meshes

	Coarse mesh	Intermediate mesh	Fine mesh
Total number of points	230,118	1,875,835	7,661,005
Total number of cells	1,242,086	10,620,245	43,949,682
Max. cell volume [$\mathtt{m}^3$]	$3.12671\ 10^{-8}$	$8.97802\ 10^{-9}$	$4.05748\ 10^{-9}$
Min. cell volume [$\mathtt{m}^3$]	$1.81795\ 10^{-11}$	$8.29479\ 10^{-12}$	$1.1828\ 10^{-12}$
Time step [$\mathtt{s}$]	$1.52\ 10^{-7}$	$0.92\ 10^{-7}$	$0.49\ 10^{-7}$
CPU-hour effort for a 10 $\mathtt{ms}$ LES	277	9,164	35,630

Conditions (NSCBC) [22, 23] are applied on inlet and outlet BC's to control the acoustic behavior of the system. Walls are adiabatic and are treated with a turbulent law-of-the-wall to take into account boundary layer effects. Side boundaries of the computational domain are axi-periodic.

4 Results

Although grid dependency of LES predictions is often presented in the context of reacting and non-reacting simple laboratory flows [24, 25, 26], it is usually not addressed for LES of real configurations especially when dealing

with reacting systems. In the following section, the statistics issued by the three LES of a helicopter chamber are presented. Assessment of resolution criteria based on the velocity predictions are presented and their convergence is analysed. Combustion quantities are then gauged in a similar manner.

4.1 Convergence of the Mean Fields

Turbulent reacting LES is usually evaluated through comparisons against DNS or experimental results. Prior to this modelling performance assessment, mean flow quantity dependency on the grid resolution is paramount. It is often observed that first mean moments become rapidly grid independent while resolved fluctuating fields will also converge but for higher grid resolutions. When dealing with complex industrial configurations, experimental data are not available and assessing the quality of LES becomes particularly difficult. First, flow scales cover a larger range of dimensions when compared to experimental rigs and this dependency is expected to be accentuated if dealing with reacting flows. Indeed, combustion regimes are difficult to identify *a priori* since they strongly rely on the local flow scales and the local mixing state itself dependents on the turbulent velocity field. Grid dependency is even more critical for these applications.

An alternative to experimental measurements used to assess LES predictions stems from the comparaison of the energy content at the resolved and sub-grid scales [24]. Likewise, ratios between the resolved fluctuating and resolved mean fields may be used. In that case, only convergence and grid dependency of the predictions can be evaluated and modelling performance becomes secondary although critical from a purely scientific point of view. Knowing the degree of grid dependency of a turbulent reacting industrial flow LES is still important and ideally modelling performances should be assessed once grid independence is reached. That last issue is the subject of the following analysis.

Impact of the grid resolution is first investigated for the mean velocity field. To do so the following ratio is constructed based on the temporally averaged LES results for the three meshes,

$$M_E = \frac{k_{sgs}}{k_{sgs} + k_{res}}. \tag{7}$$

In Eq. (7), k_{sgs} stands for the mean sub-grid turbulent kinetic energy and $k_{res} = \frac{1}{2}\langle(\widetilde{u}_i - \langle\widetilde{u}_i\rangle_T)(\widetilde{u}_i - \langle\widetilde{u}_i\rangle_T)\rangle_T$ is the mean resolved kinetic energy with $\langle\rangle_T$ denoting the temporal average. For that criterion to be computed, an additional closure is needed to evaluate k_{sgs}. Here the relation $\nu_t = C_M \Delta\sqrt{k_{sgs}}$ is used along with the SGS turbulent viscosity given by the classical Smagorinsky model [11] and C_M is a constant value [8]. For non-reacting flows, 15–20% of the total turbulent kinetic energy should be contained in the sub-grid scales for the velocity model to operate suitably [24].

Figure 2 presents the spatial distribution of M_E, Eq. (7), supplemented by an isoline corresponding to the 20% limit. Clearly, most of the three computational domains satisfies the resolution criterion. Higher limits are reached in the wall regions, the guiding jet vanes and the pre-vaporizing canes. The primary zone, where combustion is expected, is well resolved on all meshes.

Figure 3 shows the volumetric mean value of M_E (denoted by $\langle M_E \rangle$) as a function of the mean cell volume for the three computational domains. The evaluations confirm the previous findings and they are below the 20% line which confirms the predictions in a mean sense. Convergence behavior is also seen and an asymptotic state is suspected for the velocity field. Such a convergence pattern underlines the suitability of the intermediate mesh which provides a very good criterion level. Use of the fine mesh yields a slight improvement coming along with a large increase in computing effort, Table 1. The findings are confirmed by Fig. 4 (solid symbols) where the ratio between the resolved fluctuating and the resolved mean velocity energies are shown, Eq. (8).

$$\Xi(f) = \left\langle \frac{\langle (\widetilde{f} - \langle \widetilde{f} \rangle_T)(\widetilde{f} - \langle \widetilde{f} \rangle_T) \rangle_T}{\langle \widetilde{f} \rangle_T \langle \widetilde{f} \rangle_T} \right\rangle. \tag{8}$$

Increase of the ratio $\Xi(v)$ denotes an increase of energy content in the large unsteady scales which is supplemented by a decrease in the contribution of the SGS velocity field, Fig. 3. These opposite trends of the SGS field and the fluctuating unsteady field result in the asymptotic behavior of the velocity predictions.

Addition to Fig. 4 of the fluctuating to mean energy ratios obtained for the reaction rate (open triangles) and temperature (open circles) shows similar trends. For these combustion quantities, an increase of the grid resolution increases the energy content of the fluctuating scales, the mean field levels being unchanged (not shown). The asymptotic behavior (observed for velocity) is not clear for these reacting fields. At this stage, it is important to note that combustion is a process which does not occur at large scales (although it is strongly influenced by these motions). Convergence of reacting LES (if existing) is not guarantied to happen at the same grid resolution as the one issued by the velocity scales. That observation does not preclude the potential existence of a grid independent turbulent reacting LES for the studied configuration. It only underlines the fact that the fine mesh predictions do not seem to reach such a state with the mesh resolution considered.

Analysis of the instantaneous fields of combustion provides first insights on the previous results. Figure 5 shows Probability Density Functions (PDF) of burning equivalence ratios (noted Φ). These functions are obtained by conditionally classifying the equivalence ratios within the LES instantaneous snapshots provided that the local value of the burning rate is greater than 10% of the mean burning rate. Three peaks occur in the PDF's of the three simulations. The first peak corresponds to points burning near the mean chamber equivalence ratio and for which the combustion chamber is designed to

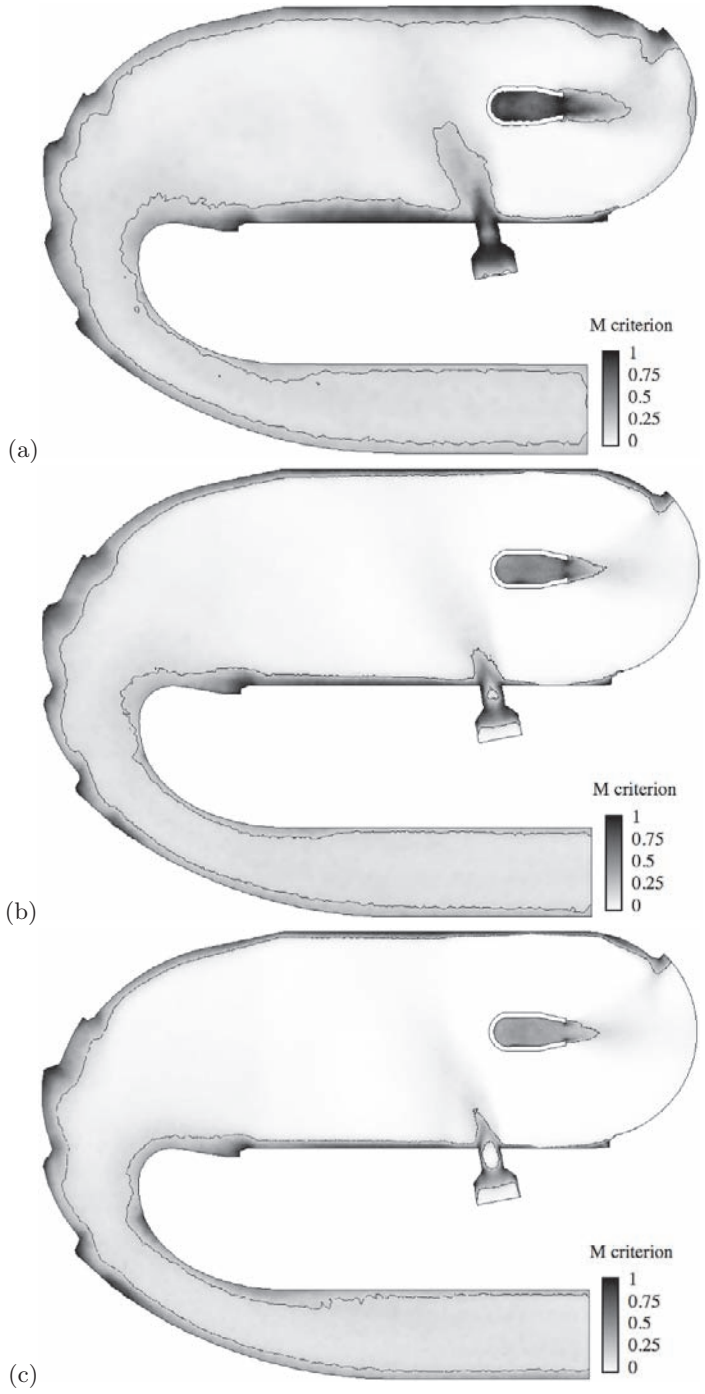

Fig. 2 Transversal view of Pope's criterion [24] in a plane going through one outlet of the pre-vaporizer: (**a**) coarse, (**b**) intermediate and (**c**) fine mesh predictions

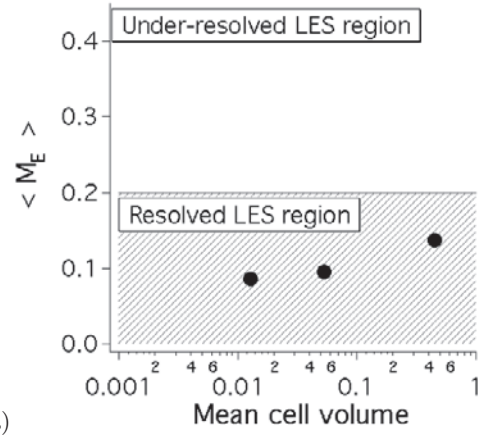

(a)

Fig. 3 Pope's mean volumic criterion as a function of the mean cell volume used in LES

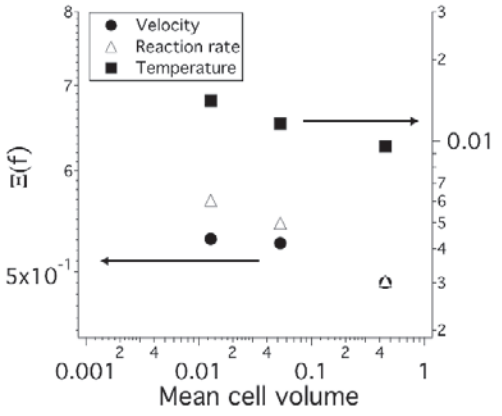

(a)

Fig. 4 Evolution of $\Xi(f)$, Eq. (8), as a function of the grid resolution

operate. The second peak, $\Phi = 1$, coincides with diffusion type combustion while the last peak, $\Phi \approx 1.7$, is rich premixed flames located near the prevaporizer outlets. As the mesh resolution is increased a change in local combustion regime is observed. Indeed, the second peak is more pronounced as the mesh is refined. That transition is initiated only when the velocity field is converged (i.e. the intermediate mesh) and is in agreement with the behaviors noted on Fig. 4 for the combustion fields. More computing effort is necessary at this stage to conclude on the full convergence of the LES model

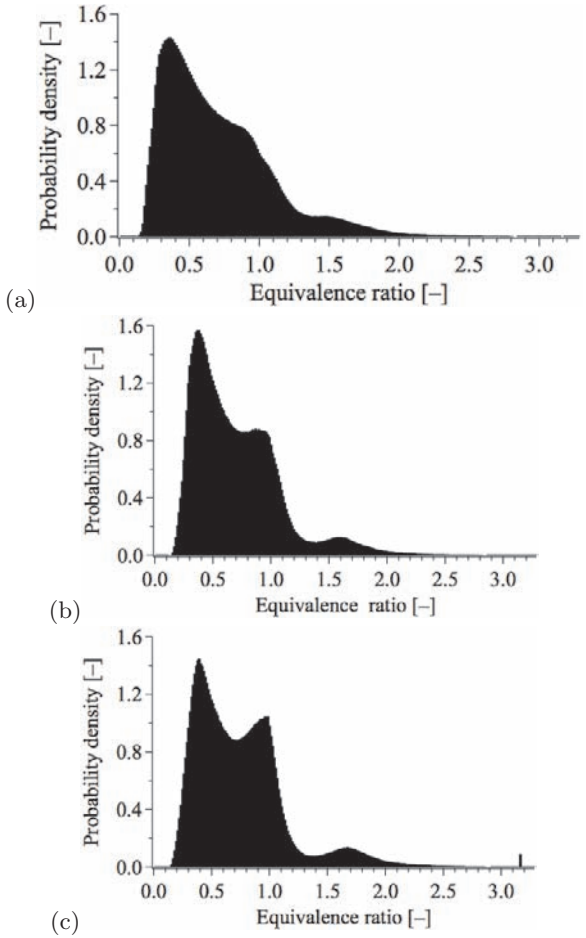

Fig. 5 Probability density function of the equivalence ratio for which the burning rate is higher than ten percent of the mean reaction rate: (**a**) coarse, (**b**) intermediate and (**c**) fine mesh

for such a complex turbulent reacting flow. These preliminary observations also underline the necessity of highly efficient and parallel flow solvers.

5 Conclusions

Convergence of reacting LES predictions for an aeronautical gas turbine combustion chamber is analysed in terms of mesh resolution. To do so three fully unstructured meshes containing respectively 1.2, 10.6 and 43.9 million tetrahedra are used to compute the fully turbulent reacting flow in an inverted-flux chamber burning gaseous fuel. Resolution criteria obtained from the mean

velocity and reacting fields depict different convergence states. The velocity predictions show good quality criteria on the intermediate mesh. The fluctuating to mean resolved velocity ratio and the sub-grid to total kinetic energy ratio prove the existence of an asymptotic state where the LES velocity statistics become independent of the grid resolution. In that sense, the intermediate mesh seems satisfactory and provides a good evaluation of velocity field as predictable by the LES velocity model. The reacting fields and more specifically combustion regimes are seen to be slightly grid dependent while maintaining mean global combustion quantities. Even on the fine mesh, criteria do not depict full convergence although the expected behavior is observed as the grid resolution is increased. Indeed energy contained in the fluctuating resolved field is increased as the mesh is refined. As the grid is refined, changes in the local combustion regimes are underlined and occur only after convergence of the velocity field. More computations are however needed to conclude on the existence of mesh independent reacting LES results for the studied configuration.

Acknowledgements

Numerical simulations and analyses have been conducted thanks to CERFACS computing facility as well as access to MARE-NOSTRUM supercomputer located in Barcelona, Spain.

References

1. Boudier G et al (2007) Proc Combust Inst 31:3075
2. Moin P, Apte SV (2006) AIAA J 44:698
3. Légier JP, Poinsot T, Veynante D, (2000) In Proceedings of the Summer Program 2000, pp. 157–168, Center for Turbulence Research, Stanford, USA
4. Poinsot T, Veynante D (2005) Theoretical and numerical combustion, 2nd edn. Edwards, Flourtown
5. Légier JP (2001) Simulations numériques des instabilités de combustion dans les foyers aéronautiques. Phd thesis, INP Toulouse
6. Schmitt P et al (2007) J Fluid Mech 570:17
7. Martin C et al (2006) AIAA J 44:741
8. Sagaut P (2000) Large Eddy simulation for incompressible flows. Springer, Berlin Heidelberg, New York
9. Ferziger J, Perić M (1997) Computational methods for fluid dynamics. Springer, Berlin Heidelberg, New York
10. Pope SB (2000) Turbulent flows. Cambridge University Press
11. Smagorinsky J (1963) Mon Wea Rev 91:99
12. Moin P et al (1991) Phys Fluids A 3:2746
13. Erlebacher G et al (1992) J Fluid Mech 238:155
14. Ducros F, Comte P, Lesieur M (1996) J Fluid Mech 326:1

15. Ghosal S, Moin P (1995) J Comput Phys 118:24
16. Lilly DK (1992) Phys Fluids A 4:633
17. Germano M (1992) J Fluid Mech 238:325
18. Meneveau C, Lund T, Cabot W (1996) J Fluid Mech 319:353
19. Colin O et al (2000) Phys Fluids 12:1843
20. Roux A et al (2008) Combust flame 152(1–2):154–176
21. Linan A, Williams F (1993) Fundamental aspects of combustion. Oxford University Press
22. Moureau V et al (2005) J Comput Phys 202:710
23. Poinsot T, Echekki T, Mungal M (1992) Combust Sci Tech 81:45
24. Pope SB (2004) New J Phys 6, Art no 35
25. Veynante D, Knikker R (2006) J Turb 7
26. Klein M (2005) Flow Turb Combust 75:131

Analysis of SGS Particle Dispersion Model in LES of Channel Flow

Jacek Pozorski and Mirosław Łuniewski

Institute of Fluid-Flow Machinery, Polish Academy of Sciences, Fiszera 14, 80952 Gdańsk, Poland. jp@imp.gda.pl

Abstract. The wall-bounded two-phase turbulent flow with the dispersed heavy particles is modelled in the Eulerian-Lagrangian approach. The large-eddy simulation (LES) method with near-wall resolution is applied to compute the dynamics of the continuous phase (fluid). The particle tracking with account for drag and lift is used for the dispersed phase. A stochastic model for the residual fluid velocity along particle trajectories is used to account for the subgrid-scale (SGS) particle dispersion. Results for the fluid and particle velocity statistics are presented. In the case of particles undergoing deposition on the channel walls, the separation velocity curve, resulting from several variants of modelling, is presented and discussed.

Keywords: Two-phase flow, Lagrangian-Eulerian approach, Large-eddy simulation, Subgrid-scale particle dispersion, Deposition

1 Introduction

The Lagrangian-Eulerian studies of turbulent polydispersed flows have traditionally been based on RANS for fluid, cf. [8] for a review and new proposals. This approach is still predominant for industrial applications because of its computational efficiency. Some recent developments and limitations of the statistical models are discussed in [12]. Nowadays, LES of particle-laden flows gains in popularity, specially for cases where the large flow scales control the particle motion [1, 11]. Consequently, there is an ongoing debate as to the importance of the residual, or subgrid-scale, flow field on the dynamics of the particulate phase, both in homogeneous turbulence [14, 19] and in wall-bounded flows [2, 4, 24]. Practical ramifications of this issue go as far as collisional flow regime [3] or spray combustion [9]. In wall-bounded flows, the importance of the lift force and a suitable expression for it are discussed [25]. Another problem is the interplay of modelling and numerical errors related, e.g., to the interpolation of flow velocity at particle locations and the integration of particle equations. So, despite a number of papers on LES studies of particle-laden flows published over the last years, e.g. [2, 24], the issue is

J. Meyers et al. (eds.), Quality and Reliability of Large-Eddy Simulations,

still perceived as open and further work is warranted regarding the effect of fluid on particle motion (such as SGS dispersion, kinetic energy, preferential concentration, collision statistics, deposition velocity) and *vice versa* (effect of the particle mass loading on the SGS stress term for the fluid phase, etc.).

In the paper, we consider the issue of particle motion one-way coupled with the fluid flow that is determined from the LES. Fluid velocity at the particle location is found with the local formulae: either the tri-linear interpolation or the second-order accuracy in each coordinate direction. To account for the subgrid-scale particle dispersion, a stochastic model of the Langevin equation type is applied for the residual fluid velocity along particle trajectories. First, with the elastic wall rebound condition for particles we compute their velocity statistics. Next, with the absorbing wall boundary condition we consider the separation of particles from the flow and compute the deposition mass flux on the channel walls.

The main emphasis of the paper is twofold. First, we report our results from a "regular" LES of particle-laden channel flow. A name "regular" means that our LES (with no reconstruction of the residual velocity) corresponds to the computational conditions of the DNS reference data for the flow case defined by the COST Action benchmark test [6] where, in particular, only the drag force acting on point-particles is considered. Second, regarding the physical modelling, by performing an "enhanced" LES we analyse the impact of the lift force term and of the reconstructed residual fluid velocity, called a subgrid-scale particle dispersion model, on particle statistics (turbulent energy, preferential concentration patterns, deposition mass flux).

2 Governing Fluid and Particle Equations

Regarding the carrier fluid, we consider incompressible viscous flow in the absence of gravity. It is governed by the Navier-Stokes equations that in LES are spatially-smoothed with a filter of length scale $\bar{\Delta}$. For the present computation, the dynamic model of Germano and Lilly (cf. [13]) is applied. As far as the dispersed phase is concerned, we treat it as dilute with the one-way momentum coupling (fluid to particles). We use a simplified particle equation of motion [12] which basically is appropriate for the case of heavy particles ($\rho_p \gg \rho_f$), i.e. with the drag term only; in some simulations, we also account for the lift force $\mathbf{F}_L$:

$$\frac{d\mathbf{x}_p}{dt} = \mathbf{U}_p \tag{1}$$

$$\frac{4}{3}\pi r_p^3 \rho_p \frac{d\mathbf{U}_p}{dt} = \pi r_p^2 C_D \frac{\rho_f}{2} |\mathbf{U}_f^* - \mathbf{U}_p|(\mathbf{U}_f^* - \mathbf{U}_p) + \mathbf{F}_L \ . \tag{2}$$

Above, $\mathbf{U}_f^*$ stands for the instantaneous fluid velocity "seen" by particles. In the context of LES, the simplest choice ("regular" LES) is to neglect the impact of the residual scales, $\mathbf{U}_f^* = \bar{\mathbf{U}}_f^* = \bar{\mathbf{U}}_f(\mathbf{x}_p, t)$. In an "enhanced" LES

formulation, the SGS fluid motions are accounted for through a model (for the residual velocity "seen", $\mathbf{u}_f^*$), and the fluid velocity "seen" by the particles is taken as $\bar{\mathbf{U}}_f^* + \mathbf{u}_f^*$. Both treatments (regular LES as well as LES with SGS particle dispersion) have been used in particle tracking reported in the paper. In both cases $\bar{\mathbf{U}}_f^*$ has been interpolated to particle locations from the large-eddy fluid velocity known at mesh points. In Eq. (2), the drag coefficient $C_D = C_D(Re_U)$ is analytically computed as $24/Re_U$ in the limit of the Stokes (creeping) flow and extended to the general case with a well-established correlation (cf. [21]):

$$C_D = (24/Re_U)(1 + 0.15Re_U^{0.687}), \tag{3}$$

where $Re_U = 2r_p|\mathbf{U}_r|/\nu_f$ is the particle Reynolds number based on the particle diameter $2r_p$, the relative particle velocity, $\mathbf{U}_r = \mathbf{U}_p - \mathbf{U}_f^*$, and the kinematic viscosity of the carrier fluid, ν_f. In the limit of small inertia particles, the particle acceleration due to the drag term in Eq. (2) becomes $-\mathbf{U}_r/\tau_p$ where $\tau_p = (2\rho_p/9\rho_f)r_p^2/\nu_f$ is the particle relaxation time.

In the near-wall region where the fluid velocity gradients are high, and in particular the component $G = \partial\bar{U}_x/\partial y$ (x and y being the streamwise and wall-normal directions, respectively), the lift force may have an impact on particle motion. An analytical expression for the lift force has been derived by Saffman [18] in the limit of the Stokes flow and with the additional assumptions on the particle Reynolds number (slip-based) $Re_U \ll 1$, the particle Reynolds number (shear-based) $Re_G = (2r_p)^2|G|/\nu_f \ll 1$, and the relative shear-to-slip parameter $\epsilon = Re_G^{1/2}/Re_U \to \infty$. The Saffman formula has further been extended by McLaughlin [7] for the general case of finite ϵ. Then, the generalized formula for lift force acting in the wall-normal direction with a unit vector $\mathbf{y}^0$ takes the form

$$\mathbf{F}_L = -\frac{9}{\pi}\mu_f r_p^2 U_r \sqrt{|G|/\nu_f}\; sgn(G) J(\epsilon)\mathbf{y}^0, \tag{4}$$

where $J = J(\epsilon)$ is a (nearly) monotonically increasing function from $J = 0$ (at $\epsilon = 0$) to $J = 2.255$ being the asymptotic (Saffman) limit (at $\epsilon = \infty$).

For the wall-bounded flow considered, we introduce the Stokes number as the particle relaxation time normalised in wall-scaling, $St = \tau_p^+ = \tau_p u_\tau^2/\nu_f$.

3 LES Results for Fluid

We computed a fully-developed turbulent channel flow for $Re_\tau = 150$ which corresponds to a benchmark test case of the COST Action LES-AID. The size of the flow domain in the streamwise (x), wall-normal (y) and spanwise (z) directions was $4\pi h \times 2h \times 2\pi h$. The $64 \times 84 \times 64$ grid was used and the mesh size (in wall units) was $\Delta x^+ = 29.4$ and $\Delta z^+ = 14.7$. In the wall-normal direction, Δy^+ varied from 0.7 at the wall up to 6.9 at the centerline. For the reasons

explained below, we have also computed the flow case for the smaller domain size in the spanwise direction, namely $(4/3)\pi h$, keeping the same number of nodes; consequently, for this case $\Delta z^+ = 9.8$. The flow was assumed periodic in the streamwise and spanwise directions. As the flow solver, we used a finite volume, second-order accuracy, open-source code `FASTEST3D` (the group of Prof. M. Schäfer, TU Darmstadt, Germany).

The results for the mean fluid velocity are illustrated in Fig. 1. Two LES runs are shown there; they differ only by the computational domain size in the spanwise direction: $2\pi h$ vs. $(4/3)\pi h$. As readily seen, both the mean velocity and the r.m.s. fluctuating velocity are considerably closer to the reference DNS data [6] when the computation is performed with a smaller mesh size, i.e. $\Delta z^+ = 9.8$. Therefore, this domain size has been kept for further simulations of particle-laden flow presented in the paper.

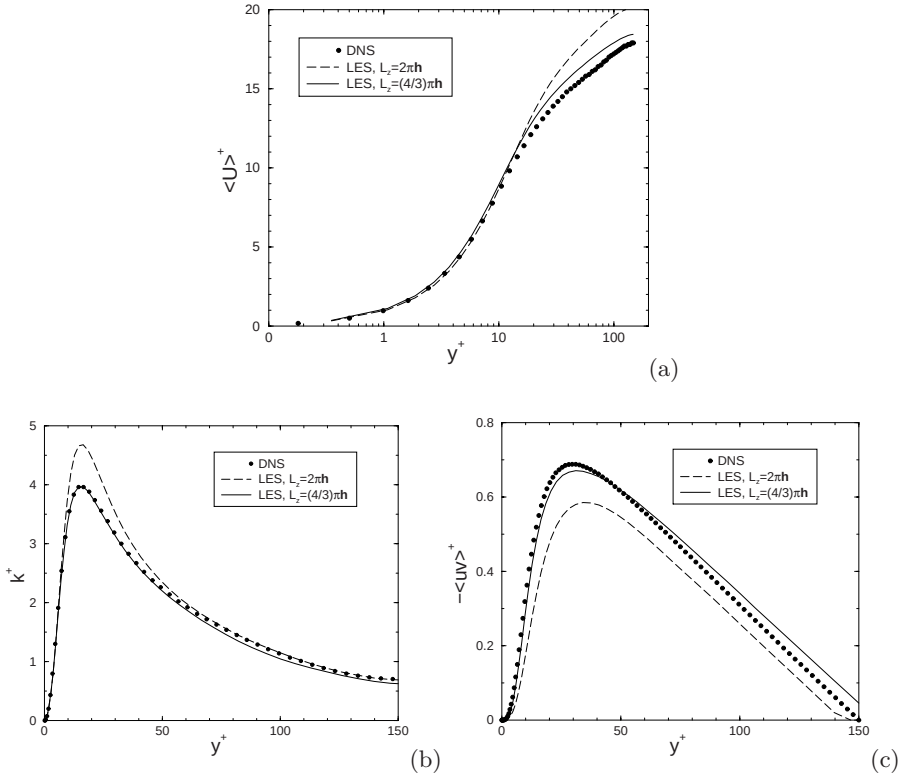

Fig. 1 LES of particle-laden channel flow at $Re_\tau = 150$: (**a**) the resolved mean fluid velocity; (**b**) the turbulent kinetic energy; (**c**) the turbulent shear stress. LES with larger Δz^+: *dashed lines*, LES with smaller Δz^+: *solid lines*, DNS [6]: (•)

4 Results of Regular LES for Particle-Laden Channel

In this section, we report results for particle tracking in the fluid velocity "seen" computed as the large-eddy velocity interpolated to the particle locations. First, we have taken only the drag term in the particle equation of motion. Particles of various inertia, ranging from $St = 1$ up to $St = 250$, have been tracked with the perfect (elastic) rebound wall boundary condition. It has been checked that the simulation time $t^+ \approx 5000$ was generally sufficient to result in a (nearly) equilibrium distribution of particles across the channel. The resulting concentration profiles are considerably non-uniform, due to the turbophoresis, with concentration peaks close to the channel walls.

First, we have assessed the impact of the fluid velocity interpolation scheme, cf. [21]. Results of the tri-linear interpolation scheme have been compared to those obtained with local second-order polynomials in each direction (also known as the sixth-order formula). For the mean particle velocity, however, no differences between the two interpolation schemes have been noticed. The comparison of the mean velocity of particles of $St = 1$ and $St = 125$ with the DNS reference data is shown in Fig. 2. The effect of the interpolation scheme becomes noticeable for the second-order particle velocity statistics. As an example, the turbulent energy is shown in Fig. 3. The general trend shows that tri-linear interpolation slightly underestimates the level of particle turbulent energy. We have checked that the results for all three fluctuating particle velocity components exhibit the same trend. Regarding now the comparison of our LES with the available DNS data for particles (taken from the site `cfd.cineca.it/cfd/repository`, cf. [6]), the mean particle velocities are consistently overpredicted in our LES (cf. Fig. 2). This is most probably due to the overprediction of the mean fluid velocity itself by the LES, as shown in

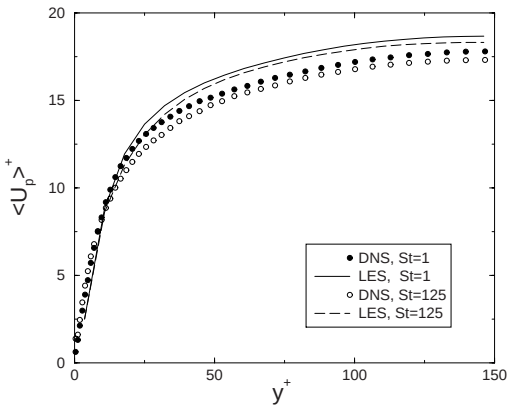

Fig. 2 LES computation of the mean particle velocity in channel flow at $Re_\tau = 150$. $St = 1$: LES (*solid line*) and DNS (•); $St = 125$: LES (*dashed line*) and DNS (○)

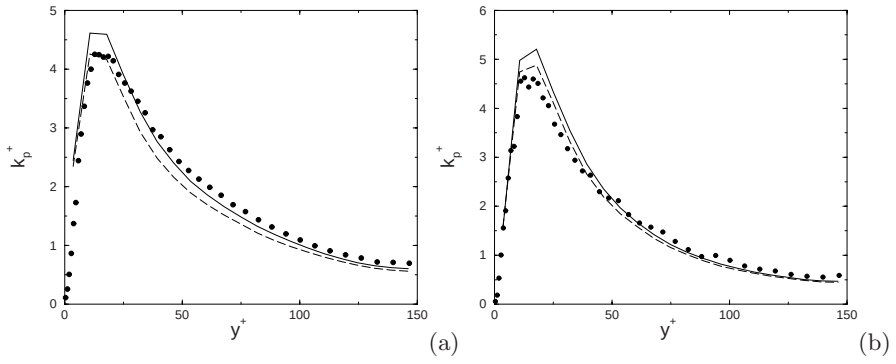

Fig. 3 Effect of the interpolation scheme for the fluid "seen" on particle turbulent energy: (**a**) $St = 1$; (**b**) $St = 25$. Tri-linear scheme: *dashed line*; tri-parabolic scheme: *solid line*; DNS (•)

Fig. 1. However, the decrease of the particle mean velocity in the core region of the channel with increasing St is correctly predicted, as demonstrated by the DNS points. As far as the turbulent particle energy is concerned, the LES tends to slightly overpredict this statistic, specially in the buffer region.

We have also assessed the effect of the lift force in the particle equation of motion. No influence is seen on the level of the mean particle velocity profiles, and there is no clear-cut dependency on St as far as the particle turbulent energy is concerned (not shown), although some differences are observed close to the maxima in the buffer layer.

5 Results of LES with SGS Particle Dispersion

The impact of a SGS dispersion is obviously related to the residual turbulent energy content, k_{sg}. Here, we estimate this quantity as [10, 19] $k_{sg} = C_I \bar{\Delta}^2 |\bar{S}|^2$ where $|\bar{S}| = (2\bar{S}_{ij}\bar{S}_{ij})^{1/2}$ is the scale of the resolved strain rate. The proportionality parameter C_I is not really a constant but varies in space and time like the Germano coefficient in the dynamic model for SGS stresses. Analogously to the estimation of the Germano coefficient, cf. [13], the dynamic procedure with double filtering is applied to solve for C_I [10, 15, 17]. As compared with an *a priori* LES study, the resulting profile of the residual turbulent energy k_{sg} is qualitatively correct, yet it is consistently overpredicted over the channel (roughly, by a factor of 3 [17]). Therefore, the present estimation of k_{sg} and its further use in the SGS particle dispersion model (below) should be treated as provisory.

A stochastic model for the SGS particle dispersion recently proposed by the authors builds on [14]. Its crucial ingredients are the subgrid scales of the fluid "seen": velocity $\sigma^*_{\rm sg}$ and time τ^*_L. We assume that $\sigma^*_{\rm sg} = \sigma_{\rm sg} = \sqrt{(2/3)k_{\rm sg}}$.

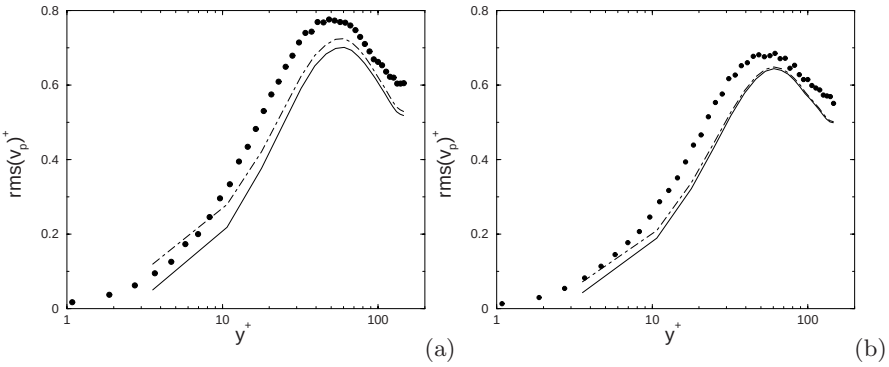

Fig. 4 Effect of the SGS particle dispersion model for the fluid "seen" on the r.m.s. fluctuating particle velocity, wall-normal component, for: (**a**) $St = 1$, (**b**) $St = 5$. Regular LES: *solid lines*; LES with the SGS particle dispersion model (with $C_{sg} = 0.01$): *dot-dashed lines*; DNS (•)

By analogy to modeling turbulent diffusion of fluid elements in the context of statistical (RANS) description [16], we assume that $\mathbf{u}^*$ is governed by the Langevin equation

$$du_i^* = -\frac{u_i^*}{\tau_L^*}\,dt + \sqrt{\frac{2\sigma_{\rm sg}^2}{\tau_L^*}}\,dW_i, \tag{5}$$

where dW_i is an increment of the Wiener process. The time scales of residual fluid motions "seen" by the particle are taken as $\tau_L^* = C_{sg}\bar{\Delta}/\sigma_{\rm sg}$. The model constant $C_{sg} = \mathcal{O}(1)$ accounts for the uncertainty concerning the time scale of the residual velocity autocorrelation.

By integrating Eqs. (1), (2) and (5) in time, the particle trajectories in the flow are determined together with some statistics of their motion. For the smallest particles considered (of $St = 1$) there is a noticeable effect of the SGS particle dispersion model on the intensity of particle velocity fluctuations, as illustrated in Fig. 4(a). Of special importance is the wall-normal component, since its level is directly connected with the separation efficiency. The impact of the SGS particle dispersion model on the r.m.s. particle fluctuating velocity components is still noticed for $St = 5$, as shown in Fig. 4(b). However, for larger inertia particles, no discernible differences are seen for these statistics.

As known from comprehensive DNS studies (cf. [20]), particles of certain inertia preferentially concentrate in near-wall streaks. We have checked the impact of filtering on the instantaneous particle structures, and a subsequent effect of applying the SGS dispersion model. The results (most pronounced for $St = 25$) are shown in Fig. 5. It is readily noticed that the preferential concentration patterns are altered in LES: they are less visible, yet the length of spatial correlation is larger in the streamwise direction. In the LES with

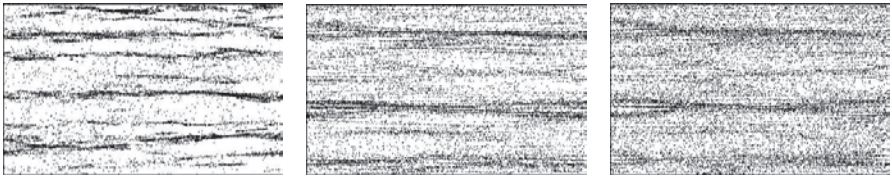

Fig. 5 Particle instantaneous locations in turbulent channel flow; a layer parallel to the wall ($0 < y^+ < 5$), particles of $St = 25$: (**a**) DNS [6], (**b**) regular LES, (**c**) LES with the SGS particle dispersion model

SGS dispersion model, the preferential concentration decreases further. This may be expected since the Langevin stochastic model is diffusive by nature. The observed trends in near-wall preferential concentration are consistent with those we observed in isotropic turbulence [14].

6 Particle Separation

The mass flux of particles separating on the channel walls is quantified as the particle deposition velocity (cf. [22, 23]). We have computed the non-dimensional deposition velocity V_{dep}^+ in several variants of our LES and plotted it vs. the particle Stokes number, i.e. the momentum relaxation time τ_p made non-dimensional with wall units. As already discussed [15], the deposition mass flux is heavily under-estimated for middle-inertia particles (for $\mathcal{O}(1) \leq \tau_p^+ \leq \mathcal{O}(10)$, say), possibly due to the neglect of SGS particle dispersion and/or the lift force effects. In the computations reported here, we have thoroughly checked this hypothesis.

First, in the "regular" LES runs, we have obtained the deposition curve with the drag force only. Subsequently, we have added the lift force term, alternatively in the asymptotic Saffman form or in the generalized McLaughlin setting, cf. Eq. (4). Results are shown in Fig. 6. As it transpires from the drag-only results (□), there is virtually no particle deposition below $St = 5$, contrary to the experimental evidence of Liu & Agarwal [5]. It has to be noted that the Brownian separation regime extends only below $St = 0.5$, say. Moreover, in the presence of lift force there is no separation beyond $St = 5$ neither. (Figure 6 is slightly misleading in this respect since results for V_{dep}^+ at smaller St are not plottable in the logarithmic scale.)

For the LES simulations with the SGS particle dispersion model, the deposition velocity can be considerably improved, depending on the model constant. Several runs with varying values of C_{sg} are illustrated in Fig. 7 (drag force only). As expected, the impact of the SGS dispersion model is largest for small-inertia particles (here, $St = 2$) and vanishes for large ones (here, $St = 250$).

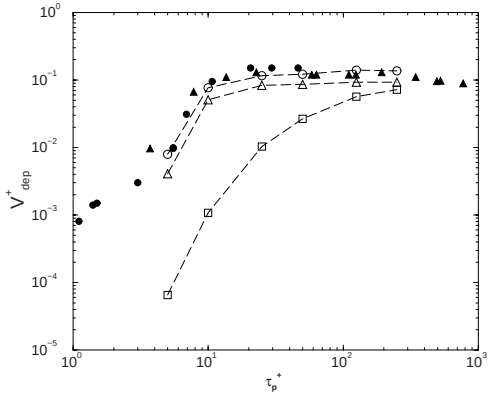

Fig. 6 Particle deposition velocity in channel flow at $Re_\tau = 150$: lift force effect. Drag only (*squares*), Saffman lift (○), McLaughlin lift (*triangles*). Experimental data [5] at $Re = 10^4$ (●), at $Re = 5 \cdot 10^4$ (▲)

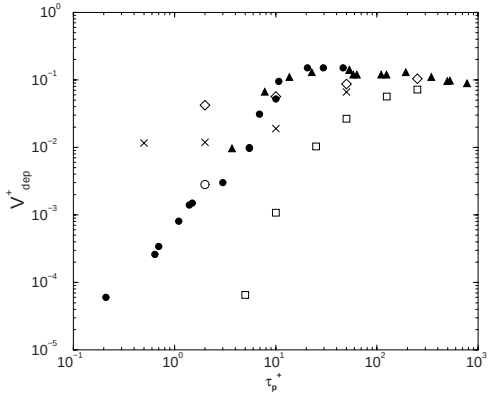

Fig. 7 LES of particle-laden channel flow at $Re_\tau = 150$. Particle separation velocity: LES with no SGS particle dispersion (□), LES with SGS dispersion model for $C_{sg} = 0.1$ (◇), $C_{sg} = 0.01$ (×), and $C_{sg} = 0.002$ (○); experiment (Liu & Agarwal 1974) at $Re = 10^4$ (●), $Re = 5 \cdot 10^4$ (▲)

Although the stochastic SGS dispersion model has got a considerable impact on particle deposition velocity, the current results are still not completely satisfactory. As noticed in Fig. 7, the quantitative agreement with the experimental value of the deposition velocity can be reached for a particular choice of the model constant ($C_{sg} = 0.002$), yet the qualitative agreement of the results remains fairly poor, since the scaling $V^+_{\mathrm{dep}} \sim (\tau_p^+)^2$ is not retrieved in the "diffusion-impaction" regime. However, as it transpires from Fig. 8, our deposition results with the McLaughlin lift force and the SGS dispersion model

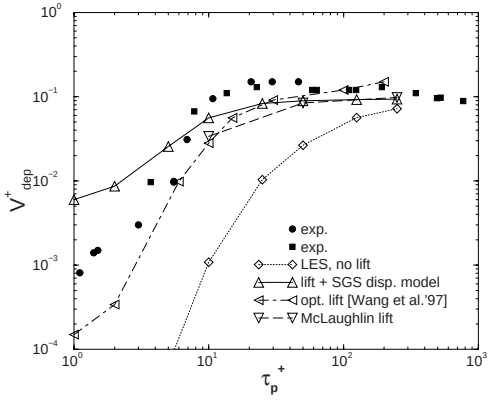

Fig. 8 Particle deposition velocity in channel flow at $Re_\tau = 150$: impact of the SGS particle dispersion model. Model constant: $C_{sg} = 0.1$ ($\diamond$), $C_{sg} = 0.01$ ($\times$), and $C_{sg} = 0.002$ ($\circ$); experimental data [5] at $Re = 10^4$ ($\bullet$), at $Re = 5 \cdot 10^4$ ($\blacktriangle$)

are quite acceptable, and arguably not worse than those obtained earlier by Wang et al. [25] with a more sophisticated lift force expression, taking into account the wall proximity.

7 Conclusion and Perspectives

In the paper, we studied LES of wall-bounded, particle-laden flow, with account on drag and lift terms in the particle equation of motion. Both the standard analytical formula of Saffman and its extension proposed by McLaughlin were implemented. Then, we analysed the effect of a stochastic model for residual (SGS) particle motion, based on the Langevin equation for the residual velocity of the fluid along particle trajectories. The statistics of the dispersed phase have been computed for the elastic rebound boundary condition. Next, for the absorbing boundary condition we computed the mass flux of particles undergoing separation on channel walls. The sources of discrepancies with respect to the available experimental and fully-resolved computation (DNS) reference data were indicated. With the account of the stochastic Langevin model for the SGS particle dispersion, a reasonable agreement of the particle deposition velocity with the experimental data has been reached. Although the SGS dispersion model has a rather small impact on the second-order velocity statistics, it considerably affects the wall deposition for smaller particles. The model, being diffusive by nature, is not able to retrieve particle concentration patterns (streaks) in the near-wall region. Therefore, further work on this and other SGS dispersion models is warranted, also for free shear flows, such as particle-laden jets.

Acknowledgements

The authors would like to thank Professor Michael Schäfer (TU Darmstadt, Germany) for a kind agreement to use and further develop the research code FASTEST3D. Some simulation runs have been carried out at the regional Academic Computer Centre (TASK) at Gdańsk, Poland.

References

1. Apte SV, Mahesh K, Moin P, Oefelein JC (2003) Large-eddy simulation of swirling particle-laden flows in a coaxial-jet combustor. Int J Multiphase Flow 29:1311–1331
2. Armenio V, Piomelli U, Fiorotto V (1999) Effect of the subgrid scales on particle motion. Phys Fluids 11:3030–3042
3. Fede P, Simonin O (2006) Numerical study of the subgrid fluid turbulence effects on the statistics of heavy colliding particles. Phys Fluids 18, Art no 045103
4. Kuerten JGM, Vreman AW (2005) Can turbophoresis be predicted by large-eddy simulation? Phys Fluids 17, Art no 011701
5. Liu P, Agarwal O (1974) Experimental observation of aerosol deposition in turbulent flow. Aerosol Sci 5:145–155
6. Marchioli C, Soldati A, Kuerten JGM, Arcen B, Tanière A, Goldensoph G, Squires KD, Cargnelutti MF, Portela L (2007) Statistics of particle dispersion in Direct Numerical Simulations of wall-bounded turbulence: results of an international collaborative benchmark test. In: Int Conf on Multiphase Flow, July 9–13, Leipzig, Germany
7. McLaughlin JB (1991) Inertial migration of a small sphere in linear shear flow. J Fluid Mech 224:261–274
8. Minier JP, Peirano E (2001) The PDF approach to turbulent polydispersed two-phase flows. Phys Reports 352:1–214
9. Moin P, Apte SV (2006) LES of multiphase reacting flows in complex combustors. AIAA J 44:698–708
10. Moin P, Squires K, Cabot W, Lee S (1991) A dynamic subgrid-scale model for compressible turbulence and scalar transport. Phys Fluids A 3:2746–2757
11. Okong'o N, Bellan J (2004) Consistent large-eddy simulation of a temporal mixing layer laden with evaporating drops. J Fluid Mech 499:1–47
12. Peirano E, Chibbaro S, Pozorski J, Minier JP(2006) Mean-field/PDF numerical approach for polydispersed turbulent two-phase flows. Prog Energy Combust Sci 32:315–371
13. Pope SB (2000) Turbulent flows. Cambridge University Press, Cambridge
14. Pozorski J, Apte SV, Raman V (2004) Filtered particle tracking for dispersed two-phase turbulent flows. In: Proceedings of the Summer Program, 329. Center for Turbulence Research, Stanford University
15. Pozorski J, Łuniewski M (2007) LES with subgrid-scale particle modelling in turbulent channel flow. Int Conf on Multiphase Flow, July 9–13, Leipzig, Germany
16. Pozorski J, Minier JP (1999) PDF modeling of dispersed two-phase turbulent flows. Phys Rev E 59:855–863

17. Pozorski J, Wacławczyk T, Łuniewski M (2007) LES of turbulent channel flow and heavy particle dispersion. J Theor Appl Mech (Warsaw) 45:643:657
18. Saffman PG (1965) The lift on a small sphere in a slow shear flow. J Fluid Mech 22:340–385
19. Shotorban B, Mashayek F (2006) A stochastic model of particle motion in large-eddy simulation. J Turbul 7, Art no 18
20. Soldati A (2005) Particles turbulence interactions in boundary layers. Z Angew Math Mech 85:683–699
21. Squires KD (2007) Point-particle methods for disperse flows. In: Prosperetti A, Tryggvason G (eds) Computational methods for multiphase flow. Cambridge University Press, Cambridge
22. Uijttewaall WSJ, Oliemans RVA (1996) Particle dispersion and deposition in direct numerical and large eddy simulations of vertical pipe flows. Phys Fluids 8:2590–2604
23. Wang Q, Squires KD (1996) Large eddy simulation of particle deposition in a vertical turbulent channel flow. Int J Multiphase Flow 22:667–683
24. Wang Q, Squires KD (1996) Large eddy simulation of particle-laden turbulent channel flow. Phys Fluids 8:1207–1223
25. Wang Q, Squires KD, Chen M, McLaughlin JB (1997) On the role of the lift force in turbulence simulations of particle dispersion. Int J Multiphase Flow 23:749–763

Numerical Data for Reliability of LES for Non-isothermal Multiphase Turbulent Channel Flow

Marek Jaszczur[1] and Luis M. Portela[2]

[1] AGH - University of Science and Technology, 30-059 Krakow, Al. Mickiewicza 30, Poland. jaszczur@agh.edu.pl
[2] Delft University of Technology, Prins Bernhardlaan 6, 2628 BW, Delft, The Netherlands. L.Portela@tudelft.nl

Abstract. Turbulent non-isothermal fully-developed channel flow laden with small particles is investigated through numerical simulation combined with the tracking of the individual particles using DNS and LES. The simulations are performed at Re_τ=180 and 395, with Pr=1.0, using the point-particle approach and neglecting the influence of the particles on the fluid and inter-particle interactions. The focus is on the interactions between particles and turbulence and their effect on the particles using DNS and LES. Presented data obtained through direct numerical simulation show new effects related to clustering and heat exchange for particles. The LES results shows that particles behaviour is very complex and to have proper results additional subgrid modelling for dispersed phase is required.

Keywords: Particle laden flow, Multiphase flow, LES/DNS

1 Introduction

One of the interesting problems in two-phase turbulent flow is prediction of transport of mass and thermal energy by small solid particles or droplets in non-isothermal turbulent flow. This type of flow occurs in large number of environmental and industrial processes e.g., clouds formation, coal combustion, catalytic cracking, filters, chemical reactors, etc. Very accurate prediction of particles behavior is important to design industrial devices or understand physics. Experiments and numerical computations demonstrate that shear flow has complex effect on the particle fluctuations. Due to the interactions between particles and turbulence, the distribution of the particles and their properties can be highly influenced. Small heavy particles immersed in a turbulent flow tend to accumulate, creating strong inhomogeneities in concentration and form cluster structures in the low-speed streaks [1]. But also due to momentum and heat exchange particles-turbulence interaction gets even more

J. Meyers et al. (eds.), Quality and Reliability of Large-Eddy Simulations,

complex and can influence thermal properties of particles. This can have important consequences on the efficiency and direction of many chemical and industrial processes.

Complexity of turbulent transfer phenomena which covers a wide range of flow scales from very small to large one introduce different mechanisms playing important role in the interaction between particles and turbulent structures. In the past a lots of work has been done for understanding influence of particle inertia on dispersed phase structure and on fluid structure using simple models [2, 3, 4]. The simulations using simple models do not promise to have high reliability and applicability and fail in more accurately analysis of the flow. On the way of understanding particle-turbulence interactions Direct Numerical Simulation plays an important role. For flows laden with a large number of small particles, Eulerian-Lagrangian point-particle DNS has been quite successfully in studies of the particle-turbulence dynamics in isothermal flows. Several important aspects of particle-turbulence interactions have been found by Maxey & Riley [5], Kulick [6], Fessler & Eaton [7], Chung [8]. Application of DNS to the study particle deposition in boundary layers by Wang and Squires [9] has clearly show accumulation of heavy particles in the low velocity streaks. Most of recent works focus on isothermal flow and very few studies deal with non-isothermal particle-laden flow. Hetsroni & Rosenblit [10] and Hetsroni [11] used infrared thermography to study the thermal interaction between the particle-laden turbulent flow and a heated plate. As a results of this experiment they reported enhancement of heat transfer, due to addition of particles. This effect can increase heat transfer of factor about 35% depending on particle size, loading and flow conditions. In recent computations Hetsroni [11] shows that the particles cause an increase in wall-normal turbulent flux. This effect probably can be directly caused by "film scraping" on "particle convection" assumed by Subramanian [12] or indirectly caused by turbulence modifications (mainly change of a level of wall-normal fluctuations) Rashidi [13] and Kaftori [14]. Oesterle [15] perform numerical studies focusing on particle collisions in heated pipe flow. He reported that flow dynamic alternation induced by particle-wall and inter-particle collisions results in significant modulation of the heat exchange rate, but direct heat exchange during inter-particle collisions (solid–solid) and for particle-wall collisions is negligible.

A number of papers on Large Eddy Simulation of particle-laden flows have been published over the last years [16, 17]. But the issue is still perceived as open and further work is warranted on the effect of subgrid-scale fluid flow on particle motion and vice versa.

In the present paper we will focus on particle-turbulence interaction in wall heated fully-developed turbulent vertical channel. We have chosen wide range of particle time scales starting from τ_v^+=2 up to τ_v^+=29 and for τ_θ^+=0.3 up to τ_θ^+=105. The choice allows us to discriminate at different mechanisms of particle interactions and covers the range of particle most responsive to the flow structures in boundary layer. For this purpose we extend the point-

particle approach in order to deal also with heat transfer. The temperature is considered as a passive scalar. We consider only one-way coupling, from both the hydrodynamic and thermal perspectives, i.e., the influence of the particles on the turbulence and particle collisions are not taken into account. We focus on how the particle-turbulence interaction affects the temperature of the particles, on the exchange heat rate and on the correlation between the properties of the particles and of the surrounding fluid. In last section LES approach have been used in comparison with DNS results. Due to complexity of particles behaviour only some of quantities (for dispersed phase) shows good agreement. Phenomena like clustering and concentration is very difficult to reproduce properly with LES and additional subgrid scale modelling for dispersed phase seems to be required.

2 Mathematical Model

For current studies of wall-bounded turbulent particle-laden flow the Eulerian-Lagrangian point-particle approach [18] has been used. Particles are dispersed in a pressure-driven heated flow of gas, assumed to be incompressible and Newtonian. Periodic boundary conditions are imposed on the fluid velocity and temperature field in streamwise and spanwise directions, no slip boundary conditions are enforced to the wall. We assume very small values of volume fraction of particles and small size of particles, so the particles have negligible effect on turbulence and the interactions between the particles and turbulence is one-way coupling. We assume also that for very small particle number density, with small particle size, heat exchange between the particles and the turbulence has an insignificant effect on the temperature of the flow.

The continuous-phase is solved using standard direct numerical simulations or large eddy simulations techniques for incompressible flow together with the tracking of the individual particles. The transfer of momentum between the particle and the fluid is considered through a force located at the particle center, which is determined from the velocities of the particle and of the surrounding fluid. The heat transfer is determined base on velocities of the particle and fluid and the temperatures of the particle and the surrounding fluid. Those approaches are valid if the particles are significantly smaller than the smallest flow scales and the Biot number is less than 0.1. Since we want to consider only the particle-turbulence interactions, the simulations are performed in a channel without gravity. The geometry of the problem under consideration is sketched in Fig. 1.

For the continuous-phase, the equations to be solved are mass, momentum and energy. For small heavy particles the only significant force is the drag force [19] and the equation of motion for a particle can be written as:

$$\frac{d\mathbf{v}}{dt} = C_d \frac{Re_p}{24} \frac{1}{\tau_v} (\mathbf{u} - \mathbf{v}) \tag{1}$$

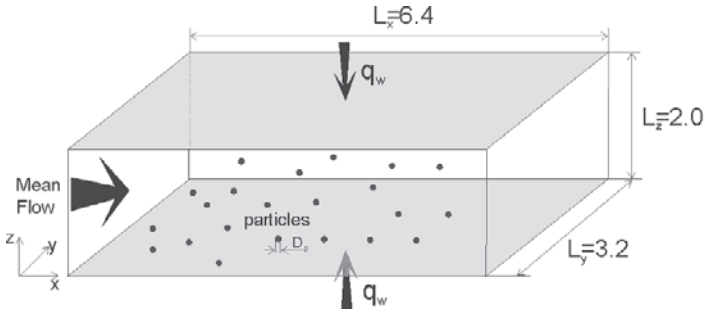

Fig. 1 Particle-laden channel flow

where u is the velocity of the fluid interpolated at the center of the particle.

The particle Reynolds number Re_p, and the hydrodynamic particle-relaxation time τ_v, are defined as:

$$Re_p = \frac{|\,(\mathbf{u}-\mathbf{v})\,|\,D_p}{\nu} \quad , \quad \tau_v = \frac{\rho_p}{\rho}\frac{D_p^2}{18\nu} \qquad C_d = \frac{24}{Re_p} \tag{2}$$

where ρ_p and ρ are the particle and fluid densities, D_p is the diameter of the particles and C_d is the drag coefficient for Stokes flow (valid for small Re_p). The equation for the particle temperature, assuming a Biot number less than 0.1 (uniform particle temperature) can be written as:

$$\frac{dT_p}{dt} = \frac{Nu}{2}\frac{1}{\tau_\theta}(T - T_p) \qquad \tau_\theta = \frac{\rho_p c_p D_p^2}{12k} \tag{3}$$

T is the temperature of the fluid interpolated at the center of the particle, and τ_θ is the thermal particle-relaxation-time. The Nusselt number was calculated from the Ranz-Marshall correlation.

The position, flow, and particle quantities are normalized by the channel half-width, δ, the friction velocity, u_τ, and the friction temperature, T_τ. The convective and diffusive terms in all the equations are discretized using a second-order central scheme. For time-advancement a second-order Adams-Bashforth scheme is used. The particle motion and particle temperature algorithms are obtained with using a second-order Adams-Bashforth scheme for the time-advancement, and a tri-linear interpolation for the velocity and temperature. Even though some times high order algorithm are used to interpolate the fluid velocity at the particle position, there is no clear agreement on the literature that this procedure has a large influence on the statistics. The flow is heated from walls with a uniform heat-flux. Periodic boundary conditions are imposed in streamwise and spanwise directions.

In the case of Large Eddy Simulations, the filtered continuity and Navier–Stokes equations, that are solved for the gas-phase are,

$$\nabla \cdot \mathbf{u} = 0 \tag{4}$$

$$\frac{D\mathbf{u}}{Dt} = -\frac{\nabla P}{\rho_f} + \nu\nabla^2\mathbf{u} + \nabla\cdot\mathbf{T} \tag{5}$$

where ρ_f and ν are the density and the kinematic viscosity of the fluid. The influence of the subgrid motion on the resolved gas-velocity is represented by the extra stress-tensor, $\mathbf{T}$. The code used to solve equations 4 and 5 is the same as in the DNS case. The stress-tensor, $\mathbf{T}$, is computed using the standard Smagorinski model, with the Smagorinski constant $C_s = 0.1$. Van Driest wall-damping is also included in the calculations [20]. More details about the single-phase solver can be found in [21].

The conditions for the dispersed phase were the same as for the DNS case. This means, no model was used to mimic the unresolved flow scales. Moreover, for simplicity, the Large Eddy Simulations where performed under isothermal conditions.

3 Results

Calculations are performed on a computational domain of 6.4x3.2x2.0 δ in x,y and z discretized with 128x128x66 (for Re_τ=180) and 256x256x128 (for Re_τ=395) on DNS and 64x64x48 on LES control volumes. For the streamwise and spanwise directions uniform grid spacing has been used. For wall normal non-uniform grid spacing with an hyperbolic-tangent stretching. The shear Reynolds number of the flow was Re_τ=180 and 395 based on the shear velocity and half channel height. In order to obtain good statistics for particle for the simulations presented here $1.5\text{x}10^6$ particles were considered.

The simulations started from arbitrary conditions (random flow and temperature field) and flow field has been time advanced to get a statistically-steady state for velocity and temperature. When a statistically steady state is reached particles are distributed uniformly over the computational domain. Their initial velocity assumed to be the same as the fluid in the center of particles location. The particles need to adapt to the new velocity and temperature which usually takes few particle response times. But upon that much longer time is required to get statistically-steady state for particles conditions necessary for reliable statistics (to obtain statistically steady state for particles takes respectively much longer time than for flow field; also, it takes longer for particles with larger response time). After initial big change in particle concentration profile, particles continue very slow process of accumulations near walls. As shown by Portela [19] this process can take enormous amount of time. In present computations time before particles start to be averaged takes at least $t^* = 200$. The statistics for the fluid and particles were averaged for $100\delta/u_\tau$ at Re_τ=180 and for $40\delta/u_\tau$ at Re_τ=395. The particle properties were obtained by averaging over a rectangular slices using simple linear model base on center of particle locations and distance from reference points and reference point corresponds to flow computational grid points. The mean streamwise velocity and mean temperature profile and other mean turbulence

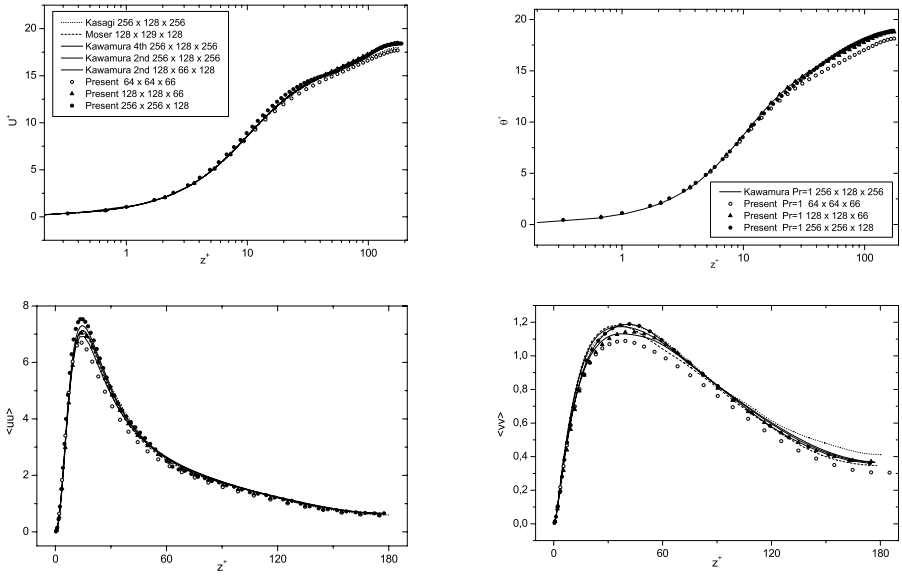

Fig. 2 Computed flow quantities for $Re_\tau = 180$ in comparison with other DNS computations [22, 23, 24]

quantities for fluid phase are compared with DNS data provided by other researchers [22, 23, 24] and shown in Fig. 2. We can notice a good agreement with the work from other authors unless some small differences can be found between data from databases mainly cause by different way of solution and differences in grids.

It is well-known that in wall-bounded shear flow particles concentrate near the wall. And particle concentration is non-uniform gives highest concentration in low-speed streaks due to particle interactions with the local turbulent flow structure. But it is also important to know how this non-uniformity influence on the temperature or heat fluxes. The particle concentration profiles are shown in Fig. 3. For all cases very high particle concentrations near the wall can be observed. Particle concentration is two orders of magnitude higher than in core flow and remain uniform only for small area close to channel center line. Even for relatively light particle with $\tau_v = 2$ concentration is one order of magnitude higher than the value in center of the channel. The small concentration of particles in core region of channel shows that in order to get accurate good statistical number of particles must be large.

The mean streamwise-velocity profiles and mean temperature for particle and fluid are also shown in Fig. 3. For $Re_\tau = 180$ and up to $z = 0.5\delta$ particle velocity is slightly smaller then the fluid velocity (except very close to the wall) and this difference increases with increasing τ_v with maximum difference around $z = 30$ in wall units. For higher z velocity of particle can be slightly larger than fluid velocity and maximum deviation was seen for particle with

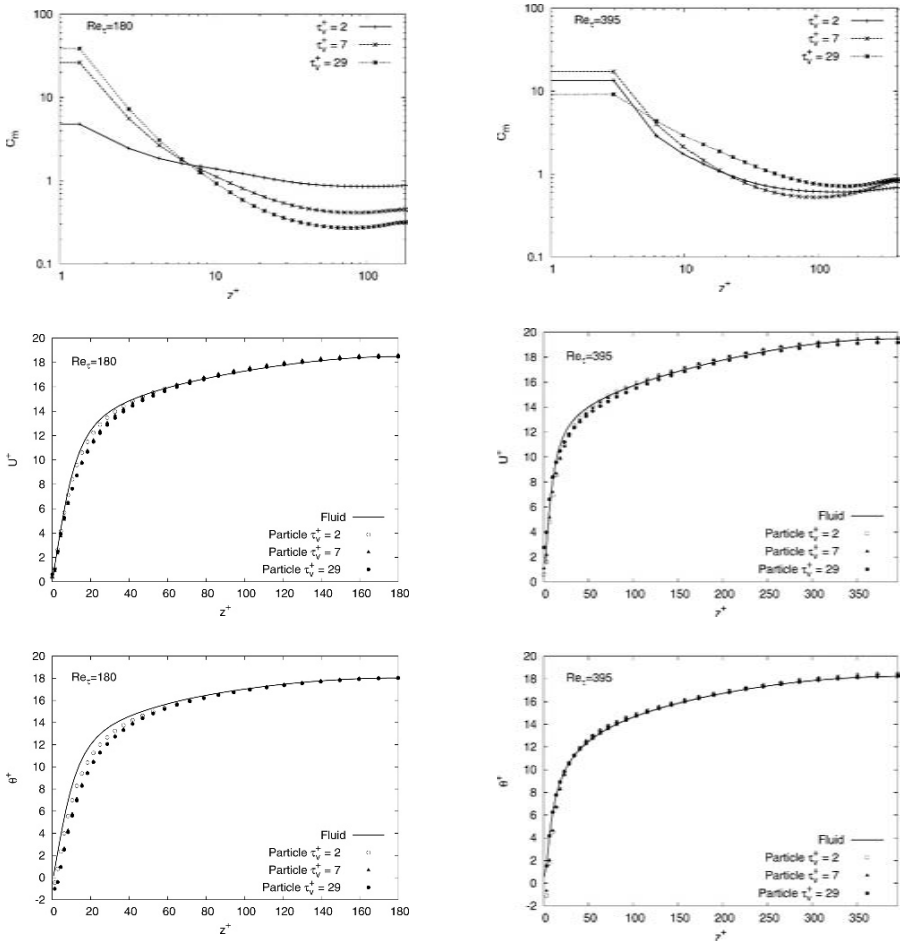

Fig. 3 Particle concentration (*top*), velocity (*middle*) and temperature (*bottom*) for particle relaxation time $\tau_v = 2$, $\tau_v = 7$ and $\tau_v = 29$

$\tau_v = 7$. Similar effect can be seen for $Re_\tau = 395$. For most of the cases temperature of particle is smaller then temperature of the fluid for all distance z. Which is different from profile of streamwise velocity where in the core of channel velocity of the particle overlap velocity of the fluid. But main difference can be seen close to the wall where temperature of the particle even very close to the wall is much smaller than temperature of the fluid. This effect occurs also for relatively light particles and is more pronounces for high Reynolds number. From this point can be seen that uniform mixing of particles in turbulent flow is non-trivial task.

On Fig. 4 thermal quantities for fluid and particles are presented. Velocity-temperature correlations are presented for the fluid and for the particles.

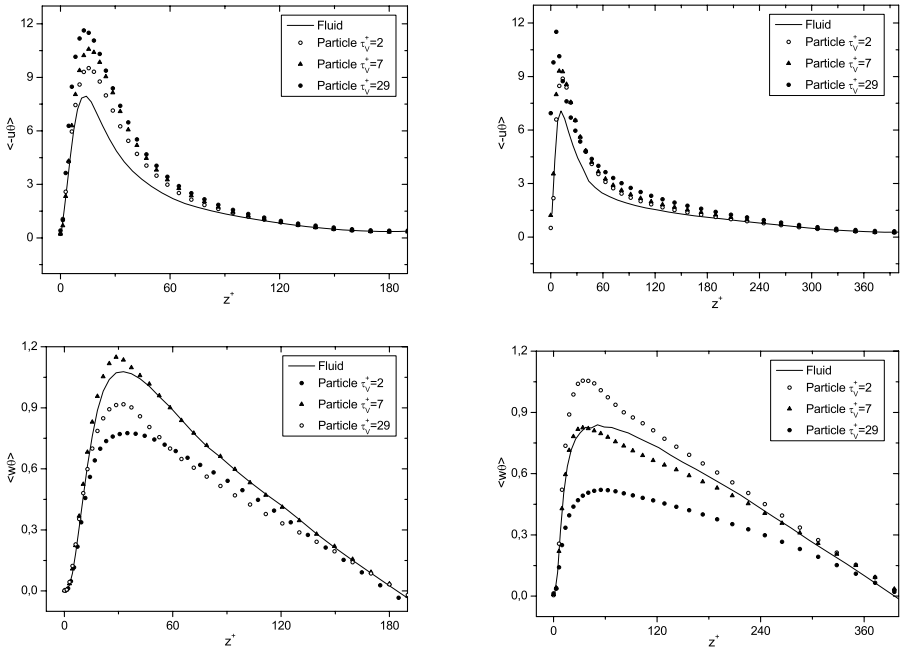

Fig. 4 Temperature and velocity-temperature correlation for particle relaxation time $\tau_v = 2, 7, 29$, and $\tau_\theta^+ = 3, 10.5, 43.5$, for $Re_\tau = 180$ (*left*) and $Re_\tau = 180$ (*right*)

For fluid with Prandtl number Pr=1 and for three types of particles with $\tau_v^+ = 2, 7, 29$ and $\tau_\theta^+ = 3, 10.5, 43.5$ respectively and for $Re_\tau = 180, 395$. Correlations of streamwise velocity fluctuations and temperature for particle are much larger than for the fluid and the difference is increasing when particle response time increases. Correlation $< w\theta >$ for light and heavy particle is smaller than for the fluid but for particle with response time $\tau_v^+ = 7$ for most of z is equal the value for the fluid or slightly exceed those value. Comparison of this component with $< uw >$ component shows that also for $< uw >$ maximum value is for middle response particle than for light and heavy which are most close to the fluid correlation [18]. This means that in this effect hydrodynamic behavior of streamwise velocity plays primary role.

To explore that effect we have drawn on Fig. 5 average distributions of the temperature in the plane x-y for $z^+ = 3.6$. For the fluid in this region mean temperature is around $\theta = 3.6$ but for the particle it depend of the momentum and thermal response time. For most light particle mean temperature is around $\theta = 2.0$ and is not decreasing if the thermal response time is 10 times faster. For heavy particle mean particle temperature is around $\theta = 0.8$ and is sligthly decreasing with decreasing τ_θ^+. This shows that particle response time is fast enough to converge particles thermally but not hydrodynamicaly. Also because of preferential concentration particle are not randomly distributed

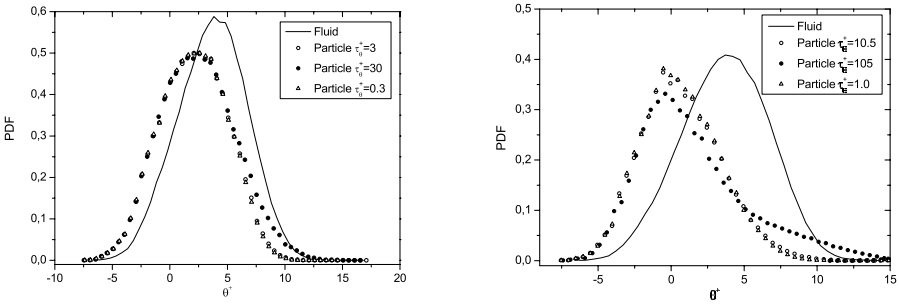

Fig. 5 Particle pdf for particle relaxation time $\tau_v = 2$ (*left*) and $\tau_v = 7$ (*right*) for $Re_\tau = 180$, and τ_θ from 0.3 up to 105

in the fluid but located in streaks more often than in other positions. This influence statistics for thermal components

3.1 Large Eddy Simulations

Large Eddy Simulations where performed for $Re_\tau = 180$, on a computational domain of size 10x4x2 measured on channel half-height. The grid had a resolution of 64x64x48, with uniform grid spacing in the stream and spanwise directions, and an hyperbolic-tangent stretching in the normalwise direction, with a high number of grid points in the near-wall region. The simulations started from an interpolated profile of a fully developed DNS velocity field. Once an statisticaly steady state flow field was obtained, particles with $\tau_v^+ = 2$ where introduced uniformely distributed in the domain. Particles where tracked for $t^* = 100$, and both fluid and particles properties where averaged from $t^* = 50$ till $t^* = 100$.

On Fig. 6 are presented the mean streamwise velocity profiles for LES and DNS, at $Re_\tau = 180$. On the left hand side are the profiles for fluid only, while on the right hand side are also included the mean velocity profiles for the particles. Both plots show a very good agreement between the DNS and

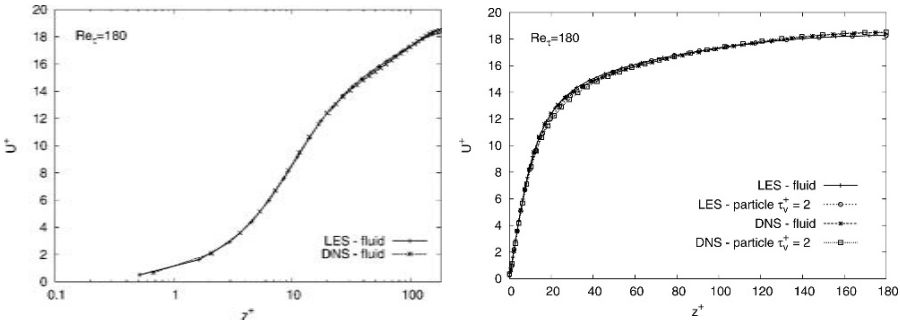

Fig. 6 Velocity profiles for LES and DNS for $Re_\tau = 180$

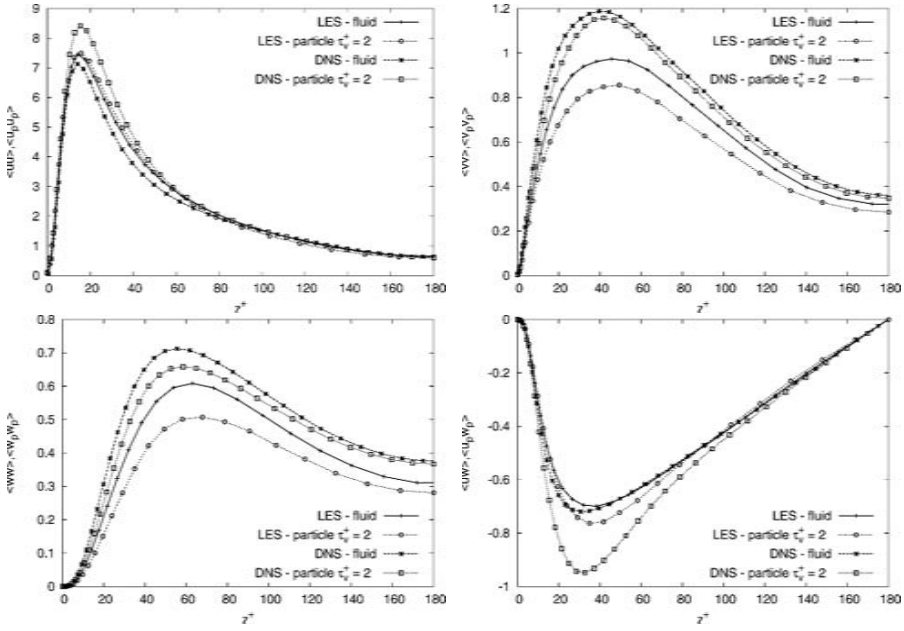

Fig. 7 Velocity fluctuation profiles for LES and DNS for $Re_\tau = 180$

LES profiles. In contrast to mean velocity field where the mean velocity for continuous and for dispersed part computed with DNS and LES shows good agreement stresses differs quite a lot. On Fig. 7 we can see that value obtained by LES are lower then for DNS for $< uu >$, $< vv >$ and $< ww >$ components for the fluid and for the particles. Level of fluctuations play key role in particle distributions and, as can be seen from Fig. 8, large eddy simulation results give much higher concentration level of particles close to the wall. Also, as can be seen on Fig. 8, the predicted slip velocity with LES is much higher than for DNS. This can be also cause by much smaller particle fluctuation.

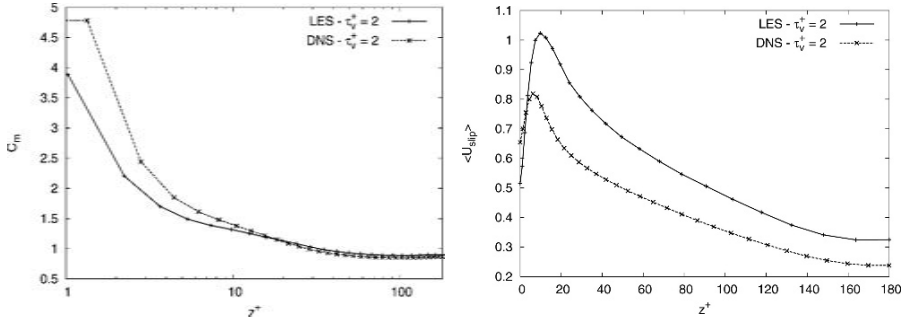

Fig. 8 Concentration profiles and slip velocity for $Re_\tau = 180$

4 Conclusion

We extended the Eulerian-Lagrangian point-particle LES/DNS approach in order to to study particle transport and heat transport in wall-bounded turbulent flow and to verify possibility of using LES in particle laden flow. Several statistical quantities for particle velocity, temperature and concentrations and flow-particle correlations for the correlations between continuous-phase and dispersed phase were obtained from the calculations. All results for the fluid phase (mean fluid velocity, mean temperature and correlations) show a good agreement with results obtained by other researchers using DNS/LES. The qualitative analysis of the turbulence and particle structures shows streaky patterns for the hydrodynamics and indicates how these patterns are associated with the patterns for the temperature of the particles. Particles tends to be highly concentrated in the region close to the wall but with increasing Reynolds number concentrations of particles in the region close to the wall does not increase. Particles agglomerate in form of long strikes. This behaviour knows as preferential concentration is very strong close to the wall but it can be also observed in whole domain. It has been shown that mean temperature of the particle is much smaller than temperature of the fluid. This occurs for all particles and also very near the wall and even on the wall. Mean streamwise velocity fluctuation in the boundary layer is different for the fluid and for the particle, and decorrelates with increasing time response opposite effect has been seen for mean wall-normal component which value for particles is smaller then for the fluid and its value for particles decrease with increasing response time. This affects the velocity-temperature correlations which are proportional to the turbulent heat fluxes. The heat flux transported by the particles in the streamwise direction can be 50% larger (most heavy particles) compared to the fluid. It has been found same similarity between streamwise velocity fluctuation and temperature fluctuations. Distributions of the temperature close to the wall shows that temperature of particle and the temperature of the fluid can be shifted quite a lot. This difference can strongly affect many industrial and chemical processes.

Calculations with LES for particle laden flow is still perceived as open and further work is warranted on the effect of subgrid-scale fluid flow on particle motion. Particle motion similar to continuous phase for proper evaluation of key properties e.g. kinetic energy, preferential concentration, collision statistics, deposition velocity etc. required additional models which will take into account not only local but also global structure of particles. Regarding the treatment of the dispersed phase, model for the residual fluid velocity along particle trajectories can be one of solution.

Acknowledgements

This research was supported by project COST P20 258/2006

References

1. Eaton JK, Fessler J (1994) Int J Multiphase Flows 20:169–209
2. Young JB, Leeming A (1997) J Fluid Mech 340:129–159
3. Sergeev YA, Johnson RS, Swailes DC (2002) Phys Fluids 14:1042–1055
4. Soldati A, Andreussi P (1996) Chem Eng Sci 51:353–363
5. Maxey MR, Riley JK (1983) Phys Fluids A 26:883–889
6. Kulick JD, Feesler JR, Eaton JK (1994) J Fluid Mech 277:109–121
7. Fessler J, Eaton JK (1994) Int J Multiphase Flows 20: 169–209
8. Chung J, Koch DL, Rani SL (2005) J Fluid Mech 536:219–227
9. Wang Q, Squires KD (2001) J Multiphase Flow 22:667–683
10. Hetsroni G, Rozenblit R, Yarin LP (1997) Int J Heat Mass Transfer 40:2201–2217
11. Hetsroni G, Mosyak A, Pogrebnyak E (2002) Int J Multiphase Flow 28:1873–1894
12. Subramanian NS, Rao DP, Gopich T (1973) Inc Eng Chem Fund 12: 479–482
13. Rashidi M, Hetsroni G, Banerjee S (1990) Int J Multiphase Flow 16:953–965
14. Kaftori D, Hetsroni G, Banerjee S (1995) Phys Fluids A 7:1095–1106
15. Chagras V, Oesterle B, Boulet P (2005) Int J Heat Mass Transfer 48:1649–1661
16. Wang Q, Squires KD (1996) Phys Fluids 8:1207–1223
17. Armenio V, Piomelli U, Fiorotto V (1999) Phys Fluids 11:3030–3042
18. Portela LM, Cota P, Olemans RVA (2002) Powder Techn 125:149–157
19. Portela LM, Oliemans RVA (2003) Int J Num Fluids 43:1045–1065
20. Moin P, Kim J (1982) J Fluid Mech 118:341–377
21. Eggels JGM (1994) PhD thesis, Laboratory for Aero & Hydrodynamics, Delft University of Technology
22. Kasagi N (1998) Int J Heat Fluid Flow 19:125–134
23. Moser RD, Kim J, Mansour NN (1999) Phys Fluids 11:943–945
24. Kawamura Laboratory (2006) Direct Numerical Simulation DATABASE for Turbulent flow `http://murasun.me.noda.tus.ac.jp`

Lagrangian Tracking of Heavy Particles in Large-Eddy Simulation of Turbulent Channel Flow

Maria-Vittoria Salvetti[1], Cristian Marchioli[2], and Alfredo Soldati[2]

[1] Dipartimento di Ingegneria Aerospaziale, Università di Pisa, 56122 Pisa, Italy
mv.salvetti@ing.unipi.it
[2] Centro Interdipartimentale di Fluidodinamica e Idraulica and Dipartimento di Energetica e Macchine, Università di Udine, 33100 Udine, Italy
cristian.marchioli@uniud.it, soldati@uniud.it

Abstract. The problem of assessing accurate Eulerian-Lagrangian modeling of heavy particle dispersion in Large Eddy Simulation (LES) is addressed. This issue is investigated in a systematic way by performing a priori and a posteriori LES coupled with Lagrangian particle tracking of fully developed channel flow, in which different grid resolutions and different values of the particle response time are considered. The accuracy in the prediction of the particle velocity statistics, near wall accumulation (turbophoresis) and preferential concentration is assessed trough comparison against DNS data. Both a priori and a posteriori tests indicate that turbophoresis and particle segregation can not be accurately predicted without introducing a model in the particle motion equations, also for particles having a response time much larger than the scales non resolved in LES. Furthermore, the present results indicate that the reintroduction of the correct level of fluid and particle velocity fluctuations is not the only issue for a closure model for particle equations.

Keywords: Large-eddy simulation, Heavy particle dispersion, Turbulent channel flow

1 Introduction

The dispersion of particles with finite inertia in wall-bounded turbulent flows is characterized by phenomena such as non-homogeneous distribution, large-scale clustering and preferential concentration in the near-wall region due to the inertial bias between the denser particles and the lighter surrounding fluid.

Direct Numerical Simulation (DNS) together with Lagrangian particle tracking has been largely used to investigate and quantify these macroscopic phenomena, for instance in vertical turbulent pipe and channel flows. Clearly, DNS is limited to low Reynolds numbers, while the simulation of turbulent flows at higher Reynolds numbers can be tackled using Large-Eddy Simulation (LES). However, only the filtered fluid velocity is available from LES,

J. Meyers et al. (eds.), Quality and Reliability of Large-Eddy Simulations,

while the particle motion depends on the actual fluid velocity and, thus, a closure model for the particle motion equations should in principle be needed. Nonetheless, this point has received only little attention, especially if compared to the huge amount of work devoted to the closure problem in LES for the fluid dynamic part. In several previous LES of particle laden turbulent flows (see, e.g., [1, 2]) no SGS model was introduced in the particle motion equations, based on the assumption that the particle response time was large compared to the smallest timescale resolved in LES [2]. It was later shown that this assumption may lead to a certain degree of inaccuracy on the prediction of particle velocity statistics and concentration. In particular, the results obtained by Kuerten and Vreman [3] and by Kuerten [4] for turbulent dispersion of heavy particles in channel flow have shown that LES underestimates the tendency of particles to move towards the wall by the effect of turbulence (turbophoresis). To overcome this problem, a closure model for the particle equation of motion based on filter inversion or approximate deconvolution was used in turbulent channel flow [4] and in homogeneous turbulent shear flow. [5] An effort was also provided to establish criteria according to which the SGS modeling for particles could be judged necessary or not. In particular, Février *et al.* [6] have shown that LES filtering has an effect on particle motion which depends on the ratio of the particle size to the filtered spatial scales. For single particle statistics such as turbulent dispersion, Fede and Simonin [7] confirm that an explicit accounting of sub-grid fluid turbulence on particle transport is not required when the particle response time is much larger than the cut-off timescale of the sub-grid velocities. However, they show also that accumulation and collision phenomena are strongly influenced by sub-grid fluid turbulence even when the particle response time is up to $\mathcal{O}(10)$ times the Kolmogorov time scale.

Aim of the present study is to build on the work of Kuerten and Vreman [3] extending the analysis of Fede and Simonin [7] on the sub-grid turbulence effects on particle accumulation to turbulent channel flow, which presents the additional complexity of a solid wall and of turbulence strong anisotropy and non-homogeneity. The analysis is based on a systematic investigation on the importance of SGS effects on particle motion through a priori and a posteriori LES carried out for different particle inertia and different LES resolutions.

2 Physical Problem and Numerical Methodology

The flow into which particles are introduced is a turbulent channel flow of air (assumed to be incompressible and Newtonian) with density $\rho = 1.3\ kg\ m^{-3}$ and kinematic viscosity $\nu = 15.7{\times}10^{-6}\ m^2\ s^{-1}$. The reference geometry consists of two infinite flat parallel walls: the origin of the coordinate system is located at the center of the channel and x, y and z denote the streamwise, spanwise and wall-normal directions respectively. Periodic boundary conditions are imposed on the fluid velocity field in x and y, and no-slip boundary conditions

are imposed at the walls. The shear Reynolds number $Re_\tau = u_\tau h/\nu$, based on the shear (or friction) velocity, u_τ, and on the half channel height, h, is equal to 150. The shear velocity is defined as $u_\tau = (\tau_w/\rho)^{1/2}$, where τ_w is the mean shear stress at the wall. The corresponding bulk Reynolds number is $Re_b = u_b h/\nu = 2100$ based on the bulk velocity $u_b = 1.65\ m\ s^{-1}$. All variables considered in this study are reported in dimensionless form in wall units. Wall units are obtained combining u_τ, ν and ρ. The dimensions of the computational domain are $4\pi h \times 2h \times 2\pi h$, corresponding to $1885 \times 942 \times 300$ wall units in x, y and z respectively.

Particles with density $\rho_p = 1000\ kg\ m^{-3}$ are injected into the flow at concentration low enough to consider dilute system conditions (particle-particle interactions are neglected). The effect of particles, which are assumed pointwise, rigid and spherical, onto the turbulent field is also neglected (one-way coupling assumption). The motion of particles is described by a set of ordinary differential equations for particle velocity and position at each time step. For particles much heavier than the fluid ($\rho_p/\rho \gg 1$) it has been shown [8] that the only significant forces are Stokes drag and buoyancy and that Basset force can be neglected being an order of magnitude smaller. To the aim of minimizing the number of degrees of freedom by keeping the simulation setting as simplified as possible, the effect of gravity has also been neglected here. Thus, the following equations are obtained, in which only inertia is considered:

$$\frac{d\mathbf{x}}{dt} = \mathbf{v}\ , \qquad \frac{d\mathbf{v}}{dt} = -\frac{3}{4}\frac{C_D}{d_p}\left(\frac{\rho}{\rho_p}\right)|\mathbf{v}-\mathbf{u}|(\mathbf{v}-\mathbf{u})\ , \tag{1}$$

where $\mathbf{x}$ is the particle position, $\mathbf{v}$ the particle velocity, $\mathbf{u}$ the fluid velocity at the particle position and d_p is the particle diameter. The Stokes drag coefficient is computed as $C_D = \frac{24}{Re_p}(1 + 0.15Re_p^{0.687})$ where $Re_p = d_p|\mathbf{v}-\mathbf{u}|/\nu$ is the particle Reynolds number.

In this study both DNS and LES have been carried out. In both cases, a pseudo-spectral method is used, based on Fourier representations for the periodic streamwise and spanwise directions and on a Chebyshev representation for the wall-normal (nonhomogeneous) direction. A two level explicit Adams-Bashforth scheme for the non-linear terms, and an implicit Crank-Nicolson method for the viscous terms, were employed for time advancement. Further details of the method can be found in [9].

In DNS the computational domain has been discretized in physical space with $128 \times 128 \times 129$ grid points (corresponding to 128×128 Fourier modes and to 129 Chebyshev coefficients in the wavenumber space). This is the minimum number of grid points required in each direction to ensure that the grid spacing is always smaller than the smallest flow scale[1] and that the limitations imposed by the point-particle approach are satisfied.

[1] In the present flow configuration, the non-dimensional Kolmogorov length scale, η_K^+, varies along the wall-normal direction from a minimum value $\eta_K^+ = 1.6$ at the wall to a maximum value $\eta_K^+ = 3.6$ at the centerline. The grid resolution in

LES calculations have been performed on the same computational domain. Two computational grids have been considered: a *coarse* grid made of $32 \times 32 \times 65$ nodes and a *fine* grid made of $64 \times 64 \times 65$ nodes. For the closure of the LES equations, the dynamic eddy-viscosity model has been used [10].

In the a priori tests the Lagrangian tracking of particles is carried out starting from the filtered velocity fields, obtained through explicit filtering of the DNS velocity by means of either a cut-off or a top-hat filter. Both filters are applied in the homogeneous streamwise and spanwise directions in the wave number space. Three different filter widths have been considered, corresponding to a grid Coarsening Factor (CF) in each homogeneous direction of 2, 4 and 8 with respect to DNS. In the wall-normal direction data are not filtered, since often in LES the wall-normal resolution is DNS-like.

To calculate particle trajectories in the flow field, we have coupled a Lagrangian tracking algorithm with the DNS/LES flow solver. It discretizes Eq. (1) using 6th-order Lagrangian polynomials to interpolate fluid velocities at particle position; with this velocity the equations of particle motion are advanced in time using a 4th-order Runge-Kutta scheme. The timestep size used for particle tracking was chosen to be equal to the timestep size used for the fluid, $\delta t^+ = 0.045$; the total tracking time was, for each particle set, $t^+ = 1200$ in the a priori tests and $t^+ = 1800$ in the a posteriori tests. These simulation times are not long enough to achieve a statistically steady state for the particle concentration. At the beginning of the simulation, particles are distributed homogeneously over the computational domain and their initial velocity is set equal to that of the fluid at the particle initial position. Periodic boundary conditions are imposed on particles moving outside the computational domain in the homogeneous directions, perfectly-elastic collisions at the smooth walls were assumed when the particle center was at a distance lower than one particle radius from the wall. For the simulations presented here, large samples of 10^5 particles, characterized by different response times, were considered. The response time is defined as $\tau_p = \rho_p d_p^2/18\mu$ where μ is the fluid dynamic viscosity: when the particle response time is made dimensionless using wall variables, the Stokes number for each particle set is obtained as $St = \tau_p^+ = \tau_p/\tau_f$ where $\tau_f = \nu/u_\tau^2$ is the viscous timescale of the flow. Particles having response times corresponding to St =0.2, 1, 5, 25, 125 have been considered in this study. We remark here that, for the present channel flow configuration, the non-dimensional value of the Kolmogorov timescale, τ_K^+, ranges from 2 wall units at the wall to 13 wall units at the channel centerline [11]. Hence, if we rescale the particle response times using the local value of τ_K^+ near the centerline, where the flow conditions are closer to homogeneous and isotropic, we obtain Stokes numbers that vary from 10^{-2} to 10 and fall in the lower range of values considered in [7].

---

the wall-normal direction is such that the first collocation point is at $z^+ = 0.05$ from the wall, while in the center of the channel $\Delta z^+ = 3.7$

3 Particle Distribution in a Priori LES

We discuss here the influence of filtering on particle distribution for particles dispersed in a priori LES flow fields, i.e. filtered DNS fields. As described in Sec. 2, the cut-off and the top-hat filters have been used. As well known, the first one provides a sharp separation between resolved and non-resolved scales and can be considered the filter corresponding to a coarse spectral simulation, in which no explicit filtering is applied. Conversely, the top-hat filter is a smooth filter and, thus, it subtracts a significant amount of energy from the resolved scales. For each filter, three different filter widths have been considered. Figure 1 sketches a one-dimensional (streamwise) frequency spectrum obtained in DNS. Since particle dynamics in the viscous sublayer is controlled by flow structures with timescale τ_f around 25 and considering that this timescale corresponds to the circulation time of the turbulence structures in the buffer layer ($5 < z^+ < 30$) [12], we show the energy spectrum at $z^+ = 25$. The cut-off frequencies corresponding to each filter width are indicated as $\omega_{\text{cut}-\text{off}}^{\text{CF}=2}$, $\omega_{\text{cut}-\text{off}}^{\text{CF}=4}$ and $\omega_{\text{cut}-\text{off}}^{\text{CF}=8}$ in increasing order. Also shown (dot-dashed lines) are the estimated response frequencies which characterize each particle set considered in the a priori tests, these frequencies being proportional to $1/\tau_p$.

Figure 2 shows the particle root mean square (rms) fluctuations of the wall-normal velocity component obtained in the a priori tests with cut-off filter for the $St = 1$, the $St = 5$ and the $St = 25$ particles, respectively. The reference values obtained injecting the particles in the DNS flow velocity fields are also reported. All profiles were obtained averaging in time (from $t^+ = 450$ to $t^+ = 1200$) and space (over the homogeneous directions). It is apparent that filtering the fluid velocity has a large impact on the turbulent velocity fluctuations. As expected, particle velocity fluctuations are reduced in particular for the larger filter widths corresponding to coarser LES grids; for the

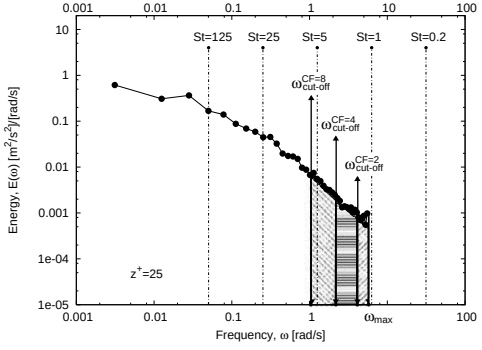

Fig. 1 One-dimensional (streamwise) frequency spectrum for turbulent channel flow, computed at $z^+ = 25$. The different cut-off frequencies, used to perform the a-priori tests, are indicated as $\omega_{\text{cut-off}}^{\text{CF}=2}$, $\omega_{\text{cut-off}}^{\text{CF}=4}$ and $\omega_{\text{cut-off}}^{\text{CF}=8}$, respectively

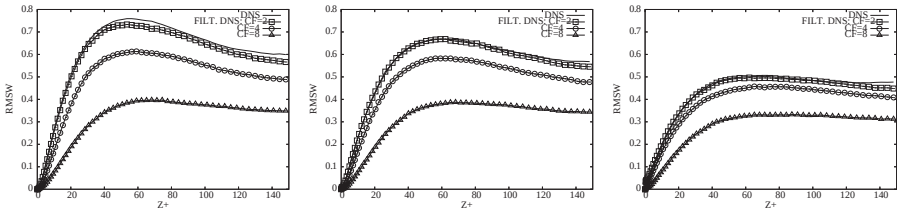

Fig. 2 Particle wall-normal velocity rms for a priori simulations (with cut-off filter). Left-hand panel: $St = 1$ particles, central panel: $St = 5$ particles, right-hand panel: $St = 25$ particles. CF indicates the LES grid coarsening factor with respect to the DNS grid: CF=2 (□), CF=4 (◯), CF=8 (△)

streamwise and spanwise components, not shown here for sake of brevity, the effect is the same. This is a consequence of the well known decrease of the flow velocity fluctuations due to filtering as felt by the particles, even if in a different measure depending on their inertia. Note that the effect of filtering is significant also on particles having characteristic response frequencies much lower than those removed by the filters (e.g. the $St = 25$ particles). Finally, for the cut-off filter, the underestimation of the particle fluctuations is a pure effect of the elimination of the SGS scales, since no energy is subtracted from the resolved ones. The results obtained with the top-hat filter (not shown here for brevity) are qualitatively similar, although, for a given filter width, the underestimation of the particle fluctuations is, as expected, larger for the top-hat filter than for the cut-off one. The reduction of the wall-normal velocity fluctuations near the wall for the a priori LES, shown in Fig. 2 is worth noting because it corresponds to a reduction of particle turbophoretic drift (namely, particle migration to the wall in turbulent boundary layers) and, in turn, to a reduction of particle accumulation in the near-wall region [3]. This is also shown in Fig. 3 where the near wall instantaneous particle concentration obtained in a priori LES is compared to the DNS one for different filter widths and different particle inertia. Concentration profiles shown here are taken at time $t^+ = 1200$: as mentioned, the particle tracking in a priori LES was not carried out long enough to reach a statistically-steady particle concentration at the wall. However, we checked many different time instants and, although the concentration values change, the trend is always the same as that shown in Fig. 3. It appears that, consistently with the results of Kuerten and Vreman, [3] filtering leads to a significant underestimation of the wall particle concentration, for all filter types and widths and for all particle sets considered in this study.

Finally, in Fig. 4 the particle segregation parameter, Σ_p, is plotted versus the particle Stokes number in two different regions of the channel: the channel centerline, where Σ_p has been computed in a fluid slab 10 wall unit thick centered at $z^+ = 150$, and in the near-wall region, where Σ_p has been computed in the viscous sublayer ($0 \leq z^+ \leq 5$). The segregation parameter (or

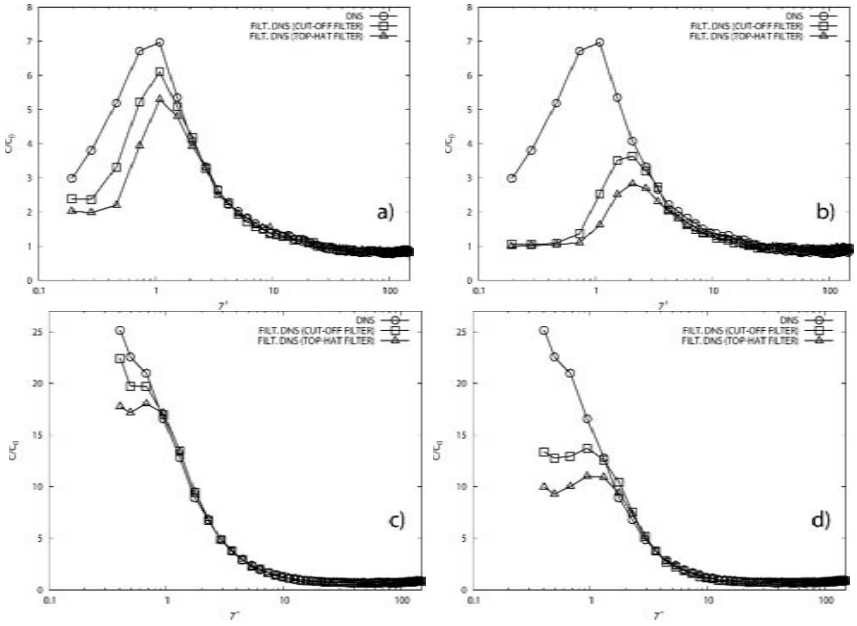

Fig. 3 Particle concentration in a-priori tests: (**a**–**b**) $St = 5$ particles, (**c**–**d**) $St = 25$ particles. DNS (◯), a-priori LES with cut-off filter (□), a-priori LES with top-hat filter (△). *Left-hand panels*: CF=2, *right-hand panels*: CF=4

maximum deviation from randomness)[13] is calculated as $(\sigma - \sigma_{Poisson})/m$, where σ and $\sigma_{Poisson}$ represent the standard deviations for the particle number density distribution and for the Poisson distribution, respectively. The particle number density distribution is computed on a grid containing N_{cell} cells of volume Ω_{cell} covering the entire computational domain. The parameter m is the mean number of particles in one cell for a random uniform particle distribution [13]. The drawback of this method is the dependence of Σ_p on the cell size. To avoid this problem, we computed the particle number density distribution for several values of Ω_{cell} and we kept only the largest value of Σ_p [6]. First, as found in previous studies [12], a peak of Σ_p occurs for $St \simeq 25$ and preferential concentration falls off on either side of this *optimum* value. As shown for instance in Fig. 3, $St = 25$ particles are thus the most responsive to the near-wall turbulent structures. When an explicit filter is applied, particle segregation is underpredicted severely in all considered cases, especially near the wall. Note that this underestimation is significant also for the smallest filter width, for which the reduction of particle fluctuations was relatively small (see Fig. 2).

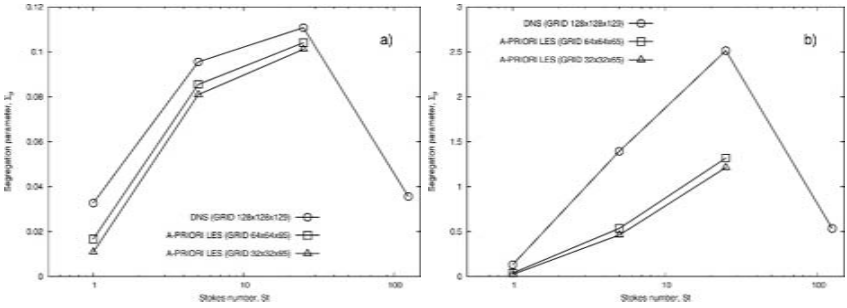

Fig. 4 Particle segregation, Σ_p, versus particle Stokes number, St, in turbulent channel flow: comparison between DNS (◯), a-priori LES on the fine $64 \times 64 \times 65$ grid (□) and a-priori LES on the coarse $32 \times 32 \times 65$ grid (△). A-priori results are relative to the cut-off filter. (**a**) channel centerline ($145 \leq z^+ \leq 150$), (**b**) near-wall region ($0 \leq z^+ \leq 5$)

4 Particle Distribution in a Posteriori LES

In this Section, we will discuss the behavior of particles dispersed in LES flow fields. As mentioned in Section 2, two different LES grids have been used. In these a posteriori tests, different sources of errors are present in addition to the filtering effects discussed in Section 3, viz. the errors due to *(i)* the SGS modeling for the fluid phase, *(ii)* the numerical discretization of the fluid governing equations and *(iii)* the interpolation in the Lagrangian particle tracking. For the used pseudo-spectral discretization the numerical error should plausibly be negligible. As for interpolation, a 6th-order interpolation scheme is used. Although we did not carry out a sensitivity study, the analysis in Kuerten and Vreman [3] indicates that the interpolation error should remain small, even if it may introduce an additional smoothing. Thus, we believe that the main source of difference with the a priori tests is represented by the SGS model closing the governing equations for the fluid phase. As in the a priori tests, no closure model is used in the equations of particle motion. In order to asses the quality of the LES for the fluid phase, Fig. 5 compares the streamwise and wall-normal rms of the fluid velocity components obtained in LES to the reference DNS values. For the more resolved LES, a good agreement with DNS is obtained and, hence, this can be considered as a *well-resolved* LES for the fluid phase. Conversely, in the coarser LES significant errors are found in the prediction of the fluid-phase velocity fluctuations and, thus, errors in the Lagrangian particle tracking are anticipated. The effect of the SGS modeling error is clearly visible if the values obtained for the coarser grid are compared with those of the a-priori tests in Fig. 2 for a corresponding coarsening factor (CF=4). Indeed, in the a posteriori LES, the introduction of the SGS model tends to counteract the decrease of the fluid velocity fluctuations due to filtering; in the coarser case this leads to an overestimation of the rms of the streamwise and wall-normal velocity components. This overestimation

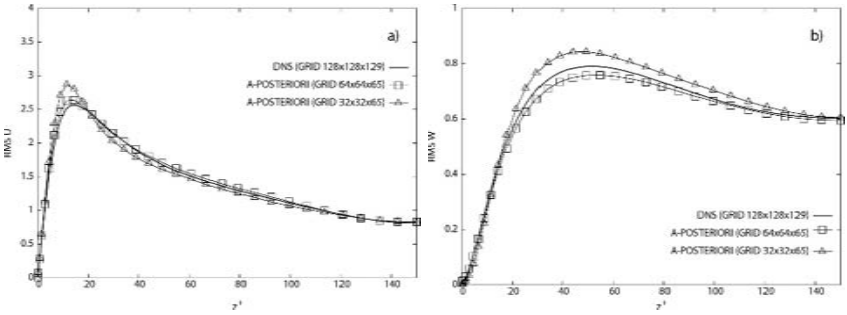

Fig. 5 Fluid velocity rms: comparison between DNS (*solid line*), a-posteriori LES on the fine $64 \times 64 \times 65$ grid (□) and a-posteriori LES on the coarse $32 \times 32 \times 65$ grid (△). (**a**) streamwise, (**b**) wall-normal velocity components

is a rather well-known behavior of coarse LES, especially for the rms of the streamwise component. Nonetheless, it is worth remarking that in actual LES the fluid velocity fields in which the particles are dispersed are not always characterized by a lack of fluctuations, as it happens in the idealized context of a priori tests. As previously mentioned, the dynamic eddy-viscosity model [10] was used to close the LES equations for the fluid phase. We also carried out LES simulations with the Smagorinsky model, but, as expected, the results were generally less accurate than those obtained with the dynamic SGS model for a fixed resolution: hence they are not shown or discussed here for sake of brevity.

In Fig. 6 the streamwise and wall-normal rms of the different particle sets obtained in LES are compared with the reference DNS data. A good agreement with DNS is obtained in the more resolved LES for all the considered particle inertia, while for the coarser simulation significant discrepancies are found. Note that in the coarse case, the rms of the wall-normal velocity component are overestimated for all the considered particle sets, as previously observed also for the fluid phase. In spite of the differences in the fluid and particle velocity fluctuations observed in a priori and a posteriori tests, the underestimation of particle concentration at the wall, already observed in the a priori tests (see Section 3), is also found in a posteriori LES, for all considered resolutions and particle sets. This is shown, for instance, by the instantaneous particle concentration profiles of Fig. 7. The same is for the underprediction of the particle preferential concentration (see Fig. 8). It is worth noting that the errors on the quantitative prediction of both particle segregation and near-wall accumulation are large also for the well-resolved LES, in which the level of fluid and particle velocity fluctuations is rather well predicted. This indicates that, in order to obtain acceptable predictions for near-wall accumulation and particle segregation, the reintroduction of the correct level of velocity fluctuations is not the only issue to devise a closure model for the particle equations. Finally, in the a posteriori LES the segregation parameter, Σ_p, was

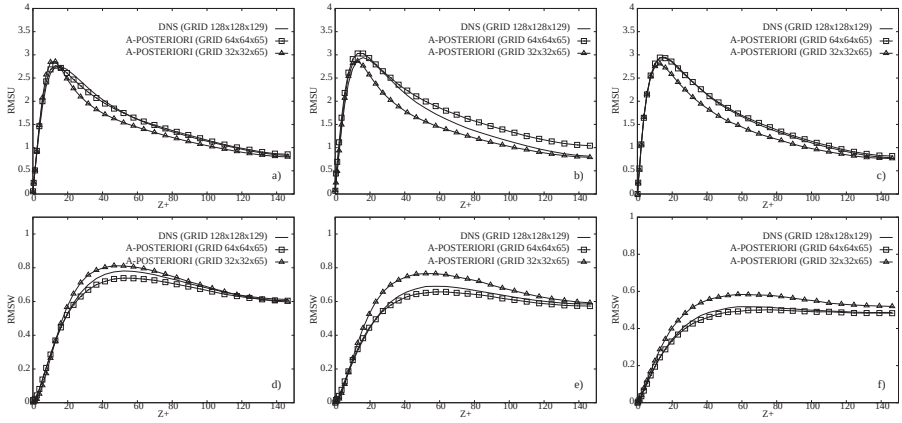

Fig. 6 Particle velocity rms: comparison between DNS (*solid line*), a-posteriori LES on the fine $64 \times 64 \times 65$ grid ($\square$) and a-posteriori LES on the coarse $32 \times 32 \times 65$ grid ($\triangle$): (**a**–**c**) streamwise component, (**d**–**f**) wall-normal component. *Left-hand panels*: $St = 1$ particles, *central panels*: $St = 5$ particles, *right-hand panels*: $St = 25$ particles

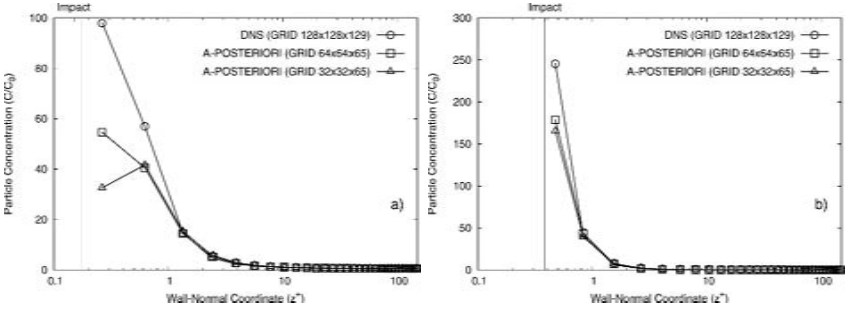

Fig. 7 Particle concentration in a-posteriori tests: comparison between DNS ($\bigcirc$), a-posteriori LES on the fine $64 \times 64 \times 65$ grid ($\square$) and a-posteriori LES on the coarse $32 \times 32 \times 65$ grid ($\triangle$). (**a**) $St = 5$ particles, (**b**) $St = 25$ particles. The vertical solid line in each diagram indicates the position where the particles hit the wall (*Impact*)

also computed for $St = 125$ particles (see Fig. 8). For this set of particles, the values obtained in both LES simulations are higher than those computed in DNS. In their a priori tests for homogeneous and isotropic turbulence, Fede and Simonin [7] found that for particles having lower inertia than a given threshold value the effect of filtering was to decrease the segregation parameter, while for particles of larger inertia the segregation was conversely increased. From our results, this scenario seems to hold also in a posteriori LES and in near wall turbulence.

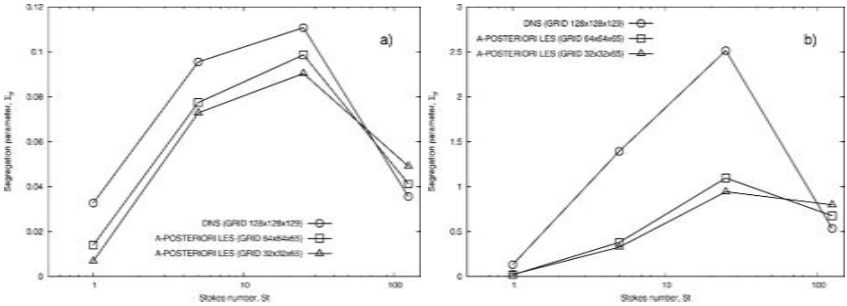

Fig. 8 Particle segregation, Σ_p, versus particle Stokes number, St, in turbulent channel flow: comparison between DNS (◯), a-posteriori LES on the fine $64 \times 64 \times 65$ grid (□) and a-posteriori LES on the coarse $32 \times 32 \times 65$ grid (△). (**a**) channel centerline ($145 \leq z^+ \leq 150$), (**b**) near-wall region ($0 \leq z^+ \leq 5$)

5 Concluding Remarks

The problem of assessing an accurate modeling of heavy particle dispersion in Large Eddy Simulation has been investigated by means of a priori and a posteriori LES coupled with Lagrangian particle tracking of fully developed channel flow. Different grid resolutions and different values of the particle response time have been considered. The accuracy in the prediction of the particle velocity statistics, near wall accumulation and preferential segregation have been assessed through comparison against DNS data.

Consistently with the results of Kuerten and Vreman [3] the effect of pure filtering in a priori tests is to decrease the fluid velocity fluctuations and, in turn, the particle velocity fluctuations, although by different amounts according to particle inertia. This leads to a severe underestimation of particle accumulation at the wall. Extending the analysis to particle segregation, quantified by a macroscopic indicator, we found that filtering leads to a significant underestimation of particle preferential concentration. In conclusion, as also found in previous studies [3, 4, 5], it appears that a closure model is needed for the particle equations. In a posteriori LES simulations, we have found that the dynamic SGS model, used to close the problem for the fluid phase, is able to reintroduce a correct level of fluid velocity fluctuations when a rather fine grid (twice the DNS grid spacing in each direction) is used; the particle velocity fluctuations are also in good agreement with those obtained in DNS. Conversely, significant discrepancies are observed with respect to the DNS reference values when a coarser resolution (typical of LES applications) is used. We observe that the velocity fluctuations of both phases are overestimated, in contrast with the a priori tests. Despite these differences, particle wall accumulation and local segregation are always severely underestimated (except for the largest considered particles ($St = 125$)). This indicates that the reintroduction of the correct level of fluid and particle velocity fluctuations is not enough to have an accurate prediction of near-wall accumulation

and local particle segregation. It may be argued that, since these phenomena are governed by complex interactions between the particles and the flow structures, the reitroduction of the correct amount of higher order moments of the velocity fluctuations for both phases is probably the key point to develop these models.

References

1. Uijttewaal WSJ, Oliemans RWA (1996) Particle dispersion and deposition in direct numerical and large eddy simulations of vertical pipe flows. Phys Fluids 8:2590–2604
2. Armenio V, Piomelli U, Fiorotto V (1999) Effect of the subgrid scales on particle motion. Phys Fluids 11:3030–3042
3. Kuerten JGM, Vreman AW (2005) Can turbophoresis be predicted by large-eddy simulation? Phys Fluids 17, Art no 011701
4. Kuerten JGM (2006) Subgrid modeling in particle-laden channel flow. Phys Fluids 18, Art no 025108
5. Shotorban B, Mashayek F (2005) Modeling subgrid-scale effetcs on particles by approximate deconvolution. Phys Fluids 17, Art no 081701
6. Février P, Simonin O, Squires KD (2005) Partitioning of particle velocities in gas-solid turbulent flows into a continuous field and a spatially-uncorrelated random distribution: theoretical formalism and numerical study. J Fluid Mech 528:1–46
7. Fede P, Simonin O (2006) Numerical study of the subgrid fluid turbulence effects on the statistics of heavy colliding particles. Phys Fluids 18:045103
8. Elghobashi SE, Truesdell GC (1992) Direct simulation of particle dispersion in a decaying isotropic turbulence. J Fluid Mech 242:655–700
9. Pan Y, Banerjee S (1996) Numerical simulation of particle interactions with wall turbulence. Phys Fluids 8:2733–2755
10. Germano M, Piomelli U, Moin P, Cabot WH (1991) A dynamic subgrid-scale eddy viscosity model, Phys Fluids 3:1760–1765
11. Marchioli C, Picciotto M, Soldati A (2006) Particle dispersion and wall-dependent fluid scales in turbulent bounded flow: implications for local equilibrium models, J Turbul 27, Art no 60
12. Picciotto M, Marchioli C, Soldati A (2005) Characterization of near-wall accumulation regions for inertial particles in turbulent boundary layers. Phys Fluids 17, Art no 098101
13. Rouson DW, Eaton JK (2001) On the preferential concentration of solid particles in turbulent channel flow. J Fluid Mech 428:149–169

Large-Eddy Simulation of Particle-Laden Channel Flow

J. G. M. Kuerten

Department of Mechanical Engineering, Technische Universiteit Eindhoven, P.O. Box 513, 5600 MB Eindhoven, The Netherlands. j.g.m.kuerten@tue.nl

Abstract. Large-eddy simulation of particle-laden turbulent channel flow is investigated for several subgrid models and Stokes numbers with the objective to investigate the accuracy of the subgrid models studied with respect to particle behavior. It is shown that the wall-normal particle velocity and particle velocity fluctuations are reduced compared to DNS, if the filtered fluid velocity calculated in the LES is used in the particle equation of motion. Better agreement with DNS is obtained if an inverse filtering model is incorporated into the particle equation. The results of the approximate deconvolution model (ADM) agree better with DNS results than results of the dynamic eddy-viscosity model and the Smagorinsky model.

Keywords: Particle-laden flow, Large-eddy simulation

1 Introduction

Particle-laden turbulent flows often occur in industry and nature. Forces exerted by the fluid influence the particles. The most important of these are drag and lift forces. If the particles are small compared to the smallest length scales of the fluid flow, a point-particle description can be employed [1]. The fluid is then modeled as a continuous phase, while for each particle an equation of motion is imposed. For simple geometries and low Reynolds number all relevant length and time scales of the flow and particles can be resolved within this approach in direct numerical simulation (DNS).

For flows at higher Stokes numbers DNS can no longer be applied. Therefore, in the last decade, particle-laden flows have also been studied by large-eddy simulation (LES). However, the equation of motion of a particle contains the fluid velocity and in an LES only the resolved part of the fluid velocity is known. If the particle relaxation time is large compared to the Kolmogorov time scale, turbulence hardly has an effect on the particle motion and the filtered fluid velocity can be used in the particle equation of motion without incorporating a model for the subgrid scales [2]. Armenio et al. [3] studied the effects of the disregard of the subgrid scales in the particle equation of

J. Meyers et al. (eds.), Quality and Reliability of Large-Eddy Simulations,

motion by *a priori* and *a posteriori* simulation of particle-laden channel flow, but they restricted to quantities and test cases where the effect of the subgrid scales is small.

In [4] it has been shown that a phenomenon as turbophoresis, where particles move towards the walls of a channel by the effect of the turbulence, cannot accurately be predicted if the subgrid scales in the fluid velocity are disregarded in the particle equation of motion. The results depend on the subgrid model applied, but even for an 'optimal' subgrid model, a substantial difference between the DNS and LES results remains, especially for particle relaxation times of the same order as the Kolmogorov time. It has also been shown that results improve in case a defiltered fluid velocity [5] is used in the particle equation of motion and an adequate subgrid model, such as the dynamic eddy-viscosity model [6], is applied.

In the present paper several subgrid models in LES of particle-laden channel flow will be studied: Smagorinsky's eddy-viscosity model [7], the dynamic eddy-viscosity model [6] and the approximate deconvolution model (ADM) [8]. Simulations will be performed with and without the defiltering procedure. Results will be compared with DNS results on a fine grid, on which all relevant length scales are resolved, and on a coarse LES grid, which serves as an LES without subgrid model.

In the next section, the equations of motion and numerical methods for particles and fluid are formulated. In Section 3 results are shown and explained for DNS and LES, including results obtained with the defiltering procedure. Finally, in Section 4 conclusions are stated and discussed.

2 Governing Equations and Numerical Method

In this section the equations of motion and numerical methods for fluid and particles are described. Moreover, the defiltering procedure is elucidated.

2.1 Fluid

The flow considered in this paper is incompressible turbulent channel flow. The Navier-Stokes equation is solved in rotation form [9]

$$\frac{\partial \mathbf{u}}{\partial t} + \omega \times \mathbf{u} + \nabla P = \nu \Delta \mathbf{u} + \mathbf{F}, \tag{1}$$

where $\omega = \nabla \times \mathbf{u}$ is the vorticity, $P = \frac{p}{\rho_f} + \frac{1}{2}\mathbf{u}^2$, ν is the fluid kinematic viscosity, p the fluctuating part of the pressure and ρ_f is the fluid density. Finally, $\mathbf{F}$ is the driving force, chosen constant in time and space. In that way the time-averaged Reynolds number based on the friction velocity u_τ, $Re_\tau = \frac{Hu_\tau}{\nu}$ can be specified, where H is half the channel height.

In the DNS all relevant length- and time scales are resolved. In the streamwise and spanwise directions periodic boundary conditions are applied. Therefore, the use of a pseudo-spectral method is very convenient. In the two periodic directions a Fourier-Galerkin approach is applied, whereas a Chebyshev-collocation method is adopted in the wall-normal direction.

The time integration is performed with a combination of the second-order accurate implicit Crank-Nicolson method for the viscous and pressure terms and a third-order accurate compact-storage explicit Runge-Kutta method for the other terms. This makes the total method second-order accurate. The nonlinear term is calculated by transforming from Fourier space to real space and back with Fast Fourier Transform. In order to prevent aliasing errors the 3/2-rule is applied in the periodic directions. The velocity field is made divergence-free within machine accuracy following the approach proposed by Kleiser and Schumann [10] applied to the collocation approximation [9].

The computational domain has a size $2H$ in the wall normal direction, $4\pi H$ in streamwise direction and $2\pi H$ in spanwise direction. In the DNS, $Re_\tau = 150$, the number of Chebyshev collocation points equals 129 and 128 Fourier modes are used in both periodic directions. This makes the dimensions of the channel in wall units equal to 300 in wall-normal direction, 1885 in streamwise direction and 942 in spanwise direction. Moreover, $\Delta x^+ = 14.7$, $\Delta z^+ = 7.4$ and Δy^+ ranges between 0.045 at the walls and 3.7 at the center of the channel. Throughout the paper x, y and z are used for streamwise, wall-normal and spanwise direction, respectively. The simulation was started from Poiseuille flow, onto which several of the least stable two- and three-dimensional disturbances according to linear stability theory were superposed. Due to nonlinear interactions transition to turbulence occurs and after a large number of time steps a state of fully-developed turbulence appears.

In the LES calculations an equation for a spatially filtered fluid velocity $\overline{\mathbf{u}}$ is solved, where

$$\overline{\mathbf{u}}(\mathbf{x}) = \int_V G(\mathbf{x};\mathbf{y})\mathbf{u}(\mathbf{y})d^3y. \tag{2}$$

The integral extends over the whole domain and $G(\mathbf{x};\mathbf{y})$ is a filter function, e.g. the top-filter or a spectral cut-off filter. Filtering of the Navier-Stokes equation for the fluid velocity leads to the turbulent stress tensor $\tau_{i,j}$ given by

$$\tau_{ij} = \overline{u_i u_j} - \overline{u}_i \overline{u}_j, \tag{3}$$

which depends on the unfiltered fluid velocity and hence is unknown in an LES. Here it is assumed that the filter operator commutates with all derivatives and that the viscosity is constant. Otherwise, more subgrid terms appear in the filtered Navier-Stokes equation. In a large-eddy simulation the turbulent stress tensor is replaced by a subgrid model which is expressed in terms of the known filtered fluid velocity.

In this work three subgrid models are considered: Smagorinsky's eddy-viscosity mnodel [7], the dynamic eddy-viscosity model [6] and the

approximate deconvolution model (ADM) [8]. Moreover, for comparison purposes calculations on a coarse LES grid without subgrid model are performed. In the dynamic eddy-viscosity model

$$\tau_{ij} = -C_d \Delta^2 |S(\overline{\mathbf{u}})| S_{ij}(\overline{\mathbf{u}}), \tag{4}$$

where S_{ij} is the rate of strain tensor given by

$$S_{ij}(\mathbf{u}) = \frac{\partial u_i}{\partial x_j} + \frac{\partial u_j}{\partial x_i}$$

and $|S(\mathbf{u})| = \frac{1}{2} S_{ij}(\mathbf{u}) S_{ij}(\mathbf{u})$. Furthermore Δ is the typical width of the filter. In the present application of channel flow the filter width in each direction is taken equal to the grid size and

$$\Delta = (\Delta_x \Delta_y \Delta_z)^{1/3}$$

is taken as the typical filter width, which depends on the wall-normal coordinate. Finally, the coefficient C_d is dynamically adjusted to the local structure of the flow. The coefficient is determined by the introduction of a test filter with filter width 2Δ and application of the Germano identity [6]. Following Lilly [11], the dynamic coefficient is averaged over the homogeneous directions. As a test filter the top-hat filter is applied. In the Smagorinsky model the coefficient C_d in (4) is replaced by a constant C_s^2. In order to avoid excessive damping near the walls the Smagorinsky constant is reduced near the walls according to:

$$C_S = C_{S,0}(1 - \exp(-y^+/A^+)),$$

where y^+ is the distance to the nearest wall in wall coordinates, $C_{S,0} = 0.1$ and $A^+ = 26$.

The basis of ADM is replacement of the unfiltered velocity in τ_{ij} by an approximate deconvolution of the filtered velocity, according to:

$$\tau_{ij} = \overline{u_i^* u_j^*} - \overline{u}_i \overline{u}_j, \tag{5}$$

where

$$u_i^* = Q_N \overline{u}_i = \sum_{k=0}^{N} (I - G)^k \overline{u}_i \tag{6}$$

and G is the filter kernel. The filter and the implementation of the model are the same as in the original paper by Stolz et al. [8]. In this work the choice of $N = 5$ is made as well. In order to represent the effects of the subgrid scales an extra regularization term is added to the Navier-Stokes equation:

$$\frac{\partial \overline{\mathbf{u}}}{\partial t} + \overline{\omega^* \times \mathbf{u}^*} + \nabla \overline{P} = \nu \Delta \overline{\mathbf{u}} + \mathbf{F} - \chi (I - Q_N G) \overline{u}, \tag{7}$$

where χ is dynamically adjusted in such a way that the kinetic energy contained in the smallest resolved scales remains constant in time [8].

The numerical method used for the LES is the same as for the DNS. The turbulent stress tensor is treated in the same way as the other nonlinear terms in the Navier-Stokes equation. For the ADM de-aliasing is also performed in the wall-normal direction. In the LES 33 Chebyshev collocation points in the wall-normal direction are used, 32 Fourier modes in streamwise and 64 in spanwise direction. Since the computational domain is the same as in the corresponding DNS, $\Delta x^+ \approx 59$ and $\Delta z^+ \approx 15$, which satisfies the requirements of a resolved LES (see for details Piomelli and Balaras [12]). This resolution corresponds with $\Delta/h_{DNS} = 4$ in the wall-normal and streamwise directions and $\Delta/h_{DNS} = 2$ in the spanwise direction. The LES simulations are started from filtered DNS fields. After some time a statistically stationary LES solution is obtained.

2.2 Particles

Particles are described by an equation of motion for each particle. In the present work only the drag force will be considered, which has been justified by Armenio et al. [13]. Particle-particle interaction and the effect of particles on the fluid will be disregarded. This is justified for the low particle concentrations considered in this paper. Hence, the equation of motion for a particle i with instantaneous position $\mathbf{x}_i$, velocity $\mathbf{v}_i$ and mass m_i reads [1]:

$$\frac{d\mathbf{v}_i}{dt} = \frac{\mathbf{u}(\mathbf{x}_i, t) - \mathbf{v}_i}{\tau_p}(1 + 0.15Re_p^{0.687}), \tag{8}$$

where $\mathbf{u}(\mathbf{x}_i, t)$ is the fluid velocity at the position of the particle. The particle relaxation time τ_p quantifies the drag by the fluid on the particle and is given by: $\tau_p = \rho_p d_p^2/(18\rho_f \nu)$, where d_p is the particle diameter. The standard drag correlation for particles with particle Reynolds number Re_p not small compared to 1 is applied [14].

In the low Reynolds number simulations shown here, $\rho_p/\rho_f = 769.23$ and three different diameters are investigated: $d_{p,1}/H = 1.02 \times 10^{-3}$, $d_{p,2}/H = 2.28 \times 10^{-3}$ and $d_{p,3}/H = 5.10 \times 10^{-3}$. This corresponds to Stokes numbers, defined as $St = \tau_p^+ = \tau_p u_\tau^2/\nu$, of 1, 5 and 25. The lowest particle relaxation time studied is lower than the smallest turbulent time scale throughout the channel. Hence, these particles are affected by all time scales present in the flow and disregard of the subgrid scales will influence the particle behavior in the whole channel. The highest particle relaxation time studied is larger than the smallest time scale of the flow, both in the DNS and in the LES. This implies that the effect of disregarding the subgrid scales in the fluid velocity will not influence the results much, since these scales hardly affect the particles in this case. Particles with $St = 5$, on the other hand, have a particle relaxation time equal to the channel-averaged Kolmogorov time. Especially

around $y^+ = 25$ the Kolmogorov time is close to the particle relaxation time, and the effect of the disregard of the subgrid scales in the fluid velocity will be appreciable. This is exactly the region where the turbophoretic velocity, which leads to particle accumulation at the walls, is largest.

In the particle-laden simulations (8) is solved with the second-order accurate Heun method. In order to find the fluid velocity at the particle position, an interpolation has to be made. In this work, in the two periodic directions fourth-order Lagrange interpolation [15], and in the wall-normal direction, fourth-order Hermite interpolation is applied. The particle-laden simulations start from a statistically stationary state of fully-developed turbulence with 100,000 particles of each Stokes number randomly distributed uniformly over the channel. A particle collides elastically with the walls when it reaches one of the walls within a distance equal to its radius. If a particle leaves the computational domain through one of the periodic boundaries, its position is still tracked and the fluid velocity at the particle position follows from periodic continuation of the velocity field.

Solution of (8) gives accurate results in DNS, but in the particle-laden LES simulations the fluid velocity present in (8) is unknown and simulations with the fluid velocity replaced by the filtered fluid velocity result in substantial deviations in statistical particle quantities compared to DNS. It is, however, possible to decrease the subgrid errors in the LES results by retrieving part of the subgrid contributions to the fluid velocity by inverse filtering. Inverse filtering frequently occurs in the literature of LES [8, 5, 16], where it is used to model the turbulent stress tensor. It has often been successful provided that a dissipation term is added to control the extra fluctuations introduced by defiltering. Recently, Kuerten and Vreman [4] and later Shotorban and Maskayek [17] showed that defiltering of the fluid velocity also yields a useful subgrid model in the particle equation of motion.

In the present work the defiltering depends on the subgrid model and is carried out in the following way. In the dynamic eddy-viscosity model a filter only appears explicitly as test filter. Assuming that the primary filter has the same shape, we adopt the top-hat filter with filter width Δ as primary filter. The inversion is performed in Fourier space in the two periodic directions, whereas in the wall-normal direction the inverse is approximated with a Taylor series up to second order in the filter width. (Note that this corresponds to $N = 1$ in the approximate deconvolution proposed by Shotorban and Mashayek [17], who applied a Gaussian filter.) At the walls the defiltered velocity is set equal to zero. In the ADM simulations the deconvolved velocity field $\mathbf{u}^*$ defined in (6) is used with $N = 5$, just as in the filtered Navier-Stokes equation. In simulations with the Smagorinsky subgrid model the same inverse filter is used as in the dynamic eddy-viscosity model.

3 Results

In this section results of the particle simulations are presented. DNS results will be compared with LES results for the three subgrid models, both with the filtered and with the defiltered fluid velocity adopted in (8). Also results without subgrid model are included. A good subgrid model should yield results better than without subgrid model. The discussion will be restricted to three quantities: mean particle velocity, particle concentration and particle velocity fluctuations. The latter quantity is of interest for particle dispersion, whereas the other two are directly related to the phenomenon of turbophoresis.

3.1 Mean Wall-Normal Particle Velocity

Although the mean wall-normal fluid velocity component equals zero, the mean wall-normal particle velocity is initially unequal to zero. This phenomenon leads to turbophoresis: the accumulation of particles near the walls and has been measured [18] and numerically predicted in DNS of turbulent channel and pipe flow [19, 20]. This particle transport mechanism is caused by the inhomogeneity of the turbulent velocity fluctuations [21, 22].

In order to quantify turbophoresis, in Fig. 1 the mean relative velocity is shown for all simulations for $St = 1$. All results have been averaged over time until $t^+ = 16,000$ and over the two homogeneous directions. A first observation from these figures is that the LES results without defiltering underpredict

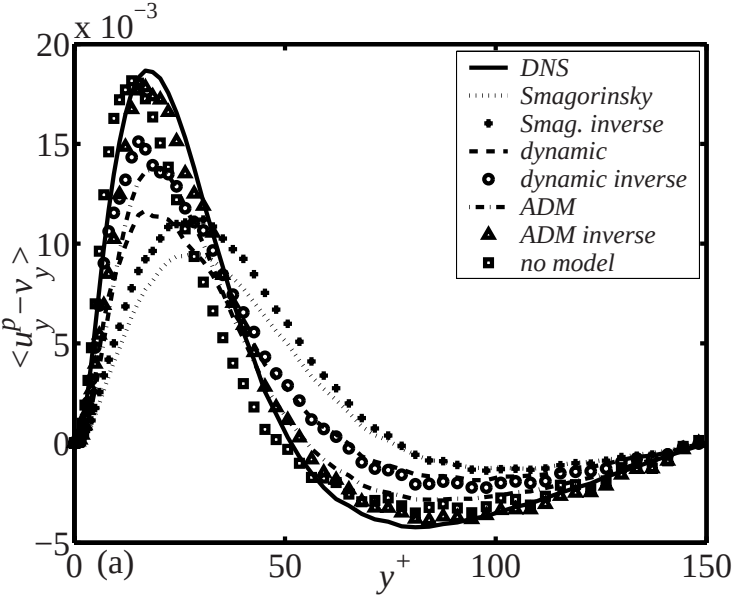

Fig. 1 Mean relative velocity at $St = 1$

the maximum in the relative velocity. Moreover, it can be seen that ADM agrees best with the DNS and that Smagorinsky is the least accurate subgrid model with not only a reduced maximum but also a peak shifted towards larger distances from the wall. This observation is related to the capability of the subgrid model to predict the wall-normal fluid velocity fluctuations. A second observation is that defiltering improves the LES results. This results in only small differences between DNS and defiltered ADM results. A final observation is that the results without subgrid modeling are almost as accurate as the best results with subgrid model (ADM with defiltering). For the largest Stokes number considered the differences between the LES results and the DNS is smaller and so is the effect of defiltering.

3.2 Particle Concentration

The non-zero mean wall-normal particle velocity leads to accumulation of particles near the walls of the channel. In Fig. 2 the concentration of particles close to the walls is plotted as a function of time for the DNS calculations at the three Stokes numbers. To this end the computational domain is divided in 40 equidistant strips parallel to the walls and the number of particles in the strips closest to both walls is counted. The particle concentration is normalized in such a way that for a uniform distribution $c = 1$.

The effect of turbophoresis is clearly visible. The concentration close to the walls increases as a function of time, first fast, and later, due to the non-uniformity of particle distribution, more slowly until a statistically stationary particle concentration is reached. The particle concentration close to the walls increases with increasing Stokes number in the regime investigated.

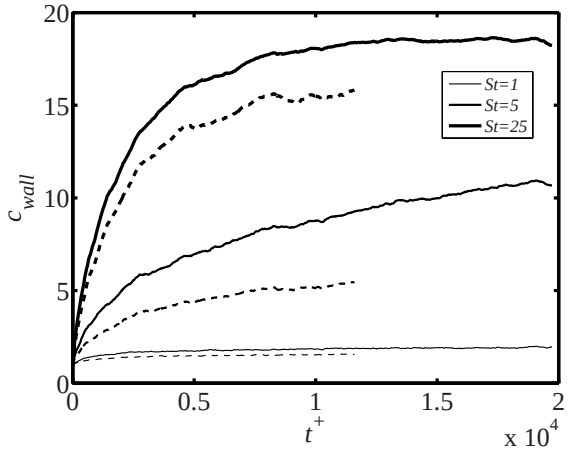

Fig. 2 Concentration of particles close to the wall as a function of time; *solid*: DNS; *dashed*: *a priori*

The stationary particle concentration is reached at $t^+ \approx 16,000$ for $St = 1$ and $St = 25$ and has not been fully reached for the middle Stokes number at $t^+ = 20,000$.

Also included in Fig. 2 are the *a priori* results until $t^+ \approx 12,000$. The particle concentration close to the walls is reduced when the fluid velocity in (8) is filtered. The effect is largest at the middle Stokes number, $St = 5$, for which the particle relaxation time is equal to the Kolmogorov time. For these particles the effect of the turbulence on their motion is largest.

In Fig. 3 the wall concentration is plotted as a function of time for all simulations and $St = 1$. As for the mean relative velocity, it can be observed that the results of the three subgrid models without defiltering underpredict the particle accumulation and again the Smagorinksy model is the least accurate and ADM the most accurate. ADM and the dynamic model correspond quite well with the *a priori* result, which indicates that the main source of error in these results is the disregard of the subgrid effects in the particle equation of motion. For ADM and the dynamic model the results with defiltering show a significant improvement. On the other hand, defiltering hardly improves the Smagorinsky results. Marchioli and Soldati [19] explained turbophoresis by the presence of secondary streamwise vortices close to the walls, which prevent particles from being entrained into the outer flow. The absence of these vortices in the Smagorinsky simulations, in contrast to the other two models, explains the strong reduction in turbophoresis and the negligible effect of defiltering.

Finally, we note that the results without subgrid model are as accurate as the results of the defiltered ADM and dynamic model and also agree quite well with the DNS results. Again, this follows from the fact that this coarse grid DNS yields almost the same wall-normal velocity fluctuations as the unfiltered DNS. Similar results are obtained at the other two Stokes numbers.

3.3 Particle Velocity Fluctuations

As a final quantity the root-mean-square of the particle velocity fluctuations is studied. In Fig. 4 the streamwise particle velocity fluctuations have been plotted for $St = 1$, averaged over time from $t^+ = 1,000$ to $t^+ = 16,000$ and over the homogeneous directions. All simulation results are included. At this low Stokes number the particle velocity fluctuations are almost equal to the fluid velocity fluctuations. Since the two eddy-viscosity models overpredict the streamwise fluid velocity fluctuations, it is not surprising that the particle velocity fluctuations are also overpredicted by these models. Defiltering only deteriorates this result. On the other hand, the defiltered ADM results agree quite well with the DNS results. Finally, the results without subgrid model are too low. In contrast with mean particle velocity, and hence particle concentration, this coarse grid DNS does not predict higher moments of fluid velocity, and hence particle velocity, accurately.

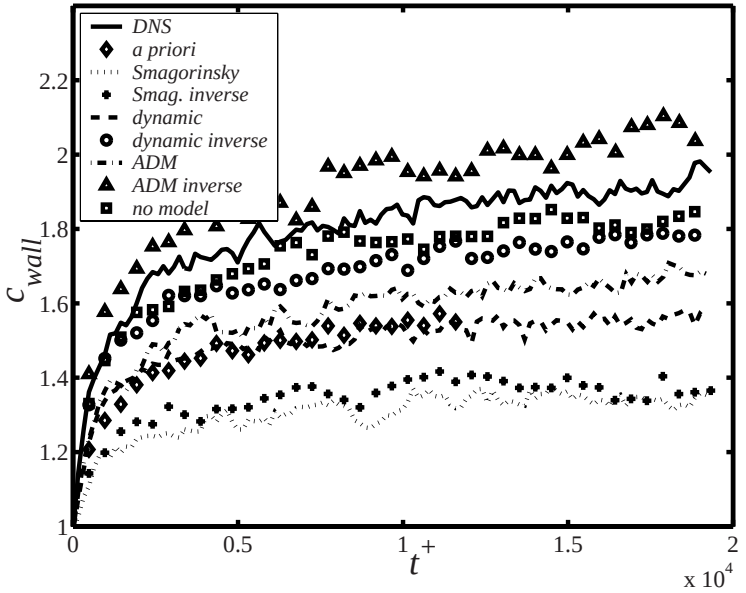

Fig. 3 Concentration of particles close to the wall as a function of time for $St = 1$

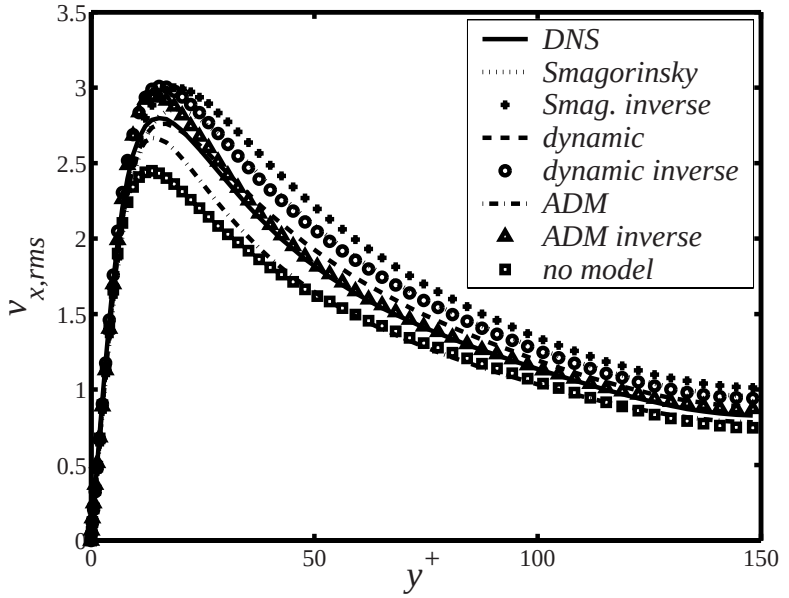

Fig. 4 Streamwise particle velocity fluctuations at $St = 1$

Similar results are obtained for the streamwise particle velocity fluctuations at the other Stokes numbers. In all cases, the defiltered ADM results slightly overpredict the peak value, but agree best with the DNS results. The peak value of the streamwise particle velocity fluctuations increases from $St = 1$ to $St = 5$ and slightly to $St = 25$, whereas the velocity fluctuations mildly decrease with increasing Stokes number near the center of the channel.

The dynamic eddy-viscosity model and ADM yield smaller wall-normal and spanwise particle velocity fluctuations than the DNS, but defiltering improves the results. The defiltered ADM results show the best agreement with DNS. Especially at $St = 5$ and $St = 25$ the difference between defiltered ADM and DNS is small.

4 Conclusions

In this paper LES of particle-laden turbulent channel flow is studied for several subgrid models and at three different Stokes numbers. In order to model the subgrid effects in the particle equation of motion the fluid velocity is deconvolved with the use of an approximate inverse of the filter.

Of the three subgrid models investigated Smagorinsky's model does not yield accurate results, both for particle concentration and particle velocity fluctuations. This model agrees less with DNS results than when no subgrid model is used. Moreover, defiltering hardly or not improves the results. The explanation for this finding is that Smagorinsky's model does not predict the structures in the fluid flow that are important for particle motion in the regime of Stokes numbers studied.

The dynamic subgrid model performs better. Predicted particle concentrations are closer to the DNS results than with Smagorinsky's model, especially if the fluid velocity is defiltered and particle velocity fluctuations are close to the DNS results. The best results, however, are obtained with the approximate deconvolution model ADM. All quantities studied agree quite well with DNS results if the fluid velocity is defiltered. From a theoretical point of view this model has the advantageous property that the same defiltering operation is used in the subgrid model for the fluid and in the subgrid model for the particles. Apparently, this also results in better agreement with DNS.

The results shown in this paper clearly indicate that the proposed subgrid model in the particle equation of motion yields a substantial improvement provided that an adequate LES model is applied. An advantage of this subgrid model is that it is very easy to implement, both in spectral methods and in finite volume methods. The additional required computing time is negligible compared to the time needed for the velocity interpolation. Moreover, the same subgrid model can be applied in case two-way or four-way coupling is applied and if other forces between fluid and particles, such as lift force, added mass and pressure drag, are taken into account. For the latter two

forces also the fluid acceleration should be defiltered and for the lift force the fluid vorticity, but that can be done in exactly the same way.

Defiltering only models the effects of the resolved scales, in sofar they are affected by the filtering operator. Subgrid scales, which are not represented on the LES grid, cannot be retrieved by deconvolution. This paper shows that in general the subgrid scales hardly affect statistical properties of particle motion, such as mean particle concentration and mean and root-mean-square of particle velocity. This can be explained by the fact that the typical time scales of the subgrid scales are small compared to the particle relaxation time in the regime investigated. At smaller Stokes numbers the small scales of turbulence become more important, but then particles follow the flow more closely, so that a phenomenon as turbophoresis is almost absent.

References

1. Maxey MR, Riley JJ (1983) Phys Fluids 26:883–889
2. Uijttewaal WJS, Oliemans RVA (1996) Phys Fluids 8:2590–2604
3. Armenio V, Piomelli U, Fiorotto V (1999) Phys Fluids 11:3030–3042
4. Kuerten JGM, Vreman AW (2005) Phys Fluids 17, Art no 011701
5. Kuerten JGM, Geurts BJ, Vreman AW, Germano M (1999) Phys Fluids 11:3778–3785
6. Germano M, Piomelli U, Moin P, Cabot WH (1991) Phys Fluids A 3:1760–1765
7. Smagorinsky J (1963) Mon Wea Rev 91:99–164
8. Stolz S, Adams NA, Kleiser L (2001) Phys Fluids 13:997–1015
9. Canuto C, Hussaini MY, Quarteroni A, Zang TA (1988) Spectral methods in fluid dynamics. Springer, Berlin
10. Kleiser L, Schumann U (1980) Treatment of incompressibility and boundary conditions. 3-D numerical spectral simulations of plane channel flows. In Hirschel EH (ed) Proceeding of the third GAMM-conference on numerical methods in fluid mechanics. Vieweg, Braunschweig
11. Lilly DK (1992) Phys Fluids A 4:633–635
12. Piomelli U, Balaras E (2002) Ann Rev Fluid Mech 34:349–374
13. Armenio V, Fiorotto V (2001) Phys Fluids 13:2437–2440
14. Clift R, Grace JR, Weber ME (1978) Bubbles, drops and particles. Academic Press Inc, Boston
15. Balachander S, Maxey MR (1989) J Comput Phys 83:96–125
16. Geurts BJ (1997) Phys Fluids 9:3585–3887
17. Shotorban B, Mashayek F (2005) Phys Fluids 17, Art no 081701
18. Liu BYH, Agarwal JK (1974) J Aerosol Sci 5:145–1148
19. Marchioli C, Soldati A (2002) J Fluid Mech 468:283–315
20. Marchioli C, Giusti A, Salvetti MV, Soldati A (2003) Int J Multiphase Flow 29:1017–1038
21. Reeks MW (1983) J Aerosol Sci 14:729–739
22. Young J, Leeming A (1997) J Fluid Mech 340:129–159